Department of Chemistry
University College London
University of London

Intermediate-range order in molten network-forming systems

Bevan Kieran Sharma

I, Bevan Kieran Sharma, confirm that the work presented in this thesis is my own. Where information has been derived from other sources, I confirm that this has been indicated in the thesis.

22/11/09

Acknowledgements

Firstly, I would like to thank my supervisor, Dr. Mark Wilson, for his guidance, encouragement, inspiration and assistance throughout my PhD, from encouraging me to embark on this project to providing sound advice during thesis-writing, with considerable help in-between.

Many thanks to my friendly and congenial colleagues of the Wilson Group at UCL: Dr Mark Wilson, Dr. Clare Bishop, Numaan Ahmed and Dr. Dominc Daisenberger, which, like the components in Trigger's broom in Only Fools and Horses, has since changed its composition in both members and location.

Thanks to people of room 105 for providing such a warm environment to work in over the years including Keith, Fedor, Davy, Miguel, Sheena, Hitesh, Martina, Kristine, Tanya, Jorge and Demetrios.

Thanks to other members of UCL Chemistry especially Dr. Dewi Lewis, Dr. Andrea Sella, Professor Fred Pearce and Professor Anthony Deeming and Dr Carlo Massobrio at CRNS in Strasbourg for a enjoyable and productive absence from Bloomsbury. Many thanks to members of the "Ramsay Lunar Society": Wai-Cheung, Manchi, Tim, soon to be married Paul and Subhadra, Dianne, Nori, Joey, Gavin, Nening and the recently married Hindy.

Thanks to all my secondary school and sixth-form college teachers, in particular Mr. MacCaoilte and Mr. Hook for teaching science at Strode's College.

Thanks to Shamsia Husseini and James Meredith, because going to school shouldn't be that difficult, and to Graham Greene for writing "The Power and The Glory".

This thesis is dedicated to my parents, Urmilla and Brendra Sharma, and sisters, Usha and Uma, for all their love and support all these years.

Intermediate-range order in molten network-forming systems

Bevan Kieran Sharma
University College London.

A thesis submitted in partial fulfillment of the requirements
for the degree of Doctor of Philosophy, November 2009.

Abstract

Molecular Dynamics simulations using the polarisable ion model (PIM), which accounts for many-body ion polarisation in addition to short-range repulsion and simple Coulombic interaction between ions, are undertaken in a study of the structure of molten network-forming liquids. The primary focus is the investigation of the structural origin of intermediate range order (IRO), the ordering of atoms beyond the nearest-neighbour in liquids and glasses often highlighted by the presence of a first sharp diffraction peak (FSDP) in total and partial structure factors. Two primary modelling approaches are applied. In the first, specific systems of MX_2 stoichiometry are targeted ($ZnCl_2$, $MgCl_2$ and $GeSe_2$) allowing for direct comparison with the results from scattering experiments. An ionic description for $GeSe_2$ represents a stern test as this system is often described as having considerable metallic character. In the second approach, key system parameters are systematically varied in order to control the network topology and examine the evolution of IRO. A key structural property, the presence of a FSDP in the concentration-concentration structure factor, $S_{CC}(k_{FSDP})$, is observed and structure factors, "coloured" according to network connectivity, show its presence to be dependent on the percolation of edge-sharing units disturbing the corner-sharing tetrahedral network. The effect on the network topology and IRO of varying both temperature and pressure, properties often difficult to obtain experimentally, are observed. The inherent structure of the systems studied shows the presence of newly resolved features, including a distortion of constituent polyhedra. Homopolar bonds are induced by combining Morse and Born-Mayer potential and their effect on the underlying IRO examined.

Contents

3 Intermediate-range order in metal halides   76

4 A Polarisable Ion Model of GeSe$_2$ 113

5 Chemical ordering in GeSe$_2$ and ZnCl$_2$ 133

6 Network topology of MX$_2$ compounds   153

7 Effect of pressure and temperature on the intermediate-range order of ZnCl$_2$ 190

8 Effect of temperature and pressure in MX$_2$ systems   228

9 The inherent structure of MX_2 systems   254

Chapter10 Homopolarity and the effect on IRO   287

11 Summary and Conclusions 305

List of Figures

List of Tables

Chapter 1

Introduction

1.1 Early models of liquid structure

The early study of liquid properties was dominated by thermodynamical and electrochemical analysis through measurement of quantities such as melting temperatures and ionic conductivities.[1-4] In comparison, the relative weakness in understanding the structure of amorphous substances was highlighted by Zacharisen[5] stating (on the structure of glasses) in 1932: "It must be frankly admitted we know nothing about the arrangement of atoms". A number of experimental techniques have since been developed to probe the structure of liquids; complementing experimental advances has been the use of modelling in understanding existing experimental data and elucidating details which are beyond experimental scope. Initial theories concerning the structure of liquids, based on the loss of order that results from fluidity and diffusion of atoms took a quasi-gaseous approach: in 1873, Van der Waals constructed an equation of state for liquids and gases.[6] Its applicability to gases is stronger and is limited to liquids such as n-alkanes.[7] The opposite approach of treating liquids as quasi-crystalline[4], due to liquid's solid-like properties of compactness and cohesion, has wider applicability to this day. This was supported by analysis of early X-ray diffraction experiments of liquids by Zernike and Prins[8] which pointed to the similarity between the peak positions in the crystal and liquid structure factors. The existence of positional defects in solids[4] has also been applied to the understanding of the melt structure: domain models[4] envisage the structure of liquids featuring remnants of crystal structures, which, although considered thermodynamically unstable in the crystalline state, are stabilised with increasing temperature into the liquid phase. One model which combines these different approaches is the significant structure model proposed by Eyring.[9] Liquids are split into sections where molecules have solid-like degrees of freedom and another which have gas-like degrees of freedom. Another approach was the geometric analysis of hard-sphere liquids by Bernal[10] where liquids are defined as "homogenous, coherent and essentially irregular assembly of molecules containing no crystalline regions, nor in their low temperature form, holes large enough to accept another molecule". From these studies it was noted that a significant property of

liquids, exhibited in contrast to solids and gases, was the variety of coordination displayed by the constituent atoms. In network melts[4,11], the focus of this thesis, charge ordering has a dominating effect on structure with packing of anions around cations and vice-versa. Within these systems lies a variety of bonding and structure, controlled through variation of the anion polarisability, α_X, which will be explored through computational study.

1.2 Network forming liquids

Network melts, in general, have high melting temperatures and ionic conductivities of the order of 1 Ω^{-1} cm^{-1} [3] As well as established uses in electronic storage[11], molten salts have potential uses in the nuclear fuel industry[11], in areas such as the process of separating actinide material for recycling. SiO_2 [12], archetypal glass-formers, are termed strong liquids for their near Arrhenius behaviour with regards to viscosity changes against T_g/T, where T_g is the glass transition temperature. Compounds which deviate away from this behaviour, such as heavy metal halides are termed fragile. A numerical relation of glass-forming strength is given by calculation of the fragility index given by:

$$m = \left(\frac{d \left(\log \eta \right)}{d \left(T_g / T \right)} \right)$$

where η is the viscosity and T_g is the glass transition temperature. The related values for the $ZnCl_2$[13] and $GeSe_2$[14], where m=30-60, indicating that its behaviour is between that of 'strong' liquids such as SiO_2[15], GeO_2[15] and BeF_2[15], where m=20-28, and 'fragile' heavy metal halides[16] (where m~200), and is therefore considered as displaying intermediate behaviour.[12] Across these compounds there is a sharp difference in the range of melting temperatures. Liquids such as SiO_2 (1996K) and GeO_2 (1389K), which consist of a strong three dimensional network, have relatively high melting points compared to $ZnCl_2$ (591K). $ZnCl_2$ is used industrially as a catalyst in the hydrocracking of coal slurries and activation of charcoal from coconut shell.[17,18] $GeSe_2$ also has a wide variety of uses including optical recording[19], photoresistors[20] and antireflection[21] coatings.

1.3 Intermediate range order: Origin in experimental studies.

The information obtained from a number of experimental probes into the liquid structure of systems concerned is outlined below:

1.3.1 Extended X-RAY Absorption Fine Spectroscopy(EXAFS): EXAFS gives information about the first coordination shell of a liquid through studying the effect of backscattering on the absorption coefficient, $\mu(k)$. From the oscillations in the absorption coefficient, $\mu(k)$, ~30 e.V past the absorption edge, information concerning the local coordination shell of atoms[22] is obtained through equation 1.1 where EXAFS scattering χ is measured as a function of the wavenumber of the photonelectron, k:

$$\chi(k) = \sum_i \frac{N_i f_i(k)}{k \cdot r_i^2} \cdot e^{-2k^2\sigma_i^2} e^{-2r_i/\lambda} \sin(2kr_i + \alpha_i(k)) \tag{1.1}$$

N_i is the coordination number, r_i is the interatomic distance, σ_i is the Debye-Waller term related to the fluctuations in bond length, $f_i(k)$ is the backscattering amplitude, α_i is the phase function and λ is the mean-free path of the photoelectron. From EXAFS experiments, for example, information about bond lengths in $ZnCl_2$ and their variation with pressure has been obtained.[23,24]

1.3.2 Mössbauer Spectroscopy: The Mössbauer effect is the recoilless emissions of a gamma ray by a neutron and resonance with an absorbing nucleus.[25] The effect is stabilised in the condensed state and gives information on the coordination environment of the atom. Due to limiting factors such as the lifetime and the linewidth of the excited nuclear state, such phenomena are limited to certain isotopes of particular elements i.e for the study of $GeSe_2$, the cation sites have to be doped with ^{119}Sn[24] whilst anion sites are doped with ^{128}Te.[25] The cations sites highlighted are corner-sharing tetrahedra and ethane-like Ge_2Se_6 units[26] while the anion sites highlighted are as bridging $GeSe_4$ tetrahedra[27] or part of a Se-Se homopolar bond and with another connection to a $GeSe_4$ tetrahedra.[26] Further information is inferred from ratios of the intensities of different sites: the presence of Se-rich clusters of 60-70Å in length are predicted from Mössbauer spectroscopy on $GeSe_2$ glass, supporting a domain model interpretation of the structure.[27]

1.3.3 Raman Spectroscopy: Raman spectroscopy highlights vibrational modes of compounds which effect changes in molecular polarisability.[28] A low frequency vibration, referred to as the *boson peak*[28,29,30], is found in the spectra of compounds displaying IRO such as $ZnCl_2$.[28] Bands associated with the corner- and edge-sharing tetrahedra are present and changes can be observed with increasing temperature, such as the increase in the presence of corner-sharing modes in $ZnCl_2$.[28]

The experimental methods highlighted above generate information concerning the short-range scale: i.e information concerning the geometry and coordination of the first coordination shell. As such, order in liquids is recognised over a length scale of a few atoms i.e short-range order (SRO). The existence of ordering on longer length scales was discovered in neutron diffraction work pioneered by Enderby and co-workers[31,32].

1.3.4 X-Ray and neutron diffraction:

Neutron and X-Ray diffraction experiments[32-35] entail the observation of the properties of compounds through the scattering characteristics of the nucleus and electrons respectively. The former method requires a source of neutrons which are either nuclear reactors, where neutrons are produced by nuclear fission, or spallation sources. The resulting neutron beam then has to be attuned by several processes; the first is moderation, where the neutrons are slowed down by hydrogenous materials. The neutron beams, which initially emerge from the moderator in all directions are then collimated by a series of apertures. The beam is then monochromatised through Bragg reflection by a single crystal. Diffraction experiments are carried out at range of temperature and pressures and recent improvements in technology have extended the real space resolutions for determining correlations up to 60Å.[30] The differential scattering-cross section $\left(\frac{d\sigma}{d\Omega}\right)$ gives the fraction of neutrons scattered into $d\Omega$ in the direction (θ,φ).

$$\left(\frac{d\sigma}{d\Omega}\right)_{tot} = \left(\frac{d\sigma}{d\Omega}\right)_{incoh} + \left(\frac{d\sigma}{d\Omega}\right)^{self}_{coh} + \left(\frac{d\sigma}{d\Omega}\right)^{dist}_{coh} \qquad (1.2)$$

The total scattering cross-section (equation 1.2) in multicomponent systems is comprised of the incoherent scattering contribution, $\left(\frac{d\sigma}{d\Omega}\right)_{incoh}$, which arises from random distributions of scattering lengths and spins, $\left(\frac{d\sigma}{d\Omega}\right)_{coh}$, which describes scattering of atoms with the same spin and isotope and coherent scattering with a further division into

the self term, $\left(\dfrac{d\sigma}{d\Omega}\right)^{self}_{coh}$, and the distinct term, $\left(\dfrac{d\sigma}{d\Omega}\right)^{dist}_{coh}$ which describes scattering from single atoms and between distinct atoms respectively.

There are a number of formalisms by which the total structure factor can be deconvoluted. In our calculations, we shall, unless stated otherwise, use the Ashcroft-Langreth formalism[36] which is described using terms with the square-root of the species concentration.

$$\frac{1}{N}\frac{d\sigma}{d\Omega} = \sum_{i=1}^{n} c_\alpha (\overline{b_\alpha^2} - \overline{b}_\alpha^2) + \sum_{\alpha,\beta=1}^{n} (c_\alpha c_\beta)^{1/2} \overline{b}_\alpha \overline{b}_\beta S_{\alpha\beta}^{AL}(Q) \tag{1.3}$$

The quantities obtained from the scattering intensity for such experiments are total structure factors, which may be expressed in terms of the partial structure factors,

$$F(k) = c_\alpha b_\alpha^2 (S_{\alpha\alpha}(k) - 1) + c_\beta b_\beta^2 (S_{\beta\beta}(k) - 1) + 2(c_\alpha c_\beta)^{1/2} b_\alpha b_\beta (S_{\alpha\beta}(k))$$

$$\tag{1.4}$$

where b_α is the coherent scattering length which describes the scattering properties of the ion a, c_α is the concentration of a given ion and $S_{\alpha\beta}$ are the partial structure factors for a ion pair. Note that, if we consider a typical MX_2 system, the experimentally available information on the cation-cation term can be limited both by the concentration weighting of $c_M c_M$ in equation 1.4 as well as by the possibility of low scattering power. In X-Ray diffraction experiments the scattering coefficient b is replaced by the k-dependent form factor f.

$$f\left(\frac{\sin(\theta)}{\lambda}\right) = \sum_{i=1}^{4} a_i \exp\left[-b_i\left(\frac{\sin(\theta)}{\lambda}\right)^2\right] + c \tag{1.5}$$

where coefficients a_i and b_i are dependent on the electron properties of each ion. The Faber-Ziman[35] structure factors are related to the Ashcroft-Langreth structure factors by the following relationship:

$$S_{\alpha\beta}^{FZ}(k) = 1 + \frac{S_{\alpha\beta}(k) - \delta_{\alpha\beta}}{(c_\alpha c_\beta)^{1/2}} \tag{1.6}$$

Neutron diffraction experiments performed on a range of molten halides show large variations in the experimental total structure factor depending upon the system. The partial structure factors were isolated by using the method of *isotopic substitution*[37,38]: in NaCl and $ZnCl_2$, for example, the stability and significant difference in scattering properties of ^{37}Cl, ^{35}Cl and ^{nat}Cl, where the scattering length is proportional to the natural isotopic mix of ^{37}Cl and ^{35}Cl. By performing separate experiments at the same state point of temperature and pressure, but where the isotopic contribution differ, the respective weightings of the three terms in equation 1.4 can be varied and, as a result, three partial structure factors ($S_{NaNa}(k)$, $S_{NaCl}(k)$ and $S_{ClCl}(k)$ and $S_{ZnZn}(k)$, $S_{ZnCl}(k)$ and $S_{ClCl}(k)$ for NaCl and $ZnCl_2$ respectively) can be extracted.[37,38]
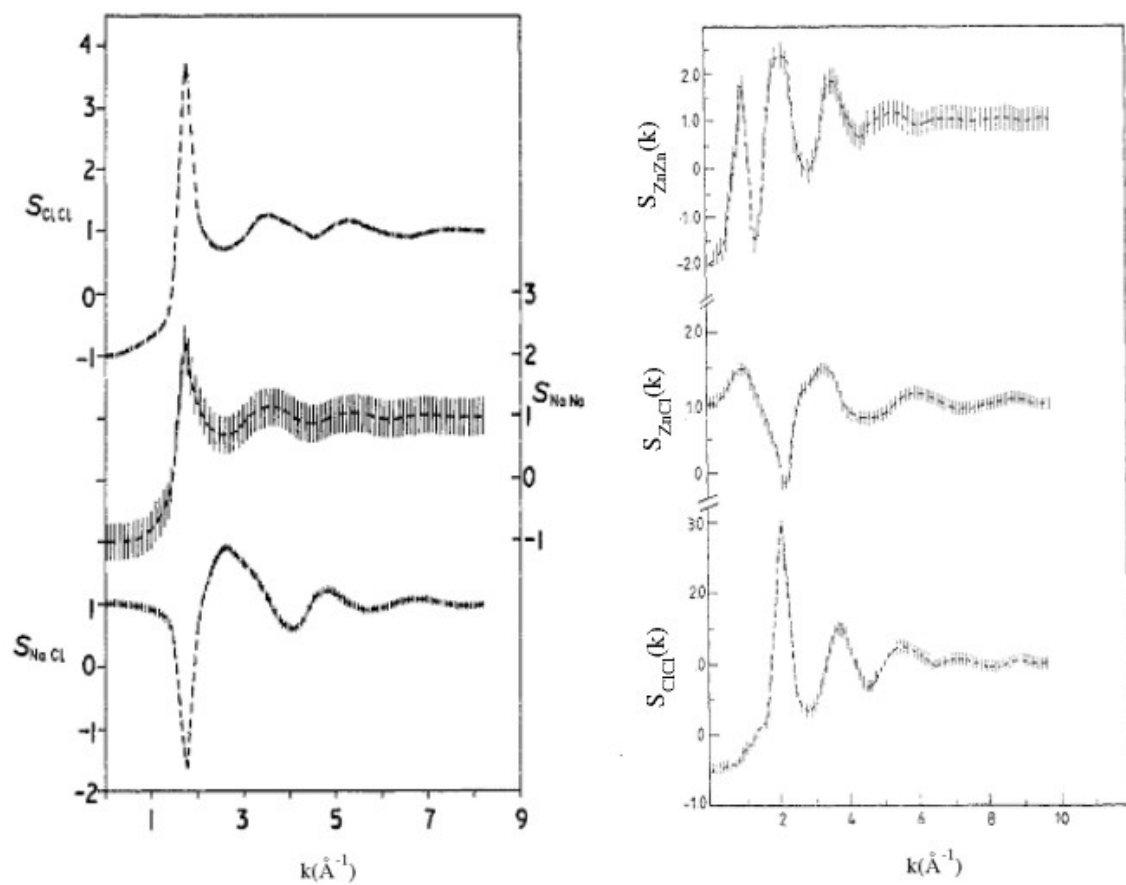
Figure 1.1: Experimental partial structure factors for NaCl (left) and $ZnCl_2$ (right) from experiments by Edwards *et al*[38] and Biggin and Enderby[37]. A First Sharp Diffraction peak is observed in $S_{ZnZn}(k)$ and $S_{ZnCl}(k)$.

For example, figure 1.1 shows the partial structure factors for $ZnCl_2$[37] and NaCl[38]. The long-range ordering of the atoms in typical crystalline environments is not present, as indicated by the increased width of peaks compared to the sharp Bragg peaks observed for crystals. The partial structure factors for NaCl show all three principal peaks are in a similar position, with the cation-anion function, $S_{NaCl}(k)$, showing a valley in contrast to

the peaks of $S_{NaNa}(k)$ and $S_{ClCl}(k)$.[38] In $ZnCl_2$, the cation-cation function, $S_{ZnZn}(k)$, shows significantly different behaviour from $S_{ClCl}(k)$ with a significant peak at k~1Å^{-1}. This results in a peak at 1Å^{-1} in F(k) known as the *First Sharp Diffraction Peak* (FSDP).[37] The presence of such a peak in F(k) is taken to be a signature of *intermediate range order* (IRO), that is ordering of atoms beyond the nearest neighbour. The position of the FSDP, k_{FSDP}, is associated with a real space periodic distance of $d \approx 2\pi/k_{FSDP}$ and width is related to a correlation length of $2\pi/\Delta k_{FSDP}$. Computational analysis can provide an effective complement to experimental data here in two respects. Firstly, as diffraction experiments are often performed at a single state point, calculations can provide information as to the effect of changes in temperature and pressure. Secondly, in those experiments where the temperature and pressure are varied, it is solely the changes in the total structure factor, F(k), which are extracted: computational analysis can be used to provide information on changes at the partial structure level. Between diffraction experiments there are disagreements about the role of particular contributions. In $ZnCl_2$, the dominance of the $S_{ZnZn}(k)$ contribution, emphasised by Enderby[37] and Salmon in a later neutron diffraction experiment[39], is contradicted by a recent High Energy X-Ray diffraction experiment by Neuefeind which states that $S_{ZnCl}(k)$ is the dominant contributor.[40]

Table 1.1 shows that the position and intensity of the FSDP varies from one compound to another and that there are number of classes of compounds which display a FSDP. The position of the FSDP in MX_2 sytems varies from 1.63Å^{-1} in BeF_2[41] to 0.99Å^{-1} in $GeSe_2$[42]. IRO is present for a number of different stoichiometries for systems MX_n where n=2-4. However, the absence of a FSDP in systems with a MX stoichiometry[38,43,44], irrespective of cation size, suggests that IRO is related to directional bonding.[45] A FSDP is observed in systems with a range of bonding from ionic systems such as $ZnCl_2$ to molecular systems[46,47] such CCl_4. In the case of CCl_4, the total structure factor, F(k), is deconvoluted into an intramolecular form factor, $f_m(k)$, and $D_m(k)$, the intermolecular form factor, describing the interaction between the tetrahedral units[47]:

$$F(k) = f_m(k) + D_m(k)$$
(1.7)

The appearance of a FSDP across a wide range of compounds, as highlighted in table 1.1, has elicited a number of general formulae (equations 1.8-1.11) which aim to give a prediction of the position of the FSDP according to quantities such as bond lengths.

Wright *et al*[48] highlighted the similarity in position of the FSDP, k_{FSDP}, in several glasses (SiO_2, $GeSe_2$, B_2O_3, and As_2S_3) if scaled according to cation-anion bond distance, r_{MX}, by calculating the product, $k_{FSDP}r_{MX}$. (equation 1.8). A notable deviation from this relationship occurs for As_2Se_3 where the product, $k_{FSDP}r_{MX}$, is 3.10. Using a wider set, Moss and Price[41] introduce different ranges for glasses and amorphous metals respectively (equations 1.9 and 1.10 respectively). A relationship proposed between the position of the FSDP and void diameter (where the void is defined as the separation between the cation centres, r_{MM}) by Bletry[49] is shown in equation 1.12. At present, there is no analogous formula which attempts to predict the *intensity* of the FSDP.

$$k_{FSDP}r_{MX} \approx 2.5 \tag{1.8}$$

$$k_{FSDP}r_{MX} \approx 2.14\text{-}3.10 \tag{1.9}$$

$$k_{FSDP}r_{MX} \approx 4.3\text{-}5.3 \tag{1.10}$$

$$k_{FSDP} = 3\pi/2d \quad \text{where } d = r_{MM} \tag{1.11}$$

	System	$k_{FSDP}(\text{Å}^{-1})$	$r_{MX}(\text{Å})$	$k_{FSDP}r_{MX}$
Oxide and Halide Glasses	BeF_2	1.63	1.54	2.51
	SiO_2	1.55	1.61	2.50
	$ZnCl_2$	1.09	2.29	2.49
Chalcogenide glasses	$P_{40}Se_{60}$	1.16	2.29	2.66
	$GeSe_2$	1.01	2.37	2.39
	As_2Se_3	1.27	2.44	3.10
Elemental semiconducting glasses	Se	1.88	2.37	4.56
	As	1.03	2.49	2.56
	Ge	1.89	2.46	4.43
Metallic glasses	$Co_{80}P_{20}$	2.30	2.34	5.38
	$Ni_{35}Zr_{65}$	1.62	2.66	4.30
	$Ni_{40}Ti_{60}$	1.90	2.60	4.94
Equi-atomic liquid alloys	NaPb**	1.25	3.19	3.99
	KPb***	0.96	3.12	3.00
	RbPb**	0.93	3.10	2.88

Table 1.1: The positions of the FSDP across several groups of compounds. All data unless stated from Moss and Price[41] **, Saboungi *et al*[50] ***, Saboungi *et al* [51].

1.4 Dynamical Properties associated with IRO and the FSDP

The presence of IRO has a number of effects on dynamical properties. A low-frequency feature which appears in Raman spectra is termed the *boson peak*[28,29,30]. The frequency of the boson peak has been linked[30,31] with the correlation length, R, obtained from the width of the FSDP, Δq, by $R = 4\pi/\Delta q$:

$$\omega_m \sim 0.9\, v_t/c\; R = 0.9\, v_t\, \Delta k_{FSDP}/4\pi c \qquad\qquad (1.12)$$

A similar relationship was put forward by Sugai[30]:

$$k_{FSDP}\, r_1 = \omega_m c/v \qquad\qquad (1.13)$$

where ω_m is the boson peak energy, v_t is the sound velocity and c is the speed of light. A significant criticism of this relation is that correlation length is not related to the position of the experimental FSDP where the scattering length, depending on the diffraction technique used, may affect the FSDP position differently[52]: in $(AgI)_{0.75}(Ag_2MoO_4)_{0.25}$, the scattering lengths affect the FSDP so that in neutron diffraction patterns, the position is at 0.65Å^{-1} and for X-Ray the position is larger at 0.95Å^{-1}.[53] Other dynamical effects exhibited by systems such as $GeSe_2$ include a companion mode observed in Raman spectroscopy.[54] A companion mode, A_C^1, observed close to the A_1 vibrations for tetrahedral units, is also a feature of compounds displaying IRO and has been attributed either to the presence of Se-Se homopolar bonds[54] or the vibrations of anions across each other in edge-sharing chains.[55]

Although there is no direct correlation between the presence and intensity of FSDP and glass-forming ability[56], computational studies have shown that the ion dynamics on the intermediate length scale may slow down more dramatically than those associated with the nearest-neighbour length scale.[57] Long time scale dynamics have shown that it is this length scale which dominates the relaxation phenomena around the glass transition temperature.[57]

1.5 Concentration fluctuations in MX$_2$ systems

The total structure factor, F(k), can be deconvoluted in more than one manner. In the

Bhatia-Thornton formalism,[58] for example, fluctuations in the number density, Δv, and

concentration density , Δc , are considered, utilising the weak scattering approximation

and the Van-Hove correlation function[59]. The weak scattering equation approximation is:

$$\Gamma(k,\omega)=\left(\frac{1}{2\pi N}\right)\int e^{-i\omega t}dt\langle A^{*}(k,0)A(k,t)\rangle, \qquad (1.14)$$

where

$$A(k,t)=\sum_{i}W_{i}(k)e^{ik\cdot R_{j}(t)} \qquad (1.15)$$

A*(k, 0) is the conjugate of the operator A(k, 0), N is the total number of atoms, R$_j$(t) the

position operator of the atom j at time t, and <....> denotes ensemble average in the

equilibrium state of the alloy.

W, is the pseudopotential matrix element is given by,

$$W_{j}(k)=\int e^{ik\cdot(r-R_{j})}V_{j}(r-R_{j})d^{3}r \qquad (1.16)$$

if $V_{j}(r-R_{j})$, is the effective potential of ion j in the alloy.

$$\Gamma(k,\omega)=|W(k)|^{2}S(k,\omega) \qquad (1.17)$$

where $S(k,\omega)$ is the dynamical structure factor

$$I(k)=\int_{-\infty}^{+\infty}\frac{\beta\omega}{e^{\beta\omega}-1}\Gamma(k,\omega)d\omega, \beta=\frac{\hbar}{k_{B}T} \qquad (1.18)$$

where k$_B$ is the Boltzmann constant and T is the temperature. I(k), related to the

resistivity of the alloy, is the function to be derived in terms of the number-number, concentration-concentration and number-concentrations interactions.

For a two component system, the fluctuations in density are given by:

$$\Delta v_A(r) = v_A(r) - n_A = \sum_k \delta(r - R_k^{(A)}) - n_A \tag{1.19}$$

v_A and n_A are instantaneous and average number densities and where the Fourier component, $\Delta v_A(r)$, is defined by:

$$\Delta v_A(r) = V^{-1} \sum_k v_A(k) e^{(ik \cdot r)} \tag{1.20}$$

then
$$N_A(k) = \int e^{(ik \cdot r)} \Delta v_A(r) \, dr$$
$$= \sum_k e^{(ik \cdot R_k^{(A)})} - n_A \int_v e^{(ik \cdot r)} \, dr \tag{1.21}$$

Similarly
$$N_B(k) = \sum_k e^{(ik \cdot R_k^{(B)})} - n_B \int_v e^{(ik \cdot r)} \, dr \tag{1.22}$$

and
$$N(k) \equiv N_A(k) + N_B(k) = \sum_{j=k,l} e^{(ik \cdot R_j)} - n_0 \int_v e^{(ik \cdot r)} \, dr \tag{1.23}$$
$$= N_1(k, t) + N_2(k, t) \tag{1.24}$$

Local deviations from the mean concentration are given by:

$$\Delta c(r) \equiv (V / \langle N \rangle)(c_B \Delta v_A(r) - c_A \Delta v_B(r)) \tag{1.25}$$

Δc is an expression of the concentration fluctuations within V.

$$\Delta c(r) = \sum_Q \Delta c(k) e^{(-ik \cdot r)} \tag{1.26}$$

and setting C(k) as $\Delta c(k)$, the Fourier transform of $\Delta c(r)$ is

$$C(k) = V^{-1} \int_V \Delta c(r) e^{(-ik \cdot r)} \tag{1.27}$$

$$= (N^{-1})[(1-c)N_1(q,t) - cN_2(q,t)]$$

$$C = \langle N \rangle^{-1}[c_B(N_A - \langle N_A \rangle) - c_A(N_B - \langle N_B \rangle)] \tag{1.28}$$

Utilising 1.22, 1.25 and 1.28, 1.15 can now be written as

$$A(k,t) = W_1 N_1(k,t) + W_2 N_2(k,t) \tag{1.29}$$

or as

$$A(k,t) = \bar{W} N(k,t) + (W_1 - W_2) NC(k,t) \tag{1.30}$$

where

$$W \equiv W_1(q), \, etc, \tag{1.31}$$

and

$$\bar{W} = cW_1 + (1-c)W_2 \tag{1.32}$$

If we replace 1.32 into 1.14 then:

$$\Gamma(k,\omega) = \left(\frac{1}{2\pi N}\right)\int e^{-i\omega t} dt \langle A^*(k,0)A(k,t)\rangle, \tag{1.33}$$

$$\Gamma(k) = (\bar{W})^2 S_{NN}(k,\omega) + (W_1 - W_2)^2 S_{CC}(k,\omega) + 2\bar{W}(W_1 - W_2)S_{NC}(k,\omega)$$
$$\tag{1.34}$$

$$S_{CC}(k,\omega) = \left(\frac{N}{2\pi}\right)\int e^{-i\omega t} dt \langle C^*(k,0)C(k,t)\rangle, \tag{1.35}$$

$$S_{NN}(k,\omega) = \left(\frac{N}{2\pi}\right)\int e^{-i\omega t} dt \langle N^*(k,0)N(k,t)\rangle, \tag{1.36}$$

$$2 S_{NC}(k,\omega) = \left(\frac{1}{2\pi}\right)\int e^{-i\omega t} dt \langle N^*(k,0)C(k,t) + C^*(k,0)N(k,0)\rangle \tag{1.37}$$

If the following equation is introduced (and similar expressions for $S_{NC}(k)$ and $S_{CC}(k)$

$$S_{NN}(k) = \int [\beta\omega(e^{\beta\omega} - 1)]S_{NN}(k,\omega)d\omega \tag{1.38}$$

The expression for I(k) becomes,

$$I(k) = (\bar{W})^2 S_{NN}(k) + (W_1 - W_2)^2 S_{CC}(k) + 2\bar{W}(W_1 - W_2)S_{NC}(k) \tag{1.39}$$

As high temperatures are involved the scattering is elastic and $\beta\omega$ $(= \hbar\omega/k_BT)<<1$ for all ω which for $S_{NN}(k,\omega)$ are far from zero. The factor, $\beta\omega(e^{\beta\omega}-1)^{-1}$, may be replaced by unity. As

$$\int e^{-i\omega t}d\omega = 2\pi\delta(t),\tag{1.40}$$

then using 1.35-1.37 and 1.38, $S_{NN}(k)$, $S_{NC}(k)$ and $S_{CC}(k)$ can be written as

$$S_{NN}(k)=\frac{1}{\langle N\rangle}\langle N(k)^{*}N(k)\rangle\tag{1.41}$$

$$S_{CC}(k)\equiv\langle N\rangle\langle C(k)^{*}C(k)\rangle\tag{1.42}$$

$$S_{NC}(k)\equiv\Re\langle N\rangle\langle N(k)^{*}C(k)\rangle\tag{1.43}$$

The Bhatia-Thornton (BT) partial structure factors [$S_{CC}(k)$, $S_{NN}(k)$, and $S_{NC}(k)$] may be expressed in terms of the Faber-Ziman functions as

$$S_{CC}(k)=c_Mc_X\{1+c_Mc_X[[S_{MM}^{FZ}(k)-S_{MX}^{FZ}(k)]+[S_{XX}^{FZ}(k)-S_{MX}^{FZ}(k)]]\}\tag{1.44}$$

$$S_{NN}(k)=c_M^2S_{MM}^{FZ}(k)+c_X^2S_{XX}^{FZ}(k)+2c_Mc_XS_{MX}^{FZ}(k),\tag{1.45}$$

$$S_{NC}(k)=c_Mc_X\{c_M[S_{MM}^{FZ}(k)-S_{MX}^{FZ}(k)]-c_X[S_{XX}^{FZ}(k)-S_{MX}^{FZ}(k)]\}\tag{1.46}$$

or from the Ashcroft-Langreth structure factors using

$$S_{CC}(k)/(c_Mc_X)=c_XS_{MM}(k)+c_MS_{XX}(k)-2\sqrt{c_Mc_X}S_{MX}(k)\tag{1.47}$$

$$S_{NN}(k)=c_MS_{MM}(k)+c_XS_{XX}(k)+2\sqrt{c_Mc_X}S_{MX}(k)\tag{1.48}$$

$$S_{NC}(k)/(c_Mc_X)=S_{MM}(k)-S_{XX}(k)-(c_Mc_X)^{-1/2}\times(c_M-c_X)S_{MX}(k)\tag{1.49}$$

The number-number structure factor describes the topological structure of the liquid, ignoring the separate identity of the ions; therefore, if $b_M=b_X$, then $S_{NN}(k)$ would be equal to the total structure factor, F(k). In systems which display IRO, the FSDP is intense in

$S_{NN}(k)$, indicative of IRO inherent in the network topology. The number-concentration term, $S_{NC}(k)$, describes the occupation of these sites with reference to ion character while the concentration-concentration term describes the ordering of atoms with each other based on atom identity; if M and X were of equal molar volume and similar shape then $S_{NC}(k)$ would be zero. $S_{CC}(k)$ observes a k-dependence if there is a preference for homopolar or heteropolar bonding. A FSDP in $S_{CC}(k)$ has been observed experimentally in a range of MX_2 systems.[60] In a fully ionic system, $S_{CC}(k)$ is related to the charge-charge structure factor, $S_{ZZ}(k)$:[2]

$$S_{CC}(k) = c_M c_X S_{ZZ}(k) \qquad (1.50)$$

The absence of a FSDP in $S_{ZZ}(k)$ was taken to be a signature feature of MX_2 compounds.[61] Electronic structure calculations show that significant differences between $S_{ZZ}(k)$ and $S_{CC}(k)$, particularly in the region of the FSDP where a FSDP is present only in the latter function. The conclusion was that charge correlations in the region of IRO are absent and coordination defects were responsible.[62] Replication of the FSDP in $S_{CC}(k)$ has proved problematical in computational methods.[63,64]
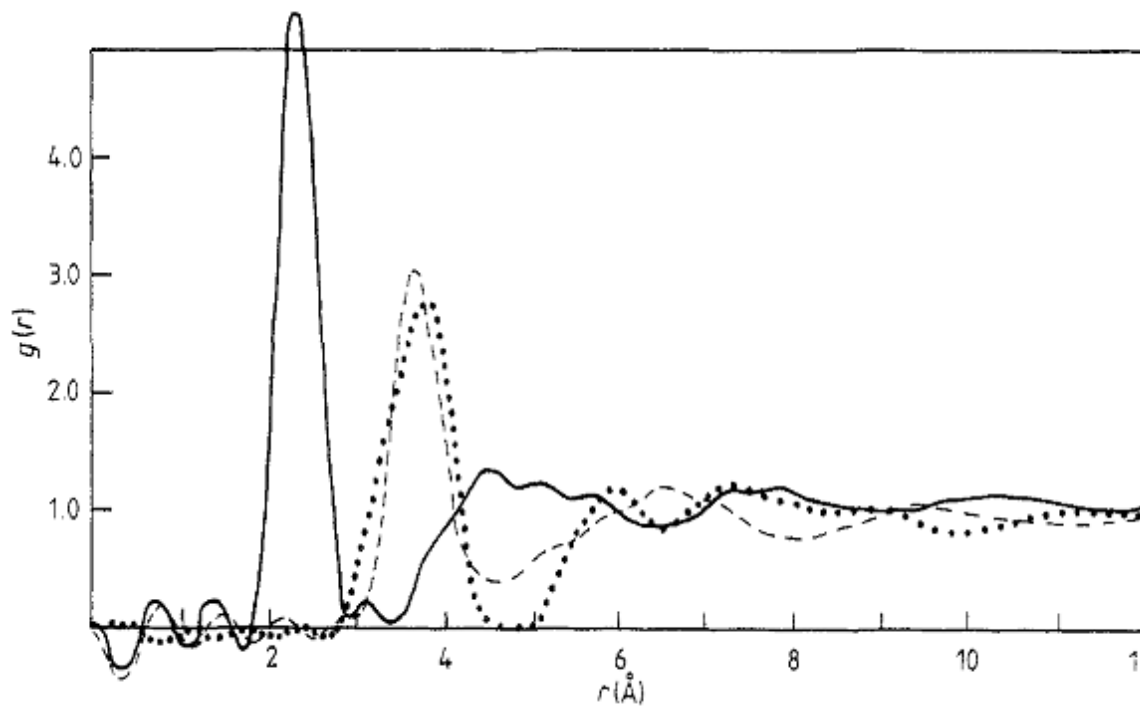
Figure 1.2:The experimental partial radial distribution functions of $ZnCl_2$ by Biggin and Enderby[37]. Full line, $g_{ZnCl}(r)$, half-line, $g_{ZnZn}(r)$; dotted line,$g_{ClCl}(r)$.

1.6 Real space representation of liquid structure.

Zernike and Prins[8] showed that partial radial distribution functions, which describe the correlation of pairs of atoms in real space, can be calculated from diffraction patterns. The partial structure factors obtained from experiments are Fourier transformed to obtain the partial radial distribution function where $g_{\alpha\beta}(r)=\{g_{--}(r), g_{++}(r), g_{+-}(r)\}$ which gives a measure of the probability of finding atom α from β at distance r:

$$g_{\alpha\beta}(r)=1+\frac{1}{2\pi^2 nr}\int_0^\infty \left[S_{\alpha\beta}(k)-1\right]k\sin kr\, dk \qquad (1.51)$$

where n is the total number density of atoms.

The main features of the radial distribution function are highlighted in the experimental functions for $ZnCl_2$ shown in figure 1.2. The major peak occurs close to atomic separations, while at larger r, g(r) damps to a value of 1, indicating the lack of long-range correlations. Inaccuracies in the experimental radial distribution functions are highlighted at very low r where the excluded volume effect sets g(r)≡0. Unphysical oscillations observed at low r are often the result of truncation effects in the Fourier transformation procedure arising from the finite k-range probed in obtaining the structure factors.[12] Early studies noted than upon an increase in the temperature, the principal peak weakened in intensity and displayed an increase in the FWHM corresponding to higher amplitude molecular vibrations as the temperature is increased.[65,66] Furthermore, it was noted that the coordination number derived from the principal peak of the radial distribution function showed a decline from that observed for the respective crystalline states. Whilst such statements are relatively easy to understand in terms of the underlying ionic short-range ordering, analogous arguments focusing on the IRO are more difficult to construct. The oscillations in the ion density responsible for IRO cannot be related simply to radial distribution functions due to low k weighting of the FSDP in the Fourier transform. One association observed is the position r of a peak in real space and the position k of a corresponding peak in Fourier space is kr≈7.7. This identifies the location of the first maximum of the spherical Bessel function, $j_0(kr)$. Salmon showed another relationship by constructing the function, I(r), which is the real space Fourier transform of the H(k), which is the FSDP with the rest of the structure factor excluded.[45] Where the FSDP was strong in intensity, such as in $ZnCl_2$, the oscillations in I(r), dominated the IRO region,

and the similarity between $g_{MM}(r)$ and I(r) is strong. In NiI_2, where the IRO is absent, and $MgCl_2$, where the FSDP intensity is weak, I(r) shows no similarity with $g_{MM}(r)$ over this range.[45]

1.7 Theoretical approach for the origin of IRO.

Wilson and Madden highlighted three mechanisms for the formation of a FSDP[67]; an induction mechanism, a size-ratio mechanism and Coulombic ordering. In the induction mechanism, an anion with a large anion polarisability situated in a site of low symmetry, results in a large dipole being formed which stabilises the relatively close separation of neighbouring cations: the larger the dipole present, the smaller the separation of cations. Similarly, for an anion of a given polarisability, smaller or intermediate-sized cation results in a larger dipole and similar stabilisation or relatively close cation-cation separation. This is shown by the similarity in principal peak position of $g_{MM}(r)$ and $g_{XX}(r)$ in MX_2 systems with small or intermediate sized-cations[37], contributing to an excess of positive charge on the local scale which is offset by a depletion over a longer-length scale. These two length scales are observed as the FSDP and principal peak. A size-ratio mechanism highlights the importance of the tetrahedrally coordinated structures, as highlighted by the larger FSDP observed for $ZnCl_2$ compared to compounds of larger-sized cations such as $BaCl_2$[68]. Iyetomi and Vashishta observed a dependence of the FSDP intensity on the atomic radius ratio using Hypernetted Chain Calculations[69]. The height of the FSDP in the simulated AX_2 glasses decreased with increasing radius ratio, $R=(\sigma_A/\sigma_X)$, where σ_A and σ_X are the respective cation and anion sizes, from 0.25 to 0.5. At higher values, the systems exhibited markedly less tetrahedral behaviour and the FSDP disappeared.[69] However, as later noted by Salmon, the radius ratio for $ZnCl_2$ is 0.41, which displays a stronger FSDP than NiI_2, where it is 0.31. Salmon included the effect of cation mobility in controlling the intensity of the FSDP.[43] Where the cation mobility is high, the clusters comprising a network structure will be short lived (less than the time 5 x 10^{-12} s predicted for IRO to be present), leading to a less intense FSDP as in the case of NiI_2 compared to $ZnCl_2$. Additionally, the separation between tetrahedral centres can be varied by changing the anion, X, in ZnX_2, where X=Cl, Br or I. This results in the function, I(r), with oscillations with increased amplitude which decay more gradually, correlating with the shift in the position of the FSDP to lower k and an increase in the FSDP sharpness.[45] The third mechanism, Coulombic ordering, is highlighted in systems

such as YCl_3 where IRO is present due to the separation of highly charged Y^{3+} cations, with a FSDP present despite the radius ratio of 0.56 for $\sigma_Y/\sigma_{Cl.}$.

There have been a number of *structural* theories put forward concerning the origin of IRO. Cervinka suggested the presence of well-defined clusters as responsible for intermediate-range ordering.[70,71] A quasicrystalline interpretation, similar to those proposed by Zernike and Prins (1927), was implied for systems such as As_2Se_3[72] and $GeSe_2$[73] and generalised over a range of systems by Gaskell and Wallis[74], stating that quasilattice planes (distinct from 2D layers observed in crystals) in the liquid are responsible for the FSDP in the F(k). Similarities between the positions of peaks in crystalline structure factors and those in the melt supports this theory although the appearance of FSDP in SiO_2[75], which has no layer structure in the solid phase, contradicts this.

The presence of layering can be detecting theoretically using a hypothetical scattering experiment.[76] The effect of layering is given by calculating the second moment, $M^{(2)}(k)$, which correspond to discrete wave vectors of the form k_i =2 /L (l_i, m_i, n_i), where L is the cell length and l_i, m_i, and n_i are integers:

$$M^{(2)}(k)=N_k^{-1}\sum_{i=1,N_k}[\langle|(A\boldsymbol{k}_i,t)|^2\rangle-S(k)^2]/S(k)^2 \tag{1.52}$$

where the sum runs over N_k wavevectors with $|\boldsymbol{k}_i|=k$ and:

$$A(\boldsymbol{k}_i,t)=N^{-1}\sum_{p,q=1,N}\exp[i\,\boldsymbol{k}_i\cdot\boldsymbol{r}^{pq}(t)] \tag{1.53}$$

where $M^{(2)}(k)$ =1 for Gaussian statistics. Figure 1.3 (right panel) shows the time evolution of A(**k**,t) for a simulation of $ZnCl_2$[74] for six **k**-vectors with |k|=(2π/L){440}. The continuous "specking" of the intensities along different directions in the simulation cell is indicative of directional structural ordering.
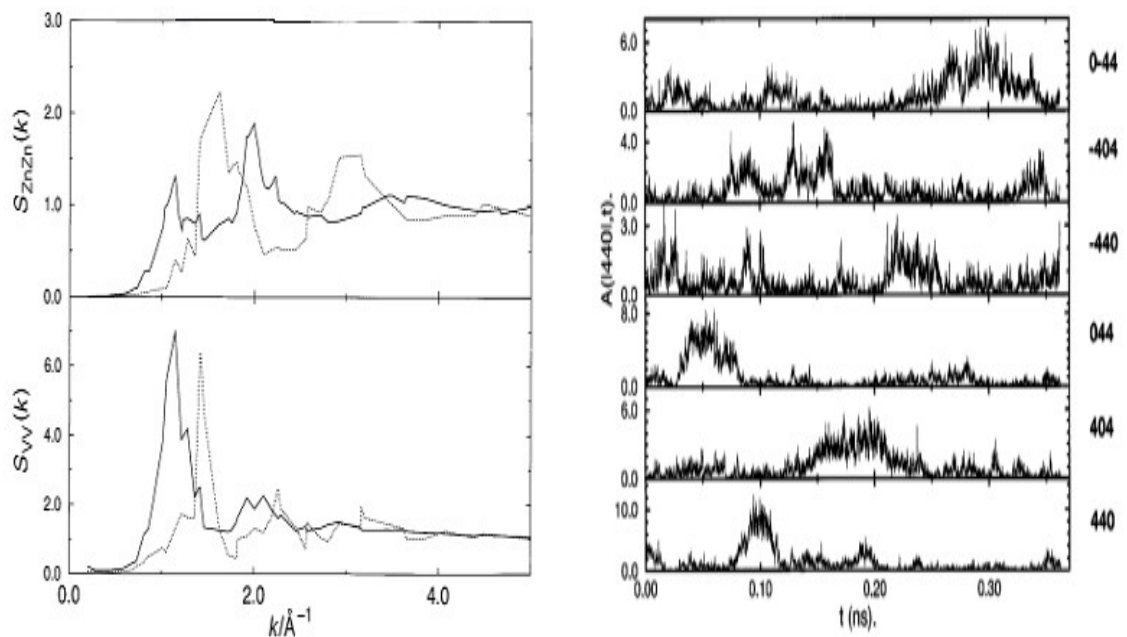
Figure 1.3 Indications of void ordering and layering[76] in $ZnCl_2$. (left) Dotted line, RIM model; solid line, PIM (right) Fluctuations in $A(\boldsymbol{k}_i, t)$ with time for [440] wavectors corresponding to the FSDP indicating presence of layering.

Other evidence supporting the quasi-crystalline interpretation is the effect of positional disorder. In a simulation[77], atoms of a crystalline lattice were displaced at distances greater than would occur at usual thermal temperatures. The peak in the total structure factor, F(k), that showed the most resilience in terms of decline in intensity was the peak with the lowest wavevector.[77] Also, experimental information on ethyl alcohol[78] shows the similarity in position and width of the FSDP in several different phases, from crystalline to rotator-phase crystals: a crystalline state with high amplitude vibrations, and into the liquid state, whilst the peaks at higher k decline in intensity. .

Another approach proposed by Elliot is based on the conception of a liquid stabilising large *voids* in a 3-dimensional network.[79,80,81] The influence of voids in producing a FSDP was demonstrated earlier in 2D models and Dense Random Packing structure with voids progressively incorporated.[49,82] According to the Bhatia-Thornton representation of a system comprised of voids and atoms, the FSDP is solely derived from the FSDP in $S_{CC}(k)$: i.e, the chemical ordering of cation-centred clusters and voids. This relationship was highlighted in theoretical calculations where the structure factors of a hypothetically scattering correlation of voids, $S_{VV}(k)$, was calculated using :

$$S_{VV}(k) = \langle N_V^{-1} \sum_{i,j=1}^{N_V} \exp(i\,\boldsymbol{k}\cdot\boldsymbol{R}^{ij}) \rangle \qquad (1.54)$$

where R^{ij} represents the distance between void centres. This theory is supported by calculations which observe an in-phase relationship, in terms of presence and position of both a principal peak and a FSDP, between $S_{VV}(k)$ and the structure factors describing the cation-cation correlation, $S_{ZnZn}^{PIM}(k)$, as highlighted in figure 1.3. In BeCl$_2$, where edge-sharing is more prominent, a FSDP appears in $S_{VV}(k)$ attributed to inter-chain separation, while the principal peak was absent due to absence of intra-chain void ordering. This was attributed to the absence of voids across the edge-sharing chains present.[82] In contrast to the simulated ZnCl$_2$ PIM model highlighted above, electronic calculations by Massobrio et al[83] have highlighted simulated systems where a FSDP is observed, but with no crystalline ordering, and another system where void-ordering is present without an accompanying FSDP.[83]

1.8 Modification of FSDP position and intensity

In addition to the variation of the position and intensity of the FDSP between compounds there are a number of ways of modifying IRO within a given compound. There are several methods where the stoichiometry is modified:

1. **Templating**: The introduction of an alkylammonium template introduces voids into a ZnCl$_2$ "array" with accompanying length scales, as indicated by the presence of FSDP at values smaller than 1Å^{-1}. The templating mixture consists of CuCl and an ACl templating salt of ZnCl$_2$ (in a 1:1:5 ratio) to form [Cu$_n$Zn$_{m-n}$Cl$_{2n}$]$^{n-}$ templated networks through reaction with the appropiate alkyammonium salt of the templating cation [A]. The templating cation, [A], vary in size from trimethylammonium ([HTMA]$^+$), tetrapropylammonium ([TPMA]$^+$) and methylammonium ([MA]$^+$); these templates correspond to sizes of 10, 4 and 1 anion respectively. The FSDP in F(k) of ZnCl$_2$ is varied in the range 0.75Å^1 for [TPMA]$^+$ to 1.40Å^{-1} for [MA]$^+$.[83]

2. **Cation substitution by addition in MX$_2$ by addition of MX** : The addition of different sized cations can be achieved by mixing ZnCl$_2$ with an alkali halide such

as KCl or LiCl.[85,86] With addition of LiCl, there is an increase in FSDP intensity is present up until 67% LiCl after which the FSDP disappears. The intensities of the FSDP in $ZnCl_2$/LiCl mixtures are smaller than that predicted by utilising the partials (weighted appropiately to the mixture) of the pure LiCl and $ZnCl_2$ liquids.[85] For KCl[86] there is an increase in intensity of the FSDP from 0-67%, show an enhancement in FSDP intensity compared to that predicted by a comibination of weighted partial strucure factors from the pure substances. The FSDP sharply collapses at the next recorded value of 81%. The origin of this difference can be understood in terms of the formation of well-defined MX_4^{2-} molecular anions in the KCl/$ZnCl_2$ mixtures which are not present in the corresponding LiCl substituted systems.

3. **Anion addition**: For systems such as $M_XSe_{1-X,}$ where M=Ge or Si, a change in stoichiometry can be achieved through the addition of Se_2 to the existing mixture. Neutron diffraction experiments on Ge_XSe_{1-X} at values of x=0.33, 0.4, 0.5, and 1.0 showed a decline in the FSDP of $S_{NN}(k)$.[87]

1.9 Polyamorphism

Another method for potentially varying IRO is achieved through variations in temperature and pressure. With increasing temperature, the intensity of the FSDP displays considerably different behaviour to other peaks in the structure factor: in As_2Se_3 [88], the FSDP intensity anomalously increases, whilst in $GeSe_2$ it collapses sharply.[87] Variations of structural properties such as the FSDP within the amorphous state have been considered as indicative of underlying change in the potential energy surface and as a possible indicator of different polymorphs in the liquid state. The presence of such transitions in the liquid state has been of recent interest.[90-93] Many of the possible candidate structures for such a transition (and that are systems of interest in our study), such as $GeSe_2$, $ZnCl_2$ and oxides such as SiO_2 and GeO_2, possess IRO.[91] High pressure experiments on liquid $ZnCl_2$ and $GeSe_2$ show changes in structure, particularly on the IRO scale. In recent experiments by Brazkhin[94,95], two phases were highlighted as occurring in the pressure range of 0-3GPa. In the first phase, a molecular-network is identified with significant IRO present highlighted. At the higher pressure of 3GPa, a sharp change in structure is highlighted as the molecular network changes to a more ionic

$CdCl_2$ type structure and the collapse of intensity in the FSDP. Recently, computational studies have been carried out on this behaviour in systems such as SiO_2, indicating a change in local ion coordination implying the presence of low and high density states.[96] $ZnCl_2$ is understood to be less open as a network than SiO_2 whilst changes in structure have been observed at relatively lower pressures[97].

1.10 Structure of Liquids.

The work highlighted so far indicates the presence of three major types of ordering present in liquids:

> **Short Range Ordering (SRO)**: SRO describes the geometry and coordination of a constituent unit, (i.e MX_4 tetrahedra) as well as the bond lengths of the constituent polyhedra. Information about short-range order can be derived from a number of experiment sources highlighted earlier.

> **Intermediate Range Ordering (IRO)**: Information about IRO is obtained primarily from diffraction experiments and is highlighted by the presence of a FSDP. Although the existence for IRO in MX_2 systems is well established, information on the atomistic origins of IRO, as well as explanations of how the intensity and position of the FSDP changes is less understood. Intermediate-range order can be defined as structural ordering on typical length-scales of 5-10Å, characterised by the presence of a feature in the static structure factor (the prepeak) at $k\sim1-1.5Å^{-1}$. The presence of such a feature is indicative of ordering on a length-scale beyond that imposed by the typical ion diameters (packing effects).

> **Extended Range Ordering (ERO)**: The development of third generation radiation sources have improved the real space resolution obtainable so that radial distribution functions can be resolved to distances of 60Å.[39] The frequency of such oscillations have been linked to the position of the principal peak rather than the FSDP.

Early interpretations of the relationship with IRO postulated a large contribution of ERO to the intensity of the FSDP: an investigation using a large cell size for a-Si concluded that the correlations at r >15Å contributed 50% of the intensity of the FSDP.[98] A later diffraction investigation concluded that there is no such relationship with IRO.[99] The interdependence between these orderings is not yet fully understood, but an important

observation is that SRO and ERO are ubiquitous features of a liquid originating in the *principal peak* which occurs $\sim 2\text{Å}^{-1}$ in F(k), whereas IRO depends on features at lower k: MX systems, highlighted as systems where IRO is absent, would observe both SRO and ERO.[99]
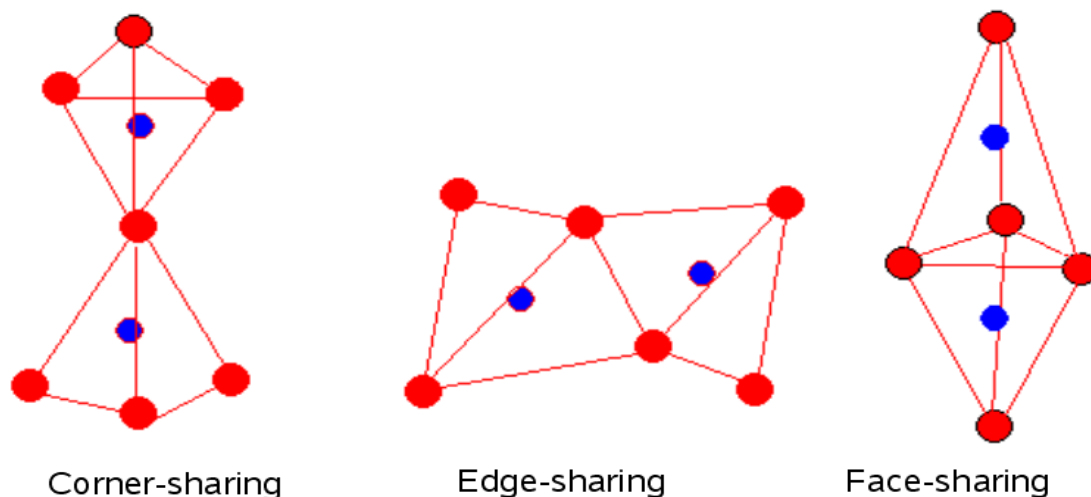
Figure 1.4: Possible connections of tetrahedral units. The central cation is blue and the surrounding anions are red.

Diffraction experiments showed that systems such as $ZnCl_2$ are comprised primarily of tetrahedral units.[100] The network topology, described by how the tetrahedral units are connected to each other, has profound implications for the material properties. In a network system, there are three possible connections between tetrahedral units (figure 1.4):

Corner Sharing: The tetrahedra are linked at the vertices by one bridging anion. This structural feature is associated with systems such as SiO_2 and BeF_2 and are characterised by relatively obtuse M-X-M bond angles ($>140°$). Pure corner-sharing produces a three-dimensional network of strong bonds.

Edge-Sharing: Cations are bridged at the edge of tetrahedral units by two anions. Edge-sharing tetrahedra are a feature of the crystal structures of compounds such as $GeSe_2$ and $SiSe_2$.. Raman spectra for $BeCl_2$ [101] highlights the edge-sharing nature of liquid $BeCl_2$ and feature prominently in models of chalcogenides such as $SiSe_2$[102]. The structure is comprised of chains of edge-sharing tetrahedra with relatively acute M-X-M bond angles ($\sim 80°$). The relatively low melting points for these systems result from the weak inter-chain forces of these charge-neutral units.

Face-Sharing: Three anions are bridging across cations. Here, the cation-cation separation is smaller than the anion-anion separation; in MX_2 compounds where the cations are charged this is highly unlikely and so far there is no evidence of their presence in molten network-forming salts.

An archetypal three-dimensional MX_2 network could be described as consisting of corner-sharing $(MX_4)^{2-}$ tetrahedra where ideal coordination numbers for the ion pairs XM, MX, XX and MM are 2, 4, 12 and 8. Departures from this network are highlighted by systems such as $ZnCl_2$ and $GeSe_2$ which display a network topology derived from a mixture of both corner and edge-sharing tetrahedra with accompanying M-X-M bond angles between 90° and 120°. The effect of this variation in inter-tetrahedral coordination on structure, specifically IRO, is not yet well understood. Also observed, is the destabilisation of chemical ordering: in systems such as $GeSe_2$, homopolar bonds, that is bonding of like atoms, are observed.

The main focus of this study is the analysis and reproduction of IRO in MX_2 compounds with a focus on the effect of different tetrahedral linkages. To study the effect of varying inter-tetrahedral connections a range of systems will be studied with the relative concentrations of the inter-tetrahedral linkages controlled by varying a single parameter (the anion polarisability). The use of a simple potential model enables a wide search of structural features. In addition to the variation of tetrahedral linkages, other factors studied include the effect of temperature and pressure.

1.11 Outline of study

Chapter 2 details the methodology behind the polarisable ion model (PIM) and the analytical methods used in studying liquid structures. Chapter 3 focuses on the halides of intermediate-sized metal cations. An improved model for $ZnCl_2$ is produced and the interpretation of several different experiments are examined for this system. A potential is produced for $MgCl_2$ and a comparison with the structure of $ZnCl_2$ is made as well as comparing the structures of $MnCl_2$, $ZnCl_2$ and $MgCl_2$. The effect of increasing anion size, through increasing the effective anion-anion separation is examined. Chapter 4 deals with the application of the PIM to $GeSe_2$. This involves the use of a larger anion polarisability than that previously used. Comparisons of the resulting structure with results from experiment and electronic structure calculations are made. Chapter 5 is a comparison of $ZnCl_2$ and $GeSe_2$ with regards to the chemical ordering present. A peak is

observed in $S_{CC}(k)$ for $ZnCl_2$ and a novel analysis is presented in which the cation structure is decomposed according to network connectivity. A wider study of the function, $S_{CC}(k)$, is made with a range of other systems which represent candidate systems which may possess a FSDP in $S_{CC}(k)$, including low-density $ZnCl_2$ system, an amended potential for $BeCl_2$ and BeF_2. Chapter 6 extends the study to a generalised MX_2 structure where the network topology is controlled by varying the anion polarisability. The FSDP intensity and position are recorded as a measure of changes in inter-tetrahedral connectivity. The variation in properties of the partial network-connectivity structure factors of $S_{MM}(k)$ including FSDP presence and variable intensity are described. Chapter 7 studies the effects of t*emperature and pressure* on the model for $ZnCl_2$, with particular emphasis on the changes in partial structure factors which, as yet, are unavailable from experiment. Chapter 8 highlights the changes with pressure and for the generalised MX_2 model using high and low anion polarisabilities. The focus in this chapter is the effect of polarisability dependence on the changes of the tetrahedral network in terms of the variations in the underlying network topology and coordination at different densities. Chapter 9 is an inherent structure analysis of the liquid systems studied previously. Steepest-descent calculations are applied on melt configurations to locate the potential energy minima and the inherent structure quantities are analysed. In Chapter 10 we observe the effect of inducing homopolar bonds into a predominantly tetrahedral MX_2 network and the effect on IRO.

1.12 References

[1] M. Rovere and M. P. Tosi. *Rep. Prog. Phys.*, **49**, 1001, (1986).

[2] J.-P Hansen and I.R. McDonald. *Theory of Simple Liquids*,
   Academic Press, New York, (1986).

[3] J. E. Enderby and A. C. Barnes. *Rep. Prog. Phys.*, **53**, 85, (1990).

[4] A. R. Ubbelohde. *The Molten State of Matter,* John Wiley and Sons, Chichester,
   (1978).

[5] W. H. Zachariasen. *J. Am. Chem. Soc.*, **54**, 3841, (1932).

[6] J. D. Van der Waals. *On the Continuity of the Gaseous and Liquid states,*
   Ph.D. Diss., Leiden, (1873).

[7] R. L. Scott and P. H. van Konynenburg. *Discuss. Faraday Soc.*, **49**, 87, (1970).

[8] F. Zernike and J. A. Prins. *Z. Phys.*, **41**, 184, (1927).

[9] H. Eyring and S. M. Jhon. *Significant Liquid Structures,* Wiley, New York, (1969).

[10] J. D. Bernal. *Proc. R. Soc. London A,* **280**, 299, (1964).

[11] *Molten Salts: From Fundamentals to Applications,* NATO Science Series, (2003).

[12] C. A. Angell. *J. Non-Cryst. Solids*, **102**, 205, (1988).

[13] E. A. Pavlatou, S. N. Yannopoulos, G. N. Papatheodorou and G. Fytas. *J. Phys.
   Chem. B,* **101**, 8748, (1997).

[14] J. Ruska and H. Thurn. *J. Non-Cryst. Solids,* **22**, 277, (1976).

[15] V. N. Novikov, Y. Ding and A. P. Sokolov. *Phys. Rev. E*, **71**, 061501, (2005).

[16] G. N. Greaves and S. Sen. *Advances in Physics*, **56,** 1, (2007).

[17] R. T. Struck and C. W. Zielke. *Fuel*, **60**, 795, (1981).

[18] H. Mozammel, O. Masahiro and S. C. Battacharya. *Biomass and Bioenergy*, **22**, 397,
   (2002).

[19] K. Sakai, T. Uemoto, H. Yokoyama, A. Fukuyama, K. Yoshino, T. Ikari and
   K. Maeda. *J. Non-Cryst. Solids*, **266-269**, 933, (2000).

[20] A. Yoshikawa, O. Ochi, H. Nagai and Y. Mizushima. *Appl. Phys. Lett.*, **31**, 161,
   (1977).

[21] J. E. Griffiths, G. P. Espinosa, J. P. Remeika and J. C. Phillips. *Phys. Rev. B*, **25**,
   1272, (1982).

[22] C. Hardacre. *Ann. Rev. Mater. Res.*, **35**, 29, (2005).

[23] C. Fillaux, B. Couzinet, C. Dreyfus, J. P. Itié and A. Polian. *Physica Scripta*. **T115**,
   339, (2005).

[24] J. Wong, and F. W. Lytle. *J. Non-Cryst. Solids*, **37**, 273, (1980).

[25] P. Boolchand. *Insulating and Semiconducting Glasses*, Chap. 5B, World Scientific, Singapore, (2000).

[26] P. Boolchand, J. Grothaus, W. J. Bresser and P. Suranyi. *Phys. Rev. B*, **25**, 2975, (1982).

[27] W. J. Bresser, P. Boolchand, P. Suranyi and J. G Hernandez. *Hyperfine Interactions*, **27**, 389, (1986).

[28] S. N. Yannopoulos, A. G. Kalampounias, A. Chrissanthopoulos and G. N. Papatheodorou. *J. Chem. Phys*., **118**, 3197, (2003).

[29] H. E. Fischer, A. C. Barnes, and P. S. Salmon. *Rep. Prog. Phys*., **69**, 233, (2006).

[30] S. Sugai and A. Ondera. *Phys. Rev. Lett*., **77**, 4210, (1996).

[31] A. P. Sokolov, A. Kisliuk, M. Soltwisch and D. Quitmann. *Phys. Rev. Lett.*, **69**, 1540, (1992).

[32] R. F. Kruh. *Chem. Rev*., **62**, 319, (1962).

[33] K. Furukawa. *Rep. Prog. Phys*., **25**, 395, (1962).

[34] N. W. Ashcroft and D. C. Langreth. *Phys. Rev*., **156**, 685, (1967).

[35] J. E. Enderby, D. M. North and P. A. Egelstaff. *Phil. Mag.*, **14**, 961, (1966).

[36] T. E. Faber and J. M. Ziman. *Philos. Mag.*, **11**, 153, (1965).

[37] S. Biggin and J. E. Enderby. *J. Phys, C.:Solid State Phys*., **14**, 3129, (1981).

[38] F. G. Edwards, J. E. Enderby, R. A. Howe and D. I. Page. *J. Phys. C*, **8**, 3483, (1975).

[39] P. S. Salmon, R. A. Martin, P. E. Mason and G. J. Cuello. *Nature* (London), **435**, 75 (2005).

[40] J. Neuefeind. *Phys. Chem. Chem. Phys.,* **3**, 3987, (2001).

[41] S. C. Moss and D. L. Price. *Physics of Disordered Materials*, 81, Plenum, New York, (1985).

[42] Q. Mei, C. J. Benmore, R. T. Hart, E. Bychkov, P. S. Salmon, C. D. Martin, F. M. Michel, S. M. Antao, P. J. Chupas, P. L. Lee, S. D. Shastri, J. B. Parise, K. Leinenweber, S. Amin and J. L. Yarger. *Phys. Rev. B,* **74**, 014203, (2006).

[43] E. W. J. Mitchell, P. F. J. Poncet and R. J. Stewart. *Phil. Mag.,* **34**, 721, (1976).

[44] S. Biggin and J. E. Enderby. *J. Phys. C*, **15**, L305 (1982).

[45] P. S. Salmon. *Proc. R. Soc. London*, Ser. A, **445**, 351 (1994).

[46] R. L. McGreevy. *Mol. Phys.,* **90**, 533, (1997).

[47] M. Misawa. *J. Chem. Phys*., **91**, 5648, (1989).

[48] A. C. Wright, R. N. Sinclair and A. J. Leadbetter. *J. Non-Cryst. Solids*, **71**, 295, (1985).

[49] J. Blétry, *Philos. Mag. B*, **62**, 469, (1990).

[50] M-L. Saboungi, D. L. Price, J. W. Richardson, K. J. Volin and H. T. J. Reijers. *Bull. Am. Phys. Soc.*, **33**, 768, (1988).

[51] M-L. Saboungi, R. Blomquist, K. J. Volin and D. L. Price. *J. Chem. Phys.*, **87**, 2278, (1987).

[52] R. J. Hemley, C. Meade and H. Mao. *Phys. Rev. Lett.*, **79**, 1420, (1997).

[53] J. Swenson. *Phys. Rev. Lett.*, **79**, 1421, (1997).

[54] P. M. Bridenbaugh, G. P. Espinosa, J. E. Griffiths, J. C. Phillips and. J. P. Remeika. *Phys. Rev. B,* **20**, 4140, (1979).

[55] S. Sugai. *Phys. Rev B*. **35**, 1345, (1991).

[56] E. A. Chechetkina. *J. Phys. Condens. Matter,* **7**, 3099, (1995).

[57] M. Wilson and P. A. Madden. *J. Phys.:Condens. Matter*, **11**, A237, (1999).

[58] A. B. Bhatia and D. E. Thornton. *Phys. Rev. B.*, **2**, 3004, (1970).

[59] L. Van Hove. *Phys. Rev.*, **95**, 249, (1954).

[60] P. S. Salmon. *Proc. R. Soc. London*, Ser. A **437**, 591 (1992).

[61] P. Vashishta, R. K. Kalia, G. A. Antonio and I. Ebbsjö. *Phys. Rev. Lett.*, **62**, 1651, (1989).

[62] C. Massobrio and A. Pasquarello. *Phys. Rev. B*, **68**, 020201 (2003).

[63] C. Massobrio, A. Pasquarello and R. Car. *Phys. Rev. Lett.*, **80**, 2342, (1998).

[64] C. Massobrio, M. Celino, and A. Pasquarello. *Phys. Rev. B*, **70,** 174202, (2004).

[65] F. H. Trimble and N. S. Gingrich. *Phys. Rev.*, **53**, 278, (1938).

[66] E. Principi, M. Minicucci, S. De Panfilis and A. Di Cicco. *Physica Scripta*, **T115**, 1059, (2005).

[67] M. Wilson and P. A. Madden. *Phys. Rev. Lett.*, **72**, 3033, (1994).

[68] F. G. Edwards, R. A. Howe, J. E. Enderby and D. I. Page. *J. Phys. C: Solid State Phys.*, **11**, (1978).

[69] H. Iyetomi and P. Vashishta. *Phys. Rev. B*, **47**, 3063, (1993).

[70] L. Cervinka. *J. Non-Cryst. Solids*, **90**, 371, (1987).

[71] L. Cervinka. *J. Non-Cryst. Solids*, **106**, 291, (1987).

[72] L. E. Busse. *Phys. Rev. B,* **29**, 3639, (1984).

[73] P. Boolchand, J. Grothaus and J. C. Phillips. *Solid State Commun.*, **45**, 183, (1983).

[74] P. H. Gaskell and D. J. Wallis. *Phys. Rev. Lett.*, **76**, 66, (1996).

[75] S. Susman, K. J. Volin, D. L. Price, M. Grimsditch, J. P. Rino, R. K. Kalia and P. Vashishta. *Phys. Rev. B*, **43**, 1194, (1991).

[76] M. Wilson and P. A. Madden. *Phys. Rev. Lett.*, **80**, 532, (1998).

[77] J. K. Christie, S. N. Taraskin and S. R. Elliot. *J. Phys.:Condens. Matter*, **16**, S5109, (2004).

[78] R. Fayos, F. J. Bermejo, J. Dawidowski, H. E. Fischer and M. A. González. *Phys. Rev. Lett.*, **77**, 3823, (1996).

[79] S. R. Elliot. *J. Phys.: Condens. Matter*, **4,** 7661, (1992).

[80] M. Wilson, P. A. Madden, N. N. Medvedev, A. Geiger and A. Appelhagen. *J. Chem. Soc., Faraday Trans.*, **94**, 1221 (1998).

[81] K. Maruyama, H. Endo, and H. Hoshino. *J. Phys. Soc. Jpn*, **76**, 024601, (2007).

[82] J. Dixmier. *J. Phys.(France)*, **I 2**, 1011, (1992).

[83] C. Massobrio and A. Pasquarello. *J. Chem. Phys.*, **114**, 7976, (2001).

[84] C. J. D. Martin, S. J. Goettler, N. Fosse and L. Iton. *Nature*, **419**, 381, (2002).

[85] Y. S. Badyal and R. A. Howe. *J. Phys. Condens. Matter*, **5**, 7189, (1993).

[86] D. A. Allen, R. A. Howe, N. D. Wood and W. S. Howells. *J. Phys. Condens. Matter,* **4**, 1407 (1992).

[87] P. S. Salmon and J. Liu. *J. Phys.: Condens. Matter*, **6**, 1449, (1994).

[88] L. E. Busse and S. R. Nagel. *Phys. Rev. Lett.*, **47**, 1848 (1981).

[89] I. Petri, P. S. Salmon and W. S. Howells. *J. Phys.:Condens. Matter*, **11,** 10219, (1999).

[90] M. C. Wilding, M. Wilson and P. F. McMillan. *Chem. Soc. Rev.*, **35**, 964, (2006).

[91] V. V. Brazhkin, S. Buldyrev, V. N. Ryzhov and H. E. Stanley. *New Kinds of Phase Transition:Transformation in Disordered Substances,* Kluwer, Dordrecht, (2002).

[92] E. G. Ponyatovsky and O. I. Barkalov. *Mater. Sci. Rep.*, **8**, 147, (1992)

[93] P. G. Debenedetti. *Metastable Liquids*, Princeton University Press, Princeton,(1997).

[94] V. V. Brazhkin, A. G. Lyapin, S. V. Popova, Y. Inamura, Y. Katayama, H. Saitoh and W. Utsumi. *J. Phys.:Condens. Matter, 19*, 246104, (2007).

[95] V. V. Brazhkin, Y. Katayama, A. G. Lyapin, S. V. Popova, Y. Inamura, H. Saitoh and W. Utsumi. *JETP Letters*, **82**, 713, (2005).

[96] D. Daisenberger, M. Wilson, P. F. McMillan, R. Q. Cabrera, M. C. Wilding and D. Machon. *Phys. Rev. B*, **75**, 224118, (2007).

[97] C. H. Polsky, L. M. Martinez, K. Leinenweber, M. A. Verhelst, C. A. Angell and G. H. Wolf. *Phys. Rev. B*, **61**, 5934, (2000).

[98] S. R. Elliot. *J. Non-Cryst. Solids*, **182**, 40, (1995).

[99] P. S Salmon. *J. Phys.: Condens. Matter*, **19**, 455208, (2007).

[100] D. S. Allen, R. A. Howe, N. D. Wood and W.S. Howells. *J. Chem. Phys.*, **94**, 5071, (1991).

[101] E. A. Pavlatou and G. N. Papatheodorou. *Phys. Chem. Chem. Phys.*, **2**, 1035, (2000).

[102] L. F. Gladden and S. R. Elliot. *Phys. Rev. Lett.*, **59**, 908, (1987).

Chapter 2

Computational Methods

2.1 Introduction.

Computational simulations in chemistry are important in complementing information gathered from experiments, particularly in the determination of structure of liquids. An advantage of simulation methodologies with respect to experiments is that positions and velocities are known precisely so we are able to highlight the microscopic structural features which comprise amorphous systems. Early liquid models were built on hard-sphere packing systems of Bernal[1], initially with hand-built ball and spoke representations.[2,3] As we have seen in Chapter 1, experimental results on MX_2 systems have shown that they possess complex ordering on intermediate-length scales. The use of computers, enabling construction of a large number of configurations, provides an effective method for constructing models for these systems.[4,5,6] There are a variety of computational techniques which are used to model the systems of interest in this study:

2.2 Electronic structure methods.

Electronic structure methods attempt to solve the Schrődinger equation for a given compound. In density functional theory (DFT), electrons are represented by functions in terms of single particle electron density, rather than many-body wave functions. *Ab initio* molecular dynamics developed by Car and Parrinello[7] adapts the electronic structure problem so that it can be solved by the steepest-descent method and Newtonian equations of motion, and has been used to model systems in this study such as $GeSe_2$. Due to computational expense, the array size is ~100 atoms and time scales of tens of picoseconds are available. The method by which electron correlations are accounted for has a significant impact on the structure calculated as it affects the electronic distribution around an atom. In the local density approximation (LDA)[8], which treats a bond as highly ionic, the simulated $GeSe_2$ system does not exhibit a FSDP; however, when the generalised-gradient approximation (GGA)[9], which results in a covalent description of

the bond, is applied, a FSDP appears.

2.3 Methods using experimental data directly in parameterisation.

There are several modelling techniques which use experimental data directly. *Reverse Monte Carlo*[10] (RMC) iterates towards a configuration which matches a set of experimental data, such as the total structure factors, $F^E(k)$, through a series of small random movements of a single atom from an initial configuration which, if accepted, provide the starting configuration for the next step. This process is repeated until the experimental data is matched to a degree of precision. Whether a step is accepted or not depends on the following cost function (equation 2.1), which measures the difference between the changes of the structure factor calculated from the configurations, $F^{Co}(Q_i)$, and those determined experimentally:

$$\chi^2 = \sum_{i=1}^{m} (F^{Co}(Q_i) - F^E(Q_i))^2 / \sigma^2(Q_i) \tag{2.1}$$

where m is number of experimental data points and σ is the experimental error. A move is accepted if $\chi_n^2 < \chi_o^2$, where the subscripts refer to results from the new (n) and old configurations(o), or if it increases it with probability $\exp(-(\chi_n^2 - \chi_0^2)/2)$. *Monte Carlo* (MC) methods utilise a potential model in conjunction with random displacements to generate configurations which are then compared to an experimental quantity. In a MC model of $ZnCl_2$ by Bassen *et al*[11], the longer range correlations between zinc ions are forced by an oscillating function, μ_{ZnZn}^{osc}:

$$\mu_{ZnZn}^{osc} = A_{ZnZn} \sin\left(\frac{\pi}{2} \frac{r_{ZnZn} - B_{ZnZn}}{C_{ZnZn}} \right) \exp\left[-(\frac{r_{ZnZn}}{D_{ZnZn}}) \right] \tag{2.2}$$

$$\mu_{ClCl}^{osc} = \mu_{ZnCl}^{osc} = 0 \tag{2.3}$$

A_{ZnZn}, B_{ZnZn}, C_{ZnZn} and D_{ZnZn} are variable parameters. Another potential based method of fitting configurations to data, empirical structure refinement (EPSR)[12], utilises an

empirical potential, with an adjustable set of parameters which feed into the modelling of experimental data, also taking into account the confidence in the reliability of the experimental data from a scale of 0 (no confidence) to 1(full confidence). It is shown that the cation-cation correlation, for which there is a low weighting in $ZnCl_2$, is reproducable over a wide confidence scale.[12]

2.4 Integral equations.

In integral theory, the energy functional of a compound is linked to the pair distribution function, $g_{\alpha\beta}(r)$, through two-body additive potentials, $u_{\alpha\beta}(r)$. The pair distribution function is split, through the Ornstein-Zernike relation (equation 2.4)[13], into a direct correlation, $c_{\alpha\beta}(r)$, which includes the atom pair and an indirect correlation term describing the effect of other particles on the pair-wise interaction.

$$h_{\alpha\beta}(r) = c_{\alpha\beta}(r) + \sum_{\gamma} n_{\gamma} \int d\boldsymbol{r}' h_{\alpha\gamma}(|\boldsymbol{r}-\boldsymbol{r}'|) c_{\gamma\beta}(\boldsymbol{r}') d\boldsymbol{r} \tag{2.4}$$

The effective pair potential can be calculated by:

$$u_{\alpha\beta}(r) = k_B T [h_{\alpha\beta}(r) - c_{\alpha\beta}(r) - \ln g_{\alpha\beta}(r) + B_{\alpha\beta}(r)] \tag{2.5}$$

$B_{\alpha\beta}(r)$ is a bridging function which describes the sum of the contribution of all elementary graphs in the cluster expansion. It is difficult to solve analytically and, as a result, an approximation is usually made. The hypernetted chain approximation[14] solves this by setting $B_{\alpha\beta}(r)$ to 0. The former expression has been used for modelling the systems we are using whilst the Percus-Yevick closure[15] has had greater success in modelling Lennard-Jones systems. Integral equations on $ZnCl_2$ and $GeSe_2$ by Ballone[16] and Iyetomi[17] respectively, where the former calculation dealt with Coulombic repulsions with distance-dependent dielectric screening and the latter treated the atoms as firstly neutral hard spheres and secondly charged hard spheres. They produced FSDPs at ~1.3Å^{-1} and ~1.4Å^{-1} for $ZnCl_2$ and $GeSe_2$ respectively. This was somewhat higher than the experimental values of ~1Å^{-1}. Once a potential model with bond bending constraints was implemented, the FSDP moved closer to ~1Å^{-1} for $GeSe_2$.[17]

2.5 Classical potential models.

Classical potential models rely on the application of simple energy functions to describe certain properties of a given compound. The choice of energy functional can vary from the hard-sphere model[18], which deals only with the short-range repulsion of atoms to more complex functions which incorporate many-body effects.[19] The advantages of such methods is that the relative simplicity of the model compared to *ab initio* electronic structure methods allows faster computation, enabling longer time-scales and larger systems to be studied. However, in order to maintain flexibility the potential models should be transferable in the sense that the models should be applicable, without parameter change, across a wide range of state-points. In addition, potential parameters for a given model should be physically transparent and transfer between systems in terms of well-defined quantities (such as ion radii). For the purposes of our investigation, we will use molecular dynamics using a simple classical-MD potential, which, as well as accounting for coulombic ordering, short-range repulsion and dispersion, also includes a representation of polarisation effects.

2.6 Molecular dynamics.

Molecular dynamics[6] involves the modelling the time evolution of a system of N particles with their trajectories determined through integration of Newton's equations of motion, the atom forces being obtained from the potential energy function. The first step of a molecular dynamics simulations is the inputting of parameters, where quantities such as the number of particles, time step, length of run and temperature are specified. Initial coordinates are then inserted into the system. The coordinates chosen are such that overlap of the atomic or molecular core is prevented. The forces are then computed on the particles. The system energy can be written as a function of the atom positions [$U(R_i)$] and, as a result, the pairwise force acting between a pair of atoms *ij* can be calculated from the simple derivative:

$$f_{ij} = -\frac{\partial U}{\partial r_{ij}}$$

(2.6)

where r_{ij} is the separation of atoms i and j. Depending on the complexity of the ionic potential, this is the most computationally expensive stage of the run as all the forces affecting an ion have to be considered. Coulombic energetics require careful consideration as the interactions are relatively long range with respect to the simulation cell size. Newton's equations of motion are then integrated.

$$F_i = m_i a_i = m \cdot \frac{d v_i}{dt} = m \cdot \frac{d^2 r_i}{d t^2} \qquad (2.7)$$

where $\mathbf{r}_i$ and $\mathbf{v}_i$ are the position and velocity vectors of particle i respectively. F_i is force exerted on particle, m_i is mass of particle and a_i is acceleration of particle. These equations of motion are then integrated using a finite difference method. In the present case we use the Verlet *leap-frog a*lgorithm[6] to solve the equations of motion. This algorithm generates the particle velocities and positions at each time step. The particular form we use is the velocity-verlet algorithm developed by Swope *et al*[23]. The velocity Verlet algorithm computes the particle velocity $v(t+\delta t)$ and particle position $r(t+\delta t)$ as follows:

$$r(t+\delta t) = r(t) + \delta t\, v(t) + \frac{1}{2}\delta t^2\, a(t) \qquad (2.8)$$

$$v(t+\delta t) = v(t) + \frac{1}{2}\delta t[a(t) + a(t+\delta t)] \qquad (2.9)$$

, where δt is the finite time step, in the present work δt=25 a.u. (equivalent to 6.047 x 10^{-15} s). For this investigation, simulations of ~60 ps will be used to generate the configurations from which structural data including radial distribution functions and structure factors are obtained.

2.7 Potential models: rigid ion model.

The form of the energy function has to effectively describe the interactions in the system so it can replicate known properties and elucidate other structural quantaties unobtainable

from experiment. In addition, it has to be computationally tractable for the system sizes and length scales dealt with in this investigation. The *rigid ion model*[24] treats ions as charged spheres, neglecting many body effects on the ion caused by the environment and as a result are computationally inexpensive compared to models that do. They account for the static structures of systems such as SiO_2 and BeF_2, where the M-X-M bond angles are of the order of $140°$, but fair less well for systems such as $ZnCl_2$, $GeSe_2$ or $BeCl_2$, where the M-X-M bond angles are more acute.[21] The Born-Huggins-Mayer potential[24] used can be expressed as the following sum:

$$U_{ij} = U_{ij}^{Coul} + U_{ij}^{sr} + U_{ij}^{disp} \qquad (2.10)$$

$$U_{ij} = \frac{Q_i Q_j}{r_{ij}} + B_{ij} e^{-a_{ij}r_{ij}} - \sum_{n=6,8.} \frac{C_n^{ij}}{r_{ij}^n} f_n^{ij} \qquad (2.11)$$

The first term on the right in 2.11, U_{ij}^{Coul}, represents the coulombic interaction between the two species i and j, with separation r_{ij}. The second term, U_{ij}^{sr}, represents the (short range) repulsion arising from the overlap of the atomic electron densities. In this potential function this interaction is controlled through two parameters, a_{ij} and B_{ij}. B_{ij} is related to the respective radii of ions i and j, whilst a_{ij} controls the hardness of the repulsive wall acting between an ion pair. The final term, U_{ij}^{disp}, describes the dispersive interactions which arise from electron correlation effects. C^6 and C^8 represent the van der Waals dipole-dipole and the dipole-quadrupole interactions respectively (in this investigation, we consider the dipole-dipole interactions only). These dispersion coefficients can be related to the ion polarisabilities using the Slater-Kirkwood[25] and Starkschall-Gordon formulae[26] respectively:

$$C_{ij}^6 = \frac{\frac{3}{2}\alpha_i \alpha_j}{\left(\frac{\alpha_i}{P_i}\right)^{\frac{1}{2}} + \left(\frac{\alpha_j}{P_j}\right)^{\frac{1}{2}}} \qquad (2.12)$$

$$C_{ij}^8 = \frac{\frac{3}{2} C_{ij}^6 \langle r_j^4 \rangle}{\langle r_j^2 \rangle} \qquad (2.13)$$

where the $\langle r_y^n \rangle$ terms are ground-state expectation values of even powers of r_i, the electron distance in the isolated atom. α_i and P_i represent the polarisability and effective electron number of the ions. The effective electron number has been shown to apply over an isoelectronic series.[27] These relations are extremely useful as ion polarisabilities may be readily obtained from both experimental studies (from the measurement of refractive indices) and by direct electronic structure calculations[28]. The damping functions f_{ij}^{n} [29] in equation 2.11 are required to correct the intrinsic overestimation of the dispersion energy arising from the overlap of ionic electron densities at short separation. Here, a function of the form suggested by Tang and Toennies[29] is utilised.

$$f_{ij}^n = -e^{-b^n r_{ij}} \sum_{k=0}^{4} \frac{(b^n r_{ij})^k}{k!} \qquad (2.14)$$

Parameter b^n controls the r damping length scale, k=6 for C^6 and 8 for C^8 respectively.

2.8 "Extended" ionic models.

As alluded to earlier with the varying success of integral equation methods, the concept of ionicity plays an important role in determining the structure of MX_2 systems. It was initially considered that a purely ionic potential could reproduce the structural features of $ZnCl_2$.[30] Similarly, covalent representations of systems such as $GeSe_2$ [31] have shown less success in reproducing elements of intermediate-length structure whilst those with a more ionic description of bonds have had more success in reproducing the associated FSDP.[31] The concept of *extended ionicity*[32], where polarisation is accounted for, in addition to Coulombic effects and short-range repulsion, is a relevant one for constructing models for these systems. There have been a number of methods used in modelling systems which include a description of polarisation. In the *Shell Model*[33], the charge of the ion is split between the core with the mass of the ion and a shell with no mass. The shell is bound to the core by a harmonic potential. This model was shown to be deficient for describing systems such as $MgCl_2$, where the crystal exhibits a layer structure of MX_2

triplets of ions where layers of anions of adjacent triplets partner each other contrary to a simple ionic model. The *polarisable ion model* (PIM)[21] develops earlier ideas of Sprik and Klein[34] used in polar liquids, and accounts for large deviations from ionic compounds in an extended ionic framework.

2.9 Environmental effects due to polarisation.

The electron density of a given anion may display considerable environmental dependence in the condensed state. The *spherical confining potential*[32] describes the potential energy well arising from placing a free ion into a crystalline environment and is an indication of the overlap of both the formal ion charges and the anion and cation electron densities (as shown in figure 2.2a). It compresses the charge density relative to the free ion (illustreated in figure 2.2b) and is responsible for stabilising the oxide ion in condensed matter. The polarisable ion model[20] utilises an 'extended' description of the ion interactions in which the electric fields, which arise from the movement of ionic charges, distort the ion electron density resulting in induced moments. The anion electron cloud may be distorted by interactions with other ions. For example, figure 2.1 shows the movement of a nearest-neighbour cation in the first coordination shell about a central anion.[20] The movement of the cation charge results in an electric field at the anion site which induces a charge distortion (dipole moment). The induction of a dipole, μ_i, on species i by a permanent charge from surrounding species j is represented as follows:

$$\boldsymbol{\mu}_i = \boldsymbol{\alpha}_i \boldsymbol{E}_i \qquad\qquad (2.15)$$

where α_i is the ion polarisabililty and E_i is the electric field at site i.

The formation of an induced dipole may be understood in terms of two contributions, as shown in figure 2.2. A displacement of a cation charge will create an electric field at the anion site, resulting in electron displacement in the anion, termed an asymptotic dipole.[20] *Ab initio* electronic structure calculations[35] indicate the presence of an additional contribution to the induced dipole moment, which acts to oppose that induced by the movement of formal (point) charges. The movement of electron density of the disturbed anion reduces the effect of the confining potential. As a result of the induced dipole the anion electron density relaxes, allowing one side of the confining potential wall to push

out. This enables a flow of electrons in the opposite direction, termed a short-range
dipole effect. The short-range dipole[20] can decrease the effect of the asymptotic dipole by
as much as 50% and can be modelled by applying a damping function of the same form
as that deployed earlier to account for the damping of the dispersive interactions at short
range.

$$\mu_{short\,range}^{i} = \sum_{i \neq j} \alpha_i f^{ij} \frac{Q_j \mathbf{r}_{ij}}{|r_{ij}^3|} \tag{2.16}$$

This short-range damping function is modelled using a Tang-Toennies damping
function[29]:

$$f\left(r_{ij}\right) = -c \sum_{k=0}^{k_{max}} \frac{\left(br_i\right)^k}{k!} e^{-br_{ij}} \tag{2.17}$$

where b is termed the short-range damping parameter. The parameter c is included to
allow for the possibility of the short-range term exceeding in magnitude the asymptotic
dipole, as highlighted by electronic calculations[36]. The parameter set $\{b,c\}$ may be
obtained by reference to high level electronic structure calculations in which the nearest-
neighbour cation shell is systematically distorted. Furthermore, these calculations indicate
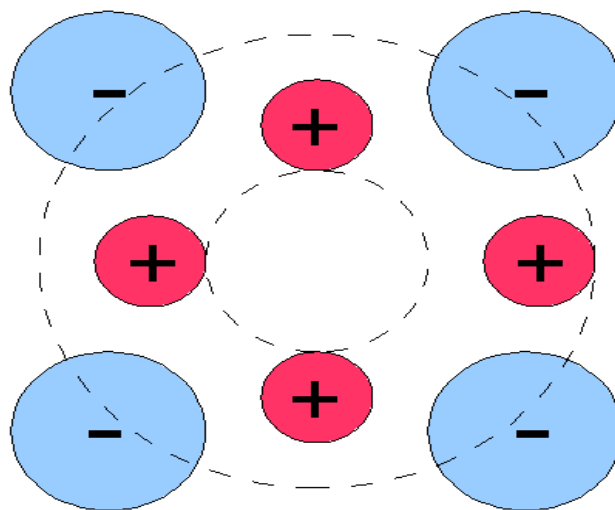
Figure 2.1: Shift of cation in cubic lattice. The resulting effect on the spherical confining potential is
shown in Figure 2.2.

that the parameter b should scale between systems as a function of the ion radii, σ,

$$b = d / (\sigma_+ + \sigma_-)$$
(2.18)

where d is a constant for a series of linked compounds, and σ_+ and σ_- are the respective cation and anion radii. As a result, parameters may be obtained for systems currently beyond the scope of the electronic structure calculations themselves.

In the condensed phase the evolution of the induced dipoles is complicated by the many-body nature of the interaction (a dipole induced on one ion affects that on another which in turn affects the dipole on the original ion). As a result, obtaining the self-consistent dipole moments on the ions (the dipole which include the results of all many-body interactions) requires the iterative solving of coupled equations of the form:

$$\mu^i_{asymptotic} = \alpha_i \frac{\sum\limits_{i \neq j} Q_j \, r_{ij}}{r_{ij}^3} - \sum\limits_{i \neq j} \left[\frac{\mu^j}{r_{ij}^3} - \frac{3 \, r_{ij} \left(r_{ij} \cdot \mu^j \right)}{r_{ij}^5} \right]$$
(2.19)
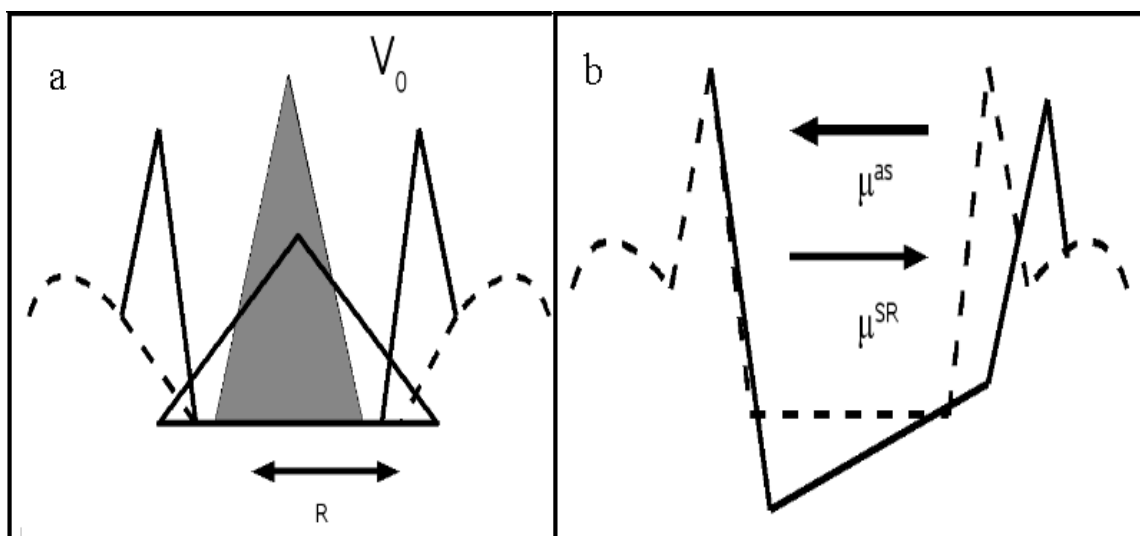
Figure 2.2a:Origin of spherical confining potential, V_o, acting on electrons around an anion in a cubic crystal. Dashed line show Madelung contribution, associated with point ionic charges, to spherical potential. V_0 compresses the free anion charge density (lightly shaded) to in crystal charge density (darkly shaded)

Figure 2.2b:Origin of asymptotic and short-range contribution to the dipole moment when cation is displaced. The dashed line represents the undistorted potential. With the shift of the anion highlighted in figure 2.1, the floor of the potential has acquired a gradient (and an associated aymptotic dipole) with the wall pushing out (an associated short-range dipole). The arrows represent the flow of electron density and are antiparallel to the associated dipole.

or, included the short-range interactions:

$$\mu^i_{coulombic} = \alpha_i \left\{ \sum_{i \neq j} \frac{Q_j r_{ij} \left(1 + f_4^{ij} \right) r^{ij}}{r_{ij}^3} - \sum_{i \neq j} \left[\frac{\mu^j}{r_{ij}^3} - 3 r_{ij} \frac{\left(r_{ij} \cdot \mu^j \right)}{r_{ij}^5} \right] \right\}$$

(2.20)

The possibility of having to solve these iterative equations at each molecular dynamics time step is a significant potential barrier to the effective employment of potential models of this type. To circumvent this problem, the PIM[20] exploits a Car-Parrinello[7] method for maintaining self-consistent values of the induced multipoles without explicit minimisation at each time step. To achieve this, the dipoles are included as additional degrees of freedom in an extended Lagrangian formalism, which allows for the construction of Newtonian equations of motion which govern the time-evolution of the dipoles (in an analogous fashion to the equations of motion for the motion of the ions themselves).[20] The equation of motion of ions in Lagrangian form is

$$\frac{d}{dt} \left(\frac{\partial L}{\partial \dot{r}_i^\alpha} \right) - \frac{\partial L}{\partial r_i^\alpha} = 0$$

(2.21)

, where L=T-U, where T and U are the system kinetic and potential energies respectively. The analogous equation of motion for the dipole time evolution, in Lagrangian form, is given by

$$\frac{d}{dt} \left(\frac{\partial L}{\partial \dot{\mu}_i^\alpha} \right) - \frac{\partial L}{\partial \mu_i^\alpha} = 0$$

(2.22)

this reduces to

(2.23)

$$m_i^\mu \ddot{\mu}_i^\alpha = \sum_{j \neq i}^{N.} - T_{ij}^\alpha Q_j + T_{ij}^{\alpha\beta} \mu_j^\beta - 2k^\mu \mu_i^\alpha$$

where T_{ij} is the interaction tensor given by

(2.24)

$$T_{ij}^{\alpha\beta\gamma\delta} = \nabla_\alpha \nabla_\beta \nabla_\gamma \cdots \frac{1}{r_{ij}}$$

When the dipole acceleration, $\ddot{\mu}_i$, is zero, the dipoles obtained are self consistent. The derivation of equations of motion in this form leads to the generation of the so-called fake kinetic energy, associated with the rate of change of the dipole moment (the dipole velocity). As a result, the total kinetic energy becomes

$$T = \frac{1}{2}\sum_{i=1}^{N} m_i \dot{r}_i^2 + \frac{1}{2}\sum_{i=1}^{N} m_i^{\mu}(\dot{\boldsymbol{\mu}})^2$$

(2.25)

where the two summations represent separate kinetic energy contributions from ionic and dipole motions and m_i^{μ} is the associated 'mass' of the dipoles. The fake kinetic energy[20], represented in the second half of equation 2.25, represents the sum total of the extra kinetic terms generated in the CP method due to the motion of the additional degrees of freedom. Once the initial self consistent dipole moments have been obtained (see below) the self consistent dipoles at the following time step can be determined by integrating the dipolar equations of motion in parallel with the standard ion equations of motion.

In order to determine the initial dipoles, an annealing process is used in which the dipoles are re-orientated in order to reach a local minimum when the fake kinetic energy is zero. This procedure is carried out using a steepest descent algorithm. The dipolar equations of motion are integrated for fixed ion positions and the fake kinetic energy is periodically quenched in order to locate the local energy minimum. Self-consistent dipoles are obtained when the dipole velocities are zero in all directions.

2.10 Origin of polarisability values used.

In tetrahedral systems, the cations are situated in high symmetry sites and, as a result, the resulting electric fields at the cation sites are small and so cation polarisation effects are expected to be small and hence are not considered in this investigation. Conversely, the anions are typically found in lower symmetry sites (often with a coordination number of two) which may result in large electric fields present at the anion sites and hence the potential for the induction of large dipole moments. As a result, it is critical to have an understanding of the anion polarisabilities. Experimentally, anion polarisabilities can be

obtained from refractive investigations on related crystals, where the link with
polarisabilty is made through the Clausius-Mossotti relation:

$$\frac{\epsilon-1}{\epsilon+2} = \frac{N_A \rho_m \alpha}{3M} \tag{2.26}$$

where M is the molecular weight, ε is the permittivity (related to the refractive index by
$\varepsilon=n^2$), N_A is Avagadro's number, ρ_m is the mass density, α is the molecular polarisability
(the weighted sum of the anion and cation polarisabilities in a single formula unit). In
addition, ion polarisabilities may be obtained from high level electronic structure
calculations, for example utilising coupled Hartree-Fock calculations and Möller-Plesset
theory to the second order to deal with correlation effects.[37] In these calculations, a central
anion is surrounded by nearest-neighbour cations and point charges to imitate an ideal
crystalline environment. These calculations indicate that the anion polarisability
decreases from the free ion values when confined in a crystal, as would be expected for
placing an anion in a potential well of the form shown in figure 2.2. Conversely, cation
polarisability increases, but only by a small amount, typically ~1%[38,39]. The anion
polarisabilites display a strong environmental dependence, varying both *between* crystal
structures and as a function of the crystal lattice parameter. The most dramatic
environmental dependencies are observed for chalcogenide anions such as O^{2-} and Se^{2-}.
These anions are unstable as free ions (positive second electron affinity) and are
stabilized in the condensed phases by the confining effect of the ionic
environment[40].

2.11 Ewald summation.

The present work utilises Ewald summation to calculate long range contributions in the
potential energy.[41] In this method the charge-charge energy in the infinitely periodic
system comprised of the simulation cell and all its images is written as a sum of three
terms for ion pairs, ij:

$$U_{ij}^{coul} = \frac{1}{2} \sum_{i,j,l}^{'} \frac{1}{r_{ij}} Q_i Q_j = U_{ij}^{real} + U_{ij}^{recip} + U_i^{const} \tag{2.27}$$

The term **l** denotes all periodic images of the simulation cell with the prime indicating that terms where i=j if **l**=0 (i.e an interaction with itself) are excluded. The *real space* term, U^{real}, is given by

$$U^{real} = \sum_i \sum_{j \neq i} Q_i Q_j \frac{erfc(\eta' r_{ij})}{r_{ij}} \qquad (2.28)$$

where *erfc*(n'r_{ij}) is the complementary error function which ensures that all the real space interactions die away to zero within the simulation cell. The longer ranged contributions are calculated in the reciprocal space term, U^{recip}, given by:

$$U^{recip} = \sum_i \sum_{j<i} \frac{Q_i Q_j}{r_{ij}} (1 - er\, fc(\eta' r_{ij})) \qquad (2.29)$$

$$= \frac{1}{2\pi V} \sum_i \sum_{j<i} \sum_{k \neq 0} \frac{Q_i Q_j}{k^2} e^{\frac{-\pi^2 k^2}{\eta'^2}} \cos(\boldsymbol{k} \cdot \boldsymbol{r}_{ij}) \qquad (2.30)$$

which involves the sum over all the vectors k_n in the reciprocal lattice of the periodically replicated system. The constant term, U^{const}, arising from the interaction of the ions with all their periodic images, is given by

$$U^{const} = -\sum_i \frac{(Q_i)^2 \eta'}{\pi^{1/2}} \qquad (2.31)$$

The parameter η' determines the rate of convergence of the real and reciprocal space parts. A value corresponding to half the cell length is used so that both terms converge reasonably quickly. In the case of the PIM, where the charge-dipole and dipole-dipole terms are also sufficiently long-ranges to require treatment via the Ewald summation method, we replace the $U_{ij}^{RIM} = \frac{1}{r_{ij}} Q_i Q_j$ term from equation 2.27 with the new long range interaction term, U_{ij}^{PIM} which is given by

$$U_{ij}^{PIM} = T_{ij} Q_i Q_j + T_{ij}^{\alpha}(Q_j \mu_i^{\alpha} - Q_i \mu_j^{\alpha}) - T_{ij}^{\alpha} \mu_i^{\alpha} \mu_j^{\beta} \qquad (2.32)$$

2.12 Central cell.

Computational expense limits the central cell size to around 1000 ions where, if applied in isolation, around 50% of the ions would occupy the surface. To produce quantities which relate to the bulk rather than the surface, periodic boundary conditions (shown in figure 2.3) are applied. The simulation cell is replicated in all directions with the longest distance of interaction between two ions at L/2, where L is the box length, limiting the interaction of two ions i and j to the distance of i and the nearest periodic image of j. Whilst the system now pertains to the bulk, it is necessary to make sure that when modelling structural properties which exist beyond the short-range of the first-coordination sphere, the central unit cell is of sufficient size. Alternative procedures such as "multiplying cells" can lead to an inherent long range ordering outside of the predicted
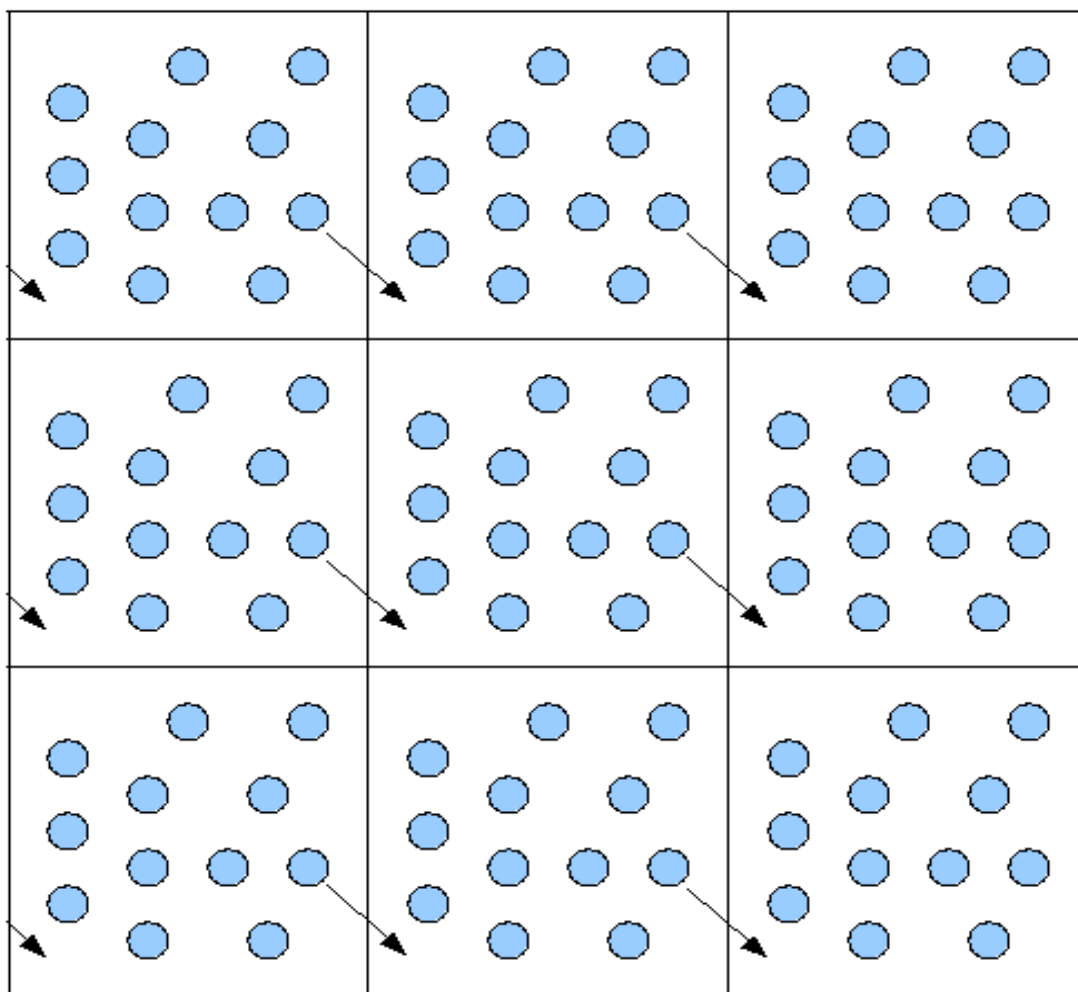
Figure 2.3: Illustration of periodic boundary conditions. If an atom leaves one side of the box its periodic image re-emerges on the other side.

structure.[42] The cell size for modelling systems IRO has varied for systems 120 atoms in electronic structure calculations[42] to 13 824 atoms in a MD simulation of a-Si.[43] One prediction of a sufficient cell size is made by stating that the diffraction pattern should be continuous over the FSDP within experimental resolution[44]. This method for determining the minimum cell length of reproducing the FSDP intensity assumes extended range correlations are significant in reproducing IRO. In a cubic-unit cell the Bragg peaks are given by:

$$Q_{hkl} = \frac{2\pi}{a_0}(h^2 + k^2 + l^2)^{1/2} = \frac{2\pi}{a_0}m^{1/2} \qquad (2.33)$$

where Q_{hkl} is the position of the Bragg peak and where integers h, k and l are integers. Differentiating and taking finite elements of the minimum lattice parameter a_{min} becomes

$$a_{min} = \frac{\pi}{Q_1}\left(\frac{2\Delta m}{(\Delta Q/Q)}\right)^{1/2} \qquad (2.34)$$

This would give a_{min} as 44-29Å for FSDP peaks at ~1Å^{-1} and ~1.5Å^{-1}. Another prediction involves multiplying the distance that extended range oscillations are present by 2 so for $ZnCl_2$ and $GeSe_2$ which have observed ERO oscillations to 60-80Å this would be upto 120-160Å. As highlighted in chapter 1, recent works[45] on $ZnCl_2$ and $GeSe_2$ indicate that such ERO derives from the principal peak and that the FSDP is dominated strongly by interactions in the region 7-10Å. Previous calculations using the PIM of a systems size of 999 atoms[46], and where the correlation length ~15Å, have been able to show a observable FSDP in the relevant structure factors.

2.13 Structural quantities

2.13.1 Radial distribution functions

The radial distribution describes the distribution of ion density around a given ion. It is defined by,

$$g_{\alpha\beta}(r) = \frac{n_{\alpha\beta}(r)}{n_{id}(r)}$$ (2.35)

where $n_{\alpha\beta}$ gives number of β ions surrounding a central ion α in the interval, $r \rightarrow r + \Delta r$, and where n_{id}, the normalisation term, is the number of ions of the ideal gas over the same distance. In computational simulation, the distances between pairs of atom are calculated, accounting for periodic boundaries, and then placed in bins of a width 0.05 a.u. building up a histogram.

2.13.2 Structure factors

The partial structure factors are calculated directly from the ion positions, $\{\mathbf{r}_i\}$, by

$$S_{\alpha\beta}(k) = \langle A_{\alpha}(k) A_{\beta}^{*}(k) \rangle$$ (2.36)

$$A_{\alpha}(k) = [1/\sqrt{N_{\alpha}}] \sum_{i=1}^{N_{\alpha}} e^{(i\,\mathbf{k}\cdot\mathbf{r}_i)}$$ (2.37)

The wavevector k is of the form $k=(2\pi/L)(m, n, p)$ where m, n and p are integers and L is the cell length. The k vectors are consistent with periodic boundary conditions and the average of those k vectors of equal length produces $S_{\alpha\beta}(k)$. Unless stated otherwise, the structure factors displayed in this thesis will be derived from the Ashcroft-Langreth formalism.[47]

2.13.3 Network connectivity statistics
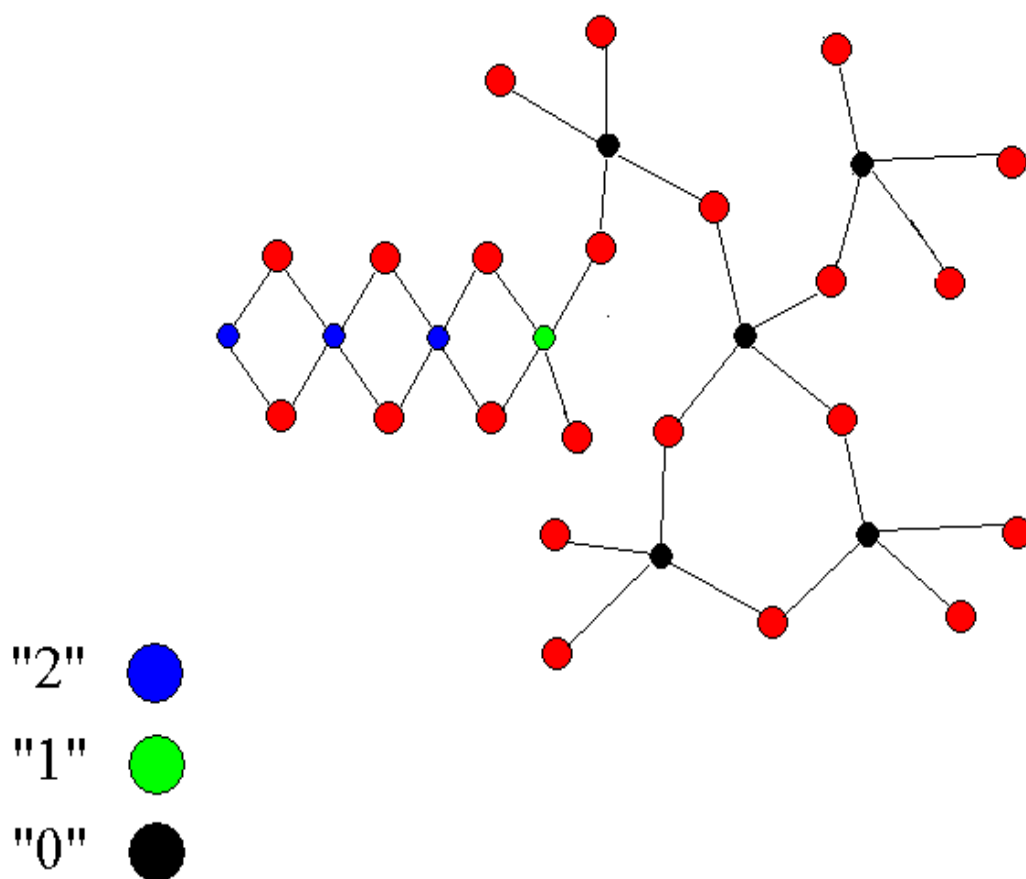
Figure 2.4: Graphical representation of the different network connectivities of a cation in a tetrahedral network.Red circles, X anions; black circles, "0" M cations; green circles, "1" M cations; blue circles, "2" M cations

The prevalence of edge-sharing units in the structure of compounds described has been highlighted in Chapter 1. The assumption that there are no face-shared tetrahedra is made and so the limit is two 4-membered rings. In a classification derived by Celino and Massobrio[48] in calculations on liquid $SiSe_2$, the cations are coloured "0", "1" or "2" depending on whether the cation-centred tetrahedra are linked to nearest-neighbour tetrahedra with 0, 1 or 2 edge-sharing connections (equivalently, the number of four-membered rings bonded to) respectively. Figure 2.4 shows a possible configuration of connected tetrahedra which include all three types of cation. These quantities are calculated by extracting pairs of cations which are bridged by two anions, as highlighted in figure 2.5. From these pairs of cations, the percentages of those which are "0", "1" or

"2" are calculated. The cutoffs used in the calculation are taken from the minima of the principal peaks in the respective radial distribution functions.
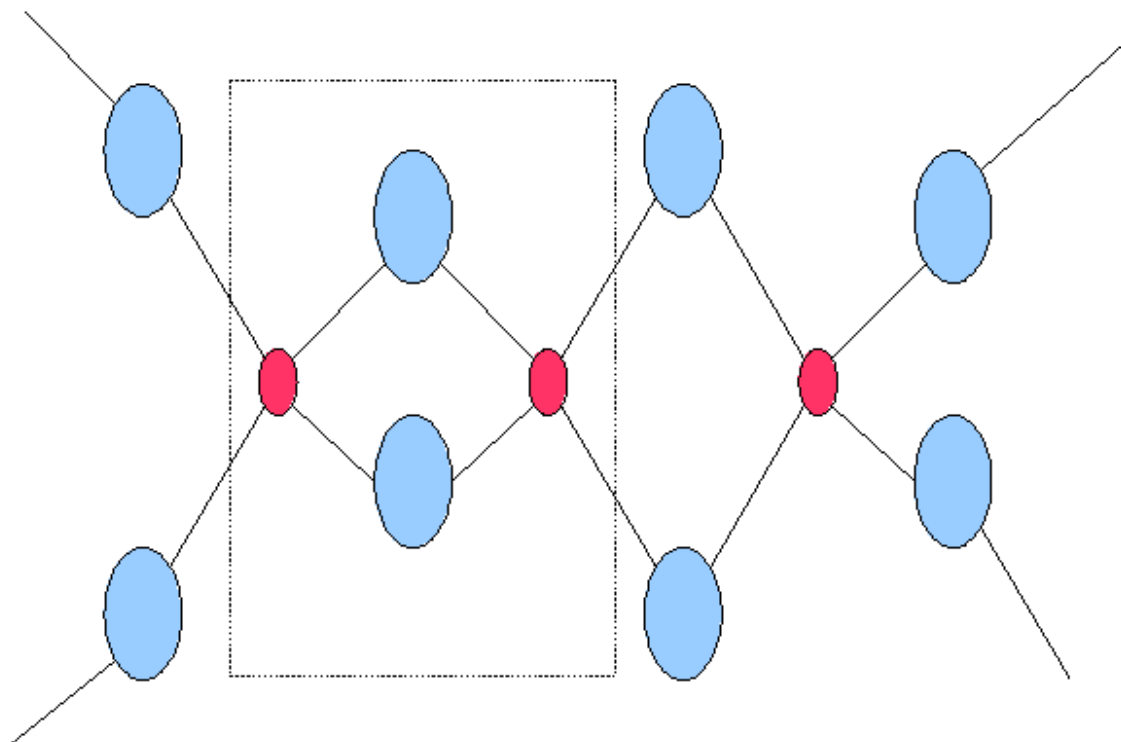
Figure 2.5:Unit defined as "edge-sharing": two cations (red circles) within a given cut-off radius which share two common anion neighbours (blue circles), where bond lengths are related to the minima of $g_{ZnZn}(r)$ and $g_{ZnCl}(r)$ respectively.

In a purely 4-coordinate system, changes in E_n, (where n={0,1,2}) the percentage of cations with n number of 4-membered rings, would represent changes in the underlying network topology. In liquid systems, the cation coordination number is likely to exhibit variation in the first coordination shell, and so the relationship of changes in network topology with changes in E_0, E_1, E_2 may be obscured by the degree to which departures from 4-coordination are present.

2.13.4 Coordination number distributions.

In experimental studies the coordination is calculated by integration of the first peak in the radial distribution function for the appropriate interaction. Deciding where the cut-off point for the first coordination sphere is the source of the most inaccuracy, magnified by r^2 in the integration. Computational analysis has the advantage of knowing the location of

the exact ion positions. The coordination number distribution was calculated by identifying, within a given radius, the number of anions X within the first coordination cell of the cation, M. In this study the cutoff was selected by locating the first minima in $g_{MX}(r)$, for calculating M-X and X-M coordination number and $g_{MM}(r)$ and $g_{XX}(r)$ for the XX and MM coordination pairs.

The average coordination number for an ion pair, M_{ij}, is calculated by:

$$M_{ij} = \sum_{l}^{m} N_{ij}^{\alpha} \alpha \qquad (2.38)$$

where l to m is the range of coordination number for ion pair, ij, considered and N_{ij}^{α} is the fraction of coordination number α.

2.13.5 Bond angle distributions.

In this investigation, we shall focus on the *bond angle distributions* for ion triplets which give an indication of how the constituent polyhedral units of a liquid connect with one another. Experimentally, they have been obtained in vitreous silica using Magic Angle Spinning NMR[49] although there are no recorded experimental distributions for the systems of particular interest in this study, $GeSe_2$ and $ZnCl_2$. Bond angle distributions are generated computationally by extracting triplets through identifying nearest neighbours of a given ion using the same cutoff used to identify the coordination environments, and calculating the angle between them. In MX_2 systems, the distributions calculated are MMM, MMX, MXM, XMX, XXM and XXX.

2.13.6 Coloured structure factors and radial distribution functions.

Total structure factors, obtainable from diffraction experiments, are illuminated once they are broken down to the respective partial structure factors. For example, the relative contributions to the FSDP are highlighted, with the cation-cation contribution usually being the strongest. In this thesis, we extend this principle to the partial structure factor and radial distribution function, by breaking down these functions according to certain "coloured" properties, either the network-connectivity as calculated by the number of

four-fold rings a cation is bonded to or by the coordination number. Previous calculations of the partial cation-cation coordination number structure factors in Al_2O_3, showed features such as phase separation, as indicated by a rise when k→0, which indicated a clustering of such species.[50] This analysis is focused on the cation-cation and cation-anion functions which are the main contributors to intermediate range order.

$$S_{\alpha\beta}^{ab} = \langle A_{\alpha}^{a*}(k) \cdot A_{\beta}^{b}(k) \rangle \qquad (2.39)$$

Three MX network connectivity functions (equation 2.40) and six MM network-connectivity functions (equation 2.41) are defined as

$$S_{MX}^{ab}(k) = \langle A_M^{a*} \cdot A_X(k) \rangle \qquad (2.40)$$

$$S_{MM}^{ab}(k) = \langle A_M^{\dot{a}}(k) \cdot A_M^{b}(k) \rangle \qquad (2.41)$$

where $ab = \{0,1,2\}$, the number of four-membered rings a cation is bonded to.
The partial cation-anion structure factor can be reconstituted according to the Ashcroft-Langreth formalism[47] by

$$S_{MX}(k) = \sqrt{c_0} S_{MX}^{0X}(k) + \sqrt{c_1} S_{MX}^{1X}(k) + \sqrt{c_2} S_{MX}^{2X}(k) \qquad (2.43)$$

Similarly, the partial cation-cation structure factor can be reconstituted by

$$S_{MM}(k) = c_0 \left(S_{MM}^{00}(k) - 1 \right) + c_1 \left(S_{MM}^{11}(k) - 1 \right) + c_2 \left(S_{MM}^{22}(k) - 1 \right) \qquad (2.44)$$
$$+ 2\sqrt{c_0 c_1} S_{MM}^{01}(k) + 2\sqrt{c_0 c_2} S_{MM}^{02}(k) + 2\sqrt{c_1 c_2} S_{MM}^{12}(k)$$

The corresponding equations according to the Faber-Zeeman formalism[51] are
$$S_{MX}(k) = c_0 S_{MX}^{0X}(k) + c_1 S_{MX}^{1X}(k) + c_2 S_{MX}^{2X}(k) \qquad (2.45)$$

$$S_{MM}(k) = c_0^2 \left(S_{MM}^{00}(k) - 1 \right) + c_1^2 \left(S_{MM}^{11}(k) - 1 \right) + c_2^2 \left(S_{MM}^{22}(k) - 1 \right) \qquad (2.46)$$
$$+ 2 c_0 c_1 S_{MM}^{01}(k) + 2 c_0 c_2 S_{MM}^{02}(k) + 2 c_1 c_2 S_{MM}^{12}(k)$$

2.14 Thermostats.

In this investigation, calculations are performed both in the isobaric-isothermal (NPT) and constant volume (NVT) ensembles. To keep constant temperature Nose-Hoover thermostats[52], later extended by Martyana,[53] are implemented. The required additional parameters are M thermostat variables $\zeta_1.......\zeta_M$, with conjugate momenta, $p_{\zeta_1}\cdots p_{\zeta_M}$. The implementation of the thermostats modifies the standard Newtonian equations of motion:

$$\dot{r}_i = \frac{p_i}{m_i} \tag{2.47}$$

$$\dot{p}_i = -\frac{\partial U(r)}{\partial r_i} - \frac{p_{\zeta 1}}{Q_1} p_i \tag{2.48}$$

$$\dot{\zeta}_k = \frac{p_{\zeta k}}{Q_k} \tag{2.49}$$

$$\dot{p}_{\zeta k} = G_k - \frac{p_{\zeta k+1}}{Q_{k+1}} p_{\zeta k} \tag{2.50}$$

$$\dot{p}_{\zeta M} = G_M \tag{2.51}$$

where the thermostat forces, G_k, are

$$G_1 = \sum_{i=1}^{N} \frac{p_i^2}{m_i} - g k_B T \tag{2.52}$$

$$G_k = \frac{p_{\zeta k-1}^2}{Q_{k-1}} - k_B T \; for \, k = 2....M \, , \tag{2.53}$$

where g is the number of degrees of freedom. Q_k is the effective mass which relates the magnitude of each thermostat force to its acceleration, and which determines a characteristic "relaxation" time scale over which the thermostat acts through a parameter τ:

$$Q_1 = g k_B T \tau^2 \tag{2.54}$$

$$Q_k = k_B T \tau^2 \; for \; k \neq 1$$

(2.55)

The term $\dfrac{p_{\zeta 1}}{Q_1}$ is a friction coefficient acting on all particle momenta, which has the

effect of coupling the system to a heat bath at the target temperature. This thermostat is

then thermostatted itself by the action of $p_{\zeta 2}$, which is thermostatted by $p_{\zeta 3}$ and so

on (a chain thermostat). In all simulations, τ is maintained at 10000 a.u.

2.15 Isobaric molecular dynamics.

The technique implemented for simulating constant pressure simulations using the PIM

was that developed by Wilson et al.[54] The constant pressure method of Andersen[55] was

extended by Parrinello and Rahman[56] to allow the simulation box to change shape as well

as size. We have implemented the equations of motion as given by Martyna et al[53]. The

ions and the barostats are both coupled to Nosé-Hoover chains of length 5.

The total stress tensor is given by

$$\Pi_{\alpha\beta}^{tot} = \frac{1}{V} \sum_i M_i \dot{r}_{i,\alpha} \dot{r}_{i,\beta} + \Pi_{\alpha,\beta}$$

(2.56)

where the configurational part of the tensor, $\Pi_{\alpha\beta}$, is obtained by:

$$-\frac{\partial U}{\partial h_{\alpha,\beta}} = \sum_\gamma \Pi_{\alpha\gamma} V h_{\beta\gamma}^{-1}$$

(2.57)

Here U is the total potential energy, V the cell volume, and h is the cell matrix, whose

elements are the components of vectors along the simulation cell edges. The rate of

change of the energy is highlighted by variation in h: in addition to the motion of ions are

the changes observed in the dipoles.

$$U \equiv U \left(\{ \boldsymbol{r}^i \}_{i=1,N}, \{ \boldsymbol{\mu}^i \}_{i=1,N} \right)$$

(2.58)

As the dipoles are calculated to their adiabatic value, the Hellman-Feynman theorem is utilised to write:

$$\frac{\partial U}{\partial h_{\alpha\beta}} = \sum_j \frac{\partial U}{\partial \boldsymbol{r}^j}(\{\boldsymbol{r}^i\}_{i=1,N}, \{\bar{\boldsymbol{\mu}}^i\}_{i=1,N}) \cdot \frac{\partial \boldsymbol{r}^i}{\partial h_{\alpha\beta}} \tag{2.59}$$

allowing the derivative of the dipoles with respect to the change in cell shape to be ignored. The long-range interactions are described by the Ewald method with a convergence parameter, η, set at $\eta r_c = 5.6$. In the Ewald construction the interaction energy is decomposed into real-space and reciprocal-space components where U^{real}, in the PIM, is a sum of pairwise addititive terms, which coverage at a range shorter than the simulation cell length, plus a Drude-like self-energy, which depends only on the dipoles and not on the ionic positions. Consequently, the real-space contributions to the stress tensor can be expressed in the standard virial form (i.e $\sim \sum_{ij,\,pairs} r_\alpha^{ij} f_\beta^{ij}$, where $\boldsymbol{f}^{ij}$ is the real space contribution). The reciprocal-space contribution was derived by developing the Appendix of Nose and Klein's paper which gives the reciprocal-space energy expression for a system of molecules with internal charges to charged, dipolar species. Expressions for the charge-charge, charge-dipole and dipole-dipole contributions are given in equations 2.61, 2.62, and 2.63 respectively.

$$U(\{\boldsymbol{r}^i\}_{i=1,N}, \{\mu^i\}_{i=1,N}) = U^{real}(\{\boldsymbol{r}^i\}_{i=1,N}, \{\mu^i\}_{i=1,N})$$
$$+ U^{recip}(\{\boldsymbol{r}^i\}_{i=1,N}, \{\mu^i\}_{i=1,N}) \tag{2.60}$$

Charge-charge

$$\Pi_{\alpha\beta}^{qq} = \frac{1}{2\pi V^2} \left\{ \sum_n Q(k_n) \sum_i q_i \cos(2\pi \boldsymbol{k}_n \cdot \boldsymbol{r}_i) \times \sum_j q_j \cos(2\pi \boldsymbol{k}_n \cdot \boldsymbol{r}_j) \right.$$
$$\left. + \sum_i q_i \sin(2\pi \boldsymbol{k}_n \cdot \boldsymbol{r}_i) \times \sum_j q_j \sin(2\pi \boldsymbol{k}_n \cdot \boldsymbol{r}_j) \right\}$$
$$\times \left[\delta_{\alpha\beta} - 2(1 + \pi^2 \eta^2 |k^2|) \right]$$

$$\tag{2.61}$$

where $Q(k_n) = e^{-\pi^2 |k_n|^2 \eta^2} / |k_n|^2$ with η the Ewald parameter, taken to be 5.0/L, where L is the shortest simulation length.

Charge-dipoles

$$\Pi_{\alpha\beta}^{q\mu}=\frac{1}{2\pi V^2}\sum_n{}' Q(k_n)2\left(\left\{-\sum_i q_i\cos(2\pi\,\boldsymbol{k}_n\!\cdot\!\boldsymbol{r}_i)\times\sum_j(2\pi\,\boldsymbol{k}_n\!\cdot\!\mu_j)\sin(2\pi\,\boldsymbol{k}_n\!\cdot\!\boldsymbol{r}_j)+\sum_i q_i\sin(2\pi\,\boldsymbol{k}_n\!\cdot\!\boldsymbol{r}_i)\right.\right.$$

$$\left.\times\sum_j(2\pi\,\boldsymbol{k}\!\cdot\!\mu_j)\cos(2\pi\,\boldsymbol{k}_n\!\cdot\!\boldsymbol{r}_j)\right\}\left\{\delta_{\alpha\beta}-2\left(\frac{1+\pi^2\eta^2|k_n|^2}{|k_n|^2}\right)k_{n,\alpha}k_{n,\beta}\right\}+\sum_i 2\pi\,k_{n,\alpha}\mu_{i,\beta}\cos(2\pi\,\boldsymbol{k}_n\!\cdot\!\boldsymbol{r}_i)$$

$$\left.\sum_j q_j\sin(2\pi\,\boldsymbol{k}_n\!\cdot\!\boldsymbol{r}_j)-\sum_i 2\pi\,k_{n,\alpha}\mu_{i,\beta}\sin(2\pi\,\boldsymbol{k}_n\!\cdot\!\boldsymbol{r}_i)\times\sum_j q_j\cos(2\pi\,\boldsymbol{k}_n\!\cdot\!\boldsymbol{r}_j)\right)$$

$$(2.62)$$

Dipole-dipole

$$\Pi_{\alpha\beta}^{\mu\mu}=\frac{1}{2\pi V^2}\sum_n{}' Q(k_n)\left\{\left(\sum_i(2\pi\,\boldsymbol{k}_n\!\cdot\!\mu_i)\cos(2\pi\,\boldsymbol{k}_n\!\cdot\!\boldsymbol{r}_i)\times\sum_j(2\pi\,\boldsymbol{k}_n\!\cdot\!\mu_j)\cos(2\pi\,\boldsymbol{k}_n\!\cdot\!\boldsymbol{r}_j)\right.\right.$$

$$+\left(\left\{\sum_j(2\pi\,\boldsymbol{k}_n\!\cdot\!\mu_j)\sin(2\pi\,\boldsymbol{k}_n\!\cdot\!\boldsymbol{r}_j)\right\}\right)$$

$$\left.\times\sum_j(2\pi\,\boldsymbol{k}\!\cdot\!\mu_j)\sin(2\pi\,\boldsymbol{k}_n\!\cdot\!\boldsymbol{r}_j)\right)\left[\delta_{\alpha\beta}-2\left(\frac{1+\pi^2\eta^2|k_n|^2}{|k_n|^2}\right)k_{n,\alpha}k_{n,\beta}\right]+2\sum_i 2\pi\,k_{n,\alpha}\mu_{i,\beta}\cos(2\pi\,\boldsymbol{k}_n\!\cdot\!\boldsymbol{r}_i)$$

$$\times\sum_j(2\pi\,\boldsymbol{k}\!\cdot\!\mu_j)\cos(2\pi\,\boldsymbol{k}_n\!\cdot\!\boldsymbol{r}_j)+2\sum_i 2\pi\,k_{n,\alpha}\mu_{i,\beta}\sin(2\pi\,\boldsymbol{k}_n\!\cdot\!\boldsymbol{r}_i)\times\sum_j(2\pi\,\boldsymbol{k}\!\cdot\!\mu_j)\sin(2\pi\,\boldsymbol{k}_n\!\cdot\!\boldsymbol{r}_j)\right\}$$

$$(2.63)$$

2.16 References.

[1] J. D. Bernal. *Nature*, **183**, 141, (1959).

[2] R. J. Bell and P. Dean. *Nature*, **212**, 1354, (1966).

[3] D. L. Evans and S. V. King. *Nature*, **212**, 1353, (1966).

[4] M. Wilson. *Phil. Trans. R. Soc. Lond. A,* **358**, 399, (2000).

[5] M. P. Allen and D. J. Tildesley. *Computer simulation of liquids*, Oxford Science Publications, New York, (1996).

[6] D. Frenkel and B. Smit. *Understanding Molecular Simulation- From Algorithms to Applications,* Academic Press, San Diego, (1996).

[7] R. Car and M. Parrinello. *Phys. Rev. Lett.*, **55**, 2471, (1985).

[8] J. P. Perdew and A. Zunger. *Phys. Rev. B*, **23**, 5048, (1981).

[9] J. P. Perdew, J. A. Chevary, S. H. Vosko, K. A. Jackson, M. R. Pederson, D. J. Singh and C. Fiolhais. *Phys. Rev B*, **46**, 6671, (1992).

[10] L. Pusztai and R. L. McGreevy. *J. Non-Cryst. Solids*, **117**, 627, (1990).

[11] A. Bassen, A. Lemke and H. Bertagnolli. *Phys. Chem., Chem. Phys*, **2**, 1445, (2000).

[12] A. Soper. *Phys. Rev B*, **72**, 104204, (2005).

[13] L. S. Ornstein and F. Zernike. *Proc. Acad. Sci. Amsterdam*, **17**, 793, (1914).

[14] J. S. Rowlinson. *Rep. Prog. Phys.*, **28**, 169, (1965).

[15] J. K. Percus and G. J. Yevick. *Phys. Rev.*, **110**, 1, (1958).

[16] P. Ballone, G. Pastore, J. S. Thakur and M. P. Tosi. *Physica B*, **142**, 294, (1986).

[17] H. Iyetomi, P. Vashishta and R. K. Kalia. *Phys. Rev. B,* **43**, 1726 (1991).

[18] L. Verlet. *Phys. Rev.*, **159,** 98, (1967).

[19] M. Wilson, U. Schönberger and M. W. Finnis. *Phys. Rev. B*, **54**, 9147, (1996).

[20] M. Wilson and P. A. Madden. *J. Phys. Condens. Matter*, **5**, 2687, (1993).

[21] M. Wilson and P. A. Madden. *Mol. Phys.*, **92**, 197, (1997).

[22] M. Wilson and P. A. Madden. *Mol. Phys.*, **72**, 3033, (1994).

[23] W. C. Swope, H. C. Andersen, P. H. Berens and K. R. Wilson. *J. Chem. Phys.*, **76**, 637, (1982).

[24] R. G. Dick and A. W. Overhauser. *Phys. Rev.*, **112**, 90, (1958).

[25] J. C. Slater and J. G. Kirkwood. *Phys. Rev.*, **37**, 602, (1931).

[26] G. Starkschall and R. G. Gordon. *J. Chem. Phys.*, **56**, 2801, (1978).

[27] D. Koutselos and E. A. Mason. *J. Chem. Phys.*, **85**, 2154, (1986).

[28] P. W. Fowler and P. A. Madden. *Phys. Rev. B*, **29**, 1035, (1984).

[29] K. T. Tang and J. P. Toennies. *J. Chem. Phys.*, **80**, 3726 (1984).

[30] S. Biggin and J. E. Enderby. *J. Phys, C.:Solid State Phys.*, **14**, 3129, (1981).

[31] C. Massobrio, A. Pasquarello and R. Car. *J. Am. Chem. Soc.*, **121**, 2943, (1999).

[32] P. A. Madden and M. A. Wilson. *Chem. Soc. Rev.*, **25**, 339, (1996).

[33] M. P. Tosi and F.G. Fumi. *J. Phys. Chem. Solids,* **25**, 45, (1964).

[34] M. Sprik and M. L. Klein. *J. Chem. Phys.*, **89**, 7558, (1998).

[35] P. W. Fowler and P. A. Madden. *Phys. Rev B*, **31**, 5443, (1985).

[36] C. Domene, P. W. Fowler, P. A. Madden, J. Xu, R. J. Wheatley and M. Wilson. *J. Phys. Chem. A*, **105**, 4136, (2001).

[37] R. P. Hurst. *Phys. Rev.*, **114**, 746, (1959).

[38] G. D. Mahan. *Solid State Ionics*, **1**, 29, (1980).

[39] C. Domene, P. W. Fowler, M .Wilson and P. A. Madden. *Mol. Phys.*, **100**, 3487, (2002).

[40] C. Domene, P. W. Fowler, P. Jemmer and P. A. Madden. *Chem. Phys. Lett.*, **299**, 51, (1999).

[41] P. P. Ewald. *Ann. Physik.*, **64,** 253, (1921).

[42] C. Massobrio, A. Pasquarello and R. Car. *Phys. Rev B*, **64**, 144205, (2001).

[43] S. R. Elliot. *J. Non-Cryst. Solids*, **182**, 40, (1995).

[44] A. C. Wright, R. A. Hulme, D. I. Grimley, R. N. Sinclair, S. W. Martin, D. L. Price and F. L. Galeener. *J. Non-Crystalline Solids*, **129**, 213, (1991).

[45] P. S. Salmon, R. A. Martin, P. E. Mason and G. J. Cuello. *Nature* (London), **435**, 75, (2005).

[46] M. Wilson and P. A. Madden. *Phys. Rev. Lett.*, **80**, 532, (1998).

[47] N. W. Ashcroft and D. C. Langreth. *Phys. Rev.*, **156**, 685, (1967).

[48] M. Celino and C. Massobrio. *Phys. Rev. Lett.,* **90**, 122502, (2003).

[49] E. Dupree and R. F. Pettifer. *Nature*, **308**, 523, (1984).

[50] M. Hemmati, M. Wilson and P. A. Madden. *J. Phys. Chem B*, **103**, 4023, (1999).

[51] T. E. Faber and J. M. Ziman. *Philos. Mag*, **11**, 153, (1965).

[52] S. Nosé and M. L. Klein. *Mol. Phys*. **50**, 1055, (1983).

[53] G. J. Martyna, D. J. Tobias, and M. L. Klein. *J. Chem. Phys.*, **101**, 4177, (1994).

[54] M. Wilson, F. Hutchinson and P. A. Madden. *Phys. Rev B*, **65**, 094109, (2002).

[55] H. C. Andersen. *J. Chem. Phys.*, **72**, 2384, (1980).

[56] M. Parrinello and A. Rahman. *Phys. Rev. Lett.*, **45**, 1196, (1980).

Chapter 3

Intermediate-range order in metal halides

3.1 Experimental background.

Zinc chloride possesses a number of interesting properties including high viscosity of the melt[1,2], low electrical conductivity[1], 'intermediate' strength glass-forming ability[3] and the presence of intermediate-range order (IRO) in the molten state.[4] Neutron diffraction experiments by Biggin and Enderby[4] in the early 1980's indicated the presence of IRO through the appearance of a first sharp diffraction peak (FSDP) at $k \sim 1 \text{Å}^{-1}$ in the total structure factor. This peak is widely attributed to density fluctuations in the *Zn-Zn* spatial correlations in the same region due to the FSDP observed in the cation-cation partial structure factor, $S_{ZnZn}(k)$[4,5]. This conclusion has been disputed in X-ray diffraction experiments by Neuefeind *et al*[6,7], claiming that the *Zn-Cl* correlation is primarily responsible for the FSDP.

Another notable feature is the similarity in the position of the principal peak for $g_{ZnZn}(r)$ and $g_{ClCl}(r)$ at $\sim 3.7 \text{Å}$. This contradicts the spatial ordering expected following simple Coulombic arguments where the nearest neighbour Zn-Zn separation would be larger than the corresponding anion-anion separation. Such ordering is observed in systems with larger cations[8] such as in $BaCl_2$. Table 3.1 shows the experimental information of the local coordination environments. X-ray diffraction experiments by Allen *et al*[9] indicate that molten $ZnCl_2$ is mainly comprised of $ZnCl_4^{2-}$ tetrahedra and that the presence of these units persist to high temperatures. Extended X-ray absorption fine structure (EXAFS) studies by Wong and Lytle[10] and later by Fillaux *et al*[11] yielded values for the Zn-Cl separation in liquid $ZnCl_2$ of 2.36Å and 2.29Å. The discrepancy between the two EXAFS experiments can be explained by the use of a six-coordinate reference crystal structure for the earlier experiment, the latter experiment using GNXAS data analysis program[12] requiring no such crystal reference. The liquid Zn-Cl coordination number varies depending on the experimental method, 5.1 for EXAFS[10] down to 3.9 for neutron scattering experiments[9] and between neutron diffraction experiments there is a variation of 0.7.[6,9]

First author (Reference)	Material	Technique	Separation			Coordination			$R=r_-/r_{+-}$
			Zn-Cl Å	Cl-Cl Å	Zn-Zn Å	Zn-Cl	Cl-Cl	Zn-Zn	
Imakoa (13)	Glass	X-ray	2.32	3.82		3.8	6		1.65
Desa (14)	Glass	Neutron	2.29	3.72	3.72	3.8	9.5	4	1.62
Wong (10)	Glass	EXAFS	2.34			5.2			N/A
Salmon(15)	Glass	Neutron	2.28	3.70	3.75	3.9	12	4	1.62
Wong (10)	Liquid	EXAFS	2.35			5.1			N/A
Fillaux (11)	Liquid	EXAFS	2.29						N/A
Triolo (16)	Liquid	X-ray	2.29	3.85	3.66	4	12	4	1.68
Biggin (4)	Liquid	Neutron	2.29	3.71	3.8	4.3	8.6	4.7	1.62
Allen (9)	Liquid	Neutron	2.29	3.79		3.9			1.66
Neuefeind (6)	Liquid	Neutron	2.33	3.77	3.8	4.6			1.62

Table 3.1 :Experimental results concerning the first coordination shell of $ZnCl_2$.

Raman spectroscopy studies on the divalent halides[17-23] show several key features with regards to structure, by linking specific Raman modes with particular structural arrangements. They have supported diffraction experiments in asserting that $ZnCl_2$ is primarily composed of tetrahedral units which persist into the liquid phase. The boson peak, a low-frequency peak linked with intermediate range-order, is found in crystalline ($39cm^{-1}$), glassy ($25cm^{-1}$) and liquid (10 cm^{-1} at $450^{\circ}C$) $ZnCl_2$[23], although over this range it weakens as temperature rises and disappears at $800^{\circ}C$. The nature of the temperature-dependent deterioration of the boson peaks has been suggested as an indicator of fragility.[24] The range of structures linked to the Raman modes found are based on:

1. Tetrahedral units linked through corner-sharing with modes attributed to isolated tetrahedral units ($(MX_4)^{2-}$, $v_{T_d} = 275$ cm^{-1}), units which form part a network ($(MX_{4/2})M$, $v_{1a}^B = 232$ cm^{-1}) and larger structural units comprised of four interconnected corner-sharing tetrahedral units ($(M_4X_6X_{4/2}M)$, $v_{1b}^B = 265$ cm^{-1}).[23]

2. Edge-sharing modes are also located, with peaks linked to units which form part of an edge-sharing chain ($(M_2X_2X_{4/2})M$, $v_1^E = 300$ cm^{-1}), designated "weak" for $ZnCl_2$, compared to "strong" for $BeCl_2$[25]. This links with theoretical work[26] on $BeCl_2$ and the experimental crystal structure for $BeCl_2$ which consists of edge-sharing chains.[27,28]

3. Terminal units such as $(MXX_{2/2})M$ which signify the presence of 3-coordinated M cations.[23]

The width of the Raman peaks (indicated by the full width half maximum-FWHM) for the ν_{T_d} vibrations appear significantly narrower (3.0cm^{-1}) for ZnBr$_2$ compared to ZnCl$_2$ (9.9cm^{-1}). This suggests a more open network for the latter which enables large amplitude vibrations. Neutron diffraction experiments[6] show that ZnBr$_2$ has a more intense FSDP than ZnCl$_2$. Whether this is due to significant structural differences or the smaller scattering length of Br (6.79 fm) compared to Cl (9.58 fm), resulting in a greater weighting of the $S_{ZnZn}(k)$ term (and, concomitantly, a larger contribution to FSDP) in F(k), is not known.

Magnesium chloride is a compound which contains a cation of similar ionic radius to zinc (0.86Å compared to the value of 0.88Å respectively) but displays vastly different properties such as weak glass forming ability, greater conductivity (2.0 Ω^{-1} cm^{-1} compared to 1 x 10^{-3} Ω^{-1} cm^{-1} for ZnCl$_2$)[29] and lower viscosity (2.2 cp against 4 x 10^3 cp).[29] Neutron diffraction[30,31] on molten MgCl$_2$ show a departure from tetrahedral coordination, as shown by the relative positions of the first peaks in the Mg-Cl and Cl-Cl partial radial distribution functions ($R=r_-/r_+$), where R=1.47, (a true tetrahedral value would be R=1.63). The difference in local coordination environment mirrors the observed ambient pressure, thermodynamically stable crystal structures. The predominant crystal phase for MgCl$_2$ is the *six-coordinate* CdCl$_2$ structure[32], whilst that for ZnCl$_2$ is the four-coordinate δ-ZnCl$_2$ structure.[33] Raman studies for liquid MgCl$_2$ emphasises the presence of [MgCl$_6$]$^{4-}$ units[18], where the basic lattice structure is predicted to persist into the liquid state, while Huang observes[19] smaller coordinated [MgCl$_4$]$^{2-}$ species.

Manganese chloride is another compound with an intermediate-sized cation whose structure has been studied by diffraction.[31,34] The results of the neutron diffraction experiment carried out by Biggin and Enderby[31] disagree significantly with an earlier X-ray diffraction experiment carried out by Ohno[34]: a Cl-Cl separation of 3.58Å[31] is obtained compared to the earlier value from X-ray diffraction of 4.10Å.[34] One notable feature of manganese chloride is the negative scattering length, b, of the cation and the effect this has on the total structure factor and the subsequent extrapolation of the partial quantities. For manganese, b=-3.73 fm, which results in the following weightings for the neutron total structure factor.[31]

$$F(k) = 0.015[S_{MnMn}(k)-1]+0.408[S_{ClCl}(k)-1]-0.159[S_{MnCl}(k)-1] \qquad (3.1)$$

This expression shows that the FSDP may be absent due to the near-negligible contribution of $S_{MnMn}(k)$ to $F(k)$, because of the small magnitude of b for manganese. The negative sign of the scattering length for manganese results also results in a *negative* contribution by $S_{MnCl}(k)$ to the FSDP in $F(k)$. The corresponding equation for the total radial distribution $G(r)$:

$$G(r) = 0.015[g_{MnMn}(r)-1]+0.408[g_{ClCl}(r)-1]-0.159[g_{MnCl}(r)-1] \qquad (3.2)$$

$g_{MnMn}(r)$ is unable to be extracted from the $G(r)$ due to its low weighting, and as a result there is no recorded experimental function for the Mn-Mn spatial correlations.

3.2 Computational studies.

Early experiments[4] suggested the use of ionic rigid-ion model potential(RIM) with no reference to polarisation effects would be satisfactory in modelling $ZnCl_2$. Early molecular dynamics simulations of zinc chloride used various forms of the Born-Huggins-Mayer potential[35-38]. They sought to reproduce such quantities as the total energy, ion separations and the partial radial distribution functions. In the work of Woodcock, Angell and Cheeseman (WAC)[35] only the Zn-Cl and Cl-Cl nearest neighbour separations could be reproduced to good accuracy. The nearest-neighbour Zn-Zn separation was significantly larger than that observed experimentally, fully consistent with simple Coulombic ordering. The models of Gardner and Hayes[36], in which partial charges were used, also failed to reproduce these features. Kumta *et al*[36] produce closer Zn-Zn separations using a rigid-ion model utilising an enormously large dispersion coefficient for the Zn-Zn interaction (C_{ZnZn}=7200 a.u).[37] compared to the range provided by electronic structure calculations[38,39] of 7.32-20.34 a.u. Abromo and Consolo[40] later adapted RIM potentials to the study of the structure of liquid $ZnBr_2$ and ZnI_2; unsurprisingly, the same deficiencies highlighted in the RIM models of $ZnCl_2$, such as an incorrect FSDP position and too large a zinc-zinc separation, were also present. It is apparent that these various attempts at closing the Zn-Zn separation are a substitution for some critical underlying physics which are inadequately represented by the RIM.

The polarisable-ion model (PIM)[41] devised by Wilson and Madden represented a significant improvement in modelling the $ZnCl_2$ structure, reproducing the closer zinc-

zinc separation and explaining the mechanistic origin of the FSDP.[42,43] Where the anion coordination is two (as expected for tetrahedral systems) then, as a consequence of the relatively high chloride ion polarisability (20 a.u)[44] and occupation of low symmetry sites, a large dipole will form. Neighbouring zinc ions are then able to move closer together, due to the shielding of their Coulombic charges by the presence of anion electron density. The reduction of Zn-Zn separation leads to the formation of two different length scales, observed in the $S_{ZnZn}(k)$ structure factor as a principal peak (at $k_{PP} \sim 2\text{Å}^{-1}$) and a FSDP at $k_{FSDP} \sim 1\text{Å}^{-1}$.[42,43] The shift of the principal peak to higher scattering angles (a small shift expected of in the principal peak position of $\sim 0.1\text{Å}^{-1}$ compared to a much larger changes in FSDP peak position) is indicative of the increase in density of the Zn-Zn correlation, due to the reduction of the Zn-Cl-Zn bond angle by anion polarisation, while the emergence of the FSDP is indicative of a decrease in Zn-Zn correlations over the longer range associated with intermediate range order in the region of 5-10Å.[42,43]

The representation of $S_{ZnZn}(k)$, and its relationship to $S_{ZnCl}(k)$ has shown significant differences in computational work, in addition to the variations observed experimentally. Implementation of the Monte-Carlo method on $ZnCl_2$ resulted in a strong FSDP in $S_{ZnZn}(k)$.[45] This was achieved by implementation of subsidiary potential forcing Zn-Zn correlation on a longer length scale.[45] A recent shell-model parameterisation of $ZnCl_2$ resulted in good agreement with, in contrast to other models, the Zn-Zn separation.[46] In reciprocal space, a shoulder rather than a FSDP appears in $S_{ZnZn}(k)$ while a clearer FSDP is observed in $S_{ZnCl}(k)$.

Reverse Monte-Carlo simulations by McGreevy and Pusztai[47] have reproduced the experimental structure factors and radial distribution functions for molten magnesium chloride. They also show important differences between the two- and three-body correlations of $MgCl_2$ and $ZnCl_2$. The Zn-Cl-Zn bond angle distribution is closer to tetrahedral values, while the corresponding distribution for $MgCl_2$ is closer to octahedral geometry around the cation. While the calculated radial distributions of both systems display glassy behaviour with many peaks observed, in $g_{MM}(r)$ and $g_{MX}(r)$ for both systems, it is noticeable that substantially smaller minima are observed between the principal and second peaks in $ZnCl_2$, although not for $g_{XX}(r)$ where it is similar to that observed in $MgCl_2$. As yet, no effective ionic pair potential has been reported for magnesium chloride.

The p^6 configuration of the lighter magnesium ion is more conducive to the use of

electronic crystal structure calculations compared with the heavier d^{10} zinc. Calculations by Harrison and Saunders[48] showed the importance of including Cl-Cl dispersion in stabilising the layer structure in the crystal state. Theoretical studies concerning the liquid structure for $MnCl_2$ have not been reported.

3.3 Simulation details

The central cell used in all calculations in this chapter consists of 999 ions (333 cations and 666 anions). The initial configuration for the $ZnCl_2$ PIM parameterisation was obtained from a previous set of calculations using the model of Wilson and Madden[43] with the parameters given in table 3.3. The advantage of using a related liquid configuration is that there is a greater certainty in maintaining liquid-like properties over melting from a crystal structure. MD simulations were carried out at elevated temperatures of 1500K, well above the melting temperature, to equilibrate the configuration for the respective $ZnCl_2$, $MgCl_2$ and ZnX_2 models dealt with in this chapter.

For each run involved in the parameter search of $ZnCl_2$ and $MgCl_2$, smaller time-scale simulations of 30 ps were carried out. The efficacy was determined by observing changes in density and radial distribution function peak positions. Structural quantities were obtained from a MD run of 60 ps at zero pressure and a temperature of 800K using an NPT ensemble and are discussed in sections 3.5-3.6. The average cell size in the simulation was 31.36Å corresponding to a liquid density of 2.42 g/cm^3, within 1% of the experimental liquid density of 2.436 g/cm^3.[53]

The initial configuration for the parameter search for the $MgCl_2$ potential was taken from the final configurations from the simulations run on the new $ZnCl_2$ PIM model. To compare the structural properties of the new $MgCl_2$ PIM model with the experimental total structure factors, the temperature was set at 1000K and the average cell size was 31.50Å, matching experimental density (1.67 g/cm^3). An equilibration run of 30 ps was carried followed by a simulation of 60 ps under NPT conditions from which structural quantities were extracted and discussed in section 3.7.

For the calculations on ZnX_2 materials discussed in section 3.8, the starting configuration was derived from the $ZnCl_2$ PIM model developed in section 3.3. The cell size was fixed at 31.36Å and the temperature maintained at 800K. Simulations were carried out increasing values of the short-range repulsion parameter B_{XX}, increased,

stepwise from 107 a.u to values of 147 a.u, 207 a.u, 307 a.u, 407 a.u and 607 a.u. Starting from B_{XX}=107 a.u and ending with B_{XX}=607 a.u, effective anion-anion separations, measured by the position of the principal peak in $g_{XX}(r)$, of 3.67Å, 3.76Å, 3.79Å, 3.81Å, 3.83Å and 3.84Å were produced. At each effective anion-anion separation, an equilibration run was undertaken for 30 ps and a further simulation runs of 60 ps undertaken under NVT conditions from which structural data was collected.

3.4 Construction of $ZnCl_2$ and $MgCl_2$ PIM potentials.

The potential models used in this investigation were derived from a previous parametrisation of the PIM for $ZnCl_2$.[43] There were several deficiencies with the old parameter set. For example, the ambient pressure experimental density was only obtained at simulation pressures of ~2 GPa. When taken down to lower pressures, as well as the expected decrease in density, peaks signifying a separate edge-and corner sharing in $g_{ZnZn}(r)$ were present. This contrasts with radial distribution functions in experiment $ZnCl_2$ where a single peak defines the cation correlation over this range. Furthermore, at simulation pressures lower than ~1.5 GPa the model became unstable. The initial parameter search focussed on two aspects: controlling the stability of the model at lower pressures and matching experimental density. The stability of the model at lower pressures was controlled by the short range damping parameter, where c was amended from a value to c=1.0 to c=1.4. Although the model was stabilised at zero pressure, the density of the model was significantly lower than that observed experimentally. Initial attempts at reducing the density by perturbing the short-range parameters failed to increase the density by a suitable amount. Experimental density was achieved by basing the Fumi-Tosi parameters on those used by Woodcock, Angell and Cheeseman, as shown in table 3.2. The initial values of the dispersion coefficients were derived from the Slater-Kirkwood formula (equation 3.3), which link the dispersion coefficients with ion polarisabilities[49]:

$$C_6^{ij} = \frac{\frac{3}{2}\alpha_i\alpha_j}{((\frac{\alpha_i}{p_i})^{\frac{1}{2}}+(\frac{\alpha_j}{p_j}))^{\frac{1}{2}}} \qquad (3.3)$$

α and p represent the polarisability and effective electron number of the ions. The effective electron number has been proved to be constant over an isoelectronic series.[50]

These parameters were perturbed until the closest match with experimental radial distribution peak positions and experimental density at 800K (2.412 g/cm^6) could be obtained. The final, old and Woodock, Angell and Cheeseman (WAC) parameter sets[35] are listed in table 3.3.

ij	α_i (a.u)	α_j (a.u)	p_i	p_j	C_{ij}^{CALC} (a.u)	C_{ij}^{PIM} (a.u)
ClCl	20	20	5.90	5.90	163	183
ZnCl	2.85	20	4.12	5.90	32.00	80
ZnZn	2.85, 5.5	2.85, 5.5	4.12	4.12	7.32, 20.34	40
MgCl	0.49	20	4.449	5.90	0.54	18.94
MgMg	0.49	0.49	4.449	4.449	2.26	2.2

Table 3.2: Related values in calculation of dispersion coefficients through the Slater-Kirkwood formula. p_i are obtained from Koutselos[50]. Polarisabilities: Cl$^-$ (from Fowler and Madden]; Zn^{2+} (2.85 a.u) from Mahan[38], Zn^{2+} (5.5 a.u) from Pyper[39]; Mg^{2+} (0.49a.u) from Mahan[52]. C_{ij}^{CALC} and C_{ij}^{PIM} refer to the dispersion coefficient values obtained from calculation from quantities in columns 1-4 and those obtained after the parameter search respectively.

One advantage of using simple potential models is the ease of transferability. A MgCl$_2$ potential model was produced by adjusting the FT parameters from the new ZnCl$_2$ PIM to better correlate with the radial distribution function peak positions obtained in neutron diffraction experiments.[31] The parameters controlling polarisability {b,c, α} were maintained due to the similar size of the cations used and the presence of the same anion. Zn^{2+} is a d^{10} cation while Mg^{2+} is p^6. Electronic structure calculations have shown the environmental dependence of the cation polarisability[51] in Zn^{2+}, greater than that for magnesium. The value of the zinc dipole polarisability is calculated as 5.5 a.u[39] (in addition, there is an older calculated value of 2.85 a.u[38]) far exceeding the value of 0.49 a.u[52] for magnesium, and results in differences for the dispersion coefficients involving the metal ion (table 3.2).

ij	PIM (new)		PIM(old)		WAC	
	B_{ij}	a_{ij}	B_{ij}	a_{ij}	B_{ij}	a_{ij}
ClCl	87	1.5564	8.00	1.00	63.00	1.5664
ZnCl	43.71	1.6000	48.00	1.56	43.17	1.5664
ZnZn	27	1.5564	27	1.60	27	1.5664
ClCl	63	1.5564				
MgCl	51.72	1.6000				
MgMg	27	1.5564				

Table 3.3: Parameters for $ZnCl_2$ and $MgCl_2$ potentials (Columns 2-3). Columns 4-5 and 6-7 show the different parameters, obtained respectively from a previous PIM used and the Woodcock, Angell and Cheeseman (WAC) potential to describe the short-range Zn-Cl and Cl-Cl interactions. All values are in atomic units.
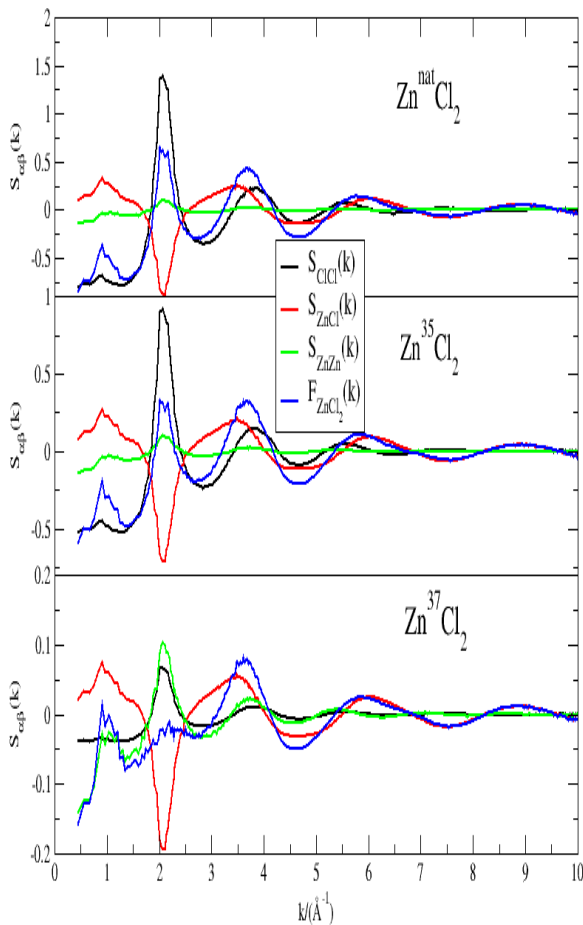
Figure 3.1: Simulated total and partial structure factors for $ZnCl_2$. Black line; $S_{ClCl}(k)$; red line, $S_{ZnCl}(k)$; green line, $S_{ZnZn}(k)$; blue line, F_{ZnCl_2}. For figures 3.1 and 3.2 the isotopes from top to bottom are; (a) ^{nat}Cl (b) ^{35}Cl (c) ^{37}Cl.
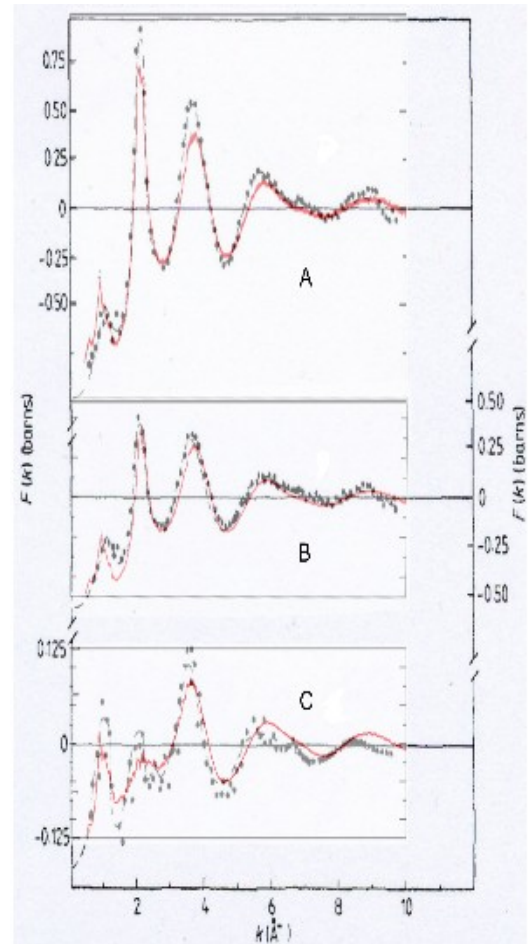
Figure 3.2: Calculated and experimental (from Biggin and Enderby[31]) total structure factors of $ZnCl_2$. Colour code: black data points, experimental; red line, calculated.

3.5 Total and partial structure factors of ZnCl$_2$.

Figure 3.1 shows the experimental[1] and calculated $F_{ZnCl_2}(k)$. The peak around the region 3.5Å^{-1} represents the short range topological order associated with excluded volume effects. At lower k values, the peak at k ~2 Å^{-1} indicates nearest neighbour bond ordering in real space. The characteristic FSDP, indicating intermediate range order, is observable in the k~1 Å^{-1} region .

The calculated total structure factors in figure 3.2 are in excellent agreement with the investigation carried out by Biggin and Enderby.[4] Figure 3.1 shows the breakdown of the three isotopically weighted total scattering factors, into the three individual weighted partial factors. The different weightings of the structure factors (given in table 3.4) are a result of the relative scattering properties of ^{35}Cl, ^{37}Cl and ^{nat}Cl (coherent neutron scattering lengths of 2.6, 11.8, 9.58 fm respectively) which explain the very different shapes of the experimental total scattering functions. The principal peak at 2 Å^{-1} is relatively strong for $F_{Zn^{35}Cl_2}(k)$ as it is dominated by $S_{ClCl}(k)$, whereas in $F_{Zn^{37}Cl_2}(k)$ this peak is largely suppressed by competition between $S_{ClCl}(k)$ and $S_{ZnCl}(k)$. Where the calculated F(k) differs from the experimental F(k) is in failing to replicate the deep trough in-between the FSDP and the principal peak in $F_{Zn^{37}Cl_2}(k)$ (conversely, for $F_{Zn^{35}Cl_2}(k)$, the intensity becomes too large here). Furthermore, the FSDP in $F_{Zn^{nat}Cl_2}(k)$ is discernibly larger than that observed in $F_{Zn^{35}Cl_2}(k)$ suggesting the model overemphasises the contribution of $S_{ZnCl}(k)$ to the FSDP.

	Individual PSF weighting factors (barns/sr/atom)		
Isotope	Zn-Zn	Zn-Cl	Cl-Cl
^{35}Cl	0.0358	0.2929	0.5982
^{nat}Cl	0.0358	0.2253	0.3541
^{37}Cl	0.0358	0.0837	0.0489

Table 3.4: Partial structure factor weightings for different isotopic combinations of ZnCl$_2$.

The contribution of $S_{ZnCl}(k_{FSDP})$ to the FSDP in F(k) is stronger than that of $S_{ZnZn}(k_{FSDP})$. This interpretation falls in between the conclusions of experimental observations of Neuefeind[6,7] and Biggin and Enderby[4] which display a dominant $S_{ZnCl}(k_{FSDP})$ and

$S_{ZnZn}(k_{FSDP})$ contribution to $F(k_{FSDP})$ respectively. In the next section, we will highlight the methods used by Neuefeind[6,7] to extract the partial structure factors for $ZnCl_2$.

3.6   Extraction methods of partial structure factors for $ZnCl_2$.

Early neutron diffraction experiments on molten salts showed that the partial structure factors could be extracted through the method of isotopic substitution. This method requires for n number of experiments to extract n(n+1) partial structure factors for a n-component liquid. Early neutron diffraction experiments were limited to momentum transfers of ~10Å and errors attributed to water contamination. High energy X-ray diffraction experiments[7] enable greater real-space resolution but have to be combined with neutron-diffraction experiments to extract partial information due to the invariability of form factors with changes in isotope identity. Due to the higher energy used (around 100 keV, far above the K edge) absorption is predicted to be reduced by three orders of magnitude compared to earlier X-ray diffraction experiments.[16] As neutron diffraction experiments are costly and certain isotopic mixtures may be hard to obtain, methods of combining X-ray and neutron diffraction studies have been utilised to extract information on the underlying partial pair structure with combine fewer than n neutron diffraction experiments and increased accuracy. The first method[7] combines X-ray and neutron diffraction data to eliminate one partial structure factor as described by the function $d_{j'k'}(k)$. $d_{j'k'}(k)$ is the linear combination of the scattering functions obtained from X-ray and neutron scattering functions, i(k) and S(k) which are defined as:

$$i(k) = \frac{\sum_i \sum_j^{uc} f_i f_j s_{ij}}{\left(\sum_i^{uc} f_i\right)^2} \tag{3.4}$$

$$S(k) = \frac{\sum_i \sum_j^{uc} b_i b_j s_{ij}}{\left(\sum_i^{uc} b_i\right)^2} \tag{3.5}$$

where f_i and b_i are the form factors and coherent neutron scattering lengths respectively. Linear combinations of i(k) and S(k) eliminate one of the partial structural correlations (defined by the ion pair j'k').

$$d_{j'k'}(k) = f_{j'} f_{k'} \left\{ \sum_i^{uc} b_i \right\}^2 S(k) - b_{j'} b_{k'} \left\{ \sum_i^{uc} f_i \right\}^2 i(k)$$

(3.6)

$$= f_{j'} f_{k'} \sum_i^{uc} \sum_j^{uc} b_i b_j S_{ij}(k) - b_{j'} b_{k'} \sum_i^{uc} \sum_j^{uc} f_i f_j S_{ij}(k)$$

(3.7)

$$= \sum_{jk \neq j'k'} \left\{ f_{j'} f_{k'} b_j b_k - b_{j'} b_{k'} f_k f_j \right\} S_{jk}(k)$$

(3.8)

Note that the jk=j'k' term could be kept from the last equation, but is zero.

Now, define

$$d_{j'k'}^{j''k''}(k) = \frac{d_{j'k'}(k)}{f_{j'} f_{k'} b_{j''} b_{k''} - b_{j'} b_{k'} f_{j''} f_{k''}}$$

(3.9)

which effectively normalises $d_{j'k'}^{j''k''}(k)$

As an example, $d_{ZnZn}^{ClCl}(k)$ ($j'k' = ZnZn$ and $j''k'' = ClCl$):

$$d_{ZnZn}(k) = \left\{ f_{Zn} f_{Zn} b_{Zn} b_{Cl} - b_{Zn} b_{Zn} f_{Zn} f_{Cl} \right\} S_{ZnCl}(k) + \left\{ f_{Zn} f_{Zn} b_{Cl} b_{Cl} - f_{Zn} f_{Zn} b_{Cl} b_{Cl} \right\} S_{ClCl}(k)$$

(3.10)

$$d_{ZnZn}^{ClCl}(k) = \frac{\left\{ f_{Zn}^2 b_{Zn} b_{Cl} - b_{Zn}^2 f_{Zn} f_{Cl} \right\} S_{ZnCl}(k) + \left\{ f_{Zn}^2 b_{Cl} b_{Cl} - b_{Zn}^2 f_{Cl} f_{Cl} \right\} S_{ClCl}(k)}{f_{Zn}^2 b_{Cl}^2 - b_{Zn}^2 f_{Cl}^2}$$

(3.11)

$$= \left\{ \frac{f_{Zn}^2 b_{Zn} b_{Cl} - b_{Zn}^2 f_{Zn} f_{Cl}}{f_{Zn}^2 b_{Cl}^2 - b_{Zn}^2 f_{Cl}^2} \right\} S_{ZnCl}(k) + S_{ClCl}(k)$$

(3.12)

In summary, the three functions considered are

$$d_{ZnZn}^{ClCl}(k) = A S_{ZnCl}(k) + S_{ClCl}(k)$$

(3.13)

$$d_{ZnCl}^{ClCl}(k) = B S_{ZnZn}(k) + S_{ClCl}(k)$$

(3.14)

$$d_{ClCl}^{ZnZn}(k) = C S_{ZnCl}(k) + S_{ZnZn}(k)$$

(3.15)

In our calculations, we replicate the derivation of these terms using our configurations from a similar temperature run of 600K. Figure 3.3 shows these three functions along with the (weighted) breakdowns in terms of respective pairs of partial structure factors. Both $d_{ZnZn}^{ClCl}(k)$ and $d_{ZnCl}^{ClCl}(k)$ appear similar to those obtained from experiment (figure 5 in [7]). For $d_{ZnCl}^{ClCl}(k)$ the simulated function shows a small indentation at $k \sim 1Å^{-1}$, reflecting the negative contribution of $S_{ZnZn}(k_{FSDP})$, whilst the experimentally-obtained function (^{nat}Cl) shows a small maximum at the same scattering angle. It is clear, however, that these features arise from the subtle interplay of the two underlying partial structure factors, shown in figure 3.4, which near-cancel in this k region. Analogous comments apply to $d_{ZnZn}^{ClCl}(k)$, which shows a significant difference between the simulated and experimental functions at $k \sim 2Å^{-1}$ (i.e. in the region associated with the principal peak).
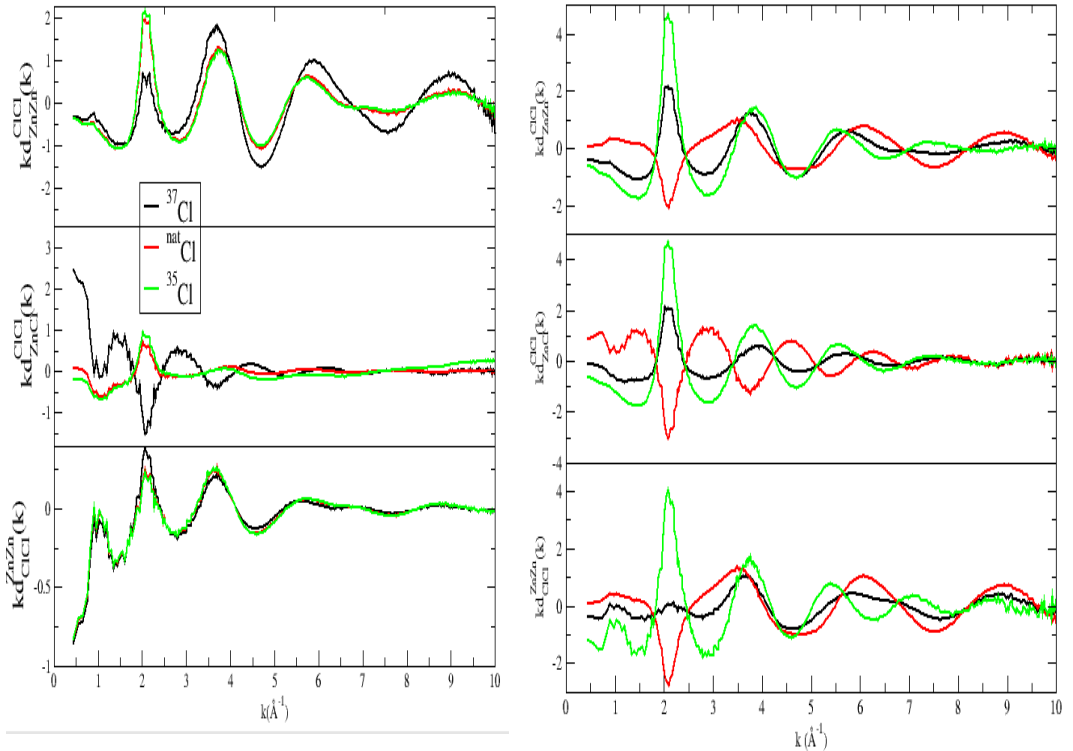
Figure 3.3: Difference functions, $d_{jk}(k)$, obtained by equations 3.13-3.15. The variation of $d_{jk}(k)$ with isotopic substitution is highlighted; black line, ^{37}Cl; red line, ^{nat}Cl; green line, ^{35}Cl. For both figures 3.3 and 3.4: Top, $d_{ZnZn}^{ClCl}(k)$; middle, $d_{ZnCl}^{ClCl}(k)$; bottom, $d_{ClCl}^{ZnZn}(k)$.

Figure 3.4: Breakdown of difference functions, $d_{jk}(k)$, into the constituent partial structure factors. Red line, weighted structure factor (with coefficients A, B and C given in table 3.5 used in equations 3.13-3.15) terms; green line, partial structure factor with the full weighting respectively.

In the experimentally-obtained function the feature at $k \sim k_{PP}$ appears as a trough whilst in the simulated function it appears as a peak. Again, however, this feature arises from the near cancellation of the principal peaks in $S_{ZnCl}(k)$ and $S_{ZnZn}(k)$.

Figure 3.3 shows that that the form of $d_{j'k'}(k)$ depends heavily on the isotope used in the neutron diffraction experiment. $d_{ZnCl}^{ClCl}(k)$ displays a significantly different form with the ^{37}Cl isotope where there is an inversion of the principal peak and it displays a strong inverted FSDP. When the ^{37}Cl isotope is used, the weighting (given in table 3.5), B, in equation 3.14 becomes strongly negative, leading to $S_{ZnZn}(k)$ dominating the $d_{ZnCl}^{ClCl}(k)$ term.

	Weighting factors		
Isotope	A $\left(d_{ZnZn}^{ClCl}(k)\right)$	B $\left(d_{ZnCl}^{ClCl}(k)\right)$	C $\left(d_{ClCl}^{ZnZn}(k)\right)$
^{35}Cl	0.391	-0.861	0.454
^{nat}Cl	0.452	-1.045	0.433
^{37}Cl	0.868	-3.568	0.288

Table 3.5: Weighting factors for difference functions $d_{j'k'}(k)$ for coefficients A, B, C in equation 3.13-3.15.

The second method Neuefeind used[6] assumes a detailed knowledge of one partial structure factor, $S_{ZnCl}(k)$, claimed to be of greater accuracy than that derived from the Biggin and Enderby experiment,to produce the other two with knowledge of X-ray and neutron diffraction experiments. The equations derived by Neuefeind for $S_{ClCl}(k)$ and $S_{ZnZn}(k)$ respectively are:

$$S_{ClCl} = \frac{\frac{^{(x)}(d\sigma/d\Omega)}{f_{Zn}^2} - \frac{^{(n)}(d\sigma/d\Omega)}{b_{Zn}^2} - S_{ZnCl}\left[\frac{4f_{Cl}}{f_{Zn}} - \frac{4b_{Cl}}{b_{Zn}}\right]}{\left[\frac{4f_{Cl}^2}{f_{Zn}^2} - \frac{4b_{Cl}^2}{b_{Cl}^2}\right]} \tag{3.16}$$

$$S_{ZnZn} = \frac{\frac{^{(x)}(d\sigma/d\Omega)}{f_{Cl}^2} - \frac{^{(n)}(d\sigma/d\Omega)}{b_{Cl}^2} - S_{ZnCl}\left[\frac{4f_{Zn}}{f_{Cl}} - \frac{4b_{Zn}}{b_{Cl}}\right]}{\left[\frac{f_{Zn}^2}{4f_{Cl}^2} - \frac{b_{Zn}^2}{4b_{Cl}^2}\right]} \tag{3.17}$$

Here, we shall define both these functions by the methods they are obtained experimentally (by Neuefeind[6]) and computationally (in this study). The neutron scattering function is defined as:

$$S^n(Q) = \frac{\frac{(d\sigma)}{(d\Omega)} - \sum_i v_i b_i^2}{\left(\sum_i v_i b_i\right)^2} + 1 \qquad (3.18)$$

and the X-ray scattering function is defined as:

$$S^X(k) = \frac{\left(\frac{d\sigma}{d\Omega}\right)^X / \sigma_{el} - \sum_i v_i f_i^2}{\left(\sum_i v_i f_i\right)^2} + 1 = i(k) + 1 \qquad (3.19)$$

where $k = (4\pi/\lambda)\sin(\theta)$, $\left(\frac{d\sigma}{d\Omega}\right)$ is the coherent differential cross section per unit of composition, b_i is the coherent scattering length, f_i is the X-ray form factor, σ_{el} is the scattering cross-section of the free electron, v_i is the stoichiometric coefficient of the atom i, and N_{uc} is the number of distinct atoms in the unit of composition, $ZnCl_2$.

$$S^{(n/X)}(k) = \sum_{ij} \omega_{ij}(k) S_{ij}(k), \qquad (3.20)$$

where $\omega_{ij} = \frac{v_i v_j f_i(k) f_j(k)}{\left(\sum_i v_i f_i\right)^2}(2 - \delta_{ij})$ for X-rays $\qquad (3.21)$

and $\omega_{ij} = \frac{v_i v_j b_i b_j}{\left(\sum_i v_i b_i\right)^2}(2 - \delta_{ij})$ for neutrons. $\qquad (3.22)$

Equation 3.18 rearranges to

$$(S^n(k) - 1)\left(\sum_i v_i b_i\right)^2 = \left(\frac{d\sigma}{d\Omega}\right)^n - \sum_i v_i b_i^2 \qquad (3.23)$$

Expand the summation

$$(S^n(k) - 1)(v_{Cl}^2 b_{Cl}^2 + v_{Zn}^2 b_{Zn}^2) = \left(\frac{d\sigma}{d\Omega}\right)^n - v_{Cl} b_{Cl}^2 - v_{Zn} b_{Zn}^2, \qquad (3.24)$$

giving,

$$S^n(k) = \frac{\left(\frac{d\sigma}{d\Omega}\right)^n - 2b_{Cl}^2 - b_{Zn}^2}{(4b_{Cl}^2 + b_{Zn}^2)} + 1 \qquad (3.25)$$

Equation 3.20 leads to:

$$S^n(k) = \sum_{ij} \frac{v_i v_j b_i b_j}{\left(\sum_i v_i f_i\right)^2} (2 - \delta_{ij}), \, S_{ij}(k),$$ (3.26)

$$= \frac{b_{Zn}^2 v_{Zn}^2 S_{ZnZn}(k) + b_{Cl}^2 v_{Cl}^2 S_{ClCl}(k) + 2 b_{Cl} b_{Zn} v_{Cl} v_{Zn} S_{ZnCl}(k)}{4 b_{Cl}^2 + b_{Zn}^2}$$ (3.27)

$$= \frac{b^2 S_{ZnZn}(k) + 4 b_{Cl}^2 S_{ClCl}(k) + 4 b_{Cl} b_{Zn} S_{ZnCl}(k)}{4 b_{Cl}^2 + b_{Zn}^2}$$ (3.28)

$$\frac{\left(\frac{d\sigma}{d\Omega}\right)^n - 2 b_{Cl}^2 - b_{Zn}^2}{4 b_{Cl}^2 + b_{Zn}^2} + 1 = \frac{b_{Zn}^2 S_{ZnZn}(k) + 4_{Cl}^2 S_{ClCl}(k) + 4 b_{Cl} b_{Zn} S_{ZnCl}(k)}{4 b_{Cl}^2 + b_{Zn}^2}$$ (3.29)

$$\left(\frac{d\sigma}{d\Omega}\right)^n - 2 b_{Cl}^2 - b_{Zn}^2 + 4 b_{Cl}^2 + b_{Zn}^2 = b_{Zn}^2 S_{ZnZn}(k) + 4 b_{Cl}^2 S_{ClCl}(k) + 4 b_{Cl} b_{Zn} S_{ZnCl}(k),$$ (3.30)

$$\left(\frac{d\sigma}{d\Omega}\right)^n + 2 b_{Cl}^2 = b_{Zn}^2 S_{ZnZn}(k) + 4 b_{Cl}^2 S_{ClCl}(k) + 4 b_{Cl} b_{Zn} S_{ZnCl}(k),$$ (3.31)

and so,

$$S_{ZnZn}(k) = \frac{\left(\frac{d\sigma}{d\Omega}\right)^n + 2 b_{Cl}^2 - 4 b_{Cl}^2 S_{ClCl}(k) - 4 b_{Cl} b_{Zn} S_{ZnCl}(k)}{b_{Zn}^2}$$ (3.32)

with the X-ray equivalent

$$S_{ZnZn}(k) = \frac{\left(\frac{d\sigma}{d\Omega}\right)^X + 2 f_{Cl}^2 - 4 f_{Cl}^2 S_{ClCl}(k) - 4 f_{Cl} f_{Zn} S_{ZnCl}(k)}{f_{Zn}^2}$$ (3.33)

So, we are now in a position to eliminate $S_{ZnZn}(k)$ by subtracting equation 3.32 from equation 3.33, giving

$$b_{Zn}^2 \left(\frac{d\sigma}{d\Omega}\right)^X + 2 f_{Cl}^2 b_{Zn}^2 - 4 f_{Cl}^2 b_{Zn}^2 S_{ClCl}(k) - 4 f_{Cl} f_{Zn} b_{Zn}^2 S_{ZnCl}(k) = f_{Zn}^2 \left(\frac{d\sigma}{d\Omega}\right)^n$$
$$+ 2 b_{Cl}^2 f_{Zn}^2 - 4 b_{Cl}^2 f_{Zn}^2 S_{ClCl}(k) - 4 b_{Cl} b_{Zn} f_{Zn}^2 S_{ZnCl}(k)$$ (3.34)

Make $S_{ClCl}(k)$ the subject,

$$S_{ClCl}(k)\{4f_{Cl}^2 b_{Zn}^2 - 4b_{Cl}^2 f_{Zn}^2\} = b_{Zn}^2 \left(\frac{d\sigma}{d\Omega}\right)^X + 2f_{Cl}^2 b_{Zn}^2 - 4_{Cl} f_{Zn} b_{Zn}^2 S_{ZnCl}(k)$$
$$-f_{Zn}^2 \left(\frac{d\sigma}{d\Omega}\right)^n - 2b_{Cl}^2 f_{Zn}^2 + 4b_{Cl} b_{Zn} f_{Zn}^2 S_{ZnCl}(k) \tag{3.35}$$

To retain consistency with Neuefeind, notice that

$$\frac{4f_{Cl}^2}{f_{Zn}^2} - \frac{4b_{Cl}^2}{b_{Zn}^2} = 4f_{Cl}^2 b_{Zn}^2 - \frac{4b_{Cl}^2 f_{Zn}^2}{f_{Zn}^2 b_{Zn}^2} \tag{3.36}$$

which allows equation 3.35 to be written as

$$f_{Zn}^2 b_{Zn}^2 \left(\frac{4f_{Cl}^2}{f_{Zn}^2} - \frac{4b_{Cl}^2}{b_{Zn}^2}\right) S_{ClCl}(k) = b_{Zn}^2 \left(\frac{d\sigma}{d\Omega}\right)^X + 2f_{Cl}^2 b_{Zn}^2 - 4f_{Cl} f_{Zn} b_{Zn}^2 S_{ZnCl}(k)$$
$$-f_{Zn}^2 \left(\frac{d\sigma}{d\Omega}\right)^n - 2b_{Cl}^2 f_{Zn}^2 + 4b_{Cl} b_{Zn} f^2 S_{ZnCl}(k) \tag{3.37}$$

and so

$$\left(\frac{4f_{Cl}^2}{f_{Zn}^2} - \frac{4b_{Cl}^2}{b_{Zn}^2}\right) S_{ClCl}(k) = \frac{\left(\frac{d\sigma}{d\Omega}\right)^X}{f_{Zn}^2} + \frac{2f_{Cl}^2}{f_{Zn}^2} - \frac{4f_{Cl} f_{Zn} b_{Zn}^2}{f_{Zn}^2 b_{Zn}^2} S_{ZnCl}(k) \tag{3.38}$$

$$-\frac{\left(\frac{d\sigma}{d\Omega}\right)^n}{b_{Zn}^2} - \frac{2b_{Cl}^2}{b_{Zn}^2} + \frac{4b_{Cl} b_{Zn} f_{Zn}^2}{f_{Zn}^2 b_{Zn}^2} S_{ZnCl}(k) \tag{3.39}$$

$$= \frac{\left(\frac{d\sigma}{d\Omega}\right)^X}{f_{Zn}^2} - \frac{\left(\frac{d\sigma}{d\Omega}\right)^n}{b_{Zn}^2} + \frac{2f_{Cl}^2}{f_{Zn}^2} - \frac{2b_{Cl}^2}{b_{Zn}^2} - \frac{4f_{Cl}}{f_{Zn}} S_{ZnCl}(k) + \frac{4b_{Cl}}{b_{Zn}} S_{ZnCl}(k) \tag{3.40}$$

$$= \frac{\left(\frac{d\sigma}{d\Omega}\right)^X}{f_{Zn}^2} - \frac{\left(\frac{d\sigma}{d\Omega}\right)^n}{b_{Zn}^2} - S_{ZnCl}(k)\left\{\frac{4f_{Cl}}{f_{Zn}} - \frac{4b_{Cl}}{b_{Zn}}\right\} + \frac{2f_{Cl}^2}{f_{Zn}^2} - \frac{2b_{Cl}^2}{b_{Zn}^2} \tag{3.41}$$

which is equivalent to equation 16 in the paper[6] (equation 3.16 here) except for the constants at the end. Neuefeind starts from an experimental perspective and hence has to get to the total functions starting from the coherent differential cross sections. We get the total structure factors directly, defining the total neutron (3.42) and X-ray diffraction (3.43) experiments:

$$F^n(k)=c_\alpha^2 b_\alpha^2(S_{\alpha\alpha}(k)-1)+c_\beta^2 b_\beta^2(S_{\beta\beta}(k)-1)+2c_\alpha c_\beta b_\alpha b_\beta(S_{\alpha\beta}(k)-1) \qquad (3.42)$$

$$F^X(k)=c_\alpha^2 f_\alpha^2(S_{\alpha\alpha}(k)-1)+c_\beta^2 f_\beta^2(S_{\beta\beta}(k)-1)+2c_\alpha c_\beta f_\alpha f_\beta(S_{\alpha\beta}(k)-1) \qquad (3.43)$$

As a result,

$$\begin{aligned} F^n(k)-F^X(k)=&(S_{\alpha\alpha}(k)-1)(b_\alpha^2-f_\alpha^2)c_\alpha^2+(S_{\beta\beta}(k)-1)(b_\beta^2-f_\beta^2)c_\beta^2\\ &+2(S_{\alpha\beta}(k)-1)(b_\alpha b_\beta-f_\alpha f_\beta)c_\alpha c_\beta \end{aligned} \qquad (3.44)$$

Rearrange equations 3.42 and 3.43 to make $S_{\alpha\alpha}(k)$ the subject.

$$S_{\alpha\alpha}(k)=1+\frac{F^n(k)}{c_\alpha^2 b_\alpha^2}-\frac{c_\beta^2 b_\beta^2}{c_\alpha^2 b_\alpha^2}[S_{\beta\beta}(k)-1]-\frac{2c_\alpha c_\beta b_\alpha b_\beta}{c_\alpha^2 b_\alpha^2}[S_{\alpha\beta}(k)-1] \qquad (3.45)$$

$$=1+\frac{F^n(k)}{c_\alpha^2 b_\alpha^2}-\frac{c_\beta^2 b_\beta^2}{c_\alpha^2 b_\alpha^2}[S_{\beta\beta}(k)-1]-\frac{2c_\beta b_\beta}{c_\alpha b_\alpha}[S_{\alpha\beta}(k)-1] \qquad (3.46)$$

$$S_{\alpha\alpha}(k)=1+\frac{F^X(k)}{c_\alpha^2 f_\alpha^2}-\frac{c_\beta^2 b_\beta^2}{c_\alpha^2 f_\alpha^2}[S_{\beta\beta}(k)-1]-\frac{2c_\beta f_\beta}{c_\alpha f_\alpha}[S_{\alpha\beta}(k)-1] \qquad (3.47)$$

Equating two expression for $S_{\alpha\alpha}(k)$ gives

$$\begin{aligned} \frac{F^n(k)}{c_\alpha^2 b_\alpha^2}-\frac{c_\beta^2 b_\beta^2}{c_\alpha^2 b_\alpha^2}[S_{\beta\beta}(k)-1]-\frac{2c_\beta b_\beta}{c_\alpha b_\alpha}[S_{\alpha\beta}(k)-1]=&\frac{F^X(k)}{c_\alpha^2 f_\alpha^2}-\frac{c_\beta^2 f_\beta^2}{c_\alpha^2 f_\alpha^2}[S_{\beta\beta(k)}-1]\\ &-\frac{2c_\beta f_\beta}{c_\alpha b_\alpha}[S_{\alpha\beta}(k)-1] \end{aligned} \qquad (3.48)$$

Make $S_{\beta\beta}(k)$ the subject:

$$\begin{aligned} \frac{c_\beta^2 f_\beta^2}{c_\alpha^2 f_\alpha^2}[S_{\beta\beta}(k)-1]-\frac{c_\beta^2 b_\beta^2}{c_\alpha^2 b_\alpha^2}[S_{\beta\beta}(k)-1]=&\frac{F^X(k)}{c_\alpha f_\alpha^2}-\frac{F^n(k)}{c_\alpha}+\frac{2c_\beta b_\beta}{c_\alpha b_\alpha}[S_{\alpha\beta}(k)-1]\\ &-\frac{2c_\beta f_\beta}{c_\alpha f_\alpha}[S_{\alpha\beta}(k)-1] \end{aligned} \qquad (3.49)$$

and so,

$$[S_{\beta\beta}(k)-1]\left\{\frac{c_\beta^2}{c_\alpha^2}\left(\frac{f_\beta^2}{f_\alpha^2}-\frac{b_\beta^2}{b_\alpha^2}\right)\right\}=\frac{F^X(k)}{c_\alpha^2 f_\alpha^2}-\frac{F^n(k)}{c_\alpha^2 b_\alpha^2}+\frac{2c_\beta}{c_\alpha}[S_{\alpha\beta}(k)-1]\left\{\frac{b_\beta}{b_\alpha}-\frac{f_\alpha}{f_\alpha}\right\} \qquad (3.50)$$

and

$$S_{\beta\beta}(k)-1=\cfrac{\cfrac{F^X(k)}{c_\alpha^2 f_\alpha^2}-\cfrac{F^n(k)}{c_\alpha^2 b_\alpha^2}+\cfrac{2c_\beta}{c_\alpha}[S_{\alpha\beta}(k)-1]\left\{\cfrac{b_\beta}{b_\alpha}-\cfrac{f_\alpha}{f_\alpha}\right\}}{\left\{\cfrac{c_\beta^2}{c_\alpha^2}\left(\cfrac{f_\beta^2}{c_\alpha^2}-\cfrac{b_\beta^2}{b_\alpha^2}\right)\right\}}$$

(3.51)

Now, note that

$$\frac{F^X(k)}{c_\alpha^2 f_\alpha^2}-\frac{F^n(k)}{c_\alpha^2 b_\alpha^2}=\frac{1}{c_\alpha^2}\left(\frac{F^X(k)}{f_\alpha^2}-\frac{F^n(k)}{b_\alpha^2}\right)$$

(3.52)

and so

$$[S_{\beta\beta}(k)-1]=\cfrac{\cfrac{1}{c_\alpha^2}\left(\cfrac{F^X(k)}{f_\alpha^2}-\cfrac{F^n(k)}{b_\alpha^2}\right)+\cfrac{2c_\beta}{c_\alpha}[S_{\alpha\beta}(k)-1]\left\{\cfrac{b_\beta}{b_\alpha}-\cfrac{f_\alpha}{f_\alpha}\right\}}{\left\{\cfrac{c_\beta^2}{c_\alpha^2}\left(\cfrac{f_\beta^2}{c_\alpha^2}-\cfrac{b_\beta^2}{b_\alpha^2}\right)\right\}}$$

(3.53)

For example, MX_2, $c_\alpha=1/3$, $c_\beta=2/3$ gives

$$[S_{\beta\beta}(k)-1]=\cfrac{\cfrac{9}{4}\cfrac{F^X(k)}{f_\alpha^2}-\cfrac{F^n(k)}{b_\alpha^2}+[S_{\alpha\beta}(k)-1]\left\{\cfrac{b_\beta}{b_\alpha}-\cfrac{f_\alpha}{f_\alpha}\right\}}{\left\{\left(\cfrac{f_\beta^2}{c_\alpha^2}-\cfrac{b_\beta^2}{b_\alpha^2}\right)\right\}}$$

(3.54)

Equation 3.54 is essentially the same as Neuefeind's. Calculations show that this equation is able to eliminate one partial (say $S_{ClCl}(k)$) and hence get $S_{ZnZn}(k)$ in terms of the two total scattering functions and the $S_{ZnCl}(k)$ partial. The latter is the function the Neuefeind claims to improve from Biggin and Enderby. Figure 3.5 shows the partial structure factor derived by Neuefeind which shows and inverted FSDP in $S_{ZnZn}(k)$, with a rise as $k\rightarrow 0$. Such a feature is likely to be an artefact from the extraction procedure rather than a true indication of the IRO ordering in $S_{ZnZn}(k)$.
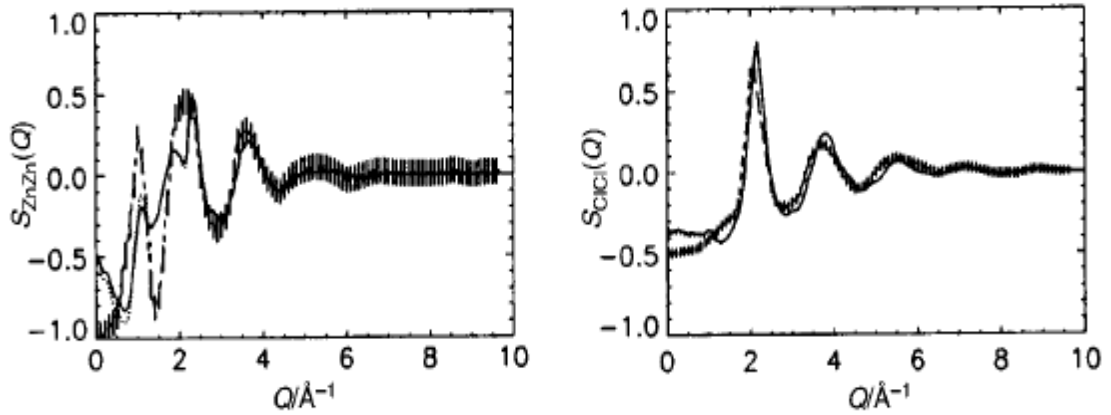
Figure 3.5: Diagram of $S_{ZnZn}(k)$ and $S_{ClCl}(k)$ obtained by Neuefeind[6] and Biggin and Enderby[4] taken from Neuefeind[6]. The structure factors obtained by Neuefeind[6] are full lines and Biggin and Enderby[4] are dot and line with error bars.

3.7 Structure of molten MgCl$_2$.
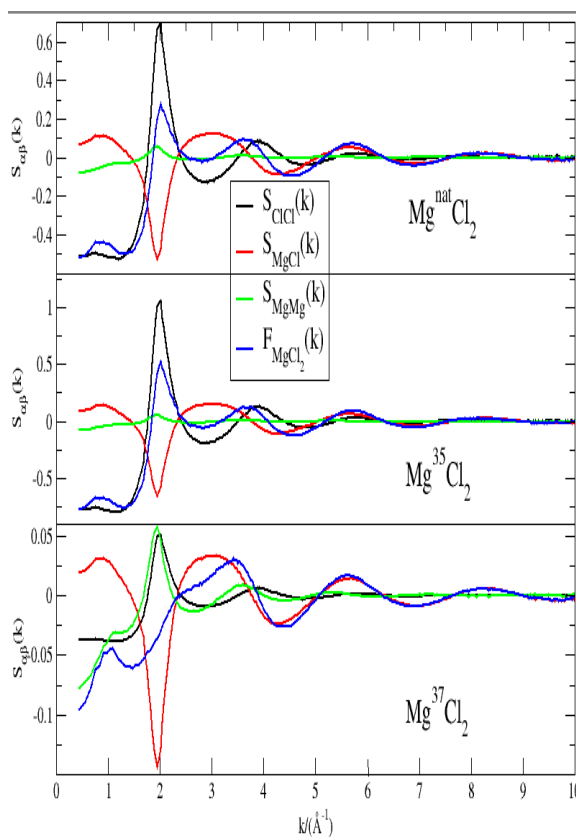
Figure 3.6: Simulated total and partial structure factors for MgCl$_2$. Black line; $S_{ClCl}(k)$; red line, $S_{MgCl}(k)$; green line, $S_{MgMg}(k)$; blue line, F_{MgCl_2}. For both figures the isotopes from top to bottom are; (a) ^{nat}Cl (b) ^{35}Cl (c) ^{37}Cl.
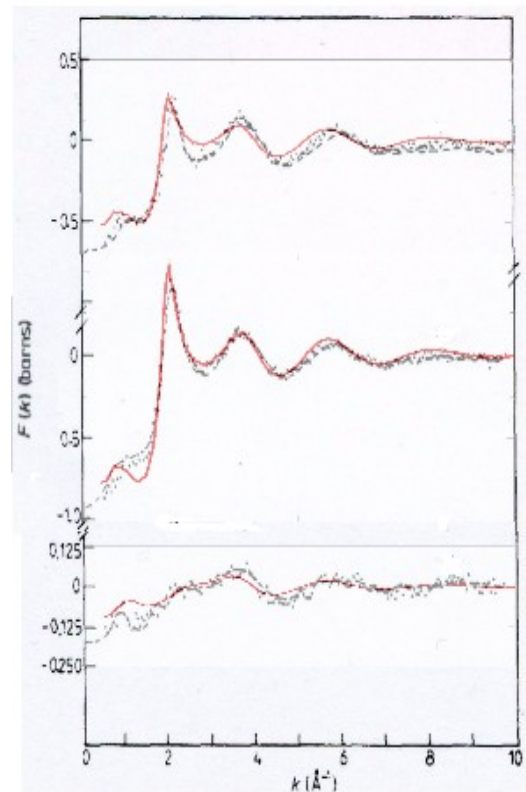
Figure 3.7: Calculated and experimental[31] total structure factors of MgCl$_2$. Colour code: black data points, experimental; red line, calculated.

The calculated structure factors in figure 3.7 show good agreement with the experimental values in reproducing the peak positions and intensities. In contrast with $ZnCl_2$ (figure 3.2) is the lack of a prominent FSDP in $F_{Mg^{37}Cl_2}(k)$ corresponding with experimental data. In the experimental F(k) for $F_{Mg^{35}Cl_2}(k)$, [29] the principal peak at $2Å^{-1}$ is considerably smaller than the $ZnCl_2$ equivalent and there is no discernible FSDP, which the calculated F(k) reproduces to a good degree. Figure 3.6 shows that the FSDP is dominated by the contribution from $S_{MgCl}(k)$. The largest difference between the experimental and calculated functions occurs in $F_{Mg^{37}Cl_2}(k)$ where the FSDP is significantly larger than the experimental value. Other differences occur in between the peaks, for instance the trough which occurs at $\sim 2.7Å^{-1}$ in $F_{Mg^{nat}Cl_2}(k)$ as well $\sim 1.5Å^{-1}$ in $F_{Mg^{37}Cl_2}(k)$, where the calculated intensity is too large. In $F_{Mg^{35}Cl_2}(k)$, the calculated trough at $\sim 1.5Å^{-1}$ is too shallow.

Figure 3.8 shows the partial structure factors of $MgCl_2$ and $ZnCl_2$ simulated at the same temperature (800K). The FSDP present in $S_{ZnZn}(k)$ is stronger than $S_{MgMg}(k)$ at 0.85 compared to 0.66, while the positions are similar at $1.027Å^{-1}$ and $0.98Å^{-1}$ respectively. For the cation-anion partial structure factors, the difference in the position of the FSDPs are smaller at the slightly lower scattering angles of $0.95Å^{-1}$ and $0.94Å^{-1}$ for $ZnCl_2$ and $MgCl_2$ respectively while the intensity is slightly greater. The principal peaks show subtle changes: in $S_{ZnZn}(k)$ and $S_{ZnCl}(k)$, the intensities are slightly smaller than for the related functions in $MgCl_2$, at 1.64 to 1.79 and -1.06 to -1.23 respectively. For $S_{ClCl}(k)$, the intensity is slightly *larger* for $ZnCl_2$ at 2.42 compared to 2.29. The position of the respective principal peaks show a slight decline from $ZnCl_2$ to $MgCl_2$ of $2.06Å^{-1}$ to $2.01Å^{-1}$, $2.09Å^{-1}$ to $2.00Å^{-1}$ and $2.09Å^{-1}$ to $2.07Å^{-1}$ for the anion-anion, cation-anion and cation-cation functions respectively. At scattering angles greater than the principal peak, the cation-anion and cation-cation functions for $ZnCl_2$, relative to $MgCl_2$, is shifted to slightly to higher values, while the anion-anion function is shifted slightly to lower scattering angles.
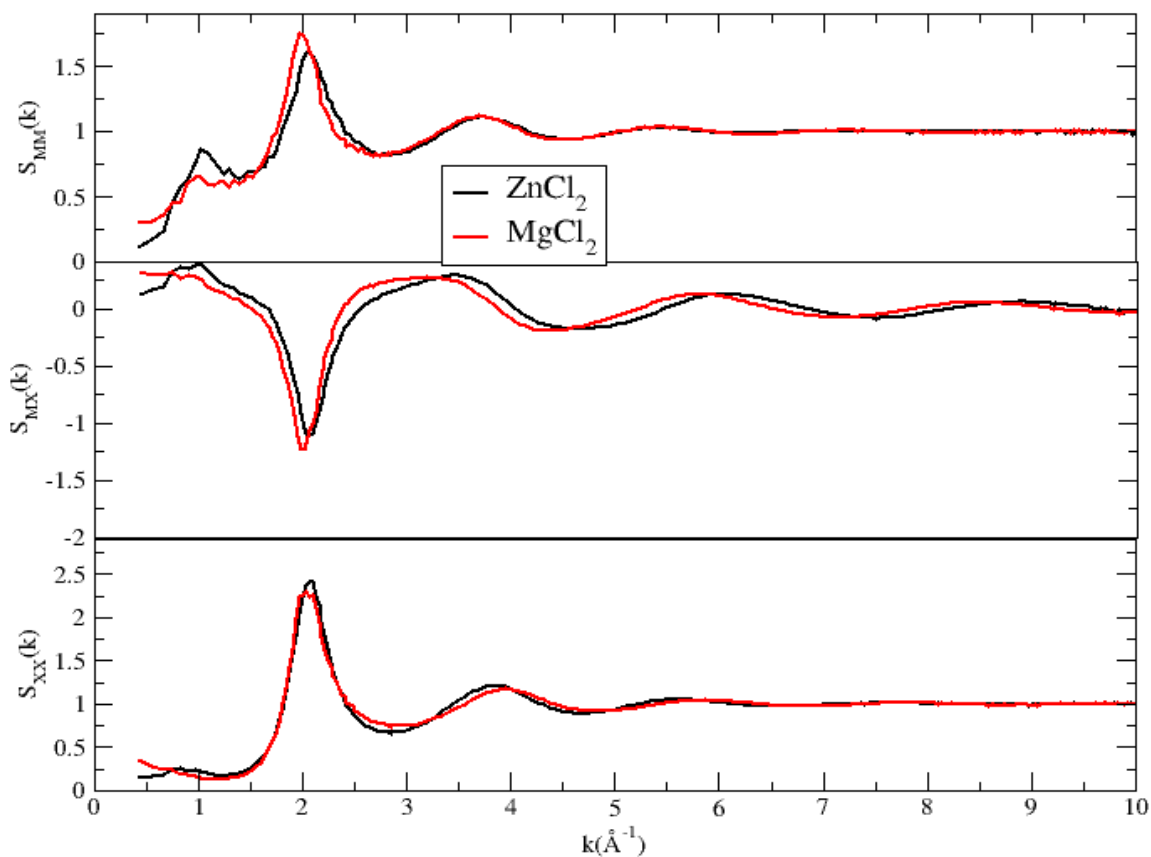
Figure 3.8: The partial structure factors of ZnCl$_2$ and MgCl$_2$. From top to bottom; S$_{MM}$(k), S$_{MX}$(k), S$_{XX}$(k),where M=Zn (black line) or Mg (red line).
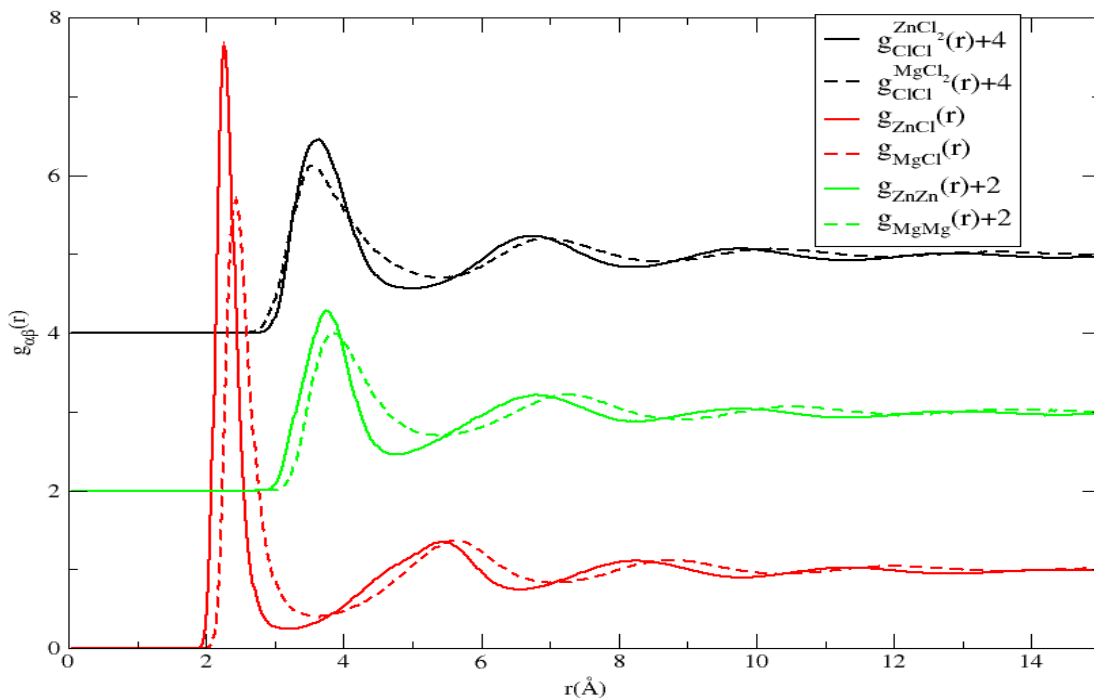
Figure 3.9: Partial radial distribution functions for ZnCl$_2$ and MgCl$_2$. Black line, g$_{ClCl}$(r); red line, g$_{MCl}$(r); green line, g$_{MM}$(r).

Figure 3.9 shows the radial distribution functions for $ZnCl_2$ and $MgCl_2$. The characteristic feature of the close proximity of $g_{ZnZn}(r)$ with $g_{ClCl}(r)$ is reproduced accurately. The nearest-neighbour principal peak positions of 2.26Å , 3.63Å and 3.77Å for the Zn-Cl, Cl-Cl and Zn-Zn separations are accurate to 0.03Å, 0.08Å and 0.03Å compared to the Biggin and Enderby experiment.[4] The related values for magnesium chloride; 2.43Å, 3.56Å and 3.86Å correlate well with the experimental results of Biggin and Enderby[31] and are accurate to 0.01Å, 0.00Å and 0.05Å. Observing the minima of the principal peak of $g_{MgCl}(r)$ gives some indication of the exchange between ions in the first coordination shell. The intensity of this minima in $g_{MgCl}(r)$ is almost double (0.40) compared to the corresponding value of 0.23 for $g_{ZnCl}(r)$. This indicates that in zinc chloride there is a cation-anion coordination shell more stable to exchange than in $MgCl_2$. The intensity and FWHM of the second peak in $g_{ZnZn}(r)$ and $g_{MgMg}(r)$ are similar, with the most significant difference being the sharper ordering between the principal peak and second peak observed in $g_{ZnZn}(r)$ with a sharper minima.

One noticeable difference between the experimental and calculated results is the intensity of the peaks. In MD simulation, the radial distribution functions are calculated directly from the coordinate positions, whereas experimentally a Fourier transformation of the structure factors is undertaken. Truncation errors in the latter process may affect the height and width of the peak, whilst maintaining their positions. For example, the neutron study by Allen *et al*[9] was undertaken at an upper k limit of 28Å^{-1} compared to 10Å^{-1} for Biggin and Enderby[4], leading to a more intense and narrower peak. A similar peak of the same distance and height was achieved by Triolo and Narten[16] by extrapolating the experimental structure factor to a longer k range of 100Å^{-1}. This is of particular relevance to the calculation of coordination numbers, the zinc-chlorine coordination number calculated experimentally by integrating to the minimum of the principal peak.

The Zn-Cl-Zn bond angle distribution in figure 3.10 shows a doubly peaked distribution with maxima at 89° and 109°. The lower value indicates the presence of edge-sharing tetrahedra while the latter indicates corner-sharing; the ratio of these peaks suggesting an equal proportion of these bonding configurations present. This in agreement with previous suggestions that zinc chloride can be considered as intermediate between strong glasses such as silicon dioxide where the Si-O-Si[54] bond angle is approximately 150° and $BeCl_2$, where the mean Be-Cl-Be bond angle is significantly

smaller at 80°.[55] The peak at 93.2° for the Mg-Cl-Mg distribution in figure 3.6 shows the predominance of square-based pyramidal and octahedral structures. This conclusion is supported by the Cl-Mg-Cl distribution where the peaks at 84.4° and 150° indicate the presence of axially and equatorially placed Cl-Mg-Cl triplets.

The newly parameterised $ZnCl_2$ model displays 56% and 37% four and five cation-anion coordination respectively. Previous calculations using the WAC[35] potential predicted a mixture of four cation-anion (75%), and five cation-anion coordination (23%). The Kumta[36] potential predicts a smaller percentage of 53% and 31% for four and five cation-anion coordination. The average Zn-Cl coordination number, M_{ZnCl}, of 4.39
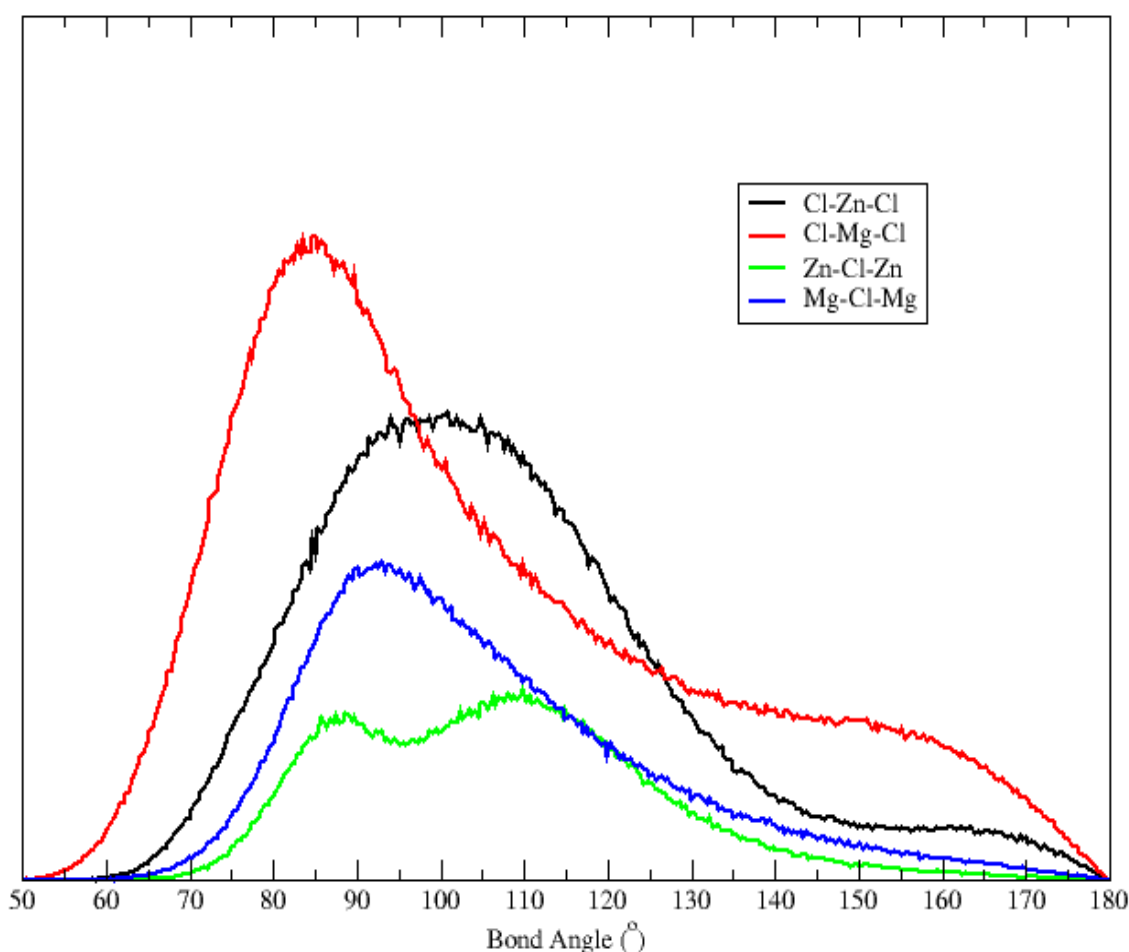
Figure 3.10: Bond angle distributions for $ZnCl_2$ and $MgCl_2$. Black line, Cl-Zn-Cl; red line, Cl-Mg-Cl; green line, Zn-Cl-Zn; blue line, Mg-Cl-Mg.

which corresponds to a good degree with the values in table 3.1, for example the values of 4.3 by Biggin and Enderby[4] and 4.0 by Triolo and Nielsen[16]. In $MgCl_2$, there is significantly greater five (49%) and six anion coordination (26%) for the ion pair, MgCl, with a decreased four-coordination (22%). In addition, $M_{ClMg} = 2.61$ is larger than M_{ClZn}

=2.16, similar to previous RMC results[47] where the cation-anion coordination had been fixed at 4. These results indicate that major difference in local coordination polyhedra between $MgCl_2$ and $ZnCl_2$ is that zinc occupies tetrahedral interstitial sites in the anion sublattice, while magnesium occupies more octrahedral sites, in agreement with the same RMC results.[47]

3.8 Predicted structure of $MnCl_2$ using $ZnCl_2$ and $MgCl_2$ partial structure factors.

$MgCl_2$ and $MnCl_2$ are considered as having similar structural properties.[31] In the solid state both $MgCl_2$ and $MnCl_2$ favour $CdCl_2$ type structures at ambient pressures, where metal cations fill half the available octahedral holes in a cubic close packed anion sublattice. In the liquid state, the values of the ratio $g_{ClCl}(r)/g_{ZnCl}(r)$ retrieved from the experimentally-determined radial distribution functions were calculated as 1.47 and 1.43 for $MgCl_2$ and $MnCl_2$ respectively. This evidence led Enderby et al[30] to suggest that $MgCl_2$ and $MnCl_2$ constitute an isomorphic pair in the molten state. In contrast, $MgCl_2$ and $MnCl_2$ are considered to have different liquid structures compared to $ZnCl_2$, after analysis of neutron diffraction results which shows a higher $g_{ClCl}(r)/g_{ZnCl}(r)$ ratio of 1.63. This was further supported by comparing the experimental F_{MnCl_2} with one created from the $MgCl_2$ partial structure factors with the appropriate weightings from equation 3.1, which resulted in a good correlation. A similar procedure can be carried out computationally by changing the scattering coefficient b for Mg and Zn to the value appropriate for manganese we can, therefore, observe any structural changes of this type.
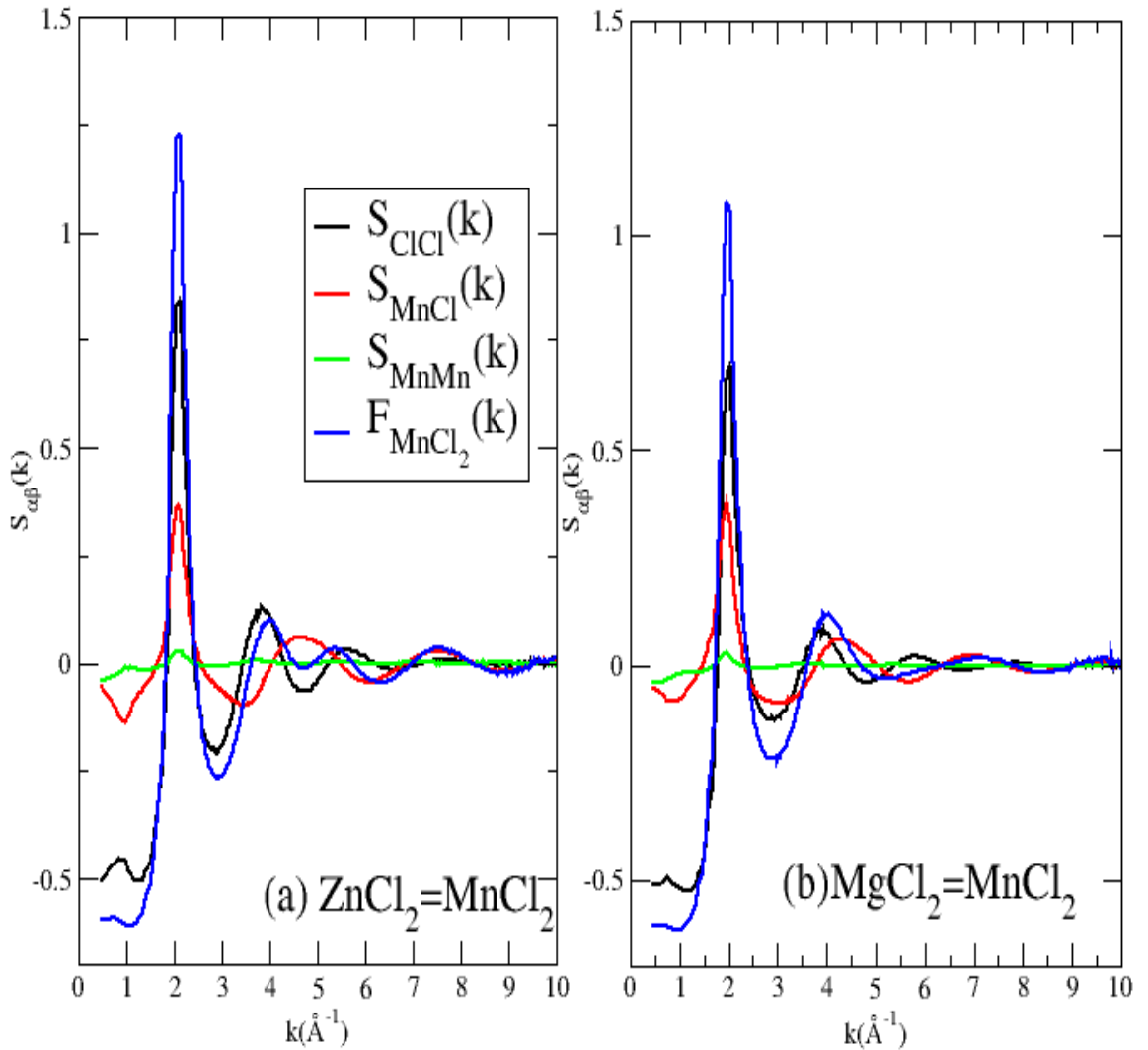
Figure 3.11:Constructed $MnCl_2$ total and partial structure factors. Left: $ZnCl_2$ scattering as $MnCl_2$.
Right: $MgCl_2$ scattering as $MnCl_2$. Black line, $S_{ClCl}(k)$; red line, $S_{MnCl}(k)$; green line, $S_{MnMn}(k)$; blue line, F(k).

Figure 3.11 shows the calculated structure factors of $ZnCl_2$ and $MgCl_2$ configurations
when b is set at the manganese value of -3.73 fm. The peak at $2Å^{-1}$ for F(k) is
significantly greater in amplitude than the equivalent for $ZnCl_2$ and $MgCl_2$. This is due
solely to the *positive* contribution of $S_{MnCl}(k)$ caused by the negative scattering of the
manganese ion. Correspondingly, the contribution of $S_{MnMn}(k)$ to the FSDP is negated by
the now negative contribution of $S_{MnCl}(k)$ in the $\sim 1Å^{-1}$ region. Both total structure factors
in figure 3.11 show good correlation with the experimental F(k) for $MnCl_2$, indicative of
the similar cation size in all three compounds of similar MCl_2 stoichiometry. Notable
differences include larger FSDP peak for M=Zn in $S_{MCl}(k)$ and $S_{MM}(k) \sim 1Å^{-1}$. Due to the
weighting attributable to the negative scattering of manganese chloride, these differences
cancel and produce a flat peak in the $1Å^{-1}$ region of F(k). The differences are further

negated by the *magnitude* of the manganese scattering which result in $S_{ClCl}(k)$ dominating $F(k)$. The relevance of the these effects is that the *absence of the FSDP* cannot necessarily be attributed entirely to the near-negligible $S_{MnMn}(k)$ contribution, but possibly by cancellation of the $S_{MnCl}(k)$ and $S_{ClCl}(k)$ terms which would otherwise contribute to the FSDP. In effect the magnitude and direction of the manganese scattering length damp all contributions to the FSDP. Furthermore, as $S_{ClCl}(k)$ dominates $F(k)$, the conclusion that $ZnCl_2$ and $MnCl_2$ were isomorphic would arise by application of the same method, using partial structure factors from $ZnCl_2$ rather than $MgCl_2$.[31]

3.9 Effect of anion-anion repulsion on IRO.

The systems so far have featured MCl_2 (where M are intermediate sized cations Mg, Mn and Zn). As mentioned in 3.1, neutron diffraction experiments have been carried out on the various halides of zinc. Changing the anion size would be expected to increase the anion polarisability and the anion-anion separation. In this section we fix the anion polarisability, α_X, at 20 a.u and observe the changes in structure with respect to IRO which occur upon increase of anion-anion separation. To achieve this increased separation, we varied the parameter, B_{XX}, at fixed density. The B_{XX} range was from 107 a.u, the value used for the $ZnCl_2$ potential, to 607 a.u, as described in section 3.3, which resulted in a shift in the effective anion-anion separation, r_{eff}^{XX}, as given by the position of the principal peak in $g_{ClCl}(r)$, from 3.67Å at 107 a.u to 3.84Å at 607 a.u.

Figure 3.12 shows the changes in the IRO properties of the partial structure factors. For $S_{ZnZn}(k)$, the FSDP shifts to higher scattering angles from 1.09Å⁻¹ at $r_{eff}^{XX}=3.67\,Å$ to 1.27Å⁻¹ at $r_{eff}^{XX}=3.84\,Å$, and a progressive merging of the principal peak and FSDP is observed. For $S_{ZnCl}(k)$, a larger shift is observed over the same range, 1.04Å⁻¹ to 1.53Å⁻¹, with a much sharper decrease in the intensity. A small FSDP observed in $S_{XX}(k)$ at r_{eff}^{XX} =3.67Å disappears with increasing r_{eff}^{XX}. The principal peak in $S_{XX}(k)$ observed the greatest change in intensity, increasing from 2.64 at $r_{eff}^{XX}=3.67\,Å$ to 4.02 at $r_{eff}^{XX}=3.84\,Å$. $S_{MM}(k_{PP})$ stays at the same intensity and $S_{MX}(k_{PP})$ changes from 1.17 to 1.33 over the same range. $S_{XX}(k_{PP})$ also observes also a slightly greater shift in position, of 2.05Å⁻¹ to 1.98Å⁻¹ from $r_{eff}^{XX}=3.67\,Å$ to $r_{eff}^{XX}=3.84\,Å$ while $S_{MM}(k_{PP})$ shifts from 2.08Å⁻¹ to 2.04Å⁻¹ and $S_{MX}(k_{PP})$ shifts from 2.06Å⁻¹ to 2.03Å⁻¹.
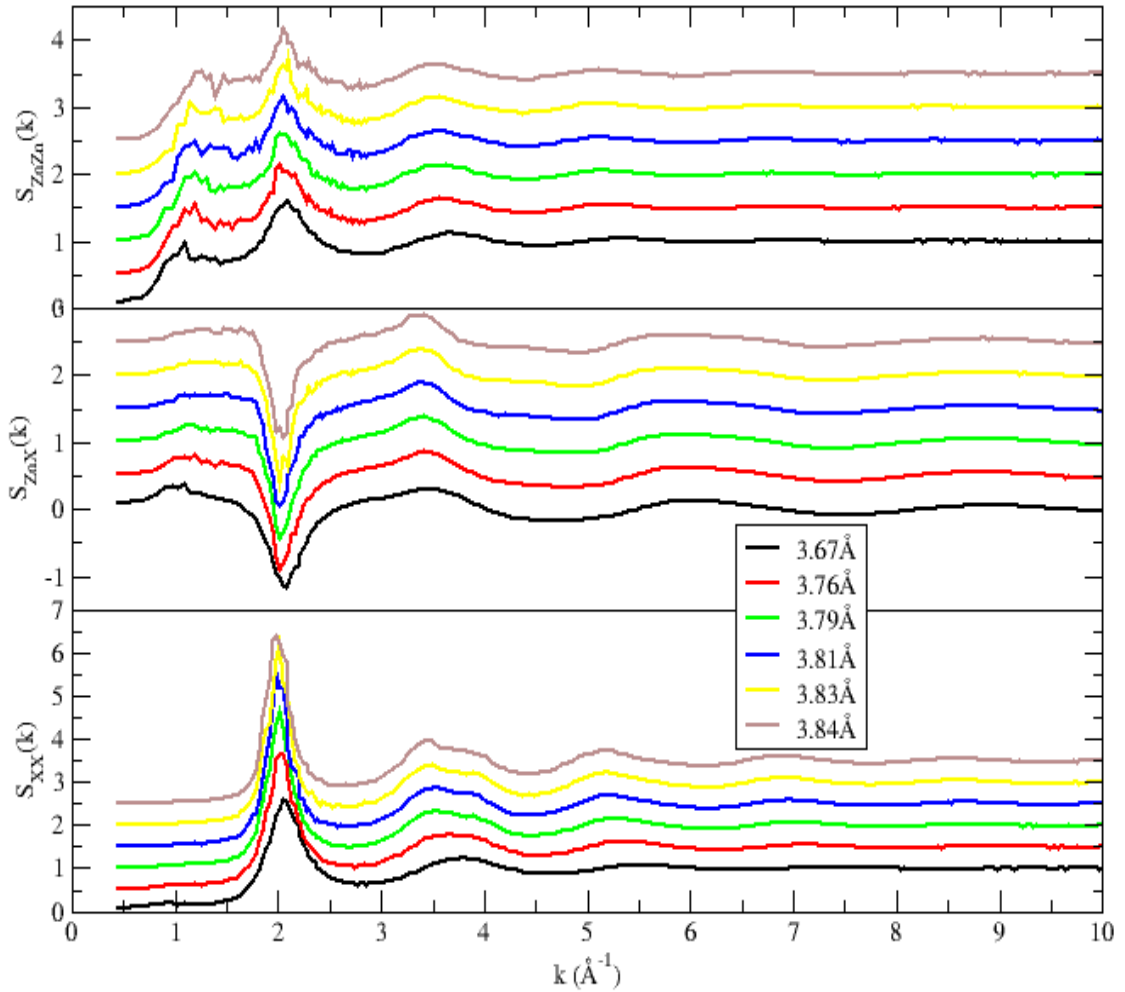
Figure 3.12: Partial structure factors of ZnX_2 with varying effective anion-anion separation, $r_{eff}^{XX.}$
Colour code (y increment in brackets): black line, 3.67Å; red line, 3.76Å (+0.5); green line, 3.79Å (+1.0);
blue line, 3.81Å (+1.5); yellow line, 3.83Å (+2.0); brown line, 3.84Å (+2.5).

Figure 3.13 shows the partial radial distribution functions in ZnX_2 with varying

r_{eff}^{XX} while table 3.6 summarises the changes in the first coordination shell of $ZnCl_2$. In

addition to the shift in principal peak position in $g_{XX}(r)$ the FWHM decreases sharply

from 0.89 at $r_{eff}^{XX} = 3.67\,\text{Å}$ to 0.56 at $r_{eff}^{XX} = 3.84\,\text{Å}$. The cation-cation radial distribution

function also shows a significant shift in peak position from 3.78Å at $r_{eff}^{XX} = 3.67\,\text{Å}$ to

3.92Å at $r_{eff}^{XX} = 3.84\,\text{Å}$; the intensity at 3.32Å (forming a shoulder in $g_{MM}(r)$ at higher

r_{eff}^{XX}) declines with increasing r_{eff}^{XX} Both these changes show that edge-sharing units

are less favourable with increasing r_{eff}^{XX}. With increasing r_{eff}^{XX}, two peaks emerge in

both $g_{XX}(r)$ and $g_{MX}(r)$ at ~4.8Å and 5.9Å. For the Zn-Cl coordination, there is an

increase in the percentage of 3-coordinate zinc ions as r_{eff}^{XX} increases with the decline of five-coordinate cations present at $r_{eff}^{XX} = 3.67\,\text{Å}$. There is also an increase in the presence of 1-coordinate anions from 1.46% to 7.56% over the r_{eff}^{XX} range. This belies a pure change of edge- to corner-sharing tetrahedra where the cation-anion coordination would to be stable; the edge-sharing units are terminated, as indicated by the presence of singly-coordinated anions acting as terminal bonds.

	% Coordination Number N_{ij}					Ion separation r_{ij}	
ij	Zn-Cl			Cl-Zn		Zn-Cl (Å)	Zn-Zn (Å)
r_{eff}^{XX}	3	4	5	1	3		
3.67	1.7	79.5	17.9	1.4	9.9	2.26	3.78
3.76	2.9	92.6	4.3	2.8	3.5	2.27	3.84
3.79	4.3	92.7	3.0	3.4	3.4	2.28	3.89
3.81	6.3	92.4	1.4	5.2	2.7	2.29	3.91
3.83	8.7	90.4	1.0	6.4	2.5	2.29	3.90
3.84	10.8	88.5	0.70	7.6	2.5	2.30	3.92

Table 3.6: Changes in the first coordination shell with increasing $r_{eff}^{XX.}$ For the Zn-Cl, the 2- and 6-coordination are neglected as they are below 1% over the whole effective anion-anion separation. The ion separations are taken from the position of the principal peak in the related $g_{ij}(r)$ functions.
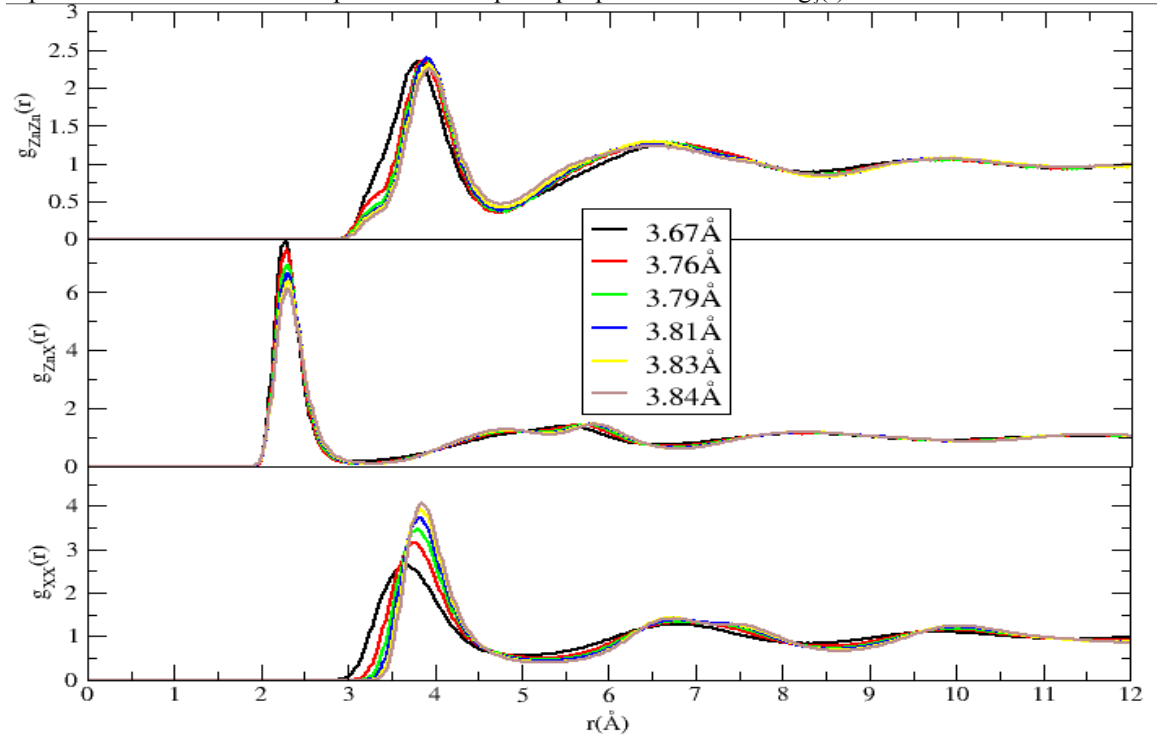
Figure 3.13: Radial distribution functions with varying effective anion-anion separation, $r_{eff}^{XX.}$ Black line, 3.67Å; red line, 3.76Å; green line, 3.79Å; blue line, 3.81Å; yellow line, 3.83Å; brown line, 3.84Å.

Figure 3.14 shows the Zn-X-Zn and X-Zn-X bond angle distributions calculated as a function of the effective anion radius. The most significant change occurs in Zn-X-Zn where the intensity at the smaller bond angle decreases with increasing r_{eff}^{XX}. This indicates that these edge-sharing tetrahedral units are reduced when the separation of anions increases. Considering the changes in coordination, the relative increase in the peak at ~120° for Zn-X-Zn is associated with trigonal planar configuration around the central cation as well as an increase in the corner-sharing proportion of cations. There is also a shift in the peak of X-Zn-X from 103° at $r_{eff}^{XX} = 3.67\,\text{Å}$ to 109° at $r_{eff}^{XX} = 3.84\,\text{Å}$. The decrease in intensity of the tail at ~150° is associated with the decline of five-coordinate sites.
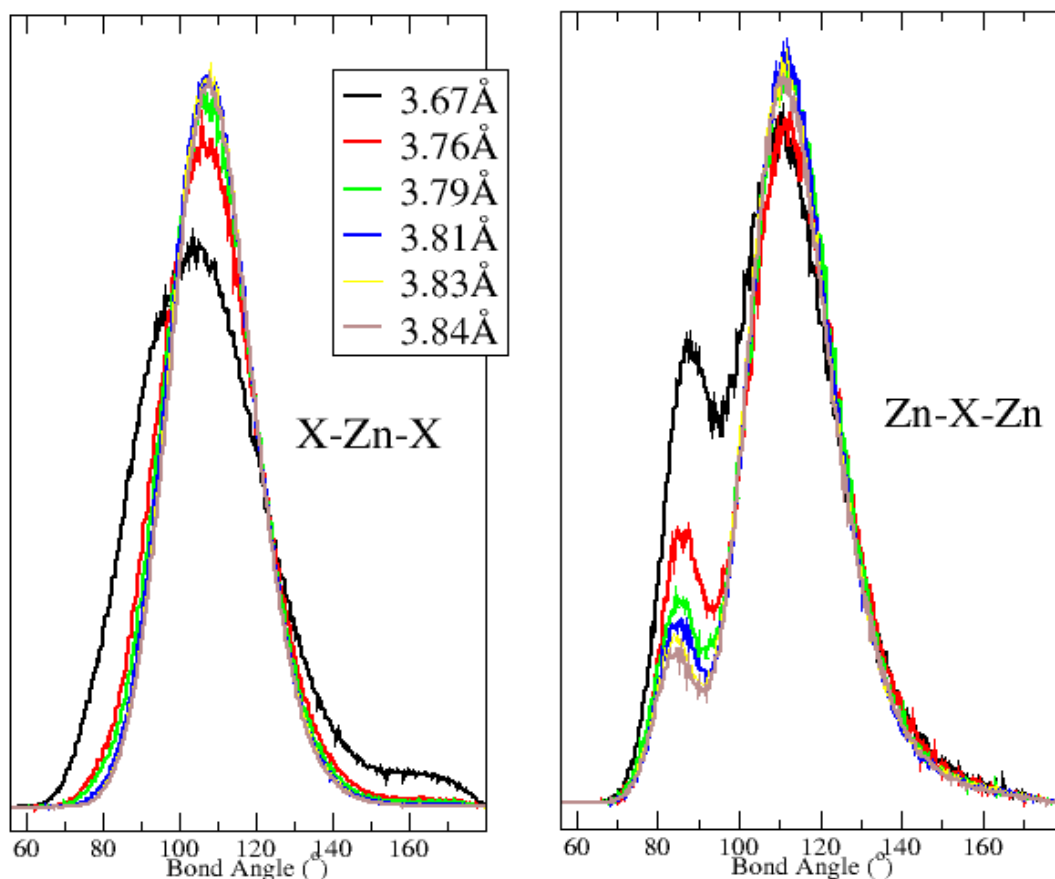
Figure 3.14:Bond angle distributions with varying effective anion-anion separation, $r_{eff}^{XX.}$ Left, Cl-Zn-Cl; right, Zn-Cl-Zn. Black line, 3.67Å; red line, 3.76Å; green line, 3.79Å; blue line, 3.81Å; yellow line, 3.83Å; brown line, 3.84Å.

The changes in network connectivity of cations with varying anion-anion separation are given in table 3.7. The rise in E^0 and decline in E^2 as the effective anion radius

increases indicates a progression towards an increasingly corner-sharing network; these changes are exacerbated with declining MX coordination. Similar systems have been simulated using the PIM on a range of MCl_3 systems where M=Fe, Al, La, Tb and Y[56,57]. In these compounds, the constituent units are in the form of dimers of the form M_2Cl_6, where a central edge-sharing unit is terminated at each end by two anions; here, due to the stoichiometry the terminating units occur with the presence of singly coordinated anions for three-coordinate cations.

r_{eff}^{XX} (Å)	E^0	E^1	E^2
3.67	44.1 (3.9)	38.4 (3.1)	17.5 (2.7)
3.76	67.4 (3.2)	28.2 (2.8)	4.3 (1.5)
3.79	71.2 (3.5)	24.2 (3.0)	2.6 (1.0)
3.81	77.5 (2.3)	21.1 (2.1)	1.5 (0.7)
3.83	79.3 (2.3)	19.9 (2.2)	0.9 (0.5)
3.84	81.0 (2.5)	24.2 (3.0)	0.6 (0.4)

Table 3.7: Cations "coloured" according to network connectivity in $ZnCl_2$ with varying effective anion-anion separation, $r_{eff}^{XX.}$

In the introduction of this chapter, the ability of models to reproduce closer cation-cation separation was highlighted as a important factor in reproducing IRO in compounds such as $ZnCl_2$. These results show that the balance between edge-sharing and corner-sharing tetrahedra can be affected by the nature of the anion-anion separation. The edge-sharing unit is visualised in achieving stabilisation of closer cation-cation separations for ions which are doubly charged. The increase in r_{eff}^{XX} shifts the balance in terms of how the system orientates to maximise *anion-anion* separation. Molecular units are favoured over edge-sharing chains as they minimise Cl-Cl repulsion by breaking MX_n chains, thereby reducing the number of anion neighbours. This increases the number of terminal units, as highlighted by the large percentage of 1-coordination for X-Zn shown in figure 3.15.
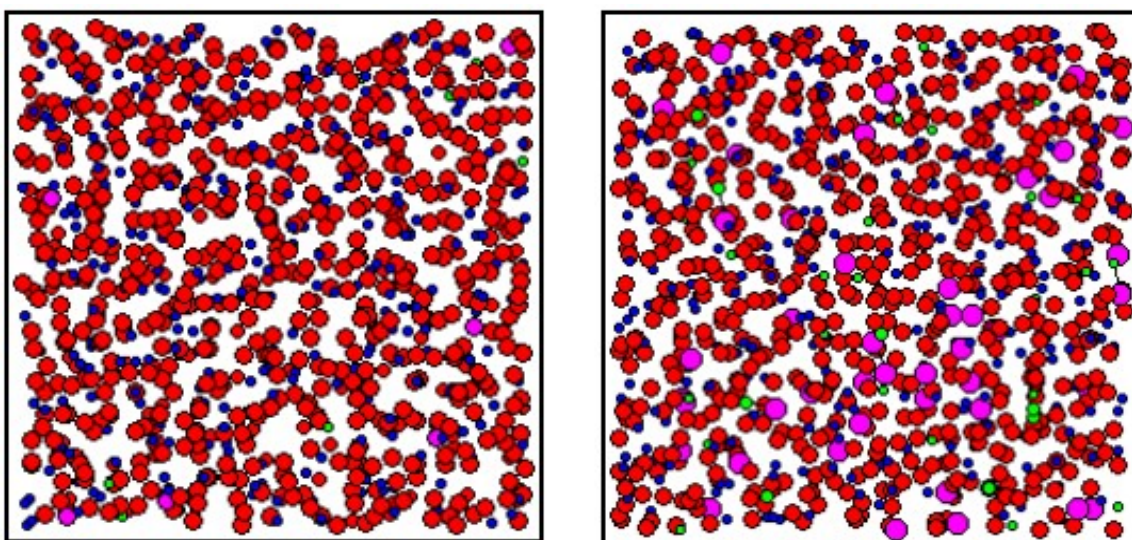
Figure 3.15:Graphical snapshots showing configurations of ZnX_2 with increasing anion-anion separation, r_{eff}^{XX}. Left, $r_{eff}^{XX} = 3.67$ Å; right, $r_{eff}^{XX} = 3.84$ Å. Red circles, 2-coordinate anions; purple circles, 1-coordinate anion; blue circles, 4-coordinate cations; green circles, 3-coordinate cations.

3.10 Conclusion

The total structure factors and peak positions of new $ZnCl_2$ and $MgCl_2$ models show good correlation with the experimental results of Biggin and Enderby.[4] One difference is that both $S_{ZnZn}(k)$ and $S_{ZnCl}(k)$ contribute significantly to the FSDP in contrast to the results of Biggin and Enderby, where $S_{ZnZn}(k)$ dominates, and Neuefeind, where $S_{ZnCl}(k)$ dominates. Further computational evidence as to the intensity of $S_{ZnZn}(k)$ in $ZnCl_2$ could be extracted from a model which produces a similar FSDP intensity in $S_{ZnZn}(k)$ (that observed in the Biggin and Enderby[4] experiment), and then observing whether the structural features present are consistent with other experimental studies of $ZnCl_2$. We have already observed the possible influence that the presence of edge-sharing may have on IRO in the calculations of ZnX_2 in section 3.9 with a decline in the proportion "1" and "2" cations resulting in a shift of the FSDP away from $\sim 1 Å^{-1}$.

Other computational models on $ZnCl_2$ have a varied interpretation of the influence of differing inter-tetrahedral connections. A Monte Carlo model of $ZnCl_2$ by Bassen et al[45] presents a highly ordered, regular tetrahedral network dominated by corner-sharing linkages (95% of cations in the equivalent of a "0" configuration). A Reverse Monte Carlo model from the same study[45] indicates a greater amount of edge-sharing in comparison, highlighted by the greater intensity of the edge-sharing peak in the Zn-Cl-Zn

bond angle distribution function. Bassen *et al*[45] have indicated that this is due to the deficiency in the Reverse Monte Carlo procedure leading to the most disordered structure. In addition to the evidence from Raman spectroscopy[23] for the presence of edge-sharing in $ZnCl_2$, the cation-cation coordination number obtained from diffraction experiments gives an indication of the inter-tetrahedral coordination. An increased presence of edge-sharing in a tetrahedral network results in a decrease in the cation-cation coordination number. Our system has a value of M_{ZnZn}=4.4 at 800K compared to Monte Carlo simulation values[45] of 6.1 and 5.2; this compares favourably with experimental results of 4.0[15,16] and 4.7[4]. It is unclear whether the screening potential used by Bassen *et al*[45] to induce intermediate-range Zn-Zn correlations is able to stabilise the presence of greater amounts edge-sharing tetrahedra, or whether the proportion of edge- and corner-sharing tetrahedra present is dependent upon the particular details of the parameters used.[45]

A common feature of computational representations of the liquid structure of $ZnCl_2$ is a more intense principal peak in $g_{ZnCl}(r)$ than that observed experimentally. Our model shows an intensity of 7.79 at $g_{ZnCl}(r_{PP})$ at 800K; the RMC model of Pusztai[47] gives an intensity of ~7; the shell model of Huang *et al*[46] at 873K shows ~10 and the MC model of Bassen *et al*[45] gives a value closest to the experimental value of ~4.5.[4] Another significant difference in the calculation of both the $ZnCl_2$ and $MgCl_2$ radial distribution functions from the RMC procedure[47] is the presence of a number spurious peaks throughout the r range, in contrast to our model. This becomes significant if changes in the radial distribution functions with variations in pressure or temperature are to be observed.

The transferability of the PIM was shown by the simple adaptation of the $ZnCl_2$ model to produce a potential model for $MgCl_2$. The cations in liquid $MgCl_2$ favour square-planar and octahedral geometries compared to $ZnCl_2$ which is dominated by tetrahedral features, as highlighted by bond angle and coordination number distribution. This is supported by Raman spectroscopy experiments of molten $MgCl_2$ where 6-coordinated Mg cations persist into the liquid state from the crystalline state.[18] These result in subtle differences in the partial structure factors where greater IRO is observed in $ZnCl_2$ as highlighted by stronger FSDPs in the cation-cation and cation-anion structure factors. Our model agrees with Puztai and McGreevy[47] that changes from the dominant tetrahedral geometry in $ZnCl_2$ (the MX coordination was fixed at 4 in the RMC procedure and so does not exhibit the increase in MX coordination observed in our model) results in a deterioration in IRO. The absence of a FSDP at $1Å^{-1}$ in $S_{ZnZn}(k)$ in a recent shell model of $ZnCl_2$ by Huang *et*

al[46], and its relationship to the radial distribution functions, can be discerned by comparing with the $ZnCl_2$ and $MgCl_2$ models produced in this chapter. In figure 7.9, the principal peaks of $g_{ZnZn}(r)$ are in phase with $g_{ClCl}(r)$, whereas in $MgCl_2$, which observes weaker IRO, $g_{MgMg}(r_{PP})$ is at a greater distance than $g_{ClCl}(r)$: a similar relationship between a weak FSDP and the out of phase relationship for cation-cation and anion-anion separations in the radial distribution functions is observed for the $ZnCl_2$ shell model.

With increasing anion-anion separation in ZnX_2, a reduction in the intensity of the FSDP and shift to higher scattering angles is observed from $k\sim 1\text{Å}^{-1}$ at the smallest anion-anion separation $(r_{eff}^{XX}=3.67\,\text{Å})$ is observed. Further structural analysis shows that the anions minimise repulsion by adopting structures which favour corner-sharing between tetrahedra and reduce MX coordination. In this chapter we have observed how the effect of the balance between edge- and corner-sharing, whether by distortion of the constituent polyhedra (as in the case of $MgCl_2$) or varying anion-anion separation can have a dramatic influence on IRO. Increasing anion-anion separation does not effectively simulate the effect of increasing anion size from chlorine to iodine, moving the FSDP position further away position exhibited by all the zinc halides[9] of $k\sim 1\text{Å}^{-1}$, indicating that the effect on anion polarisability (explored in chapter 4) needs to be taken into account. A previous set of calculations using a rigid-ion model (RIM) to represent $ZnCl_2$, $ZnBr_2$ and ZnI_2 utilised larger values for the anion-anion repulsion parameters to represent the increases in anion size.[40] In those calculations, the perturbing of the anion-anion separation did not result in a significant change from the IRO described, where the FSDP was present at $\sim 1.3\text{Å}^{-1}$ in all three systems.[40] Using a similar procedure, our calculations showed a larger range of changes in the position of the FSDP, indicating the PIM is more sensitive to changes in the anion-anion repulsion parameters than the RIM. This is due to the ability of the PIM to represent a greater range of inter-tetrahedral connections than the RIM.

3.11 References

[1] J. D. Mackenzie and W. K. Murphy. *J. Chem. Phys.*, **33**, 366, (1960).

[2] M. V. Susic and S. V. Mentus. *J. Chem. Phys.*, **62**, 744, (1975).

[3] C. A. Angell. *J. Non-Cryst. Solids*, **102**, 205, (1988).

[4] S. Biggin and J. E. Enderby. *J. Phys, C.:Solid State Phys.*, **14**, 3129, (1981).

[5] P. S. Salmon, R. A. Martin, P. E. Mason and G. J. Cuello. *Nature* (London), **435**, 75, (2005).

[6] J. Neuefeind. *Phys. Chem. Chem. Phys.*, **3**, 3987, (2001).

[7] J. Neuefeind, K. Tödheide, A. Lemke, H. Bertagnolli and H. E. Fischer. *J. Non-Cryst. Solids*, **224**, 205, (1998).

[8] F. G. Edwards, R. A. Howe, J. E. Enderby and D. I. Page. *J. Phys. C*, **8**, 3483, (1975).

[9] D. S. Allen, R. A. Howe and N. D. Wood. *J. Chem. Phys.*, **94**, 5071, (1991).

[10] J. Wong and F. W. Lytle. *J. Non-Cryst. Solids*, **37**, 273, (1980).

[11] C. Fillaux, B. Couzinet, C. Dreyfus, J. P. Itie and A. Polian. *Physica Scripta*. **T115**, 339, (2005).

[12] T. E. Westre, A. Di Cicco, A. Filipponi and C. R. Natoli. *J. Am. Chem. Soc.*, **117**, 1566, (1995).

[13] M. Imakoa, Y. Konagaya and H. Hasegawa. *Yogyo Kyokai Shi*, **79**, 91, (1971).

[14] J. A. E. Desa, A. C. Wright, J. Wong and N. Sinclair. *J. Non-Cryst. Solids*, **57**, 51, (1982).

[15] P. S. Salmon, R. A. Martin, P. E. Mason and G. J. Cuello. *Nature* (London), **435**, 75, (2005).

[16] R. Triolo and A. H. Narten. J. Chem. Phys., **74**, 703, (1981).

[17] K. Balasubrahmanyam. *J. Chem. Phys.*, **44**, 3270, (1966).

[18] R. J. Capwell. *Chem. Phys. Lett.*, **12**, 433, (1972).

[19] C. Huang and M. H. Brooker. *Chem. Phys. Lett*, **40**, 180, (1976).

[20] D. E. Irish and T. F. Young. Jr. *J. Chem. Phys.*, **43**, 1765, (1965).

[21] R. B. Ellis. *J. Electrochem. Soc.*, **113**, 485, (1966).

[22] W. Bues. *Z. Anorg. Allg. Chem.*, **279**, 104, (1955).

[23] S. N. Yannopoulos, A. G. Kalampounias, A. Chrissanthopoulos and G. N. Papatheodorou. *J. Chem. Phys.*, **118**, 3197, (2003).

[24] H. Tanaka. *J. Phy. Soc. Japan*. **70**, 1178, (2001).

[25] E. A. Pavlatou and G. N. Papatheodorou. *Phys. Chem. Chem. Phys*, **2**, 1035, (2000).

[26] M. Wilson and P. A Madden. *Mol. Phys.*, **92**, 197, (1997).

[27] R. E. Rundle and P. H. Lewis. *J. Chem. Phys.*, **20**, 132, (1952).

[28] A. Buïchler and W. Klemperer. *J. Chem. Phys.*, **29**, 121, (1958).

[29] M. P. Tosi. *J. Phys.: Condens. Matter*, **6**, A13, (1994).

[30] R. L. McGreevy and L. Pusztai. *Proc. R. Soc. London, Ser. A*, **430**, 241, (1990).

[31] S. Biggin, M. Gay and J. E. Enderby. *J. Phys. C.:Solid State Phys.*, **17**, 977, (1982).

[32] K. Hirao and N. Soga. *J. Non-Cryst, Solids*, **95**, 577, (1987).

[33] J. Brynstaed and H. L. Yakel. *Inorg. Chem.*, **17**, 1376, (1978).

[34] H. Ohno, K. Furukawa, K. Tanemoto, Y. Tagaki and T. Nakamura. *J. Chem. Soc. Faraday Trans*. **174**, 804, (1978).

[35] L. V. Woodcock, C. A. Angell and P. Cheeseman. *J. Chem. Phys.*, **65**, 1565, (1976).

[36] P. J. Gardner and D. M. Heyes. *Physica B*, **131**, 227, (1985).

[37] P. N. Kumta, P. A. Deymier and S. H. Risbud. *Physica B*, **153**, 85, (1988).

[38] N. C. Pyper, C. G. Pike, P. Popelier and P. P. Edwards. *Mol. Phys.*, **86**, 995, (1995).

[39] G. D. Mahan. *J. Chem. Phys.*, **76**, 493, (1982).

[40] M. C. Abromo and A. Consolo. *Physica B*, **205**, 408, (1995).

[41] M. Wilson and P. A. Madden. *Chem. Soc. Rev.*, **25**, 339, (1996).

[42] M. Wilson and P. A. Madden. *Phys. Rev. Lett.*, **72**, 3033, (1994).

[43] M. Wilson and P. A. Madden. *Phys. Rev. Lett.*, **80**, 532, (1998).

[44] P. W. Fowler and P. A. Madden. *Phys. Rev. B*, **29**, 1035, (1984).

[45] A. Bassen, A. Lemke and H. Bertagnolli. *Phys. Chem. Chem. Phys.*, **2**, 1445, (2000).

[46] S. Huang, F. Yoshida and W. Wang. *J. Mol. Liq.*, **115**, 81, (2004).

[47] L. Pusztai and R. L McGreevy. *J. Phys.: Condens. Matter*, **13**, 7213, (2001).

[48] N. M. Harrison and V. R. Saunders. *J. Phys. Condens. Matter*, **4**, 3873, (1992).

[49] J. C. Slater and J. G. Kirkwood. *Phys. Rev.*, **37**, 602, (1931).

[50] D. Koutselos and E. A. Mason. *J. Chem. Phys.*, **85**, 2154, (1986).

[51] P. Fowler and N. C. Pyper. *Proc. R. Soc. London, Ser. A*, **398**, 377, (1985).

[52] G. D. Mahan. *Solid State Ionics*, **1**, 29, (1980).

[53] R. Aich, K. Ismail and K. Tödheide. *High Pressure Res.*, **4,** 607, (1990).

[54] F. Mauri, A. Pasquarello, B. G. Pfrommer, Y. G. Yoon and S. G. Louie. *Phys. Rev. B*, **62**, R4786, (2000).

[55] M. Wilson and M. C. C. Ribeiro. *Mol Phys.*, **96**, 867, (1999).

[56] F. Hutchinson, A. J. Rowley, M. K. Walters, M. Wilson and P. A. Madden. *J. Chem. Phys.*, **111**, 2028, (1999).

[57] F. Hutchinson, M. K. Walters, A. J. Rowley and P. A. Madden. *J. Chem. Phys.*, **110**, 5821, (1999).

Chapter 4

A Polarisable Ion Model of GeSe$_2$

4.1 Introduction.

At the end of chapter 3, the effect of changing anion size on the structure of MX$_2$ liquids was highlighted. This was achieved by varying the short-range parameters whilst maintaining the anion polarisability at a constant value. In this chapter, we shall utilise the PIM on a system, germanium diselenide, and represent the change in anion size by varying the PIM to accommodate the presence of a larger anion polarisability. Germanium diselenide is a system which can be largely described through the interlinking of GeSe$_4$ tetrahedra. The structure of GeSe$_2$ has been studied through a number of neutron[1-5] and X-Ray diffraction[6,7,8] experiments. The results show several features in reciprocal space similar to ZnCl$_2$, including the presence of a FSDP in the total structure factor, which is primarily assigned to the contribution from $S_{GeGe}(k)$. There are, however, potentially significant differences between the functions obtained for GeSe$_2$ and those obtained for the metal dihalides. In comparison to the divalent halides discussed in Chapter 3, $S_{GeGe}(k)$ displays a more intense FSDP. Homopolar bonds (nearest neighbour spatial correlations between like atoms) are observed in the radial distribution functions, $g_{SeSe}(r)$ and $g_{GeGe}(r)$, and hence show evidence of broken chemical order.[3,4] The intensity of these low r peaks is small in comparison to the main (Ge-Se) nearest-neighbour peak, so are more susceptible to experimental errors and evidence of their existence has been contested by using the results of the high-energy X-Ray diffraction experiment of Petkov.[8] The percentage of cations in edge-sharing units is experimentally derived at 34%.[4] Recent diffraction work[5] on these two systems has identified the presence of an *extended range order*, as defined by correlations up to 60Å in the respective radial distribution functions.
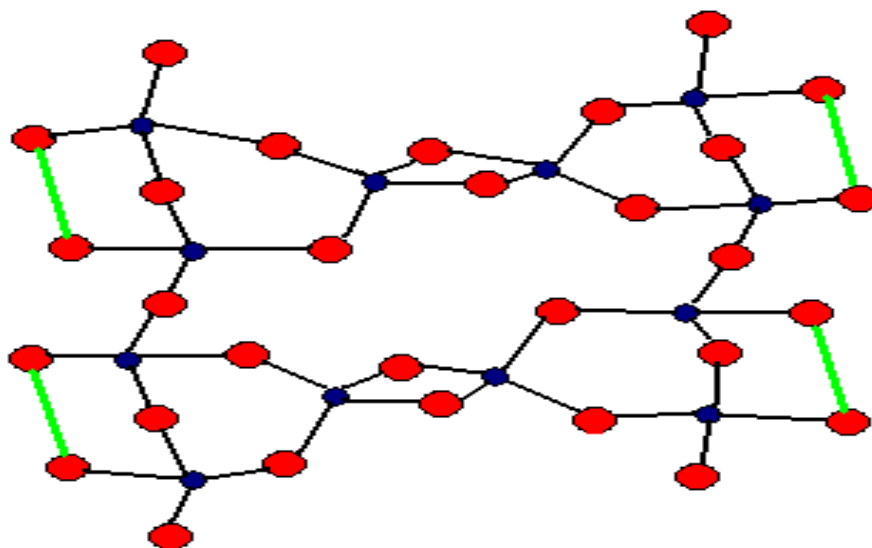
Figure 4.1: Fragment of outrigger-raft model for GeSe$_2$. Picture is based on figure from Bridenbaugh *et al*[16]. Blue circles, germanium; red circles, selenium. Homopolar bonds between the selenium atoms are green compared to black heteropolar bonds.

Whilst sharing the same tetrahedral motif as other AX$_2$ compounds, the nature of the structure of GeSe$_2$ continues to attract diverging opinions. In contrast to ZnCl$_2$, Ge$_x$Se$_{1-x}$ can have its stoichiometry readily altered.[9] Variations in stoichiometry either side of GeSe$_2$ (where x=0.33), envisage selenium rich areas containing floppy chains of Se$_n$ when x < 0.33, and germanium rich areas containing Ge$_2$Se$_4$ ethane-like molecules when x > 0.33. There are two prominent models for the structure of GeSe$_2$. One model suggests that GeSe$_2$ is based on a continuous random network model (CRN)[10] model with chemically ordered-defects incorporated (the chemically ordered continuous random network model COCRN)[11] and is supported by evidence from various experiments.[7, 12-16] Other experiments[16-22] support the "outrigger raft" model[16], as shown in figure 4.1, where the broken chemical disorder observed in germanium or selenium rich mixtures is present at x=0.33; GeSe$_2$ is comprised of units of Ge$_6$Se$_{14}$ units, where a central edge-sharing unit connects two units of corner-shared tetrahedra, which are linked through a chalcogenide-chalcogenide bond. These selenium-rich clusters are offset by Ge-rich ethane-like units of Ge$_2$(Se$_{1/2}$)$_6$.

Raman spectroscopy experiments on chalcogenides[13, 14, 16] show several key features, particularly the presence of a companion mode, A_C^1, which originates from a splitting

of the symmetrical A$_1$ stretch associated with tetrahedral vibrations. In the system, Ge$_x$Se$_{1-x}$, the A_C^1 mode decreases in intensity in the range of x from 0.33 to 0. Assignments of the companion mode reflect the different interpretations of GeSe$_2$ structure; the first assignment by Brindenbaugh et al[16] attributes the companion mode to the vibrations of the chalcogenide atoms in homopolar bonds as shown in figure 4.1. A later assignment[13] attributes the vibration of chalcogenide atoms to those placed in an edge-sharing unit. The change in frequency of the A_C^1 mode with composition x has been shown to be a signature for the onset of network rigidity[23,24] (that the elastic properties of compounds can be understood through the mean coordination number, <r>, where a rigid system is predicted to occur[25] at <r>=2.4).

4.2 Computational background.

A previous classical potential model for GeSe$_2$ developed by Vashishta[26,27] used bond-bending constraints to achieve the more acute Ge-Se-Ge bond angles required to promote the formation of edge-sharing units. Whilst reproducing features such as the presence of edge-sharing tetrahedra and a FSDP in F(k), other features, such as the presence of a FSDP in S$_{CC}$(k)[28] and homopolarity, were absent. Electronic structure calculations[29-37] have had varying success in reproducing properties of GeSe$_2$. Early calculations showed that a FSDP in the total structure factor would not be produced using a density functional calculation applying the Local Density Approximation, and a description which represented greater ionicity of the bond was needed to reproduce this feature.[29] The LDA[38] approximation tended to favour too much homopolarity, with 60% of Se atoms and 25% of Ge atoms in homopolar bonds. On applying a gradient corrected method (the generalized gradient approximation-GGA[39]) these proportions are reduced to 39% and 10% respectively. In addition to the potential effects of the details of the electronic structure calculation (of which the use of LDA and GGA is an example), electronic structure calculations tend to use relatively small system sizes (typically ~120 atoms[32]) and so the details of the FSDP, which require the system cell to be large enough so as to contain the related intermediate-range length scales, may be difficult to establish. In addition, the time-scales accessible to such methodologies may also be limited and so structural relaxation, in particular at low temperature, may be a problem.[32] As a result of these factors, the FSDP intensity can exhibit variations of 20% in intensity during a

simulation run.[32] Drabold and Tafen[35] have used FPMD-based methodologies (employing the FIREBALL density functional code[40] with LDA) on GeSe$_2$ and related chalcogenides, such as SiSe$_2$ and GeSe$_4$, showing good agreement with the total structure factors of these compounds. Cobb and Drabold[33,34] used DFT methods with several essential approximations including, most successfully, the Harris functional[41]. A substantial FSDP was reproduced in S$_{GeGe}$(k) by this method and the a possible link of IRO with the internal ring structure was highlighted by colouring the partial structure factors according to the presence of four and six-membered rings. Another technique, experimentally constrained molecular relaxation (ECMR), combines Reverse Monte Carlo simulation with first-principles molecular dynamics[36]. The model produces good correlation with the total structure factor and a similar percentage of edge-sharing tetrahedra (38% compared to the experimentally observed 34%). A recent model on glassy GeSe$_2$ utilised Møller-Plesset perturbation theory to fit a Morse-potential[37] on a 1200 atom system. The model reproduced qualitatively several aspects of the GeSe$_2$ structure including homopolar bonds between anions (although homopolar bonds between cations were absent) and the presence of deformed tetrahedra, with significant variations in the constituent bond lengths and angles, as observed experimentally.[3] Recently, Reverse Monte Carlo calculations[42] have been utilised to simulate experimental F(k) and partial structure factors, where S$_{GeSe}$(k) and S$_{SeSe}$(k) showed good correlation over the whole k range, but S$_{GeGe}$(k) showed a considerably sharper FSDP than that experimentally observed. By utilising the PIM we will show the usefulness of models with reference to an *extended ionic* description of bonding on the structure of GeSe$_2$.

4.3 Simulation details.

The central cell used in all calculations in this chapter consists of 999 ions (333 cations and 666 anions). The initial configuration for the parameterisation of the GeSe$_2$ PIM was obtained from a previous calculation for ZnCl$_2$ using the rigid-ion model with parameters given in table 3.3 for the previously used ZnCl$_2$ PIM potential.[47] For each run involved in the parameter search (stabilising each polarisability increase of 10 a.u by varying short-range damping parameters b and c) in forming the GeSe$_2$ potential model, simulations of a smaller time-scale of 500 MD steps under NPT conditions were carried out. At α_X=40 a.u, to get the model within 1.5% of experimental density[48] (3.976 g/cm^3 at 1023K) at an

average cell size of 31.80Å under NPT conditions was 6x10^{-4} a.u. Initial calculations at the experimental melting temperature at 1100K showed that the liquid diffusivity was too slow and the temperature was raised to 3000K. A simulation was carried out at an elevated temperatures of 7000K, well above the melting temperature, to equilibrate the configuration for the model. A simulation run of 100ps for calculating the structural properties of the system (discussed in sections 4.5-4.7) was carried out afterwards at a pressure of 6x10^{-4} a.u under NPT conditions.

4.4 GeSe$_2$ potential construction.

Whilst the PIM has been applied with success to compounds where the anion polarisability is of the order 5-20 a.u, estimates of selenide polarisability range from of 47-67 a.u.[43] As a result, an emphasis in the construction of the parameter set for the GeSe$_2$ model was focused on stabilizing the PIM using higher polarisabilities. Initially, a GeSe$_2$ rigid ion model was produced by using the formal valence charges for the ions involved. The initial Fumi-Tosi coefficients relating to short-range repulsion used to stabilise the potential GeSe$_2$ were derived from equation 4.1, the Busing form of the Born-Mayer potential[44] which connects the Fumi-Tosi coefficients with the charges and ion size:

$$\Phi_{ij}(r) = \frac{z_i z_j}{r} + \left(1 + \frac{z_i}{n_i} + \frac{z_j}{n_j}\right) b\exp\left|(\sigma_i + \sigma_j - r_{ij})/\rho\right| \qquad (4.1)$$

n_i and z_i are the number of outer shell electrons and charge associated with ion i, whilst ρ governs the decay of the (short-range) repulsive wall and σ_i is the ion radius
From 4.1, the Fumi-Tosi coefficient, B_{ij} is calculated as:

$$B_{ij} = (1 + \frac{z_i}{n_i} + \frac{z_j}{n_j}) b\exp\left|(\sigma_i + \sigma_j)/\rho\right| \qquad (4.2)$$

The values used, listed in Table 4.2, were based on the parameters from the rigid ion models of SiO$_2$ (RIM-SiO$_2$) and ZnCl$_2$ (RIM-ZnCl$_2$) produced by Woodcock et al.[45] The final parameter set shows that the latter model had greater success in stabilising the RIM. Dispersion coefficients were included and calculated using the Slater-Kirkwood formula (equation 3.3), the coefficients for which are listed in Table 4.1, using a polarisability range of α=47-67 a.u for Se^{2-}. Starting from the GeSe$_2$ RIM, the anion polarisability was

raised by 10 a.u and, at each stage, the short-range damping parameters (b and c used to control polarisability) and the Fumi-Tosi short-range repulsion parameters were perturbed to stabilize the model and avoid a *polarisation catastrophe*.[46] A polarisation catastrophe occurs when a unphysically close separation of two anions is stabilised (this was observed in g$_{SeSe}$(r), calculated using configurations from a few MD steps before collapse of the calculation); this leads to an ever increasing dipole moment across the two anions which causes a collapse in the calculation. At each step the anion-anion separation had to be ramped up offset the tendency towards collapse. The final parameters for the model are shown in Table 4.2. Pressure also had to be applied to maintain the model at experimental density.

ij	α_i	α_j	p$_i$	p$_j$	C_{ij}^{SK}	C_{ij}^{Final}
SeSe	40	20	6.70	6.70	630.4-1076.2	1000.60
GeSe	40	20	6.70		0.00	380.00
GeGe						0.00

Table 4.1: Table of Dispersion coefficients calculated from Slater Kirkwood formula (C_{ij}^{SK}) and those from the final parameter set (C_{ij}^{Final}). The values α and p are the respective polarisability and effective electon numbers used in equation 4.3. All values are in atomic units.

(a)	GeSe$_2$ PIM		RIM(ZnCl$_2$)		RIM(SiO$_2$)	
ij	B$_{ij}$	a$_{ij}$	B$_{ij}$	a$_{ij}$	B$_{ij}$	a$_{ij}$
SeSe	1185.64	1.5564	155.664	1.5564	16.6	1.5564
GeSe	199.38	1.5564	59.388	1.5564	47.665	1.5564
GeGe	12.25	1.5564	12.25	1.5564	75.73	1.5564

(b)			RIM(ZnCl$_2$)				RIM(SiO$_2$)			
ij			b	σ	σ	ρ	b	σ	σ	ρ
SeSe			0.190	1.90	1.90	0.34	0.342	1.42	1.42	0.29
GeSe			0.190	1.35	1.90	0.34	0.211	1.32	1.42	0.29
GeGe			0.190	1.35	1.90	0.34	0.081	1.32	1.32	0.29

(c)	α	b	c							
Se^{2-}	40	1.65	2.00							

Table 4.2: Parameter values in development of GeSe$_2$ PIM. The parameters of the final GeSe$_2$ model are shown in columns two and three for (a) Fumi-Tosi coefficients and (c) parameters associated with polarisability; α, anion polarisability and short-range damping parameters b and c. Section (b) shows the parameter values used in equation 4.2 for calculation of FT coefficients listed in section (a) for RIM-ZnCl$_2$ and RIM-SiO$_2$ models. (all units in a.u)

4.5 Comparison of the new GeSe$_2$ PIM with other potentials.

In this section we shall present the structural results for the GeSe$_2$ PIM and compare it with results from previous classical and electronic structure calculations. A direct comparison is made with the trajectories generated from first principles molecular dynamics calculations (FPMD) by Carlo Massobrio.[32] In these calculations, a central unit cell of 120 atoms was used in box size of 15.7Å, matching experimental density, at a temperature of 1025K. The generalized-gradient approximation (GGA) with suitable pseudopotentials was used to describe the core-valence interactions, while the valence electrons were described explicitly. The calculations were taken from a 21 ps run with a time step of 0.54 fs. Such a comparison assists the longer term aim of applying the two techniques together, utilizing the greater timescales and system sizes available from classical methods with electronic information of FPMD calculations.
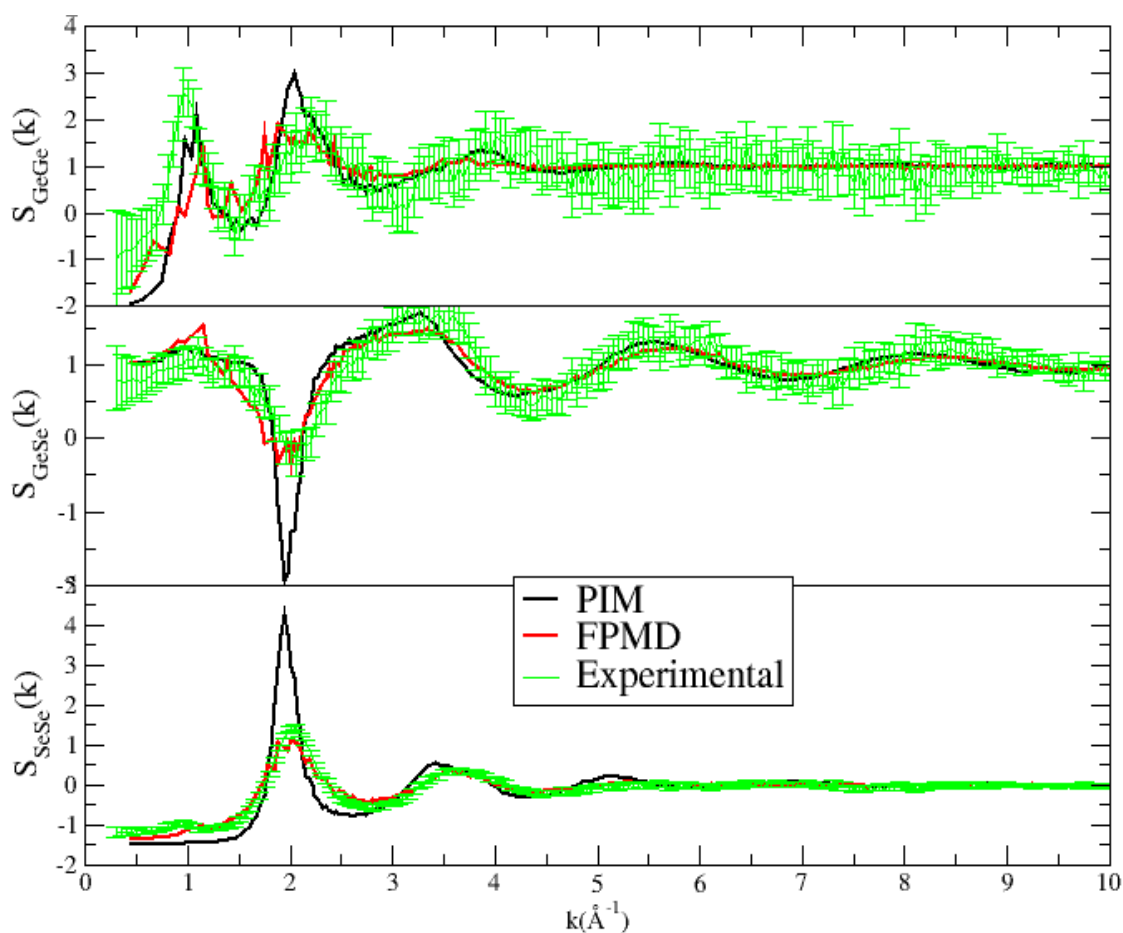
Figure 4.2: Partial structure factors of germanium selenide obtained from theory and experiment[4]. Top, $S_{GeGe}(k)$; middle, $S_{GeSe}(k)$; bottom, $S_{SeSe}(k)$. Black line, PIM; red line, FPMD; green line, experimental[4].

Figure 4.2 shows the partial structure factors calculated using the both the PIM and FPMD. There is a stronger FSDP in $S_{GeGe}^{PIM}(k)$ compared to the $S_{GeGe}^{FPMD}(k)$ and that displayed by the potential (CMD) model of Vashishta.[27] One possible explanation for the reduced intensity of $S_{GeGe}^{FPMD}(k)$ in current FPMD calculations is structural relaxation. The relatively small system size coupled with the relatively short time scales used may mean that the actual configurations reflect the high temperature states frozen in. This issue was addressed in part Tafen and Drabold[35] who used the WWW[49,50] method which tightens the coordination shell by restricting Ge-Se coordination to 4. This resulted in better agreement with high k features, thus improving the description of the first coordination, but had little effect in increasing the intensity of the FSDP, indicating that the linkages between tetrahedral units needed a better description. The principal peaks in $S_{SeSe}^{PIM}(k)$ and $S_{GeSe}^{PIM}(k)$ are at a larger intensity than the experimental observed functions, indicating an overstructuring of the anion-anion and cation-anion sublattice,
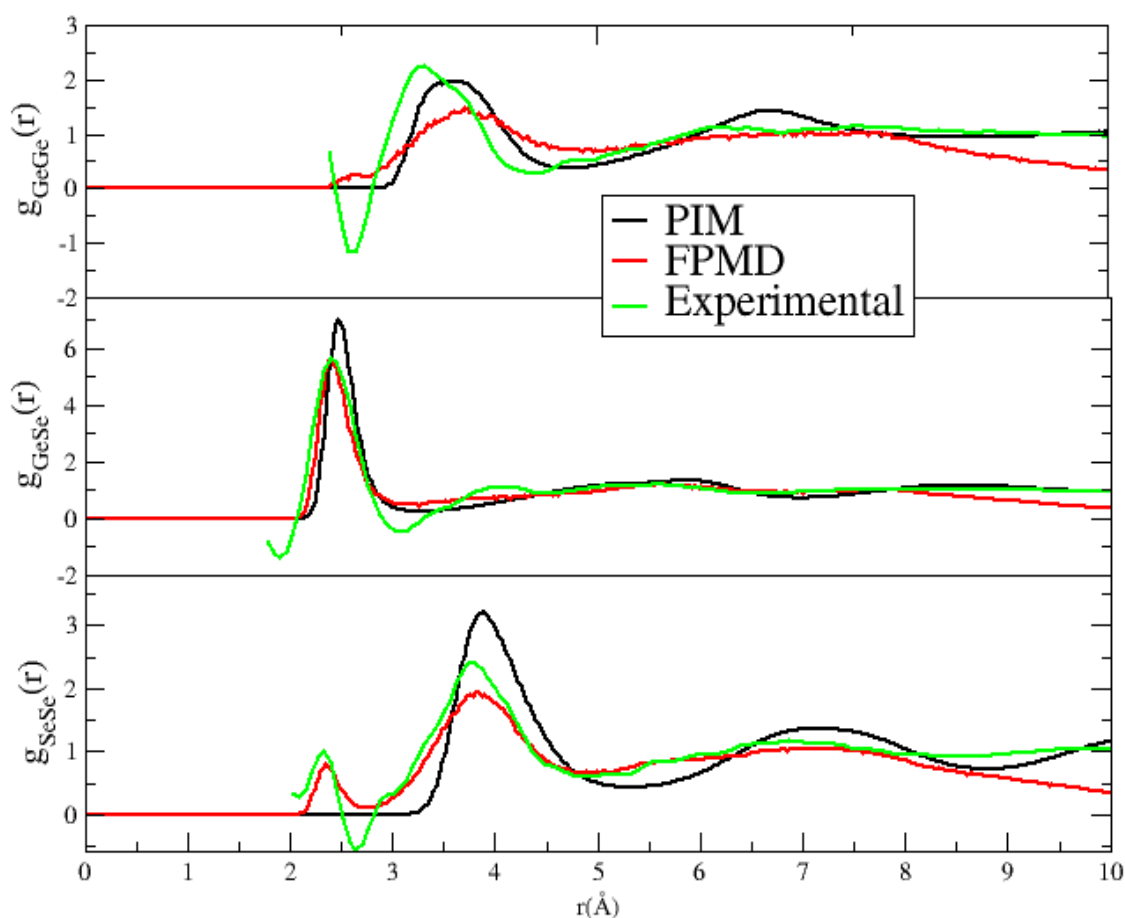
Figure 4.3:Partial radial distribution functions of germanium selenide obtained from theory and experiment[4]. Top, S$_{GeGe}$(k); middle, S$_{GeSe}$(k); bottom, S$_{SeSe}$(k). Black line, PIM; red line, FPMD; green line, experimental[4]. For the experimental function low r oscillations have been deducted.

whereas the FPMD results show better correlation.

Figure 4.3 shows that $g_{GeGe}^{PIM}(r)$ differs from $g_{GeGe}^{exp}(r)$ in not exhibiting a peak at low r (indicative of the presence of Ge-Ge homopolar bonds) and displaying greater intensity in the peak ~7Å. $g_{GeGe}^{FPMD}(r)$, in contrast, does display a peak at short separations and has approximately the same intensity at longer range values as $g_{GeGe}^{exp}(r)$. For the replication of the principal peak, $g_{GeGe}^{PIM}(r)$ has a better correlation with the peak position and in the decline of intensity at the high r side than the FPMD calculations. $g_{SeSe}^{PIM}(r)$ and $g_{GeSe}^{PIM}(r)$ displays a greater intensity than for the experimental functions at both the principal peak and the second peak indicating an overstructured representation of these interactions. In contrast, the FPMD results show better correlation; the low r peak in $g_{SeSe}^{exp}(r)$ is replicated, although at a lower intensity, while $g_{GeSe}^{FPMD}(r)$ shows the best match with experimental results over the whole range of separations.
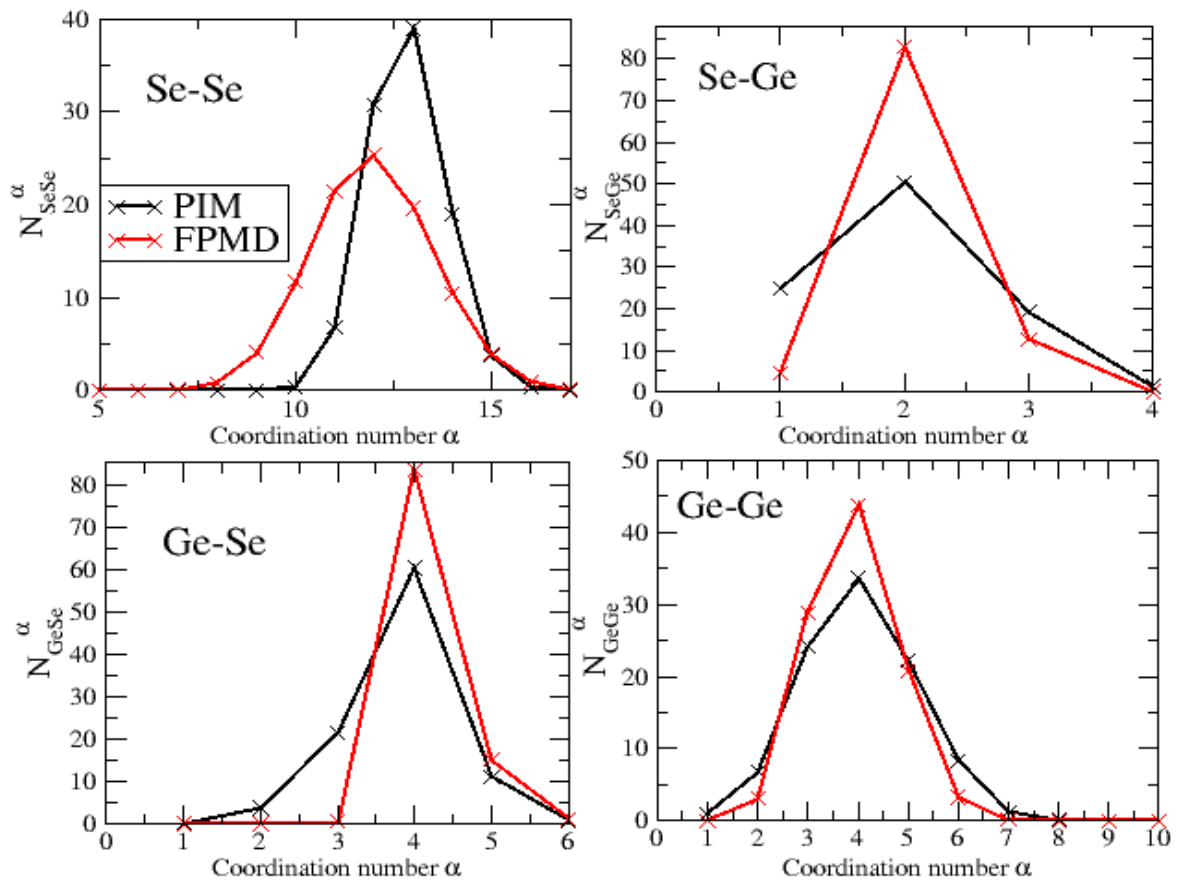
Figure 4.4:Coordination number distributions for ion pairs in GeSe₂. Black line, PIM; red line, FPMD.

Figure 4.4 shows the coordination number distributions of the four ion pairs for the PIM and FPMD models. They indicate that both models display a variety of coordinations for each ion pair. For the Ge-Se pair, the PIM shows a tighter coordination shell, with 88.4% of four coordinate cation compared to 60.3% in FPMD, but also with non-neglible miscoordinations present with 15.0 and 0.50% of 5 and 3-coordinate cations respectively. In the FPMD model, the more diffuse coordination shell of the Ge-Ge pair is expected after observation of the intensity on the high r side of the $g_{GeGe}(r)$ principal peak in figure 4.2 in addition to low-coordinated Ge atoms in homopolar bonds where 17% of Ge atoms are involved. The greater propensity for regular coordination numbers in the PIM is further highlighted by the Se-Se function. The large difference between the FPMD and PIM functions can be attributed, in part, by the presence of Se-Se homopolar bonds in the FPMD model which involve 32% of Se atoms but not in the PIM. Homopolar bonds can be inserted into a tetrahedral network in two ways: they may be contiguous with a tetrahedral network model due to a close separation of Se atoms which bridge two Ge cations or they can exist in isolation, bridging between cation-centred tetrahedral units. Figure 4.5 shows that in the FPMD calculations the homopolar bonds occur through the latter mechanism with an Se-Se bond linking units cation centred units together.
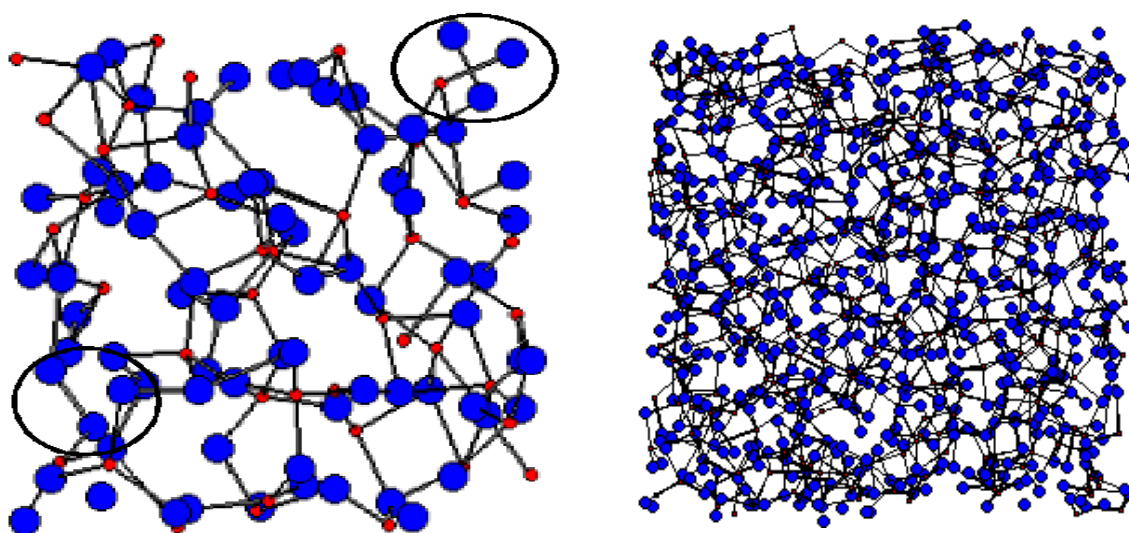
Figure 4.5. Molecular graphics snapshots of PIM and FPMD configurations. Left: FPMD (120 atoms) configuration of GeSe$_2$. The circles around the selenium (blue) ions highlight the presence of homopolar bonds. Right: PIM (999 atoms) configuration of GeSe$_2$; there are no homopolar bonds present.

Source	M$_{SeSe}$	M$_{GeSe}$	M$_{GeGe}$	M$_{SeGe}$
PIM	12.82	4.18	3.93	2.08
FPMD	11.81	3.73	3.93	1.89
Exp-Liquid[4]	9.6	3.7	2.9	
Exp-Glass[4]	9.3	3.5	3.2	

Table 4.3: Table of mean coordination numbers, M$_{ij}$, of ion pairs in GeSe$_2$ from theory and experiment[4].

Table 4.3 shows the mean coordination number of ion pairs comparing the theoretical and experiment results. For FPMD and PIM, the mean coordination numbers for a given ion pair, M$_{ij}$, were obtained using equation 4.3:

$$M_{ij} = \sum_l^m N_{ij}^\alpha \alpha \qquad (4.3)$$

where l to m is the range of coordination numbers for ion pair, ij, considered and N_{ij}^α is the percentage of coordination number α. Experimentally, this was calculated by integrating the principal peaks in the related radial distribution functions. Whilst M$_{GeSe}$ is similar, there is a large discrepancy between theory and experiment for the M$_{GeGe}$, indicating that edge-sharing, which leads to a decreased Ge-Ge coordination number, may be underepresented in the model.
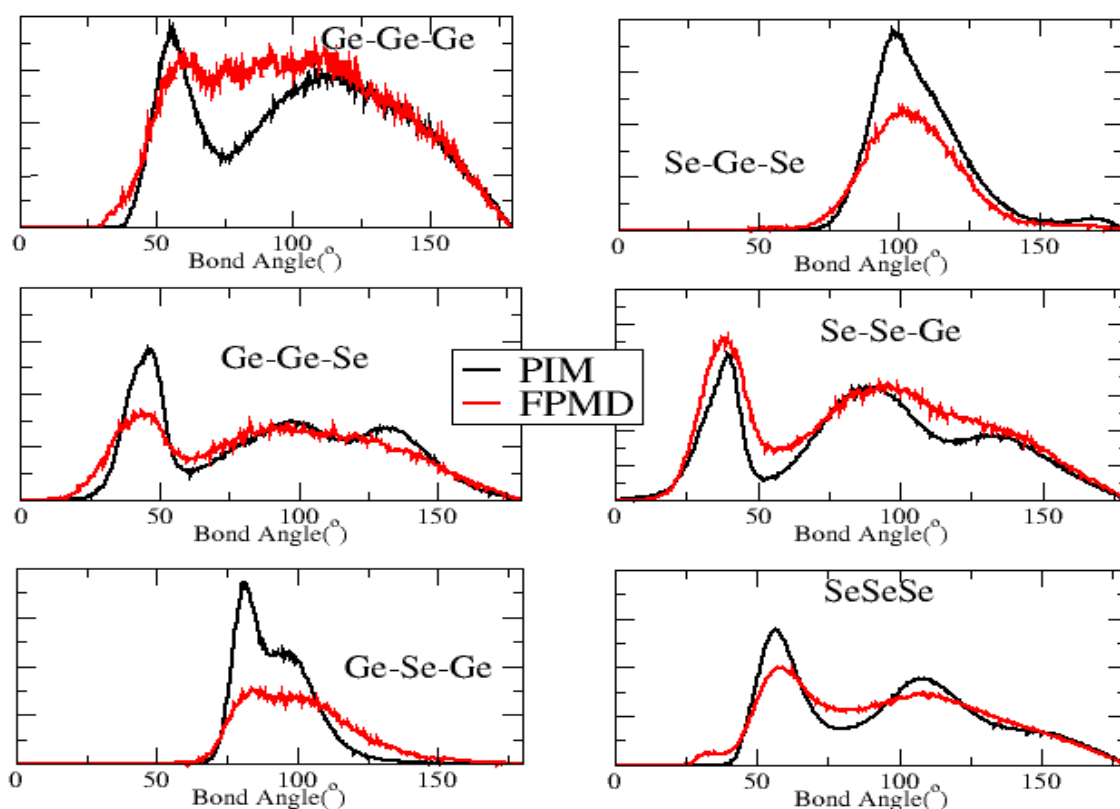
Figure 4.6: Bond angle distributions for ion triplets in GeSe$_2$. Black line, PIM; red line, FPMD.

Figure 4.6 shows the six bond angle distributions calculated for both the PIM and FPMD. The peaks observed in the bond angle distributions in GeSe$_2$ are similar for both FPMD and PIM, indicative of the fact that both are describing largely tetrahedral systems. The significant difference between the two sets of functions lies in the intensities of the peaks. The functions calculated from the FPMD configurations show a significantly weaker character than those calculated using the PIM. In Ge-Se-Ge, for example, the peak at 90° appears stronger for the PIM owing to the much larger concentration of edge-sharing units. The FWHM is also larger from the FPMD, as highlighted in the Ge-Ge-Ge distribution, as would be expected from the wider variety of coordination environments in the FPMD model. The Ge-Ge-Ge distribution has a much sharper peak 55° and larger peak 112°; in the Vashishta model (figure 6 in [26]), there is less distinction and the most intense peak is at the larger bond angle. The same feature arises in the Ge-Ge-Se distribution which differs from the PIM and FPMD models which have a larger intensity peak at lower angles. The increased connection of edge-sharing tetrahedra in the PIM will result in more acute Ge-Ge-Se angles due to the closure of the Ge-Ge-Se units which occurs with the formation of an edge-sharing unit, in comparison to a corner-shared configuration.

Netwok connectivity,E^n (where n is number of 4-membered rings a cation is bonded to)	E^0	E^1	E^2
FPMD	40.5(8.4)	40.3(7.5)	19.2(6.8)
PIM	18.1 (2.4)	49.4(2.7)	32.6(3.1)

Table 4.4:Percentage of cations according to network connectivity for FPMD and PIM GeSe$_2$ models

4.6 Relationship of network-connectivity with radial distribution function, $g_{MM}(r)$.

Table 4.4 shows the percentages of "0", "1" and "2" cations with their respective standard deviations. The greater amount of edge-sharing in the PIM distinguishes it from the FPMD and could be highlighted as one of the causes for the strengthening of the $S_{GeGe}(k)$ contribution to the total structure factor. It is uncertain whether the experimentally quoted figure of 34% edge-sharing refers to purely edge-sharing cation i.e "2" or refers to both fully and partially edge-sharing linked cations. A noticeable difference in the standard

deviation of the percentage values of "0", "1", and "2" cations. The results for FPMD exhibit a much greater standard deviation than PIM, an indication of the effects of structural relaxation which arise from a small system size. The PIM shows increased amounts of edge-sharing compared to results from diffraction and spectroscopic experiments and compared with the models of Vashishta and Massobrio. However, our model implies that a large proportion of edge-sharing units is required to reproduce the liquid structure of GeSe₂. This viewpoint is supported in recent calculations[51] in which the configurations from molecular dynamics simulations were selected according to the percentage of edge-sharing units. The partial structure factors calculated using configurations containing a relatively high proportion of edge-sharing units showed an improved representation of the FSDP in $S_{CC}(k)$ when compared with the analogous functions calculated by averaging over all configurations. In the experiment by Salmon *et al,* from which the edge-sharing figure for glassy GeSe₂ is derived[4], the high temperature crystalline phase[52] (which contains edge-and corner-sharing) is used as a guide to provide two length scales, one associated with corner-sharing (3.55Å) and the other associated with edge-sharing tetrahedra (3.05Å). Our results show that in the liquid phase, the separation between edge- and corner-sharing length scales (equivalent to "2-2" and "0-0" cation interactions) weakens and that the intermediate terms overlap. Figure 4.7 shows the network connectivity radial distribution functions, $g_{ab}^{GeGe}(r)$, where ab represents the different combinations of "0", "1" and "2" cations. These functions are normalised according to the concentrations of the coloured species (i.e $g_{ab}^{GeGe}(r)$ tends to one as r→∞). As expected, the position of the principal peaks show significant differences for $g_{00}^{GeGe}(r)$ and $g_{22}^{GeGe}(r)$ at 3.83Å and 3.46Å respectively; these represent, in extrema, corner- and edge-sharing length scales respectively. This contrasts with the experimental results of Susman *et al*[6] which indicate that the edge-sharing separation is even smaller than that given by the crystalline state at 2.85Å. These functions, in addition to the intermediate functions, $g_{01}^{GeGe}(r), g_{11}^{GeGe}(r), g_{12}^{GeGe}(r)$ and $g_{02}^{GeGe}(r)$, with principal peak positions of 3.79Å, (3.34Å and 3.76Å), 3.38Å and 3.88Å respectively show a significant amount of overlap with each other. This highlights the intractable difficulty of extracting edge-sharing statistics for liquids from radial distribution functions. This is reflected in the change of the percentage of edge-sharing cations, with variation of the Ge-Ge cutoff radius, as shown in figure 4.8. A large dependence with r is observed, in the

region 3.15Å to 3.75Å, with the total amount of edge-sharing units (E^1+E^2) increasing

until 3.90Å, approximately the same value as the principal peak position for $g_{00}^{GeGe}(r)$.
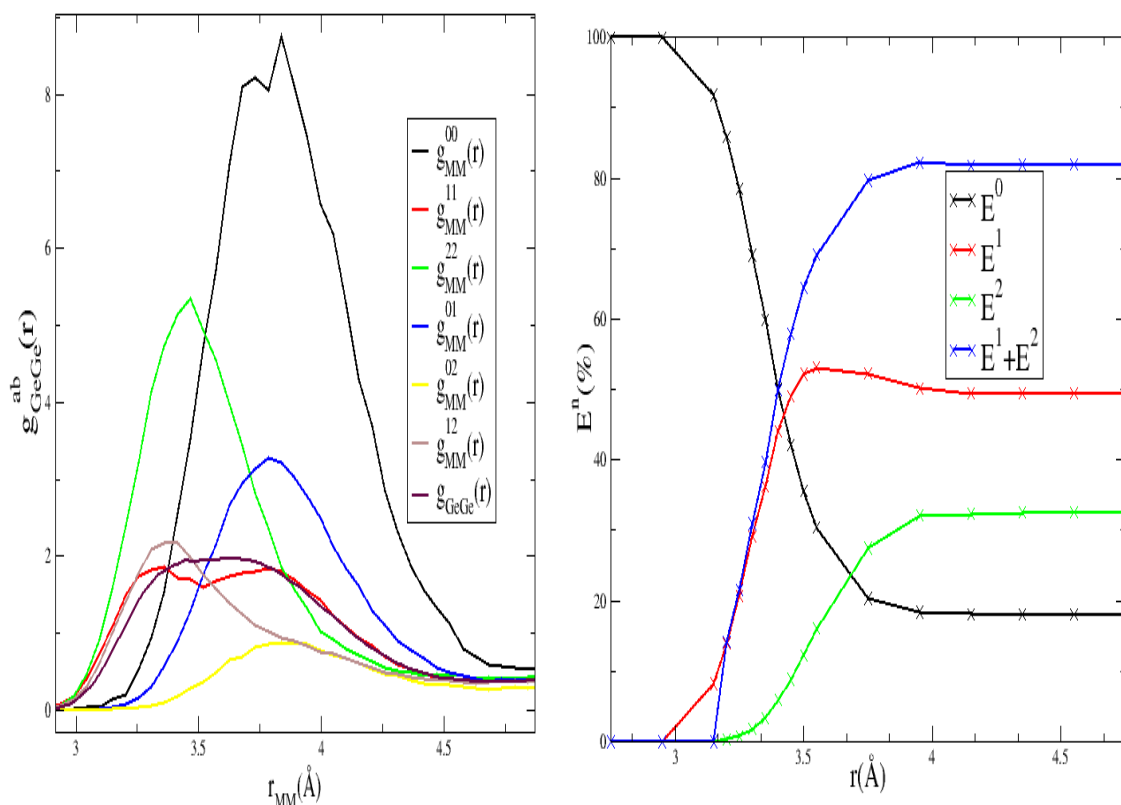
Figure 4.7 (left): Breakdown of g$_{GeGe}$(r) according to network connectivity of cations; black line,

$g_{MM}^{00}(r)$; red line, $g_{MM}^{11}(r)$; green line, $g_{MM}^{22}(r)$; blue line, $g_{MM}^{01}(r)$; yellow line, $g_{MM}^{02}(r)$;

brown line, $g_{MM}^{12}(r)$; mauve line, g$_{GeGe}$(r).

Figure 4.8(right): Percentage of cations according to network connectivity, E^n; black line, E^0; red line, E^1;

green line, E^2; blue line, E^1+E^2.

4.7 Conclusion.

A new model using the PIM has been produced for the structure of GeSe$_2$. In comparison

to recent FPMD calculations[32], the strength of the PIM representation is the description of

Ge-Ge correlations which are closer to the experimental results. FPMD provides a better

description of features such as homopolar bonds and better representation of the GeSe

and SeSe correlations, as evidenced by a similar intensity of the principal peak. However,

the absence of homopolar bonds do not appear to substantially affect the ability to

reproduce IRO as SeSe interactions are significantly less important than the

corresponding cation-cation functions. This is highlighted in the increased amount of

edge-sharing tetrahedral units which are exhibited by the PIM compared to FPMD and the Vashishta potential[26]. While the use of diffraction patterns has been questioned as suitable probe for measuring the efficacy of potential models[53], without further recourse to spectroscopic calculations, these results highlight that diffraction experiments, particularly the information at low k, are able to distinguish between a number of computational models in describing the structure. The model produced in this chapter enables the colouring of cations according to network connectivity and calculation of constituent partial structure factors, to perturb single parameters such as anion polarisability, temperature and density to observe the evolution of IRO. In this chapter, network connectivity radial distribution functions have been used to show the variety of edge-and corner-sharing environments and length scales associated with them in GeSe$_2$ demonstrate the difficulty of elucidating the percentage of edge-sharing cations from the radial distribution function $g_{GeGe}(r)$.

These results, and comparison with other GeSe$_2$ models show that there are two important strands to simulation work with regards to the structure of GeSe$_2$. The first is the importance of representing the connections between constituent tetrahedra. The prominence of edge-sharing is stronger in the PIM than in FPMD and previous classical models of Vashishta[26], leading to a stronger FSDP in $S_{GeGe}(k)$. The influence of edge-sharing in the representation of GeSe$_2$ has also been observed in systems such as calculations of Cobb and Drabold[34] where the partial structure factors are in good qualitative agreement with the experimental functions, but the relative intensities are much smaller (for $S_{GeSe}(k)$, ~10% of that observed experimentally). Another advantage of the model produced in this chapter is that it is a significantly larger system calculations of similar structural accuracy (999 atoms compared to 218 atoms used for the model used by Cobb and Drabold[34]). The edge-sharing present in a recent Monte Carlo model[45] of GeSe$_2$ is much weaker than present in our model and Cobb and Drabold's calculations[34]. This is indicated by the presence of an edge-sharing peak at 3.30Å which is much less intense than the corner-sharing peak at higher r. In a recent Reverse Monte Carlo simulation on GeSe$_2$ by Murakami *et al*[42], a FSDP in $S_{GeGe}(k)$ is reproduced but of a much weaker intensity (about half as intense as the principal peak) than that observed experimentally. There is also a good correlation in the principal peak intensities of all three correlations in addition to the FSDP of $S_{GeSe}(k)$. Another feature is the slower damping of high k oscillations in $S_{SeSe}(k)$ and $S_{GeGe}(k)$ than is observed in our model and experimentally

(possibly related to the initial configuration in the RMC procedure being crystalline). Again, the GeSeGe bond angle distribution shows the presence of edge-sharing is less significant than in our model. Ongoing work in electronic structure calculations is looking for stronger intermediate-range GeGe correlations by application of different exchange-correlation functionals including the BLYP (Becke exchange function[54] with Lee Yang and Parr correlation functional[55]) and Perdew-Wang[56] GGA approximations for exchange and correlation energy. The former, which does not assume uniform electron gas character of the correlation energy is more successful at reproducing liquid GeSe$_2$ structure. The improved model with the BLYP functional displays many structural features which correlate with our model including a steeper decline in the intensity at the high r side of the principal peak in $g_{GeGe}(r)$; a clearer separation between edge- and corner-sharing tetrahedra as highlighted by the presence of two peaks in the Ge-Se-Ge bond angle distribution; and a more intense FSDP in $S_{GeGe}(k)$.

The second important strand is the effect of the coordination shell of the ions; the PIM has a strong tetrahedral nature while FPMD induces a certain amount of disorder in terms of the coordination distribution and the presence of homopolar bonding. As highlighted in the introduction, too much chemical disorder through the presence of a significant amount of homopolar bonds leads to a relatively weakened FSDP. In comparison with recent results for glassy GeSe$_2$ by Mauro et al[37], no significant defect feature was observed in the radial distribution function at 3.04Å compared to the typical Ge-Se bond length of 2.36Å of $g_{GeSe}(r)$, as exhibited in structure factors of glassy GeSe$_2$[1]. This peak has been highlighted as a possible termination ripple, similar to other low r features caused by the truncation of the structure factor[8] in the Fourier transform of High Energy Diffraction experiments where it is present when k_{max} is 20Å^{-1} but absent when k_{max}=35Å^{-1}. In the RMC model of Murakami, $g_{GeSe}(r)$ has a strong intensity of ~13, over double to that observed experimentally, in addition to the presence of homopolar bonds in SeSe and GeGe correlations; the former feature may be caused by using a crystalline configuration at the beginning of the RMC procedure. DFT calculations on glassy-GeSe$_2$ by Giacomazzi[53] show good correlation in the FSDP and higher k range of the partial structure factors except for the FSDP in $S_{GeGe}(k)$. In several models produced, one utilising the Vashishta potential[26,27] to generate the initial configuration for relaxation by electronic structure methods, and another using solely electronic structure methods, show two varying interpretations of the structure. The first is predominantly ionic with 5% of

Se atoms involved in homopolar bonds and 33% edge-sharing, while the latter model has 24% of Se atoms in homopolar bonds with 55% edge-sharing, both resulting in a significantly weaker than experimental feature for $S_{GeGe}(k)$.[53] Our model, in contrast, shows an ability to stabilise a larger presence of edge-sharing units and exhibits greater stability in terms of the chemical ordering of the coordination shell, resulting in a better correlation to the experimental FSDP for $S_{GeGe}(k)$.

4.7 References

[1] I. T. Penfold and P. S. Salmon. *Phys. Rev. Lett.*, **67**, 97, (1991).

[2] I. Petri, P. S. Salmon and W. S. Howells. *J. Phys.: Condens. Matter,* **11**, 10219, (1999).

[3] I. Petri, P. S. Salmon and H. E. Fischer. *Phys. Rev. Lett.*, **84**, 2413, (2000).

[4] P. S. Salmon and I. Petri. *J. Phys.: Condens. Matter,* **15**, S1509, (2003).

[5] P. S. Salmon, R. A. Martin, P. E. Mason and G. J. Cuello. *Nature* (London), **435**, 75, (2005).

[6] S. Susman, K. J. Volin, D. G. Montague and D. L. Price. *J. Non-Cryst. Solids*, **125**, 168, (1990).

[7] A. Fischer-Colbrie and P. H. Fuoss. *J. Non-Cryst. Solids*, **69**, 271, (1985).

[8] V. Petkov. *J. Am. Ceram. Soc.*, **88**, 2528, (2005).

[9] P. S. Salmon and J. Liu. *J. Phys.: Condens. Matter*, **6**, 1449, (1994).

[10] W. H. Zachariasen. *J. Am. Chem. Soc*, **54**, 3841, (1932).

[11] I. T. Penfold and P. S. Salmon. *Phys. Rev. Lett.*, **68**, 253, (1992).

[12] R. J. Nemanich, F. L Galeener, J. C. Mikkelsen Jr, G. A. N. Connell, G. Etherington, A. C. Wright and R. N. Sinclair. *Physica B*, **117**, 959, (1983).

[13] S. Sugai. *Phys. Rev. B*, **35**, 1345, (1987).

[14] P. Tronc, M. Bensoussan, A. Brenac and C. Sebenne. *Phys. Rev. B*, **8**, 5947, (1973).

[15] R. J Nemanich, G. A. N.Connell, T. M. Hayes and R. A. Street. *Phys. Rev B,* **18**, 6900, (1978).

[16] P. M. Bridenbaugh, G. P. Espinosa, J. E. Griffiths, J. C. Phillips and J. P. Remeika. *Phys. Rev. B,* **20,** 4140, (1979).

[17] P. Boolchand, J. Grothaus and J. C. Phillips. *Solid State Commun.,* **45**, 183, (1983).

[18] J. M. Peters and L. E. McNeil. *J. Non-Cryst. Solids,* **139**, 231, (1992).

[19] P. Boolchand, J. Grothaus, W. J. Bresser and P. Suranyi. *Phys. Rev B*, **25**, 2975, (1982).

[20] P. Boolchand and J. C. Phillips. *Phys. Rev. Lett.*, **68**, 252, (1992).

[21] W. J. Bresser, P. Boolchand, P. Suranyi and J. P. de Neufville. *Phys. Rev. Lett.*, **46**, 1689, (1981).

[22] P. H. Fuoss, P. Eisenberger, W. K. Warburton and A. Bienenstock. *Phys. Rev. Lett.*, **46**, 1537, (1981).

[23] J. C. Phillips. *Phys. Today*, **35**, 27, (1982).

[24] M. F. Thorpe. *J. Non-Cryst. Solids*, **57**, 355, (1983).

[25] X. Feng, W. J. Bresser and P. Boolchand. *Phys. Rev. Lett*., **78**, 4422, (1997).

[26] P. Vashishta, R. K. Kalia and I. Ebbsjö. *Phys. Rev. B*, **39**, 6034, (1989).

[27] P. Vashishta, R. K. Kalia, G. A. Antonio and I. Ebbsjö. *Phys. Rev. Lett*., **62**, 1651, (1989).

[28] P. S. Salmon. *Proc: Math. and Phys. Sci*., **437**, 591, (1992).

[29] C. Massobrio, A. Pasquarello and R. Car. *J. Am. Chem. Soc*., **121**, 2943, (1999).

[30] C. Massobrio, M. Celino and A. Pasquarello. *Phys. Rev. B,* **70**, 174202, (2004).

[31] C. Massobrio, A. Pasquarello and R. Car. *Phys. Rev. Lett*., **80**, 2342, (1998).

[32] C. Massobrio, A. Pasquarello and R. Car. *Phys. Rev B*, **64**, 144205, (2001).

[33] M. Cobb, D. A. Drabold and R. L. Cappelletti. *Phys. Rev. B*, **54,** 12162, (1996).

[34] M. Cobb and D. A. Drabold. *Phys. Rev. B*, **56,** 3054**,** (1997).

[35] D. Tafen and D. A. Drabold. *Phys. Rev B*, **68**, 165208, (2003).

[36] P. Biswas, D. N. Tafen, and D. A. Drabold. *Phys. Rev. B*, **71**, 054204, (2005).

[37] J. C. Mauro, A. K. Varshneya. *J. Am. Ceram. Soc*., **89**, 2323, (2006).

[38] J. P. Perdew and A. Zunger. *Phys. Rev. B*, **23**, 5048, (1981).

[39] J. P. Perdew, J. A. Chevary, S. H. Vosko, K. A. Jackson, M. R. Pederson, D. J. Singh and C. Fiolhais. *Phys. Rev B*, **46**, 6671, (1992).

[40] O. F. Sankey and D. J. Niklewski. *Phys. Rev. B*, **40**, 3979, (1989).

[41] J. Harris. *Phys. Rev. B*, **31**, 1770, (1985).

[42] Y. Murakami, T. Usuki, M. Sakurai and S. Kohara. *Materials, Science and Engineering A*, **449**, (2007).

[43] G. D. Mahan. *Solid State Ionics*, **1**, 29, (1980).

[44] W. R. Busing. *J. Chem. Phys*., **57**, 3008, (1972).

[45] L. V. Woodcock, C. A. Angell and P. Cheeseman. *J. Chem. Phys*., **65**, 1565, (1976).

[46] M. P. Tosi and M. Doyama. *Phys. Rev*., **160**, 716, (1967).

[47] M. Wilson and P. A. Madden. *Phys. Rev. Lett*., **80**, 532, (1998)

[48] J. Ruska and H. Thum. *J. Non-Cryst. Solids*. **22**, 277, (1976).

[49] F. Wooten and D. Weairem. *Solid State Physics*, Academic, p40, New York, (1987)

[50] G. T. Barkema and N. Mousseau. *Phys. Rev. B*, **62**, 4985, (1996).

[51] C. Massobrio, A. Pasquarello and R. Car. *Phys. Rev B*, **75**, 014206, (2007).

[52] G. Dittmar and H. Schäfer. *Acta Crystallogr. B*, **32**, 2726, (1976).

[53] L. Giacomazzi, C. Massobrio and A. Pasquarello. *Phys. Rev B*, **75**, 174207, (2007).

[54] A. D. Becke. *Phys. Rev. A*, **38**, 3098, (1988).

[55] C. Lee, W. Yang, and R. G. Parr. *Phys. Rev. B*, **37**, 785, (1988).

[56] J. Perdew and Y. Wang. *Phys. Rev. B*, **45**, 13244, (1992).

Chapter 5

Chemical ordering in GeSe$_2$ and ZnCl$_2$

5.1 Introduction.

In the MX$_2$ stoichiometry, GeSe$_2$ and ZnCl$_2$ represent an archetypal pair of materials possessing intermediate-range order.[1,2] In both cases, the network structure can be considered as constructed from a mix of corner-sharing and edge-sharing MX$_4$ tetrahedra. Both systems show a FSDP at scattering angles corresponding to $k_{FSDP} \sim 1$Å^{-1} (compared with the principal peak at 2Å^{-1}) in their structure factors.[3-7] Furthermore, the existence of suitable isotopes allow the partial structure factors to be experimentally resolved for both systems.[3,5-7,8] rendering these systems excellent targets for simulation models. Neutron scattering studies[3,5-7] indicate that the respective FSDPs are dominated by the cation sublattice (although this view has been questioned[9]). Both systems display complex morphological changes as a function of temperature[5-7,10] and pressure.[11,12] Despite their clear similarities, these systems also show distinct differences often assigned to a fundamental difference in their inherent bonding, as indicated by the greater ionicity of the Zn-Cl bond with a value of 43% according to the Pauling electronegativity scale compared to 7% for GeSe$_2$. Additionally, GeSe$_2$ shows a small fraction of homopolar bonds[13-18,19-23] not present in ZnCl$_2$, which may have implications for network-dependent properties.

The difference in structure is naturally expressed in the Bhatia-Thornton structure factors, which separate structural (network) ordering from that imposed by the underlying chemistry (chemical ordering),[24,25] with GeSe$_2$ showing a significantly stronger FSDP in the concentration-concentration function $S_{CC}(k)$, indicative of the chemical ordering on an intermediate length scale. Simulation work has tended to focus on the individual systems. For GeSe$_2$, *ab initio* electronic structure calculations have reproduced a large number of static and dynamic properties.[14-18, 19-23] However, the emergence of a FSDP in $S_{CC}(k)$ is found to be heavily dependent on the details of the calculation. Pair potential based models augmented with explicit three body terms, which constrain specific bond angles, fail to reproduce such a feature.[26,27] The success of electronic structure calculations in

reproducing the FSDP in S$_{CC}$(k) varies. Neither the LDA (Harris first order functional) of Drabold *et al*[20,21] or the calculations of Massobrio et al, either in LDA or GGA schemes,[16,19] reproduce this feature. An understanding of the structural origin of the FSDP in S$_{CC}$(k) is lacking. Massobrio *et al*,[13-18] define three classes of IRO in which structural disorder is correlated with the FSDP intensity. Class 1 encompasses near perfect networks and have no FSDP in S$_{CC}$(k). In class II, significant structural disorder leads to a FSDP, while in class III the degree of disorder is such as to remove the FSDP. For systems such as ZnCl$_2$ and GeSe$_2$ the polarisation effects are balanced such that these systems can be considered as a dynamic mix of edge-sharing and corner-sharing units. The relative flexibility of the PIM lies in the ability to readily stabilise both corner-sharing and edge-sharing polyhedral links as a function of the anion environment, rather than relying on more restrictive explicit bond-angle constraints.[26,27]

In order to exploit this inherent flexibility this chapter is divided into two main sections. In the first half, the current best fit models for both ZnCl$_2$ and GeSe$_2$ are studied with emphasis on the low-k properties of S$_{CC}$(k). In the second half, additional models are considered as well as the density dependence of S$_{CC}$(k), allowing for the structural origins of the low k features to be further understood.

5.2 Simulation Details

The central cell used in all calculations in this chapter consists of 999 ions (333 cations and 666 anions).The Bhatia-Thornton[24] and network connectivity correlation functions discussed in section 5.3, were obtained by using the configurations generated from the calculations for ZnCl$_2$ and GeSe$_2$ detailed in Chapters 3 and 4 respectively. The cell for GeSe$_2$ was held to experimental density (average cell size 31.80Å) by application of a pressure of 6×10^{-4} a.u and at a temperature of 3000K while for ZnCl$_2$ the run was at zero pressure and 800K, both under NPT conditions, and the results are discussed in section 5.3.

In section 5.4, we compare the S$_{CC}$(k) of ZnCl$_2$ and GeSe$_2$ with BeF$_2$, MgCl$_2$, ZnCl$_2$ at lower density and BeCl$_2$, where the short-range damping parameter c is reduced from 0.90 to 0.50 in steps of 0.1. In all simulations in this section, equilibration runs of 30 ps were carried before an additional simulation run of 60 ps length. The potential parameters for all these systems are given in Appendix B. For BeF$_2$, the potential[28] was applied to a

previous configuration using the ZnCl$_2$ RIM model. The simulation was run at 1100K under NPT conditions in a cell with an average cell size of 22.17Å, within 1% of experimental density of 1.96 g/cm^3 at 973K.[29] Using a potential model which used an older parameter set for the ZnCl$_2$ PIM potential model[30], the range of densities analysed were obtained by varying the pressure from 5x10^{-5} a.u to 1.5x10^{-5} a.u pressure increments of 1.25x10^{-6} a.u. Data was taken at each increment where, beginning with the lowest pressure configuration, the average cell sizes were 35.05Å, 34.27Å, 33.79Å, 33.41Å, 33.02Å, 32.73Å, 32.46Å, 32.15Å and 31.97Å. The temperature for these simulations was set constant at 800K. S$_{CC}$(k) for BeCl$_2$ was calculated for the configurations generated with the short-range damping parameter carried out in steps of 0.1 from c=0.90 to c=0.50 in the procedure highlighted in section 6.9. S$_{CC}$(k) for MgCl$_2$ was calculated using the configurations generated in Chapter 3.

5.3 Comparison of GeSe$_2$ with ZnCl$_2$.

Figure 5.1 shows the network connectivity structure factors for the ZnCl$_2$ and GeSe$_2$ models calculated at T=800K and T=3000K, respectively (in the liquid regimes for both systems). The strongest FSDPs are observed in the cation-cation functions, with significant features in the corresponding metal-anion functions. The major difference in these two systems lies in the relative intensities of the FSDP in S$_{MM}$(k) compared with the principal peak in S$_{MM}$(k). The feature in GeSe$_2$ is significantly more intense than in ZnCl$_2$ (~90% and ~55% of the principal peak heights, respectively)[3, 5-7, 8] consistent with experiment and *ab initio* simulations.[13-18] The Bhatia-Thornton (BT) partial structure factors [S$_{CC}$(k), S$_{NN}$(k), and S$_{NC}$(k)] may be expressed in terms of the Faber-Ziman functions as:

$$S_{CC}(k) = c_M c_X \{ 1 + c_M c_X [[S_{MM}(k) - S_{MX}(k)] + [S_{XX}(k) - S_{MX}(k)]] \} \qquad (5.1)$$

$$S_{NN}(k) = c_M^2 S_{MM}(k) + c_X^2 S_{XX}(k) + 2 c_M c_X S_{MX}(k) \qquad (5.2)$$

$$S_{NC}(k) = c_M c_X \{ c_M [S_{MM}(k) - S_{MX}(k)] - c_X [S_{XX}(k) - S_{MX}(k)] \} \qquad (5.3)$$
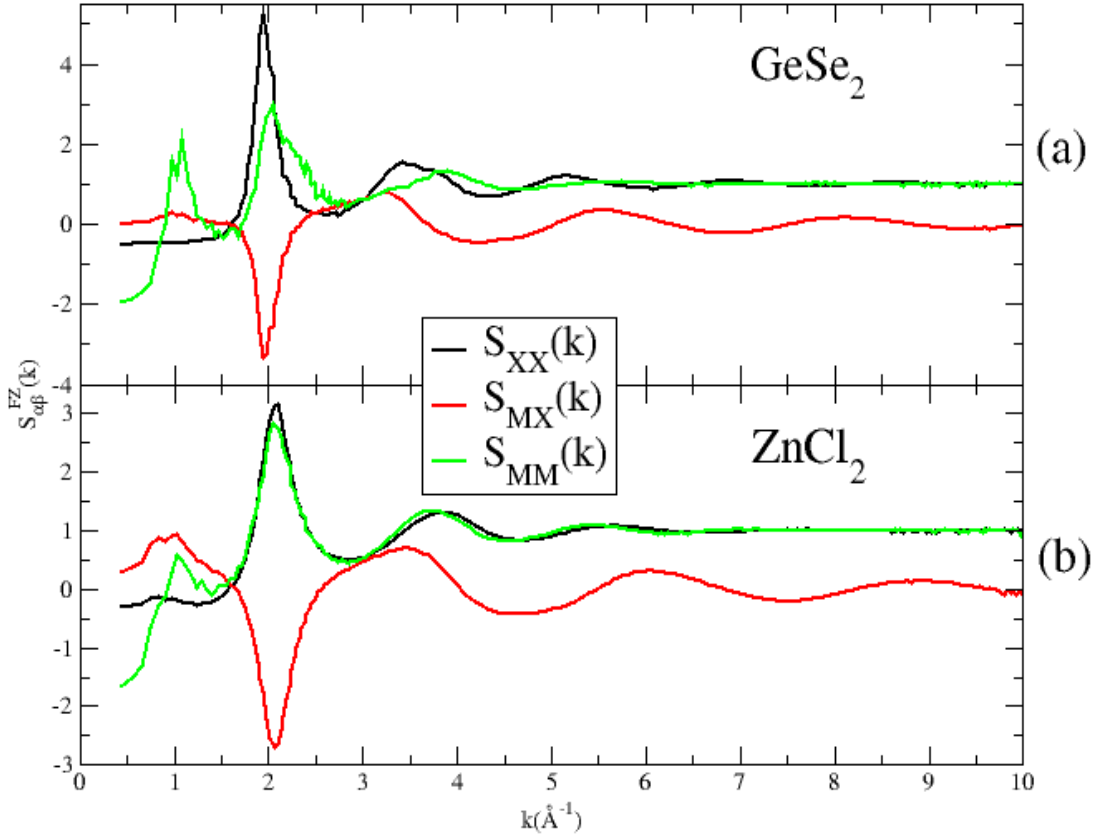
Figure 5.1:Faber-Ziman partial structure factors obtained for the ZnCl$_2$ and GeSe$_2$ models at 800K and 3000K respectively. Black line, S$_{XX}$(k); red line, S$_{MX}$(k); green line, S$_{MM}$(k), where M=Ge and X=Se for top panel and M=Zn and X=Cl for bottom panel.

Figure 5.2 shows the BT structure factors for the simulated GeSe$_2$ and ZnCl$_2$ systems. Clear FSDPs are observed in both S$_{NN}$(k) functions (again, consistent with experiment[5-7]). Significantly, a FSDP appears in the S$_{CC}$(k) for the GeSe$_2$ model but not for the ZnCl$_2$. Although recent scattering experiments suggest the appearance of an S$_{CC}$(k) in both systems,[8] the signature for ZnCl$_2$ appears significantly weaker than for GeSe$_2$. As a result, we envisage the two models considered here may represent *extrema* in terms of their IRO and its relation to S$_{CC}$(k). Figure 5.3 shows the breakdown of S$_{CC}$(k) into the weighted contributions from the FZ functions. [Eq 5.1] At $k \geqslant k_{PP}$ S$_{CC}$(k) is a simple superposition of three FZ functions, with the two like-like functions [S$_{MM}$(k) and S$_{XX}$(k)] equally weighted and S$_{MX}$(k) weighted double. At $k \leqslant k_{PP}$ however, S$_{XX}$(k$_{FSDP}$)~0 and so S$_{CC}$(k) approximates to a simple combination of S$_{MM}$(k) and S$_{MX}$(k) [S$_{CC}$(k)~c$_M$c$_X$\{1+c$_M$c$_X$[S$_{MM}$(k)-2S$_{MX}$(k)]\}]. For the ZnCl$_2$ model these two functions can effectively cancel out on the length scale associated with the FSDP. It appears, therefore,

that the greater intensity of $S_{GeGe}(k)$ [compared with $S_{ZnZn}(k)$ in ZnCl$_2$] leads to an incomplete cancellation from the respective anion-cation function and hence to the significant FSDP in $S_{CC}(k)$.
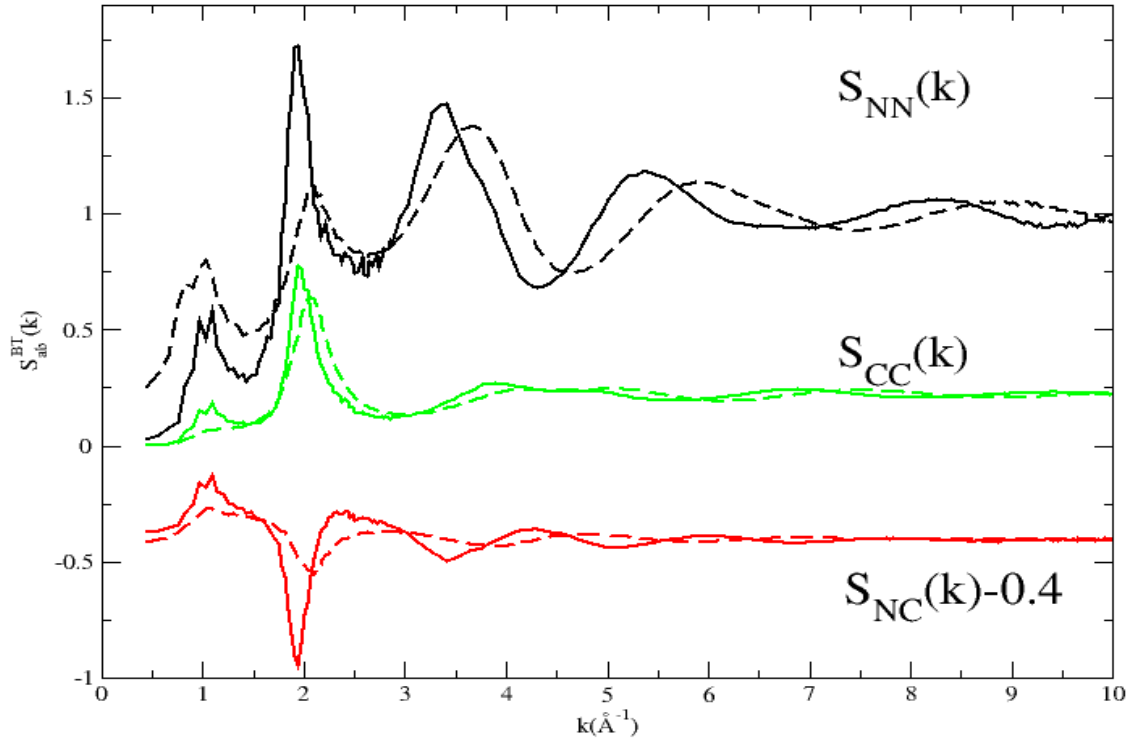
Figure 5.2: Bhatia-Thornton partial structure factors obtained for the ZnCl$_2$ and GeSe$_2$ models at 800K and 3000K respectively. Black line, $S_{NN}(k)$; red line, $S_{NC}(k)$; green line, $S_{CC}(k)$, where full line is GeSe$_2$ and half-line is ZnCl$_2$.

In order to understand the structural origins of this difference in $S_{CC}(k_{FSDP})$, $S_{MM}(k)$ and $S_{MX}(k)$ are decomposed into additional partial structure factors (network connectivity structure factors) generated by "colouring" each cation in the terms of the local environment. A cation at the centre of a tetrahedron which only corner shares with neighbouring polyhedra is labelled "0", while those with structural units containing one and two edge-sharing units are labelled "1" and "2" respectively.[15] Table 5.1 lists the fraction of each cation type for the two systems averaged over 100ps of molecular dynamics. The GeSe$_2$ model contains a significantly greater proportion of edge-sharing units.
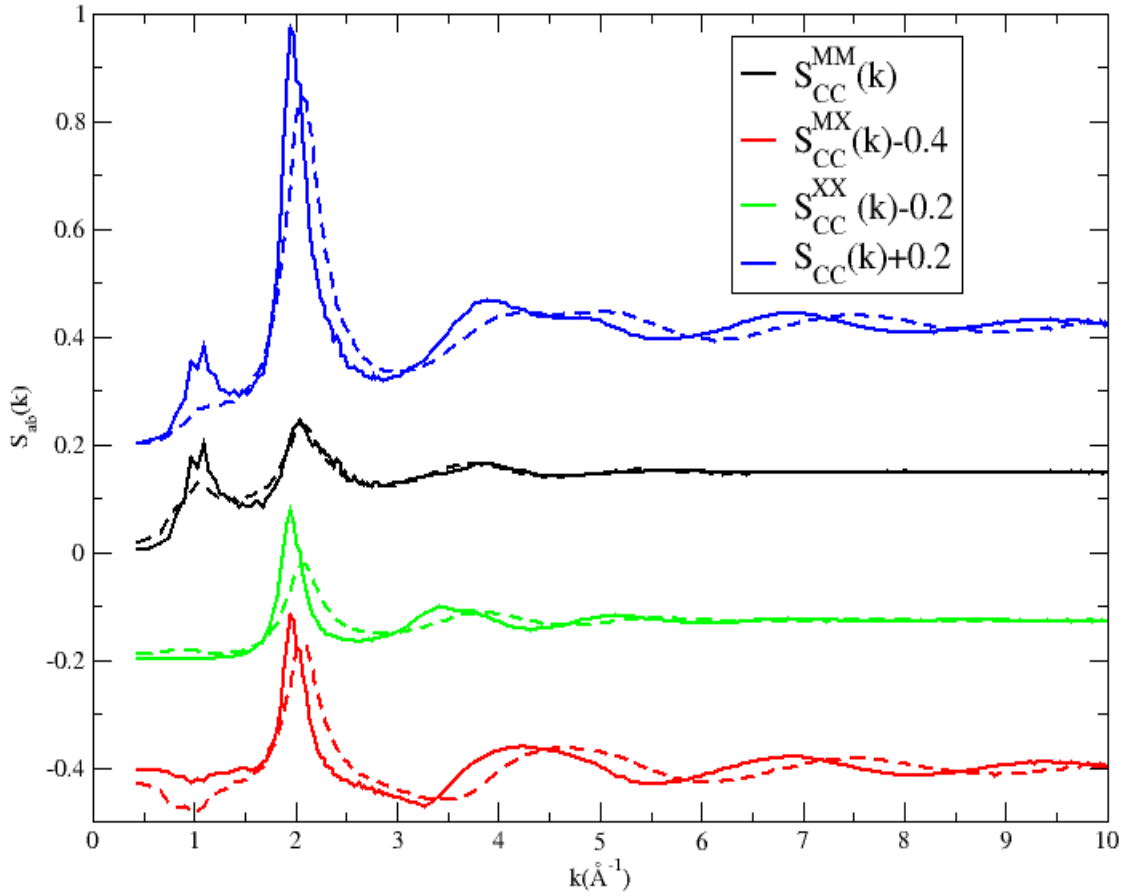
Figure 5.3: Breakdown of the Bhatia-Thornton concentration-concentration structure factors, S$_{CC}$(k), into the weighted Faber-Ziman functions for the GeSe$_2$ (solid lines) and ZnCl$_2$ (dashed lines) models. The GeSe$_2$ shows a clear FSDP which is absent for ZnCl$_2$. Black line, anion-anion contribution $S_{CC}^{XX}(k)$; red line, cation-anion contribution $S_{CC}^{MX}(k)$; green line, cation-cation contribution $S_{CC}^{MM}(k)$; blue line, $S_{CC}(k)$.

Connectivity	*GeSe$_2$*	*ZnCl$_2$*
0	18	33
1	49	40
2	33	27

Table 5.1: Percentage of cations coloured according to their network connectivity.

An additional six MM and three MX structure factors can be defined as

$$S_{MM}^{ab}(k)=\langle A_M^{\grave{a}}(k)\cdot A_M^b(k)\rangle \tag{5.4}$$

$$S_{MX}^{aX}(k)=\langle A_M^{a'}(k)\cdot A_X(k)\rangle \tag{5.5}$$

where {a,b} = {0,1,2}. These functions can be combined to produce network connectivity cation-cation and cation-anion structure factors.

$$S_{MX}(k) = c_0 S_{MX}^{0X}(k) + c_1 S_{MX}^{1X}(k) + c_2 S_{MX}^{2X}(k)$$

(5.6)

$$S_{MM}(k) = c_0^2 \left(S_{MM}^{00}(k) - 1 \right) + c_1^2 \left(S_{MM}^{11}(k) - 1 \right) + c_2^2 \left(S_{MM}^{22}(k) - 1 \right) + 2 c_0 c_1 S_{MM}^{01}(k) + 2 c_0 c_2 S_{MM}^{02}(k)$$
$$+ \quad 2 c_1 c_2 S_{MM}^{12}(k)$$

(5.7)

where c_1 and c_2 are the mole fractions of atoms labelled "0", "1, and "2" respectively. Figure 5.4 shows the breakdown of the respective $S_{MM}(k)$ and $S_{MX}(k)$ structure factors into the (weighted) network connectivity functions defined above. For GeSe$_2$, the strongest contributions to the FSDP in $S_{MM}(k)$ arise from $S_{MM}^{11}(k)$, $S_{MM}^{12}(k)$, and $S_{MM}^{02}(k)$, with $S_{MM}^{12}(k)$ and $S_{MM}^{02}(k)$ both having a FSDP intensity greater than the principal peak. [$S_{MM}(k_{FSDP})/S_{MM}(k)(k_{PP}) = 1.13$ and 1.79 respectively]. For ZnCl$_2$, the six functions appears similar in terms of the $S_{MM}(k_{FSDP})/S_{MM}(k_{PP})$ ratio (in the range 0.6 to 0.9), with each appearing to contribute significantly to the FSDP in $S_{ZnZn}(k)$ with their relative contributions dictated by the concentration weightings in equation 5.6. In addition, the GeSe$_2$ function FSDPs differ in position, with k_{FSDP}=0.97, 1.08, 1.02 and 1.03Å^{-1} for $S_{MM}^{01}(k)$, $S_{MM}^{02}(k)$, $S_{MM}^{11}(k)$ and $S_{MM}^{12}(k)$ respectively. These differences indicate that the presence of edge-sharing units in the GeSe$_2$ model exerts a major influence on the static structure by effectively breaking up the corner-sharing network and introducing subtle variations in the IRO.

Further clues as to the nature of this network are afforded by considering the width of the FSDPs in Figure 5.4. The $S_{MM}^{11}(k)$, $S_{MM}^{12}(k)$ and $S_{MM}^{02}(k)$ functions show widths (at half the peak height) of 0.35, 0.39, and 0.67Å^{-1} respectively. The significantly greater width of $S_{MM}^{02}(k)$ at k_{FSDP} results from the pseudo one-dimensional nature of the percolating edge-shared chains. These chains are effectively charge neutral and so are only weakly bound to the network perpendicular to the chain major axis. The weak-bonding results in the formation of an ordered intermediate-ranged length scale in addition to that imposed by the corner sharing network. Unlike $S_{MM}(k)$, the $S_{MX}(k)$ functions appear to map onto each other when the concentration weightings are accounted
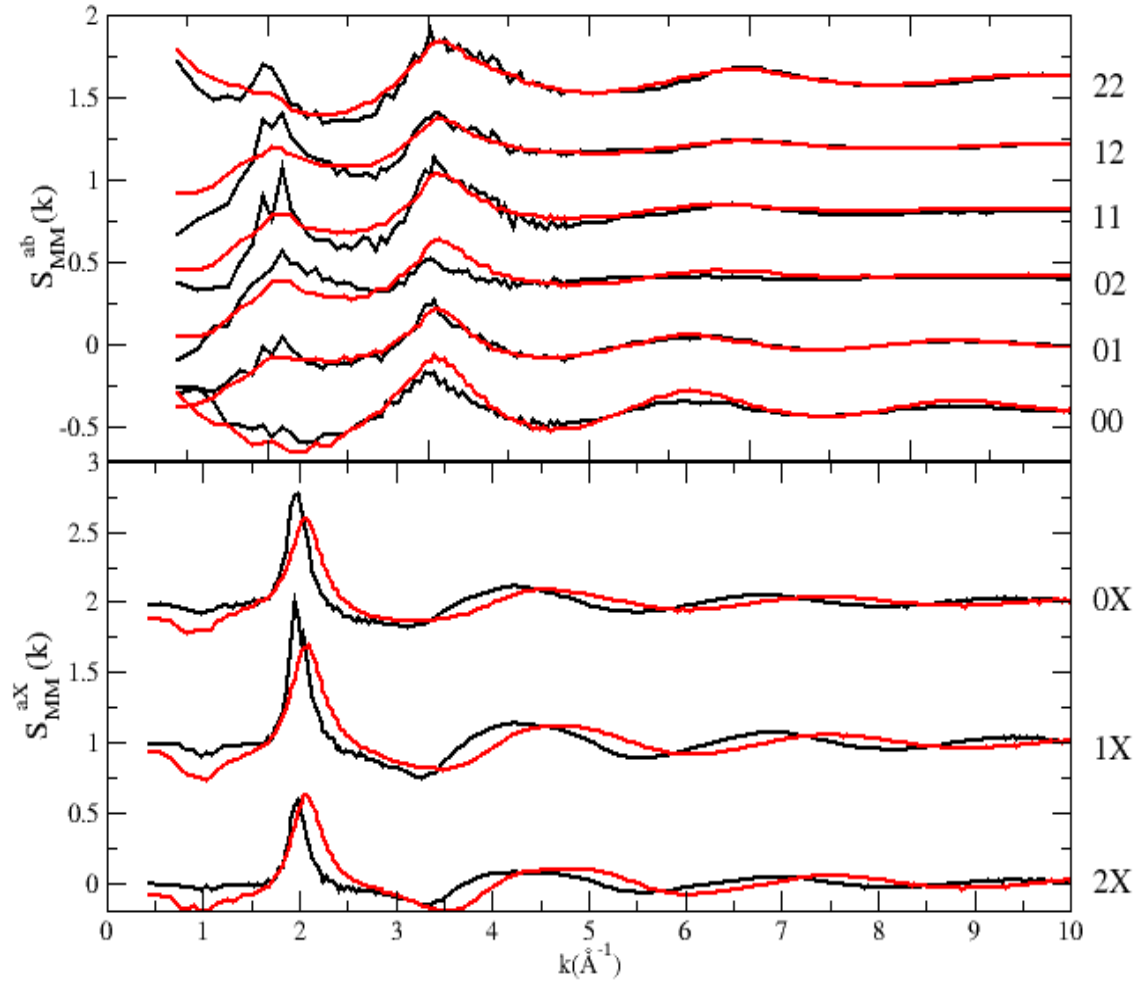
Figure 5.4:Breakdown of the cation-cation (upper panel) and cation-anion (lower panel) structure factors in terms of the cation environment. The functions are weighted by the respective concentrations of the coloured cations.

for. The difference in the two systems, therefore, lies in the relative intensities of the S$_{MM}$(k) which is directly correlated to the differing proportions of edge-sharing units.

Two further differences between the MM functions are noteworthy. First, both $S_{MM}^{00}(k)$ and $S_{MM}^{22}(k)$ are increasing as k→0 indicative of the effect of "phase separation" or clustering of these coloured cation sites. Secondly the long k oscillations appear quite different in these two set of functions. For the ZnCl$_2$ model, the six functions appear to contain the oscillations (at $k \geqslant k_{PP}$) at approximately the same frequency. In the GeSe$_2$ model, the oscillation frequencies and their intensities appear to be significantly different between the six different functions. To further understand these differences the corresponding real space network connectivity pair distribution functions, $g_{MM}^{ab}(r)$ are calculated.
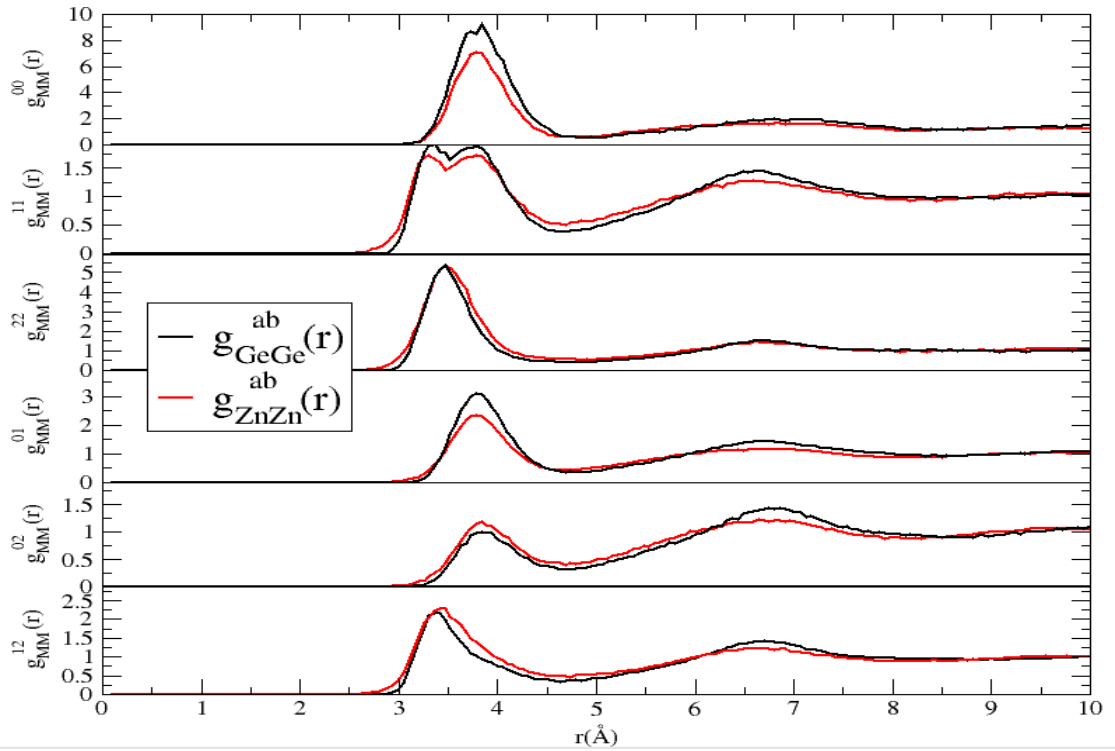
Figure 5.5: Network connectivity radial distribution functions, $g_{MM}^{ab}(r)$, for ZnCl$_2$ and GeSe$_2$ according to network connectivity of cations.

Figure 5.5 shows the six network connectivity radial distribution functions for the two systems. ZnCl$_2$ and GeSe$_2$ functions display peaks on three length scales; $g_{MM}^{00}(r)$ and $g_{MM}^{01}(r)$ show a peak at 3.86Å, $g_{MM}^{11}(r)$ at ~3.60Å, and $g_{MM}^{12}(r)$ and $g_{MM}^{22}(r)$ at ~3.35Å. The resolution of the different cation length scales supports the existence of relatively long-lived species built around the corner- and edge-sharing in the molten state. For $g_{GeGe}^{02}(r)$ and $g_{GeGe}^{12}(r)$, a less intense principal peak compared to $g_{ZnZn}^{02}(r)$ and $g_{ZnZn}^{12}(r)$ is coupled with a more intense second peak; the ratio of the intensities being significantly larger for $g_{GeGe}^{02}(r)$ at 1.45, compared to 0.97 for $g_{ZnZn}^{02}(r)$. The function, $g_{MM}^{12}(r)$, displays the only significant difference in terms of principal peak position with $g_{GeGe}^{12}(r)$ showing a peak at 3.35Å compared 3.45Å for $g_{ZnCl}^{12}(r)$. $g_{GeGe}^{00}(r)$, $g_{ZnZn}^{01}(r)$ and $g_{GeGe}^{11}(r)$ show more intense principal and second peaks compared to their zinc counterparts.

Figure 5.6 shows two graphical snapshots of the respective cation distributions with the different polyhedral linkages highlighted. For the GeSe$_2$ system a significant number

of edge-sharing units form into chains. The percolation of the edge-sharing units form into chains. This percolation of edge-sharing units leads to an effective clustering of these units with resultant phase separation of sites labelled "0" and "2". The presence of a cation labelled "2" precludes the nearest neighbour labelled "0" (since these neighbours must have one edge-shared link). The percolation of these edge-sharing units (equivalent) to chains of "2" cations results in an additional ordering of the sublattice beyond that imposed by a simple corner-sharing polyhedral network. The percolated edge-sharing units introduce a short cation-cation length scale resulting in a region of relatively high cation density.
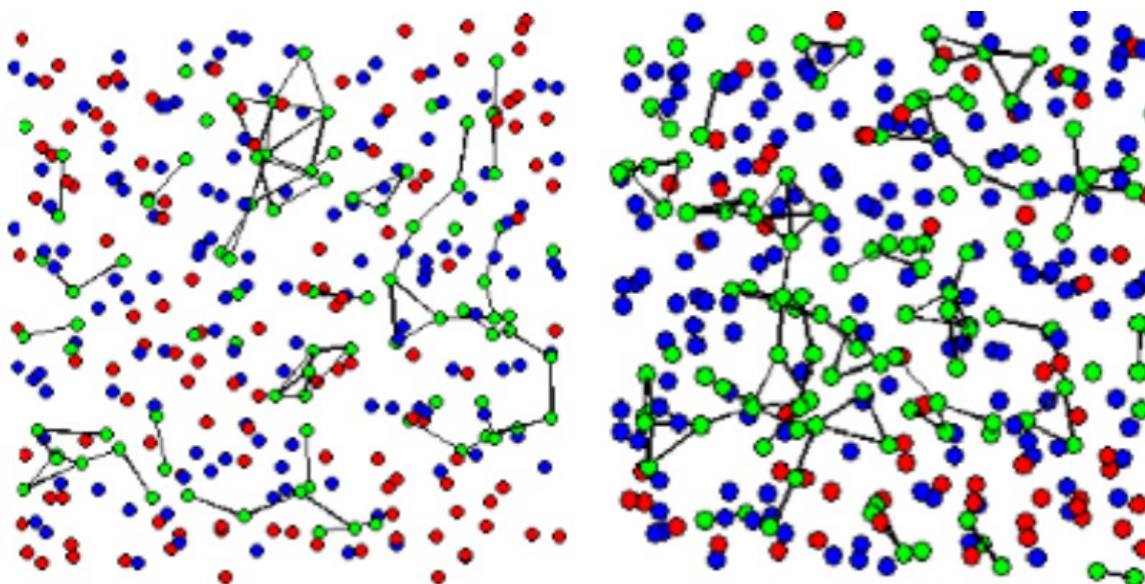
Figure 5.6: Molecular graphics snapshots for ZnCl$_2$ (left) and GeSe$_2$ (right) showing cations coloured according to their network connectivity: red circles, "0" cations; blue circles, "1" cations; green circles, "2" cations.

Figure 5.7 shows the effect of the additional cation-cation length scales on the real space concentration-concentration Bhatia-Thornton functions, g$_{CC}$(r) calculated by the equation 5.7:

$$g_{CC}(r) = c_M c_X [g_{MM}(r) + g_{XX}(r) - 2 g_{MX}(r)] \qquad (5.7)$$

The GeSe$_2$ system shows significant features at r+/r-~1.33 attributable to the existence of a significant number of the percolating edge-shared units. The presence of the percolating edge-shared units, therefore creates fluctuations in the cation subdensity on both the short and intermediate length scales. The pseudo one-dimensional nature of these units leads to
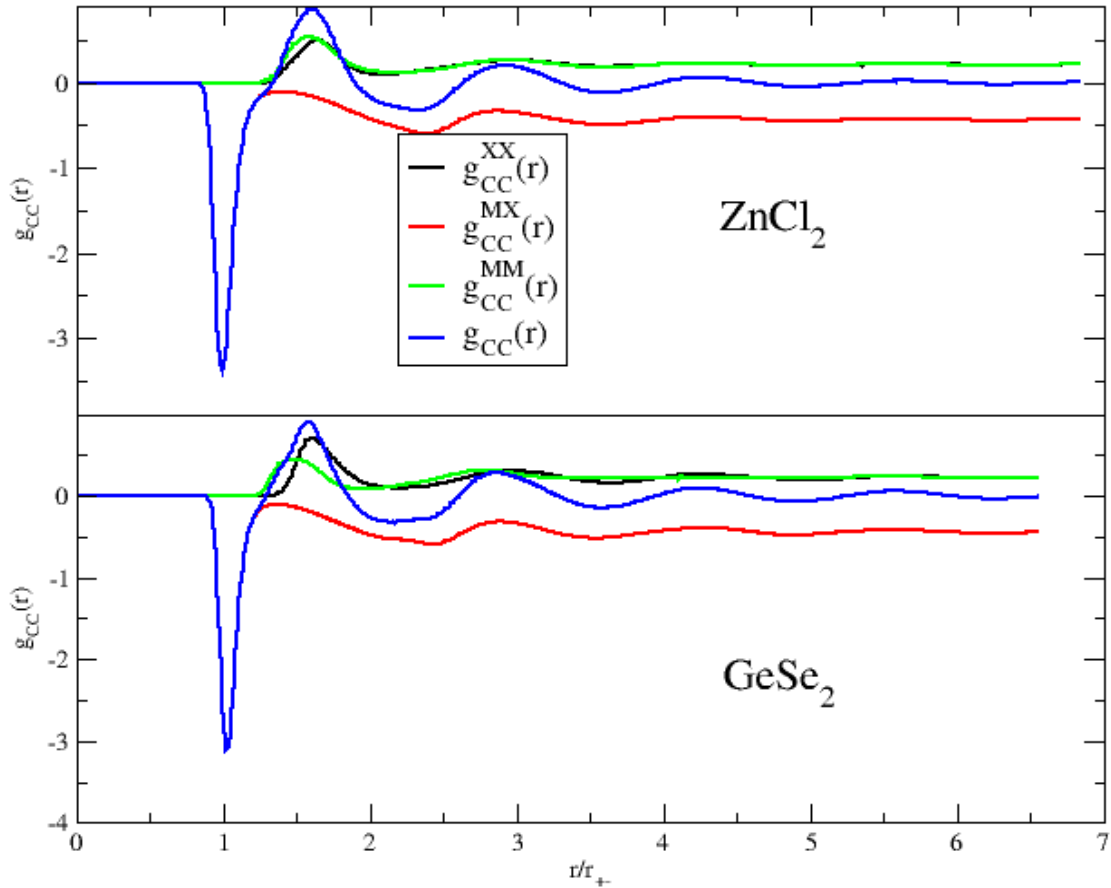
Figure 5.7: Real space Bhatia-Thornton concentration-concentration pair distribution functions for the GeSe$_2$ (bottom panel) and ZnCl$_2$ (top panel) along with the three Faber-Ziman contributions. Black line, anion-anion contribution $g_{CC}^{XX}(r)$; red line, metal-anion contribution $g_{CC}^{MX}(r)$; green line, cation-cation contribution $g_{CC}^{MM}(r)$; blue line, $g_{CC}(r)$.

fluctuations in the cation charge density over the intermediate length scale and hence causes the FSDP in $S_{CC}(k)$. For ZnCl$_2$, the chain percolation is strictly limited and so these additional length scales are only transient.

In this section the difference in the intermediate–range order observed in two specific systems (ZnCl$_2$ and GeSe$_2$) has been investigated. The variations in IRO have been attributed to difference in the number of edge-sharing tetrahedral units present in the two systems. For GeSe$_2$, these edge-sharing polyhedral units are found to percolate into persistent charge neutral (one-dimensional) chain structures which act to break up the (three-dimensional) corner-sharing network (predominant in ZnCl$_2$). These chains act to introduce an additional intermediate-range length scale leading to an excess intensity of the $S_{MM}(k_{FSDP})$ which is not counterbalanced by the corresponding $S_{MX}(k)$ function and hence leads to the FSDP in $S_{CC}(k)$.

5.4 The FSDP in concentration-concentration structure factor, S$_{CC}$(k), in MX$_2$ systems.

A study by Salmon of a group of MX$_2$ compounds found the presence of a first sharp diffraction peak in S$_{CC}$(k) in ZnCl$_2$, MgCl$_2$ and GeSe$_2$, although absent in NiCl$_2$, NiBr$_2$, NiI$_2$, SrCl$_2$, CaCl$_2$ and BaCl$_2$.[25] Subsequent computational study has found it difficult to reproduce this feature.[16,19] In the case of classical calculations, the inability to reproduce homopolar bonds may have been a factor; in the case of electronic structure calculations, structural relaxations due to the small size of the array, and an overestimation of the amount of covalency could be reasons why the observation of the FSDP in S$_{CC}$(k) remains problematic. The appearance of a FSDP in S$_{CC}$(k) in section 5.2 is the first to be found in classical-MD calculations. The appearance of such a feature in the present work enables a systematic study of the S$_{CC}$(k) peak with regards to temperature and pressure, and in particular on the structural origin. Our work so far has shown the FSDP in S$_{CC}$(k) to be present in GeSe$_2$-like systems while a less intense shoulder is present is ZnCl$_2$. The major structural difference in GeSe$_2$ and ZnCl$_2$ was the presence of a tighter 4-coordination with the presence of larger amounts of edge-sharing. Preliminary calculations, with a previously used parameter set[30] for ZnCl$_2$, showed that with density changes an increased amount of edge-sharing was present. As a result, we pose the question as to whether a FSDP in S$_{CC}$(k) could be produced by calculating the structure of *low-density* ZnCl$_2$, where we expect a larger proportion of edge-shared tetrahedral units. In addition, we considered another candidate system, BeCl$_2$, which displays dominant edge-sharing linkages in the molten state as indicated by Raman spectroscopy.[31] Furthermore, a potential model has been developed using the PIM had shown to contain significant edge-sharing units. BeCl$_2$ is also shown to have significant presence of three and four coordinate cations. Other candidate systems for the observations of the presence of a FSDP in S$_{CC}$(k) are BeF$_2$: a system dominated by the presence of corner-sharing tetrahedra and MgCl$_2$: a system with similar features to ZnCl$_2$ but as shown in chapter 3 differs particularly in the local geometry of the anions around the central cation in constituent polyhedral units. This would complete the range of structures we would expect from molten MX$_2$ systems in this cation size range.
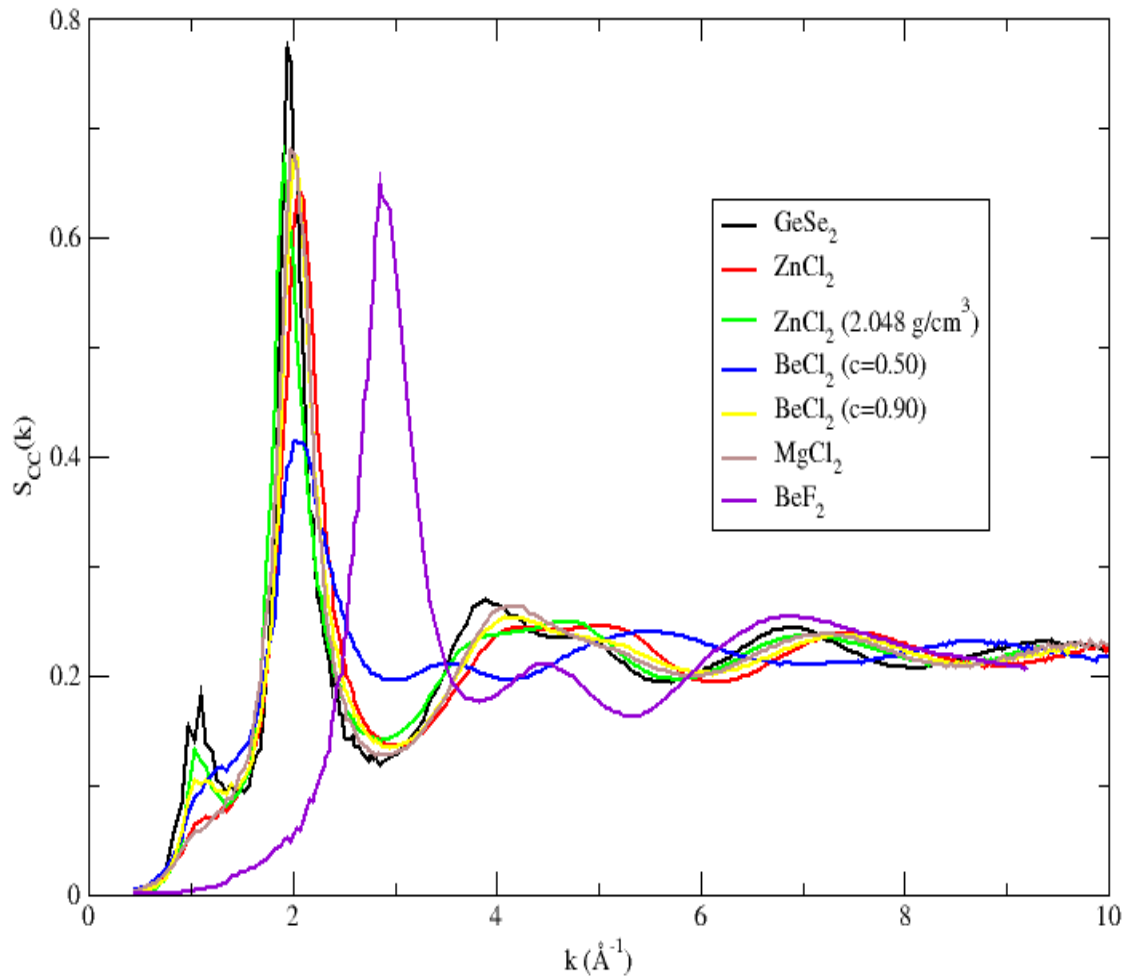
Figure 5.8:Concentration-concentration structure factor, $S_{CC}(k)$, for various compounds: Black line, GeSe$_2$ (3000K, exp. density); red line, ZnCl$_2$ (800K, 2.41 g/cm^3); green line, ZnCl$_2$ (800K, 2.05 g/cm^3); blue line, BeCl$_2$ (short-range damping parameter (SRDP) c=0.50); yellow line, BeCl$_2$ (SRDP c=0.90); brown line, MgCl$_2$ (800K); purple line, BeF$_2$.

Figure 5.8 highlights the $S_{CC}(k)$ functions for the different compounds. BeF$_2$ displays the least intensity at 1Å^{-1}. GeSe$_2$ displays the strongest $S_{CC}(k)$ whilst the lower density configuration of ZnCl$_2$ displays a much stronger FSDP compared the experimental density configuration. The simulated BeF$_2$ system is strongly 4-coordinate with negligible amounts of edge-sharing tetrahedra. As a result, the length scales which are stabilised for systems such as GeSe$_2$ and ZnCl$_2$ are not present and so concentration fluctuations are not observed over the intermediate-range near 1Å^{-1}. The $S_{CC}(k)$ functions of MgCl$_2$ and ZnCl$_2$ do not show a significant FSDP unlike the experimental functions by Salmon[25]. At lower densities, ZnCl$_2$ forms a small pre-peak in $S_{CC}(k)$. The change in the intensity of $S_{CC}(k_{FSDP})$ highlighted in table 5.2 shows that there is not a simple linear relationship with

decrease in density. The intensity of $S_{CC}(k_{FSDP})$ observed for ZnCl$_2$ across the density-range of 1.73 to 2.28 g/cm^3 varies from 0.11 to 0.13, with the maximum value occuring at the intermediate density values of 2.05 g/cm^3 and 2.11 g/cm^3. Over the same range of densities, the FSDP in $S_{NN}(k_{FSDP})$ shows much larger changes from 0.47 at the highest to 1.26 at the lowest density. Figure 5.9 shows the change in the partial structure factors for ZnCl$_2$ over this density region. With decreasing density both $S_{ZnZn}(k_{FSDP})$ and $S_{ZnCl}(k_{FSDP})$
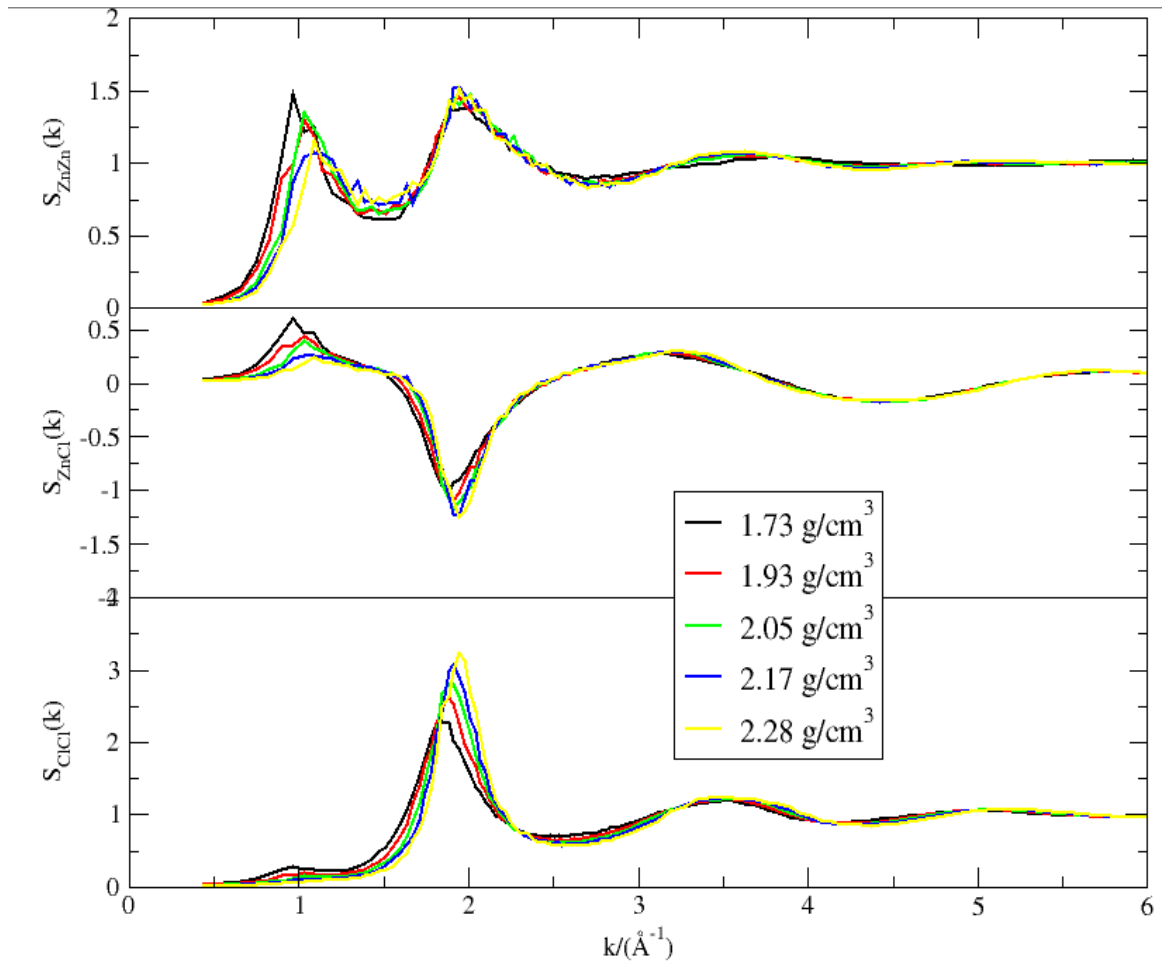
Figure 5.9: Partial structure factors of ZnCl$_2$ in the density range 1.73-2.28 g/cm^3. Top panel, $S_{ZnZn}(k)$; middle panel, $S_{ZnCl}(k)$; bottom panel, $S_{ClCl}(k)$. Black line, 1.73 g/cm^3; red line, 1.93 g/cm^3; green line, 2.05 g/cm^3; blue line, 2.17 g/cm^3; yellow line, 2.28 g/cm^3.

increase in intensity and shift to lower k. The balance of $S_{ZnZn}(k_{FSDP})$ against $S_{ZnCl}(k_{FSDP})$ which is responsible for the FSDP in $S_{CC}(k)$ fluctuates over this density region.

At the lowest density sampled, 1.73 g/cm^3, $S_{ZnZn}(k)$ displays a large FSDP similar to that of GeSe$_2$ in section 5.2, but the intensity of the related $S_{CC}(k_{FSDP})$ (given in table 5.2) is not similarly the strongest (observed at 2.05 g/cm^3) because of the larger intensity of $S_{ZnCl}(k_{FSDP})$. Whereas $S_{CC}(k)$ represents the difference between $S_{ZnZn}(k)$ and $S_{ZnCl}(k)$

equation 5.2 shows that $S_{NN}(k)$ is essentially a weighted summation of the changes in the partial correlations. However, the subtle balance of the cation-cation and cation-anion terms in $S_{CC}(k)$ results in a non-linear relationship of the intensity at the FSDP compared with the relatively clear fall in intensity observed in $S_{NN}(k)$. Table 5.2 also shows that structural features over the density range remain similar, both in the percentage of cations coloured by their respective network connectivities and the coordination numbers, highlighted by the similarity in 4-coordination in the Zn cation. This indicates that the changes are largely to do with the accommodation of larger voids within essentially the same network.

Density (g/cm^3)	E^0	E^1	E^2	N$_{Zn\text{-}Cl}$=4	N$_{Cl\text{-}Zn}$=1	S$_{CC}$(k$_{FSDP}$)	S$_{NN}$(k$_{FSDP}$)
1.73	19	54	26	82.7	8.96	0.12	1.26
1.85	26	57	17	82.9	8.4	0.11	1.02
1.93	31	54	15	83.6	7.81	0.12	0.98
2.00	30	54	15	84.6	6.74	0.12	0.93
2.05	26	55	20	85.7	4.46	0.13	0.89
2.11	36	48	16	83.8	5.66	0.13	0.72
2.17	34	52	15	83.6	4.63	0.12	0.67
2.24	35	48	17	81.1	4.62	0.11	0.65
2.28	35	51	15	81.2	4.05	0.11	0.47

Table 5.2: Summary of structural information of low-density ZnCl$_2$ configurations. Columns 2-4: percentages of cations coloured according to their network connectivity; columns 5 and 6: percentage of four coordination for Zn-Cl ion pair and 1 coordination for Cl-Zn ion pair; columns 7 and 8: intensities of the FSDP in concentration-concentration and number number structure factors.

So far we have observed the presence of a FSDP in systems where edge-sharing connectivity between tetrahedra is more prominent i.e in GeSe$_2$ and the low-density ZnCl$_2$ configurations. Whilst a minimum is highlighted in the intensity of $S_{CC}(k_{FSDP})$ in the case of BeF$_2$, the possibility of a maximum in the intensity of $S_{CC}(k_{FSDP})$ can be investigated by using an amended BeCl$_2$ potential which enables larger polarisation effects, such as increased propensity for edge-sharing to occur. The short-range damping parameter c was varied in the region 0.50-0.90. Figure 5.8 shows that a peak is resolved ~1Å^{-1} at c=0.90 while at c=0.50 the intensity is observed as a shoulder. Table 5.3 highlights the $S_{CC}(k)$ intensity with changing value of c. In contrast to the low density configurations of ZnCl$_2$

where coordination is similar, changing c causes large changes in coordination: table 5.3 shows with decreasing c lower Be-Cl coordination is favoured. There is also a large increase of miscoordinated anions. Over this range of coordination changes, the $S_{CC}(k_{FSDP})$ intensity remains similar. In chapter 6 we show that at c=0.50, an ionic to molecular transition occurs: this is highlighted by the steep drop in coordination number for Be-Cl coupled with the rise in miscoordinated anions, indicating the formation of molecular units. Although there is a sharp decline in $S_{BeBe}(k)$ this is matched by a similar drop in $S_{BeCl}(k)$; the net effect is that though $S_{CC}(k)$ is observed as a shoulder rather than a peak in figure 5.7 it observes a similar intensity to $S_{CC}(k)$ at c=0.90.

SRDP c	k_{FSDP} (Å^{-1})	$S_{CC}(k_{FSDP})$	$N_{Be-Cl}=2$	$N_{Be-Cl}=3$	$N_{Be-Cl}=4$	$N_{Be-Cl}=5$	$N_{Be-Cl}=6$	$N_{Cl-Be}=1$
0.50	1.08	0.10	10.3	45.8	39.7	4.2	0.11	40.4
0.60	1.14	0.13	1.37	24.3	63.6	10.2	0.43	20.1
0.70	1.14.	0.13	0.17	10.5	70.1	18.1	1.08	9.7
0.80	1.09	0.12	0.018	4.30	65.3	27.9	2.56	4.5
0.90	1.09	0.10	0.017	3.42	61.5	31.5	3.58	3.2

Table 5.3: Summary of structural information of BeCl$_2$ configurations. Columns 2-3, intensities and position of the FSDP in concentration-concentration structure factors; columns 4-8, percentage of coordination number for ion pair BeCl, N_{Zn-Cl}; column 9, percentage of 1-coordination for Cl-Zn ion pair.

5.5 Conclusion.

The section of the London underground map in figure 5.10 provides an effective 2D analogy of the cation-cation correlations which are responsible for the presence of a FSDP in $S_{CC}(k)$. Stations represent cations with the section pictured here representing an amorphous system. In a system where Coulombic repulsion was paramount in determining the structure of a cation sublattice, they would, to a reasonable approximation, be spaced out equally with an even distribution of voids between them. The presence of an anion with significant polarisability stabilises closer packing of the cations (stations). This results in an increasing in cation bonded together through edge-shared units ("1" cations). In GeSe$_2$, where a larger anion polarisability is present this

results in chain formation (track lines) with cations in wholly edge-sharing configurations ("2" cations) connected together.

Figure removed for
copyright reasons

Figure 5.10: Section of the London Underground Map. Variations in void sizes between cations (train stations) are exacerbated with the presence of train tracks inducing concentration fluctuations.

The effect of this chain formation is a closer separation of atoms at local density. To offset this increase in local density voids are stabilised by the larger separation of bonds between remaining cations. It is primarily the ordering across these larger voids which are responsible of both longer length scale and a wider range of M-M bond distances to a greater degree in systems such as GeSe$_2$ compared to ZnCl$_2$. The importance of the presence of a significant amount of edge-sharing has been highlighted here and in recent work by Massobrio[32] where GeSe$_2$ configurations derived from those displaying a relatively high value of S$_{CC}$(k) showed greater edge-sharing than configurations displaying a relatively low value.

Our calculations show the influence of percolating edge-sharing chains in systems such as molten GeSe$_2$ which are responsible for the presence of a FSDP in S$_{CC}$(k). Previous work[26] on the presence of a FSDP in S$_{CC}$(k) in MX$_2$ systems was hindered by the inability to stabilise the presence of enough edge-sharing tetrahedra to stabilise the interactions responsible for the FSDP. An early interpretation of the FSDP in S$_{CC}$(k) by Salmon[2] indicated its presence as being a ubiquitous feature in systems of MX$_2$ stoichiometry which are comprised of tetrahedral units. Due to the stoichiometry of the constituent tetrahedra (MX_4^{-2}), charge propagates along the bonds and, as this occurs in an open network, concentration fluctuations occur as a result.[2] The focus of proceeding electronic structure calculations was on the relationship between the charge-charge

structure factor, $S_{ZZ}(k)$, and the concentration-concentration structure factor, $S_{CC}(k)$. FPMD calculations on GeSe$_4$ showed that charge fluctuations on an intermediate-range length scale were not responsible but structural disorder.[19] This structural disorder was viewed in terms of miscoordination (i.e for MX$_2$ systems higher or lower than 4-coordination for M ions) and broken chemical order in terms of the presence of homopolar bonding, rather than the importance of the varying presence of edge- and corner-sharing tetrahedral linkages which our model indicates. Similarly, the scheme of Massobrio[15] described in section 5.1 focuses on a small amount of disorder (combination of miscoordination and homopolar bonding) as being required for the presence of a $S_{CC}(k_{FSDP})$. As we have shown in this chapter, it is the presence of percolating edge-sharing chains breaking up a corner-sharing network which is required for a significant FSDP in $S_{CC}(k)$.

In the second half of the chapter we observed a range of systems and the varying manner by which they displayed a FSDP in $S_{CC}(k)$. BeF$_2$ observes the weakest intensity in the range of the FSDP in $S_{CC}(k)$ and it was found that systems which tended towards edge-sharing behaviour and strong tetrahedral coordination, such as the low-density ZnCl$_2$ configurations generated, displayed a stronger FSDP in $S_{CC}(k)$. A non-linear dependence was found in ZnCl$_2$, where the temperature and pressure affected the subtle balance between the relative intensities of $S_{ZnZn}(k_{FSDP})$ and $S_{ZnCl}(k_{FSDP})$. Of all the systems analysed here, GeSe$_2$ displayed the strongest intensity in $S_{CC}(k_{FSDP})$. The range of systems exhibiting a peak in $S_{CC}(k_{FSDP})$ in simulated systems is smaller than those observed in experimental systems. This gap has decreased by, firstly, the observation of the FSDP in $S_{CC}(k)$ in a simulated system and, secondly, the elucidation of the major structural features responsible for it. Our interpretation of the $S_{CC}(k_{FSDP})$ indicates support for the presence of significant peaks systems such SiSe$_2$ and GeSe$_2$, medium intensity for systems such as ZnCl$_2$ and MgCl$_2$ at 1Å^{-1} and the absence of a peak and any significant intensity for systems such as BeF$_2$. This correlates with experiments[8] on glassy GeSe$_2$ and ZnCl$_2$ which show that GeSe$_2$ has a visibly more intense FSDP in $S_{CC}(k_{FSDP})$ than ZnCl$_2$, although the latter systems observes a peak experimentally compared to the shoulder observed in figure 5.2 from our calculations. Our model is also in contradiction with the presence of a FSDP observed experimentally in $S_{CC}(k)$ of glassy GeO$_2$ from experiments of Salmon *et al*[33] at ~1.53Å^{-1} in addition to earlier experiments[2] which showed a FSDP present at ~1Å^{-1} in MgCl$_2$.

5.6 References.

[1] S. R. Elliott. *Nature* (London), **354**, 445, (1991).

[2] P. S. Salmon. *Proc. R. Soc. London, Ser. A*, **445**, 351, (1994).

[3] J. A. E. Desa, A. C. Wright, A. C. Wong and R. N. Sinclair. *J. Non-Cryst. Solids*, **51**, 57, (1982).

[4] I. Petri, P. S. Salmon and H. E. Fischer. *Phys. Rev. Lett.*, **84**, 2413, (2000).

[5] T. Penfold and P. S. Salmon. *Phys. Rev. Lett.*, **67**, 97, (1991).

[6] P. S. Salmon and I. Petri. *J. Phys.: Condens. Matter,* **15**, S1509, (2003).

[7] I. Petri, P. S. Salmon and W. S. Howells. *J. Phys.: Condens. Matter,* **11**, 10219, (1999).

[8] P. S. Salmon, R. A. Martin, P. E. Mason and G. J. Cuello. *Nature* (London), **435**, 75, (2005).

[9] J. Neuefeind. *Phys. Chem. Chem. Phys.,* **3**, 3987, (2001).

[10] D. A. Allen, R. A. Howe, N. D. Wood and W. S. Howells. *J. Chem. Phys.,* **94**, 5071, (1991).

[11] W. A. Crichton, M. Mezouar, T. Grande, S. Stølen and A. Grzechnik. *Nature,* **414**, 622, (2001).

[12] C. H. Polsky, L. M. Martinez, K. Leinenweber, M. A. VerHelst, C. A. Angell and G. H. Wolf. *Phys. Rev. B,* **61**, 5934, (2000).

[14] C. Massobrio, F. H. M van Roon, A. Pasquarello and S. W. De Leeuw. *J. Phys.: Condens. Matter,* **12**, L697, (2000).

[15] C. Massobrio, M. Celino and A. Pasquarello. *Phys. Rev. B,* **70**, 174202, (2004).

[16] C. Massobrio, A. Pasquarello and R. Car. *Phys. Rev. Lett.*, **80**, 2342, (1998).

[17] C. Massobrio, A. Pasquarello and R. Car. *Phys. Rev. B,* **64**, 144205, (2001).

[18] C. Massobrio and A. Pasquarello. *J. Chem. Phys.,* **114**, 7976, (2001).

[19] C. Massobrio and A. Pasquarello. *Phys. Rev. B,* **68**, 020201, (2003).

[20] M. Cobb, D. A. Drabold, and R. L. Cappelletti. *Phys. Rev. B,* **54**, 12162, (1996).

[21] M. Cobb and D. A. Drabold. *Phys. Rev. B,* **56**, 3054, (1997).

[22] M. Durandurdu and D. A. Drabold. *Phys. Rev. B,* **65**, 104208, (2002).

[23] P. Biswas, D. N. Tafen and D. A. Drabold. *Phys. Rev. B,* **71**, 054204, (2005).

[24] A. B. Bhatia and D. E. Thornton. *Phys. Rev. B,* **2**, 3004, (1970).

[25] P. S. Salmon. *Proc: Math. and Phys. Sci*., **437**, 591 (1992).

[26] P. Vashishta, R. K. Kalia, G. A. Antonio and I. Ebbsjö. *Phys. Rev. Lett.,* **62**, 1651, (1989).

[27] H. Iyetomi, P. Vashishta, and R. K. Kalia. *Phys. Rev. B,* **43***,* 1726, (1991).

[28] R Brookes, *Part II Thesis*, *University of Oxford*, (1998).

[29] F. Vaslow and A. H. Narten, *J. Chem. Phys*., **59**, 4949, (1973).

[30] M. Wilson and P. A. Madden. *Phys. Rev. Lett*., **80**, 532, (1998).

[31] E. A. Pavlatou and G. N. Papatheodorou. *Phys. Chem. Chem. Phys.,* **2**, 1035, (2000).

[32] C. Massobrio and A. Pasquarello. *Phys. Rev. B,* **68**, 014206, (2007).

[33] P. S. Salmon, A. C. Barnes, R. A. Martin and G. J. Cuello. *J. Phys.:Condens. Matter,* **19**, 415110, (2007).

Chapter 6

Network topology of MX₂ compounds

6.1 Introduction.

The systems which form our primary focus are those whose structure can be considered network-like and formed by connecting MX_4 local coordination polyhedra. As a result, for a given class of polyhedra of a given stoichiometry the underlying network structure is dependent on the details of the cation-cation and cation-anion linkages.

Figure 6.1:Compounds classified according to the nature of the connection between tetrahedra.

A common feature of such networks is the presence of so-called intermediate range order (IRO), that is, ordering present on length scales longer than those associated with the position of the principal peak in experimental diffraction patterns.[1] Figure 6.1 shows a series of compounds, based on a characterization of varying connectivity of edge- and corner-sharing tetrahedral units. This chapter deals with the MX_2 stoichiometry and systems which are predominantly tetrahedrally coordinated systems. Previous work, using the PIM[2] and integral equation methods[3], has shown that, within a series of MCl_2 compounds, increasing cation size leads to a weakening of medium range order due to the reduction of the number of tetrahedral units. The example systems listed in the above

table can be considered as having significant IRO. However, the origin of IRO can be classified in more than one manner. One classification scheme is based on the mechanism for the origin of IRO:

1. *Coulombic ordering.* Figure 6.2 shows that tetrahedral units can be arranged in an edge- and corner-sharing configuration; the configuration adopted is determined by the strength of the dipole on the central anion.[4] The result is that these linkages may percolate differently depending on the strength of the anion polarisability.[5] On the right hand side of figure 6.1 are systems such as BeF_2[6] and SiO_2[7] which are characterized by ions having relatively low anion polarisabilities.[7] In these systems the origin of IRO is primarily based on Coulombic ordering, in which highly charged cations tend to spatially avoid each other, highlighted by a large M-X-M bond angle and a FSDP at ~1.5Å^{-1}.

2. *Inductive effects.* In the centre are compounds such as $ZnCl_2$[8,9] and $MgCl_2$[10] where inductive effects are more apparent. These systems show a similarity in the nearest-neighbour principal peak position in $g_{MM}(r)$ and $g_{XX}(r)$ and show a FSDP at k~ 1Å^{-1}. On the left hand side are systems such as $GeSe_2$[11] and $SiSe_2$[12], where inductive effects are larger, resulting in significantly more edge-sharing; this is highlighted by the crystal states of such compounds which include edge-sharing[13] in contrast to SiO_2 and $ZnCl_2$. Homopolar bonds are also observed in these systems.[14]

An alternative classification of IRO compounds is presented by Massobrio[15] in terms of the uniformity of the coordination shell (and the implied chemical ordering and coordination environments), and its subsequent effect on the presence of the FSDP in $S_{CC}(k)$. Unlike the above classification, this scheme accounts for the observation of homopolar bonds in these systems. In this classification, class I includes those compounds, such as BeF_2, where there is limited disorder: strongly four coordinate systems where a FSDP in $S_{CC}(k)$ is absent. $SiSe_2$ is an example of a class II compound, where there is a little disorder: miscoordination, small percentage of homopolar bonds and the presence of $S_{CC}(k_{FSDP})$. Class III includes $GeSe_2$ as modelled by Massobrio[16]: large percentage of homopolar bonds and $S_{CC}(k_{FSDP})$ is absent again.

One advantage of using a simple classical model is the robustness of the potential: many parameters can be changed with ease in order to model a wide variety of systems. The aim of this part of the investigation is to understand the origin of the IRO as a

function of the underlying network topology by systematically observing changes in the tetrahedral framework. As shown in Chapter 5, the difference in structural properties described in $GeSe_2$ from $ZnCl_2$ can be understood in terms of the proportions of the corner- and edge-sharing units in the network which, in the PIM, are controlled by both the anion polarisability and cation polarising power. Our strategy, therefore, is to understand the changes in the structure for a generalised MX_2 system as a result of varying the anion polarisability. In doing so, the changes in structure may mirror compounds where the anion polarisability is smaller and also changes which occur in systems such as Ge_xSe_{1-x}[17], where the stoichiometry can be changed experimentally.
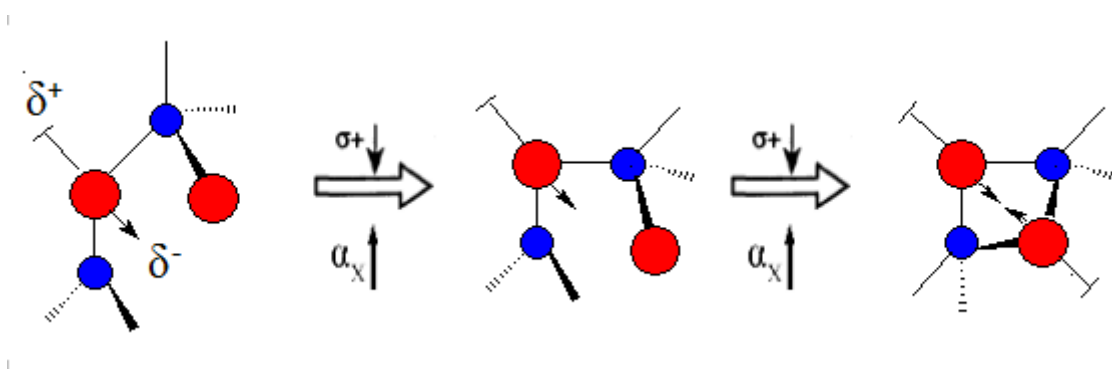
Figure 6.2: Relationship of edge and corner-sharing tetrahedral units with increasing dipole moment (based on figure from Wilson and Madden[4]). α_X and $\sigma+$ refer to anion (red circles) polarisability and cation (blue circles) size respectively. With increasing α_X and decreasing $\sigma+$ the dipole moment on the anion highlighted increases.

6.2 Simulation Details.

The initial parameters for the generalised MX_2 system were those used for the $GeSe_2$ PIM model in chapter 4. The use of the $GeSe_2$ short-range (repulsive) parameters favours the formation of relatively tight local tetrahedral geometry. The central cell used in all calculations in this chapter consists of 999 ions (333 cations and 666 anions). The initial starting configuration of MX_2, where $\alpha_X=40$ a.u, was used from the end of simulations carried out on $GeSe_2$ in Chapter 4. The pressure was maintained constant at 6×10^{-4} a.u in an NPT ensemble. The anion polarisability value is then reduced down in steps of 2.5 a.u from 40 a.u to 10 a.u with the short-range damping parameters b and c fixed. The temperature used for these calculations is 3000K: a temperature at which system can be considered as the low-temperature liquid. The initial box size is 31.81Å at $\alpha_X=40$ a.u and with each step with a slight declines to 31.40Å at $\alpha_X=10$ a.u (the evolution of cell

volume is given in figure 6.17). At each anion polarisability step, the system was equilibrated for 30 ps and a simulation run of 60 ps from which structural correlations (discussed in sections 6.3-6.8) were calculated. The initial configuration for the next polarisability was generated from the end of the simulation of the system at the previous polarisability. For section 6.6, where configurations are generated where 4-MX coordination is greater than 95% over the whole polarisability range, the pressure of the MX$_2$ system when α_X=40 a.u was reduced to 3 x 10^{-4} a.u. Calculations were then carried out in the same way as those at higher pressure of 6x10^{-4} a.u.

To represent systems with extreme anion polarisability, which are explored in section 6.9, a BeCl$_2$ model with the parameters from Wilson[4] was used (given in Appendix B). To remove memory of the previous configuration, a MD simulation was carried out at elevated temperatures of 1500K, well above the melting temperature, to equilibrate the configuration for the model. Pressure (3 x 10^{-5} a.u) was applied to get the model with damping parameter c=0.90 at a similar density to that observed for MX$_2$ at α_X=40 a.u. NPT calculations were run at 800K and the short-range damping parameter c was varied in steps of 0.1 down to c=0.50. The average cell sizes from c=0.50 to c=0.90 in steps of 0.1 are 30.93Å, 31.38Å, 31.49Å, 31.95Å and 32.31Å. At each short-range damping parameter step, the system was equilibrated for 30 ps and a simulation run of 60 ps from which structural correlations were calculated.

6.3 Structure Factors.
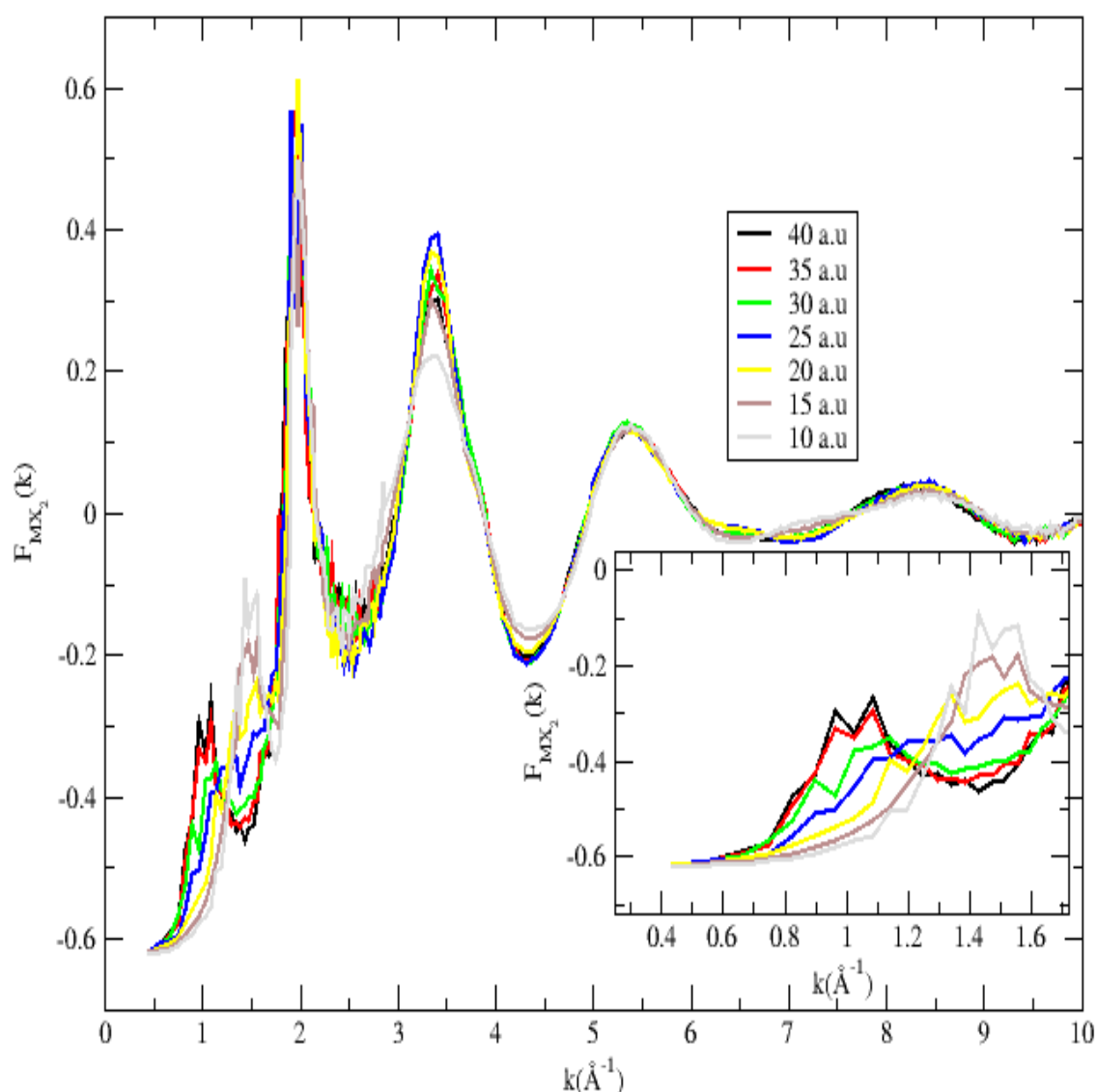
Figure 6.3: Change in total structure factors, F(k), of MX_2 systems with varying anion polarisability in the range α_X=10-40 a.u. Inset: close-up of changes in First Sharp Diffraction Peak of F(k).

The changes in the total structure factor, $F_{MX_2}(k)$, as a function of the anion polarisability are shown in figure 6.3. These functions are calculated by combining the partial structure factors using the Ge and Se neutron scattering lengths (8.185 fm and 7.97 fm respectively), allowing a direct comparison to be made between functions obtained using different anion polarisabilities. As the polarisability is decreased the FSDP is observed to shift to higher-k with the most significant shift between anion polarisabilities of 25 a.u and 10 a.u. The FSDP intensity decreases from -0.248 to -0.36 when moving from α_X=40 a.u to 25 a.u. From α_X=25 a.u to 10 a.u, where the major shift

in position occurs from 1.25Å^{-1} to 1.46Å^{-1}, the intensity of the FSDP increases sharply to -

0.095. The form of $F_{MX_2}(k)$ at $k > k_{PP}$, where little change is observed as a function

of anion polarisability, is largely a function of the short-range ordering; this indicates

strongly that the changes in IRO which vary with polarisability, are primarily determined

by the linkages *between* tetrahedral units. The convergence of k_{FSDP} at high polarisabilities

is consistent with the observation that features significantly lower than k~0.9 Å^{-1} can only

be created by templated liquids, where large alkylammonium cations create large voids

leading to the presence of longer-range ordering across them.[18]
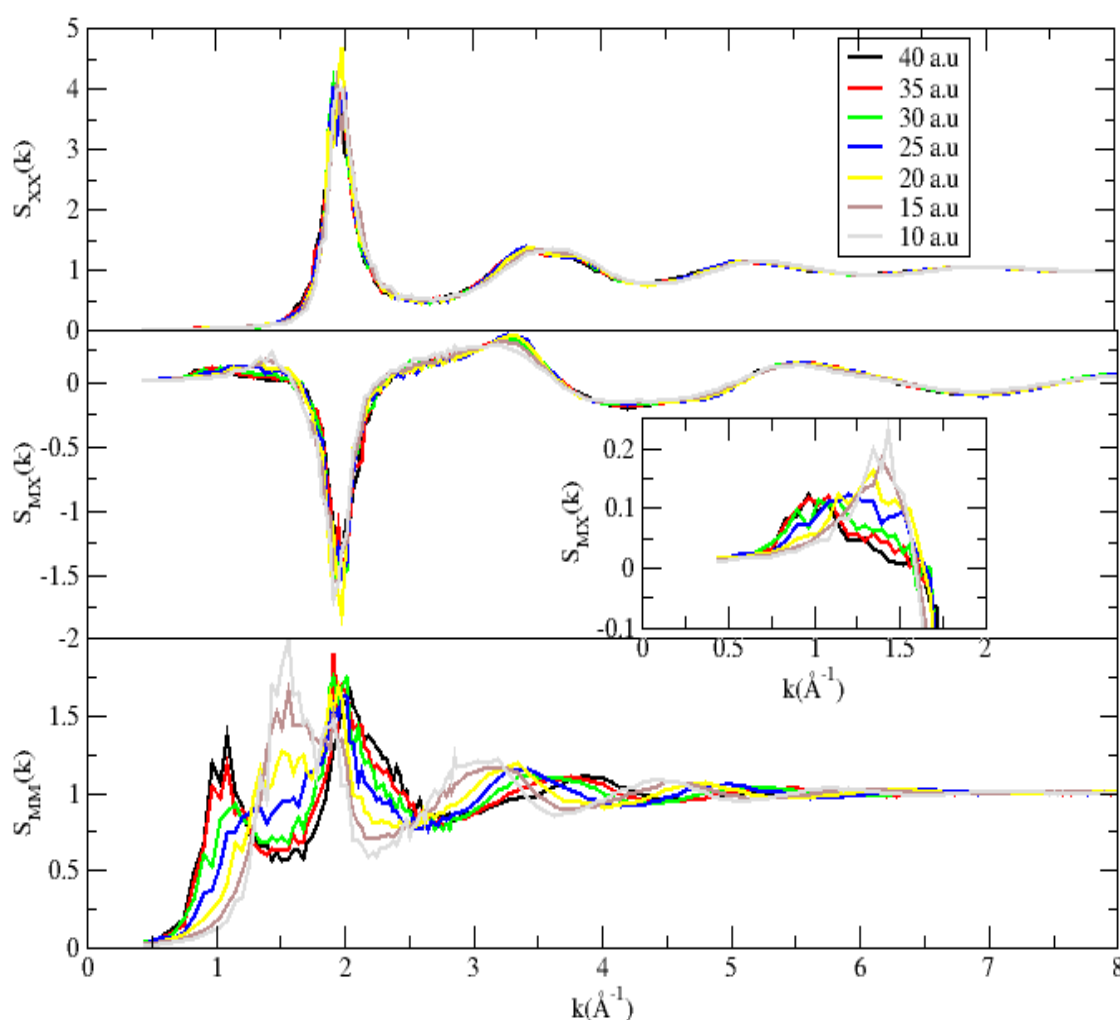
Figure 6.4:Partial structure factors according to polarisability in the range α_X=10-40 a.u. Top, $S_{MM}(k)$; middle, $S_{MX}(k)$; bottom, $S_{XX}(k)$. Inset: close-up of changes in First Sharp Diffraction Peak of $S_{MX}(k)$.

The partial structure factors in figure 6.4, show that $S_{MM}(k)$ is the dominant

contributor to the FSDP. However, as shown in figure 6.5, the ratio of $S_{MM}(k_{FSDP})$/

$S_{MX}(k_{FSDP})$ changes considerably over this polarisability range. This may explain in part

the controversy over the dominant contributor to the FSDP[8,9] in systems such as $ZnCl_2$, where in the region 25 to 32.5 a.u, the disparity in contributions of $S_{MM}(k)$ and $S_{MX}(k)$ to IRO is weakest. In compounds such as $GeSe_2$ and SiO_2, where the positions of the FSDP are very different, the $S_{MM}(k)$ contribution dominates.
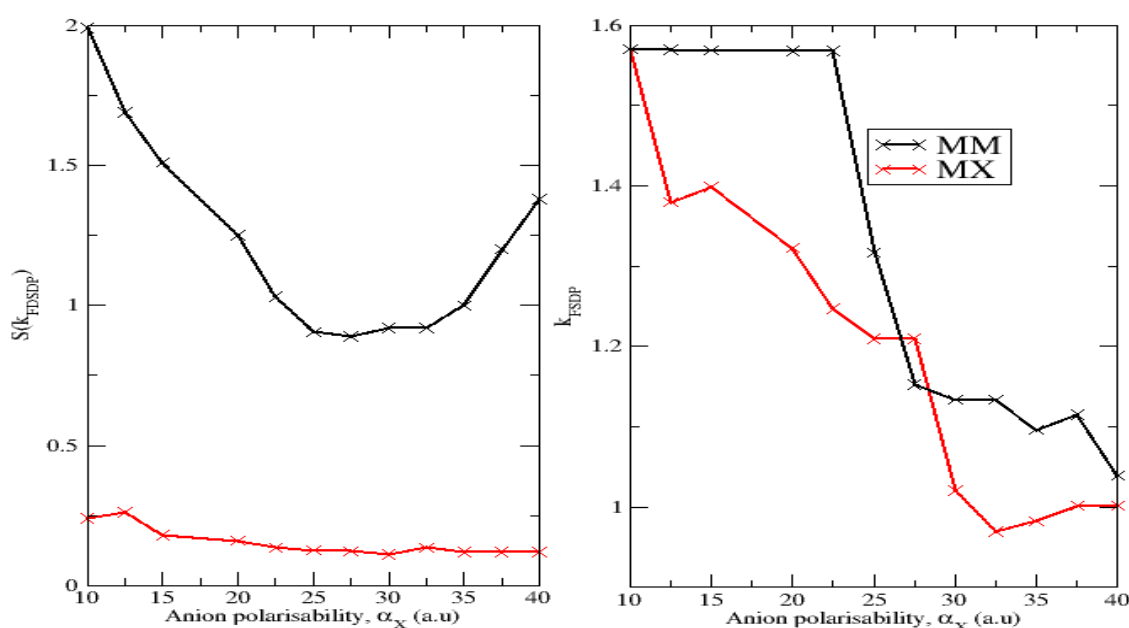
Figure 6.5:Intensities (left) and positions (right) of the First Sharp Diffraction Peak in $S_{MM}(k)$ (black line) and $S_{MX}(k)$ (red line).

$S_{XX}(k_{FSDP})$ contributes negligible amounts to intermediate range order over the whole polarisability range. The position of $S_{MM}(k_{FSDP})$ shifts to higher k with decreasing polarisability from a minimum of 1.03Å^{-1} at 40 a.u to 1.55Å^{-1} at 10 a.u. The intensity of the peak varies non-linearly over this polarisability range, decreasing in the range 40-20 a.u from $1.38\rightarrow1.20$, and then increasing up to 1.99 at 10 a.u. Concomitantly, the position of the principal peak, $k_{PP,}$ displays a smaller shift to lower k from 2.06Å^{-1} to 1.89Å^{-1}. The opposite movements in k_{PP} and k_{FSDP} is a result of the induction mechanism behind intermediate range order. The stabilising of a close cation-cation separation due to an induced dipole on an anion causes a local increase in cation density which can only be offset by a decrease in intensity over a longer range.[19] This effect is represented by the formation of two length-scales. The peaks at higher k in $S_{MM}(k)$ are shifted to the right with declining polarisability; these changes are effectively hidden in F(k) due to the larger concentration weighting of $S_{MX}(k)$ and $S_{XX}(k)$ over this range. $S_{MX}(k)$ varies

similarly to $S_{MM}(k)$ in terms of the position of the FSDP and is present over all polarisabilities but exhibits a much smaller range of intensities of 0.26-0.10 compared to 0.89-1.98 for $S_{MM}(k)$.

6.4 Radial distribution functions and coordination numbers.
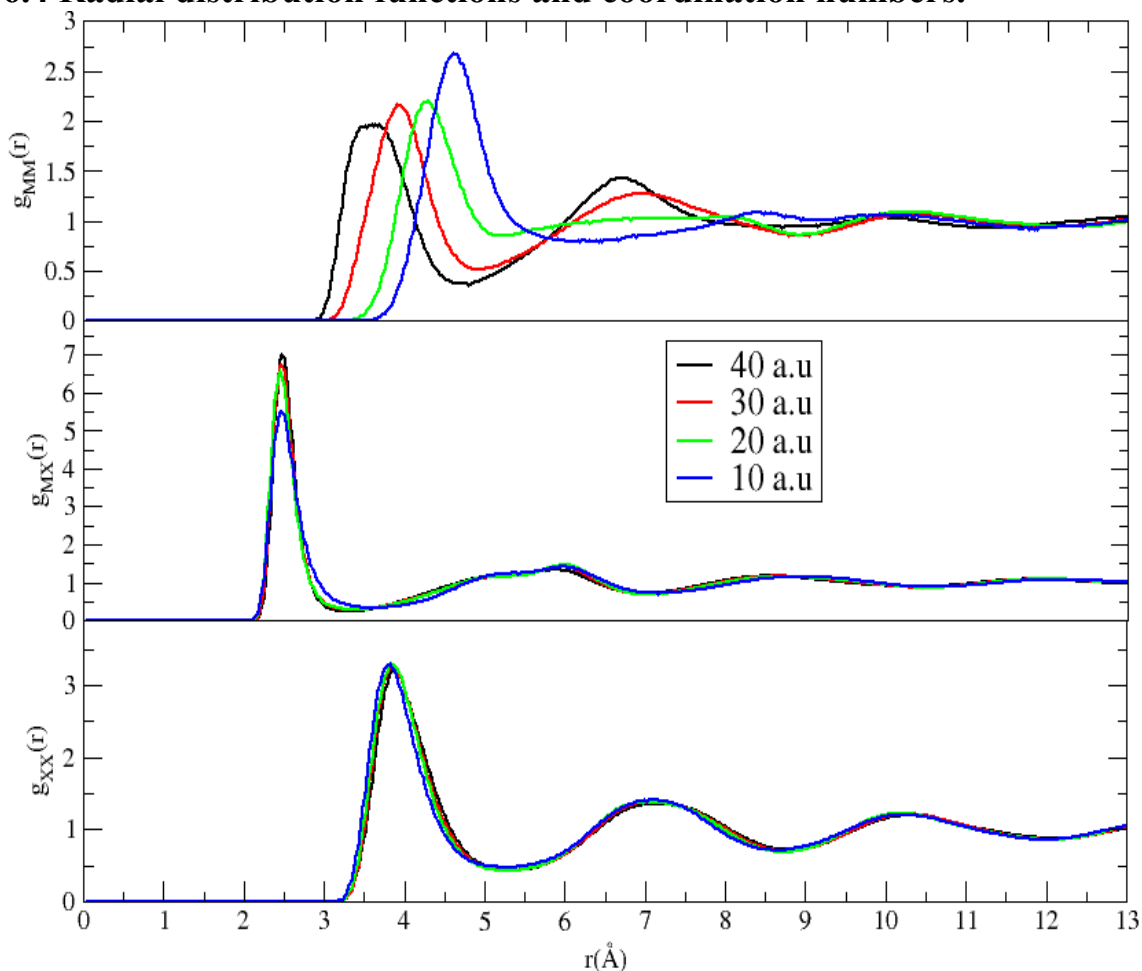
Figure 6.6: Radial distribution functions, $g_{\alpha\beta}(r)$, of MX$_2$ systems with varying anion polarisability in the range α_X=10-40 a.u.

The radial distribution functions are shown in figure 6.6 and accompanying changes in the principal peak positions are given in table 6.1. The largest shift in principal peak position occurs in $g_{MM}(r)$ from 3.57Å at 40 a.u to 4.60Å at 10 a.u. The decreasing M-M distance is indicative of the increasing presence of edge-sharing tetrahedral configurations. The correlation with experimental observations is shown in the ratio $g_{MM}^{PP}(r)/g_{MX}^{PP}(r)$, where the values for selected systems such as GeSe$_2$, ZnCl$_2$ and SiO$_2$, corresponding to strongly edge-sharing, mixed edge- and corner-sharing, and strongly

corner-sharing systems, show a strong similarity with MX$_2$ systems at α_X=40, 30 and 10 a.u respectively. The FWHM is similar at both high and low polarisabilities. The largest changes occur in the region of 5 to 10Å where at α_X=40 a.u a much larger intensity is observed compared to the damped equivalent at low polarisabilites. For g$_{MX}$(r) the changes are much less significant, while for g$_{XX}$(r) there is a small shift in principal peak from 3.91Å at 40 a.u to 3.80Å at 10.a.u. The changes in g$_{MX}$(r) are smaller, with the principal peak shifting from 2.47Å to 2.43Å and a decrease in the intensity. At higher r values both g$_{MM}$(r) and g$_{XX}$(r) remain similar. This indicates that the changes with anion polarisability are strongly to do with changes in the cation subdensity.

Compound	Ref	$g_{MX}(r_{PP})$ (Å)	$g_{MM}(r_{PP})$ (Å)	$g_{XX}(r_{PP})$ (Å)	$g_{MM}(r_{PP})$ / $g_{MX}(r_{PP})$	$g_{XX}(r_{PP})$ / $g_{MX}(r_{PP})$	$g_{XX}(r_{PP})$ / $g_{MM}(r_{PP})$
GeSe$_2$	20	2.42	3.59	3.75	1.48	1.55	1.04
ZnCl$_2$	8	2.29	3.72	3.72	1.62	1.62	1.00
SiO$_2$	21	1.62	3.15	2.64	1.94	1.63	0.84
MX$_2$(α_X=40 a.u)		2.47	3.57	3.87	1.39	1.50	1.08
MX$_2$(α_X=30 a.u)		2.43	4.08	3.86	1.62	1.59	0.95
MX$_2$(α_X=20 a.u)		2.44	4.46	3.84	1.82	1.57	0.86
MX$_2$(α_X=10 a.u)		2.47	4.60	3.80	1.86	1.54	0.83

Table 6.1: Radial distribution function peak positions in MX$_2$ compounds and the values for the ratios, $g_{MM}(r_{PP})/g_{MX}(r_{PP})$, $g_{MM}(r_{PP})/g_{XX}(r_{PP})$ and $g_{XX}(r_{PP})/g_{MM}(r_{PP})$ with experimental analogues.

The dominance of the variations in the cation distribution is reflected in the average coordination numbers, M$_{ij}$, shown in figure 6.7. M$_{ij}$ were obtained using equation 6.1:

$$M_{ij} = \sum_l^m N_{ij}^\alpha \alpha \qquad (6.1)$$

where l to m is the range of coordination number for ion pair, ij, considered and N_{ij}^α is the fraction of coordination number α, where the boundary for the coordination shell is the minimum of the principal peak from the related radial distribution function.

As anion polarisability decreases, the propensity for four-coordination, around a central cation, is largely stable at 83%-75% in the range α_X=40-22.5 a.u. From α_X=22.5-10 a.u the 4-coordination decreases to 53%. The values of average coordination values of 12.87, 4.15, 2.08 for M$_{XX}$, M$_{MX}$ and M$_{XM}$ respectively are in the range of expected
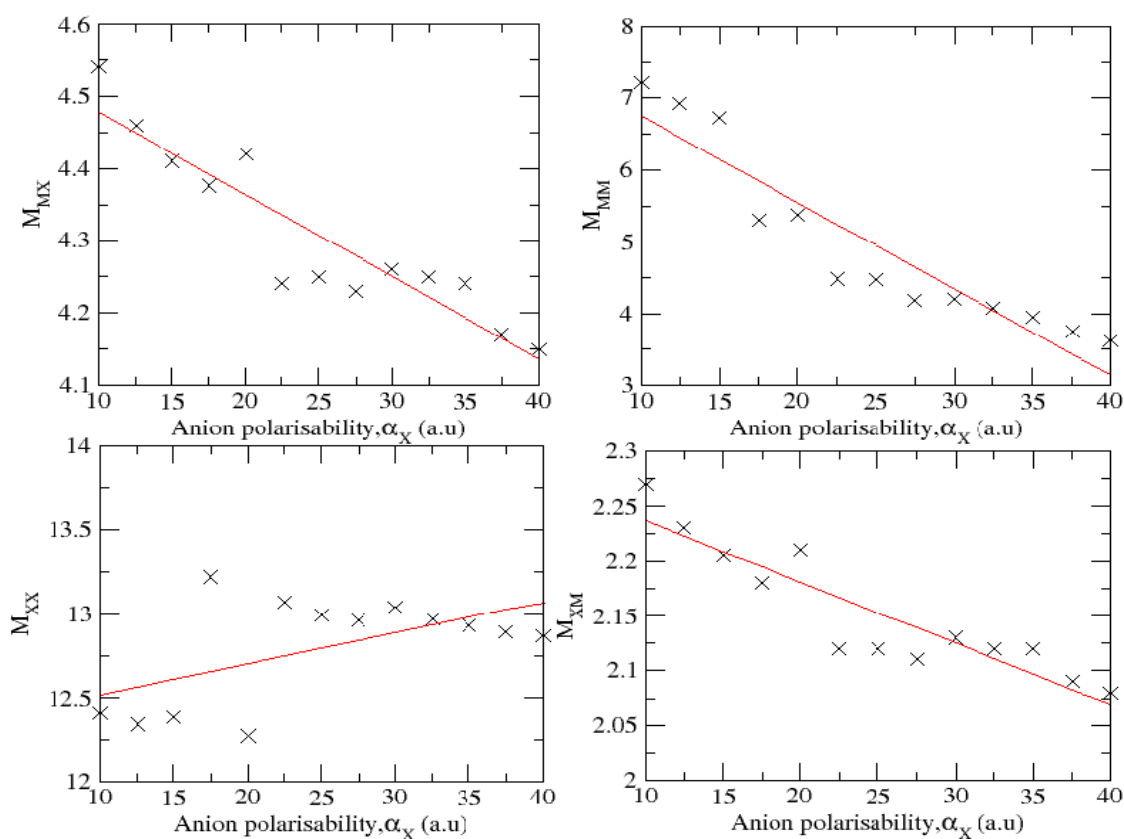
Figure 6.7: Change of mean coordination number, M$_{\alpha\beta}$, in MX$_2$ systems with anion polarisability, α_X.

coordination for a tetrahedral liquid. M$_{MM}$ shows the largest change, increasing 92% over the polarisability range compared for M$_{MX}$, M$_{XX}$ and M$_{XM}$ with values of 7%, -4% and 10% respectively although the pattern of the changes in M$_{XX}$ are less discernible. At α=40 a.u, where there are large amounts of edge-sharing, M$_{MM}$ is as low as 3.6. At lower polarisabilities, the larger M-M coordination (e.g M$_{MM}$=7.22 at 10.au) is indicative of the increasing influence of a corner-sharing network, where each central cation has singly bridging connections with other cations.
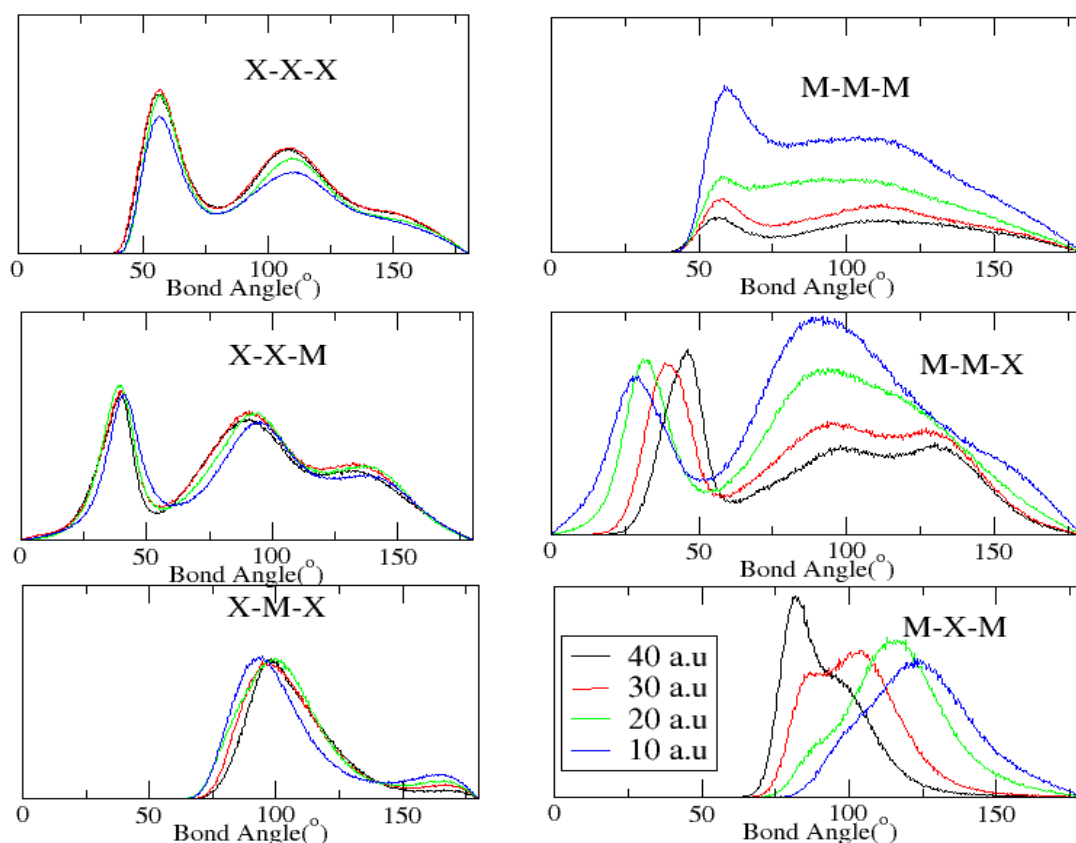
Figure 6.8: Bond angle distributions for MX_2 according varying anion polarisability

The changes in the bond angles distributions (figure 6.8) highlight further the general trend of large changes in the cation distribution. Bond angle distributions which involve X atoms; X-X-X, X-M-X and X-X-M, show little polarisability dependence and we can assume have little effect on IRO through the polarisability range. Those distributions involving changes in the angles of M atoms; M-M-M, M-M-X and M-X-M, show much larger changes in terms of intensity, peak positions and shape. The bond angle distributions show an increase in M-X-M angle with decreasing polarisability from 40 a.u where a peak is observed at 82° to 121° at 10 a.u. This indicates that with decreasing polarisability, the M-M bond distances are getting larger, leading to smaller and less distinct edge-sharing geometries while favouring corner-sharing geometries. The FWHM for M-X-M decreases from 37.2° at 10 a.u to 26.0° at 40 a.u: an indication of increased ordering. The larger peak intensity $\sim 90^\circ$ compared to the peak at $29^\circ\sim$ in M-M-X was a feature of a previous classical potential for $GeSe_2$[22]; however, our model shows this to be a feature of systems where anion polarisability is lower than that exhibited by Se^{2-}. With the increasing presence of edge-sharing, the acute M-M-X bond angle involving the

anion X bridging the cations of the edge-sharing unit dominates the distribution.
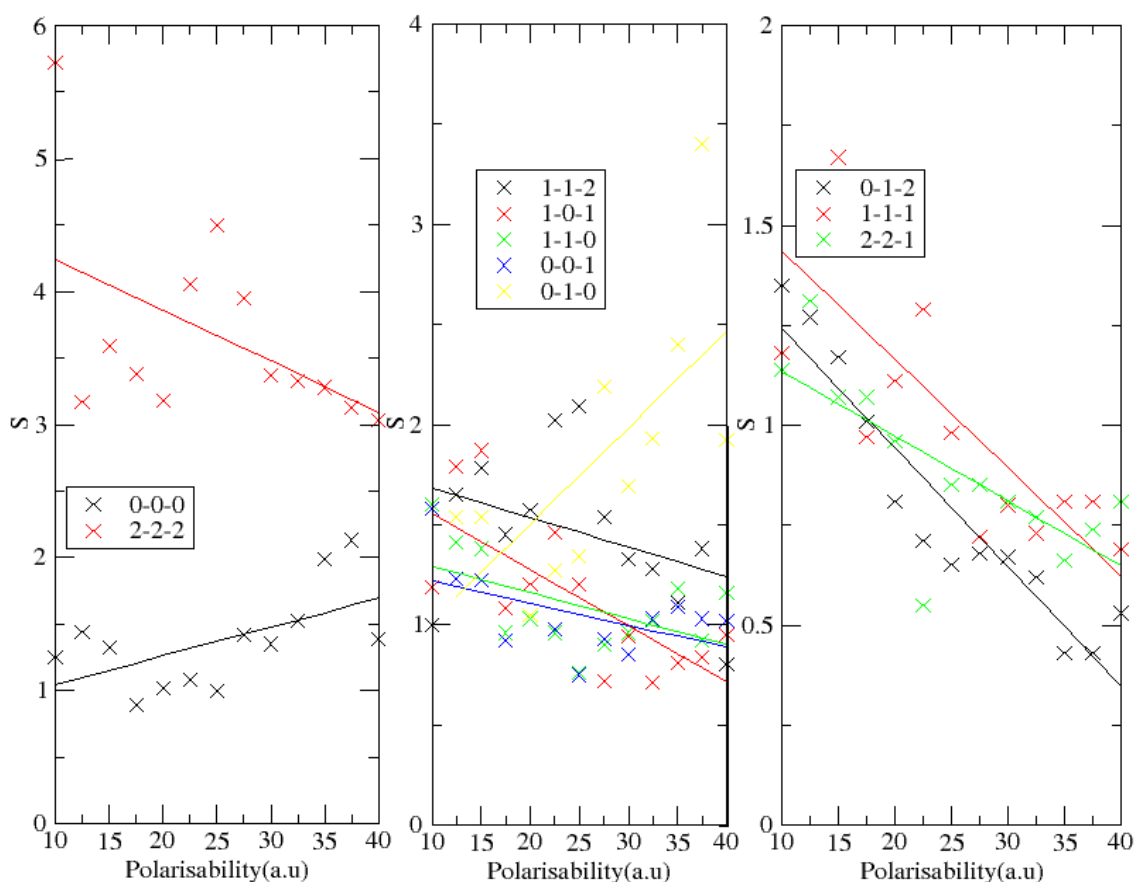
Figure 6.9:Variation of ratio S with anion polarisability, α_X.

The M-M-M distribution shows two prominent features at large polarisabilities: a band at larger angles and a sharp peak around 50°. At larger polarisabilities a sharp peak at small bond angles dominates the larger angle peak. This ratio changes with increasing polarisability. In an analogous fashion to the network connectivity cation-cation structure factor, $S_{MM}^{ab}(k)$ where {a,b}={0,1,2}, the bond angle distribution, M-M-M, can also be decomposed according to a cation's identity based on the number of four-membered rings it is bonded to. The partial contributions vary significantly in the relative proportion of these two features compared to the total M-M-M distribution. Figure 6.9 shows the changes, with polarisability, of S: the ratio of the intensities of the low angle peak over the high angle peak for each of the partial M-M-M functions. The functions are separated into three groups: clustering (S>1 over whole polarisability range), bridging (S<1 for range 40-27.5 a.u) and intermediate (those functions which satisfy neither of the criteria for the first two functions). The 0-0-0 and 2-2-2 functions show a sharp peak at low angles and in line with the idea of clustering of "0" and "2" cations,

show large values of S. The 0-1-2 function is the most easily understood bridging function: the connection of clusters of "0" and "2" cations is more likely to observe higher angles, due to the resulting in values where S < 1, especially at high polarisabilities where clustering of "0" and "2" cations is more apparent.

6.5 Network-connectivity structure factors.

As shown in Chapter 5, the $S_{MM}(k)$ function can be decomposed into further partial structure factors according to the identity of cations based on number of four-membered rings they are bonded to. By changing the anion polarisability, we are able to observe how features such as the intensity and shape of the network connectivity cation-cation terms change with the underlying network topology. Figure 6.10 shows that the network connectivity cation-cation functions at different polarisabilities display a wide variation at low k in the presence and intensity of a FSDP. In $S_{MM}^{00}(k)$ and $S_{MM}^{11}(k)$, the position of the FSDP, when present, remains in the narrow range of $1.08Å^{-1}$-$1.15Å^{-1}$ from 40 a.u to 25 a.u for $S_{MM}^{11}(k)$ and $1.44Å^{-1}$ -$1.55Å^{-1}$ from 17.5 to 10 a.u for $S_{MM}^{00}(k)$. These two functions highlight two different mechanisms for IRO: an induction mechanism where the anion is able to stabilise the closer separation of cations, and a Coulombic mechanism where repulsion of like charges is the dominant factor. The latter mechanism only allows for a FSDP at $1.5Å^{-1}$ whereas the induction mechanism enables a FSDP at peaks lower than $1.5Å^{-1}$ and closer to $~1Å^{-1}$. The induction mechanism for IRO is highlighted in $S_{MM}^{02}(k), S_{MM}^{11}(k)$ and $S_{MM}^{12}(k)$ which exhibit two peaks in the 0-$2Å^{-1}$ region and with decreasing polarisability the intensity of the FSDP decreases. $S_{MM}^{12}(k)$, as might be expected for terms involving edge-sharing units, behaves similarly to $S_{MM}^{11}(k)$ in the narrow range of FSDP positions from $1.02Å^{-1}$-$1.08Å^{-1}$ for 10-40 a.u. Of the six functions, $S_{MM}^{01}(k)$ is the only function which displays a FSDP at low and high polarisabilities in the range $1.55Å^{-1}$-$1.08Å^{-1}$ from 10 to 40 a.u. Figure 6.10 shows the changes in cation sublattice evident in perturbing $S_{MM}^{01}(k)$ from a double peaked structure to that of a single peak; a function which displays both mechanisms due to varying concentrations of cations labelled "0" i.e corner-sharing to "1" , where it has mixed corner- and edge-sharing character. A FSDP

appears in $S_{MM}^{22}(k)$ at 40 a.u only at k~1.08Å^{-1}. This is the only example of clear FSDP

present in a function with significant phase separation signified by the rise in $S_{MM}^{22}(k)$

as k→0. This is due to the preponderance of "2" clusters at this polarisability. $S_{MM}^{02}(k)$

is the only function to have a FSDP more intense than the principal peak at the highest

polarisability values of 37.5 a.u and 40 a.u. The weak short range ordering and damped

oscillations at high k, a feature uncommon to the other network connectivity cation-

cation functions, are consistent through all polarisabilities. At anion polarisabilities of

α_X=20 a.u and lower, where the percentage of "2" cations is small, $S_{MM}^{02}(k)$ becomes

similar to $S_{MM}^{01}(k)$, observing a large shift in the FSDP position.

   The variation in the ratio of the heights of the FSDP and principal peak,

$S_{MM}^{ab}(k_{FSDP})/S_{MM}^{ab}(k_{PP})$, where {a,b} ={0,1,2} was highlighted in the comparison of

GeSe$_2$[23] and ZnCl$_2$[23] The ratios for MX$_2$ decreasing anion polarisability are shown in table

6.2 for the polarisability range of α_X=40-25 a.u where edge-sharing is prominent. Over

this range, large changes are observed in the ratios in all the functions considered, with a

decrease observed in accordance with corresponding decrease of intensity in S$_{MM}$(k).

$S_{MM}^{ab}(k_{FSDP})/S_{MM}^{ab}(k_{PP})$ is strongest for $S_{MM}^{02}(k)$ at the highest polarisability.

The values $S_{MM}^{ab}(k_{FSDP})/S_{MM}^{ab}(k_{PP})$ observed for $S_{MM}^{01}(k)$, which lie in the range 0.26-

0.45 are smaller than $S_{MM}^{12}(k)$, $S_{MM}^{11}(k)$ and $S_{MM}^{02}(k)$ where the ranges are

0.33-0.98 , 0.36-0.89 and 0.42-1.23 respectively. This indicates that while the presence

of edge-sharing units is necessary for IRO to be observed around ~1Å^{-1} region, there is

no significant increased contribution from any changes that occur in the corner-sharing

structures over the polarisability range to intermediate-range ordering.
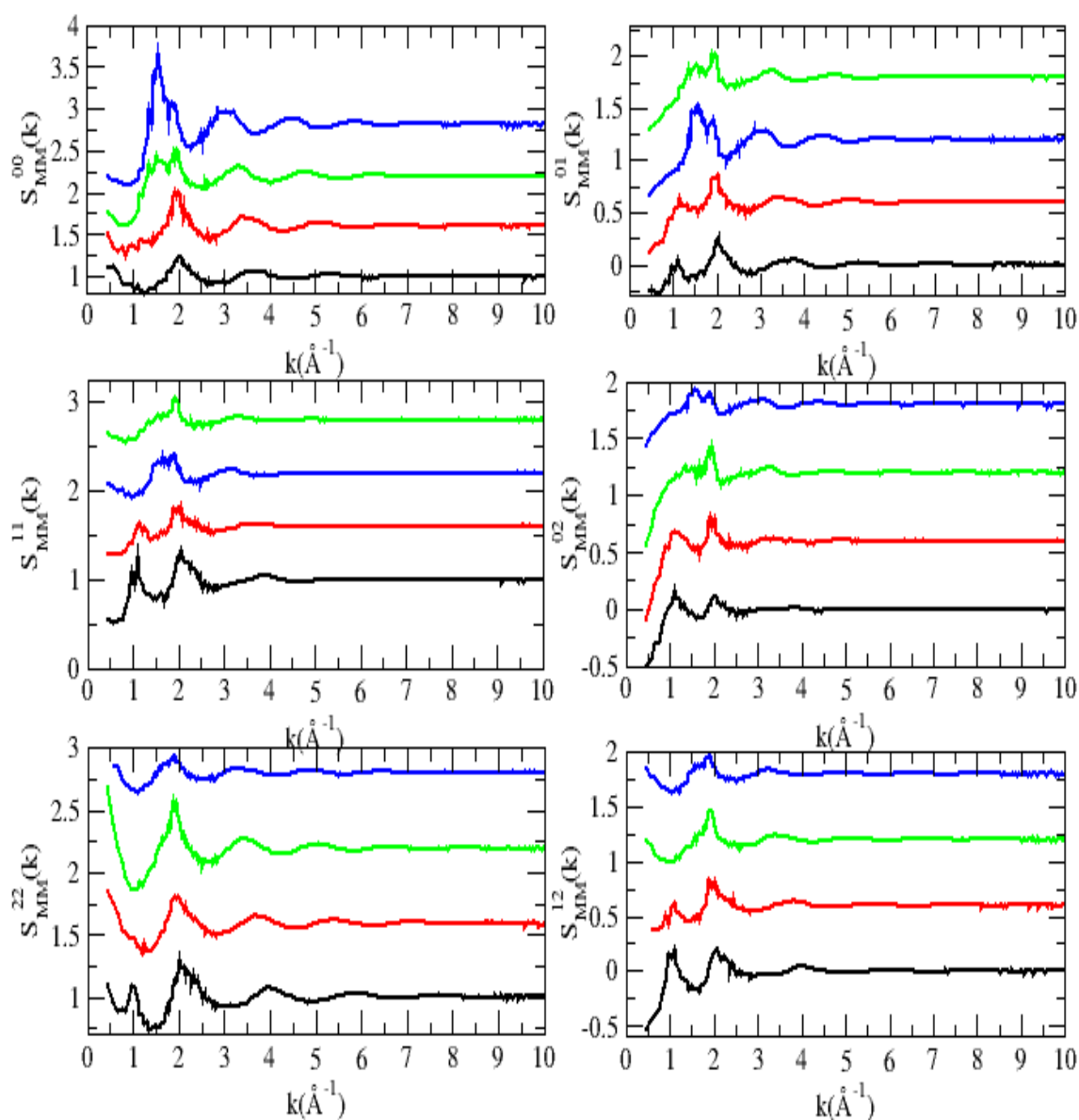
Figure 6.10: Network connectivity cation-cation structure factors according to varying anion polarisability. Colour code with y increments in brackets: black line; 40 a.u; red line, 30 a.u (+0.6); green line 20 a.u(1.20); blue line 10 a.u (+1.80).

The various $S_{MM}^{ab}(k)$ functions at low k show sharply diverging characteristics depending on the identity of the function involved and the anion polarisability. An effective phase separation is characterized in reciprocal space when $S_{MM}^{ab}(k)$ increases in magnitude sharply as k→0. Archetypally, phase separation occurs in liquid mixtures where two immiscible liquids are present; here, we are concerned with interactions of cations coloured according to network connectivity. Phase separation has been modelled in a binary fluid composed of molecules of sharply varying atom size at liquid packing

fractions[24,25]; in our system, the factors to be considered are concentration of the cations and how the changing network connectivity at each anion polarisability affects their distribution.

Polarisability, α_X (a.u)	$S_{MM}^{11}(k_{FSDP})$ / $S_{MM}^{11}(k_{PP})$	$S_{MM}^{01}(k_{FSDP})$ / $S_{MM}^{01}(k_{PP})$	$S_{MM}^{12}(k_{FSDP})$ / $S_{MM}^{12}(k_{PP})$	$S_{MM}^{02}(k_{FSDP})$ / $S_{MM}^{02}(k_{PP})$
40.0	0.89	0.42	0.98	1.23
37.5	0.80	0.42	0.70	1.20
35.0	0.63	0.45	0.70	0.66
32.5	0.49	0.26	0.57	0.42
30.0	0.59	0.31	0.86	0.64
27.5	0.42	0.44	0.42	0.60
25.0	0.36	0.32	0.33	0.55

Table 6.2: Table of ratios of the FSDP and principal peak intensities of network connectivity cation cation structure factors.

Table 6.3 highlights the phase separation behaviour of the network connectivity cation-cation terms. In our systems, the low concentration of each partial goes some way in explaining this phase separation. However, the propensity for the separate cation functions to display phase separation effects is not solely dependent on the concentration of the interaction, as shown by the varying phase separation behaviour of the network connectivity cation-cation terms. Although $S_{MM}^{01}(k)$ displays no phase separation over the whole polarisability range: a property which can be correlated with a relatively large concentration term over the whole polarisability range, $S_{MM}^{02}(k)$ and $S_{MM}^{22}(k)$ provide contrasting examples where even at low fractions, $S_{MM}^{02}(k)$ does not display phase separation, whereas $S_{MM}^{22}(k)$ does. $S_{MM}^{22}(k)$ and $S_{MM}^{02}(k)$ represent the two extremes of functions which have varying degrees of inherent separation. At a given density, $S_{MM}^{22}(k)$ will describe clustering cations in edge-sharing chains whilst $S_{MM}^{02}(k)$ represents an ordering across a larger enforced separation. This is highlighted in figure 6.11b and 6.11c which show molecular graphics snapshots of the coloured cations taken from the system with anion polarisability of 40 a.u. These snapshots highlight the origin of the features observed in $S_{MM}^{02}(k)$ and $S_{MM}^{22}(k)$. In figure 6.11c, edge-sharing chains are evident as well as significant clustering which result in large voids. The interaction between the edge-sharing chains is through weak Van der Waals forces. In

contrast, the bonds between "0" and "2" cations, as expected, show no sign of clustering. For the polarisability range considered, the "0"-"2" interaction will have stronger long range ordering than the "2"-"2" interaction. As a reference, 6.11a shows the cations coloured "0" (highlighting the origin of the features displayed by $S_{MM}^{00}(k)$) which, despite the relatively low concentration, also show signs of clustering.

(a)   (b)   (c)
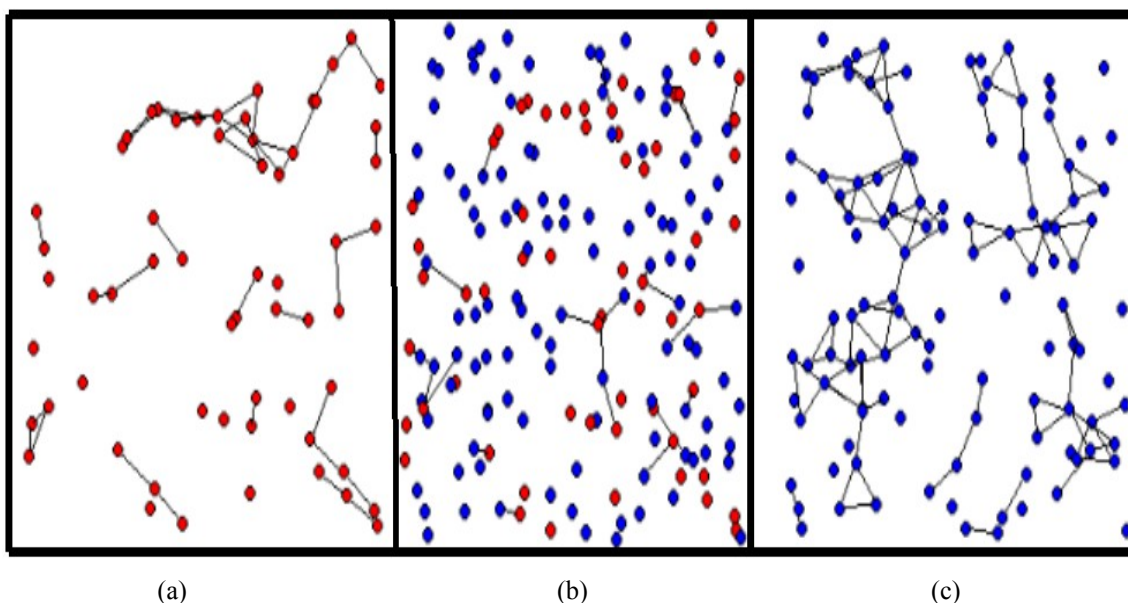
Figure 6.11: Graphical snaphots of arrangement of "0" and "2" cations at α$_X$=40 a.u. (a), "0"-"0"; (b), "0"-"2"; (c),"2"-"2". Figure shows strong clustering is observed for "0"-"0" and "2"-"2" compared to "0"-"2".

Partial Structure	c_a	c_b	$c_a c_b$	Phase Separation(a. u)*
$S_{MM}^{00}(k)$	0.18-0.71	0.18-0.71	0.035-0.50	0-40
$S_{MM}^{11}(k)$	0.22-0.50	0.22-0.50	0.050-0.24	17.5-10
$S_{MM}^{22}(k)$	0.063-0.33	0.063-0.33	0.0040-0.11	0-40
$S_{MM}^{01}(k)$	0.18-0.71	0.22-0.50	0.089-0.166	None
$S_{MM}^{02}(k)$	0.18-0.71	0.063-0.33	0.048-0.091	None
$S_{MM}^{12}(k)$	0.22-0.50	0.063-0.33	0.015-0.16	25.0-10

Table 6.3: Phase separation behaviour of network-connectivity cation-cation structure factors.* The ranges describe the polarisability value boundaries where phase separation occurs.

To observe the effect of reducing cation concentration on the structure factor $S_{MM}(k)$, randomly selected cations were chosen from configurations generated at α_X=40 a.u to create arrays of varying cation density. This is intended to give some indication as to the effect of selecting random cations against colouring cations according to network connectivity. There were two methods of selection:

1. n cations were selected at random from the initial configuration (t=0). These cations were then extracted from every configuration onwards as the simulation progresses.
2. n cations were selected at random at each time step.

The network connectivity structure factor, $S_{MM}^{n/333}(k)$, where n is the number of ions, is calculated from the configurations generated. Figure 6.12 shows the structure factors calculated from configurations with the procedure applied once. At high k, there is little difference between the structure factors produced. At low k, the related network connectivity structure factor produced from method 2 shows sharp fluctuations over this region, in contrast to that produced by method 1. These fluctuations are stronger at low n compared to the high n, as shown by the similarity in $S_{MM}^{200/333}(k)$ for both methods. The relatively good statistics observed using method 1 indicate that the coloured functions obtained earlier (section 6.5) are statistically valid. The dynamic implication of the results is that the ions change their identity (in terms of their colour) on timescales which are short with respect to typical simulation time-scales.
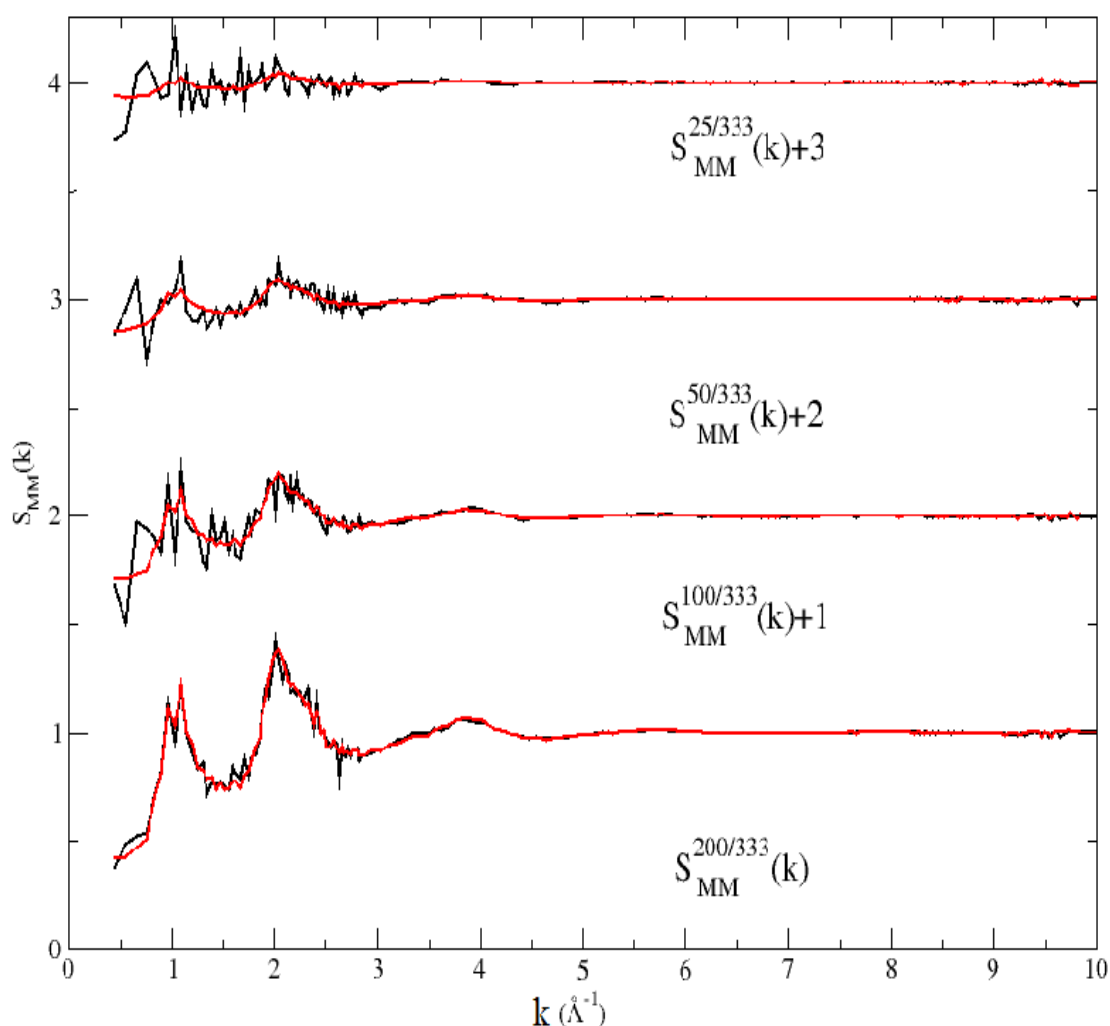
Figure 6.12: Random network connectivity cation-cation structure factors, $S_{MM}^{n/333}(k)$, where n is the number of cations extracted. Black line: a set of n atoms is taken from the first step and then the same ions are repeatedly extracted in every step thereafter. Red line: a set of n atoms is taken from the first step and then a *new* set of n ions are taken from every step thereafter.

As described earlier, the FSDP in S$_{MX}$(k) shifts to higher k and increases in intensity with decreasing anion polarisability. The partial changes that are responsible for this can be elucidated from calculating the structure factors, $S_{MX}^{aX}(k)$, where a= 0, 1 and 2. The functions in figure 6.13 show less variability with anion polarisability than S$_{MM}$(k) functions with common features for all functions at all polarisabilities; a FSDP of varying intensity and position, and the absence of phase separation effects observed in S$_{MM}$(k). For $S_{MX}^{0X}(k)$ there is a sharp rise in intensity of the FSDP with decreasing polarisability and a the position shifts to higher k. This is to be expected from gradual change from an edge-sharing network to a corner-sharing one with the increasing

percentage of "0" cations. $S_{MX}^{1X}(k)$ and $S_{MX}^{2X}(k)$ behave similarly with regards to the concentration of the interaction, but at high polarisabilities, where they are most prominent, the FSDP is ~1Å^{-1}. The decrease in the intensity of the FSDP at higher polarisability can be ascribed primarily to the damped $S_{MX}^{0X}(k_{FSDP})$ function, which of the three functions displays the greatest maximum intensity: 0.225 for $S_{MX}^{0X}(k_{FSDP})$ at 12.5 a.u compared to 0.09 for $S_{MX}^{1X}(k_{FSDP})$ at 40.0 a.u and 0.09 for $S_{MX}^{2X}(k)$ at 37.5 a.u. Larger changes are observed in the principal peak intensities for $S_{MX}^{0X}(k_{PP})$ and $S_{MX}^{2X}(k_{PP})$ over the polarisability range than $S_{MX}^{1X}(k_{PP})$.
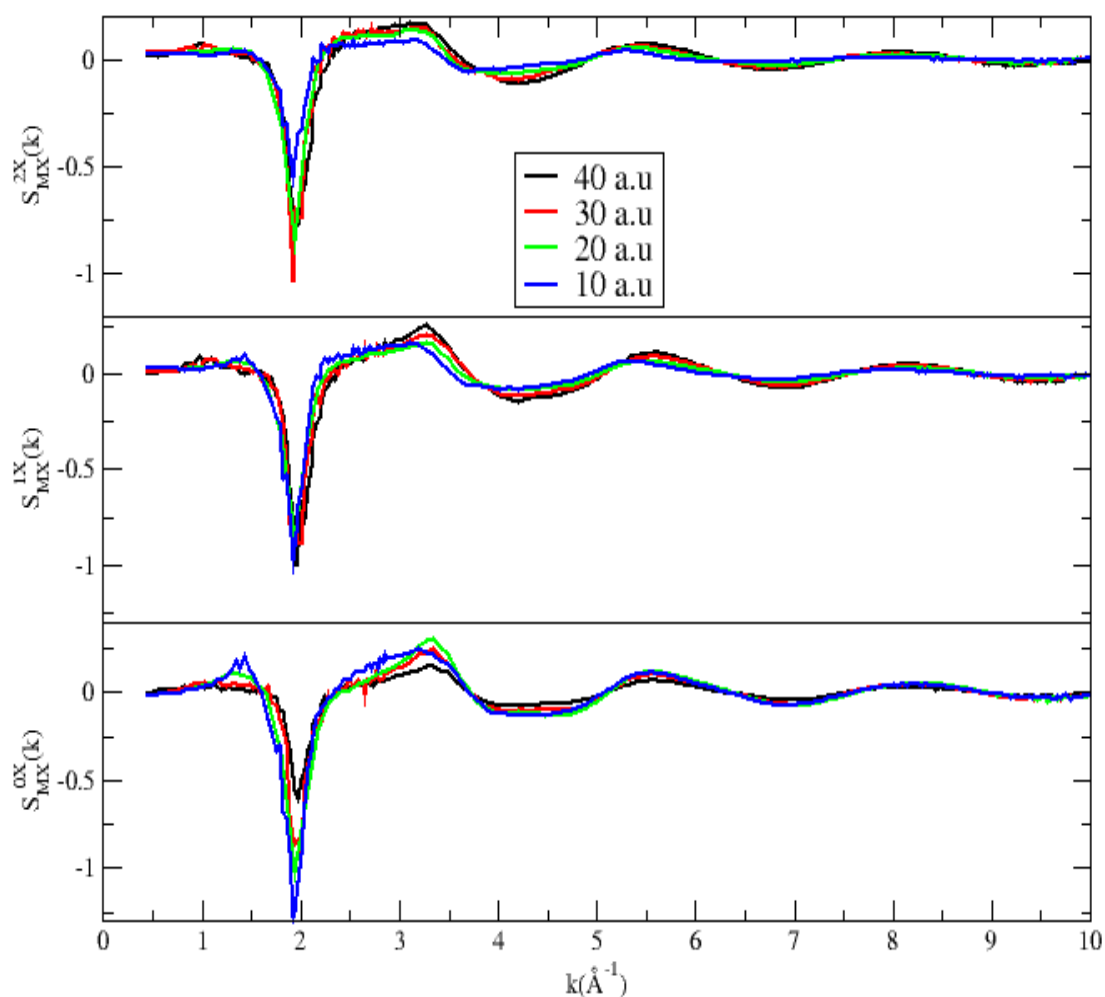
Figure 6.13: Network-connectivity cation-anion structure factors according to varying anion polarisability. Black line; 40 a.u; red line, 30 a.u; green line 20 a.u; blue line 10 a.u.

6.6 Bhatia-Thornton Structure Factors.
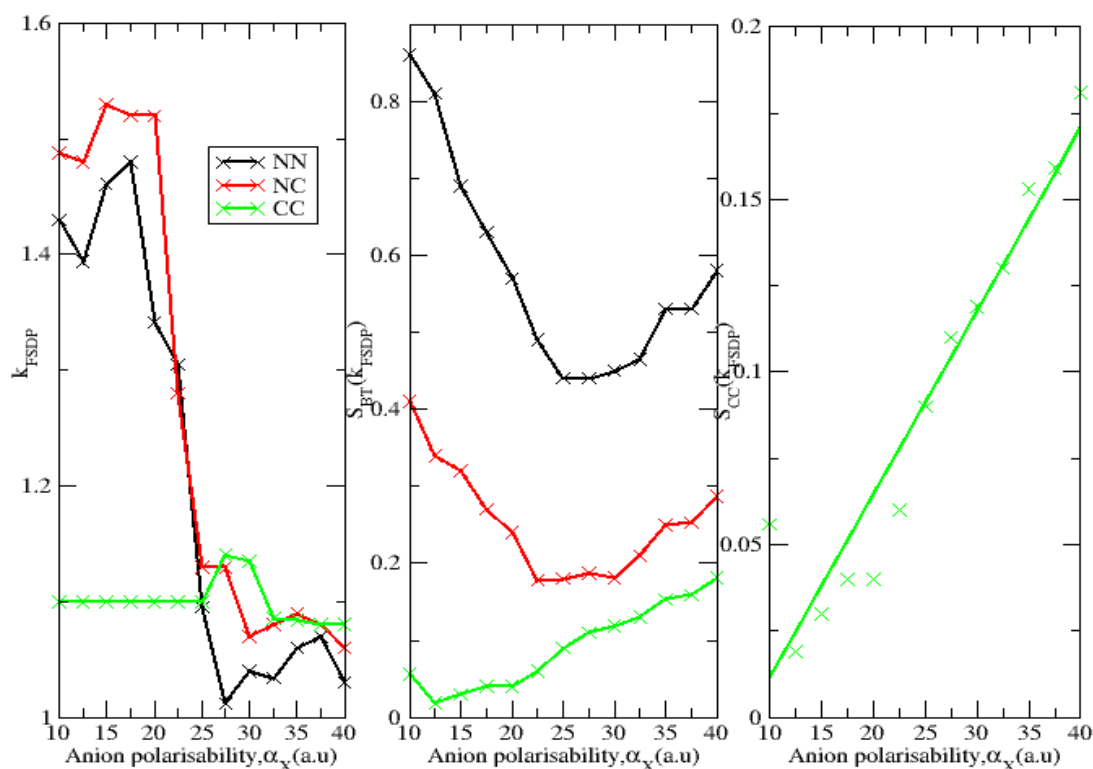
Figure 6.14:Graph showing relationship of FSDP intensities and positions of Bhatia-Thornton structure factors with anion polarisability. Left, Position of FSDP in Bhatia-Thornton functions; middle: intensity of FSDP in Bhatia-Thornton functions; right, intensity of $S_{CC}(k_{FSDP})$ with anion polarisability. Black, number-number (NN); red, number-concentration (NC); green, concentration-concentration (CC).

The Bhatia-Thornton formalism[26] is able to separate changes in the underlying topology from chemical ordering. The positions and intensities of all three Bhatia-Thornton functions with anion polarisability are shown in figure 6.14. The feature of the FSDP in $S_{CC}(k)$, which, hitherto, had not been observed in previous classical type calculations, is present as a peak in the polarisability range 40-27.5 a.u. At lower polarisabilities, intensity is observed as a shoulder ~1Å^{-1} and the intensity recorded in figure 6.14 is at the same position as the higher polarisability functions. Rather than being a function of ordering, the FSDP in $S_{CC}(k)$ is clearly attributed to the presence of edge-sharing units. The $S_{CC}(k)$ is formed by the superposition of $S_{MM}(k)$, $S_{MX}(k)$ and $S_{XX}(k)$; the latter is ignored due to negligible contribution over small k values, and so it is reduced to

$$S_{CC}(k) \approx c_M c_X \{ c_X S_{MM}(k) + c_M S_{XX}(k) - 2\sqrt{c_M c_X} S_{MX}(k) \},$$ using the Ashcroft-Langreth

formalism. The decline of $S_{CC}(k)$ in the region 40-27.5 a.u can be explained by the declining intensity of $S_{MM}(k_{FSDP})$; the remergence of a large FSDP at lower polarisabilites

does not produce an FSDP in $S_{CC}(k) \sim 1.5\text{Å}^{-1}$ but a wider principal peak. In contrast,
sharp changes occur in the intensity and position of $S_{NN}(k_{FSDP})$ where the FSDP shifts
in position from 1.43Å^{-1} at 40 a.u to 1.03Å^{-1} at 10 a.u. Here, the absence of a FSDP in
$S_{XX}(k)$ reduces $S_{NN}(k_{FSDP})$ to $S_{NN}(k) \approx c_M S_{MM}(k) + 2\sqrt{c_M c_X} S_{MX}(k)$. This indicates the
prevalence of chemical ordering in the intermediate range is limited to high
polarisabilities, whilst number-number ordering can be attributed to a wider range of
accessible morphologies.
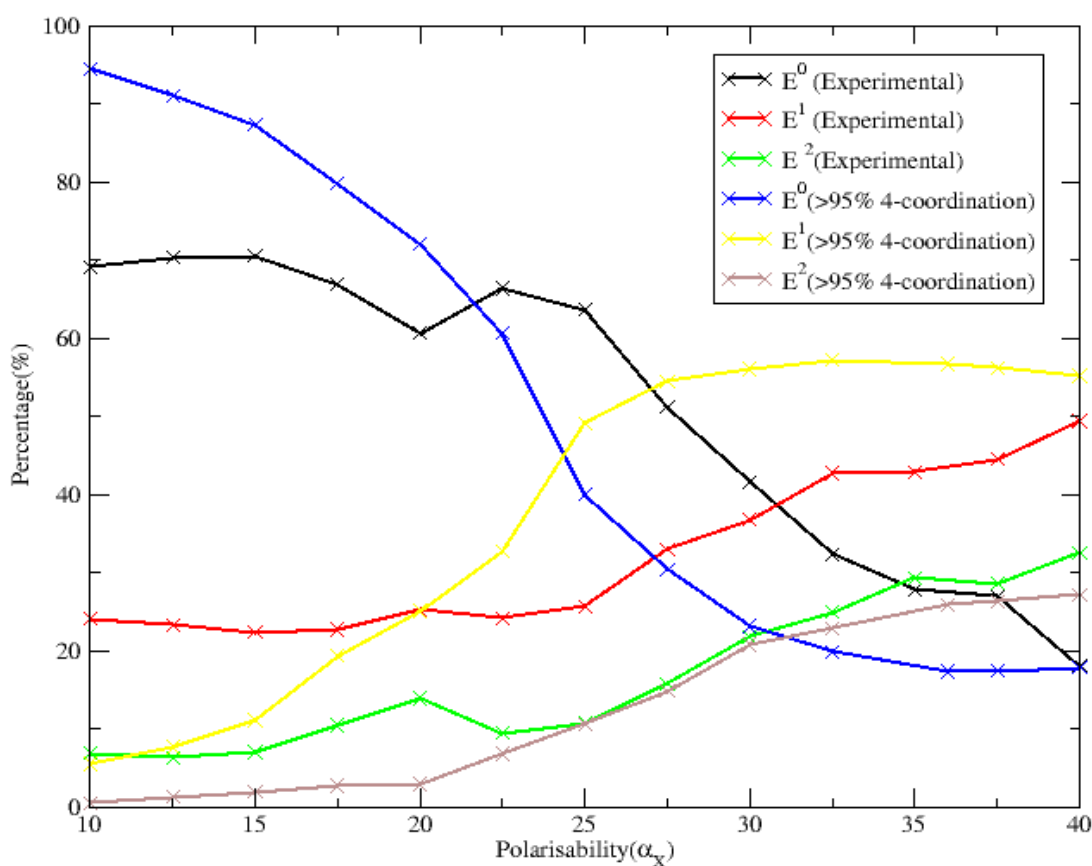
Figure 6.15:Change in network connectivity with anion polarisability as indicated by changes in the
percentage of cations with n number of four-membered rings, E^n, where n=0-2.

Figure 6.15 shows the changes in percentage of "0","1" and "2" cations according to
anion polarisability. To observe the effects of coordination difference on the
polarisability dependence of the edge-sharing configurations, the same functions were
calculated at a lower density where the proportion of four-coordinate cations is greater
than 95% over the whole polarisability range. This gives a closer topological account of

the changes in network connectivity statistics. While the values are similar, the changes follow a curvature which in the higher density configurations is "damped" due to the weakening 4-coordination. Increasing anion polarisability changes the network topology from a corner-sharing, 3D system to a system with 2D character with a combination of corner- and edge-sharing units. The graphical snapshots of two MX$_2$ configurations (figure 6.16) at different polarisabilities show the general features of high and low polarisability systems. The preponderance of "2" cations in the higher polarisability configurations, where chains and significant clustering can be observed is contrasted with the configuration at 15 a.u, where "0" cations predominate. The changes in cell volume, as shown in figure 6.17, are related directly to the changes in the network structure. With increasing polarisability, the volume increases due to the breakdown of a 3 dimensional network into relatively less dense edge-sharing regions which are charge
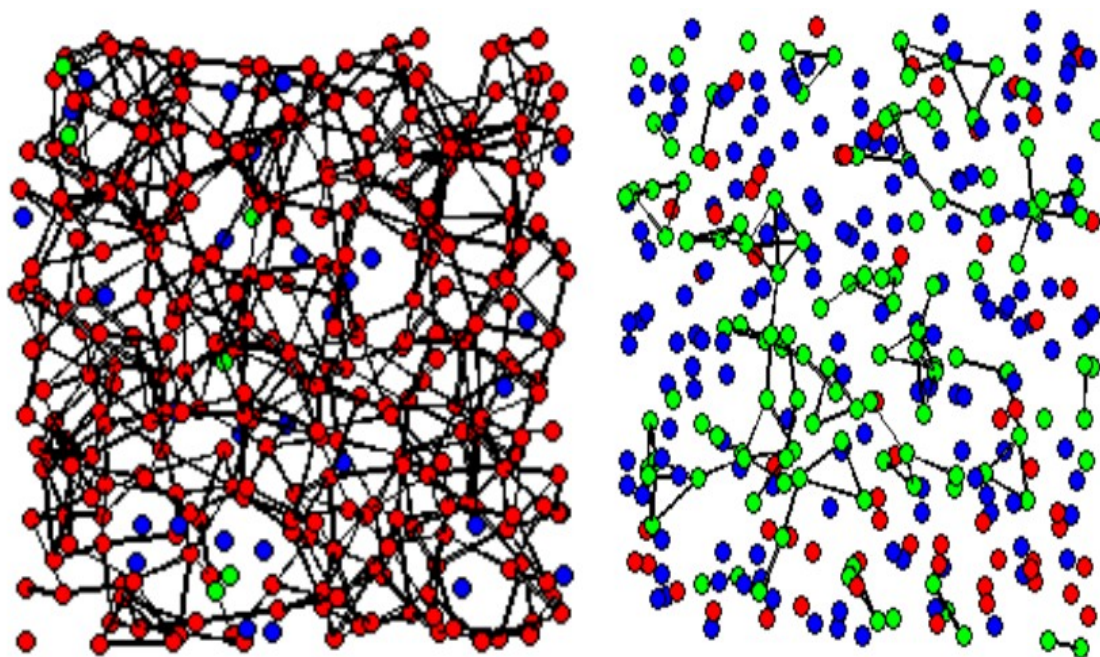
Figure 6.16:Graphical snapshots of configurations at α_X=15.a.u (left) and 40 a.u (right). "0","1" and "2" cations are represented by red, blue and green circles respectively.

neutral and are held together by weak Van der Waals forces. The levelling out of the cell volume from α_X=27 a.u onwards, is commensurate with a plateau in the edge-sharing unit percentage (which appears more significant for configurations where N_{MX}=4>95%).
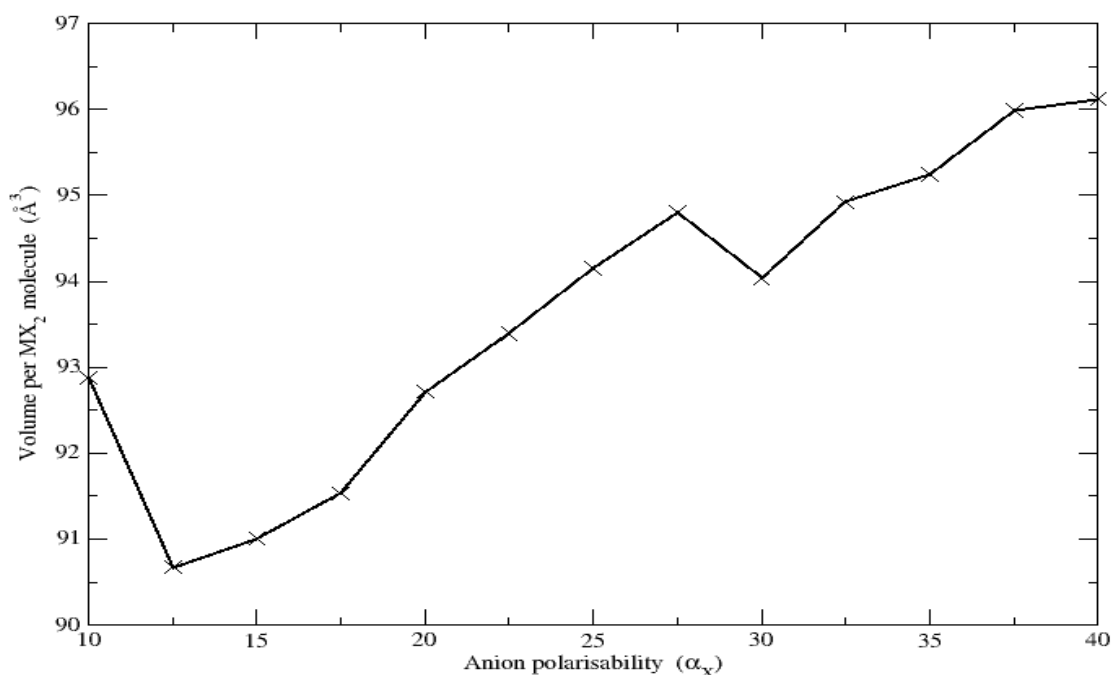
Figure 6.17: Change in volume per MX$_2$ molecule with anion polarisability.

Figure 6.18 shows the changes in the network connectivity triplet structure according to polarisability. These triplets are the various combinations which can be obtained from combination of the cations identified according to the number of four-membered rings they are bonded to. Notable features include an obvious difference in rates of change with respect to the proportion of different triplets. At low polarisabilities, triplets associated with "0" and "1" cations dominate, particularly 0-0-0 and 0-1-0. The influence of these two triplets declines sharply as $\alpha \rightarrow 27.5$ a.u. The region 27.5-40 a.u is characterised by two features: firstly, there are more triplet combinations involving just "1" and "2" cations in significant percentages: an indication of the variety of cation environments present. Secondly, the percentage of these triplet combinations do not change significantly at the highest polarisability values. As with the values in figure 6.15, the calculations carried out where $N_{MX=4} > 95\%$ show clearer changes, though the overall pattern remains similar. One noticeable difference is that the maximum in 0-0-0 is at a lower percentage due to the higher miscoordination of the respective systems at low polarisabilities.
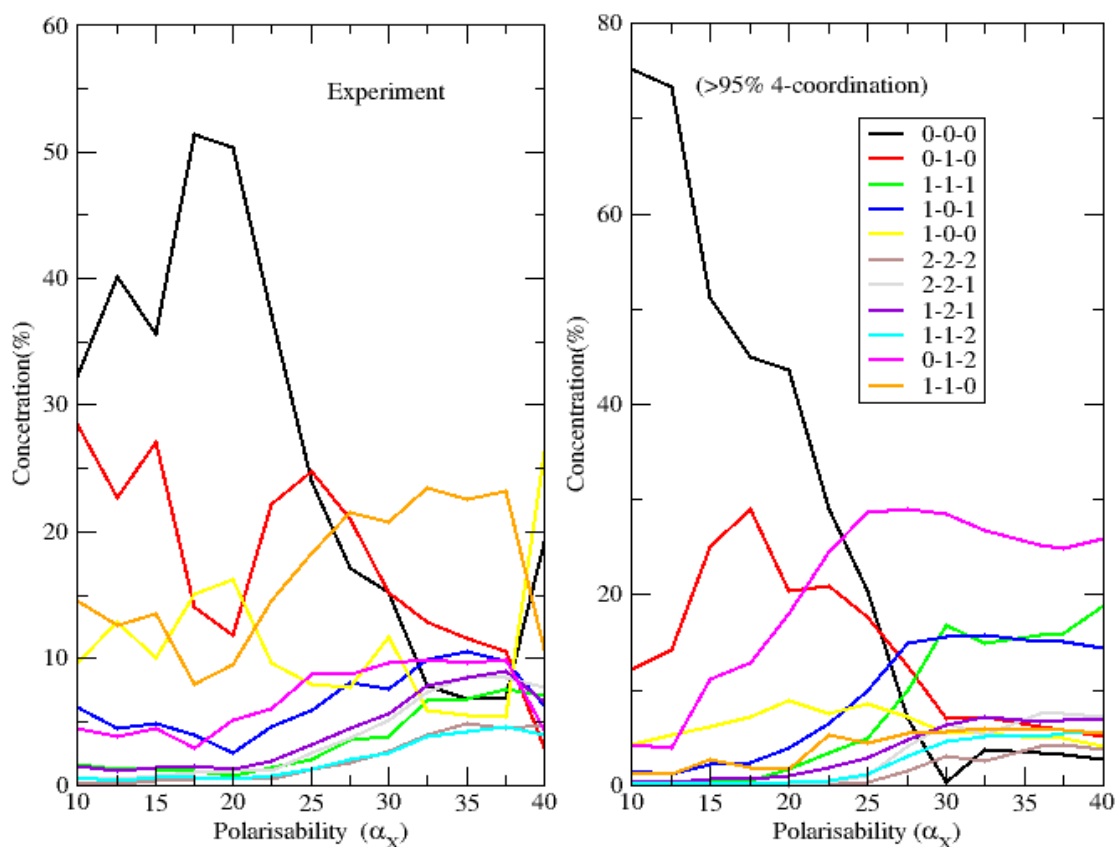
Figure 6.18: Percentage of network connectivty triplets in MX$_2$ configurations with varying anion polarisability.
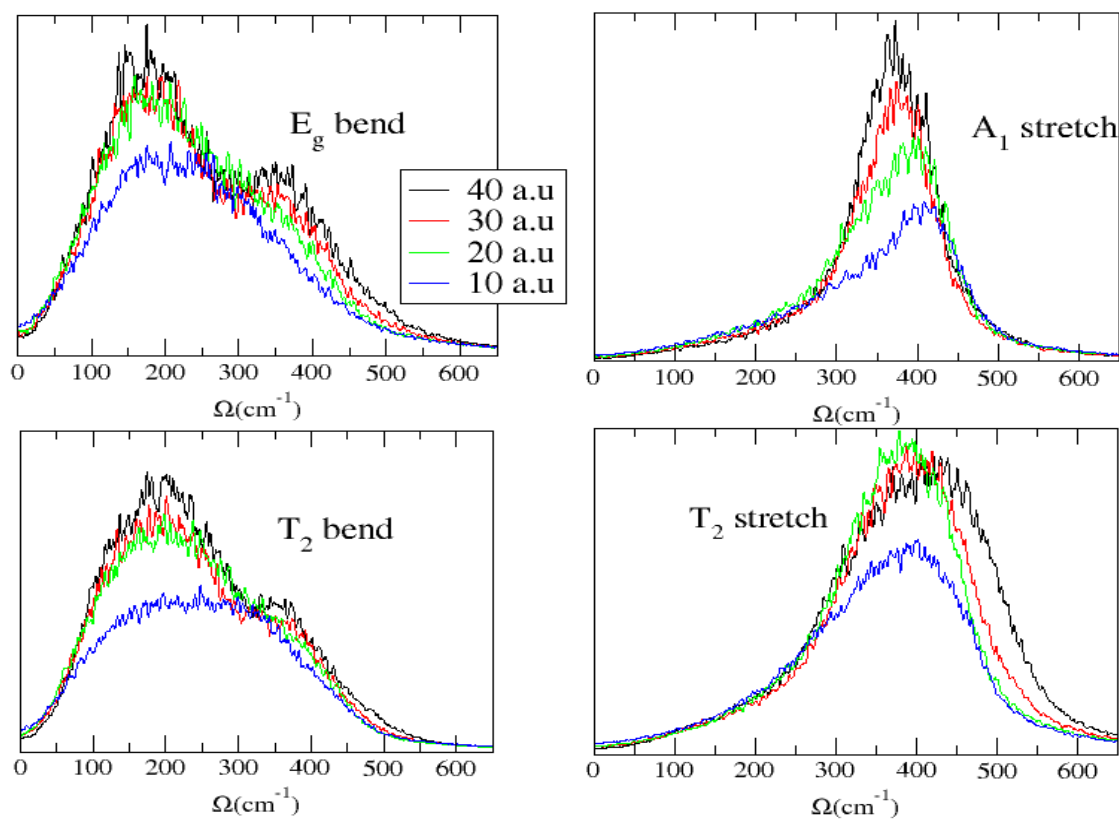
Figure 6.19: Vibrational frequencies of MX$_2$ systems.

6.7 Vibrational dynamics in MX_2 systems.

The vibrational frequencies[27] corresponding to several tetrahedral modes were calculated across the anion polarisability range. The full method of calculating vibrational densities is given in Appendix B. Note that, whilst collective modes of vibration would be expected to be significant for highly connected systems of the sort under study here, a local mode model, in which vibrations of local coordination polyhedra are considered, provides a useful reference point in the sense that the frequencies (and intensities) of specific features can be tracked as a function of the network topology.

The vibrational frequencies, shown in figure 6.19, for the E_g bend show two modes at higher polarisabilities. The first mode, present at all polarisabilities in situated around ~ 170 cm^{-1}. The second mode is at a higher frequency ~ 350 cm^{-1} is present from 40 to 27.5 a.u (at 25 a.u it appears as a shoulder). The A_1 symmetric stretch shows the greatest change in intensity with increasing polarisability in contrast to the other modes. The peak shifts from 371cm^{-1} at 40 a.u to 409 cm^{-1} at 10 a.u. The T_2 bend also resolves two features; an early mode at 200 cm^{-1} and a higher frequency mode at ~ 355 cm^{-1} disappears at lower polarisability of 25 a.u. The T_2 stretch maintains approximately the same position, 392cm^{-1} at 40 a.u and 397cm^{-1} at 10 a.u. The shifts with polarisability are partly to do with the increasing coordination number distribution as polarisability decreases. With an increasing number of coordinated anions, the average distance from the central cation increases, and consequently the bond strength and vibrational frequency of the complex increases. This explains the changes in position, although not the appearance of a second identifiable modes in the E_g and T_2 bends, whose appearance correlates with the establishment of large amounts of edge-sharing. Although the modes are higher than the corresponding experimental values, indicating that the potential is too stiff, the appearance of other modes with changing polarisability mirrors the changes in systems such as Ge_xSe_{1-x}, where new bands are observed with changing x.[28] This indicates that varying proportion of edge- and corner-sharing tetrahedra can be a cause of changes in Raman rather than the continuation of broken chemical order in systems such as Ge_xSe_{1-x} where x=0.33.

6.8 Relationship of ^{29}Si MAS-NMR data on SiSe$_2$ with network-connectivity of MX$_2$ compounds.

A large range of structures, as shown by the variation in position and intensity of quantities such FSDP's, bond angle distributions and coordination numbers have been sampled by varying the anion polarisability in a MX$_2$ model. While comparison of radial distribution functions and structure factors have been made in the thesis, the results concerning the network-connectivity of cations can be linked with ^{29}Si MAS-NMR experimental data. Such data is available for SiSe$_2$, highlighting the percentage value of "0", "1" and "2" cations[29]. SiSe$_2$ is similar to GeSe$_2$ in that edge-sharing tetrahedra are present in both the liquid and crystalline phases, but where homopolar bonds have been detected to level of ~1%.[30,31]

	E^n					
n	CMD-a-SiSe$_2$	Ex-a-SiSe$_2$	a-SiSe$_2$ (FPMD)	PIM(0) (31.89 a.u)	PIM(1) (40 a.u)	PIM(2) (37.86 a.u)
0	48	26	30	22	18	26
1	46	52	61	38	49	45
2	6	22	9	41	32	29

Table 6.4: Percentages of cations in different network connectivities observed experimentally and computationally in SiSe$_2$. CMD, calculated values from calculations by Vashishta[32]; Ex-a-SiSe$_2$, experimental values from Tenhover[29]; FPMD, calculated values from Massobrio calculations[33]; PIM (n), where n=0-2, the cation identity of the value E^n to be taken from experimental data that is used to locate the relates anion polarisability value (in brackets). The two remaining E^n values are then obtained using this polarisability value in conjunction with figure 6.15.

To compare the results from the PIM, "0", "1" and "2" percentages were extracted from figure 6.15 by fixing one of terms according to the experimental figure, or in the case of "1", where the experimental figure is not reached in the polarisability range, the closest figure possible. Table 6.4 show these results and the comparison with a previous classical model[32] and electronic structure calculations.[33] The PIM results compares favourably with the experimental results; the polarisabilities ranging from 31.89-40 a.u. The simulations show that $S_{SiSi}(k)$ is primarily responsible for the FSDP in F(k), although experimental partials have yet to be extracted. The major discrepancy lies in the failure

of FPMD calculations and Vashishta's classical model to produce a sufficiently high percentage of "2" cations, highlighting that the ability of models to allow these edge-sharing units to percolate, as the PIM is able to do, is important. A previous model[3] for $SiSe_2$, which centred on the edge-sharing motif of the crystalline form, is supported by the results of experiment and this model. This also enables a better prediction of the distribution of the triplets in $SiSe_2$, as the accuracy of these figures is inherently linked with the correspondence with the MAS-NMR data. Amongst the configurations with edge-sharing units, Massobrio's model predicted 1-2-1 as the most common triplet combination, and our model agrees with this.[33]

6.9 Systems with extreme anion polarisation.

The next question which leads from the results discussed in sections 6.1-6.10 is what happens if the polarisability is increased further? An alternative measure of the effect of polarisability is the polarisation energy as a fraction of the total energy. By this measure a range of 8.7% at $\alpha_X = 40$ a.u to 1.8% at $\alpha_X = 10$ a.u is covered in sections 6.1-6.8. In this section we utilise a potential that was previously used for $BeCl_2$[4], a system with substantial edge-sharing, and amend it to predict structures of larger polarisabilty. This was done by amending the value of c in the short-range damping function[34] from c=0.50 to c=0.90, which accesses a range of polarisation energies of 9% at c=0.90, to 19% at c=0.50.

Figure 6.20 shows the effect of the increased polarisability on the partial structure factors. In the range c=0.90-0.60, $S_{MM}(k)$ is similar to that observed at high polarisabilities, as highlighted by the presence of a FSDP at $k\sim 1\text{Å}^{-1}$; from b=0.90 to c=0.60, there is a shift in position from 1.03Å^{-1} to 1.10Å^{-1} and a small rise in the intensity of the FSDP from 1.04Å^{-1} to 1.18Å^{-1}. At c=0.50, the FSDP intensity decreases to 0.93 and the FSDP becomes a broad shoulder with peak position of 1.14Å^{-1}.
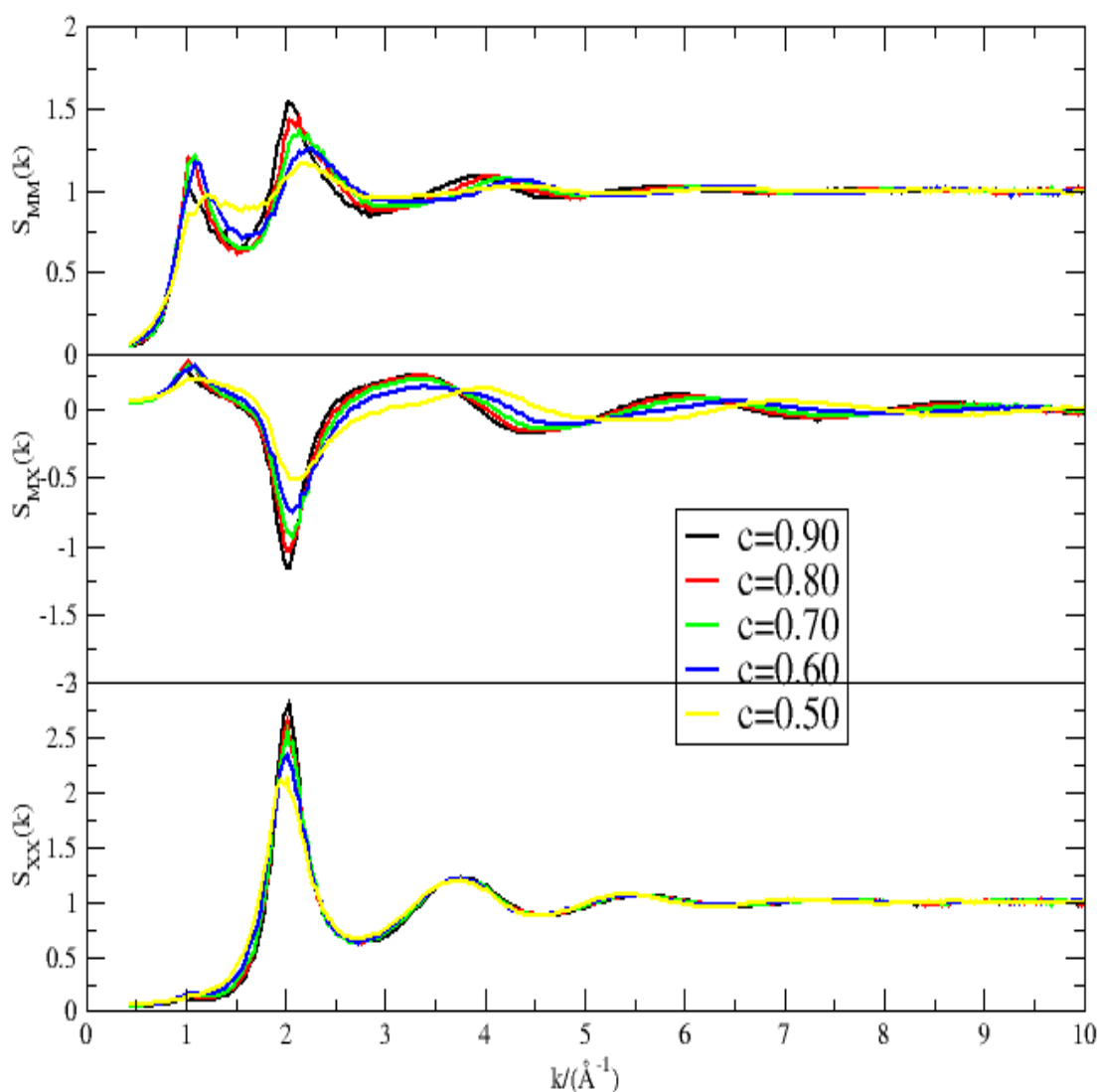
Figure 6.20: Partial structure factors for MX₂ with extreme anion polarisability. Black, c=0.90; red, c=0.80, green, c=0.70, blue, c=0.60, yellow, c=0.50

This process is distinct from that observed which changes from high to low anion polarisability (i.e $\alpha_X = 40$ a.u-10a.u) in that *both* the FSDP and the principal decrease in intensity. In $S_{MX}(k)$, the FSDP follows a similar pattern to the changes observed in $S_{MM}(k)$ shifting from 1.00Å⁻¹ to 1.07Å⁻¹ from c=0.90 to c=0.60, then shifting back to lower scattering angles at 1.02Å⁻¹. The intensity over the range increased slightly from 0.29 to 0.34 from c=0.50 to c=0.60 and then declines to 0.23 at c=0.50. The small FSDP in $S_{XX}(k)$ stays at similar intensity over the c range with similar changes in FSDP position as $S_{MM}(k)$ and $S_{MX}(k)$ from 0.13 at 0.97Å⁻¹ to 0.16 at 1.08Å⁻¹ from c=0.90 to c=0.60 to 0.14 at 1.05Å⁻¹ when c=0.50. This effective transition is a change from ionic systems, with features attributed to covalency such as significant edge-sharing, to systems which can be described as having a molecular interaction. In systems such as

CS_2 no FSDP is observed in the experimental $F(k)$[35] indicating a weak interaction between the constituent polyhedral units.

Figure 6.21 shows the changes in the radial distribution functions with decreasing c. In $g_{MM}(r)$, the position of the principal peak shifts from 3.57Å to 3.13Å in the range c=0.90-0.60, increasing in intensity from 1.91 to 2.20; this is indicative of an increasing effect of anion polarisation that we have observed in section 6.5. At c=0.50, the intensity of the principal peak decreases sharply in intensity to 1.31 with the position of the principal peak, now a broad shoulder, staying constant at 3.13Å. The minima of the principal peak at this value of c rises sharply in comparison with those at c=0.90-0.60.
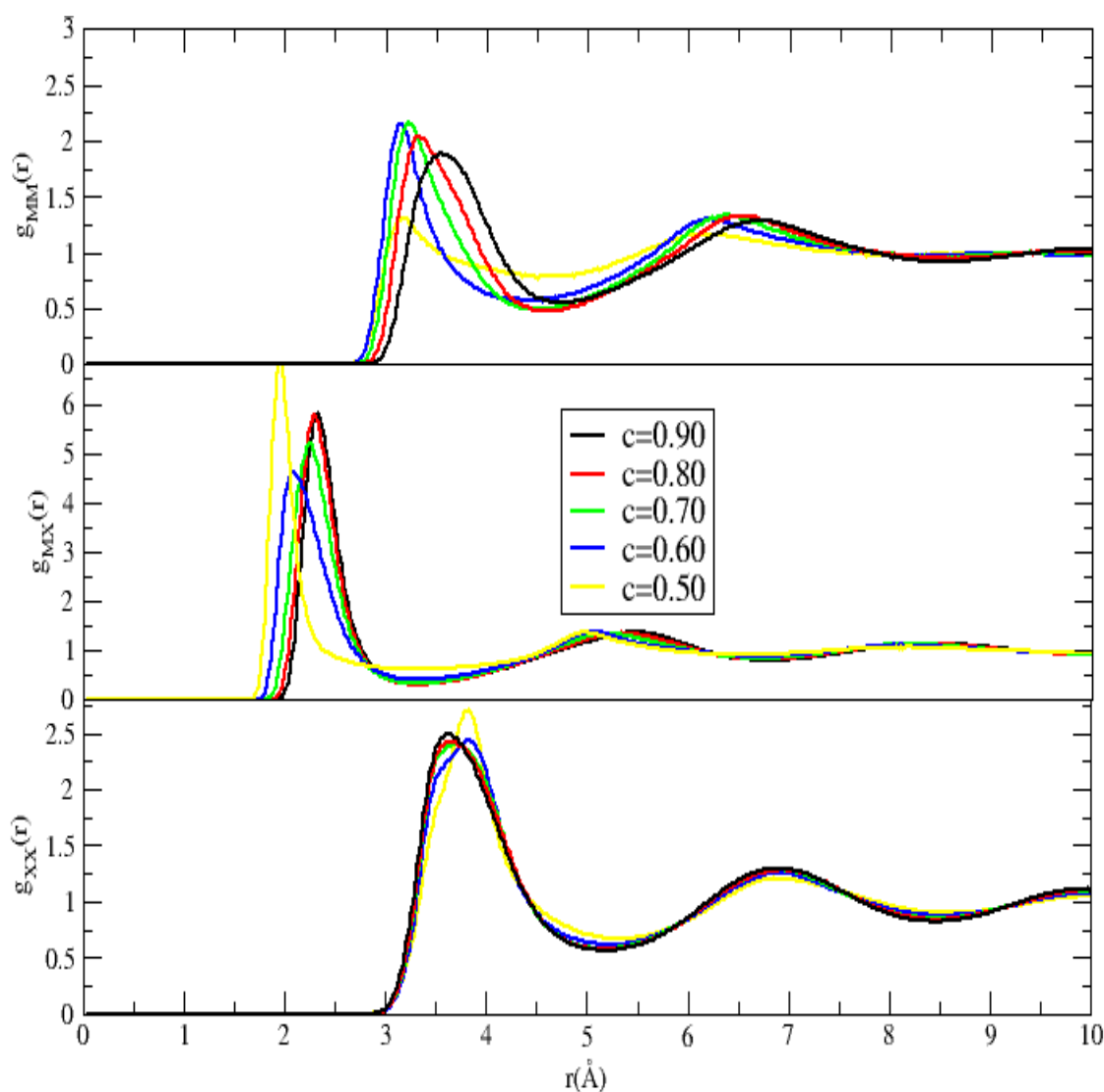
Figure 6.21: Radial distribution functions for MX_2 with extreme anion polarisability. Black, c=0.90; red, c=0.80, green, c=0.70, blue, c=0.60, yellow, c=0.50.

The principal peak position in $g_{MX}(r)$ observes a shift from 2.31Å at c=0.90 to 2.09Å at

c=0.60. At c=0.50, the principal peak shifts again to 1.94Å with a sharp rise in intensity. These changes are much larger than those observed in section 6.5 (which varied by 0.04Å over the anion polarisabililty range) indicating that significant changes the cation-anion short-range ordering occur in the presence of extreme anion polarisability. The position of the principal peak in g$_{XX}$(r) shift from 3.60Å at c=0.50 to 3.83Å at c=0.90 with similar intensities of 2.52 and 2.44. At c=0.50, the intensity rises to 2.75 with the position at 3.84Å.

The value of the cation-cation coordination number, M$_{MM}$, ranges from 2.40 at c=0.50 to 4.07 at c=0.90 and is indicative of the stronger polarisability effect of using this potential. The corresponding M$_{MX}$ values are 3.38 and 4.35 which are a further indication of deviations in the local tetrahedra compared to simulations described in section 6.5.
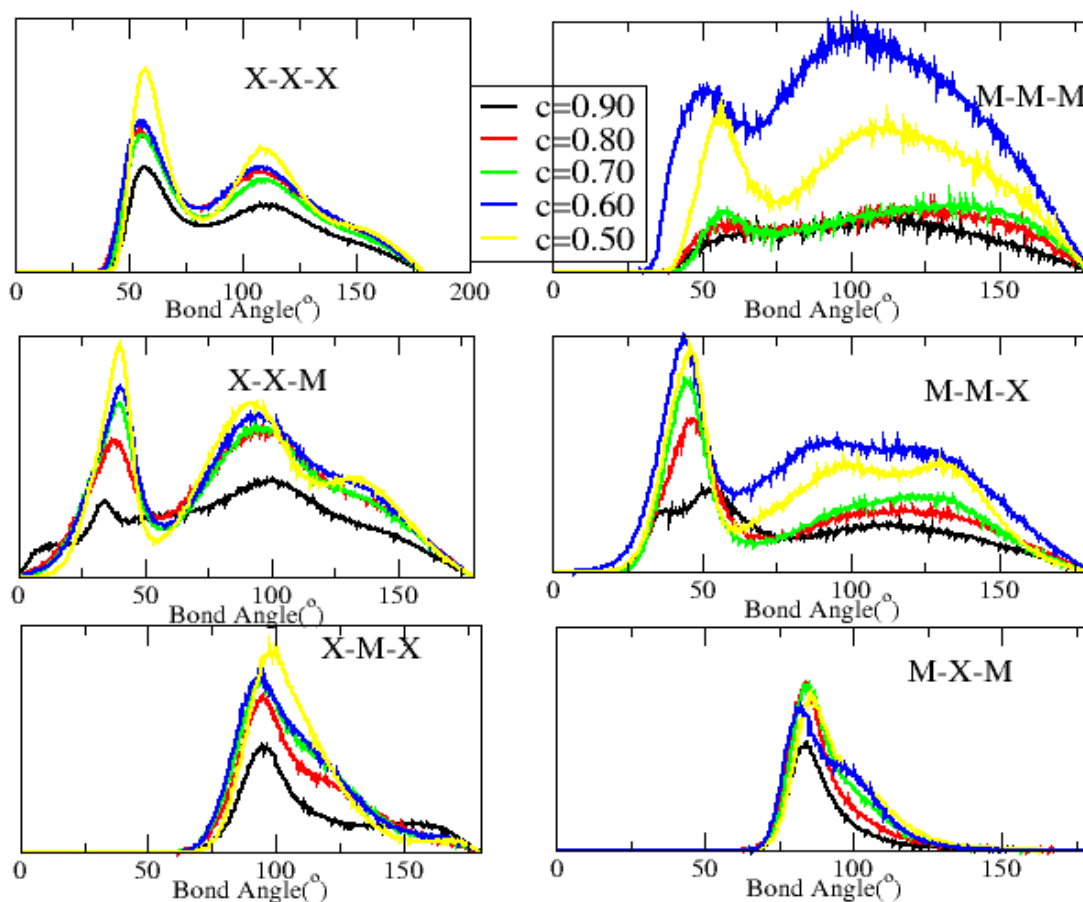
Figure 6.22: Bond angle distribution functions for MX$_2$ with extreme anion polarisability. Black, c=0.90; red, c=0.80, green, c=0.70, blue, c=0.60, yellow, c=0.50.

The bond angle distributions, shown in figure 6.22, exhibit smaller changes in structure

when c decreases from 0.90 to 0.50, compared to the radial distribution functions and structure factors. For the M-X-M bond angle distribution the major peak is at ~85° for all values of c covered, indicative of a system with strongly polarisable anions, where close separation of cations is favored (and with an associated lack of intensity at ~110°). The X-M-X distribution shows a strong peak ~95° which increases in intensity with decreasing c and also relatively against the higher angle tail ~150°. The M-M-M bond shows similar features in the range of c=0.90-0.70. At c=0.60 and 0.50, the acute peak ~55° increasing sharply in intensity relative to the higher angle values.

Short-range damping parameter, c	0	1	2
0.50	32.3(3.3)	40.3(7.5)	19.2(6.8)
0.60	8.3(1.7)	43.9(2.8)	47.8(3.3)
0.70	6.9(1.7)	39.0(3.2)	54.0(3.7)
0.80	9.0(1.9)	41.3(3.2)	49.8(3.8)
0.90	18.1 (2.4)	49.4(2.7)	32.6(3.0)

Table 6.5: Percentages of cations in different network connectivities observed in MX$_2$ systems with varying short-range damping parameter c.

The percentages of cations coloured "1" and "2" (shown in table 6.5) are larger than in comparison with MX$_2$ (where α_X=40 a.u) whereas the percentage of "0" cations is similar over the c range 0.90-0.60. The values at c=0.90 are similar with those at α_X=40 a.u and the subsequent increase in edge-sharing, showing that there is no significant gap in the sampling of systems observed between section 6.1-6.8 and section 6.9. With decreasing c (from c=0.90), there are small changes until c=0.50, where a sharp transition occurs with a steep rise in the percentage of "0" cations with a decline in "2" cations. The main cause of this is the abrupt change in percentage of 2- and 3-coordinate cations which rises from 1.3% and 24.3% respectively at c=0.60 to 10.5 and 45.8% at c=0.50. The effect of this is to break edge-sharing chains into units where there are terminal M-X bonds also leading to increase in 1-coordination of the X-M ion pair from 20.1% at c=0.60 to 40.4% at c=0.50. It also noticeable that the standard deviation of "0","1" and "2" cations is much larger at c=0.50 than at higher c values indicating a greater flux in identity at c=0.50.

6.10 Conclusion.

In this chapter we have investigated the origin of intermediate range order in largely tetrahedral systems as a function of polarisability. The FSDP position, linked directly to the presence of IRO, moves from $k_{FSDP} \sim 1.5 \text{Å}^{-1}$ at low anion polarisabilities to $\sim 1 \text{Å}^{-1}$ at high polarisabilities. At polarisabilities higher than that sampled in sections 6.1-6.8, an ionic to molecular transition is observed, which results in a sharp reduction in the intensity of FSDP.

At high polarisabilities, the increased presence of edge-sharing units has several effects on the underlying structure: a reduction in the cation-cation coordination number and significant changes in those bond angle distributions involving metal cations. The dominance of the changes in the cation distribution allow a further analysis of the network connectivity cation-cation functions, where the characteristic features of presence of FSDP, phase separation and value of the ratio $S_{MM}^{ab}(k_{FSDP}) / S_{MM}^{ab}(k_{PP})$ are related to the nature of edge- and corner-sharing linking, rather than simple concentration effects. Analogously, the bond angle distribution M-M-M can be broken down and understood in terms of clustering and bridging terms. With increasing polarisability, the separation of "0" and "2" cations is highlighted through the large intensity of $S_{MM}^{02}(k_{FSDP})$ and the 0-1-2 bond angle distribution showing the strongest preference for larger bond angles. In contrast to a previous study[3], we have focused on predominantly tetrahedral systems. The presence of a FSDP in $S_{CC}(k)$ is shown to be reproducible over a series of polarisabilities; it is intrinsically linked to rising a proportion of edge-sharing tetrahedra, independent of the presence of homopolar bonds. Vibrational frequency calculations also showed the formation of a second bending mode in T_g and E_g which corresponds to increasing percentage of edge-sharing cations. Section 6.11 showed that upon the presence of extreme anion polarisability molecular units are stabilised which effectively break up the mixed edge- and corner-sharing network structure. As a result, a rapid decline is observed in the FSDP in $S_{MM}(k)$.

Iyetomi and Vashishta[3] highlighted the effect of increasing tetrahedral coordination on the presence of IRO by varying the ratio of cation to anion radius, with those systems exhibiting a higher ratio displaying strong deviation away from tetrahedral coordination and consequently lack a FSDP. In this chapter we have shown the variety of IRO present within predominantly tetrahedral conditions where only anion polarisability is varied.

The use of a simple potential model able to stabilise large anion polarisabilities enables the study of the evolution of IRO as a function of anion polarisability and underlying network topology. In addition, by applying a further set of calculations to describe the effect of extreme anion polarisability effects, we have described a range of MX$_2$ systems which encompasses a large range of bonding behaviour from strongly Coloumbic, systems with significant inductive effects and systems which display molecular-type behaviour, and the IRO related to their structures. This is highlighted by the range FSDP positions observed from 1-1.5Å^{-1}, larger than that observed by Iyetomi and Vashishta[3] where the FSDP position are centred around 1.4Å^{-1}. We can therefore define a set of groups analogous to those described by Massobrio[15] highlighted in section 6.1. Group 1 describe systems consisting of primarily corner-sharing tetrahedra which do not exhibit a peak in $S_{CC}(k_{FSDP})$. In group 2, where a peak in $S_{CC}(k_{FSDP})$ is observed, the number of "1" cations is approximately 50%. In group 3, we define those systems where "1" cations decline below 50% in systems where the percolating edge-sharing threshold is passed leading to a transition to a molecular system. In all three groups, due to the strongly ionic nature of our model, broken chemical order through homopolar bonding is absent, although a degree of miscoordination is present in all three systems.

Experimentally, a similar shift in FSDP position to that observed in figure 6.3 was highlighted in X-ray diffraction experiments on As$_X$Se$_{1-X}$ by Bychkov et al[36], where x was varied from 0.62 to 0.10. At x=0.62, the FSDP position is ~1Å^{-1}, and, with declining x, the FSDP position shifts to higher scattering angles (~1.5Å^{-1} at x=0.10). The FSDP intensity with varying x displays a similar curve to that exhibited in figure 6.5. In contrast with our systems, the principal peak at ~2Å^{-1} observed greater fluctuations in intensity (intensity largest at high values of x). Additionally, no collapse of the FSDP at ~1Å^{-1} occurs, such as that exhibited by extreme anion polarisability systems in section 6.9. IRO is also linked with increasing content of As whereas in our systems the cation concentration is fixed.

A model of understanding IRO through network connectivity is analogous to other generic models based on cluster-void ordering[37] and presence of quasi-crystalline layering[38] in seeking an understanding of IRO which is applicable across a range of compounds. In this chapter we have shown that this method catalogues the subtle changes in network topology with vary anion polarisability. There are some limitations: the effect of homopolarity on the structure of the system is not considered, and the effect

of deviations away from a tetrahedral network will damp the significance of the edge-sharing statistics. Experimental interest may lie in systems which lie at the transitions between the groups highlighted. Firstly, the transition between systems with isolated edge-sharing present to those where edge-sharing units percolate. In our calculations, this is highlighted more clearly in the sharp changes in network connectivity over a relatively small polarisability change from α_X=22.5 to 25 a.u for calculations at lower density (figure 6.18). A second possible transition occurs between systems with percolating edge-sharing units to molecular systems.

6.11 References.

[1] S. R. Elliott. *Nature*, **354**, 445, (1991).

[2] M. Wilson and P. A. Madden. *J. Phys.: Condens. Matter,* **5**, 2687, (1993).

[3] H. Iyetomi and P. Vashishta. *Phys. Rev. B,* **47**, 3063, (1993).

[4] M. Wilson and P. A. Madden. *Mol. Phys.,* **92**, 197, (1997).

[5] P. A. Madden and M. Wilson. *Chem Soc Rev.*, **25**, 339, (1996).

[6] A. C. Wright, A. G. Clare, G. E. Etherington, R. N. Sinclair, S. A. Brawer and M. J. Weber. *J. Non-Cryst. Solids*, **111**, 139, (1989).

[7] P. Vashishta, R. K. Kalia, J. Rino and I. Ebbsjö. *Phys. Rev. B,* **41**, 12 197, (1990).

[8] S. Biggin and J. Enderby. *J. Phys. C.:Solid State Phys.,* **14**, 3129, (1981).

[9] J. Neuefeind. *Phys. Chem. Chem. Phys.,* **3**, 3987, (2001).

[10] S. Biggin, M. Gay and J. Enderby. *J. Phys. C.:Solid State Phys.,* **17**, 977, (1984).

[11] P. S. Salmon, R. A. Martin, P. E. Masonand G. J. Cuello. *Nature (London)*, **435**, 75, (2005).

[12] M. Tenhover, M. A. Hazle and R. K. Grasselli. *Phys. Rev. Lett.*, **51**, 403, (1983).

[13] J. Peters and B. Krebs. *Acta Crystallogr. B*, **38**, 1270, (1985).

[14] I. T. Penfold and P. S. Salmon. *Phys. Rev. Lett.*, **67**, 97, (1991).

[15] C. Massobrio and A. Pasquarello. *Phys. Rev. B*, **68**, 020201, (2003).

[16] C. Massobrio, A. Pasquarello, and R. Car. *Phys. Rev. Lett.,* **80**, 2342 (1998).

[17] P. S. Salmon and J. Liu. *J. Phys.: Condens. Matter*, **6**, 1449, (1994).

[18] C J. D. Martin, S. J. Goettler, N. Fosse and L. Iton. *Nature*, **419**, 381, (2002).

[19] M. Wilson and P. A. Madden. *Phys. Rev. Lett.,* **72**, 3033, (1994).

[20] P. S. Salmon and I. Petri. *J. Phys.: Condens. Matter,* **15**, S1509, (2003).

[21] S. Susman, K. J. Volin, D. G. Montague and D. L. Price. *Phys. Rev B*, **43**, 11 076, (1991).

[22] P. Vashishta, R. K. Kalia, G. A. Antonio and I. Ebbsjö. *Phys. Rev. Lett*., **62**, 1651, (1989).

[23] B. K. Sharma and M. Wilson. *Phys. Rev. B*, **73**, 060201, (2006).

[24] X. S. Chen, M. Kasch and F. Forstmann. *Phys. Rev. Lett*., **67**, 2674, (1991).

[25] T. Biben and J. P. Hansen. *Phys. Rev. Lett.,* **66**, 2215, (1991).

[26] A. B. Bhatia and D. E. Thornton. *Phys. Rev. B*, **2**, 3004, (1970).

[27] M. C. C. Ribeiro, M. Wilson and P. A. Madden. *J. Chem. Phys.*, **110**, 4803, (1999).

[28] P. Boolchand, J. Grothaus, M. Tenhover, M. A. Hazle and R. K. Grasselli. *Phys. Rev. B*, **33**, 5421, (1986).

[29] M. Tenhover, R. D. Boyer, R. S. Henderson, T.E. Hammond and G. A. Shave. *Solid State Commun.*, **65**, 1517, (1998).

[30] P. Boolchand and W. J. Bresser. *Philos. Mag. B*, **80**, 1757, (2000).

[31] M. Arai, D. L. Price, S. Susman, K. J. Volin and U. Walter. *Phys. Rev. B*, **37**, 4240, (1988).

[32] G. A. Antonio, R. K. Kalia, A. Nakano and P. Vashishta. *Phys. Rev. Lett.,* **62**, 1651, (1992).

[33] M. Celino and C. Massobrio. *Phys. Rev. Lett.,* **90**, 122502, (2003).

[34] M. Wilson and P. A. Madden. *J. Phys.: Condens. Matter*, **5**, 2687, (1993).

[35] P. Jovari. *Mol. Phys.*, **97**, 1149, (1999)

[36] E. Bychkov, C. J. Benmore and D. L. Price. *Phys. Rev. B*, **72**, 172107, (2005).

[37] S. R. Elliot. *J. Phys.: Condens. Matter*, **4,** 7661, (1992).

[38] P. H. Gaskell and D. J. Wallis. *Phys. Rev. Lett.*, **76**, 66, (1996).

Chapter 7

Effect of pressure and temperature on the intermediate-range order of $ZnCl_2$

7.1 Introduction.

In previous chapters the underlying network structures have been analysed for a variety of models (and hence network morphologies). In this chapter we will consider the effect of temperature and pressure for a single potential model, that for $ZnCl_2$. The evolution of the system structure as a function of pressure and temperature can be monitored through changes in the total structure factor, F(k), particularly in the FSDP when considering the evolution of intermediate-range order.

The FSDP in the total structure factor is often distinguished from the other peaks in terms of the anomalous properties it exhibits with regards to temperature and pressure. The general behaviour of the FSDP with pressure has been interpreted by Elliot[1]. With changing temperature and at a constant pressure the change in intensity of a given peak in F(k) can be written as:

$$\left(\frac{\partial I}{\partial T}\right)_p = \left(\frac{\partial I}{\partial T}\right)_\rho + \left(\frac{\partial I}{\partial \rho}\right)_T \left(\frac{\partial \rho}{\partial T}\right)_p \tag{7.1}$$

The first term on the right $\left(\frac{\partial I}{\partial T}\right)_p$, is expected to be negative due to the Debye-Waller effect. The third term, $\left(\frac{\partial \rho}{\partial T}\right)_p$, is related to thermal expansivity which would also usually be negative. The second term, $\left(\frac{\partial I}{\partial \rho}\right)_T$, differs between the FSDP, for which it is large and negative; and the principal peak, for which it is small and positive. A similar understanding of the behaviour of the peak intensity with pressure, where the change in the peak intensity can be written as:

$$\left(\frac{\partial I}{\partial p}\right)_T = \frac{\rho}{B}\left(\frac{\partial I}{\partial \rho}\right)_T \tag{7.2}$$

The partial derivative on the right, $\frac{\rho}{B}\left(\frac{\partial I}{\partial \rho}\right)_T$, is negative due to network relaxation as density decreases, and where B is the bulk modulus.

7.2 Experimental methods.

The first system displaying IRO which was studied at high pressure and high temperature was SiO_2[2-5] which showed that FSDP declined in intensity by 50% with increasing pressure in the pressure range 0-28GPa.[3] Experiments highlighting the effect of increased temperature on SiO_2 showed, contradictorily, both an increase in FSDP intensity (from X-ray diffraction)[4] and a 10% decline from room temperature to 1036°C (from neutron diffraction).[5] Early difficulties associated with high temperature, high pressure neutron diffraction included large amounts of Compton scattering from pressure anvils used in comparison to the relatively low scattering from amorphous materials. This problem was overcome using high energy synchrotron sources. Other difficulties include sample preparation and pressure and temperature control of the sample. A number of recent experiments have been carried out on the effect of changes in temperature and pressure of $ZnCl_2$.[6-9] $ZnCl_2$ is a hygroscopic material and highly corrosive at elevated temperatures. In the experiment by Pfleiderer et al,[6] $ZnCl_2$ was filled and closed into a quartz glass ampoule, resistant to corrosiveness, in an inert atmosphere. The molten salt was transported to the container where neutron diffraction takes place by breaking the point of the ampoule with a molybdenum rod which is connected to the pressure-valve spindle. There was no contact with the atmosphere unlike in the experiment by Brazkhin et al,[8,9] where there was a 1 minute transfer time between the container to the pressure apparatus, which resulted in ~1-2% hydroxide contamination.

Several different apparatus have been used for high temperature-high pressure experiments. In the experiment by Pfleiderer et al a high pressure neutron diffraction apparatus is fixed on the aluminium bell-jar of the instrument D4B at Institute Laue-Langevin (ILL). The high temperatures are produced by a jacket heater comprised of a cylinder of brass wound with wire. For cooling, water jackets are integrated with the water circuit of the ILL. A gas compressor is used to produce the extra pressure utilising helium as the pressure medium for the experimentally accessible pressure range of 1-5000 bar. The X-ray diffraction experiment by Brazkhin et al was carried out at the MAX-80 setup at the SPring-8 synchrotron BL14B1 beam in Japan, covering a much larger temperature and pressure range (up to 1000°C and 4.5 GPa). The latter experiment

was carried out at diffraction scattering angles, $2\theta=4°$ and $8°$.

These experiments display a common observation: a deterioration of the FSDP in F(k) with pressure. Similar observations have been made in a related compound, $ZnBr_2$.[10] The term, *network collapse*, has been applied to his phenomena, primarily as it has been the intermediate-range order that is modified. The short-range order of the compounds remains, as indicated by no significant change in principal peak intensity over the experimental pressure range. Changes in the real space quantities are reflected by an increase in intensity at a length scale of 7-10Å in the total correlation function G(r). EXAFS data on $ZnCl_2$, taken over a wider pressure range (0-12 GPa)[11], shows that a rise in the Zn-Cl bond distance is observed from 2.30Å at atmospheric pressure to 2.45Å at 4GPa, declining to 2.40Å at the highest pressure at 12GPa. In chapter 3, the Raman modes describing the structure of molten $ZnCl_2$ were highlighted.[12] Within the temperature range of this investigation the only mode predicted to change is the $v_{1b}^{B}(A_1)$ which is present at 350°C but disappears at 800°C. It is attributed to a large cage unit comprising four corner-shared $ZnCl_4^{2-}$ units.[12] In the neutron diffraction experiment of Allen *et al*[13], the structure of $ZnCl_2$ was measured at 330°C and 600°C where little change was observed in the pre-peak intensity, although the rest of F(k) diminishes by ~25% in keeping with the general observations of Elliot.[1] High energy X-ray diffraction experiments predicts that Zn-Cl first coordination is largely stable to changes in bond length from 623K to 853K, increasing slightly from 2.281Å to 2.289Å.[14]

Whilst the contributions of different individual correlation functions to F(k) have been highlighted, there is currently no elucidation of the changes in the *partial structure factors* as a result of changes in pressure. Furthermore, the total structure factors obtained from X-ray and neutron diffraction experiments may appear to evolve in a different manner as a function of both pressure and temperature, as was the case with SiO_2[3,4]. However, it is likely that these apparent differences are due to the differing weightings of the underlying partial structure factors in the total X-ray and neutron scattering functions. In this chapter, we highlight the changes of *partial* structure factors as a function of pressure and temperature, elucidating structural changes which contribute to any network collapse. The pressure range analysed will include the current experimental range for high-temperature neutron diffraction (1-5000 bar) as well as observing larger pressure effects up to 29000 bar. It is known from crystal studies[15] that a pressure transition is obtained in $ZnCl_2$ at 23000 bar and, in keeping with recent work on liquid polyamorphism,[16-18] we could expect significant structural changes over this regions as

well. The temperature these calculations take place will be at 600K, 800K, 1000K and 1200K. This temperature range covers a significant spectrum of where, at zero pressure, the FSDP was shown to have considerable variation. At each pressure, the system was run for 40 ps from which structural quantities were carried out for the last 25 ps.

.

7.3 Simulation details.

All calculations in this chapter consists of 999 ions (333 cations and 666 anions). The $ZnCl_2$ potential used in this chapter is the same as that developed in chapter 3. Runs between 600-1200K and 1 bar were generated from an initial starting configuration taken from simulations on $ZnCl_2$ from chapter 3. The cell sizes for the different temperatures at 1 bar were 31.50Å, 31.58Å, 31.96Å and 32.42Å for 600K, 800K, 1000K, and 1200K respectively. After the initial pressure run, further simulations were carried out at ~1 bar 0.00000 a.u, 5000 bar (1.75×10^{-5} a.u), 15000 bar (5.0×10^{-5} a.u), 22000 bar (7.5×10^{-5} a.u) and 29000 bar (1.0×10^{-4} a.u) at all four temperatures. After initial observation of the pressure dependence of IRO, further calculations were carried out in the 1-15000 bar range where changes in IRO were greatest. At 29000 bar, the average cell size was 27.78Å, 27.92Å, 28.13Å and 28.35Å for 600K, 800K, 1000K and 1200K respectively. At each state point, the system was equilibrated for 30 ps and a simulation run of 60 ps under NPT conditions from which structural correlations were calculated.

7.4 Total structure factors.

Figure 7.1 shows the total neutron structure factor, F(k), for simulated $ZnCl_2$ using the scattering lengths for ^{35}Cl, ^{37}Cl, and ^{nat}Cl. As the pressure is increased, the FSDP is shifted to longer scattering angles until it is no longer discernible as a distinct peak. Peaks at $k>1Å^{-1}$ *increase* in intensity, following the trend observed experimentally. The isotope dependence of F(k) is shown in figure 7.1 where the principal peak in $F_{Zn^{37}Cl_2}(k)$ (top panel) is noticeably damped compared to $F_{Zn^{35}Cl_2}(k)$ and $F_{Zn^{nat}Cl_2}(k)$. Noticeably, the FSDP does persist at pressure higher than the experimentally accessible range of 1-5000 bar.[7] With variations in temperature, shown in figure 7.2, the isotopic dependence is further highlighted by the uneven changes in FSDP intensity, with similar intensities observed for $F_{Zn^{35}Cl_2}(k)$ and $F_{Zn^{37}Cl_2}(k)$, and a *decrease* for $F_{Zn^{nat}Cl_2}(k)$. Whilst

total structure factors are the most common functions extracted from diffraction experiments, by their very nature, they do not describe the detailed partial interactions which are present in a multi-atomic system. An understanding of how the partials change in structure through pressure can only readily be implied through changes in F(k) if it is dominated by $S_{ZnZn}(k)$ and other contributions from $S_{ClCl}(k)$ and $S_{ZnCl}(k)$ are negligible such that $F\left(k_{FSDP}\right)=c_{Zn}^2 b_{Zn}^2 S_{ZnZn}\left(k_{FSDP}\right)$.
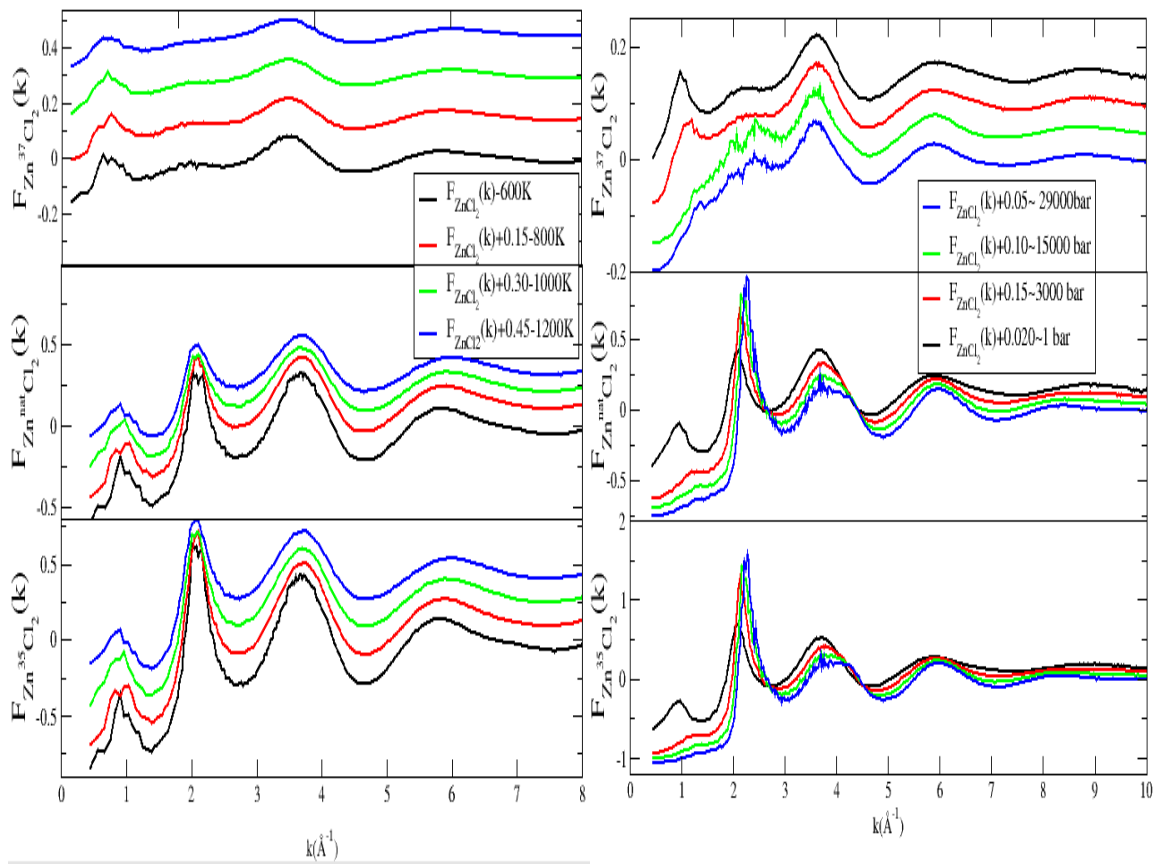
Figure 7.1:The total structure factor, $F_{ZnCl_2}(k)$, of simulated ZnCl$_2$ configurations with varying temperature. Top, ^{37}Cl; middle, ^{nat}Cl; bottom, ^{35}Cl. Colour code (increment of $F_{ZnCl_2}(k)$ in bracket): black line, 600K; red line, 800K (+0.15); green line, 1000K (+0.30) ; blue line, 1200K (+0.45).

Figure 7.2:The total structure factor, $F_{ZnCl_2}(k)$, of simulated ZnCl$_2$ configurations with varying pressure. Top, ^{37}Cl; middle, ^{nat}Cl; bottom, ^{35}Cl. Colour code (increment of $F_{ZnCl_2}(k)$ in bracket): black line, 1 bar; red line, 3000 bar (+0.15); green line, 15000 bar (+0.30) ; blue line, 29000 bar (+0.45)

7.5 Partial structure factors: Effect of temperature and pressure.

The major contributor to IRO in $ZnCl_2$ has been a source of significant debate citing the results of diffraction experiments.[19-21] An analysis of the partial structure factors shows the relative contributions to the presence of a FSDP in the total structure factor change considerably with pressure. Figure 7.3 shows the pressure-evolution of the three partial structure factors. At very low pressure (~1 bar), a strong FSDP is observed in both $S_{ZnZn}(k)$ and $S_{ZnCl}(k)$. With increasing pressure, the FSDP of $S_{ZnCl}(k)$ decreases in intensity and moves to higher k values (1.01Å^{-1} at ~1 bar to 1.24Å^{-1} at 29000 bar). The decay of the FSDP in $S_{ZnCl}(k)$ as a function of pressure is noticeably slower than for $S_{ClCl}(k)$ and $S_{ZnZn}(k)$. The principal peak intensity in $S_{ZnZn}(k_{PP})$ changes the least with an increase in height of from 1.58 to 1.99 (26%) compared to the respective changes for $S_{ZnCl}(k_{PP})$ and $S_{ClCl}(k_{PP})$ of -1.08 to -1.54 (43%) and 2.34 to 3.65 (56%) over the same pressure range.
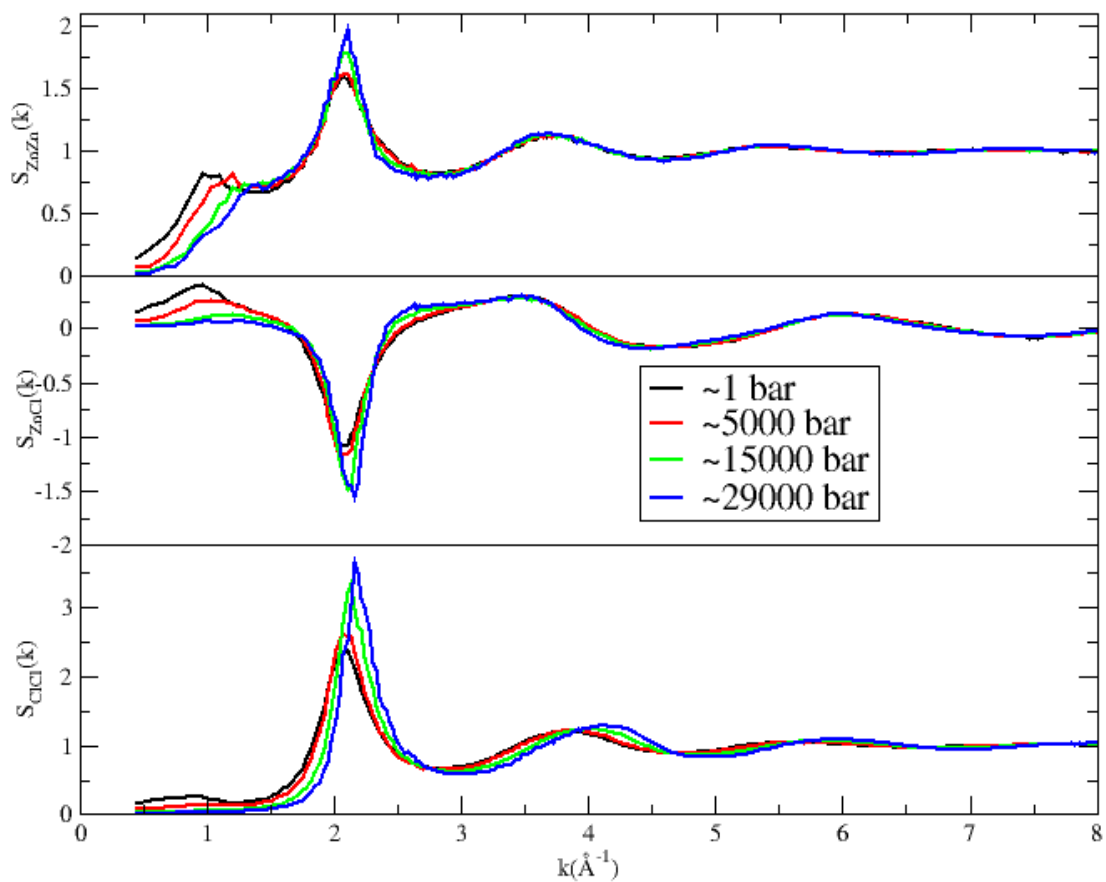
Figure 7.3:Partial structure factors in $ZnCl_2$ according to pressure in the range 1-29000 bar. (Temperature=800K). Top, $S_{ZnZn}(k)$; middle, $S_{ZnCl}(k)$; bottom, $S_{ClCl}(k)$. Black line, ~1 bar; red line, 5000 bar; green line, 14000 bar; blue line, ~29000 bar.

This explains the change in $F(k_{PP})$ where the contributions from $S_{ZnZn}(k_{PP})$ and particularly $S_{ClCl}(k_{PP})$ dominate that from $S_{ZnCl}(k_{PP})$. $S_{ClCl}(k)$ also displays a slight FSDP at 0.88Å^{-1} which rapidly shifts with pressure to 1.00Å^{-1} at 5000 bar, and then disappears at higher pressures. At higher pressures, the *position* of the peaks at $k>1\text{Å}^{-1}$ shift towards higher k values, indicating a possible change in the short-range ordering of the anion sublattice.

Figure 7.4 shows the temperature-evolution of the three partial structure factors at ~1 bar. With increasing temperature, the FSDP in $S_{ZnZn}(k)$ diminishes in intensity, from 1.09 to 0.72, while for $S_{ZnCl}(k)$ it shows an *increase* from 0.34 to 0.42 over the same temperature range. This feature is inconsistent with Debye-Waller effects but consistent with experimental observations of FSDP peak of the total structure factor, $F(k)$, in systems such as As_2Se_3.[22] For the rest of the k range a decrease in intensity is observed. The FSDP of the respective partial structure factors observe a shift in position to lower scattering angles. For $S_{ZnZn}(k)$, $S_{ZnCl}(k)$ and $S_{ClCl}(k)$ shifts of $1.12\text{-}1.09\text{Å}^{-1}$, $1.07\text{-}0.89\text{Å}^{-1}$ and $1.03\text{-}0.98\text{Å}^{-1}$ are observed from 600K to 1200K: the position of k_{FSDP} in $S_{ZnCl}(k)$ observes the greatest temperature dependence . The peaks are also shifted to lower scattering
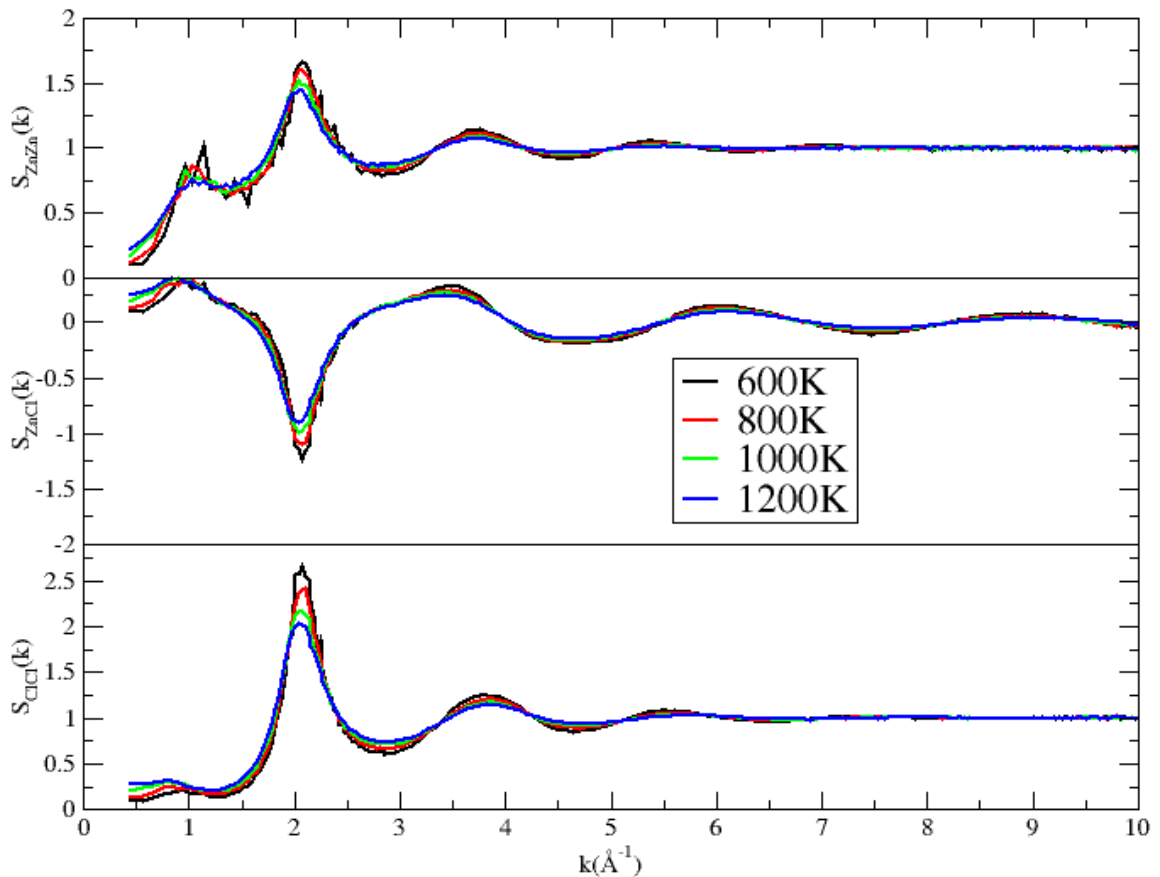
Figure 7.4:Partial structure factors according to temperature in the range 600K-1200K.(Pressure ~1 bar). Top, $S_{ZnZn}(k)$; middle, $S_{ZnCl}(k)$; bottom, $S_{ClCl}(k)$. Black line, 600K; red line, 800K; green line, 1000K; blue line, 1200K.

angles as would be expected with a density decrease. This disparity in rates of decline of IRO indicates that different mechanisms may be responsible for the contributions to IRO from $S_{ZnCl}(k)$ and $S_{ZnZn}(k)$.

7.6 Coordination numbers
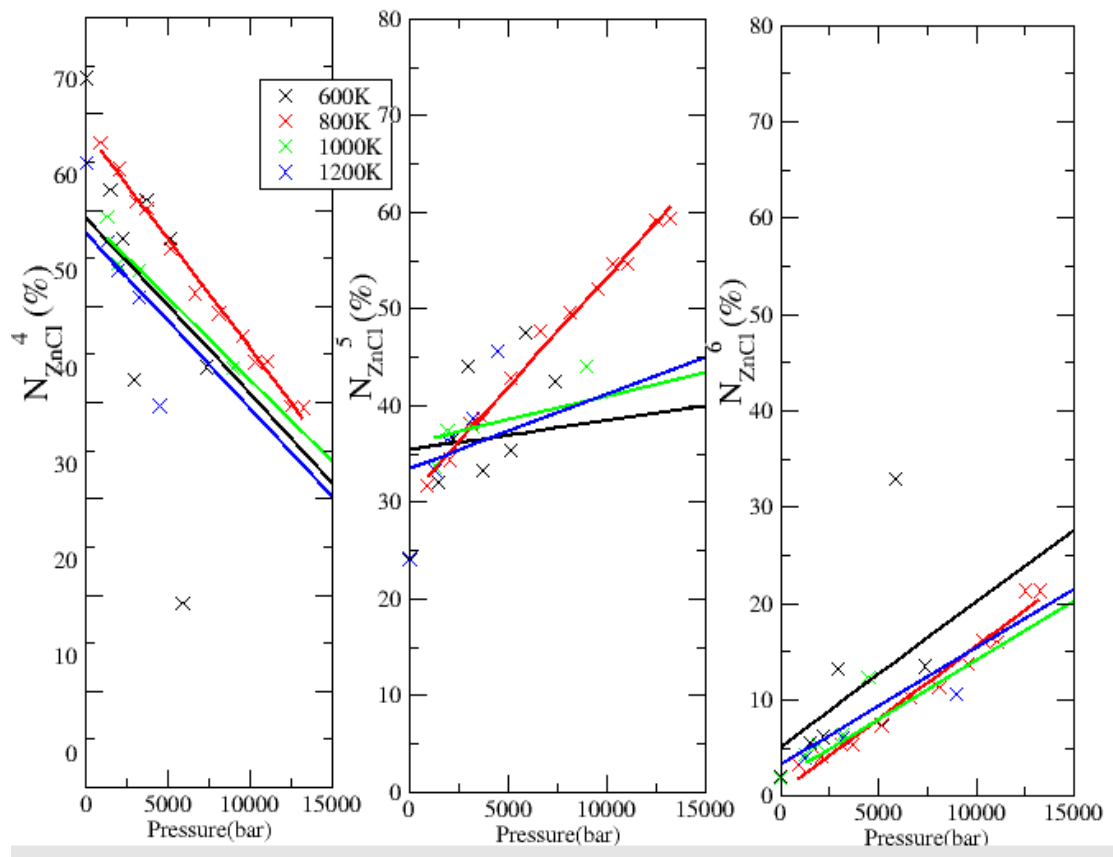
Figure 7.5:Changes in the cation-anion coordination number, N^{α}_{ZnCl}, where α={4,5,6}, with temperature and pressure. Black line, 600K; red line, 800K; green line, 1000K; blue line, 1200K.

The total neutron structure factors indicate significant structural changes in the sample as pressure is applied. To further understand the nature of these structural changes, figure 7.5 shows the variation in the dominant cation-anion coordination numbers (N^{α}_{ZnCl}, where α=4,5,6) as a function of pressure. The distributions in figure 7.5 show that increasing the pressure results in dramatic changes in the Zn-Cl coordination number. At zero pressure, zinc is predicted to have 73% four coordination with chlorine at 600K and 65% at 1200K. With increasing pressure there is a steady shift towards five and six coordination. For the different temperatures sampled, the rates of decline in four
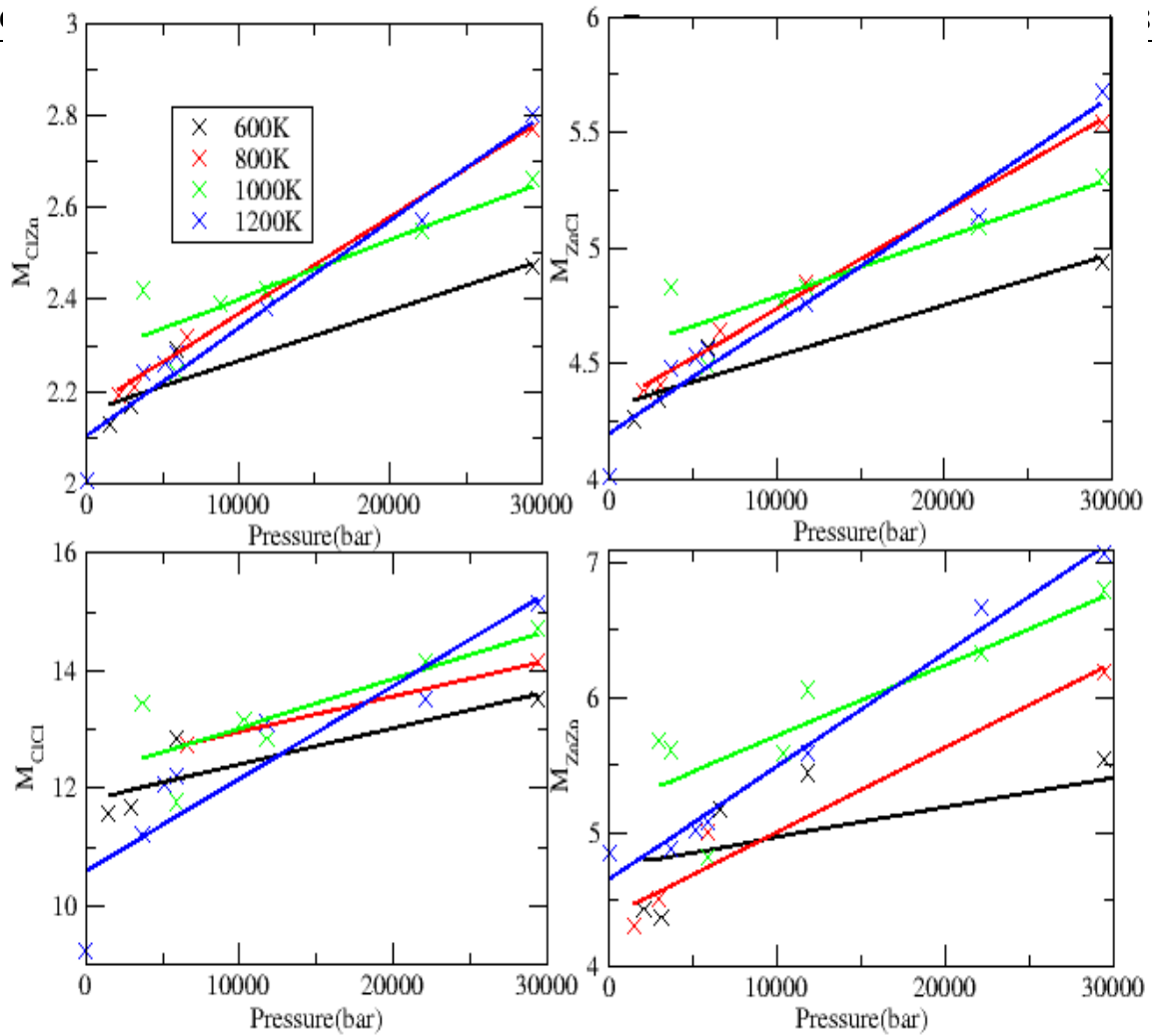
Figure 7.6: Mean coordination numbers, $M_{\alpha\beta}$, with variation in temperature and pressure. Black line, 600K; red line, 800K; green line, 1000K; blue line, 1200K.

coordinate sites is most

apparent at 1200K. In the experimental range of 1-5000 bar the changes in coordination are not as significant, and are in agreement with both the studies of Heusel et al[9] (up to 3000 bar) and Pfleiderer et al[6] (up to 5000 bar) in that there is no significant change in the tetrahedral coordination of zinc at this pressure range. At pressures of around 25000 bar, the six-coordinate zinc ions become predominant over the four and five coordinate sites. This change in the local cation environment correlates with the solid-state phase transition observed by Polsky[15] in which the four-coordinate γ-$ZnCl_2$ structure changes to the six coordinate $CdCl_2$ structure at 27000 bar. The pattern of the other coordination numbers are shown in the calculated mean values for the Zn-Zn, Cl-Cl, and Cl-Zn bonding distributions shown in figure 7.6. The propensity for miscoordination in terms of the Cl-Zn coordination number increases with increasing pressure, as shown by the large deviation of M_{ClZn} away from 2. The gradients of the change for respective coordination

number show no significant differences except at 1200K which rises faster with pressure than at other temperatures.

7.7 Radial distribution functions.

In the diffraction experiment of Pfleiderer *et al*[7], the changes in total radial distribution function, G(r), in the region 5 to 8Å are highlighted. Figure 7.7 shows G(r) obtained from using the experimental equation[7]:

$$G_{exp}(r) = 0.353g_{ZnCl}(r) + 0.595g_{ClCl}(r) + 0.052g_{ZnZn}(r) \qquad (7.3)$$
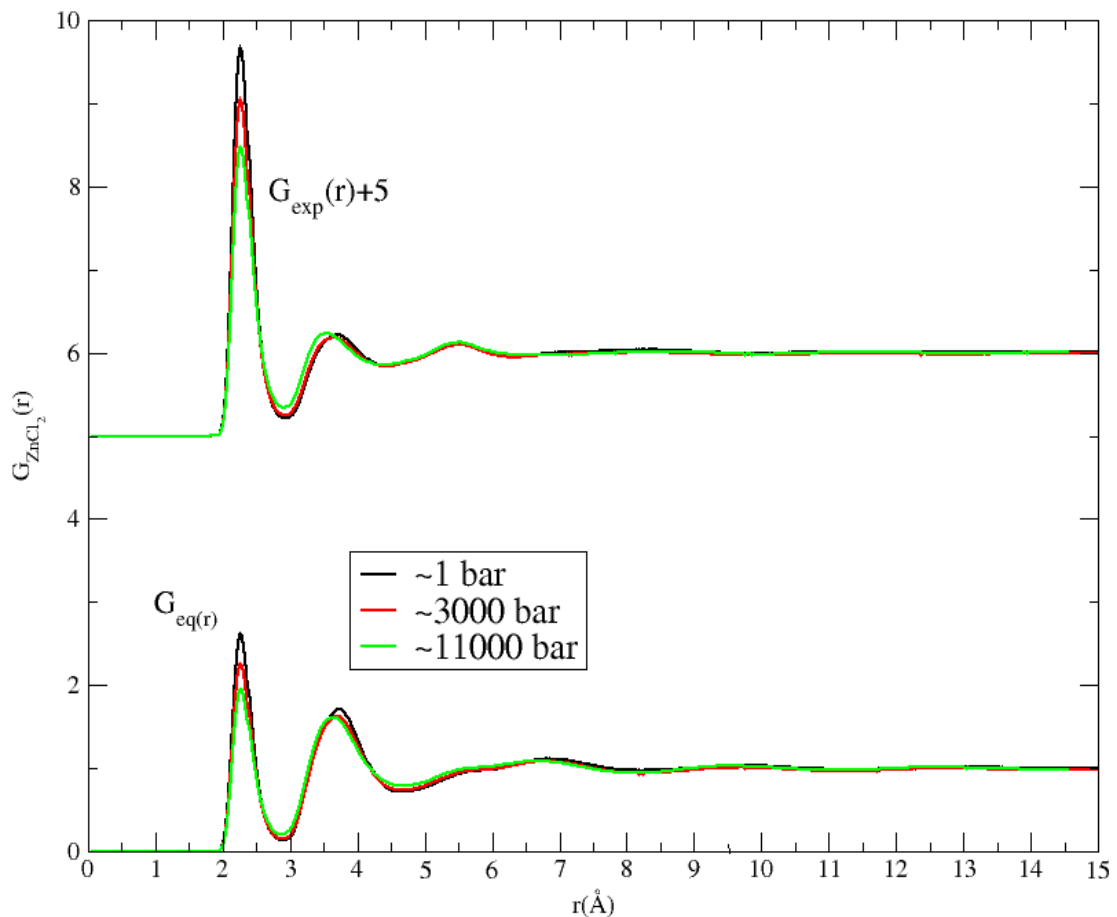
Figure 7.7:Changes in the total radial distribution functions at different pressures. $G_{eq}(r)$ is comprised of equal weightings from the different partial radial distribution functions and $G_{exp}(r)$ with the contributions given in equation 7.3. Black line, ~1 bar; red line, 5000 bar; green line, 11000 bar. The value of $G_{exp}(r)$ is raised by 5.

where the pre-factors arise from the respective ion mole fractions and neutron scattering

lengths. In addition, the total pair distribution function, G_{eq}, is calculated using an equal weighting of the three partial pair distribution functions. Both functions are calculated for 5000 bar, the high pressure limit of the current neutron scattering experiments, and at a higher simulated value of 11000 bar. The simulated $G_{exp}(r)$ features a principal peak at 2.27Å, close to the experimental value of 2.30Å.[14] The intensity of the simulated $G_{exp}(r)$ is much more intense than those experimentally observed.[7] This is possibly caused by problems in the Fourier transform procedure used to obtain G(r) from the experimentally-determined F(k). With increasing pressure, features at higher r range such as a deepening minimum at 5.0Å and a rise in intensity at ~5.6 Å, compared to respective experimental distances of ~4.7 Å and ~5.7 Å from Heusel et al[9]. The related figures of Pfleiderer et al[7] are ~5.0Å and ~6.5Å. In the latter experiment, the minimum is broader, with a small maximum which increases with pressure. A noticeably faster decline in the intensity of the principal peak of $G_{exp}(r_{PP})$ occurs than is observed experimentally.[6,9]

The change in contributions to G(r) can be highlighted by a difference function, $P_{\alpha\beta}^{P_n - P_1}(r)$, which highlights the effect of a change in one of the constituent partial radial distribution function terms on G(r) as a function of temperature and pressure defined as:

$$P_{\alpha\beta}^{P_n - P_1}(r) = G_{\alpha\beta}^{P_n - P_1}(r) - G_{\alpha\beta}^{P_n}(r) \tag{7.4}$$

where $G_{\alpha\beta}^{P_1}(r)$ and is the total radial distribution function at pressure, P_1:

$$G_{\alpha\beta}^{P_1}(r) = c_{Zn}^2 f_{Zn}^2 \left(g_{ZnZn}^{P_1}(r) \right) + c_{Cl}^2 f_{Cl}^2 \left(g_{ClCl}^{P_1}(r) \right) + 2c_{Zn} c_{Cl} f_{Zn} f_{Cl} \left(g_{ZnCl}^{P_1}(r) \right) \tag{7.5}$$

$G_{\alpha\beta}^{P_n - P_1}(r)$ is the total distribution with one of the partial radial distribution terms at a different pressure from the other two, in this case, $g_{ZnZn}^{P_n}(r)$:

$$G_{\alpha\beta}^{(P_n - P_1)}(r) = c_{Zn}^2 f_{Zn}^2 \left(g_{ZnZn}^{P_n}(r) \right) + c_{Cl}^2 f_{Cl}^2 \left(g_{ZnCl}^{P_1}(r) \right) + 2c_{Zn} c_{Cl} f_{Zn} f_{Cl} \left(g_{\alpha\beta}^{P_1}(r) \right) \tag{7.6}$$

Equation 7.4 reduces to

$$P_{ZnZn}^{P_n - P_1}(r) = g_{ZnZn}^{P_n}(r) - g_{ZnZn}^{P_1}(r) \tag{7.7}$$

Figure 7.8 shows the partial contributions responsible for the changes at 5-6Å. Over this range there are contributions from $g_{ZnZn}(r)$ and $g_{ClCl}(r)$ causing the minima to rise and a shoulder to appear. At larger r values, $P_{ZnZn}^{P_{5000}-P_1}(r)$ decays and the effect is much weaker. Such a feature becomes more pronounced in our simulations due to the increased weight of the Zn-Zn interaction which is effectively hidden in the experimental G(r). Oscillatory character for $P_{\alpha\beta}^{P_n-P_1}(r)$ indicates either a change in peak intensity or a shift in peak position upon pressure. For the Zn-Cl correlation, the peak at 2.27Å reflects the decrease in the intensity of the principal peak. This oscillation is damped rapidly to zero and the similarity of $P_{ZnCl}^{P_{5000}}(r)$ and $P_{ZnCl}^{P_{11000}}(r)$ at r > 5Å indicates that the long range Zn-Cl interactions are not significantly affected over this pressure range. The oscillations in the Cl-Cl correlation, $P_{ClCl}^{P_n-P_1}(r)$, indicate that all length scales are shifted with increasing pressure.
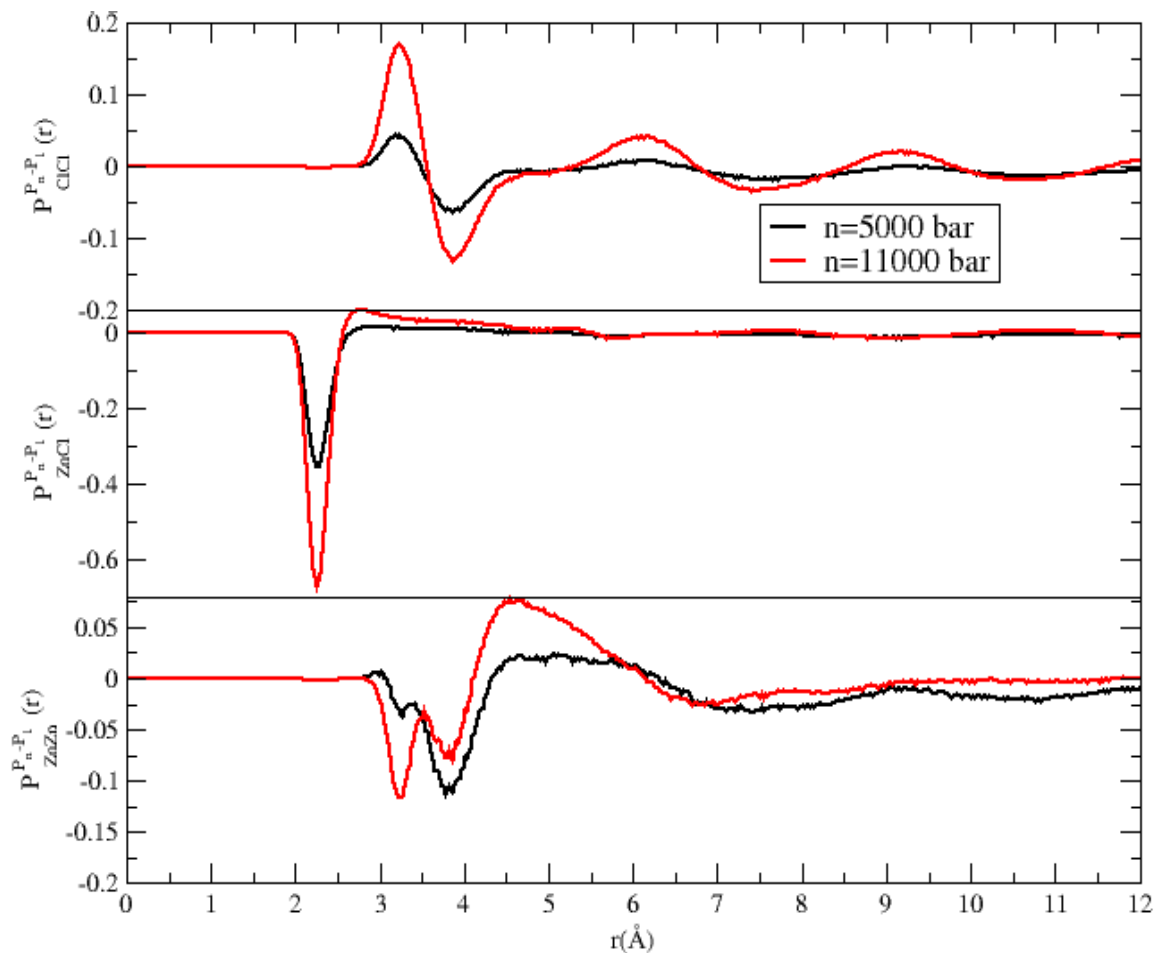
Figure 7.8: Difference functions, $P_{\alpha\beta}^{P_n-P_1}(r)$, for ZnCl₂ at 1000K. Top, $P_{ClCl}^{P_n-P_1}(r)$; middle, $P_{ZnCl}^{P_n-P_1}(r)$; bottom, $P_{ZnZn}^{P_n-P_1}(r)$. Black line, n=5000 bar; red line , n=11000 bar.

For g$_{ZnZn}$(r), where the peak intensity is similar at the pressures sampled, the respective difference functions, $P_{ZnZn}^{P_n-P_1}(r)$ highlight the widening of the first Zn-Zn coordination shell. The peaks at 3.26Å and 3.9Å for $P_{ZnZn}^{P_{5000}-P_1}(r)$ and $P_{ZnZn}^{P_{11000}-P_1}(r)$ represent the largest difference in intensity with the principal peak of g$_{ZnZn}$(r) at ~1 bar. Previously (in Chapter 4), we observed that the principal peak of g$_{MM}$(r) can be considered as comprising of coloured radial distribution functions which represent the different edge- and corner-sharing configurations. The changes in the intensity of the peaks, close to the previously highlighted edge- and corner-sharing peaks, represent the changes in the underlying network connectivity which have subtle effects on the function, g$_{ZnZn}$(r). Figure 7.8 shows that as pressure increases the relative intensities of these two peaks switch from 5000 bar, where a small decline in intensity is observed at distances associated with corner-sharing, to 11000 bar, where there is a greater decline at the distance associated with edge-sharing. At r is greater than r$_{PP,}$ where r$_{PP}$ is the position of the principal peak, there is a small and persistent intensity in $P_{ZnZn}^{P_n-P_1}(r)$. This is the result of a change in the intensity of large r oscillations for Zn-Zn correlations with increasing pressure.
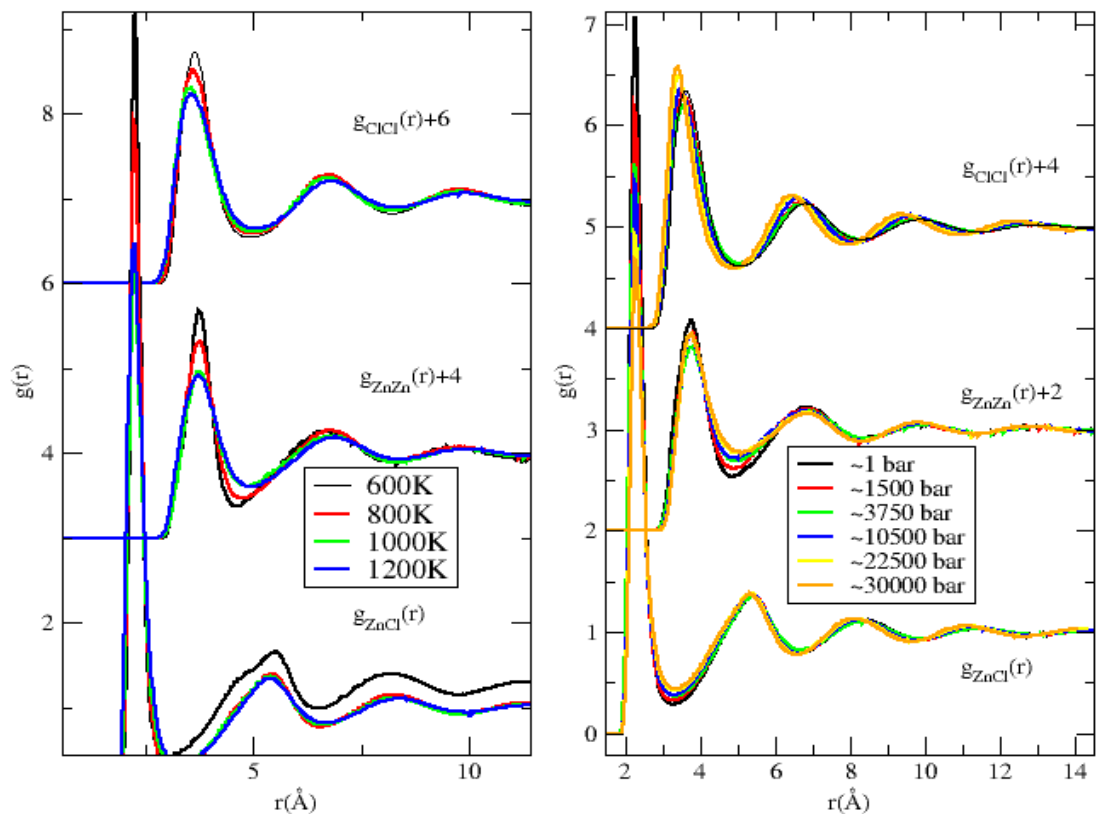
Figure 7.9:Changes in radial distribution functions, g$_{\alpha\beta}$(r), according to (left) temperature(600K-1200K at ~1bar) and (right) pressure(~1 bar ~30000 bar) at 1000K. g$_{ZnCl}$(r) at 600K is elevated by 0.3 to highlight the shoulder in the second peak.

Figure 7.9 shows the pressure and temperature evolution of the partial radial distribution functions with increasing pressure at different temperatures. With increasing temperature, the position of $g_{ZnCl}(r_{PP})$ decreases from 2.28Å to 2.25Å from 600K to 1200K. The intensity decreases, from 9.16 at 600K to 6.16 at 1000K and rising slightly again to 6.48 at 1200K. The position of $g_{ClCl}(r_{PP})$ changes from 3.64Å at 600K to 3.59Å at 1200K. The intensity changes from 2.74 to 2.23. The position of $g_{ZnZn}(r_{PP})$ changes from 3.76Å to 3.74Å and the intensity declines from 2.66 to 1.93. There were several notable changes that occur in the radial distribution functions with temperature at ~1 bar. For $g_{ZnZn}(r)$, the minimum rises again but there is also a decrease in the intensity of the first coordination shell. Similar effects are observed for $g_{ZnCl}(r)$, while in $g_{ClCl}(r)$ the minimum remains similar while the intensity of the principal peak increases. A strongly temperature dependent feature of the correlation functions was observed in the second peak of $g_{ZnCl}(r)$ (highlighted at 600K in figure 7.9) where a shoulder in the second peak becomes apparent at high pressures at 800K (at ~59000 bar) and 600K (at ~1 bar). At 1000K and 1200K this feature is not seen is the highlighted pressure range suggesting that the dynamics of this length scale are strongly temperature dependent. Further calculations to higher pressures of 150000 bar do not produce this feature in configurations at 1000K and 1200K. Although there is no reference to this phenomenon with similar network compounds, this is the pre-cursor to a feature commonly known as the *split second peak*.[23,24] Theories have attributed it to the onset of a liquid-amorphous solid phase transition, a property of the inherent structure of the liquid. Recent theories[24] have highlighted, that at higher packing densities, there are less available packing combinations over these length scales and as such this shoulder is isolated.

For $g_{ClCl}(r)$ at very high pressures the principal peak decreases from 3.62Å at 1 bar to 3.35Å at 29000 bar, in contrast to $g_{ZnZn}(r)$ and $g_{ZnCl}(r)$ where the principal peak positions remain constant in the same pressure range at 2.26Å and 3.77Å respectively. The intensity changes of the principal peak with increasing pressure show a sharp decrease for $g_{ZnCl}(r_{PP})$, declining from 7.06 to 4.69 over the pressure range; in contrast, $g_{ClCl}(r_{PP})$ and $g_{ZnZn}(r_{PP})$ observe intensity minimums at intermediate pressure of 3750 bar, 1.82 and 2.19 respectively, where the 1 bar and 29000 bar values are 2.08 and 1.92 for $g_{ZnZn}(r_{PP})$ and 2.34 and 2.59 for $g_{ClCl}(r_{PP})$. The changes in principal peak positions contrast with EXAFS data which showed an increase in the Zn-Cl bond distance with increasing pressure.[11] The experimental data is in keeping with the pressure-density anomaly where an increase in pressure with a corresponding change in coordination leads to an increase in the Zn-Cl

bond distance. In our system, it is the chlorine-chlorine sublattice which accommodates this change. The change in coordination can affect the radial distribution function in two possible ways: an increase in the intensity of the first coordination shell or a widening of it. The latter case is highlighted by the changes in $g_{ZnZn}(r)$ and $g_{ZnCl}(r)$, where the minima of the first coordination shell rises significantly whereas in the former case is represented by $g_{ClCl}(r)$ where the intensity of the principal peak rises.

7.8 Bond angle distribution functions.
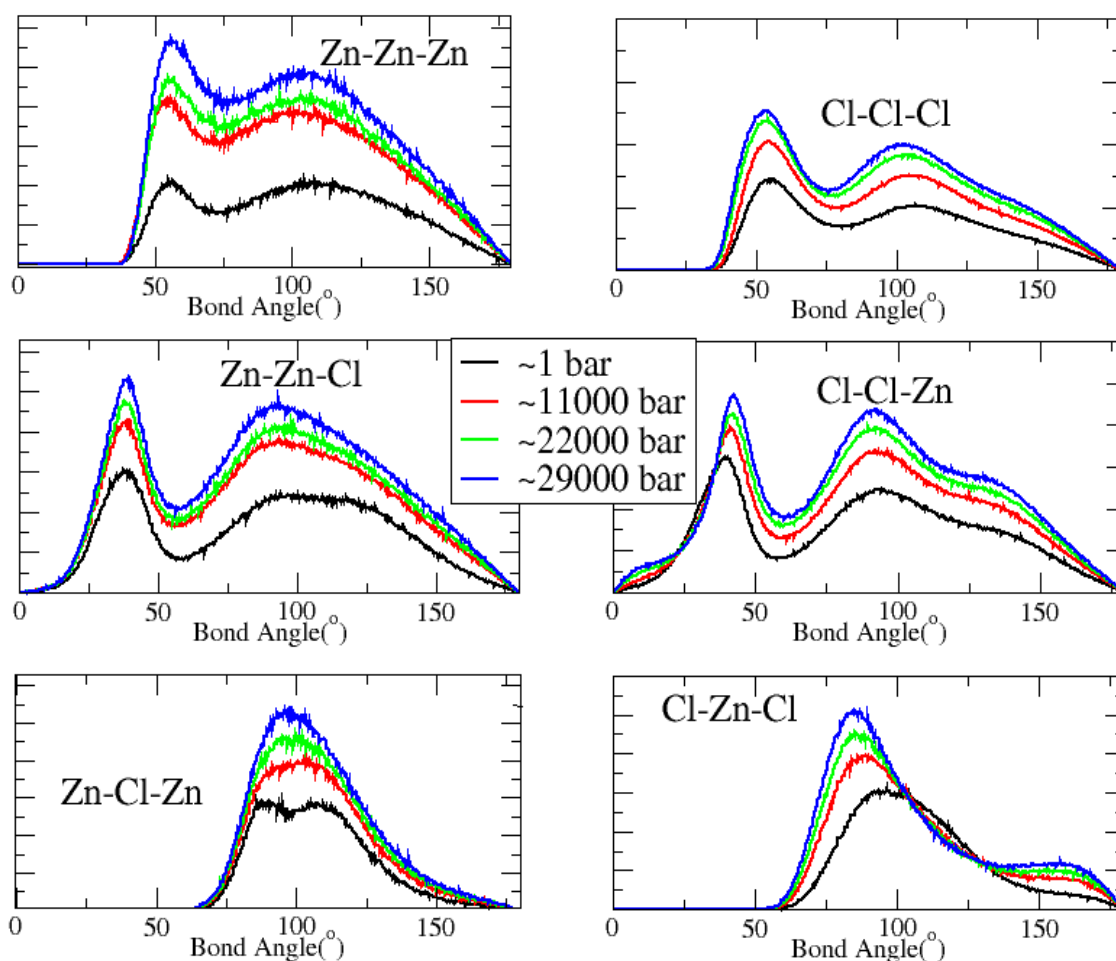
Figure 7.10: Bond angle distribution for $ZnCl_2$ with variations in pressure at 1000K. Black line, ~1 bar; red line, ~11000 bar; green line, ~22000 bar; blue line, ~29000 bar.

Upon increasing pressure it has been indicated that the tetrahedral units will accommodate the reduction in cell volume by reducing the bond angle between them.[26] In the pressure sampled we have observed large changes in coordination around the cation

which must be accounted for in the bond angle distribution. The changes in the bond angle distribution with pressure in figure 7.10 support the case for a predominantly tetrahedral network changing to an octahedral structure. The Cl-Zn-Cl becomes increasing bi-modal with prominent peaks at ~90° and 160°. This indicates an octahedral configuration where the equatorial Cl-Zn-Cl contribute to the 90° peak and the axial Cl-Zn-Cl peak contributes, less frequently, to the higher angle peak. In contrast with Cl-Zn-Cl and Zn-Cl-Zn, the Zn-Zn-Zn, Cl-Cl-Cl, Zn-Zn-Cl and Cl-Cl-Zn bond angle distributions do not change their shape with increasing pressure but do exhibit an increase in the intensity: this is due to the large increase in coordination highlighted. For Zn-Cl-Zn, a two peaked distribution is observed with peaks observed at 90.5° and 106° at ~1 bar. Increasing the pressure results in a single peak Zn-Cl-Zn distribution due to the breaking of these edge-sharing units and by the formation of larger coordinate zinc ions, with the associated square-planar and octahedral geometries.

Figure 7.11 shows the change in bond angle distribution with temperature at ~1 bar. At 600K, the latter peak ~150° in Cl-Zn-Cl is noticeably sharper than that observed at higher temperatures, an indication of the effect dynamics has on the bond angle distribution. *Two* peaks are observed for Zn-Cl-Zn at 89° and 111° at 600K. These two peaks are due to the presence of edge and corner-sharing tetrahedral units which occur at lower temperatures and low pressures. If the ratio of the intensity at ~89° and ~111° is an indication of the amount of edge-sharing then it indicates at 1200K there is a greater presence of edge-sharing. At higher temperatures the two peaks merge. As with the changes in Zn-Zn-Zn, Cl-Cl-Cl, Zn-Zn-Cl and Cl-Cl-Zn with pressure, the peak positions these functions remain similar but there is much smaller change in the intensity due to the smaller changes on coordination observed with temperature at ~1 bar.
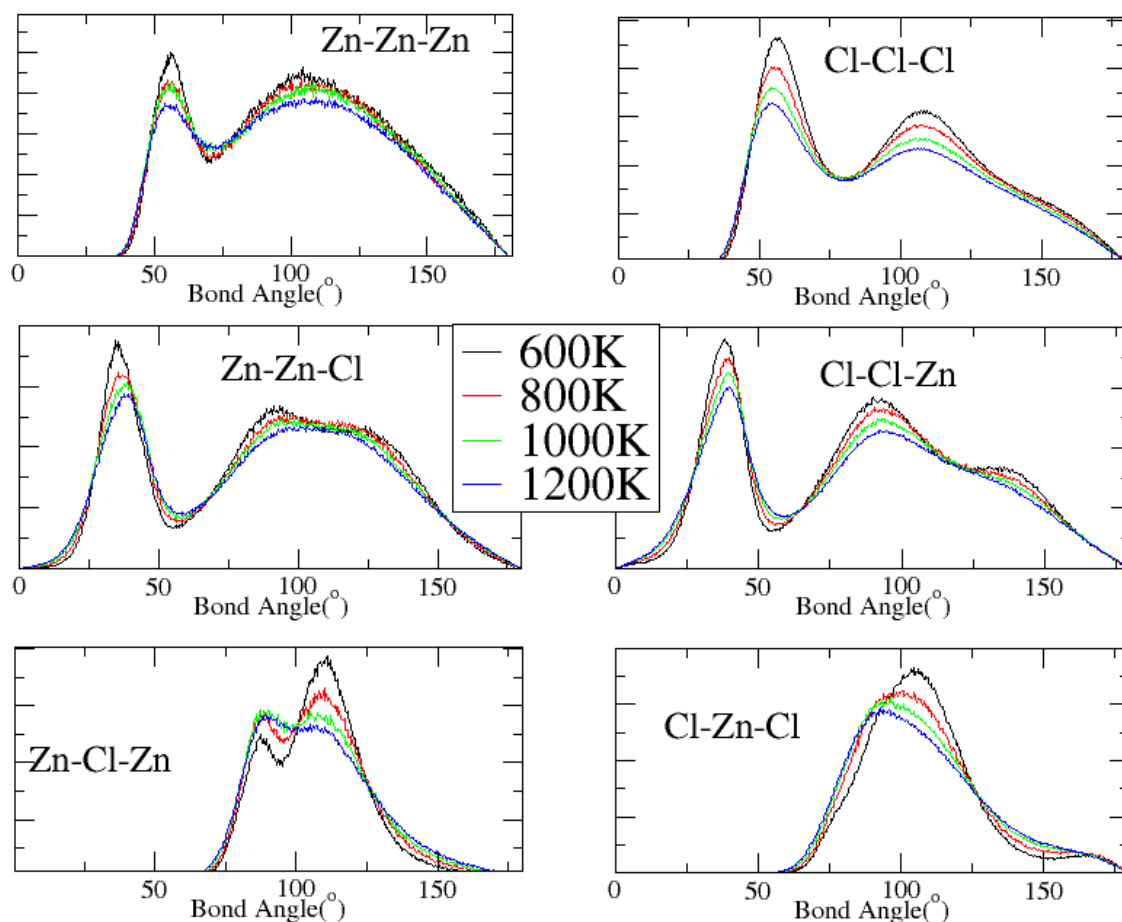
Figure 7.11: Bond angle distribution for $ZnCl_2$ with variations in temperature. Black line, 600K; red line,800K;green line, 1000K; blue line, 1200K.

7.9 Change in network connectivity with temperature and pressure.

The dramatic decline in the intensity of the FSDP in $S_{ZnZn}(k)$ indicates structural changes in the cation sublattice, occuring in the pressure range 1-5000 bar. Recent neutron diffraction experiments on $GeSe_2$ highlighted a transition between 2D edge-sharing and 3D corner-sharing phases due the application of pressure.[25] In chapter 5 we explained the significant structural similarities between $ZnCl_2$ and $GeSe_2$, although the former shows a much weaker edge-sharing character in comparison. For systems under pressure with underlying coordination changes, it becomes necessary to investigate the effect of coordination of the underlying network topology.

Calculations were carried out to find out which cations were in a "0", "1" or "2"

conformation, referring to the number of four-membered rings the central cation is bonded to. If the coordination sphere of the central cation was constant at around four this would ordinarily tell us information of the nature of the network connectivity in the system; in this chapter, there are larger changes in coordination which affect how we can interpret these quantities. The pattern of changes in the percentages of these cation, E^0, E^1 and E^2 may correspond to the three following mechanisms:

1. Strongly coordination-dependent mechanism.
   The results show there is increasing tendency towards higher coordination with pressure. A coordination dependent mechanism envisages that the changes in E^0 and E^2 arise solely from variation in the cation-anion coordination. "0" cations decrease with the addition of cation-anion bonds while E^2 cations increase. The percentage of "1" cations is expected to follow similar behaviour with 5-coordination, increasing at first, then declining as "1" cations are converted to "2" cations.

2. Edge-sharing to corner-sharing mechanism.
   Following from the experimental observations of $GeSe_2$ under high pressure, a change in network connectivity is envisaged where edge-sharing units are broken to form corner-sharing ones: E^2 is expected to decrease to form "1" and "0" cations.

3. Edge-sharing to six-coordinate mechanism.
   Four coordinate edge-sharing tetrahedral units are converted into 5- and 6-coordinate units faster than corner-sharing ones: E^0 would decrease while E^1 and E^2 would rise simultaneously.

   Figure 7.12 shows that large changes in the values of E^0, E^1 and E^2 are observed with changes in temperature and pressure. A smaller range of 1-15000 bar was used to focus on the changes in E^n which occur where the IRO changes most rapidly. E^0 and E^1 declines with increasing pressure while E^2 increases: an indicator of a dominant coordination-dependent mechanism. The change in E^1 is the strongest indicator for which mechanism may take place: with increasing pressure, it declines showing that accompanying coordination changes lead to a faster rise in E^2.
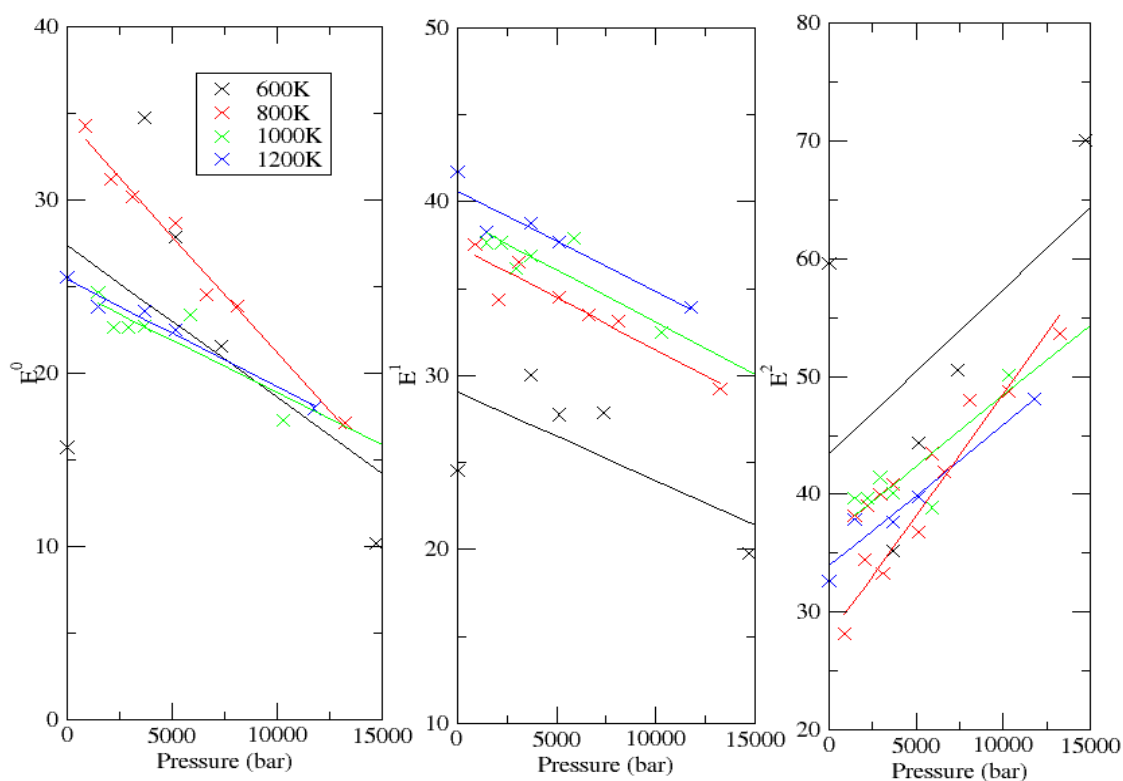
Figure 7.12: Changes in network connectivity in $ZnCl_2$ at different temperature and pressure as indicated by changes in the percentage of cations with n number of four-membered rings, E^n where n=0-2.

With increasing temperature, E^1 specifically is found to rise in a configuration, while E^2 and E^0 are largely similar at most temperatures except at 600K where E^2 is more abundant for a given pressure. In contrast to the systems studied in Chapter 6, the presence of significant miscoordination in Zn obfuscates the changes in network connectivity which can be linked readily to the changes in E^n. Another method of analysing the changes influencing intermediate-range order is to calculate structure factors and radial distribution functions coloured according to network connectivity and, due to the large changes which occur with temperature and pressure, coordination.

7.10 Coloured cation-cation structure factors.

So far we have observed changes in coordination and in network topology with temperature and pressure. We shall now decompose the partial structure factors, $S_{ZnZn}(k)$ and $S_{ZnCl}(k)$, further down into partials based on coordination numbers ($S_{MM}^{cd}(k)$ where cd={4,5,6}) and cation network-connectivity ($S_{MM}^{ab}(k)$ where ab={0,1,2}). As figure

7.5 showed, the spread of cation-anion coordination numbers, N_{ZnCl}^{α}, is significant

enough for combinations of cation-anion coordination numbers, N_{ZnCl}^{α}, where α=4,5,6,

to constitute tangible contributions to both S$_{ZnZn}$(k) and S$_{ZnCl}$(k). According to

concentration terms, listed in table 7.1, the most important contributions to S$_{ZnZn}$(k) are

$S_{ZnZn}^{4X}(k)$ where x=4,5,6. Figure 7.13 shows that $S_{ZnZn}^{44}(k)$ and $S_{ZnZn}^{45}(k)$ are the only

functions to exhibit a significant FSDP. With increasing temperature, the FSDP in

$S_{ZnZn}^{44}(k)$ becomes damped and, in contrast to the other functions, the principal peak

intensity decreases noticeably with increasing temperature.

Pressure(bar) (T=1000K)	Zn-Cl coordination			Temperature (K) (P=1 bar)	Zn-Cl coordination		
	N_{ZnCl}^{4}	N_{ZnCl}^{5}	N_{ZnCl}^{6}		N_{ZnCl}^{4}	N_{ZnCl}^{5}	N_{ZnCl}^{6}
1	68	27	2	600	72	26	2
5000	54	38	5	800	64	31	3
11000	44	44	11	1000	68	27	2
29000	16	47	34	1200	61	30	3
Pressure(bar) (T=1000K)	Network connectivity			Temperature (K) (P=1 bar)	Network connectivity		
	E^0	E^1	E^2		E^0	E^1	E^2
1 bar	30	42	28	600K	41	36	23
5000 bar	23	38	40	800K	33	40	27
11000 bar	17	33	50	1000K	30	42	28
29000 bar	7	21	72	1200K	26	42	32

Table 7.1:Percentage values for cation-anion coordination number in the range N_{ZnCl}^{α}, where α={4,5,6}
and the values for different cation network connectivities for the temperature range, 600K-1200K at 1 bar,
and the pressure range 1-29000 bar at 1000K.

Figure 7.14 shows the changes in the coordination-dependent cation-cation structure

factors with pressure. The pattern of changes with varying concentration are most

strongly observed in $S_{ZnZn}^{66}(k)$ which exhibits phase separation up to 29000 bar where a

shallow intensity is observed. The absence of phase separation in $S_{ZnZn}^{45}(k)$ and

$S_{ZnZn}^{44}(k)$ and the persistence of either a FSDP or a shoulder at low scattering angles

throughout the pressure range suggests that these terms are concomitant with network

ordering. The character of $S_{ZnZn}^{45}(k)$ changes from a FSDP ~1 bar to a broad shoulder ~29000 bar. As we saw in the Chapter 6, with the pattern of changes in $S_{MM}^{01}(k)$ highlighting the changing degree in how the Coulombic and induction mechanisms influence IRO with anion polarisability, the $S_{ZnZn}^{46}(k)$ term highlights the breaking up of network ordering, due to the changes in coordination, observing phase separation at high pressures despite a slight increase in the c_4c_6 term from 0.0129 at ~1 bar to 0.054 at ~29000 bar. Small values are observed for the ratio, $S_{MM}^{cd}(k_{FSDP})/S_{MM}^{cd}(k_{PP})$, (in contrast to the values observed for high polarisability systems in Chapter 6) for the functions that exhibit a FSDP (0.42-0.57 at 600K and 0.30-0.47 at 1200K), with little variation between them, indicating that the occupation of sites by sampling through cation coordination samples the system nearly isotropically.
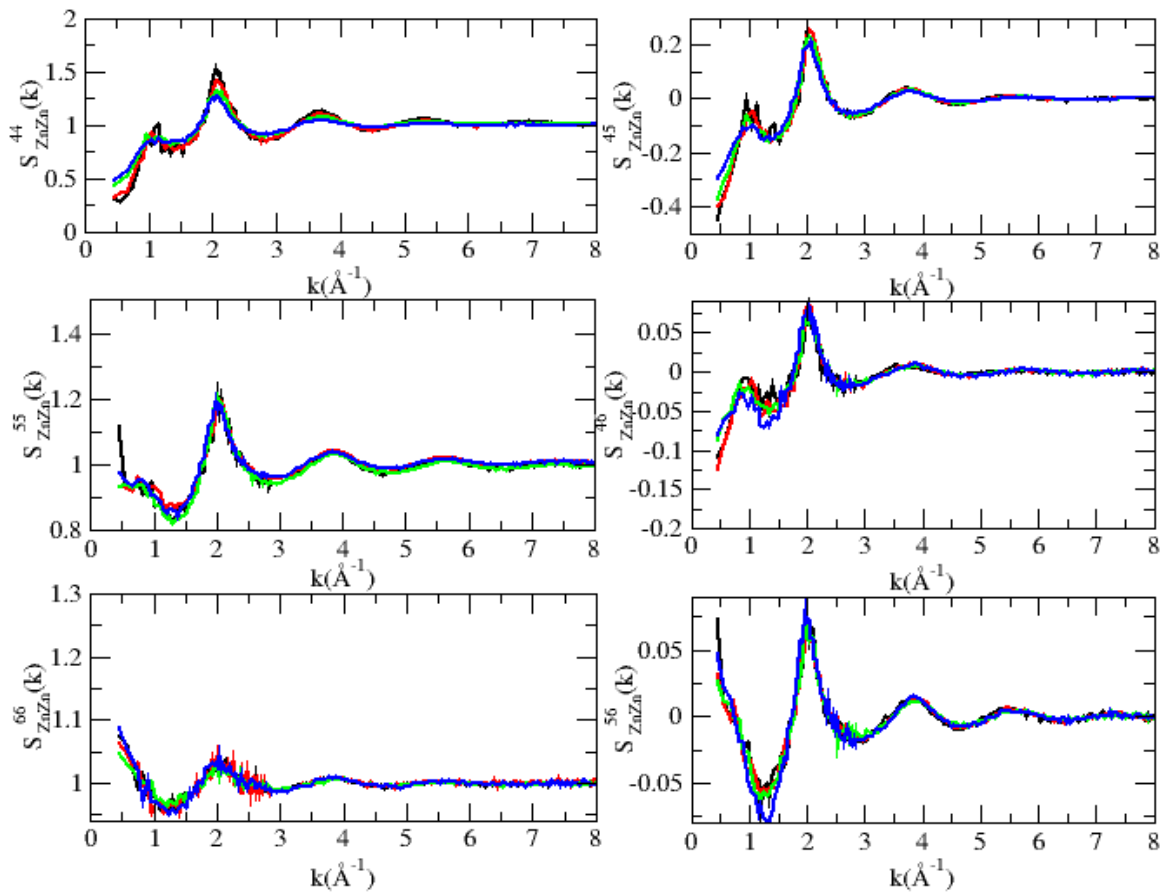
Figure 7.13 :Changes in coordination-dependent cation-cation structure factors, $S_{MM}^{cd}(k)$, with temperature (at 1 bar). Black line, 600K; red line, 800K; green line, 1000K;blue line, 1200K.
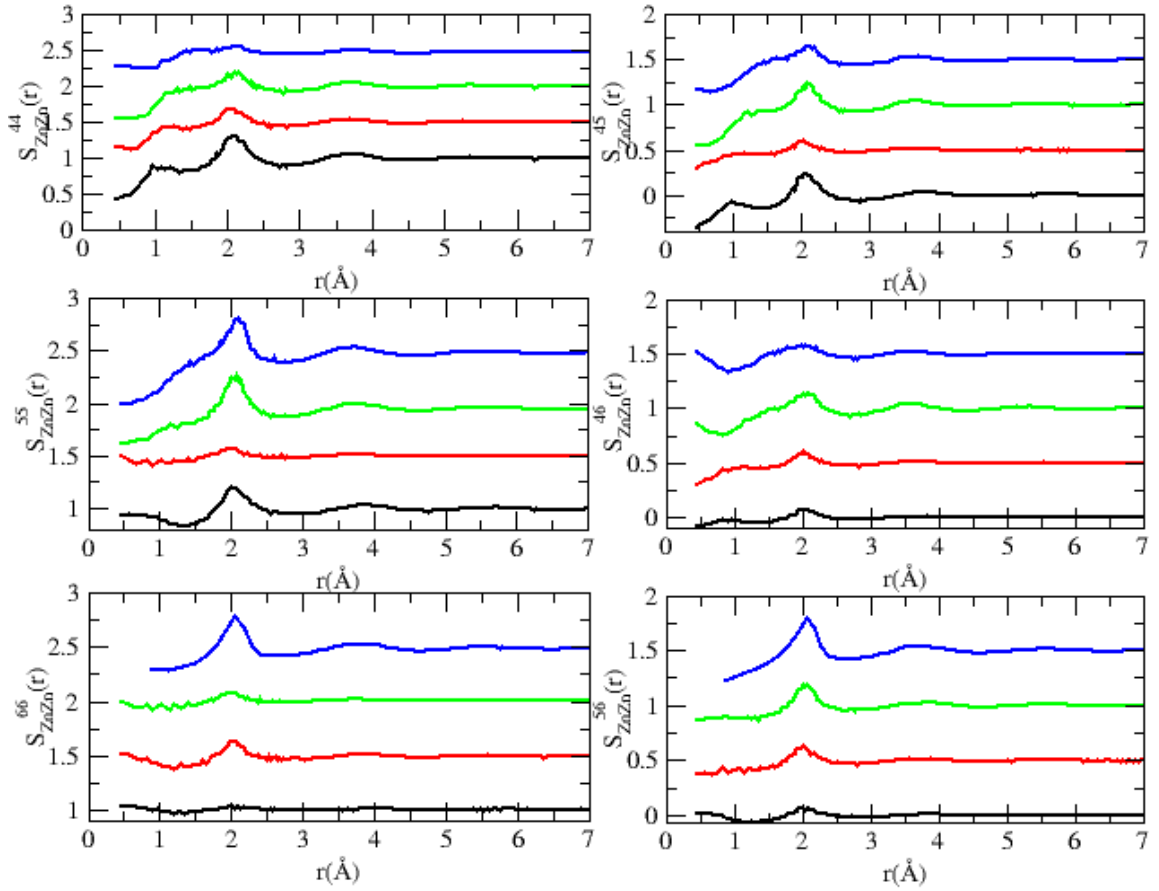
Figure 7.14 :Change in coordination-dependent cation-cation structure factors, $S_{MM}^{cd}(k)$, with pressure (at 1000K). Colour code (y increment in brackets): Black line, 1 bar; red line, 5000 bar (+0.5); green line, 11000 bar (+1.0); blue line, 29000 bar (+1.5).

A comparison of the network-connectivity cation-cation functions showing the effect of pressure contrasts significantly with that observed in chapter 6. Firstly, pressure and not polarisation is the order parameter; this means much larger cell volume changes are observed. Secondly, the coordination number change over the pressure range is much larger than that observed for changing polarisability: this could damp IRO related features of the network connectivity functions such as values of the ratio, $S_{MM}^{ab}(k_{FSDP})/S_{MM}^{ab}(k_{PP})$, being greater than one (in systems such as GeSe$_2$). Figure 7.15 shows the change of these network-connectivity structure factors with changing temperature. There is a much larger variation in the ratio of $S_{MM}^{ab}(k_{FSDP})/S_{MM}^{ab}(k_{PP})$ for the network-connectivity structure factors, where at 600K and 1 bar, for $S_{ZnZn}^{02}(k)$, this value is 0.89 compared values of 0.38, 0.53, and 0.49 for $S_{ZnZn}^{12}(k)$, $S_{ZnZn}^{11}(k)$ and $S_{ZnZn}^{01}(k)$.
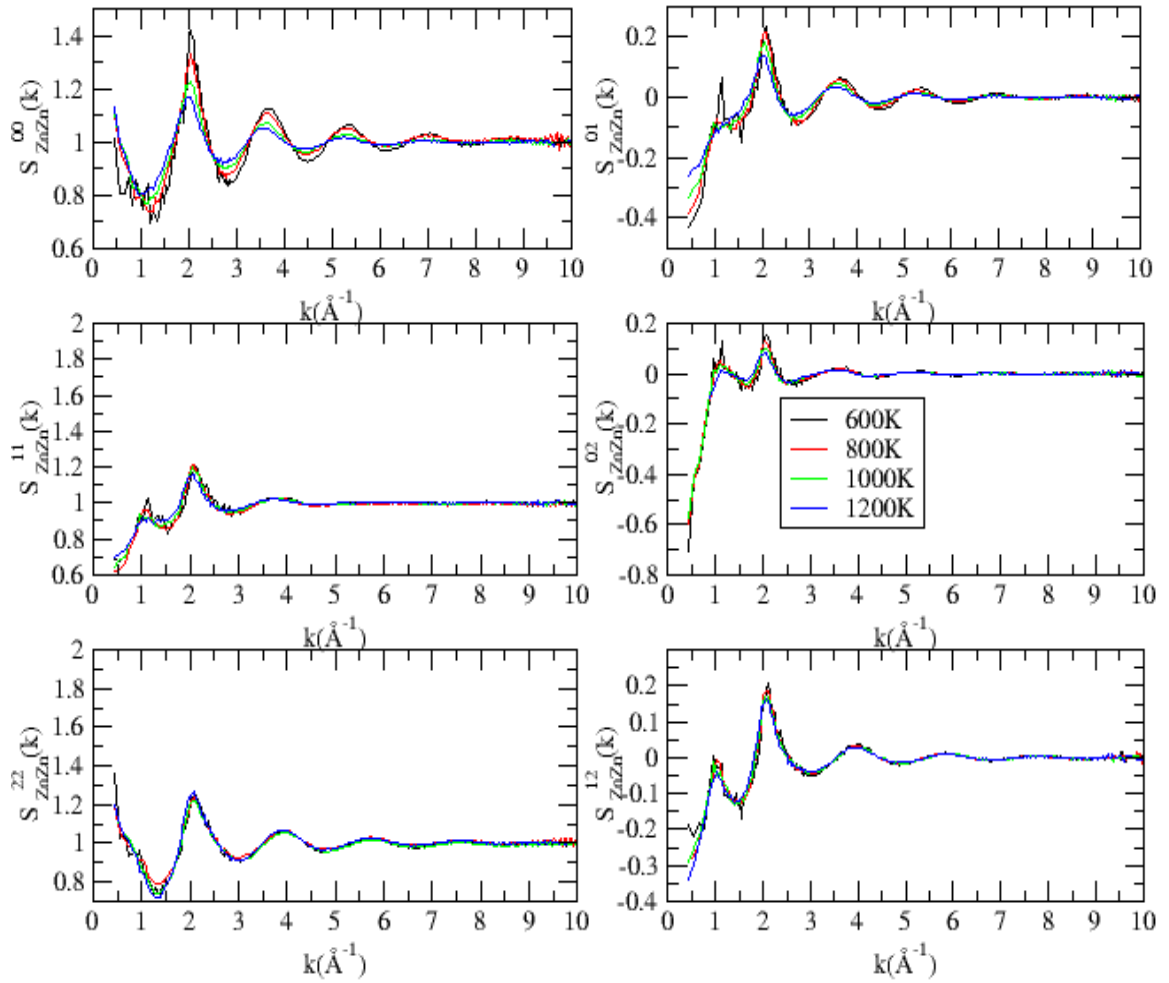
Figure 7.15: Change in network connectivity cation-cation structure factors, $S_{MM}^{ab}(k)$, with pressure. Black line, 600K; red line, 800K; green line, 1000K; blue line, 1200K.

At 1200K, a FSDP is observed in $S_{ZnZn}^{01}(k)$, $S_{ZnZn}^{11}(k)$ and $S_{ZnZn}^{02}(k)$ with the intensity decreasing from maximum values at 600K to the smallest intensities observed at 1200K. The FSDP in $S_{ZnZn}^{01}(k)$ and $S_{ZnZn}^{11}(k)$ shows a sharp decrease with increasing temperature while $S_{ZnZn}^{12}(k)$ and $S_{ZnZn}^{02}(k)$ show smaller changes. There is a small decrease in the positions of the FSDP by 0.04Å^{-1}, 0.03Å^{-1}, 0.02Å^{-1}, 0.07Å^{-1} for $S_{ZnZn}^{11}(k)$, $S_{ZnZn}^{01}(k)$, $S_{ZnZn}^{02}(k)$ and $S_{ZnZn}^{12}(k)$ respectively. At high scattering wave vectors changes are observed for $S_{ZnZn}^{00}(k)$ and $S_{ZnZn}^{01}(k)$ where a decrease in the intensity of the peaks is observed with increasing temperature. As k→0 the behaviour of $S_{ZnZn}^{01}(k)$ and $S_{ZnZn}^{12}(k)$ are heavily temperature dependent: as temperature increases the value of $S_{ZnZn}^{01}(k)$ as k→0 rises while for $S_{ZnZn}^{12}(k)$ it declines. $S_{ZnZn}^{01}(k)$ mirrors

$S_{ZnZn}^{44}(k)$ in this regard as well as the decline of both the FSDP and principal peak occuring with increasing temperature in these functions.
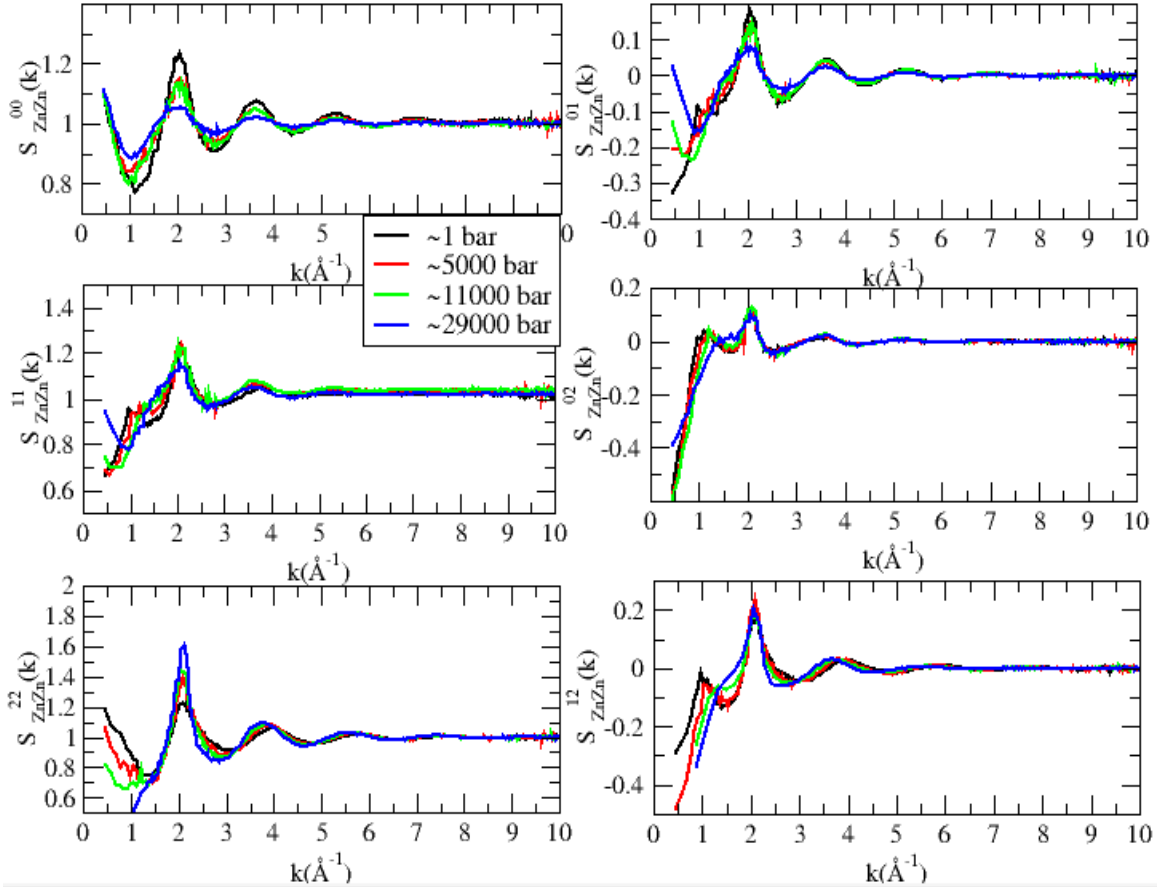
Figure 7.16 :Change in network connectivity cation-cation structure factors, $S_{MM}^{ab}(k)$, with pressure. Black line, 1 bar; red line, 5000 bar; green line, 11000 bar; blue line, 29000 bar.

Figure 7.16 shows the changes in network-connectivity functions with pressure. At ~1 bar, $S_{ZnZn}^{02}(k)$ displays similar properties as the MX₂ systems in Chapter 6, with the ratio of FSDP to principal peak ~1 at low pressures. As pressure increases, the position of the peak shifts to 1.43Å⁻¹ at 29000 bar from 1.07Å⁻¹ at 1 bar with a decline in intensity.

$S_{ZnZn}^{12}(k)$ displays similar behaviour in showing a decline in intensity and a shift in position from 0.98Å⁻¹ at 1 bar to 1.32Å⁻¹ at 29000 bar. $S_{ZnZn}^{00}(k)$ and $S_{ZnZn}^{22}(k)$ observe phase separation over most of the pressure range except $S_{ZnZn}^{22}(k)$ which, due to the increased concentration term (c_6 rises from 0.02 at 1 bar to 0.34 at ~29000 bar), forms a shoulder at 1.34Å⁻¹ at 29000 bar. $S_{ZnZn}^{01}(k)$ and $S_{ZnZn}^{11}(k)$ show a small FSDP at ~1 bar, but then observe phase separation at 11000 and 29000 bar respectively. At higher k where

$k > 3\text{Å}^{-1}$, $S_{ZnZn}^{02}(k)$ and $S_{ZnZn}^{11}(k)$ show the smallest changes with variations in temperature and pressure. Of the network-connectivity and coordination-based functions which might be expected to overlap, $S_{ZnZn}^{22}(k)$ and $S_{ZnZn}^{66}(k)$, display a shoulder at high pressures and exhibit phase separation through the pressure range. The similarity of $S_{ZnZn}^{01}(k)$ and $S_{ZnZn}^{44}(k)$ exhibited with temperature changes is weaker for changes in pressure: whilst the FSDP and principal peak intensity declines, phase separation occurs at an earlier pressure range of 5000-11000 bar for $S_{ZnZn}^{01}(k)$, compared to $S_{ZnZn}^{44}(k)$ where it occurs in the 11000-29000 bar pressure range.
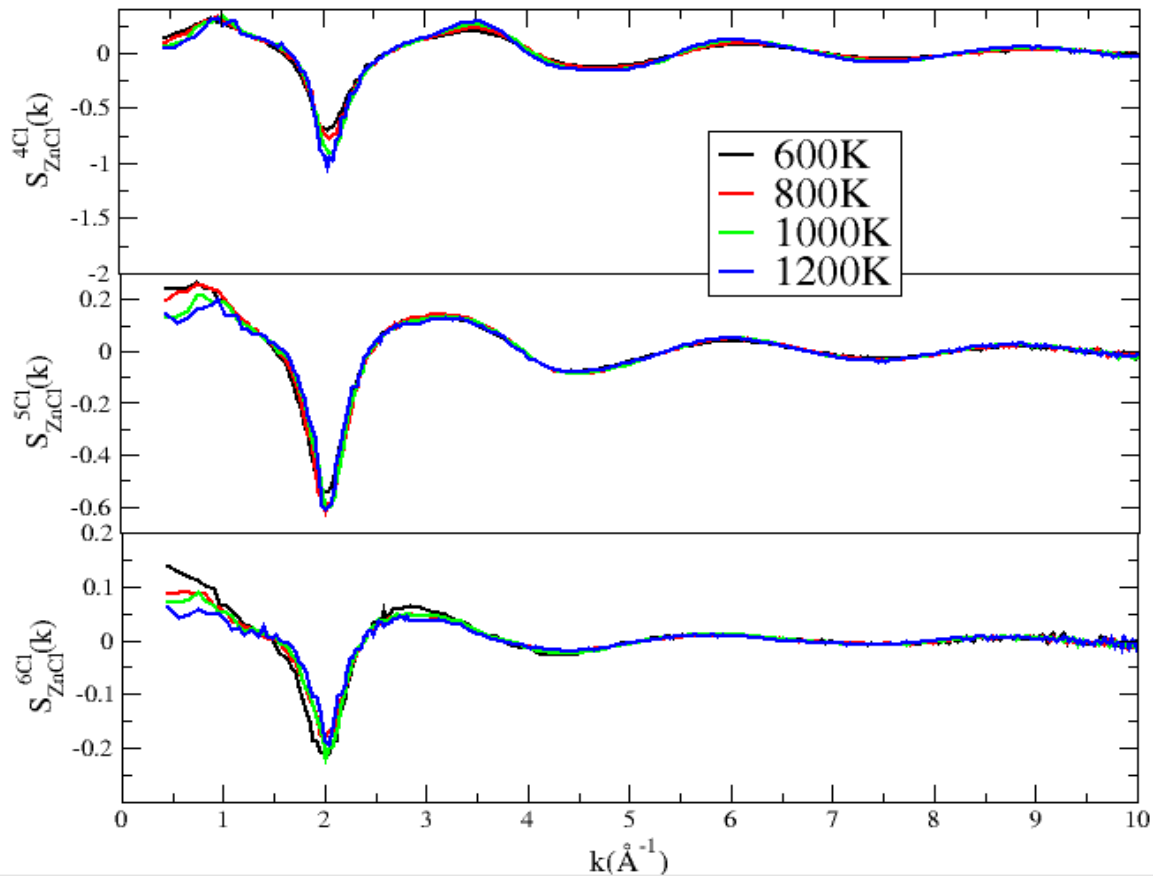
Figure 7.17 :Change in coordination-dependent cation-anion functions, $S_{ZnZn}^{cCl}(k)$, where c={4,5,6}, with temperature. Black line, 600K; red line, 800K; green line, 1000K; blue line, 1200K.

7.11 Coloured cation-anion structure factors.

It was shown earlier that the FSDP intensity $\sim 1\text{Å}^{-1}$ in $S_{ZnCl}(k)$ increases with temperature and declines with pressure, but at a slower rate compared to $S_{ZnZn}(k)$. Figure 7.17 shows

that the changes in coordination-dependent cation-anion functions, $S_{ZnZn}^{cCl}(k)$, where

c={4,5,6}, with temperature. The FSDP observed in $S_{ZnCl}^{4Cl}(k)$, which dominates the

weighting at all temperatures (at ~ 1 bar), increases with temperature in spite of a

decrease in the concentration, c_4, from 0.75 at 600K to 0.61 at 1200K Phase separation

effects, as highlighted by a rising intensity as k→ 0 is observed for $S_{ZnCl}^{6Cl}(k)$ over the

temperature range. Phase separation is also observed for $S_{ZnCl}^{5Cl}(k)$ at 1000K and 1200K.

The increase in phase separation behaviour is related to changes in density and the

concentration terms, c_5 and c_6. The position of the FSDP in $S_{ZnCl}^{5Cl}(k)$ at 1000K is at

noticeably lower scattering angles at 0.84Å^{-1} than $S_{ZnCl}^{4Cl}(k)$ at 0.97Å^{-1}.

Figures 7.18 shows the related functions with an increase in pressure. The FSDPs,

$S_{ZnCl}^{4Cl}(k_{FSDP})$ and $S_{ZnCl}^{5Cl}(k_{FSDP})$, decline in intensity but persist as shoulders to 29000

bar. A significant FSDP is absent in $S_{ZnCl}^{6Cl}(k)$ at all pressures. $S_{ZnCl}^{6Cl}(k)$ displays a

wide variation in the principal peak height over the pressure range, smallest when IRO is

present in the other two functions at low pressures. Over the pressure range a shift is

observed in the principal peaks from 2.05-2.18Å^{-1}, 2.01-2.09Å^{-1} and 1.96-2.09Å^{-1} for

$S_{ZnCl}^{4Cl}(k_{PP}), S_{ZnCl}^{5Cl}(k_{PP})$ and $S_{ZnCl}^{6Cl}(k_{PP})$ respectively. At 29000 bar, an abrupt shift is

observed for $S_{ZnCl}^{4Cl}(k_{PP})$ from 2.02Å^{-1} to 2.18Å^{-1}. This is in contrast with $S_{ZnCl}^{5Cl}(k_{PP})$

and $S_{ZnCl}^{6Cl}(k_{PP})$ which observe shifts of 0.05Å^{-1} and 0.06Å^{-1} over the same pressure

increase.
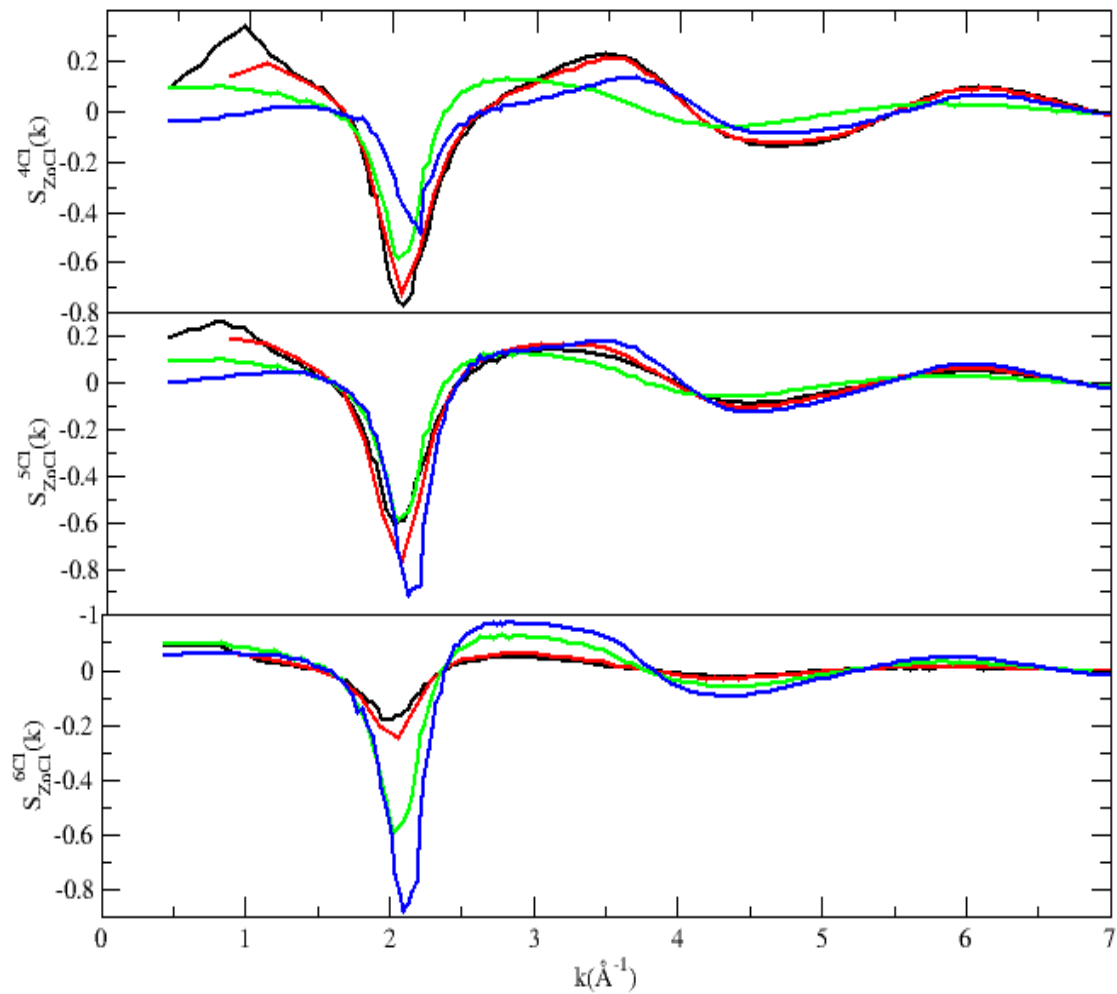
Figure 7.18: Change in coordination-dependent cation-anion structure factors, $S_{ZnZn}^{cCl}(k)$, with temperature. Black line, 1 bar; red line, 5000 bar; green line, 11000 bar; blue line, 29000 bar.

Figure 7.19 shows the network-connectivity cation-anion structure factors. At 1 bar, $S_{ZnCl}^{1Cl}(k_{FSDP})$ and $S_{ZnCl}^{2Cl}(k_{FSDP})$ observed increases in the FSDP intensity from 0.206 and 0.198 at 600K to 0.268 and 0.262 at 1200K, while for $S_{ZnCl}^{0Cl}(k_{FSDP})$ the intensity *declines* from 0.220 to 0.162; at 600K, there is also a noticeably sharper decrease as k→0 compared to the higher temperature functions. Larger changes are observed in the principal peak intensity for $S_{ZnCl}^{0Cl}(k_{PP})$ from -0.77 to -0.42 compared to $S_{ZnCl}^{1Cl}(k_{PP})$ and $S_{ZnCl}^{2Cl}(k_{PP})$ which have smaller changes of -0.65 to -0.53 and -0.56 to -0.69 respectively. The position of the FSDP shows a marked difference for $S_{ZnCl}^{2Cl}(k_{FSDP})$ at 1200K, 0.83Å^{-1} compared to 0.92Å^{-1} and 0.90Å^{-1} for $S_{ZnCl}^{0Cl}(k_{FSDP})$ and $S_{ZnCl}^{1Cl}(k_{FSDP})$ respectively. At 600K, the positions are much closer to each other: 0.96Å^{-1}, 0.98Å^{-1} and

0.95Å^{-1} for $S_{ZnCl}^{0Cl}(k_{FSDP})$, $S_{ZnCl}^{1Cl}(k_{FSDP})$ and $S_{ZnCl}^{2Cl}(k_{FSDP})$ respectively. The position of the FSDP in $S_{ZnCl}^{5Cl}(k)$ at low pressure is 0.82Å^{-1} which is similar to the distances observed for $S_{ZnCl}^{2Cl}(k)$ at the same pressure.
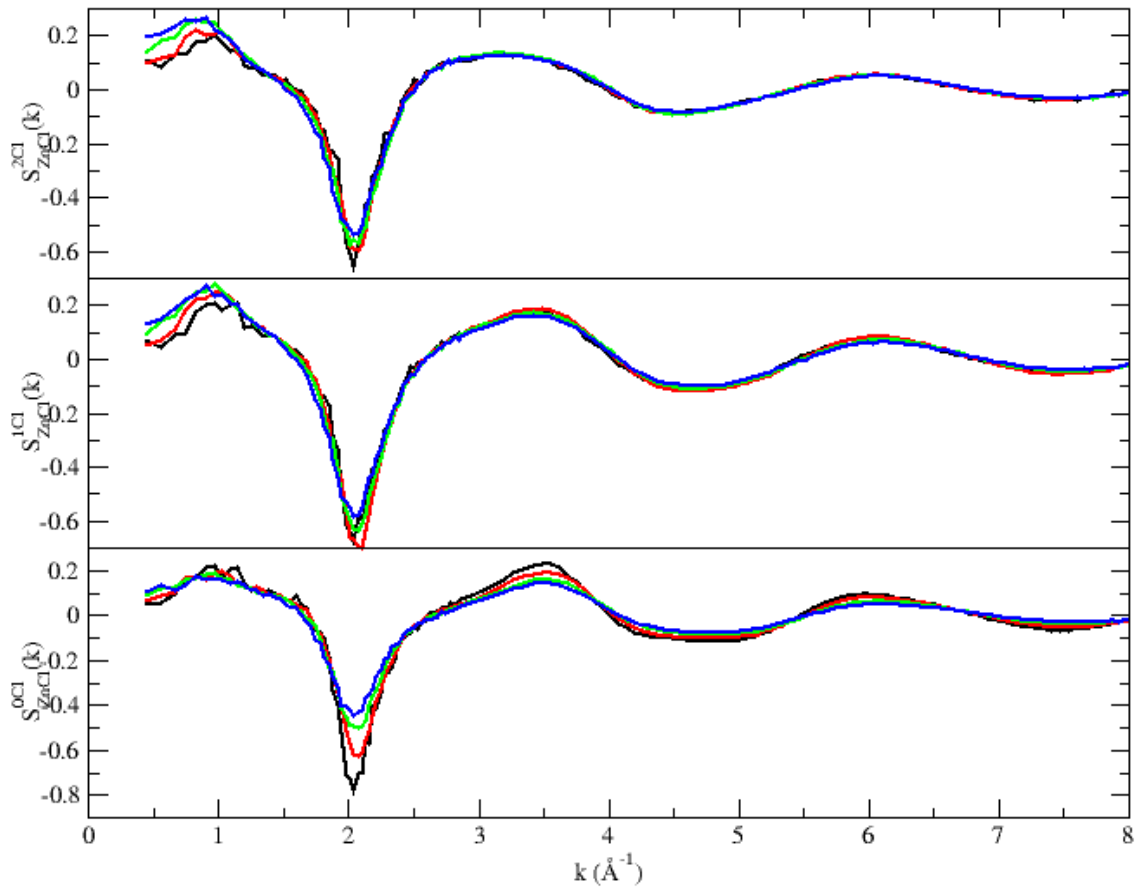
Figure 7.19 :Change in network connectivity cation-anion structure factors, $S_{ZnZn}^{aCl}(k)$, where a={0,1,2} with temperature. Black line, 600K; red line, 800K; green line, 1000K; blue line, 1200K.

Is is noticeable that phase separation occurs more readily for the coordination-dependent functions than those derived from the description of network connectivity. A consideration of $S_{ZnCl}^{5Cl}(k)$ shows, that at 1200K, it observes greater phase separation effects at low k compared to $S_{ZnCl}^{2Cl}(k)$ over the temperature range of 600-1000K and $S_{ZnCl}^{0Cl}(k)$ at 1200K even though the concentration terms, c_2 and c_1 in the respective cases are weaker than c_5. Figure 7.20 shows that the FSDP in $S_{ZnCl}^{aCl}(k)$ where a={0,1,2) is observable to higher pressures than those exhibited in the cation-cation functions, analogous to the changes observed in the coloured structure factors, $S_{ZnCl}(k)$ and $S_{ZnZn}(k)$. With increasing pressure, the FSDP shifts to higher wavevectors and declines to a similar

plateau in all three functions. The rates of change for $S_{ZnCl}^{0Cl}(k_{FSDP})$ and $S_{ZnCl}^{2Cl}(k_{FSDP})$ are similar, observing shifts of 0.23Å^{-1} from 1 bar to 5000 bar, and 0.07Å^{-1} from 5000 bar to 11000 bar; $S_{ZnCl}^{1Cl}(k_{FSDP})$ observes an initially weaker shift of 0.07Å^{-1}, and then a larger shift of 0.16Å^{-1} over the second interval of pressure. The changes in the principal peak positions with pressure are smaller than the related changes in coordination-based functions with increases of 0.07Å^{-1}, 0.02Å^{-1} and 0.04Å^{-1} for $S_{ZnCl}^{0Cl}(k_{PP}), S_{ZnCl}^{1Cl}(k_{PP})$ and $S_{ZnCl}^{2Cl}(k_{PP})$ over the pressure range.
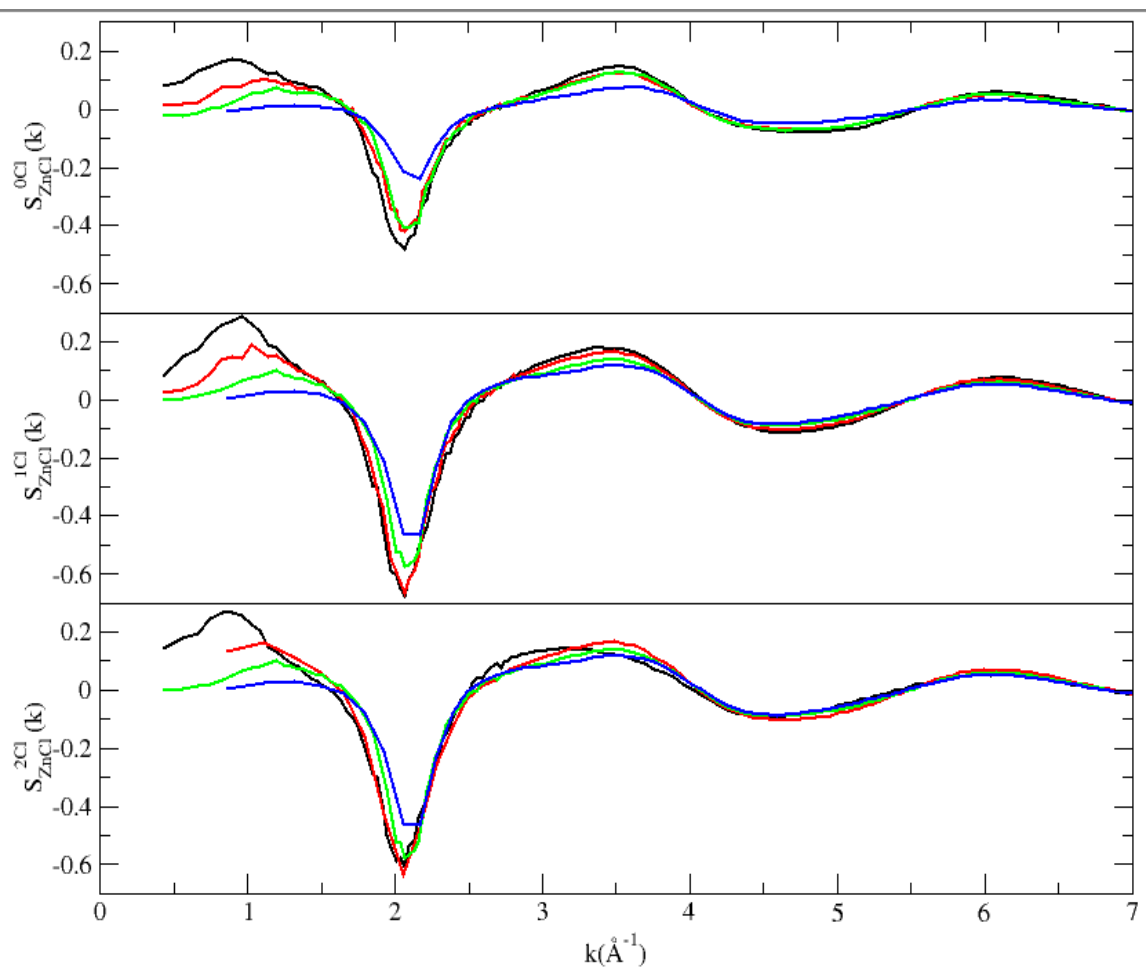
Figure 7.20 :Change in network connectivity cation-anion structure factors, $S_{ZnZn}^{aCl}(k)$, where a={0,1,2} with pressure. Black line, 1 bar; red line, 5000 bar; green line, 11000 bar; blue line, 29000 bar.

7.12 Coloured radial-distribution functions.
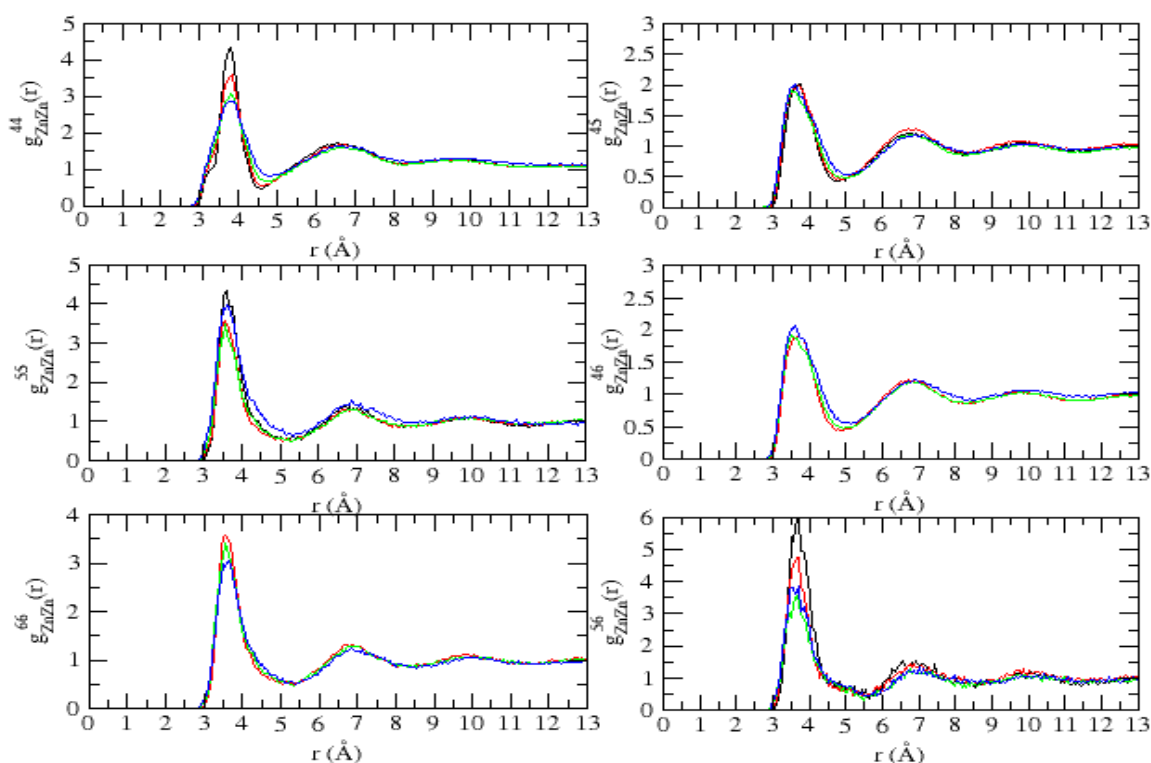
Figure 7.21:Changes in coordination-dependent radial distribution functions, $g_{ZnZn}^{cd}(r)$, with temperature. Black line, 600K; red line, 800K; green line, 1000K;blue line, 1200K.

In section 7.7, we observed that with increasing temperature and pressure the intensity of the principal peak in $g_{ZnZn}(r)$ stays the same. The intensity changes in the temperature range were much large than exhibited with pressure, 2.67-1.93 in the range 600K-1200K, and 4.07-3.97 for 1-29000 bar. The coordination-dependent radial distribution functions, shown in figure 7.21 (changes in temperature) and 7.22 (changes in pressure), do not elucidate significant variations in the shape of the principal peak. There are, however, a number of significant changes associated with increasing temperature and pressure in terms of peak shifts and intensity changes. With increasing pressure, $g_{ZnZn}^{46}(r_{PP})$,

$g_{ZnZn}^{66}(r_{PP}), g_{ZnZn}^{55}(r_{PP})$ and $g_{ZnZn}^{45}(r_{PP})$ exhibit large shifts in the position of the principal peak of 3.56 to 3.87Å, 3.58 to 3.88Å, 3.57 to 3.79Å and 3.52 to 3.80Å respectively. $g_{ZnZn}^{44}(r_{PP})$ and $g_{ZnZn}^{56}(r_{PP})$ change from 3.78-3.78Å and 3.71-3.62Å respectively. With increasing temperature, the changes are much smaller with only

$g_{ZnZn}^{46}(r_{PP}), g_{ZnZn}^{56}(r_{PP})$ and $g_{ZnZn}^{45}(r_{PP})$ exhibiting increases larger than 0.01Å, with decreases in position of 0.04Å, 0.03Å and 0.07Å from 3.65Å, 3.69Å and 3.75Å

respectively.
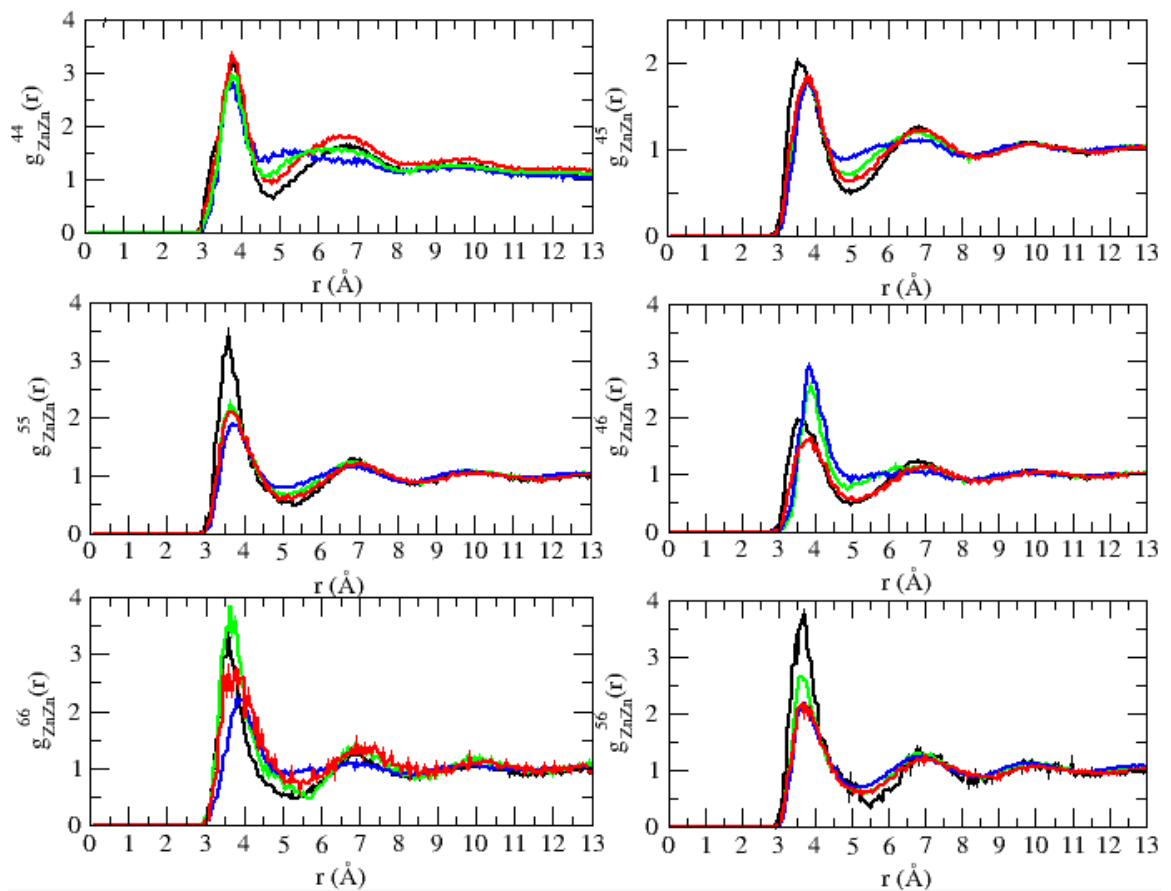
Figure 7.22 :Change in coordination-dependent cation-cation radial distribution functions, $g_{ZnZn}^{cd}(r)$, with pressure. Black line, 1 bar; red line, 5000 bar; green line, 11000 bar; blue line, 29000 bar.

The network connectivity cation-cation radial distribution functions in contrast to the coordination-dependent functions, show a wider range of principal peak positions, with ranges of 3.29Å-3.86Å compared to 3.59Å-3.80Å respectively. The functions

$g_{ZnZn}^{00}(r_{PP})$, $g_{ZnZn}^{01}(r_{PP})$, $g_{ZnZn}^{02}(r_{PP})$ and $g_{ZnZn}^{11}(r_{PP})$ show a substantial widening of the FWHM with increasing temperature (shown in figure 7.23) and a decrease of short range order. $g_{ZnZn}^{11}(r_{PP})$, $g_{ZnZn}^{22}(r_{PP})$ and $g_{ZnZn}^{02}(r_{PP})$ possess the largest FWHM at 1200K of 1.34Å , 1.69Å and 1.15Å while $g_{ZnZn}^{00}(r)$, $g_{ZnZn}^{12}(r_{PP})$ and $g_{ZnZn}^{01}(r_{PP})$ and have smaller corresponding values of 0.53Å, 0.85Å and 0.90Å. $g_{ZnZn}^{12}(r_{PP})$ and $g_{ZnZn}^{22}(r_{PP})$ show very similar FWHM at each end of the temperature range, with changes of 22% and 11% respectively, compared to the other functions which show widening with temperature of 30-50%.
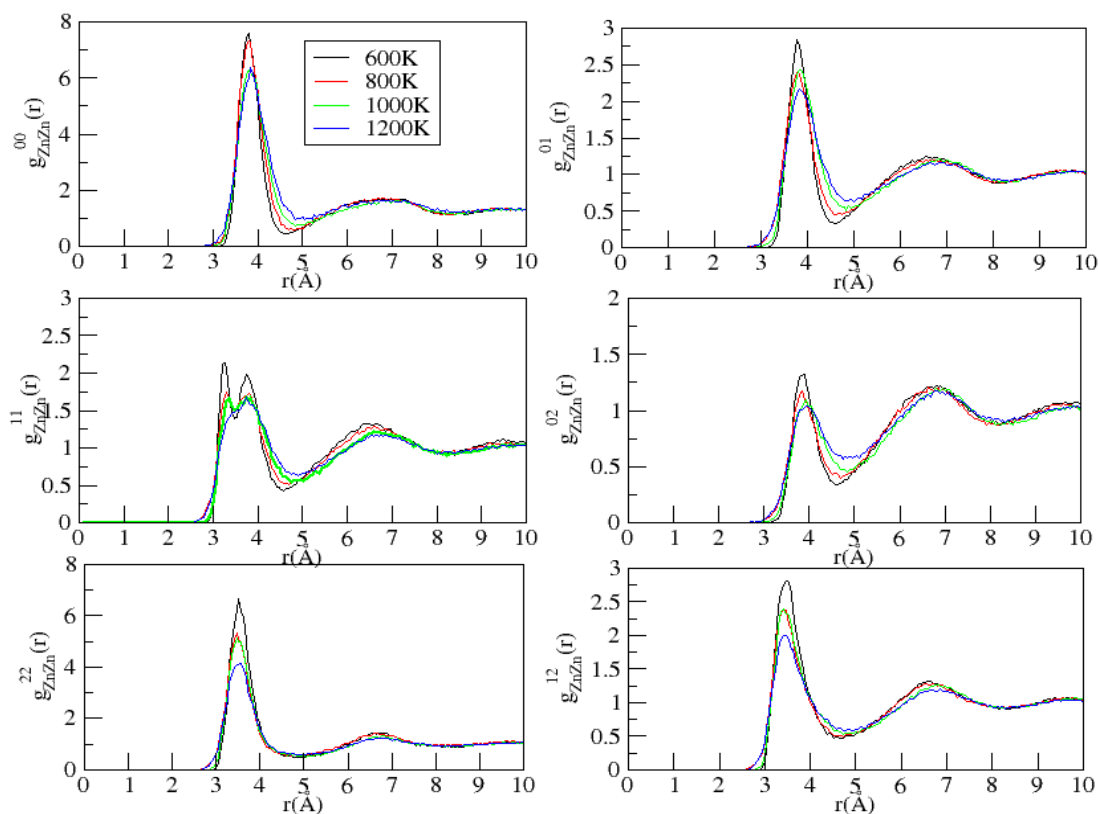
Figure 7.23:Changes in network connectivity radial distribution functions, $g_{ZnZn}^{ab}(r)$, with temperature. Black line, 600K; red line, 800K; green line, 1000K; blue line, 1200K.

$g_{ZnZn}^{12}(r_{PP})$ and $g_{ZnZn}^{22}(r_{PP})$ also observe the smallest shifts in principal peak position of 0.03Å and 0.01Å compared to 0.06Å, 0.09Å and 0.09Å for $g_{ZnZn}^{00}(r_{PP})$, $g_{ZnZn}^{01}(r_{PP})$ and $g_{ZnZn}^{02}(r_{PP})$. The rigidity of these functions in terms of position and FWHM may be expected from rigid edge-sharing chains compared to the corner-sharing configurations and those where one edge-sharing unit is involved. $g_{ZnZn}^{11}(r_{PP})$ shows a split in the principal peak, with peaks at 3.24Å and 3.76Å. This feature, not observed in the full radial distribution function, $g_{ZnCl}(r)$, is indicative either of relatively slow dynamics or a particularly strong ordering of the tetrahedra. The split in $g_{ZnZn}^{11}(r_{PP})$ is an indication of two length scales as shown in figure 7.24. The earlier edge-sharing peak reflects the bonding of two "1" cations through bridging anions, where the presence of intermediate edge-sharing unit ellicits a closer separation. The longer corner-sharing peak occurs when two E^1 cations are bonded through one bridging anion with edge-sharing unit in the opposite direction.
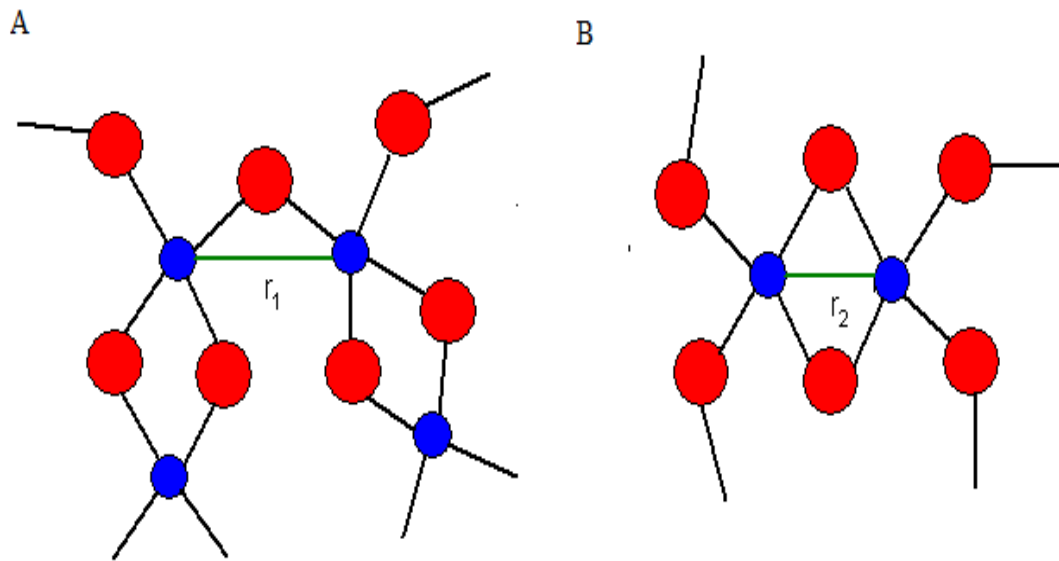
Figure 7.24: Schematic diagrams of two bond length scales for "1"-"1" cation cation interaction. A: Long bond, r_1, between two "1" cations where there is a singly bridging anion. B: Short bond, r_2, where there are two bridging anions present.

The corresponding functions calculated for the pressure range, 1-29000 bar, shown in figure 7.25, at 1000K, show changes in the principal peak and intensity. $g_{ZnZn}^{11}(r_{PP})$ at low pressure exhibits intensity a edge-sharing peak at 3.39Å, in addition to the corner-sharing peak at 3.80Å, which declines at higher pressure and only a single peak is observed at 3.85Å. There is noticeably sharper decline in the intensity of the second peak at ~7Å which flatten to a plateau at the highest pressure for $g_{ZnZn}^{01}(r_{PP})$ and

$g_{ZnZn}^{11}(r_{PP})$. $g_{ZnZn}^{02}(r_{PP}), g_{ZnZn}^{22}(r_{PP})$ and $g_{ZnZn}^{12}(r_{PP})$ exhibit larger changes in the increasing FWHM of the principal peak (0.31-61) over the pressure range compared to $g_{ZnZn}^{00}(r_{PP}), g_{ZnZn}^{01}(r_{PP})$ and $g_{ZnZn}^{11}(r_{PP})$ (0.04-0.19). $g_{ZnZn}^{22}(r_{PP})$ shows the smallest change in the minima at ~5Å which is also the case for the functions in figure 7.23.

$g_{ZnZn}^{12}(r_{PP}), g_{ZnZn}^{11}(r_{PP})$ and $g_{ZnZn}^{22}(r_{PP})$ show the largest changes in terms of position in the principal peak shifting from 3.43Å to 3.96Å and 3.34Å to 3.93Å, and 3.45Å to 3.68Å respectively. Smaller changes of 3.77Å to 3.77Å, 3.93Å to 3.93Å and 3.94Å to 4.01Å are observed for $g_{ZnZn}^{00}(r_{PP}), g_{ZnZn}^{01}(r_{PP})$ and $g_{ZnZn}^{02}(r_{PP})$ respectively. In contrast to the changes in $g_{ZnZn}^{02}(r_{PP})$ with temperature, the weakening of the separation between the principal and second peak is accompanied by a rise in the ratio of principal peak intensity over second peak from 0.88 at ~1 bar to 1.30 at 29000 bar.
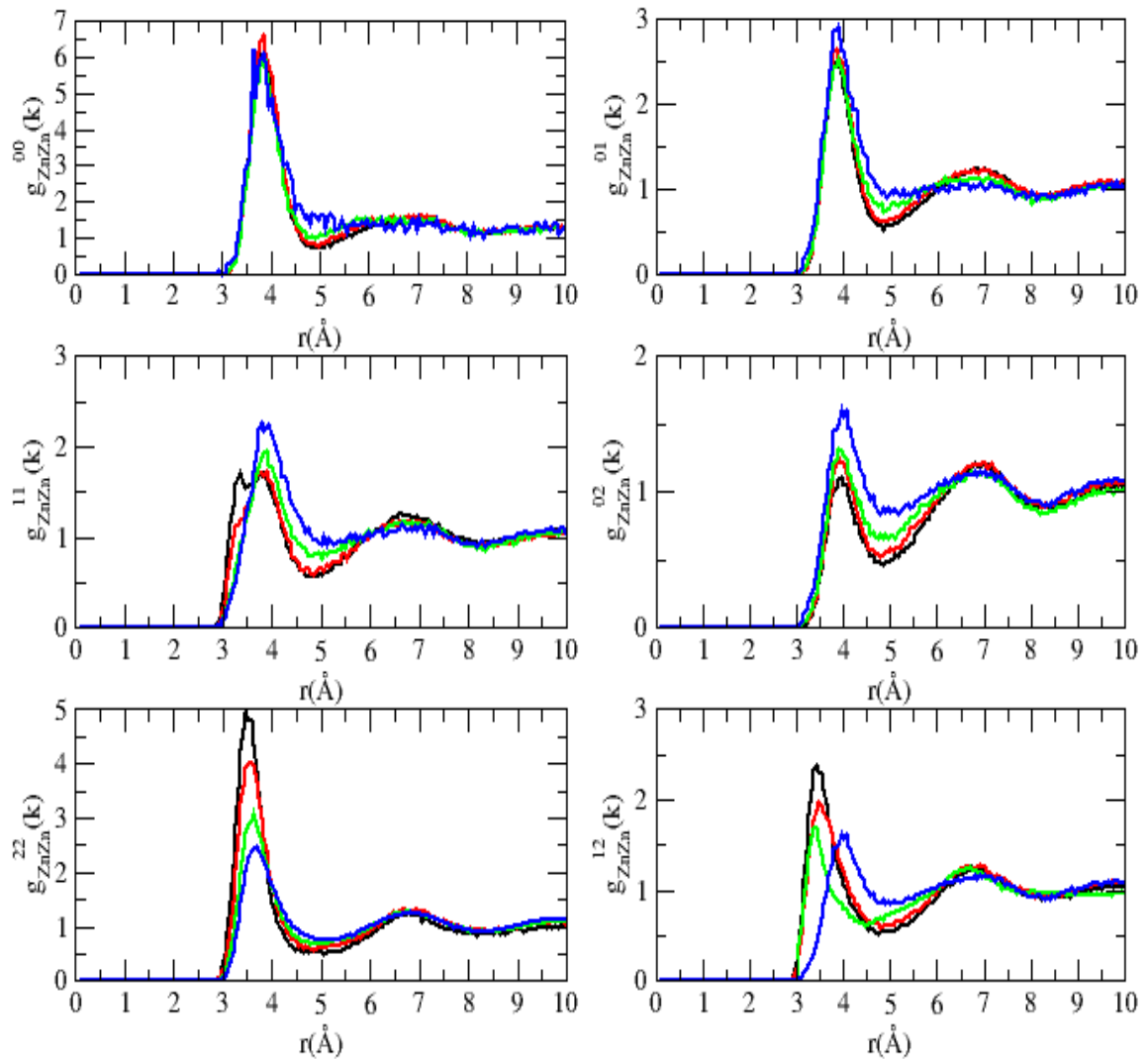
Figure 7.25 :Change in network-connectivity cation-cation radial distribution functions, $g^{ab}_{ZnZn}(r)$, with pressure. Black line, 1 bar; red line, 5000 bar; green line, 11000 bar; blue line, 29000 bar.

7.13 Conclusion.

The changes in the structure of ZnCl₂ with temperature and pressure have been highlighted. With increasing temperature, the FSDP intensity in F(k), depending on the isotopic weighting, either stays at a similar intensity or declines, whilst with pressure it declines (over all isotopic weightings). The pattern of changes of the variation in the intensity of $S_{ZnCl}(k)$ and $S_{ZnZn}(k)$ differ; the integrity of the peak in $S_{ZnCl}(k)$ persists to higher temperatures and pressure than that observed in $S_{ZnZn}(k)$ which becomes a shoulder at higher scattering angles. As expected, the cation-anion coordination increases with pressure, but the change is not substantial over the range of detailed neutron diffraction

investigations of Pfleiderer[6] and Heusel[9]. The anion sublattice is predicted to accommodate the changes with pressure with a significant reduction in the nearest neighbour anion-anion distance. Changes in the principal peak of g$_{ZnZn}$(r) are made clearer through the difference functions, $P_{\alpha\beta}^{P_n-P_1}(r)$. The separation between edge and corner-sharing peaks is highlighted further in the function, $g_{ZnZn}^{11}(r_{PP})$, which shows a split correlated with changes to the relative intensities of the edge- and corner-sharing peaks. While broad patterns are observed by the change of these variables with pressure, the details of changes in structure were better understood when the partial structure factors and radial distribution functions are coloured according to both network connectivity and ZnCl coordination. At low pressure and temperature, the network connectivity functions show similar features with the high polarisability systems studied in previous chapters. With increasing temperature and pressure they show a diminishing of features associated with IRO. The network connectivity functions show greater variation in certain properties such as propensity for phase separation and the ratio of the FDSP to principal peak intensities. It is shown that decomposing the partial structure factor according to network connectivity is a more effective probe than colouring by coordination.

Previous ZnCl$_2$ models have focused on the structure at a single state point.[28-33] In chapter 3 we showed that the ZnCl$_2$ PIM displayed a good correlation with experimental densities and quantities such as the total structure factors at zero pressure. Here we produced the first set of calculations on ZnCl$_2$ showing the effect on IRO across the temperature and pressure range. Equations by Elliot[1], highlighted in the introduction, expressing the temperature and pressure dependence of the FSDP of F(k), the total structure factor were shown. Elliot's model based on cluster-void ordering relies on the packing of cation-centred clusters, and by implication a strong cation-cation ordering which neglects other ion correlations. As we have observed in chapter 6, in systems of intermediate polarisability, the relative contributions of S$_{MM}$(k) and S$_{MX}$(k) to the FSDP are closest so this assumption is weakest with regards to systems such as ZnCl$_2$ whose anion polarisability is close to this range. We have shown that the cation-cation and cation-anion contributions display a different temperature dependence in their respective contributions to IRO. This indicates that the cation-anion contributions are not as structurally dependent upon the cation-cation correlations as the void model implies.

Our results showed a good correlation with the experimental results of Allen et al[9] with increasing temperature with the FSDP intensity more stable to changes in temperature than peaks at higher k. Our decomposition into partial structure factors

shows this is due to the stability of the FSDP in $S_{ZnCl}(k)$ with increasing temperature. This is supported by the slight decline in the position of the k_{FSDP} in $F(k)$ experimentally from 1.005^{-1} at 603K to $0.944Å^{-1}$ at 873K which corresponds with the pattern of decline in position of $S_{ZnCl}(k_{FSDP})$ we have observed in our results from $0.96Å^{-1}$ at 600K to $0.90Å^{-1}$ at 1200K.

In recent pressure experiments on $ZnCl_2$, it was commented by Brazkhin[8] that with increasing pressure the structure of $ZnCl_2$ becomes similar to that of compounds such as $MgCl_2$. Some evidence in support of this statement is that, at increased pressure, $ZnCl_2$ displays a coordination similar to that exhibited by $MgCl_2$. In comparing the partial structure factors of $ZnCl_2$ at higher pressures and $MgCl_2$, while they exhibit a decline in the intensity of the FSDPs, they show a number of significant differences. In $MgCl_2$, only the principal peak position in $S_{MgMg}(k)$ shifts significantly whereas with increasing pressure in $ZnCl_2$, principal peaks for all three correlations shift in position. The greatest change in principal peak intensity also occurs for $S_{MgMg}(k)$ in $MgCl_2$ compared to the change in pressure with $ZnCl_2$ where it is the changes in anion-anion term $S_{ClCl}(k_{PP})$ term which is notably greater than $S_{ZnCl}(k)$ and $S_{ZnZn}(k)$. For higher k oscillations, $S_{MgMg}(k)$ and $S_{MgCl}(k)$ are observed to shift while for increasing pressure in $ZnCl_2$ it is only the oscillations in the anion-anion term, $S_{ClCl}(k)$ that do so.

7.14 References

[1] S. R. Elliot. *J. Phys.: Condens. Matter*, **4**, 7661, (1992).

[2] S. Susman, K. J. Volin, D. L. Price, M. Grimsditch, J. P. Rino, R. K. Kalia and P. Vashishta. *Phys. Rev B*, **43**, 1194, (1991).

[3] S. Susman, K. J. Volin, D. G. Montague and D. L. Price. *Phys. Rev B*, **43**, 11 076, (1991).

[4] A. I. Soklakov and V. V. Nechaeva. *Fiz. Tverd. Tela*, **9**, 921, (1967).

[5] J. Paauwe and M. Dekker. *High Pressure Technology, ed. L,* vol 1, Spain, New York, (1977).

[6] T. Pfleiderer, I. Waldner, H. Bertagnolli, K. Todheide and H. E. Fisher. *Phys. Chem. Chem. Phys.,* **5**, 5313, (2003).

[7] V. V. Brazhkin, Y. Katayama, A. G. Lyapin, S. V. Popova, Y. Inamura, H. Saitoh and W. Utsumi. *JETP Letters*, **82**, 713, (2005).

[8] V. V. Brazhkin, A. G. Lyapin, S. V. Popova, Y. Inamura, Y. Katayama, H. Saitoh and W. Utsumi. *Journal of Physics:Condens. Matter, 19*, 1, (2007).

[9] G. Heusel, H. Bertagnolli, M. Kreitmeir, J. Neuefeind and A. Lemke. *Phys. Chem. Chem. Phys*., **4**, 4155, (2002).

[10] G. Heusel, H. Bertagnolli and J. Neuefeind. *J. Non-Cryst. Solids.,* **352**, 3210, (2006).

[11] C. Fillaux, B. Couzinet, C. Dreyfus, J. P. Itié and A. Polian. *Physica Scripta,* **T115**, 339, (2005).

[12] S. N. Yannopoulos, A. G. Kalampounias, A. Chrissanthopoulos and G. N. Papatheodorou. *J. Chem. Phys*., **118**, 3197, (2003).

[13] D. S. Allen, R. A. Howe and N. D. Wood. *J. Chem. Phys*., **94,** 5071, (1991).

[14] J. Neuefeind, K. Tödheide, A. Lemke and H. Bertagnolli. *J. Non-Cryst. Solids*, **224**, 205, (1998).

[15] C. H. Polsky, L. M. Martinex, K. Leinenweber, M. A. Verhelst, C. Austen Angell and George H. Wolf. *Phys. Rev B*, **61**, 5934, (2000).

[16] M. C. Wilding, M. Wilson and P. F. McMillan. *Chem. Soc. Rev.*, **35**, 964, (2006).

[17] V. V. Brazhkin, S. Buldyrev, V. N. Ryzhov and H. E. Stanley. *New Kinds of Phase Transition:Transformation in Disordered Substances,* Kluwer, Dordrecht, (2002).

[18] E. G. Ponyatovsky and O. I. Barkalov. *Mater. Sci. Rep*., **8**, 147, (1992).

[19] S. Biggin and J. E. Enderby. *J. Phys, C.:Solid State Phys*., **14**, 3129, (1981).

[20] P. S. Salmon, R. A. Martin, P. E. Mason and G. J. Cuello. *Nature* (London), **435**, 75, (2005).

[21] J. Neuefeind. *Phys. Chem. Chem. Phys*., **3**, 3987, (2001).

[22] L. E. Busse and S. R. Nagel. *Phys. Rev. Lett*. **47**, 1848, (1981).

[23] G. S. Cargill. *J. Appl. Phys*.,**41**, 248, (1970).

[24] B. O'Malley and I. Snook. *J. Chem. Phys.,* **123**, 054511, (2005).

[25] W. A. Crichton, M. Mezouar, T. Grande, S. Stølen and A. Grzechnik. *Nature,* **414**, 622, (2001).

[26] S. Sampath, C. J. Benmore, K. M. Lantsky, J. Neuefeind, K. Leinenweber, D. L. Price and J. L Yarger. *Phys. Rev. Lett.,* **90**, 115502, (2003).

[27] M. Hemmati, M. Wilson and P. A. Madden. *J. Phys. Chem B*, **103**, 4023, (1999).

[28] L. V. Woodcock, C. A. Angell and P. Cheeseman. *J. Chem. Phys*., **65**, 1565, (1976).

[29] P. J. Gardner and D. M. Heyes. *Physica B*, **131**, 227, (1985).

[30] P. N. Kumta, P. A. Deymier and S. H. Risbud. *Physica B*, **153**, 85, (1988).

[31] M. C. Abromo and A. Consolo. *Physica B*, **205**, 408, (1995).

[32] A. Bassen, A. Lemke and H. Bertagnolli. *Phys. Chem. Chem. Phys*., **2**, 1445, (2000).

[33] S. Huang, F. Yoshida and W. Wang. *J. Mol. Liq*., **115**, 81, (2004).

Chapter 8

Effect of temperature and pressure in MX$_2$ systems

8.1 Introduction.

In Chapter 7 we studied the effect of temperature and pressure in ZnCl$_2$; this corresponds to a system of MX$_2$ stoichiometry where anion X has an intermediate polarisability value of 20 a.u. In this chapter, we shall focus primarily on systems which lie either side (in the context of the magnitude of the underlying polarisation) by application of a MX$_2$ model, with the anion polarisability, α_X, set to 35 a.u and 15 a.u; these systems might be expected to correspond to systems such as GeSe$_2$ and GeO$_2$ respectively. It has been observed in diffraction experiments for GeSe$_2$[1] that the FSDP in the number-number structure factor, S$_{NN}$(k), rapidly diminishes when the temperature is raised from 800°C to 1100°C, with a shift in the position from 0.99Å^{-1} to 1.05Å^{-1}.[1] A possible explanation for this change was that upon increasing temperature the structure of GeSe$_2$ becomes similar to GeSe; this was supported by the similarity with the absence of a FSDP of GeSe at 727°C and also the similar values in conductivities of 60 Ω^{-1} cm^{-1}.[2] Pressure studies in *liquid* GeSe$_2$[3] have shown a change from a 2D system, where there are significant amounts of edge-sharing, to a 3D network, where corner-sharing dominates the linkages between tetrahedral units. Raman spectroscopy supports this by observing a reduction in the presence of edge-sharing tetrahedra in an experiment carried out to ~3 GPa.[4] This change was accompanied by a decrease in the intensity of the FSDP. The accompanying coordination changes predicted are for Ge to gradually increase from 4 to 6 coordination and for Se to increase from 2 to 4 coordination.[9] Recent neutron diffraction experiments by Mei *et al*[5] on glassy GeSe$_2$ show that the FSDP observes a 31% reduction in intensity from 0-3.9 GPa followed by a 8% reduction from 3.9 to 9.3 GPa.[5] Other structural features include a shift in the position of both the FSDP from 1.010Å^{-1} to 1.225Å^{-1} and the principal peak from 2.042Å^{-1} to 2.262Å^{-1}.[5] A double peak between 4.5 and 7.5Å^{-1}, previously associated with well defined tetrahedral units,[6,7] and the weakening of the

shoulder at 6.92Å^{-1} with increasing pressure was associated with diminution of these units.[5] An increase in Ge-Se bond length, from 2.32Å to 2.46Å, is measured for liquid GeSe$_2$,[3] up to an experimental pressure range of 4.1 GPa, whereas for glass the corresponding figures were 2.364Å to 2.377Å up to 9.3 GPa[5]. The Ge-Se coordination number increases from 4.0 to 4.2 at 3.9 GPa, and then up to 4.5 at 9.3 GPa.[5] The results disagree with earlier work by Prasad et al[8] which predicted a semi-conductor to metallic transition at 9GPa whilst observing that GeSe$_2$ remains amorphous up to these pressures.

There have been several representations of the effect of pressure and temperature on GeSe$_2$ using computational simulations.[9-13] Electronic structure calculations by Durandurdu et al predict[9,10] that with increasing pressure, the percentage of homopolar bonds initially deteriorates, then increases over the pressure range considered. Likewise, electronic structure calculations on the effect of temperature predict an increase in homopolarity with increasing temperature, leading to a reduction in the FSDP intensity.[11] In calculations by Vashishta for GeSe$_2$,[12,13] a similar FSDP intensity is observed at 300K and 1100K, temperatures corresponding to the glassy and liquid regimes respectively.

At the lower end of the polarisability spectrum we would expect the effect of pressure to relate with changes in systems such as GeO$_2$[14-18] which displays a FSDP at ~1.5Å^{-1} and a larger M-X-M bond angle ~130° compared to the smaller values associated with GeSe$_2$. With increasing pressure, the FSDP in GeO$_2$ glass broadens and shifts to higher k values.[17] EXAFS experiments on liquid GeO$_2$ show stable 4-coordination up to 2.5 GPa, followed by an increase in coordination number from 4 to 6 from 2.5 GPa to 4 GPa.[16] Difference functions, which use X-Ray and Neutron diffraction data to eliminate one of the partial structure factors were derived by Sampath et al[17]. The results showed that Ge-O and O-O correlations were largest contributors to the change in the structure factor. This is in contrast with the changes in IRO we have studied which so far have been dominated by cation-cation and cation-anion interactions. One proposed mechanism for densification envisages the collapse of the cage structure of GeO$_2$ enabled by rotation in the [GeO$_4$]$^{2-}$ tetrahedra occurring in the pressure region below 6GPa.[18] This is followed by coordination increase in the pressure range of 6-15GPa. Molecular dynamics simulations on GeO$_2$ show an increase in coordination, changing from a tetrahedral to octahedral network with increasing pressure.[19-26] GeO$_2$ and GeSe$_2$ may densify through a combination of different effects. The presence of edge-sharing tetrahedra in GeSe$_2$ enables a 2D-3D transition with density changes; in contrast, GeO$_2$, which is dominated

by corner-sharing connections, may be dominated by coordination changes.

8.2 Simulation details.

In this chapter, we will observe the changes in network structure over a large change in density for MX$_2$ using anion polarisability values of 15 a.u and 35 a.u (the recorded densities correspond to the molecular weight of 230.53 g/mol for GeSe$_2$). The accessing of low density is intended to observe both the structural changes upon densification according to two different anion polarisabilities. In addition, the breakdown of partial structure factors and radial distribution functions calculated at low densities, where coordination tends strongly to four-coordination, will highlight the influence of network topology in comparison to coordination-defects and frustration caused by packing. The effect of temperature on a system corresponding to GeSe$_2$, (α_X=35 a.u) will be observed by recording the structure at temperatures corresponding to low (2000K) and high temperature (7000K) liquids.

The MX$_2$ potential used in this chapter is the same as that developed for GeSe$_2$ in chapter 4 with the anion polarisability, α_X, changed to 35 a.u and 15 a.u. All calculations in this chapter consists of 999 ions (333 cations and 666 anions). The starting configurations for the calculations for α_X=15 a.u and α_X=35 a.u were obtained from the end of the simulations described in Chapter 6. Initial calculations were carried out by raising the pressure to 1x10^{-3} a.u. The lower density calculations were generated by decreasing the pressure applied via the barostats by increments of 1 x 10^{-4} a.u. At each pressure an equilibration run of 30 ps was carried out. Simulation runs, using an NPT ensemble,were carried out for 60 ps. Structural correlations (discussed in sections 8.3-8.6) are calculated in this chapter for both systems across a similar range of density and pressure change. At α_X=35.a.u, the structural correlations were highlighted for the pressures at 9.0x10^{-4} a.u, 7.0x10^{-4} a.u, 4x10^{-4} a.u and 1x10^{-4} a.u corresponding to average cell sizes of 34.74Å (3.00 g/cm^3), 32.30Å (3.73 g/cm^3), 31.28Å (4.11 g/cm^3) and 30.73Å (4.34 g/cm^3). At α_X=15.a.u, the structural correlations were highlighted for the pressures at 1.0x10^{-4} a.u, 3.0x10^{-4} a.u, 6.0x10^{-4} a.u and 9.0x10^{-4} a.u corresponding to average cell sizes of 34.25Å (3.13 g/cm^3), 32.37Å (3.71 g/cm^3) , 31.08Å (4.19 g/cm^3) and 30.38Å (4.49 g/cm^3).

For calculating high temperature liquid configurations for MX$_2$ (α_X=35 a.u), analysed in section 8.7, an initial starting configuration was taken from the end of a simulation run

at 2000K. The average cellsize was 32.30Å corresponding to a density of 3.71 g/cm^3. The temperature was raised by 1000K to 7000K over series of runs of 30 ps at each stage. At 7000K upon a further equilibration run, a simulation of 60 ps in an NPT ensemble was carried out from which structural correlations were calculated. The average cell size was 33.85Å corresponding to density of 3.25 g/cm^3.

8.3 Change in partial structure factors of MX$_2$ systems with density.

Figure 8.1 shows the partial structure factors of MX$_2$ at α_X=15 a.u in the density range 3.13-4.49 g/cm^3. At high densities, the principal peak and FSDP are effectively merged in $S_{MM}(k)$ at 1.65Å^{-1}. With decreasing density, there is little change until 3.13 g/cm^3 when a split in the FSDP occurs so that a peak is observed at 1.33Å^{-1} and 1.85Å^{-1}. The split in the FSDP indicates the nascent formation of two separate length scales, where the lower value peak tends towards ~1Å^{-1} and the higher value peak towards ~2Å^{-1}: these features are typical of higher anion polarisability systems. $S_{MX}(k_{FSDP})$ decreases sharply in intensity with increasing density with the position of the peak shifting to lower k values from 1.19Å^{-1} at 3.13 g/cm^3 to 1.38Å^{-1} at 3.71 g/cm^3. Although no observable FSDP is present in $S_{XX}(k)$, the intensity at 3.13 g/cm^3 is considerably larger at 0.29 than that observed at 4.49 g/cm^3 of 0.05. The principal peak intensities of $S_{MX}(k)$ and $S_{XX}(k)$
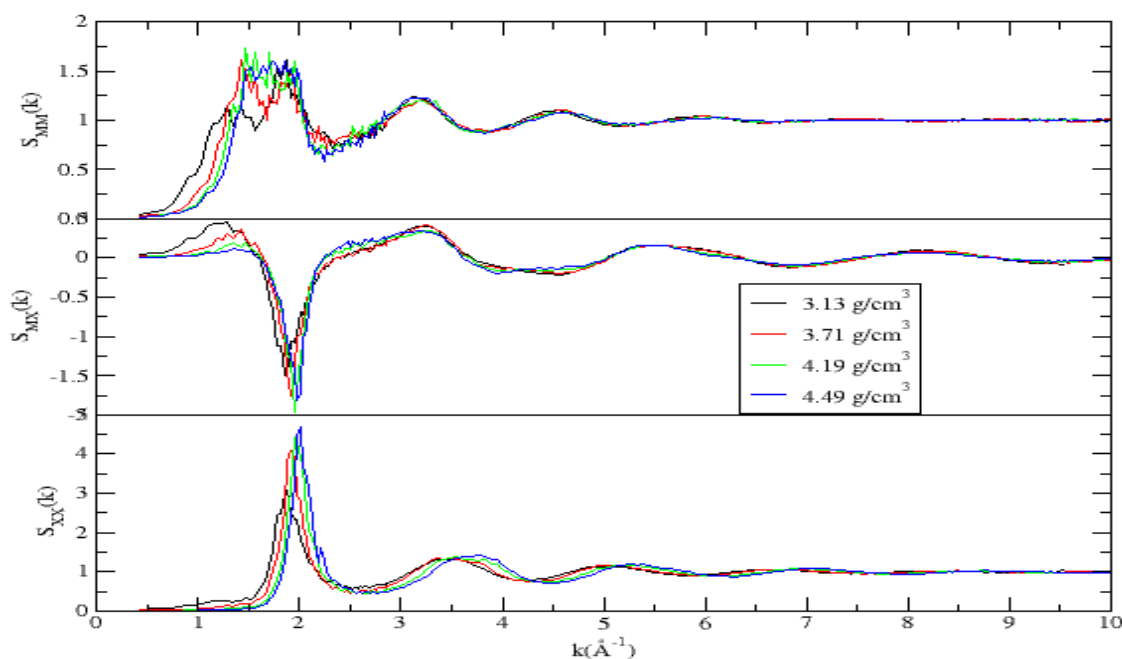
Figure 8.1:Partial structure factors of MX$_2$ when α_X=15.0 a.u, according to density range 3.13-4.49 g/cm^3. Top, $S_{MM}(k)$; middle, $S_{MX}(k)$; bottom, $S_{XX}(k)$. Black line, 3.13 g/cm^3; red line, 3.71 g/cm^3; green line, 4.19 g/cm^3; blue line, 4.49 g/cm^3.

change from -1.48 to -1.82 and 3.07 to 4.72 over the density range while both observe similar shifts of 1.87Å^{-1} to 1.97Å^{-1} and 1.86Å^{-1} to 2.00Å^{-1} respectively.

Figure 8.2 shows that for the anion polarisability of 35 a.u, there is a reduction in the intensity of the FSDP in $S_{MM}(k)$ with increasing pressure. The FSDP also shifts to higher k from 0.96Å^{-1} at 3.00 g/cm^3 to 1.14Å^{-1} at 4.34 g/cm^3. $S_{MX}(k_{FSDP})$ decreases sharply in intensity with increasing density from 0.49 at 3.00 g/cm^3 to 0.04 at 4.34 g/cm^3 and its position shifts to higher k values from 0.94Å^{-1} at 3.00 g/cm^3 to 1.05Å^{-1} at 3.73 g/cm^3. A FSDP is observed in $S_{XX}(k_{FSDP})$ only at the lowest density in contrast to $S_{MM}(k)$ and $S_{MX}(k_{FSDP})$ which is observed over the whole density range. The principal peak intensities increase with increasing density: $S_{MM}(k_{PP})$, $S_{MX}(k_{PP})$ and $S_{XX}(k_{PP})$ increase from 1.58-1.69, -1.00 to -1.33 and 2.82 to 3.33 respectively; the change in $S_{XX}(k)$ is weaker than that exhibited at α_X=15.0 a.u. The changes in position of $S_{MX}(k_{PP})$ and $S_{XX}(k_{PP})$ are similar with shifts of 1.79Å^{-1} to 1.99Å^{-1} and 1.80Å^{-1} to 2.00Å^{-1} respectively, whilst for $S_{MM}(k_{FSDP})$ it is much smaller from 1.96Å^{-1} to 1.99Å^{-1}. $S_{XX}(k_{PP})$ also shows changes at higher k, unlike $S_{MX}(k_{PP})$ and $S_{MM}(k_{PP})$, as the function is translated by 0.32Å^{-1} over the density range.
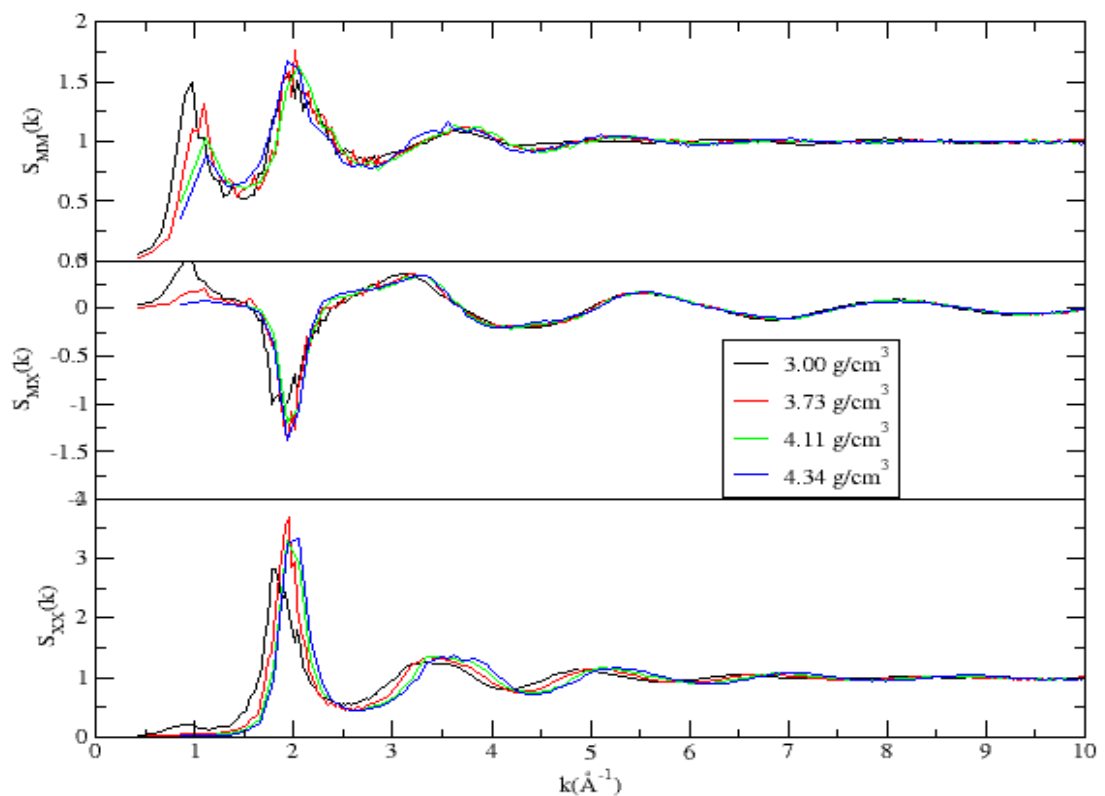
Figure 8.2:Partial structure factors of MX$_2$, when α_X=35.0 a.u, according to density range 3.00-4.34 g/cm^3. Top, $S_{MM}(k)$; middle, $S_{MX}(k)$; bottom, $S_{XX}(k)$. Black line, 3.00 g/cm^3; red line, 3.73 g/cm^3; green line, 4.11 g/cm^3; blue line, 4.43 g/cm^3.

8.4 Changes in radial distribution functions in MX$_2$ with density.

For α_X=15.0 a.u, a small pre-preak is observed in g$_{MM}$(r) at 3.00 g/cm^3, as highlighted in the inset of figure 8.3, indicating the formation of edge-sharing units. In the region of r > r$_{PP}$, g$_{MM}$(r) shows considerable variation between densities. Noticeably at 5.14Å, the intensity of g$_{MM}$(r) is substantially weak at 3.00 g/cm^3 but observes a stronger peak at 6.56Å. At higher densities the separation between these two lengths weakens, with an increasing intensity ~5.14Å. The intensity of the principal peak in g$_{MX}$(r) declines from 11.11 at 3.13 g/cm^3 to 5.81 at 4.79 g/cm^3, while the position stays constant at 2.46Å. At higher densities, the principal peak position of g$_{XX}$(r) is perturbed by shifting to lower r from 4.00Å to 3.74Å over the same density range. The peaks at r >r$_{PP}$ also shift by a similar amount in contrast to g$_{MM}$(r).
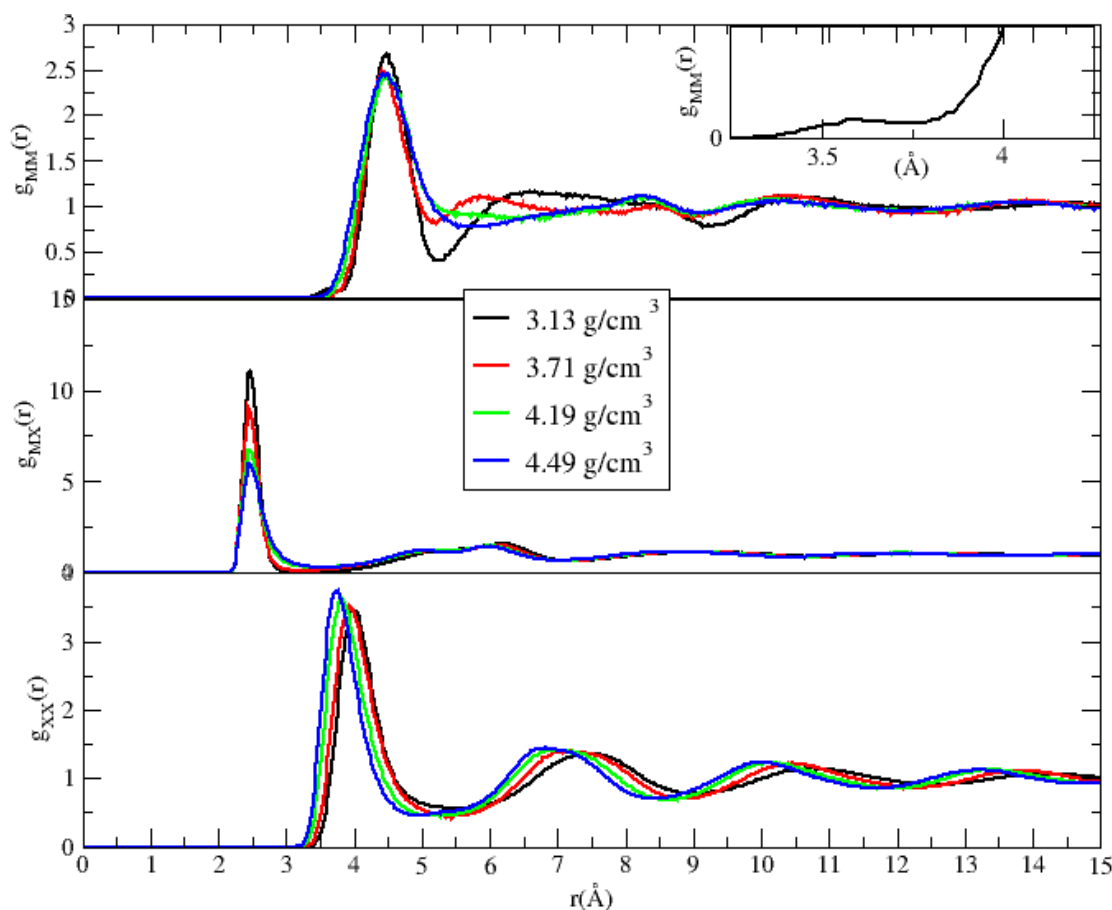
Figure 8.3: Radial distribution functions, g$_{\alpha\beta}$(r), of MX$_2$ systems, when α_X=15.0 a.u, in the density range 3.13-4.49 g/cm^3. Inset: small edge-sharing peak observed in g$_{MM}$(r) at 3.13 g/cm^3. Black line, 3.13 g/cm^3; red line, 3.71 g/cm^3; green line, 4.19 g/cm^3; blue line, 4.34 g/cm^3.

Figure 8.4 shows the changes in the radial distribution functions with density for α_X=35.0 a.u. There is little shift of the position in the principal peak in $g_{MX}(r)$, which remains at 2.47Å from 3.00 g/cm^3 to 4.34 g/cm^3, but there is a significant change in the intensity from 7.96 to 6.80. In $g_{XX}(r)$ the greatest shift in principal peak position occurs, changing from 4.08Å at 3.00 g/cm^3 to 3.76Å at 4.34 g/cm^3; the intensity also declines from 3.69 to 3.13. The change in $g_{MM}(r)$ is different from $g_{XX}(r)$ and $g_{MX}(r)$ in that the *shape* of the principal peak varies significantly. At low densities a separate peak is observed at 3.42Å in addition to a peak at 3.86Å which is observed over the whole density range. With increasing density, the intensity at this separation decreases until no second peak is observed at 4.11 g/cm^3. The changes in the intensity of the principal peak are comparatively small, from 2.40 to 2.21 over the density range. Larger variations are observed at the minima of $g_{MM}(r_{PP})$~4.65Å, which are not observed in the other two functions.
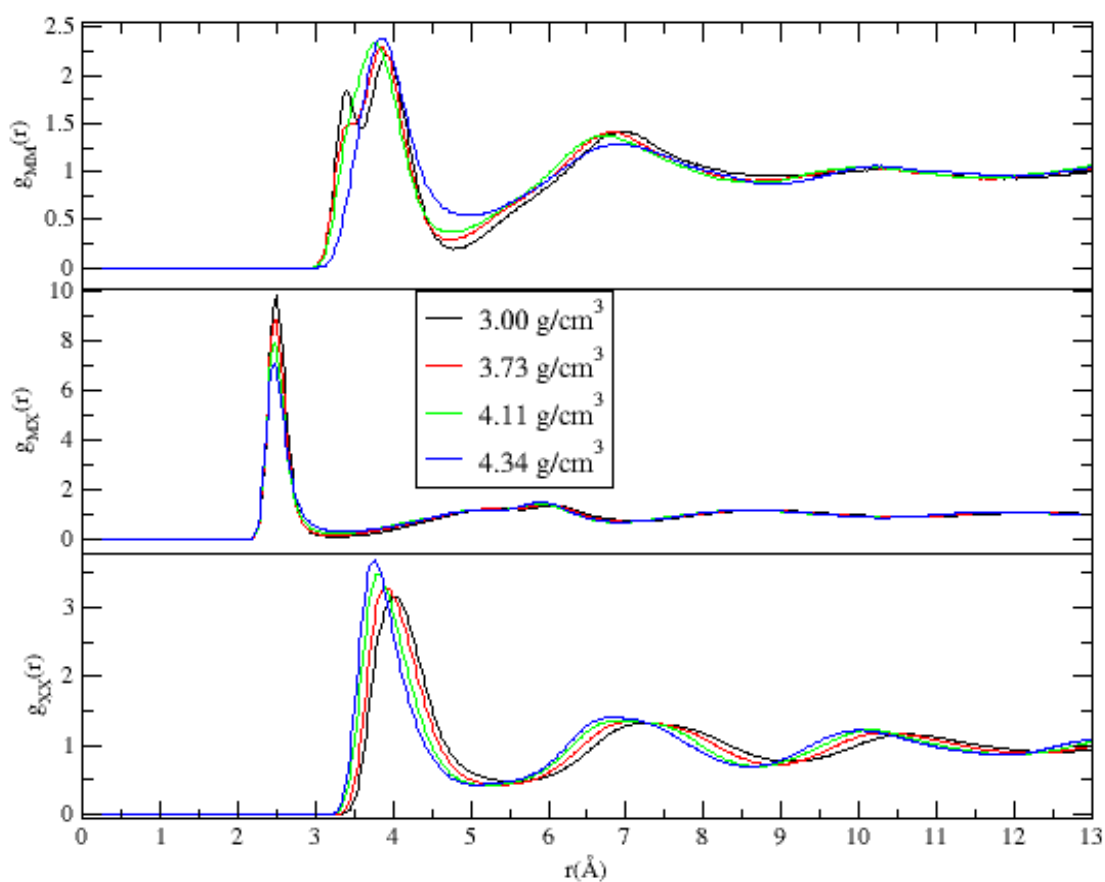
Figure 8.4: Radial distribution functions, $g_{\alpha\beta}(r)$, of MX$_2$ systems, when α_X=35.0 a.u, in the density range 3.00-4.34 g/cm^3. Black line, 3.00 g/cm^3; red line, 3.73 g/cm^3; green line, 4.11 g/cm^3; blue line, 4.34 g/cm^3.

Figure 8.5 shows the changes in the mean coordination number, M_{ij}, for the different ion-pairs for varying densities for both α_X=15 a.u and α_X=35 a.u. For α_X=15 a.u, the changes in M_{XM} and M_{MX} shows a faster rise in increasing coordination than for α_X=35 a.u. The changes with density for M_{XX} and M_{MM} are similar; the values for M_{MM} at all densities are greater for α_X=15 a.u whilst the reverse occurs for M_{XX} at α_X=35 a.u. At lower densities, the cation-anion coordination number tends towards a strongly four coordinate system with percentage values of 96.93% and 98.45% at 3.00 g/cm^3 and 3.13 g/cm^3 for α_X=35 a.u and 15 a.u respectively. At the highest density, these values reduce to 63.28% and 38.31% for α_X=35 a.u and 15 a.u respectively. This shows that the increase in density can be accommodated by changes in the bonding between tetrahedra for the higher anion polarisabililty systems; at lower anion polarisabilities, the changes in coordination dominate.
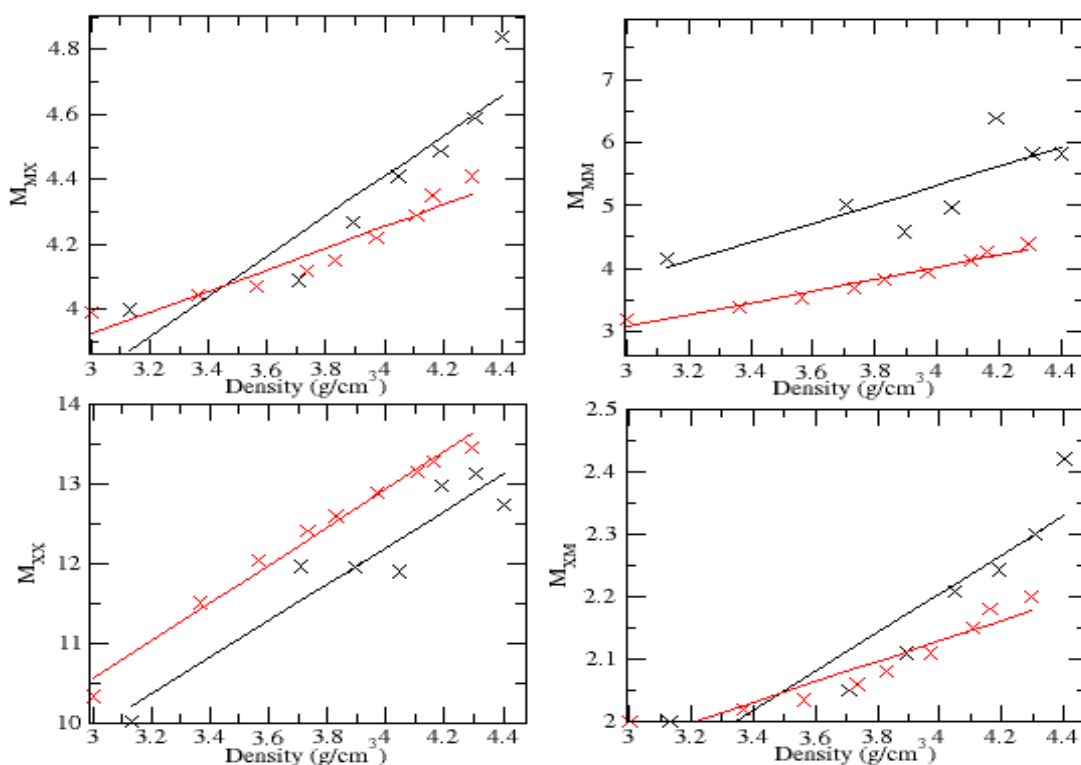
Figure 8.5:Mean coordination number, $M_{\alpha\beta,}$ of ion pairs in MX$_2$ where α_X=15 a.u (black) and 35 a.u (red)

8.5 Changes in bond angle distribution functions in MX$_2$ with density.

Figure 8.6 shows the changes in the bond angle distribution for α_X=15 a.u. For M-M-M, there is an increased overall area with increasing density and an increasingly sharp peak at 50º. For M-M-X, the early peak at 30º decreases in relative magnitude compared to the

latter 100° peak with increasing density. With increasing density, there is a widening of the FWHM in the M-X-M bond angle distribution. The intensity at ~96° increases, arising from the larger presence of 5 and 6 coordinate M cations at higher densities. There are two contrasting X-M-X distributions over the density range: firstly, at low densities a symmetrical peak around 105° is observed, indicating a strongly tetrahedral distribution; the second limit, at high densities, is signified by the characteristic tail at ~160° and an earlier peak at 90° indicating a strongly square-planar/octahedral geometry.
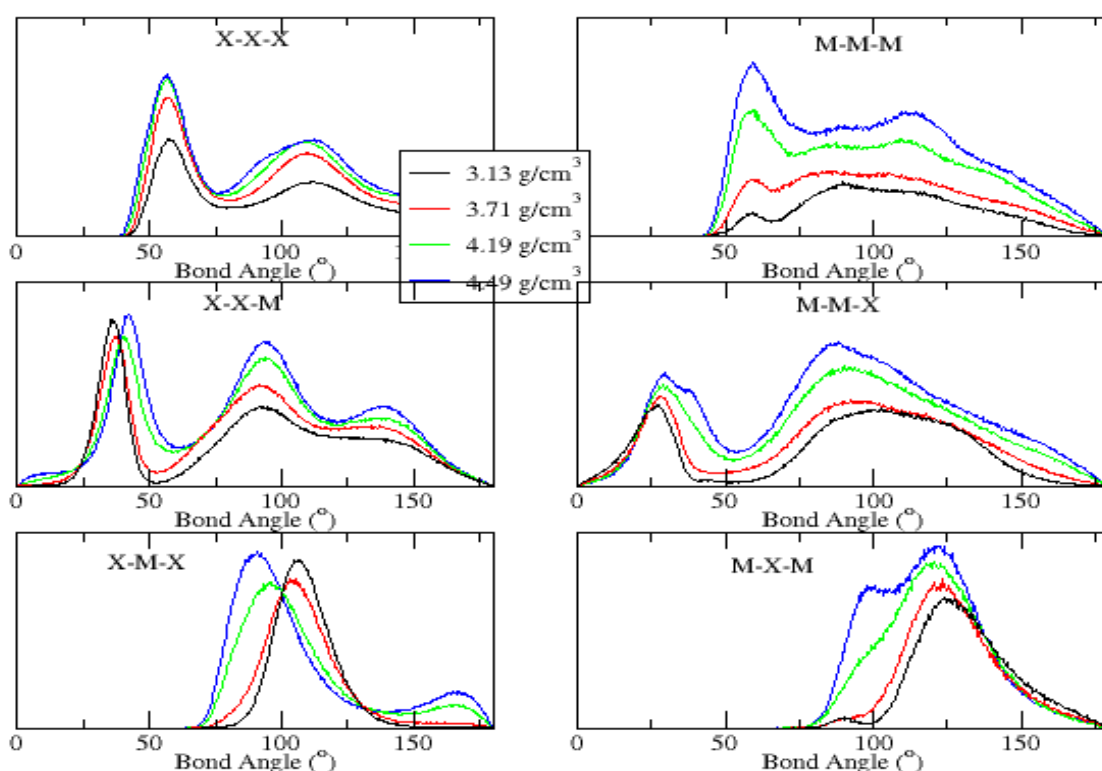
Figure 8.6:Bond angle distributions for MX$_2$, when α_X=15.0 a.u in the density range 3.13-4.49 g/cm^3. Black line, 3.13 g/cm^3; red line, 3.71 g/cm^3; green line, 4.19 g/cm^3; blue line, 4.49 g/cm^3.

Figure 8.7 shows the accompanying changes in the bond angle distribution for α_X=35 a.u. With decreasing density, the M-X-M bond angle distribution increasingly separates into two resolved peaks at ~83° and ~104°. From 4.11 g/cm^3 to 3.00 g/cm^3, the M-X coordination is highly 4-coordinate so the divergence of the two peaks, as highlighted by the declining intensity of the minima at 91°, shows that the corner and edge-sharing geometries are increasingly distinguished from intermediate configurations resulting from miscoordination or frustration caused by packing at higher densities. These changes are also reflected in the X-M-X distribution where the tail at ~160° diminishes with

declining density and the X-M-X increasingly takes the form of a symmetrical peak around 108°. The M-M-X distribution observes a split in the peak at 43° at the lowest density in contrast to the analogous functions for α_X=15 a.u.
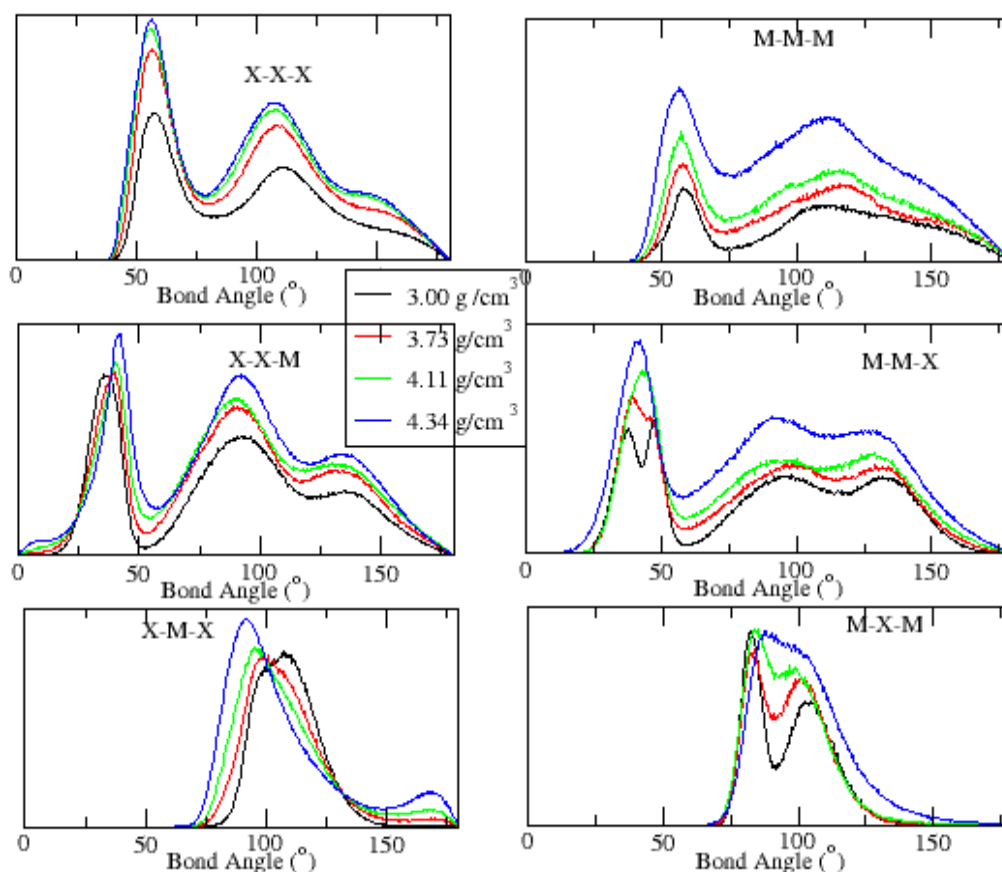
Figure 8.7:Bond angle distributions for MX$_2$, when α_X=35.0 a.u in the density range 3.00-4.34 g/cm^3. Black line, 3.00 g/cm^3; red line, 3.73 g/cm^3; green line, 4.11 g/cm^3; blue line, 4.34 g/cm^3.

The results so far show that in the density-range covered, there are two separate changes occurring in the MX$_2$ structure. At α_X=15 a.u, the system moves from one that is corner-sharing to one with a small amount of edge-sharing; this change occurs at very low densities and is responsible for the splitting of the FSDP in figure 8.1. When α_X=35 a.u, the system already has significant edge-sharing present and the decrease in density is accommodated by strengthening of the edge- and corner-sharing tetrahedral network, both in increasing four-coordination and the arrangement of geometry as shown in figure 8.7.

8.6 Changes in network-connectivity functions in MX$_2$ with density.

As shown in Chapter 5, S$_{MM}$(k) can be decomposed into partial structure factors based on the network connectivity of cations according to the number of four-membered rings they are bonded to. Figure 8.8 shows the breakdown of configurations taken at densities of 4.34 and 3.00 g/cm^3 for the MX$_2$ system at α_X=35 a.u. The results show that $S_{MM}^{22}(k)$ and $S_{MM}^{00}(k)$ display phase separation at both densities and so are not responsible for the change in in the FSDP of S$_{MM}$(k). $S_{MM}^{01}(k), S_{MM}^{02}(k), S_{MM}^{11}(k),$ and $S_{MM}^{12}(k)$ exhibit FSDP at both densities although in all cases they are reduced at the higher density, by 0.12, 0.05, 0.28 and 0.11 respectively. The biggest decrease in FSDP intensity is clearly observed in $S_{MM}^{11}(k)$. There is also a shift to higher scattering angles, with $S_{MM}^{02}(k_{FSDP})$ exhibiting the largest change from 0.95-1.16Å^{-1} while $S_{MM}^{11}(k_{FSDP}), S_{MM}^{12}(k_{FSDP}), S_{MM}^{12}(k_{FSDP}),$ and $S_{MM}^{01}(k_{FSDP})$ observe changes of 0.96-1.04Å^{-1}, 0.99-1.10Å^{-1}, and 0.97-1.10Å^{-1} respectively. Large changes are observed in the principal peak intensities of $S_{MM}^{22}(k_{PP}), S_{MM}^{01}(k_{PP})$ and $S_{MM}^{02}(k_{PP})$. $S_{MM}^{22}(k_{PP})$ increases by 0.3 from 0.10, while the latter two collapse from 0.36 to 0.09 and 0.39 to
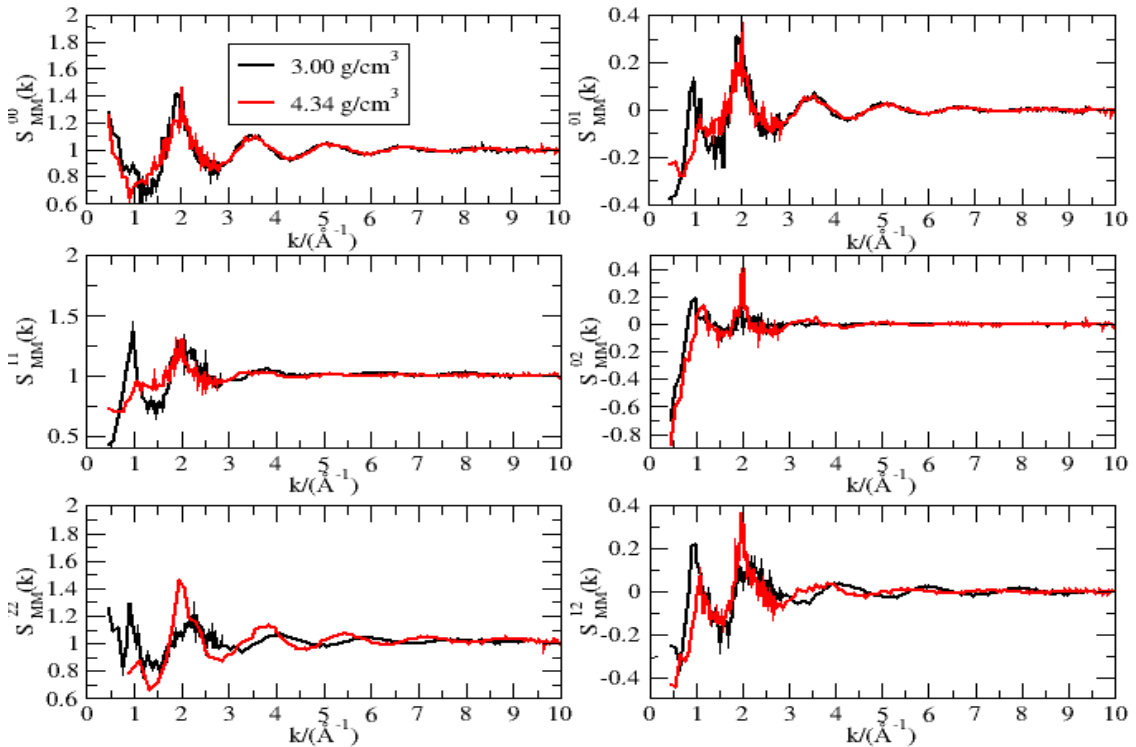
Figure 8.8 : Change in network connectivity cation-cation structure factors, $S_{MM}^{ab}(k)$, with density. Black line, 3.00 g/cm^3; red line, 4.34 g/cm^3.

0.03. The remaining functions, $S_{MM}^{11}(k_{PP})$, $S_{MM}^{12}(k_{PP})$ and $S_{MM}^{00}(k_{PP})$ show much smaller changes of 0.01, 0.02 and 0.01.

Figure 8.9 shows the related network connectivity radial distribution functions. In all the functions, there is a decrease in the value of the minima at ~4.7Å with decreasing density. $g_{MM}^{02}(r)$ shows dramatic changes with regards to the intensity of the principal peak showing a sharp decline with decreasing density from 1.52 at 4.34 g/cm^3 to 0.46 at 3.00 g/cm^3. This is understood if we idealise the interaction between the "0" and "2" cations as having an especially weak ordering over the usual cation-cation separation due to the presence of a "1" cation as an intermediate site. The large difference between this, close to ideal, $g_{MM}^{02}(r)$ and those exhibited at experimental densities (in Chapter 5) shows the effect of increased coordination in perturbing the network structure. In contrast, features such as similar minima in $g_{MM}^{22}(r)$ show that this feature is not dependent on the density: the presence of two edge-sharing units around a central cation effectively fixes the short-range ordering at ~4.5Å. $g_{MM}^{22}(r_{PP})$ and $g_{MM}^{12}(r_{PP})$ also observe changes in intensity of 10.07 to 4.49 and 5.67 to 1.99, whilst the corresponding values for $g_{MM}^{00}(r_{PP}), g_{MM}^{01}(r_{PP})$ and $g_{MM}^{11}(r_{PP})$ of 10.79 to 7.28, 4.75 to 4.75, and 2.88 to 2.18 are smaller. $g_{MM}^{11}(r)$ shows a split of the principal peak into an edge-sharing peak at 3.36Å and a corner-sharing peak at 3.95Å which is observed from 4.11 g/cm^3 to 3.00 g/cm^3, in contrast to the highest density configuration where the edge-sharing peak is reduced to a shoulder. As might be expected, the distinction between the corner- and edge-sharing peaks is much stronger than observed for ZnCl$_2$ in chapter 7. The ratio of the intensities of the edge-sharing peak to the corner-sharing peak increases with decreasing density showing that the effective distribution of "1" cations adopts morphologies which maximise the edge-sharing character.
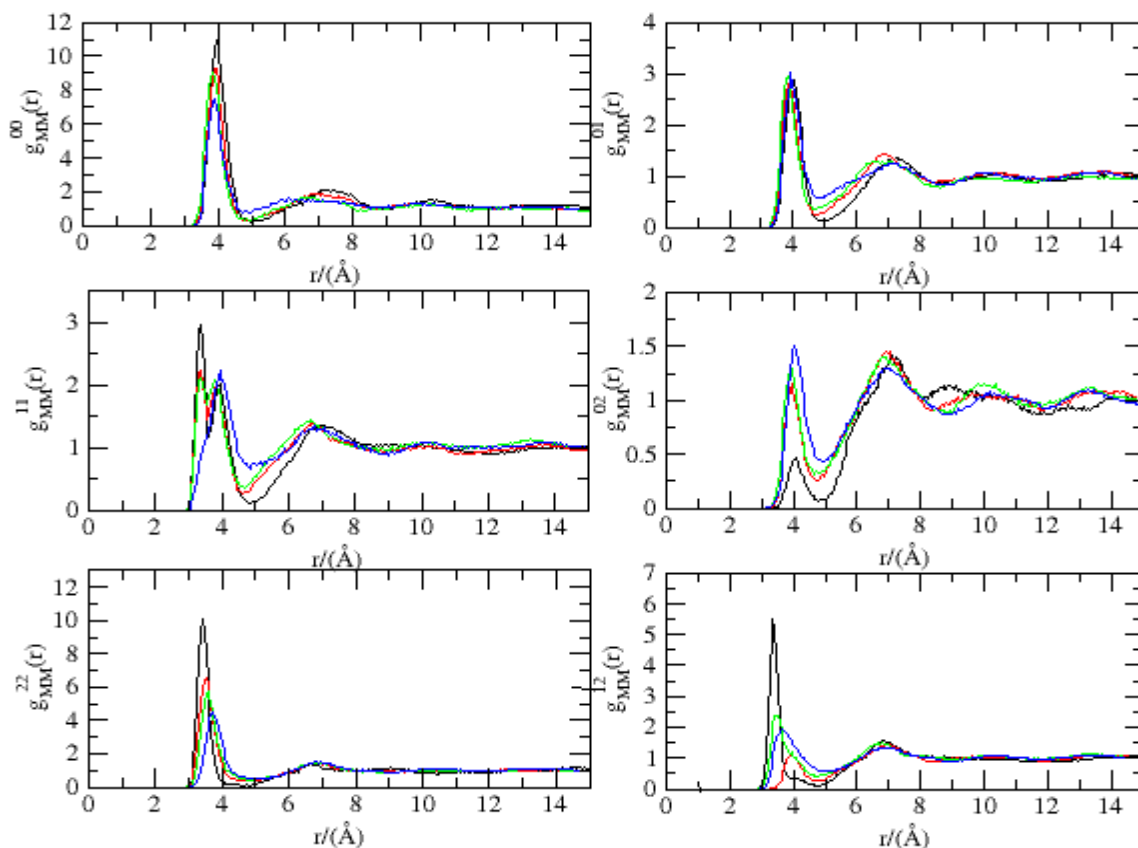
Figure 8.9:Changes in the network connectivity based radial distribution functions, $g_{MM}^{ab}(r)$, where a,b ={0,1,2}, with density. Black line, 3.00 g/cm^3; red line, 3.73 g/cm^3; green line, 4.11 g/cm^3; blue line, 4.34 g/cm^3.

8.7 Change of MX$_2$ (α_X=35.0 a.u) structure with increasing temperature.

In order to study the effect of increasing temperature on systems with high anion polarisability, the temperature of the system at a density of 3.73 g/cm^3 was raised in 1000K increments to 7000K. Figure 8.10 shows that at the higher temperature there is a sharp decline observed in the intensity of $S_{MM}(k_{FSDP})$ with a 34% drop in the intensity of the FSDP from 1.22 to 0.81. There is no significant FSDP in $S_{XX}(k)$ and $S_{MX}(k)$ at either temperature. The position of the FSDP in $S_{MM}(k)$ shifts from 1.04Å^{-1} at 2000K to 1.18Å^{-1} at 7000K. A larger drop in the intensity of the principal peak is observed for $S_{MM}(k_{PP})$ of 17% (1.80 to 1.49) compared to 8% for $S_{MX}(k)$ (-1.202 to -1.10) and 9% for $S_{XX}(k)$ (3.29 to 2.99). There is also a large shift in the position of both the FSDP and principal peak in $S_{MM}(k_{PP})$ with increasing temperature of 0.14Å^{-1} compared to no shift in $S_{MX}(k_{PP})$ and 0.02Å^{-1} increase for $S_{XX}(k_{PP})$. For systems displaying larger FSDPs in $S_{MM}(k)$, it shows a

simple model is able to predict the deterioration of the FSDP with temperature without the presence of homopolar bonding.
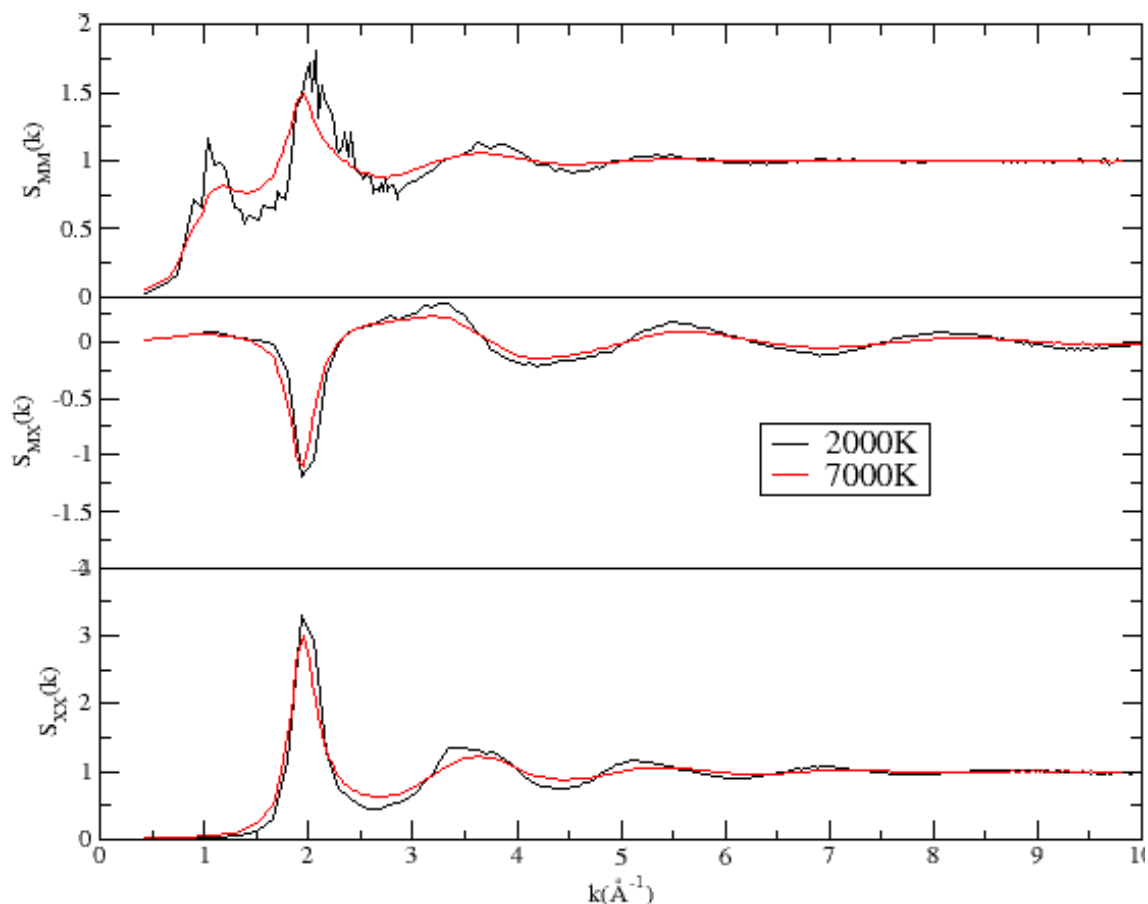
Figure 8.10:Partial structure factors of MX$_2$ at 2000K and 7000K. Top, S$_{MM}$(k); middle, S$_{MX}$(k); bottom, S$_{XX}$(k)

Figure 8.11 shows the changes in the radial distribution functions with increasing temperature. The intensity of the principal peaks decrease with increasing temperature; the change is largest in g$_{MX}$(r$_{PP}$), from 8.09 to 4.53, compared to 2.35 to 1.63 for g$_{MM}$(r$_{PP}$) and 3.52 to 2.55 for g$_{XX}$(r$_{PP}$) where there is a slightly smaller reduction. In contrast to the changes observed with pressure, there is a shift in position of the principal peak of g$_{MX}$(r$_{PP}$) from 2.46Å at 2000K to 2.42Å at 7000K. The respective changes for g$_{MM}$(r$_{PP}$) and g$_{XX}$(r$_{PP}$) are from 3.75Å to 3.83Å and 3.83Å to 3.77Å. The second peak in g(r), observes differing behaviour between the ion pairs: the intensity of the second peak in g$_{MM}$(r) decreases in intensity from 1.41 to 1.18 while the changes in g$_{MX}$(r) and g$_{XX}$(r) are much smaller at 1.43 to 1.35 and 1.36 to 1.28 respectively.
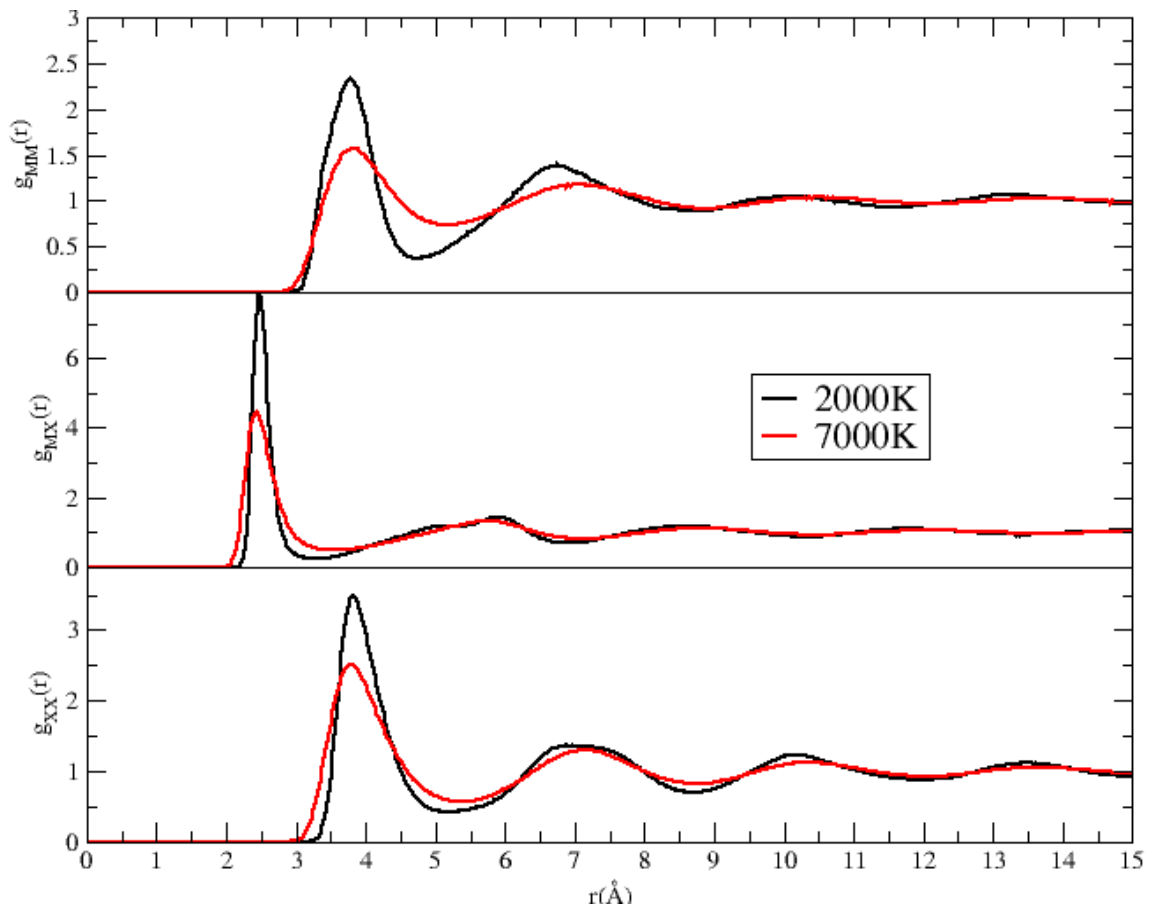
Figure 8.11: Radial distribution functions, $g_{\alpha\beta}(r)$, of MX$_2$ systems at 2000K and 7000K.

Table 8.1 highlights the changes in coordination. At the higher temperature, there is an increase in disorder, as defined by the increasing percentage of miscoordinated M-X and X-M ion pairs diverging from the ideal tetrahedral values of 4 and 2 respectively. The percentage of 1-coordinate anions increased from 1.85% at 2000K to 11.09 at 7000K, while four (cation-anion) coordination declines from 72.29% to 59.87%, with 3-coordination increasing to 10.23%, much higher than the values exhibited at the lowest density at 2000K (3.08% at 3.00 g/cm^3).

Temperature	N_{MX}=3	N_{MX}=4	N_{MX}=5	N_{MX}=6	N_{XM}=1	N_{XM}=2	N_{XM}=3
2000K	0.27	72.29	26.85	2.93	1.85	81.63	20.19
7000K	10.23	59.87	24.66	2.77	11.09	67.70	16.23

Table 8.1: Effect of temperature on the coordination pairs MX and XM in a MX$_2$ system.
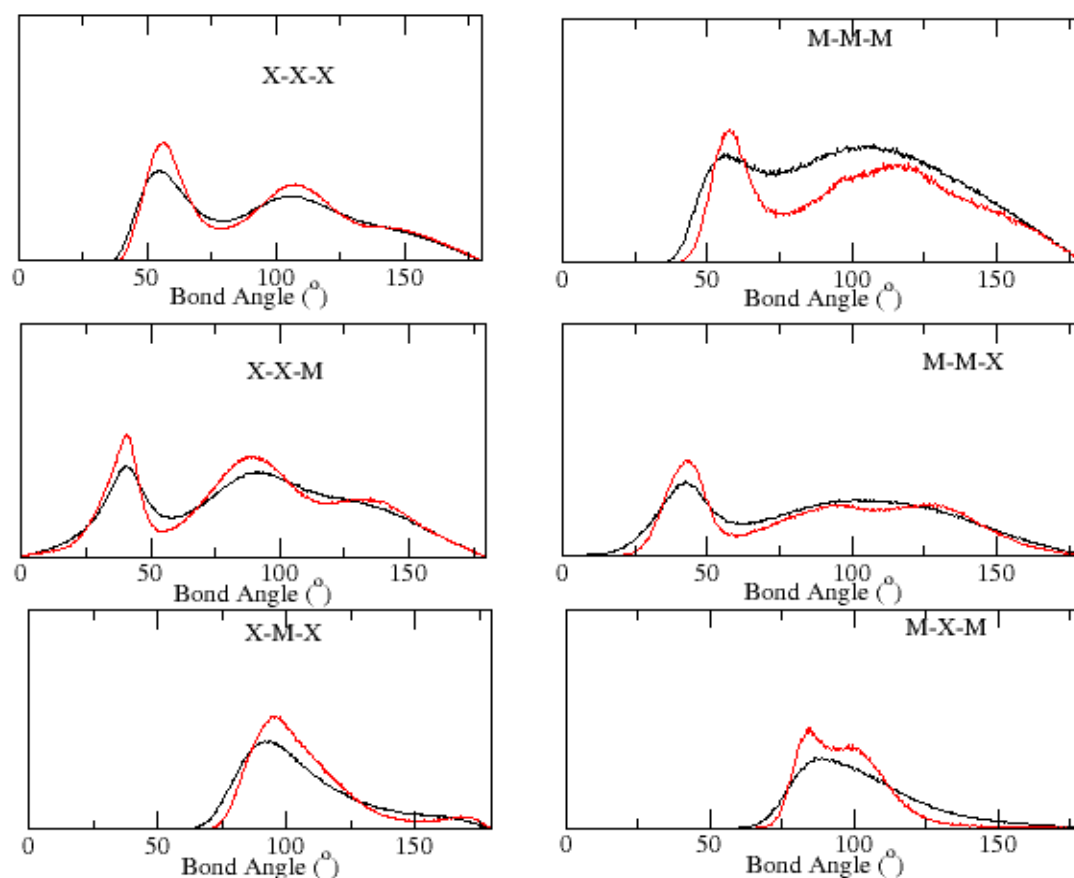
Figure 8.12:Bond angle distributions for MX_2 at 2000K and 7000K. Black line, 2000K; red line, 7000K

The bond angle distributions of the higher temperature configurations (figure 8.12) show a weakening of the features associated with the mixed edge- and corner-sharing tetrahedral network present at 2000K. This is highlighted in the M-X-M distribution where the peaks at 84° and 101° representing the bond angles associated with edge and corner-sharing tetrahedra are reduced in intensity and a single peak is formed. The related change in X-M-X is more subtle; the peak shifts from 97° to 92° at 7000K and there is a weakening of the distinction between this peak and the tail at 160°. The changes in M-M-M are larger than those in other functions with a substantial reduction in the minima at 75° which separates the low and high peaks. This is an indication of the effect of coordination change and the transition of a mixed edge- and corner-sharing tetrahedral network to one with more molecular features present.
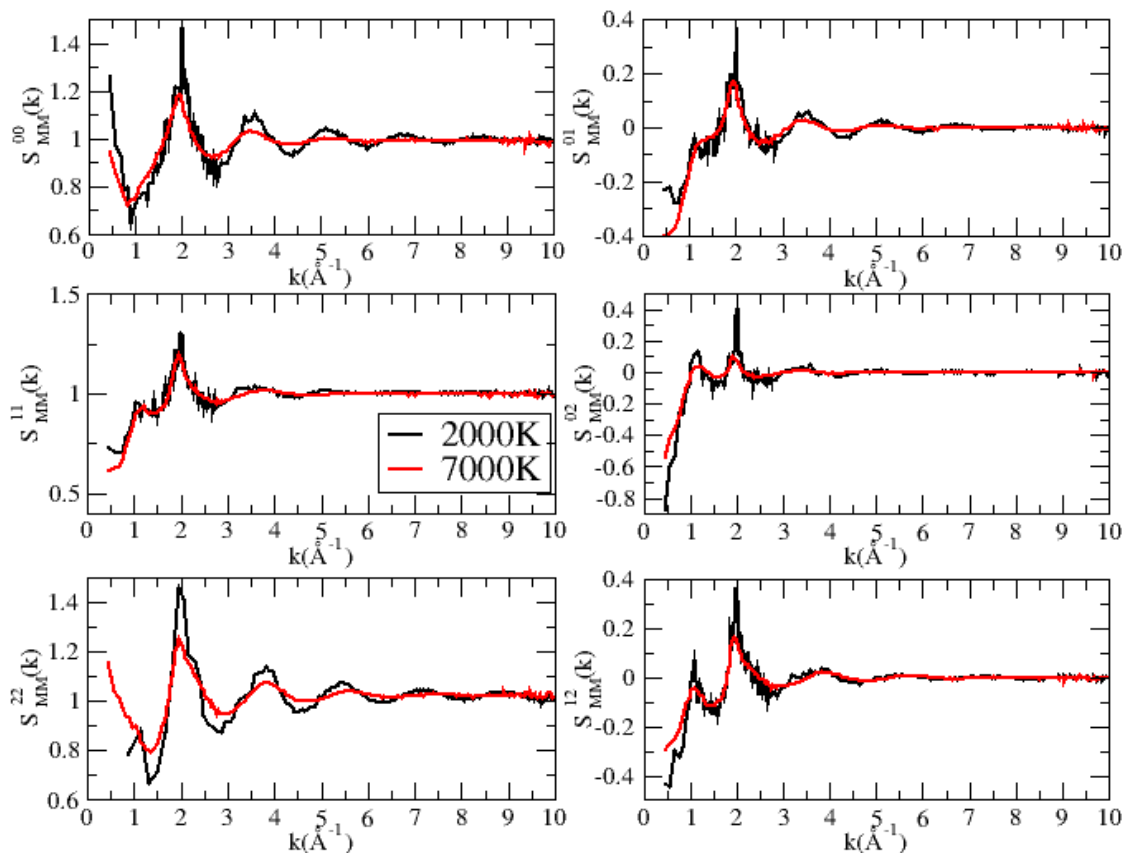
Figure 8.13 :Change in network connectivity cation-cation structure factors, $S_{MM}^{ab}(k)$, with temperature. Black line, 2000K; red line, 7000K.

The network connectivities at the two temperatures are shown in table 8.2. With increasing temperature, there is a sharp reduction in the percentage of "2" cations and an increase in "0" cations. This is further evidence that changes in the structural properties are indicative of an underlying change in network-connectivity with increasing temperature. These values are closer to that observed in the FPMD calculations in Chapter 4.

Network Connectivity	*MX$_2$(2000K)*	*MX$_2$(7000K)*
E^0	29.1 (2.4)	42.3 (3.5)
E^1	40.2 (2.1)	42.7 (2.8)
E^2	30.7 (2.7)	15.0 (2.7)

Table 8.2: Percentage of cation colored according to their network connectivity for high and low temperature configurations of MX$_2$.

Figure 8.13 shows the partial network connectivity structure factors at 2000K and 7000K. $S_{MM}^{22}(k)$ and $S_{MM}^{00}(k)$ exhibit phase separation at both temperatures with sharply damped oscillations at k >4Å. $S_{MM}^{02}(k)$ and $S_{MM}^{12}(k)$ show the sharpest decline in FSDP intensity with increasing temperature and is responsible for the loss of intensity of the FSDP at ~1Å^{-1} at the higher temperature. $S_{MM}^{01}(k)$ and $S_{MM}^{11}(k)$ show the smallest change in FSDP intensity, although $S_{MM}^{01}(k_{FSDP})$ becomes a shoulder. This shouldering, due to the relatively large c_0c_1 at the higher temperature, dominates the character of the partial structure factor, S$_{MM}$(k), especially over the range of 1-2Å where similar shouldering is observed. $S_{MM}^{01}(k)$ and $S_{MM}^{02}(k)$ also show the largest movement in position with an increase of 0.11Å^{-1} and 0.13Å^{-1} from 1.09Å^{-1} and 1.05Å^{-1} respectively. The changes in $S_{MM}^{11}(k)$ and $S_{MM}^{12}(k)$ are smaller with shifts of 0.04Å^{-1} and -0.05Å^{-1} from 1.09Å^{-1} and 1.13Å^{-1} respectively. The principal peak intensity observes a decline in all structure factors, particularly in $S_{MM}^{02}(k)$ and $S_{MM}^{22}(k)$. $S_{MM}^{11}(k_{PP})$ shows the smallest decline in intensity.

The network-connectivity radial distribution functions are exhibited in figure 8.14. Figure 8.11 showed large changes in g$_{MM}$(r) with a decline in principal peak intensity, increase in the minima of the principal peak and the decline in intensity of the second peak. $g_{MM}^{00}(r)$ shows the sharpest decrease in the intensity of the principal peak of declining from 9.75 to 3.79. The principal peak position in $g_{MM}^{01}(r)$ increases by 0.19Å from 3.81Å at 2000K. The changes in the position in the other functions are smaller with increases of 0.04Å , 0.06Å , 0.13Å and 0.07Å for $g_{MM}^{00}(r), g_{MM}^{22}(r), g_{MM}^{02}(r)$ and $g_{MM}^{12}(r)$. The split peak feature resolved at 2000K in $g_{MM}^{11}(r)$ is removed at 7000K. All functions except $g_{MM}^{22}(r)$ show a substantially increased minima of the principal peak at ~4.7Å; the largest change occurs in $g_{MM}^{02}(r)$. The intensity of the oscillations r>r$_{PP}$ decrease at the increased temperature with this effect being particularly strong in $g_{MM}^{00}(r)$.
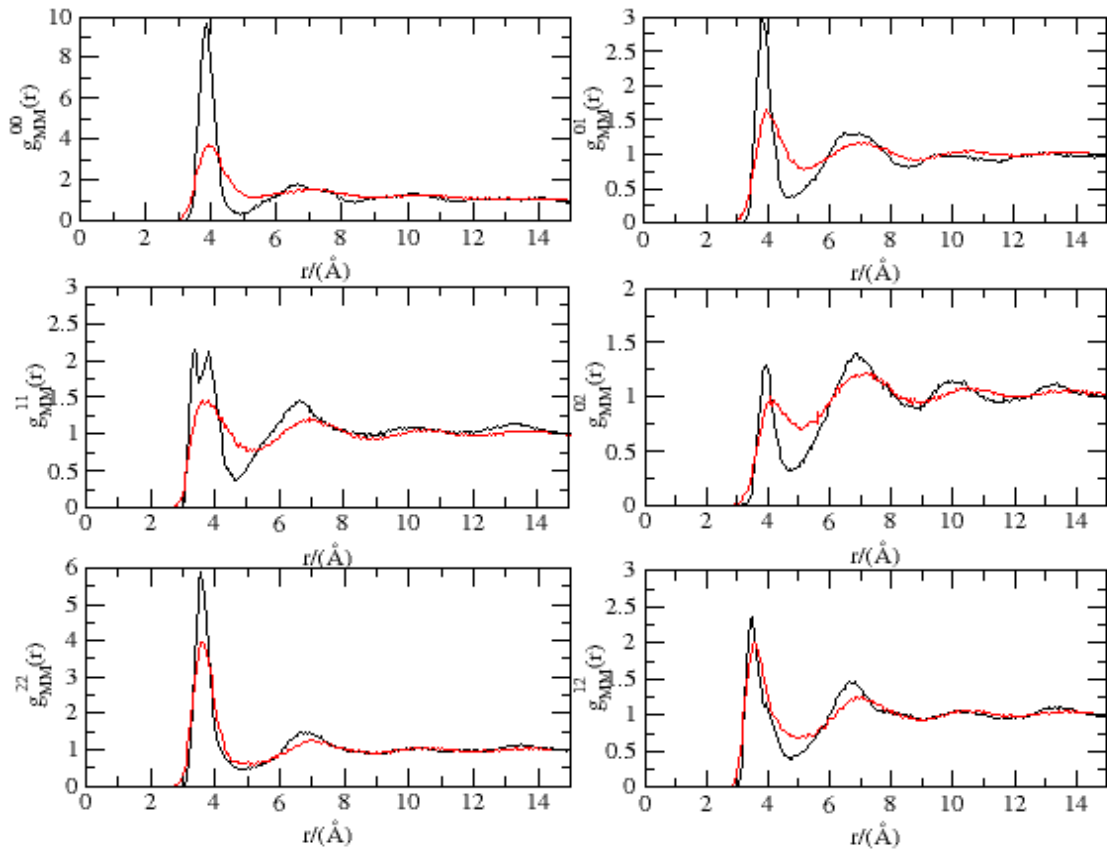
Figure 8.14: Changes in network connectivity radial distribution functions, $g_{MM}^{ab}(r)$, where a,b = {0,1,2}, with temperature. Black line, 2000K; red line, 7000K.

8.8 Conclusion.

The structural behaviour of systems with high and low anion polarisability at various densities has been studied. The anion polarisability can be considered as controlling the network topology (via constraining the cation-anion-cation bond angle), whilst changes in density may control the distribution of local ion coordination environments.

At α_X=15 a.u, the principal peak of $S_{MM}(k)$ splits at the lowest density, indicating the formation of a longer length scale associated with IRO; the FSDP in $S_{MX}(k)$ also increases over the range. These relatively low k features at ~1.2Å^{-1} at 3.13 g/cm^3 are not observed experimentally in systems such as GeO$_2$[14] and are taken to be a feature of reducing the density from experimental values. The structure factors of glassy GeO$_2$ from neutron diffraction experiments by Salmon *et al*[14] show a FSDP in $S_{OO}(k)$ which is not observed at any density in our model. As the model was based on the short-range repulsion parameters of GeSe$_2$, the actual correlation lengths are larger than that

exhibited in GeO$_2$ (3.16Å, 1.73Å, 2.83Å for the experimental GeGe, GeO, and OO separations[15] compared to 4.45 -4.30Å , 2.47Å and 4.08-3.76Å observed over the density range in our calculations). Our main priority in this chapter was to observe the densification mechanism and how it affects IRO for systems of high and low anion polarisability. A continuous rise in MX coordination at α_X=15 a.u is observed with changing density in our results. Pressure studies on GeO$_2$ have shown that with increasing pressure the coordination increases. The nature of the coordination increase varies with glassy GeO$_2$ show a sharp increase in coordination to ~5 at 6GPa and ~6 at 15GPa.[16] EXAFS experiments on liquid GeO$_2$ indicate a sharp rise in coordination at 2.5GPa to 3GPa[18], indicating that such such transformation of rigid tetrahedra is responsible for the densification mechanism up to this pressure. Our model, which does not show the discontinuous rises in coordination observed experimentally, agrees with MD calculations on GeO$_2$[20], where the predominant structural unit GeO$_X$ is stable with increased pressure with x=5,6 increasing while those units of x=4 declines.

In contrast to changes at high polarisability, the principal peak in g$_{MM}$(r) decreases in position with increasing density from 4.45Å to 4.30Å from 3.13 to 4.49 g/cm^3. In the related radial distribution functions, greater changes were observed in 5-9Å range of g$_{MM}$(r) than in the principal peak, except at the lowest density, where a small edge-sharing peak was observed. This is in contrast with recent MD simulations where a smaller distance peak in g$_{MM}$(r) in GeO$_2$ is attributed to edge-sharing (as part of five and six coordinate species) at higher pressures[19]. The same study displays a decline in the anion-anion separation with increasing density similar to our results. Experimental studies also show an elongated GeO correlation length with increasing pressure from ~1.7Å to 2.5Å[16] which was not observed in our results.

One densification mechanism proposed after neutron diffraction experiments with glassy GeO$_2$ by Sampath *et al*[17] involves the rotation of rigid tetrahedral units before any increase in MX coordination. This mechanism is suppported in part by a MAS NMR experiment on glassy SiO$_2$ which shows a decline in the Si-O-Si bond angle with increasing pressure[27]. The related bond angle distribution functions in our system shows increasingly tetrahedral behaviour at lower densities. With increasing density, our bond angle distributions show evidence of distortion of the corner-sharing tetrahedra, as indicated by a small decline in the position of the higher angle peak in M-X-M, and associated bond angles of higher coordinate species, as indicated by the increased

intensity of lower bond angle peaks in figure 8.6. Our results show a coordination-dependent densification mechanism dominates for the lower anion polarisability system in addition to changes in the bond angle distribution.

At α_X=35 a.u, the intensity of the FSDP in $S_{MM}(k)$ and $S_{MX}(k)$ increases and moves to slightly higher scattering angles with increasing density. The shift in FSDP of $S_{MM}(k)$ observed over the density range (0.96Å^{-1} at 3.00 g/cm^3 to 1.14Å^{-1} at 4.34 g/cm^3) is similar to that observed for increasing pressure in glassy[3] (1.010Å^{-1} to 1.225Å^{-1}) and liquid[5] GeSe$_2$, where the FSDP position increases from ~0.9Å^{-1} (upper limit unspecified). At higher polarisabilities, where there is already significant edge-sharing at higher-pressures, the effect of decreasing density is to effectively sharpen these edge-sharing features, as indicated in the bond angle distribution, with clearer edge- and corner-sharing peaks observed in M-X-M distributions, and by the tightening of the coordination shell to strongly 4-MX coordination. These effects are further highlighted in the network connectivity functions, where the interaction of "0" with "2" cations results in a collapsed principal peak in $g_{MM}^{02}(r)$. This change supports the experimental interpretation where a 2D-3D transition (from a system with edge-sharing to a corner-sharing system) is proposed as the cause for the decline in FSDP intensity in liquid GeSe$_2$ when pressure is applied.[3]

Our calculations indicate that at α_X=35 a.u there is a greater dependence on the MM correlations on IRO with changes than density, than at α_X=15 a.u, where MM and MX contribute to the smaller IRO present. In the experimental total structure factors of GeSe$_2$[5], the ratio of the principal peak (at ~2Å^{-1}) against the third peak (at ~3.5Å^{-1}) is observed to increase with increasing pressure. Our model shows a stronger increase in the intensity of the principal peak in $S_{XX}(k)$ compared to a smaller increase in $S_{MX}(k_{PP})$ which would result in a similar increase in F(k). A shift in the $g_{MM}(r)$ principal peak position to higher values indicative of an increase in corner-sharing tetrahedra is observed in our results. This agrees with the result highlighted experimentally by the difference functions in experiments of densified glassy GeSe$_2$ where SeSe correlations are removed, and the second peak is observed to shift from 3.63Å to 3.72Å[5]. When GeGe correlation are removed, there is no significant shift of this peak which disagrees with our results describing the decline in anion-anion separation. In the experimental total radial distribution function of liquid GeSe$_2$ with increasing pressure[3], the largest change occurs at ~3Å, corresponding to the minimum of $g_{GeSe}(r)$; our results show no correlation

with this observed feature with the minimum of $g_{MX}(r)$ (figure 8.4) stable to changes in density. In contrast to experimental results, an elongation of the GeSe bond[3] (from 2.32Å to 2.46Å) is not observed here and the effects of homopolar bonds (observed at atmospheric pressure but no experimental evidence as to their changing abundance with increasing pressure) on any densification mechanism are not considered here. As such, our results contrast with electronic structure calculations on GeSe$_2$[9] which show large changes in the chemical ordering upon application of large pressure (upto 60GPa), with substantial increases in homopolar bonding with increased pressure.
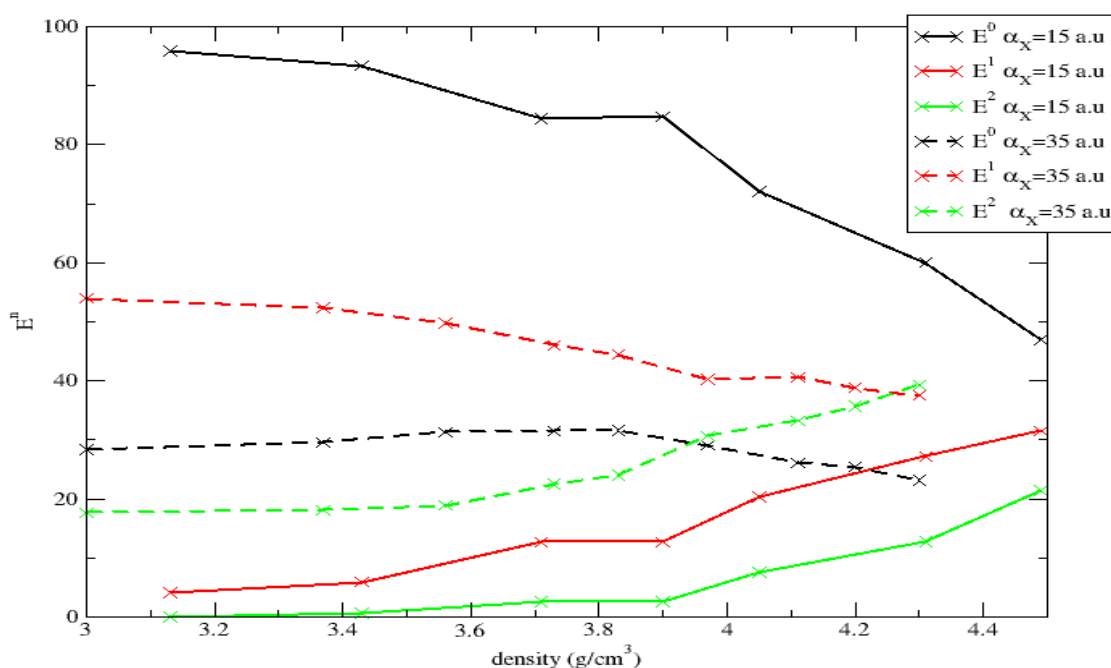
Figure 8.15:Change in network connectivity with density at α_X=15 a.u (full line) and α_X=35 a.u (dashed line) as indicated by changes in the percentage of cations with n number of four-membered rings, E^n where n=0-2.

Figure 8.15 shows the changes in network connectivity at α_X =15 a.u and α_X =35 a.u, with changing density. Larger changes in network connectivity are observed at α_X =15 a.u, driven in part by faster changes in coordination. The sharpening of the coordination distribution for both polarisabilities results in a better correlation of the network connectivity statistics with the structure observed. For α_X =15 a.u, the formation of a small number of edge-sharing units, indicated by the small "1" percentage at the lowest density (3.13 g/cm^3), and this correlates with $g_{MM}(r)$, where a small edge-sharing peak observed in figure 8.3, in addition to the overwhelmingly dominant corner-sharing peak.

In addition, no significant FSDP intensity was observed at 1Å^{-1} at any density when α_X=15 a.u, indicating that the density decline does not impose IRO on the systems and that the structural origin for the nature of IRO is dominant. For α_X=35 a.u, the decline in density results in a strengthening of the 4-coordination. In contrast to α_X=15 a.u, where "0" cations increase, an increase in the preponderance of edge-sharing linkages are observed. The edge-sharing "1" cations increase with decreasing density while the proportion of "0" and "2" cations decline. The rise in "0" cations is much smaller than that observed at α_X=15 a.u, an indication of the strong presence of edge-sharing units. In section 7.9, we highlighted three possible mechanism for changes in network connectivity with pressure: strongly coordination-dependent, edge-sharing to corner-sharing and edge-sharing to six-coordinate mechanisms. At α_X=15 a.u, moving from high to low density, the reduction in "1" and "2" cations with strengthening 4-coordination are an indication that a coordination-dependent mechanism is dominant. In contrast, at α_X=35 a.u, an increase in "1" cations, a slower rise in "0" cations than is observed at α_X=15 a.u, and a reduction in "2" cations indicates of a mixture of coordination-dependent and corner-to edge-sharing mechanisms occurring.

With increasing temperature, the system at high polarisability shows a decrease in FSDP intensity in S$_{MM}$(k) and S$_{MX}$(k). Other indications of increased disorder include increased miscoordination and weakening of the intensity of peaks in the bond angle distribution. Also highlighted is the reduction in separation of the edge- and corner-sharing peaks in $g_{MM}^{11}(r)$. Electronic structure calculations with increasing temperature also show that with increasing temperature the FSDP declines.[11] In addition to the FSDP, the principal peak in S$_{SeSe}$(k) and S$_{GeGe}$(k) show a sharper decline in intensity than is observed with increasing temperature in our calculations. We attribute this to the different deterioration in short-range order an extended ionic model has compared to FPMD. In our model, where due to the strong Coulombic interactions present, homopolar bonding is precluded, the effect of increased temperature is to break up the presence of edge-sharing units as shown by declining proportions of "1" and "2" cations, favouring of corner-sharing connections between the coordination polyhedra, and increased presence of lower coordinate M and X species. In the FPMD calculations of Massobrio[11], in addition to the decrease in coordination, there is also predicted to be a decline in chemical order with increased homopolar bonding. The major structural features which occur in GeSe$_2$ with increasing temperature is the decline in the intensity

of the FSDP. In addition, the third peak at ~3.5Å^{-1} in the experimental S$_{NN}$(k) declines in intensity faster than the smaller changes observed in the principal peak; electronic structure calculations exhibit a collapse of chemical order with increasing temperature and show a merging of the third and second peak with increasing temperature. No significant change in mean coordination number is observed with the increase in temperature experimentally[1], and our results highlight the same; it is the distribution of coordination numbers around the mean which shows greater variation at higher temperature. A shift in the position of the FSDP, observed experimentally from 0.95Å^{-1} to 1.04Å^{-1} from 1073K to 1373K, while our system observes a shift from 1.05-1.18Å^{-1}. Our model indicates that many of the structural changes observed experimentally in GeSe$_2$ can be observed in a model where chemical order is maintained.

8.9 References.

[1] I. Petri, P. S. Salmon and W. S. Howells. *J. Phys.:Condens. Matter*, **11,** 10219, (1999)

[2] J. Ruska and H. Thum. *J. Non-Cryst. Solids.* **22**, 277, (1976).

[3] W. A. Crichton, M. Mezouar, T. Grande, S. Stølen and A. Grzechnik. *Nature,* **414**, 622, (2001).

[4] F. Wang, S. Mamedov, P. Boolchand, B. Goodman, and M. Chandrasekhar. *Phys. Rev. B,* **71**, 174201, (2005).

[5] Q. Mei, C. J. Benmore, R. T. Hart, E. Bychkov, P. S. Salmon, C. D. Martin, F. M. Michel, S. M. Antao, P. J. Chupas, P. L. Lee, S. D. Shastri, J. B. Parise, K. Leinenweber, S. Amin and J. L. Yarger. *Phys. Rev. B,* **74**, 014203, (2006).

[6] A. C. Wright. *J. Non-Cryst. Solid*s, **179**, 84, (1994).

[7] C. J. Benmore, R. T. Hart, Q. Mei, D. L. Price, J. Yarger, C. A. Tulk, and D. D. Klug. *Phys. Rev. B,* **72**, 132201, (2005).

[8] S. Asokan, M. V. N. Prasad, G. Parthasarathy and E. S. R. Gopal. *Phys. Rev. Lett*. **62**, 808, (1989).

[9] M. Durandurdu and D. A. Drabold. *Phys. Rev. B,* **65**, 104208, (2002).

[10] M. Durandurdu. *phys. stat. sol(b)*, **242**, 3085, (2005).

[11] C. Massobrio, F. H. M van Roon, A. Pasquarello and S. W. De Leeuw. *J. Phys.: Condens. Matter,* **12**, L697 (2000).

[12] P. Vashishta, R. K. Kalia, G. A. Antonio and I. Ebbsjö. *Phys. Rev. Lett.,* **62**, 1651, (1989).

[13] P. Vashishta, R. K. Kalia and I. Ebbsjö. *Phys. Rev. B* **39**, 6034 (1989).

[14] P. S. Salmon, A. C. Barnes, R. A. Martin and G. J. Cuello. *J. Phys.:Condens. Matter,* **19**, 415110, (2007).

[15] D. L. Price, M. L. Saboungi and A. C. Barnes. *Phys. Rev. Lett*., **81**, 3207, (1998).

[16] M. Guthrie, C. A. Tulk, C. J. Benmore, J. Xu, J. L. Yarger, D. D. Klug, J. S. Tse, H-k. Mao and R. J. Hemley. *Phys. Rev. Lett.,* **93**, 115502, (2004)

[17] S. Sampath, C. J. Benmore, K. M. Lantzky, J. Neuefeind, K. Leinenweber, D. L. Price and J. L Yarger. *Phys. Rev. Lett.,* **90**, 115502, (2003).

[18] O. Ohtaka, H. Arima, H. Fukui, W. Utsumi, Y. Katayama and A. Yoshiasa. *Phys. Rev. Lett*., **92**, 155506, (2004).

[19] M. Micoulat. *J. Phys.: Condens. Matter*, **16**, L131, (2004).

[20] P. K. Hung, N. V. Hong, N. T. Nhan and L. T. Vinh. *Modelling Simul. Mater. Sci. Eng*, **15**, 845, (2007).

[21] V. V. Hoang, N. H. Tuan Anh and H. Zung. *Physica B*, **390**, 17, (2007).

[22] P. K. Hung, H. V. Hue and D. M. Nghiep. *J. Non-cryst. Solids*, **353**, 2163, (2007).

[23] G. Gutierrez and J. Rogan. *Phys. Rev. E*, **69**, 031201, (2004).

[24] M. Micoulat, Y. Guissani and B. Guillot. *Phys. Rev. E*, **73**, 031504, (2006).

[25] V. V. Hoang. *J. Phys.:Condens. Matter*, **18**, 777, (2006).

[26] P. K. Hung, L. T. Vinh, N. T. Nhan, N. V. Hong and T. V. Mung. *J. Non-Cryst. Solids*, **354**, 3093, (2007).

[27] R. A. B. Devine, R. Dupree, I. Farnan and J. J. Capponi. *Phys. Rev. B*, **35**, 2560, (2006).

Chapter 9

The inherent structure of network-forming liquids

9.1 Introduction.

So far, our study into the structure of liquids has been carried out through simulations at liquid temperatures. The advantage of this method is that comparison can be made with experimental results and other liquid systems. Another approach, the study of the inherent structure[1-2], is rooted in the crystallographic conception of the structure of liquids: that they consist of defined geometric structures. This idea was first espoused by J.D Bernal[3] who applied this to monatomic hard-spheres liquids. The application of the potential energy landscape[4] into the structure of liquids is accessed through inherent structure calculations. Stillinger and Weber[1,2] separated the structure of liquids into two components: the temperature-independent inherent structure and the component attributed to thermal excitations. The inherent structure describes a liquid which is rapidly quenched to zero temperature, removing fluctuations and pushing the liquid to its local lowest energy state. More formally, the inherent structure represents a local minimum in the potential energy surface. For any given configuration, these local minima can be located by the use of a steepest descent calculation as outlined in Figure 9.1. The configurational degrees of freedom, D, are determined by the number of distinguishable species and the number of degrees of freedom (rotational, vibrational and conformational), $3 + n_\alpha$ (the following derivation is from Debenedetti $et\ al$[5]):

$$D = \sum_{\alpha=1}^{v} \left(3 + n_\alpha \right) N_\alpha \tag{9.1}$$

The related quantity, $\Phi(\mathbf{X}|V)$ is the potential energy function for the system and is related to the number of particles present and where V is the volume and B are the basins of attraction:

$$\phi \geq B\left(N_1/V, \ldots N_V/V\right)N \tag{9.2}$$

Newton's equations of motion can be used to describe the movement of configuration point **X**, on the the Φ hypersurface where M is the diagonal matrix of appropriate masses:

$$\boldsymbol{M} \cdot \ddot{\boldsymbol{X}}(t) = -\nabla_X \Phi(\boldsymbol{X}) \tag{9.3}$$

and where X is the shorthand notation for the complete set of individual particle vectors:

$$\boldsymbol{X} \equiv \left(x_{1,} \ldots x_N\right) \tag{9.4}$$

The potential energy surface can be divided into local minima and their associated basins of attraction. The inherent structure is the minimum in the potential energy hypersurface which satisfies the relation.

$$\nabla_X \Phi = 0 \tag{9.5}$$

The basins of attraction are defined by the set of configuration vectors which tend towards a given inherent structure by steepest descent on the Φ hypersurface:

$$d\boldsymbol{X}(s)/ds = -\nabla_X \Phi[\boldsymbol{X}(s)|V] \qquad s \geq 0 \tag{9.6}$$
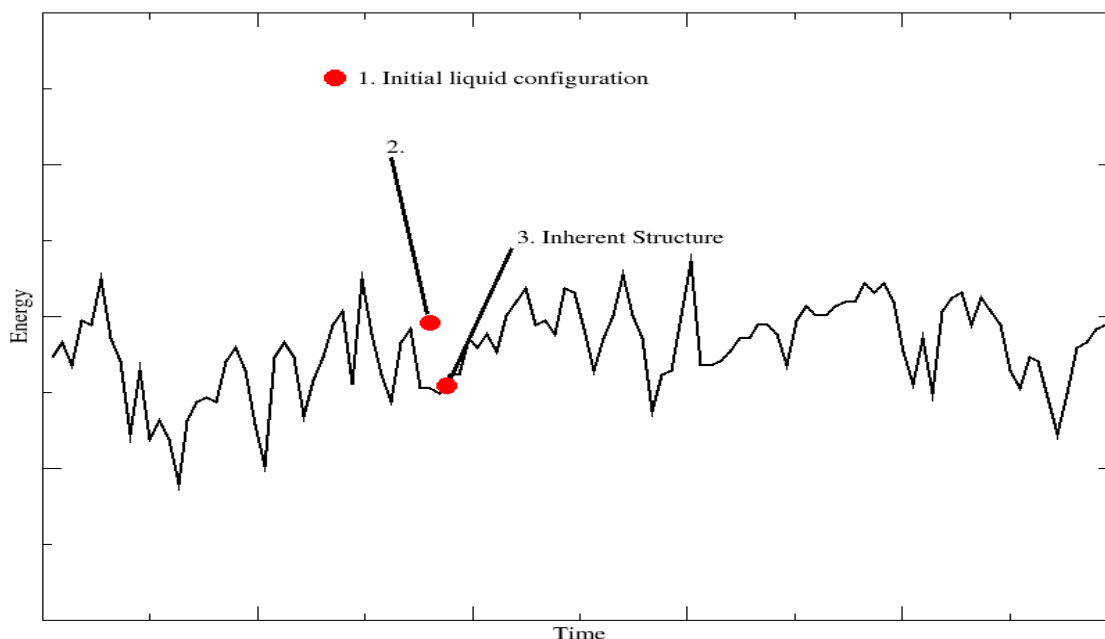
Figure 9.1: Schematic representation of calculating the inherent structure.

1. A configuration is selected from a liquid simulation; at this stage the energy of this system is such that vibrational effects weaken the effects of the underlying potential energy surface.

2. A steepest-descent algorithm is applied to locate potential energy minima.

3. The inherent structure is calculated when the local minima in the potential energy surface is located. For computational expense, this process is limited to 1.2 ps of molecular dynamics.

9.2 Previous inherent structure calculations.

The precursor of recent inherent structure calculations, carried out in the mid-1970s, were steepest descent calculations on metallic alloys of Ni-P[6,7] and molecular dynamics on quenched configurations of Lennard-Jones systems[8,9] and MX_2 salts[10]. For the latter, changes in the pair correlation function $g_{MX}(r)$ were observed, including a resolution of a double-peak feature in the second peak, known as the *split second peak*.[11] More recently, inherent structure calculations have been carried out on systems such as H_2O[12,13], $ZnBr_2$[14] and monoatomic systems such as Argon[15] and Silicon[16,17]. In the system which corresponds closest to those we have studied so far, $ZnBr_2$, these changes include splitting of the principal peak in $g_{ZnZn}(r)$ observed at low density and formation of a new peak in $g_{BrBr}(r)$ at a position intermediate between the principal and second peak.[14] Stillinger *et al* hint at a possible link with a solid-solid phase transition which occurs at a similar density.[14] Noticeably, the model used was a Born-Huggins Mayer potential with no accounting for polarisability effects.

9.3 Simulation details.

Inherent structure calculations were carried out on the range of systems examined in Chapters 3-8; $ZnCl_2$ at different temperatures and pressures; ZnX_2 systems with a variable anion-anion separation range; MX_2 with varying anion polarisability from α_X=10-40 a.u; MX_2 systems at varying density for both α=15 a.u and 35 a.u (2000K and 7000K); and the extreme anion polarisability systems. By studying this range of systems we enable an observation of the inherent structure of a wide range of systems not examined previously through inherent structure calculations: systems with a description of polarisability where there are large changes in the underlying network topology as evidenced by the presence of differing mixtures of edge- and corner- sharing features as well as a range of local ion coordination environments.

All calculations in this chapter consists of 999 ions (333 cations and 666 anions). All starting configurations for each inherent structure calculation were generated from the related MD runs highlighted in the related chapters of each type of materials. In addition to the single temperature calculation carried out at 7000K in section 8.6, further calculations were carried out for a range of other densities. These were calculated from pressure range of 6.0×10^{-4} to 1.0×10^{-4} a.u in steps of 1.0×10^{-4} a.u, resulting in average cell sizes of 32.31Å, 32.58Å, 33.16Å, 33.85Å, 34.84Å and 36.92Å..

At each state point, a sample of 100 configurations was extracted from the last 25 ps of the related simulations. In view of the time taken for each inherent structure calculation of a single configuration and the range of parameter space being sampled, this number was deemed sufficient to highlight the structural properties at each state point. The velocities of the extracted configurations were quenched by setting the thermostats to 0K, and a steepest descent algorithm was applied for 1.2 ps to locate the potential minima. Figure 9.2 shows the evolution of the total energy with time, indicating that the final energy structure can be considered the inherent structure. The average resolution of the calculation, as determined by the energy separation of the last two steps, was 0.08kJ/mol, comparable with previous calculations where a cutoff of 0.0042 kJ/mol was applied. The decision to use the steepest-descent algorithm was based on computational expense. A previous comparison of descent-minimization methods showed that using different techniques would result in different inherent structures due to the rugged nature of the energy landscape.[18] Properties such as the radial distribution functions, $g_{\alpha\beta}(r)$, and bond

angle distributions are time-averaged over the 100 inherent structure configurations.
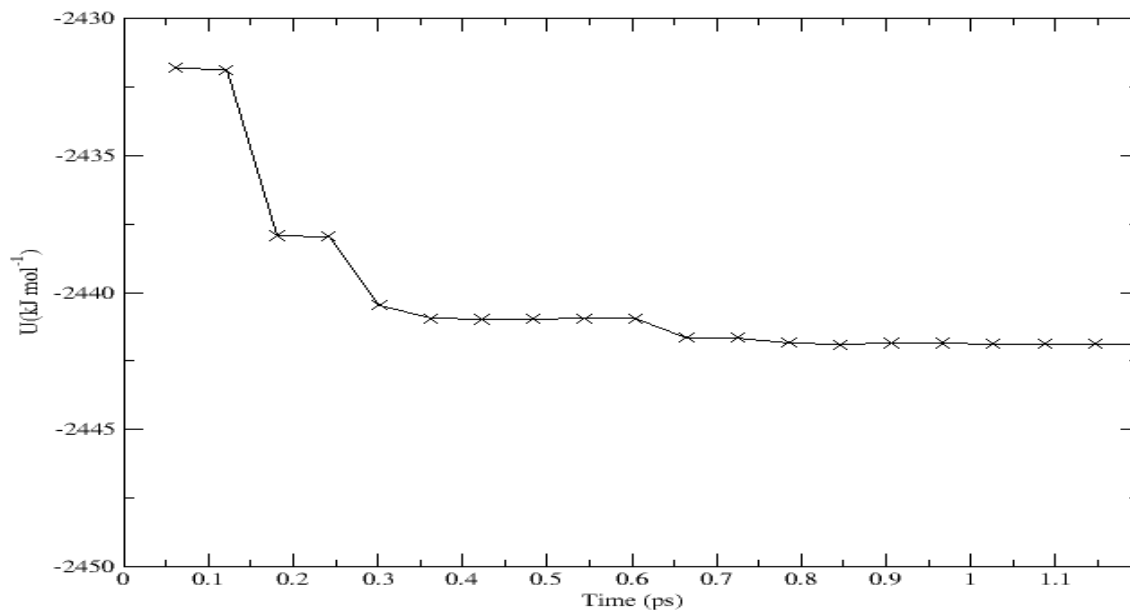
Figure 9.2: Total energy against time for a single configuration in a steepest-descent energy calculation.

9.4 The inherent structure of ZnCl₂ at varying temperature and pressures.

In Chapters 3 and 7, we observed that at low temperature and pressures, there was more IRO present in $ZnCl_2$ as indicated by a more intense FSDP. With increasing temperature and pressure, a decline in the intensity of the FSDP was observed. A comparison of $GeSe_2$ and $ZnCl_2$ in chapter 5 showed that $ZnCl_2$ displayed less strongly features responsible for an intense FSDP at $1Å^{-1}$: edge-sharing character in the network and 4-coordination of the cation-anion coordination pair.

Figure 9.3 compares the inherent radial distribution function, $g_{ZnCl}^{IS}(r)$, with $g_{ZnCl}^{Crystal}(r)$, the related function for a β-ZnCl₂ configuration[19] at the same density of 3.18 g/cm³. This shows us that while the first coordination shell of $g_{ZnCl}^{IS}(r)$ maybe analogous to a crystal structure, with a sharply increased intensity of the principal peak when compared with the functions obtained from the liquid configurations, the extended range is still amorphous showing greater similarity with liquid $g_{ZnCl}^{liq}(r)$, where a single peak is observed in the range 3-6Å.
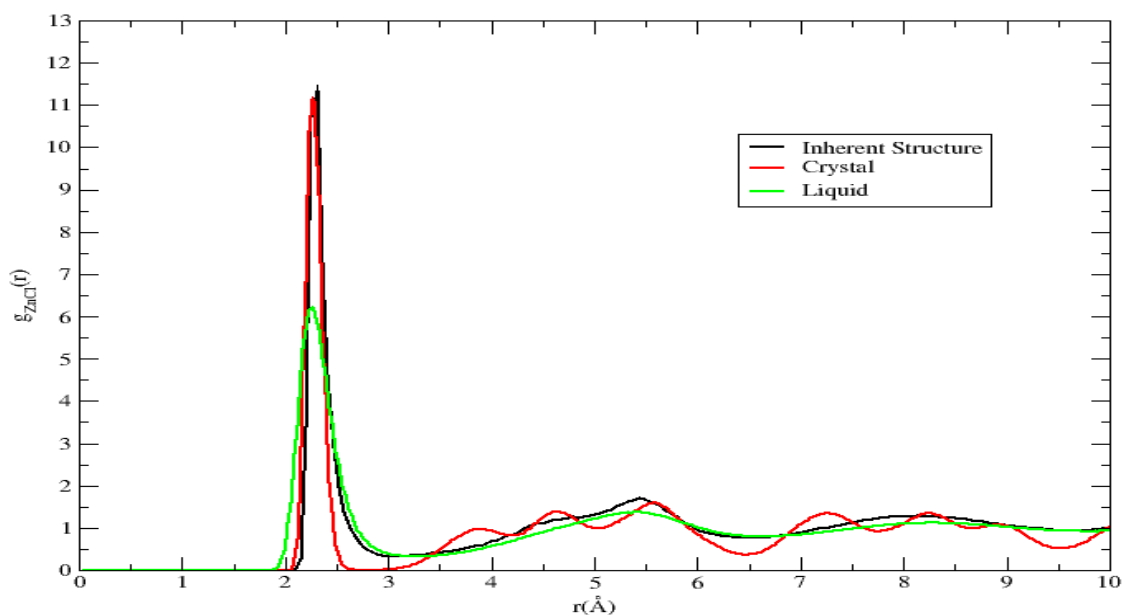
Figure 9.3: A comparison of the inherent structure radial distribution functions with crystalline function at the same density.

Figure 9.4 shows a comparison of inherent and liquid radial distribution functions in the temperature range 600K-1200K at 1 bar. At constant pressure, the increase in temperature results in a decline in the intensity of the principal peak in $g^{IS}_{ZnCl}(r_{PP})$ from 23.1 at 600K to 18.7 at 1200K. The principal peak of $g^{IS}_{ZnZn}(r_{PP})$ splits into an edge-sharing peak at ~3.25Å and a corner-sharing peak at ~3.78Å. With increasing temperature, a more intense edge-sharing peak is observed from a peak height of 1.22 at 600K to 1.98 at 1200K, and a less intense corner-sharing peak, from 3.93 to 2.63 over the same temperature range. The intensity of the principal peak in $g^{IS}_{ClCl}(r_{PP})$ at 3.67Å declines from 6.05 to 4.86, while a shoulder observed at 3.33Å increases in intensity from 2.02 to 3.01.
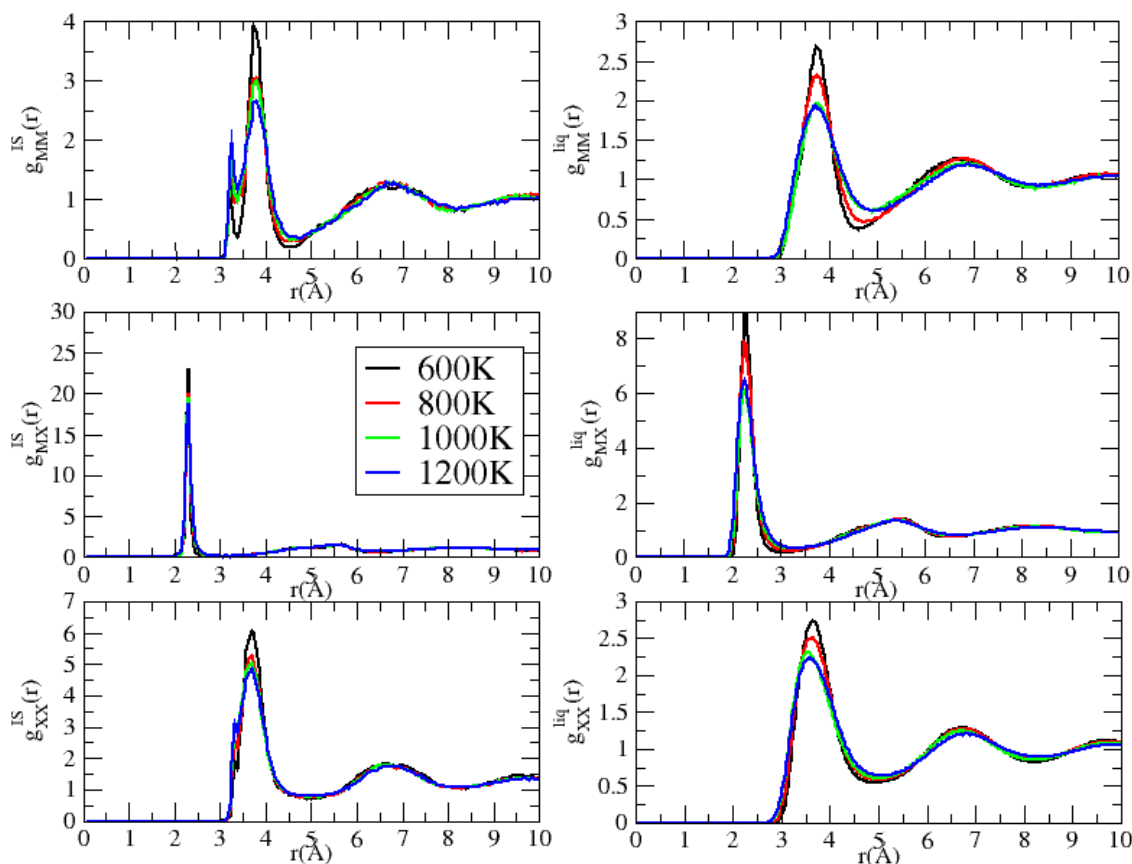
Figure 9.4: The inherent and liquid structure radial distribution functions of $ZnCl_2$ with varying temperature. Black line, 600K; red line, 800K; green line,1000K; blue line, 1200K.

Figure 9.5 show the changes of the inherent radial distribution functions at 1200K with pressure in the range, 1-29000 bar. The intensity of the principal peak in $g^{IS}_{ZnCl}(r_{PP})$ changes from 18.92 at 1 bar, peaking at 20.15 at 2000 bar and then declining to 10.72 at 29000 bar. At pressures of under 12000 bar the edge- and corner-sharing peaks in $g^{IS}_{ZnZn}(r)$ are present. Over this range, the intensity of the edge-sharing peak declines in intensity from 2.07 at 1 bar to a shoulder with an intensity of 0.71 at 29000 bar. The decrease in this peak indicates that these units break-up with increasing pressure: an observation unable to be made from the liquid radial distribution functions. The pattern of change in intensity of the corner-sharing peak at 3.78Å of $g^{IS}_{ZnZn}(r)$ is similar to the changes in $g^{IS}_{ZnCl}(r)$: from 2.72 at 1 bar , a peak of 2.97 is observed at 2000 bar, followed by a decline to 2.31 at 29000 bar.

The split in $g^{IS}_{ZnZn}(r)$ which arises is larger than that previously observed for the rigid-ion $ZnBr_2$ potential used by La Violette[14] et al where a smaller fracture in the

principal peak was observed only at much lower densities. This is an indication of the effect of including polarisation where edge-sharing configurations are stabilised at experimental densities in contrast to rigid-ion models where this is a feature at only much lower densities than is observed experimentally. The changes observed in the principal peak of $g_{ClCl}^{IS}(r_{PP})$ are similar to those with varying temperature in that the change in principal peak intensity is relatively small, ranging from 3.56Å to 3.41Å over the pressure range; however it does not display the shoulder at low r observed earlier.
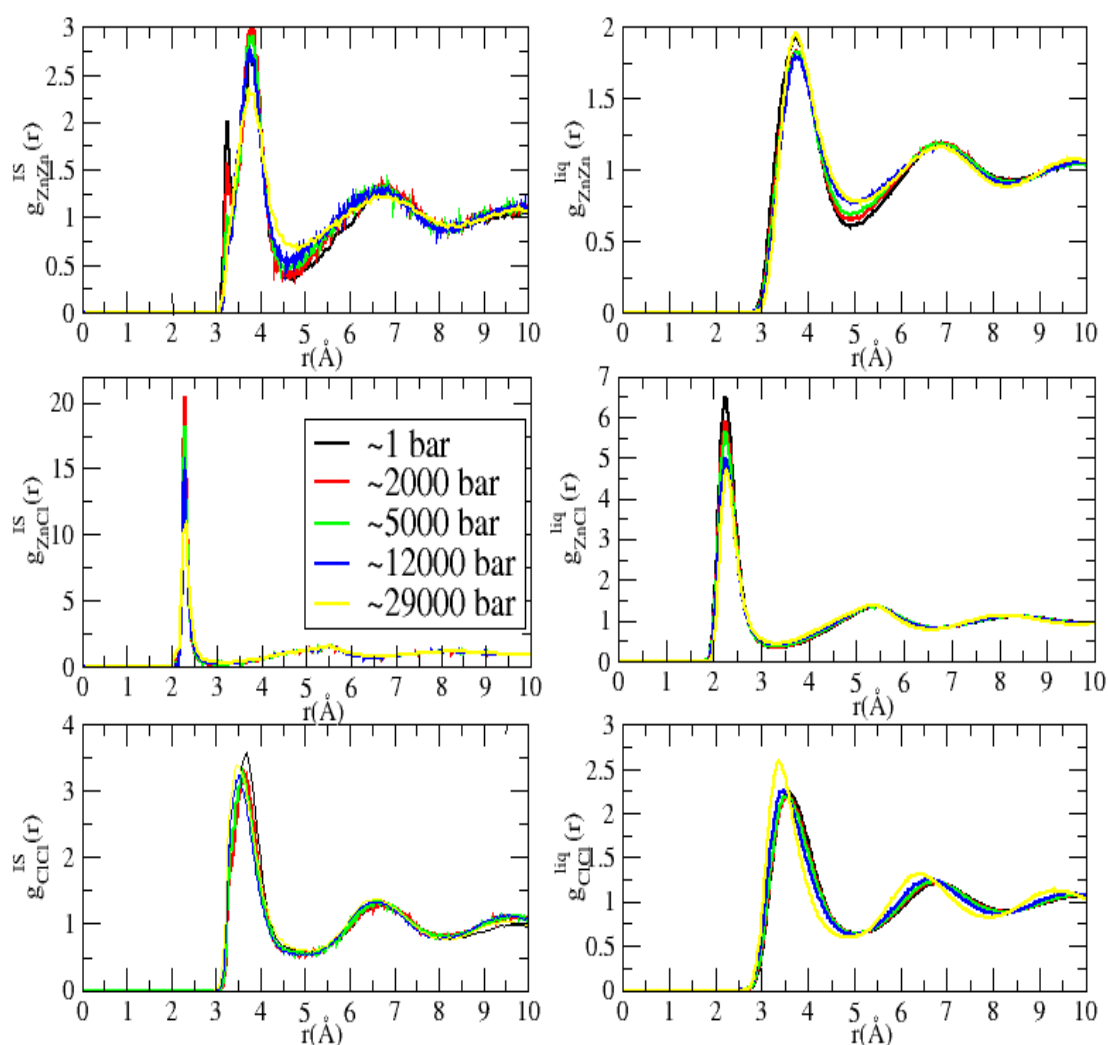
Figure 9.5: Radial distribution functions of the inherent and liquid structure of ZnCl₂ with varying pressure. Black line, 1bar; red line, 2000 bar ; green line, 5000 bar; blue line, 12000 bar; yellow line, 29000 bar.

The inherent structure also resolve a small prepeak, $g_{ZnCl}(r_{SB})$, where SB signifies shortened bond. The position of this peak is at ~2.10Å compared to the position of the principal peak at 2.29Å. This is shown in figure 9.6 which focuses in the region of the
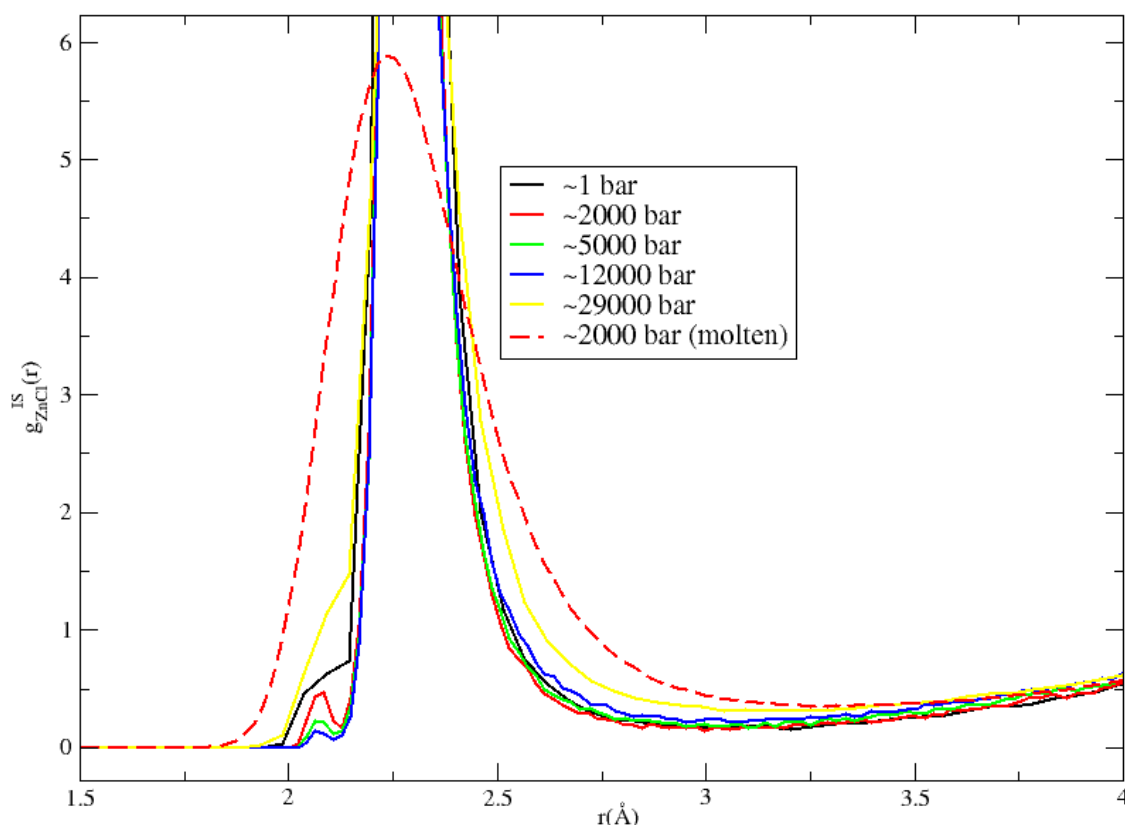
Figure 9.6: The prepeak feature in $g_{ZnCl}(r)$ in the pressure range 1-29000 bar. Black line, 1 bar; red line, 2000 bar; red line (dotted), 2000 bar (liquid); green line, 5000bar; blue line, 12000 bar; yellow line, 29000 bar.

principal peak for $g_{ZnCl}^{IS}(r_{SB})$; upon calculation of the inherent structure, the FWHM of the principal peak reduces, in addition to the formation of a new peak. The intensity of the prepeak is considerably smaller than that observed for the principal peak, typically around 2-5% of the intensity of $g_{ZnCl}^{IS}(r_{PP})$. This is the first instance of a prepeak in the cation-anion function, $g_{MX}^{IS}(r)$, found in the current body of work on inherent structures. The appearance of this peak is strongly temperature dependent, not appearing at any densities at 600K and 800K but at 1000K and 1200K. This suggests the peak intensity is possibly linked with diffusive effects. At a given temperature, the intensity of the bump increases with decreasing pressure in the range, 1-12000 bar; the intense shoulder at 29000 bar in figure 9.6 is possibly a result of increasing amorphisation of the first coordination shell of Zn-Cl where there are increasing amounts of 5 and 6 coordination.

As the changes in structure are largely concentrated around the first coordination shell, and that larger variations are observed in the intensity of $g_{ZnCl}(r_{PP})$, the bond angle distributions were restricted to Zn-Cl-Zn and Cl-Zn-Cl. Figure 9.7 shows the Zn-Cl-Zn and Cl-Zn-Cl bond angle distributions for $ZnCl_2$ at 1 bar in the temperature range 600K-
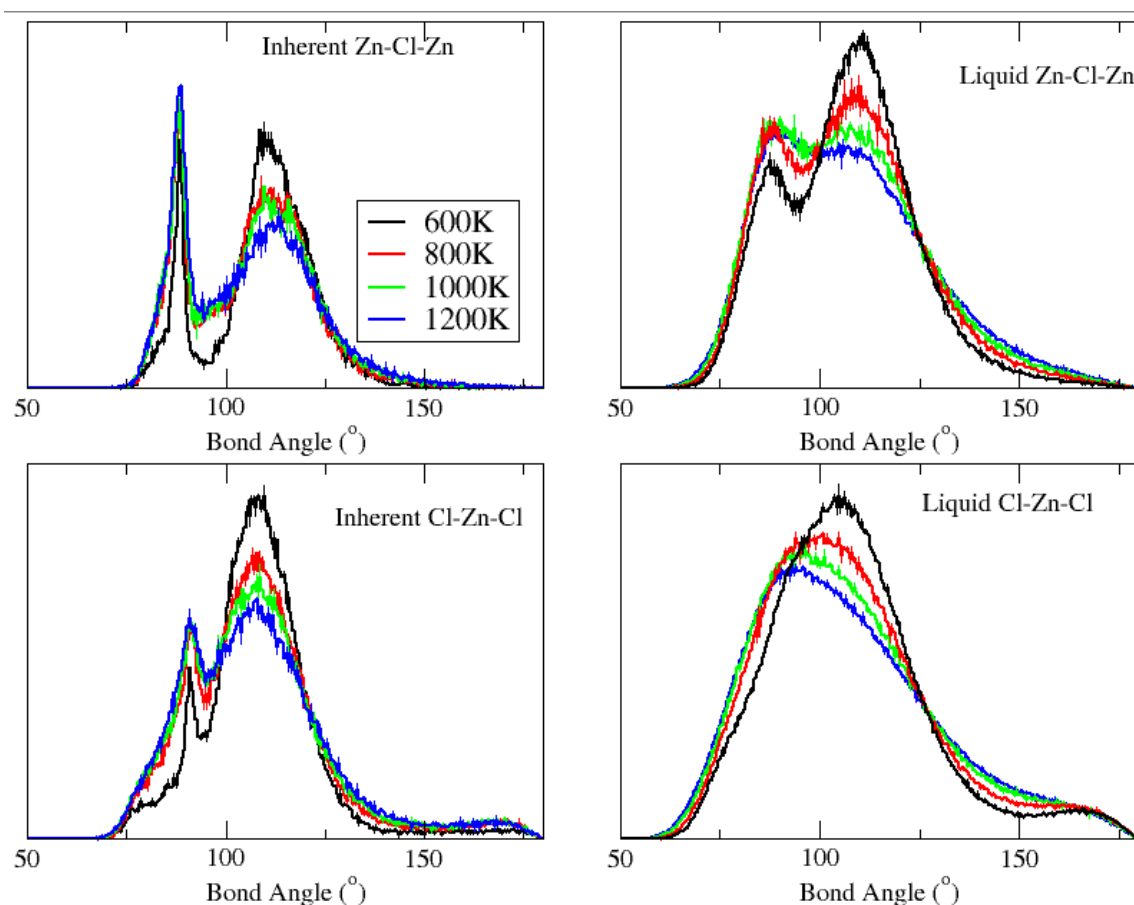
Figure 9.7: Bond angle distributions of the inherent and liquid structure of ZnCl$_2$ at different temperatures. Black line, 600K; red line, 800K; green line, 1000K; blue line, 1200K.

1200K. With increasing temperature, the peak at 89° in Zn-Cl-Zn increases in intensity while the peak at 109° (600K)-113°(1200K) decreases. Though these features are apparent to a smaller degree in the liquid configurations, the edge-sharing peak is sharpened in comparison through both a reduction in the FWHM and a reduction in the minima between the two peaks. In Cl-Zn-Cl, a peak appears at 91° in the inherent structure which increases with increasing temperature. There is also a relative contraction of intensity close to 50° and in particular the tail near 180° from the liquid to inherent structure distributions.

The changes in the Zn-Cl-Zn and Cl-Zn-Cl bond angle distributions with changing pressure are shown in figure 9.8. At lower pressure a sharp peak at 90° is featured in Zn-Cl-Zn with a second peak at 110°. At higher pressures, the distinction between the two arrangements weakens as shown by the increasing height of the minima in between the two peaks. This is due to the increase of higher coordinate zinc ions with the associated range of Zn-Cl-Zn bond angles due to the square-planar and octahedral geometry. Similar

features are observed in the Cl-Zn-Cl bond angle distribution (significant peak at ~90°
and a second peak at 110°.) With increasing pressure, the distinction weakens and features
of axially placed anions in square-planar and octahedral units becomes stronger.
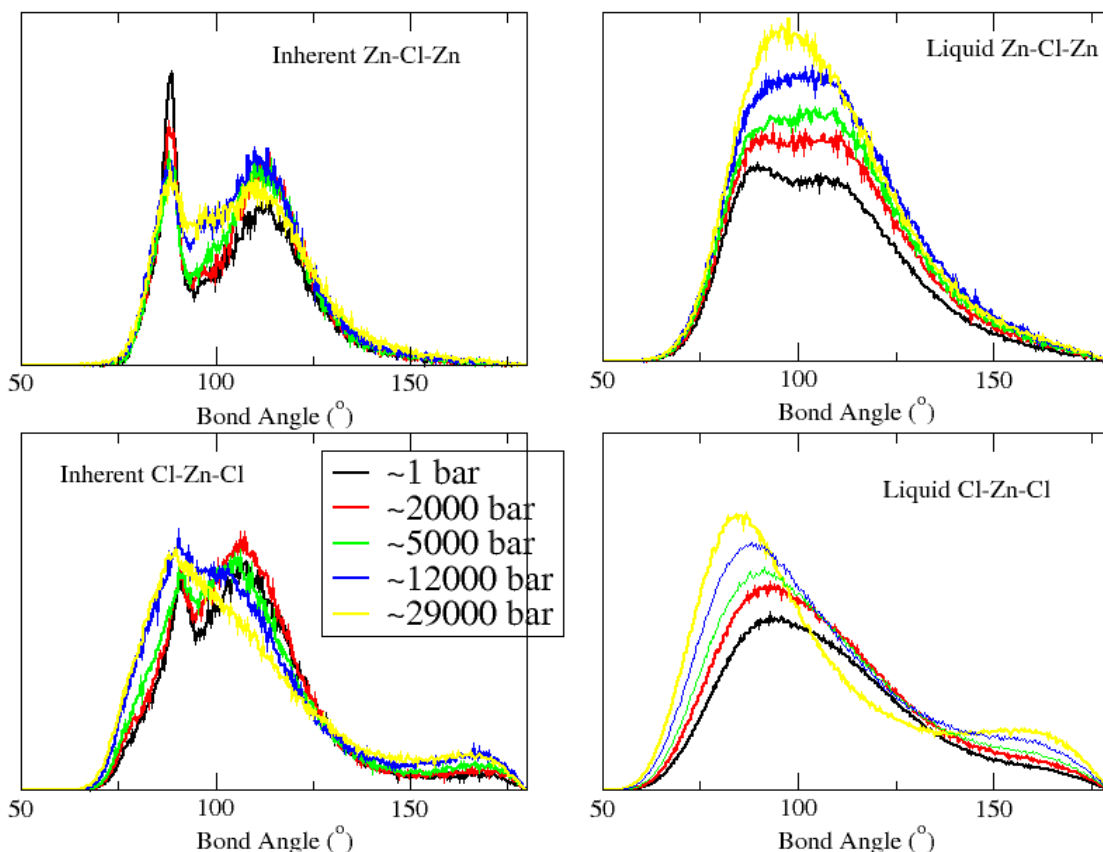
Figure 9.8: Bond angle distributions of the inherent and liquid structure of $ZnCl_2$ at different pressures.
(1200K) Black line, 1 bar; red line, 2000 bar ; green line, 5000 bar; blue line, 12000 bar; yellow line,
29000 bar.

9.5 The structural origin of the $g_{MX}(r_{SP})$ prepeak.

The prepeak, $g_{ZnCl}^{IS}(r_{SB})$, highlights a smaller length-scale than we have observed
previously; however, as shown in figure 9.6, the width of the liquid peak exceeds that in
the inherent structure indicating that vibrational motion associated with the larger peak
may mask the short-range structural feature at elevated temperatures. The assumed shape
of the principal peak of the cation-anion radial distribution function is regarded a
symmetrical peak.[20] The broadness of the peak is a result of the vibrations which occur in
the liquid state. As indicated by the absence of the prepeak in liquid configurations and its

subsequent resolution in the inherent structure, the prepeak is not expected experimentally as a separate moiety but integrated in the $g_{ZnCl}^{liq}(r_{PP})$ principal peak. Although there is no direct reference to a principal peak in literature, the influence of such a peak on $g_{ZnCl}^{liq}(r)$ is implied in the neutron diffraction experiment on $NiCl_2$ by Wood and Howe.[20] In this study, it was noted there was a better correlation in the back Fourier-Transform if the principal peak of $g_{NiCl}(r)$ was attributed an uneven intensity towards the lower r side: this was accomplished either through a soft leading edge or a prepeak shoulder.[21] Another example of deviations away from a symmetrical principal peak include EXAFS studies of AgBr.[22] The study shows that with increasing temperature the first coordination shell becomes increasingly asymmetrical, with a greater intensity this time on the high r side of the principal peak.[22] Experiments on glassy systems, taken at 300K, lower than corresponding liquid temperatures but still higher than that of the inherent structure calculations, may give further indication of the existence of such a peak. In neutron diffraction studies[23,24] of glassy $ZnCl_2$ and $GeSe_2$, the former shows a slight deviation on the low r side of the $g_{ZnCl}(r)$ (figure 3 in paper). In glassy $GeSe_2$, low intensity peaks at a positions smaller than the principal peak were observed in $g_{GeSe}(r)$ but their presence was attributed to truncation errors in the Fourier transform of $F(k)$ to $G(r)$.

Intuitively, it might be expected that these features are the result of three coordinate species, correlating with their expected greater abundance for low density systems; however, when the cations involved in these shorter cation-anion bonds are isolated, it is found that the shortened bond is attached to cations with varying MX coordination including 5-coordinate cations. Figure 9.9 below shows that in fact the shortened-bond is due to a second effect of polarisation, indicating that it is rather the environment of the anion which is responsible for the presence of $g_{ZnCl}(r_{SB})$. Previously, the effect of anion polarisability was discussed in terms of three bodies, where two cations are drawn closer together by a dipole on the central anion. This assumption holds true most of the time for systems of AX_2 stoichiometry, where the anion-cation coordination is strongly 2-coordinate. Figure 9.9a , a snapshot of a cluster of atoms taken from an inherent structure calculation, shows a situation where this assumption is invalid. Within the effective range of the dipole moment of the anion, if there is only one cation present, the net effect of the dipole is to attract the cation towards it. This results in the shortened Zn-Cl bond observed in $g_{ZnCl}^{IS}(r)$. The presence of these defects presents a possible mechanism for diffusion.
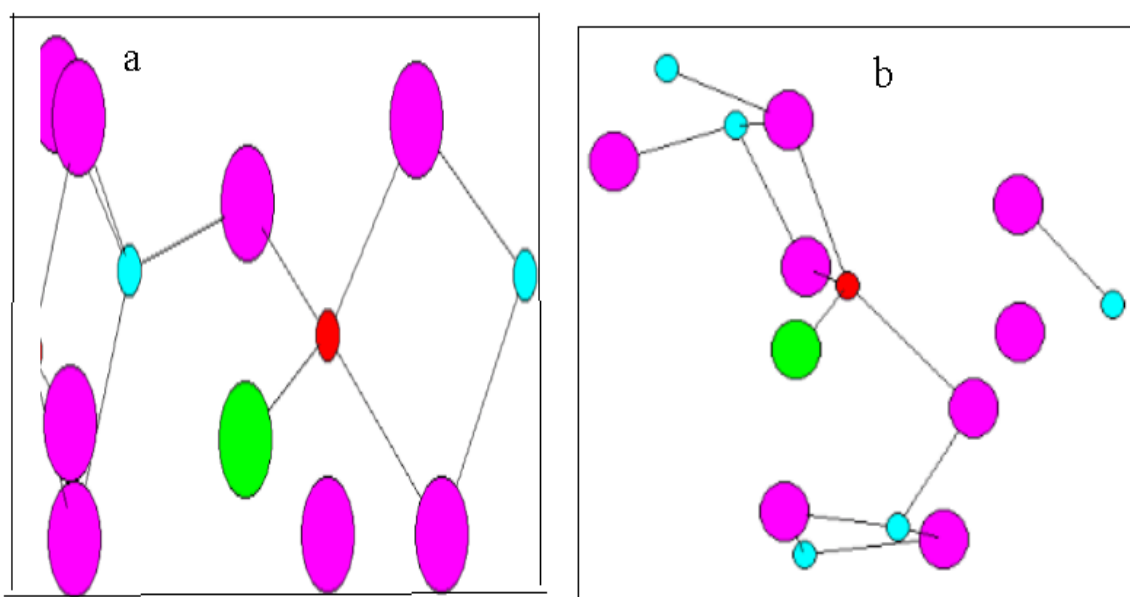
Figure 9.9: Graphical snapshot of "shortened" cation-anion bond in (a) inherent structure and (b) the equivalent set of ions in the melt configuration. Blue circle, cations in "normal" length bonds; purple circle, anions in normal length bonds; red circle, cation in shortened bond; green circle, anion in shortened bond. In both configurations, the common feature is the single coordination of the anion with the cation but the shorter bond distance (2.08Å) is not retained in the melt configuration where the bond is 2.21Å.

Figure 9.9b shows the related liquid identity of the anion involved in a Zn-Cl short bond in the inherent structure (shown in figure 9.9a). Although the anion is not involved in a shortened bond, it retains the feature highlighted from the inherent structure of being singly coordinated. There is a strong correlation between the temperatures which exhibits this prepeak in $g_{ZnCl}(r)$ and the larger presence of the defect 1-coordination in the ion coordination pair, Cl-Zn. At 1 bar, the percentage of single Cl-Zn coordination is 0.21% compared to 14.5% for 1200K at the same pressure. This effect diminishes with increasing pressure as the 1-coordinate Cl-Zn pair percentage declines to 0.05% at 29000 bar for 600K. Figure 9.10 shows which cations features in a shortened cation-anion bond over the time of the simulation. It shows that it is present among all cations over a time range with the intensity flowing intermittently in and out of different ions, indicating that such bonds are involved in diffusion. Some of these bonds last 0.604 fs while others last much longer for periods of ~12 fs.
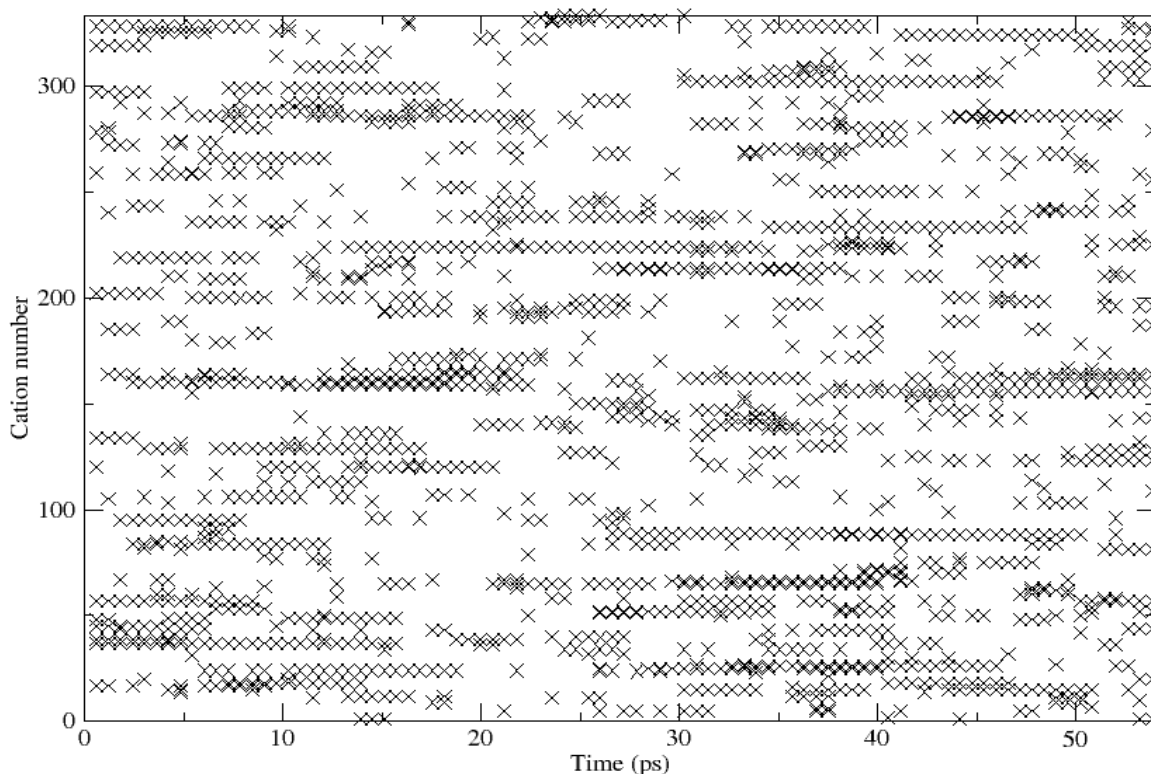
Figure 9.10: Appearance of shortened cation-anion bond with cation number according to time.

9.6 The inherent structure of ZnX$_2$ with varying anion-anion distance.

With increasing anion-anion separation, a decrease in the intensity of the FSDP was observed in Chapter 3 as well as a shift in its position to higher scattering angles. In contrast with other systems, the cell size was fixed over the whole parameter range of effective anion-anion separation, $r_{eff}^{XX} = 3.67 - 3.84 \, \text{Å}$. Figure 9.11 shows the effect of increasing the effective anion-anion separation on the inherent structure. The cation-cation functions, $g_{ZnZn}^{IS}(r)$ displays a split into edge- and corner-sharing features. With increasing r_{eff}^{XX}, the intensity of the edge-sharing peak at ~3.21Å decreases, while the intensity of the corner-sharing peak ~3.78Å increases. Analogously, $g_{XX}^{IS}(r)$ observes a distinct shoulder on the low r-side of the principal peak, and which over the range r_{eff}^{XX} =3.67-3.84Å moves in position from 3.31Å to 3.56Å; the intensity diminishes from 0.91 to 0.23 where it merges into the main principal peak. The presence of a prepeak in $g_{ZnX}^{IS}(r)$ is apparent with increasing r_{eff}^{XX} with the intensity increasing from a weak shoulder of intensity 0.16 at $r_{eff}^{XX} = 3.67 \, \text{Å}$ to 0.90 at $r_{eff}^{XX} = 3.84 \, \text{Å}$. This correlates with

the changes in the miscoordination observed in the liquid systems where the single X-Zn coordination rises from 1.46% at $r_{eff}^{XX} = 3.67\,\text{Å}$ to 7.56% at $r_{eff}^{XX} = 3.84\,\text{Å}$. The intensity of the principal peak of $g_{ZnX}^{IS}(r_{PP})$ decreases with increasing r_{eff}^{XX} from 21.47 at $r_{eff}^{XX} = 3.67\,\text{Å}$ to 13.76 at $r_{eff}^{XX} = 3.84\,\text{Å}$.
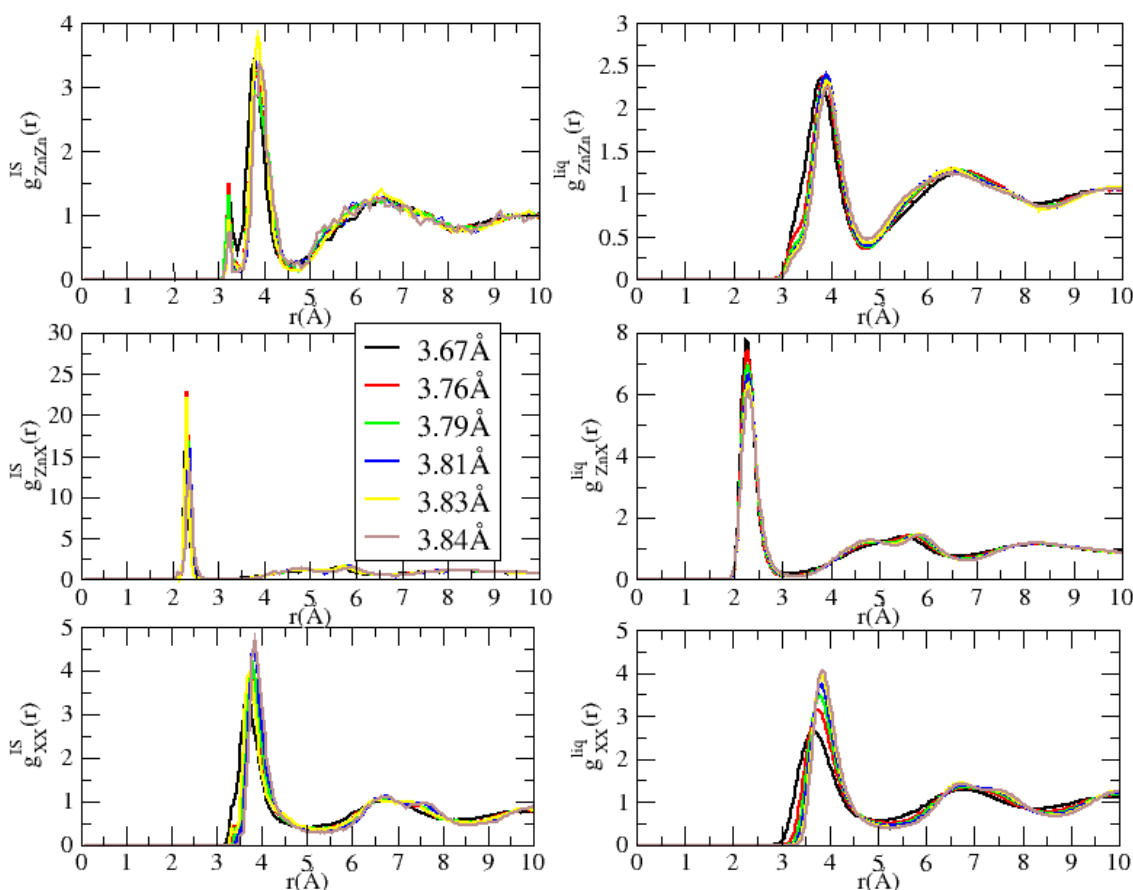
Figure 9.11: Radial distribution functions of the inherent and liquid structure of ZnX_2 systems where the anion-anion separation, r_{eff}^{XX}, is varied in the range 3.67-3.84Å. Black line, 3.67Å; red line, 3.76Å; green line, 3.79Å; blue line, 3.81Å; yellow line, 3.83Å; brown line, 3.84Å.

The Zn-X-Zn bond angle distribution in figure 9.12 shows two peaks at 88° and 110°; the former peak, associated with edge-sharing tetrahedra, declines with increasing r_{eff}^{XX}. while the latter peak, associated with corner-sharing tetrahedra, increases over the same range. The minima in between the two peaks changes sharply from $r_{eff}^{XX} = 3.67\,\text{Å}$ to $r_{eff}^{XX} = 3.76 - 3.84\,\text{Å}$. Whilst the smaller FWHM of the edge-sharing peak compared to the corner-sharing peak is consistent with the results for $ZnCl_2$, a noticeable difference

lies in the intensity of the peak at 88° at $r_{eff}^{XX} = 3.67 \, \text{Å}$ which is much more intense compared to higher values of r_{eff}^{XX} in the liquid distribution than in the inherent structure. The X-Zn-X bond distribution displays a small peak 91° which, as with the low angle peak in Zn-X-Zn declines with increasing r_{eff}^{XX}, and a larger peak at 107°, which increases with increasing r_{eff}^{XX}.
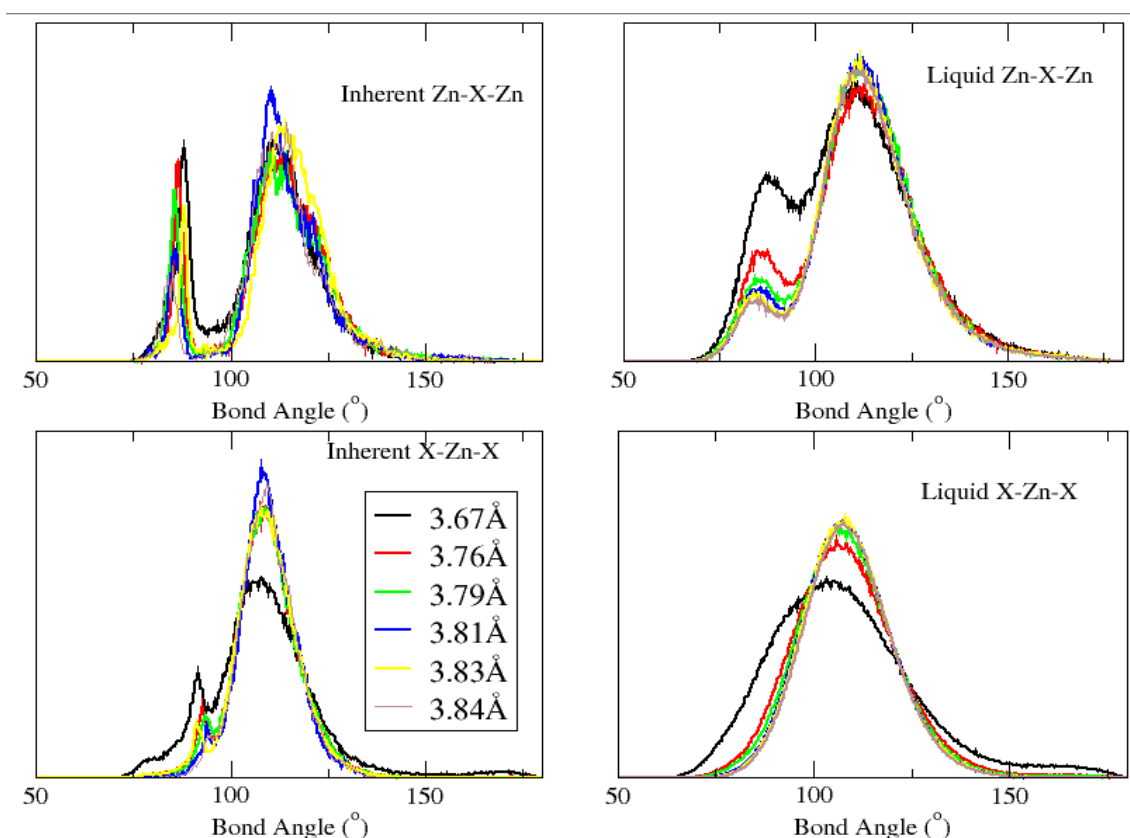
Figure 9.12: Bond angle distribution functions of the inherent and liquid structure of ZnX$_2$ systems where the anion-anion separation, r_{eff}^{XX}, is varied in the range 3.67-3.84Å. Black line, 3.67Å; red line, 3.76Å; green line, 3.79Å; blue line, 3.81Å; yellow line, 3.83Å; brown line, 3.84Å.

9.7 The inherent structure of MX$_2$ systems where anion polarisability, α_X, varies from α_X=10-40 a.u.

In chapter 6, the anion polarisability was varied in the range α_X=10-40 a.u and the changes in IRO were correlated with changes in the structural features, from tetrahedral systems dominated by corner-sharing at low anion polarisabilities to those with large

amounts of edge-sharing at high polarisabilities. Figure 9.13 shows that the radial distribution functions of the inherent structure show several features in common with the calculations on $ZnCl_2$; increased short-range ordering signified by the large increase in the value of $g_{MX}^{IS}(r)$ and little change in the intensity of $g_{XX}^{IS}(r)$. The prepeak feature in $g_{MX}^{IS}(r)$ is not present at any polarisability; this correlates with the smaller presence of the single X-M coordination which lies in the range of 4.4% (α_X=40 a.u)-1% (α_X=10 a.u) for MX_2 compared to the maximum of 14.5% for $ZnCl_2$ observed at 1200K (~1 bar). Figure 9.13 shows that the changes in intensity for $g_{XX}^{IS}(r)$ do not vary significantly over the polarisability range and, unlike the functions observed in the sections 9.4 and 9.6, does not display a shoulder or splitting. The intensity of $g_{MX}^{IS}(r)$ follows a similar pattern in the range 40-20 a.u, where a maximum of 21.58 is observed at α_X=25.0 a.u and a minimum of 17.91 at 30.0 a.u, but declines sharply from α_X=20 to 10 a.u from 18.86 to 11.30. This may be partly to do with the change in presence of 4 cation-anion coordination which decreases to 53% at 10 a.u from 83% at α_X=40 a.u, where the sharpest decline occurs between 25-10 a.u. The cation-cation term, $g_{MM}^{IS}(r)$, shows significant splitting into edge- and corner-sharing peaks at high polarisabilities, significantly more strongly than that observed in $ZnCl_2$. At α_X=40 a.u, $g_{MM}^{IS}(r)$ displays a larger edge-sharing peak at 3.29Å, which is greater in intensity than the corner-sharing peak at 3.77Å, at a ratio of 1.25. This correlates with the large amount of edge-sharing observed in these systems. As the polarisability decreases, this peak declines, while the corner-sharing peak maintains intensity and shift to the right, following the changes in structure determined in Chapter 6. This ratio declines to 0.13 at α_X=25.0 a.u, after which only the corner-sharing peak is present. The intensity of the minima in-between the two peaks is due to deviations, in terms of coordination and geometry, from edge and corner-sharing tetrahedra.
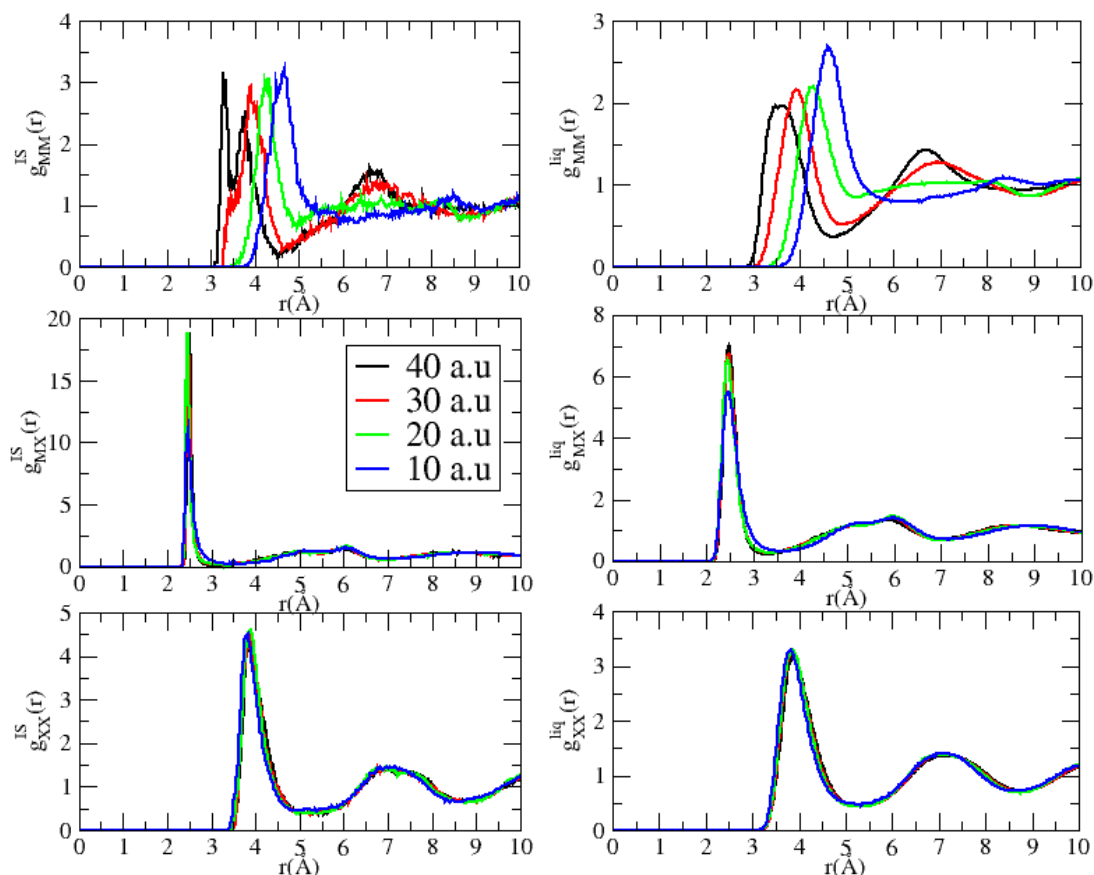
Figure 9.13: Radial distribution functions of the inherent and liquid structure of MX_2 in the anion polarisability range, α_X=10-40 a.u. Black line, 40 a.u; red line, 30 a.u; green line, 20 a.u; blue line, 10 a.u.

The related bond angle distributions, shown in figure 9.14, for M-X-M resolve two sharp peaks at α_X=40 a.u; this is in contrast to the liquid configurations where the intensity at 81° and 98° are resolved only as shoulders. Analogous to the changes in $g_{MM}(r)$, the peaks in the bond angle distribution move to higher values: the corned-shared peak moves from 98° to 124° at α_X=10 a.u. With decreasing polarisability, a relative decline in the edge-sharing peak is observed, and at α_X=25.0 a.u only a corner-sharing peak is present. In contrast, the X-M-X bond angle distribution is similar to the liquid equivalent in displaying a main peak around 98° and with a tail at 150° which increases with decreasing polarisability in keeping with the increase of 5 and 6 coordinate M cations.
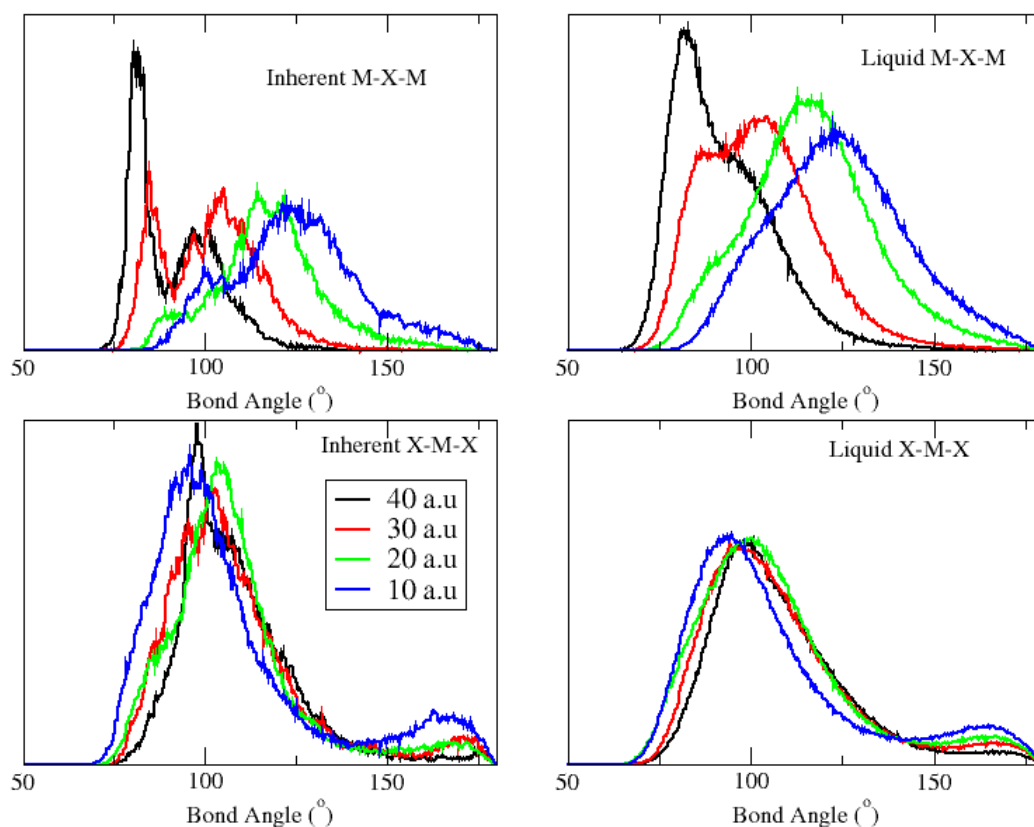
Figure 9.14: Bond angle distribution functions of the inherent and liquid structure of MX_2 in the anion polarisability range, α_X=10-40 a.u. Black line, 40 a.u; red line, 30 a.u; green line, 20 a.u; blue line, 10 a.u.

Figure 9.15 shows the inherent structure and liquid curves for the changes in "0", "1" and "2" cations with anion polarisability where the number refer to the number of four-membered rings that a cation is bonded to. The bars show the standard deviations; the standard deviation for "0","1" and "2" cations changes from 3.18, 2.61 and 2.41 in the liquid configuration to 1.99, 1.84 and 1.60 for the inherent structure calculation. The largest deviation of the inherent structure values of E^0, E^1, E^2 and the molten liquid values occur in the region, α_X=15-25 a.u. The equivalent inherent structure values for higher temperature configurations (7000K) taken in the density range 2.48-3.73 g/cm^3, and at α_X=35 a.u, are 3.46, 3.11 and 2.95 indicating that the underlying potential energy surface is sharply affected by changes in temperature.
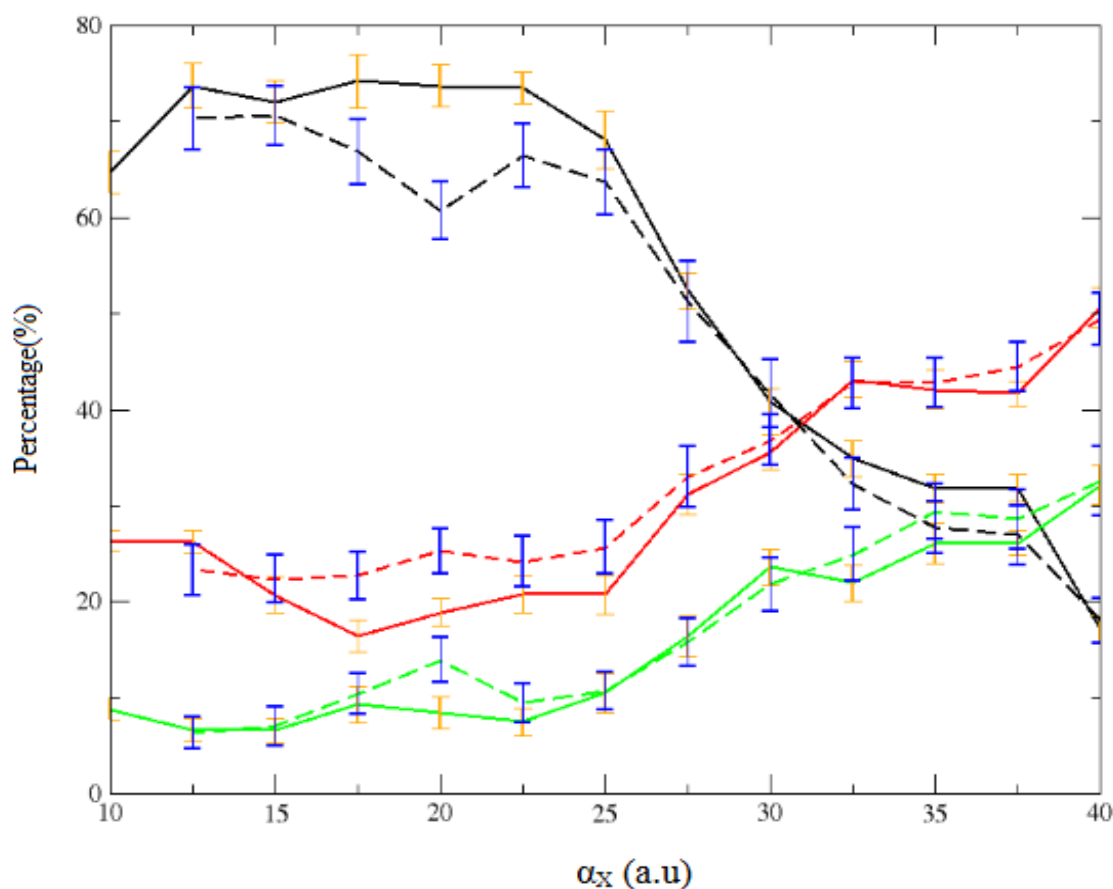
Figure 9.15: Change in network connectivity in the inherent structure and liquid configurations of MX_2 where anion polarisability, α_X, varies in the range α_X=10-40 a.u. The standard deviation bars are coloured orange for the inherent structure and blue for liquid. Black, "0"; red,"1";green,"2" (referring to percentage of cations with n number of four-membered rings, E^n, where n=0-2.) Full line, inherent calculations; half-lines, liquid configuration.

9.8 The inherent structure of MX_2, where α_X=15 and 35 a.u with varying density.

In chapter 8 changes in the structure with temperature and density were highlighted for the MX_2 systems where the anion polarisability, α_X, was 15 a.u and 35 a.u. The most prominent change with decreasing density included increased ordering effects associated with IRO: the induction of edge-sharing units and a tightened first coordination shell where the percentage of 4-coordinate M cations reached over 95%. With increasing temperature, a large decline in the IRO was observed for the MX_2 model where α_X=35 a.u. Figures 9.16 and 9.17 show the respective comparisons of the calculated inherent

structure radial distribution functions for MX_2 systems in the density ranges of 3.13-4.49 g/cm^3 and 3.00-4.34 g/cm^3 for α_X=15 a.u and 35.a.u respectively. As with $ZnCl_2$ at different pressures, the intensity of the principal peak in $g^{IS}_{MX}(r_{PP})$ varies significantly over the respective density ranges; the largest intensity is observed at the lowest densities, 43.49 for 15 a.u and 32.79 for 35 a.u. The values of 10.12 and 15.0 at the highest densities indicate that a faster decline is observed α_X=15 a.u. There are no prepeaks in $g^{IS}_{MX}(r)$ over either density range; the respective ranges for the single X-M coordination are small at 0.19-0.43% for 15 a.u and 1.60-3.08% for 35 a.u. The intensity of $g^{IS}_{XX}(r)$ is similar over the density range for both α_X=15 a.u and 35 a.u, lying in the ranges 5.47-4.94 and 4.28-4.48 over the density ranges of 3.13-4.49 g/cm^3 and 3.00-4.34 g/cm^3 respectively. The function, $g^{IS}_{MM}(r)$, when α_X=15 a.u, is similar to the liquid equivalent in maintaining a single principal peak at ~4.3Å in the density range 4.49-3.71g/cm^3.
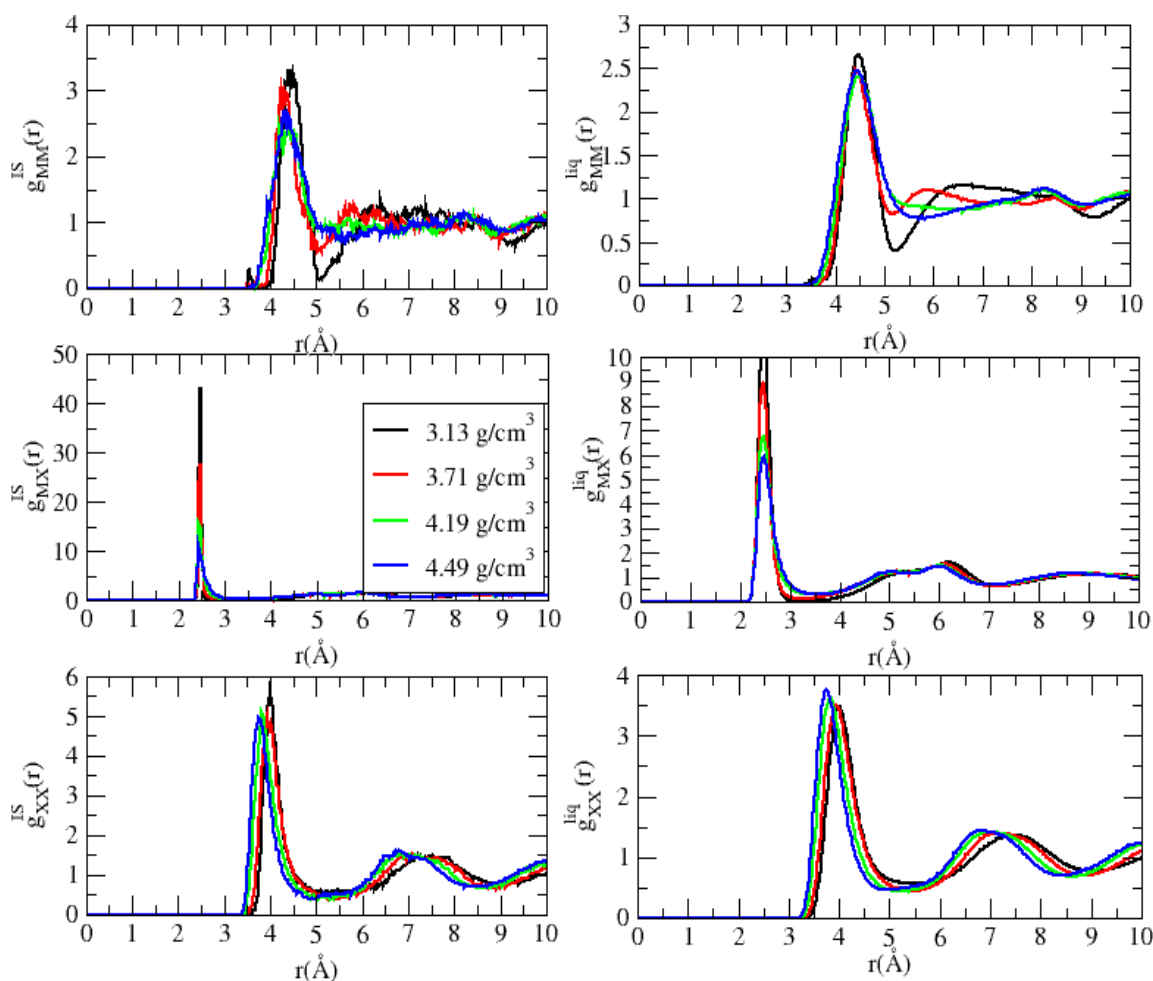
Figure 9.16: Radial distribution functions of the inherent and liquid structure of MX_2 in the density range 3.13-4.49 g/cm^3 where α_X=15.0 a.u. Black line, 3.13 g/cm^3; red line, 3.71 g/cm^3; green line, 4.19 g/cm^3; blue line, 4.49 g/cm^3.

At 3.13 g/cm^3 , a small edge-sharing peak is observed at ~3.55Å, representative of edge-sharing and in keeping with the liquid result.

At α_X=35 a.u, this effect is much stronger; at 3.00g/cm^3 there is a sharp increase in the intensity of the peak at 3.35Å and a decrease in the minima at ~3.65Å, which indicates a strong ordering of the corner- and edge-sharing tetrahedra. In comparison with the liquid configurations this is partly reflected in a small prepeak at 3.39Å at 3.00 g/cm^3, but the inherent structure magnifies this effect and elucidates a sharper distinction of the edge- and corner-sharing tetrahedral units. Analogously, the position of the principal peak at

$g_{XX}^{IS}(r_{PP})$ at 3.00 g/cm^3 is shifted to 4.09Å in comparison to the higher density

configurations and a prepeak is resolved at 3.78Å. The intensity of $g_{XX}^{IS}(r)$ remains

similar over the density range mirror the changes of the liquid structure over the density

range for both α_X=15 a.u and 35 a.u. The sharp change in intensity of $g_{MM}^{IS}(r)$ at 3.00 g/

cm^3 is in contrast to the step-wise decline in the intensity of $g_{MX}^{IS}(r_{PP})$:   this may be a

feature of calculating the inherent structure from the low-temperature liquid.
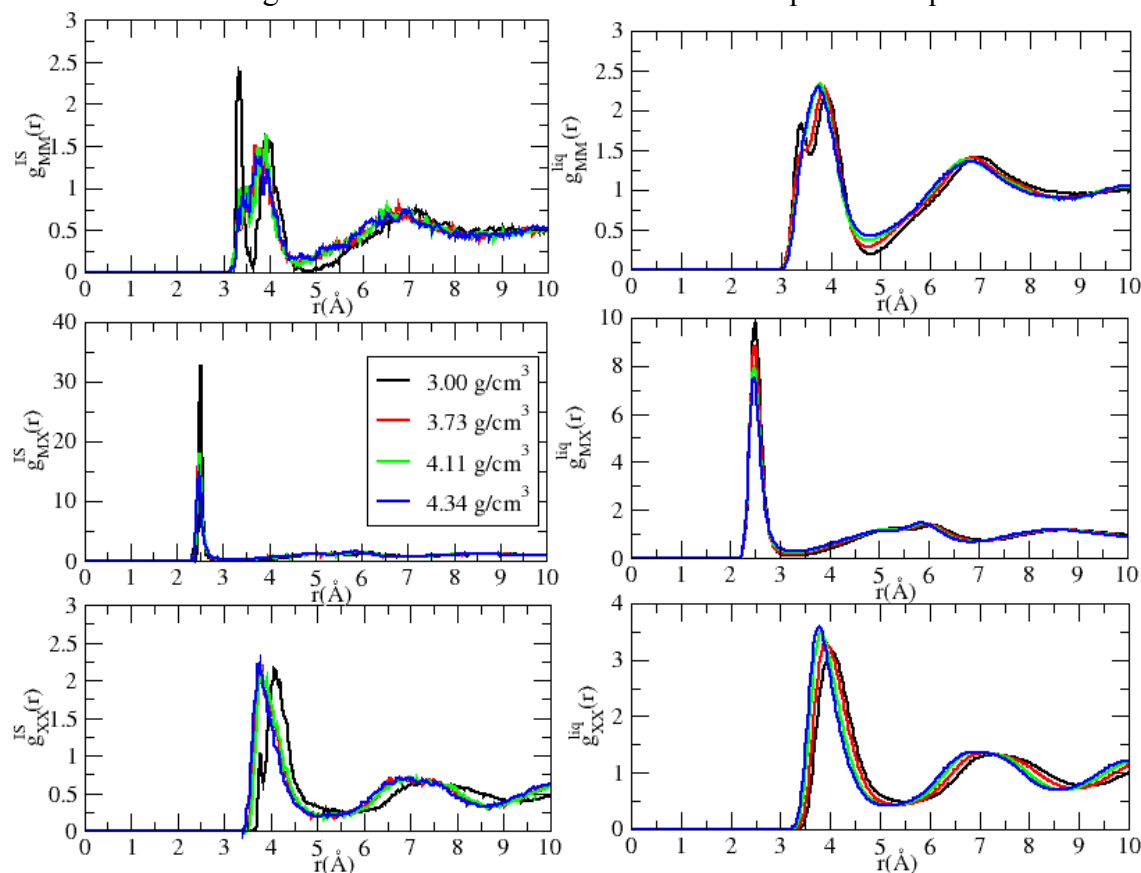
Figure 9.17: The inherent and liquid structure radial distribution functions of MX$_2$ in the density range 3.00-4.34 g/cm^3 where α_X=35.0 a.u. Black line, 3.00 g/cm^3; red line, 3.73 g/cm^3; green line, 4.11 g/cm^3; blue line, 4.34 g/cm^3.

The M-X-M bond angle distribution for α_X=15 a.u in figure 9.18 shows similar changes over the density range compared to the liquid configurations with the peak at 91-95° increasing in intensity with increasing density. In the X-M-X distribution, the relative intensities of the main peak vary with density unlike the liquid configurations where they are similar: the peak at 106° for 3.13 g/cm³ is sharpened with a larger intensity compared to the higher density configurations. At α_X=35.0 a.u, as shown in figure 9.19, the inherent structure M-X-M contrast with those obtained for α_X=15 a.u in sharpening features associated with the different edge- and corner-sharing connectivities. At 3.13 g/cm³, the M-X-M distribution displays a sharpened edge-sharing peak at 83° and the minima at 93° between the edge- and corner-sharing peaks is sharply reduced compared to the liquid configuration. The X-M-X bond angle distribution from 4.34 to 3.73 g/cm³ shows similar features with the liquid equivalents, with a main peak at 94° and a tail at 170° indicating the increasing of 5 and 6 coordinate sites. At 3.00 g/cm³, a sharp new peak at 96° is resolved which does not feature in the corresponding liquid distributions.
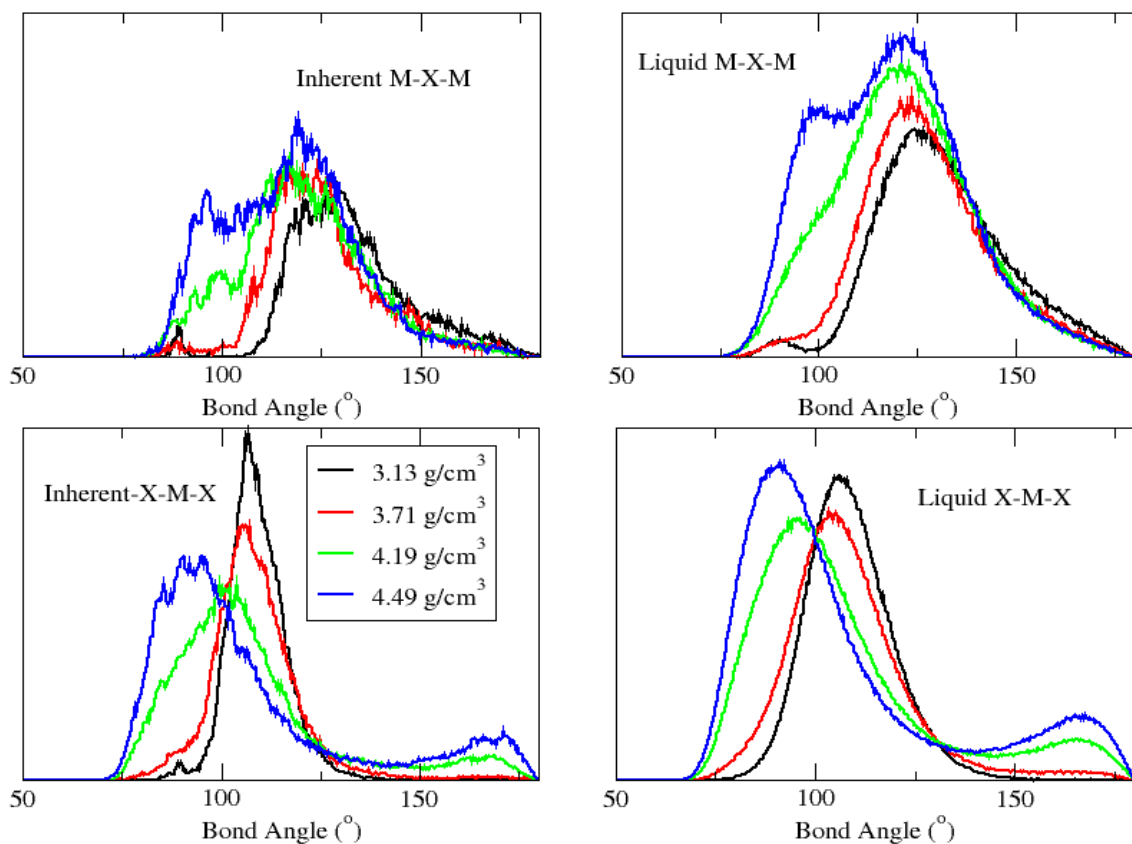
Figure 9.18: The bond angle distribution functions of MX₂ in the density range 3.13-4.49 g/cm³, where α_X=15.0 a.u. Black line, 3.13 g/cm³; red line, 3.71 g/cm³; green line, 4.19 g/cm³; blue line, 4.49 g/cm³.
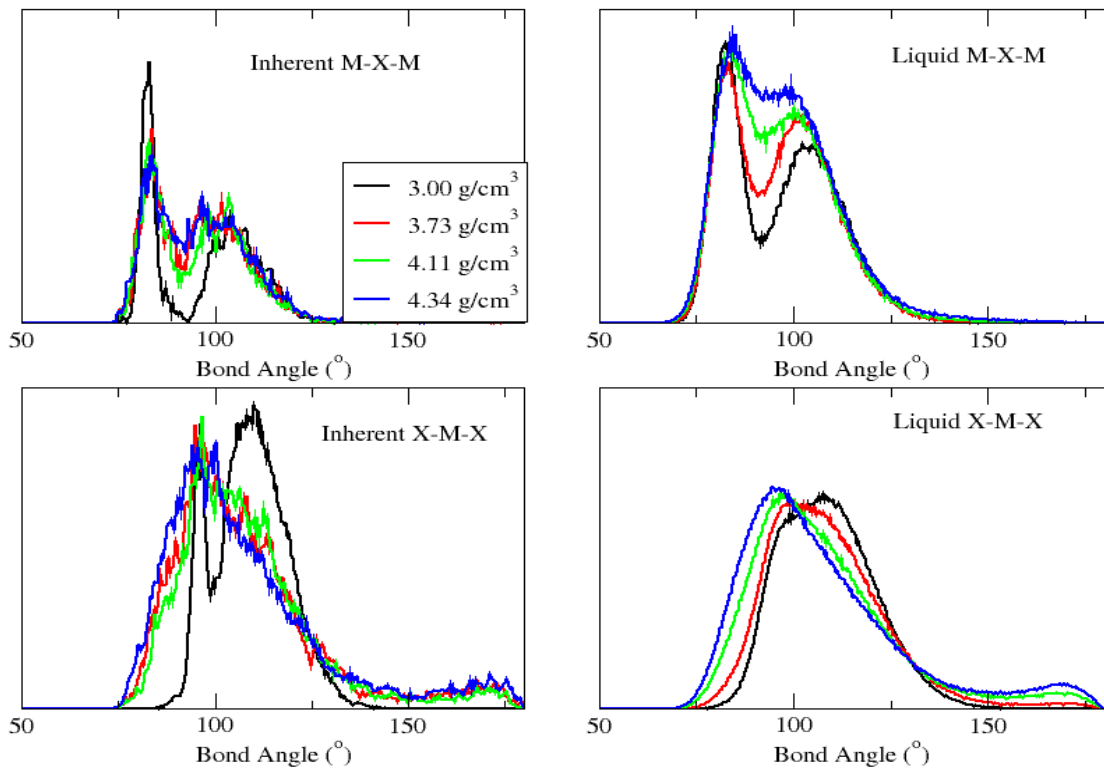
Figure 9.19: Bond angle distribution functions of the inherent and liquid structure of MX_2 in the density range 3.00-4.34 g/cm^3, when α_X=35.0 a.u. Black line, 3.00 g/cm^3; red line, 3.73 g/cm^3; green line, 4.11 g/cm^3; blue line, 4.34 g/cm^3.

9.9 The inherent structure of MX_2, where α_X= 35.a.u, at T=7000K.

Figure 9.20 shows the inherent structure radial distribution functions for high temperature configurations of MX_2 systems in the density range 2.48-3.73 g/cm^3. In $g_{MX}^{IS}(r)$, a reduction in the FWHM of the principal and resolution of a prepeak is observed over the density range of 2.48-3.73 g/cm^3. This correlates with an increased single X-M coordination at the higher temperature, from 27.8% at 2.48 g/cm^3 to 9.77% at 3.73 g/cm^3, compared to the lower temperature values of 3.08% and 1.60% at 3.00 and 4.34 g/cm^3 respectively. The prepeak intensities vary substantially over the density range, peaking at 4.21 at 2.48 g/cm^3, then declining with increased density to 1.16 at 3.37 g/cm^3. For $g_{MM}^{IS}(r)$, there is a separation of the principal peak into edge- and corner-sharing peaks at ~3.4Å and 3.90Å respectively with more gradual changes in intensity between densities compared to the lower temperature where there is a sharp change at the lowest density. Also, for 3.00 g/cm^3 at 7000K, $g_{MM}^{IS}(r)$ does not exhibit a minima close zero at 3.6Å

compared to the result at 2000K; there is a smaller ratio of the relative intensities of the edge-sharing peak against the corner-sharing peak from 1.52 to 0.79 indicating the break up of edge-sharing units. This is additional evidence that the deterioration in the FSDP with temperature shown in Chapter 8 is a result of both an increase in vibrational effects and a change in the non-vibrational structure. As with previous systems, $g_{XX}^{IS}(r)$ shows the smallest changes in the intensity of the principal peak with a range of 5.77-5.22 over the density range. At 2.48 and 3.00 g/cm^3, prepeaks at 3.80Å and 3.58Å are observed with respective intensities of 3.66 and 1.72.
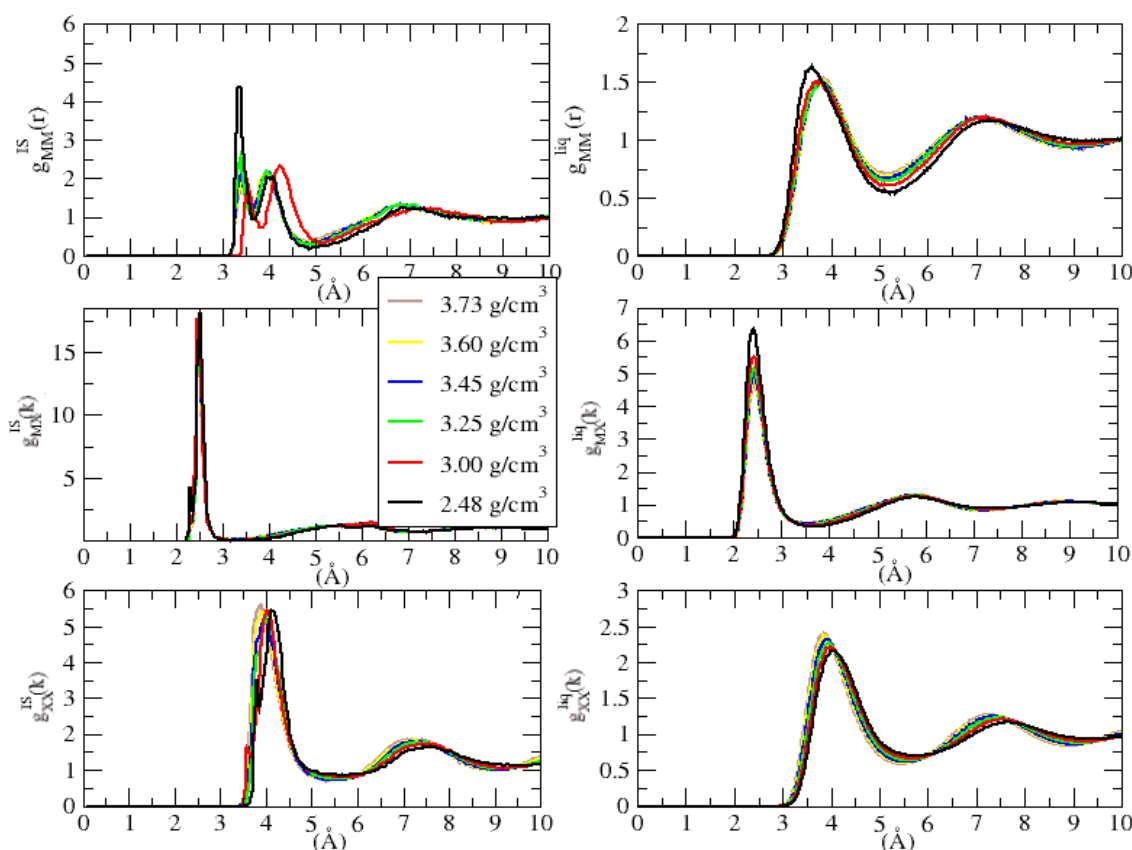
Figure 9.20: Radial distribution functions of inherent and liquid structure of high temperature MX$_2$ in the density range 2.48-3.73 g/cm^3 where α$_X$=35.0 a.u. Black line, 2.48 g/cm^3; red line, 3.00 g/cm^3; green line, 3.25 g/cm^3; blue line, 3.45 g/cm^3; yellow line, 3.60 g/cm^3; brown line, 3.73 g/cm^3.

The changes in the M-X-M and X-M-X bond angle distributions in figure 9.21 are once again reflective of the changes in the radial distribution functions with peaks at 82° and 103° indicate the presence of edge and corner-sharing tetrahedra. As with the changes in $g_{MM}^{IS}(r)$, this separation is not observed at similar densities at 2000K. The deep minimum observed at 93° for 2000K is not repeated for the lower density configurations

at 7000K. Two peaks at 96° and 107° are resolved in X-M-X in the density range 2.48-3.45 g/cm³, similar to the low density configuration at 2000K.
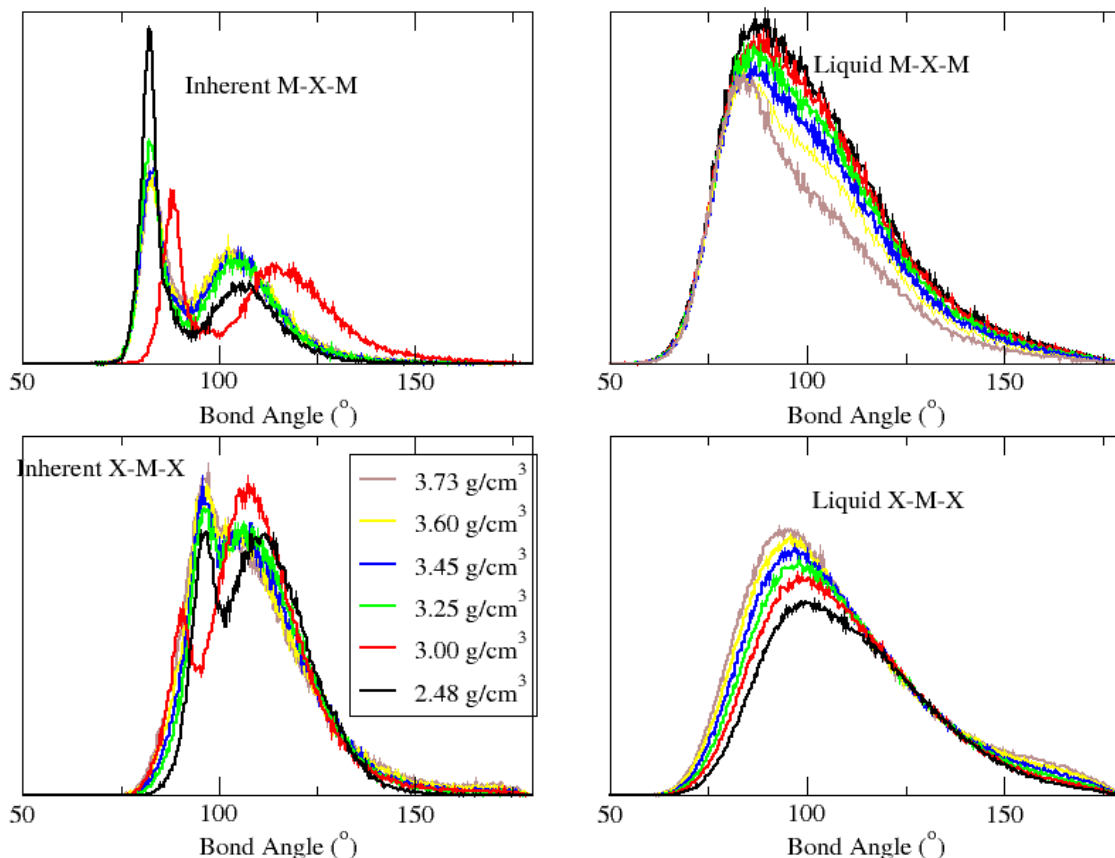
Figure 9.21: Bond angle distribution functions of the inherent and liquid structure of high temperature MX₂ in the density range 2.48-3.73 g/cm³ where α_X=35.0 a.u. Black line, 2.48 g/cm³; red line, 3.00 g/cm³; green line, 3.25 g/cm³; blue line, 3.45 g/cm³; yellow line, 3.60 g/cm³; brown line, 3.73 g/cm³.

9.10 The inherent structure of system with extreme anion polarisation.

An analysis of the MX_2 system with extreme anion polarisation exhibited in Chapter 6, will illustrate several features. Firstly, this set of systems was shown to have the highest proportion of mis-coordinated anions due to their molecular nature where there is a high proportion of terminal units. It would be expected that a significant prepeak feature in $g_{MX}(r)$ would be observed. Figure 9.22 shows the inherent radial distribution functions; the presence of a significant prepeak is clearly observed, and it considerably larger in intensity than those observed in $ZnCl_2$ both in absolute values and the ratio of the intensity of the prepeak against that of the principal peak. These systems highlight the effect of

structure on the presence of the prepeak in $g^{IS}_{MX}(r)$. When c=0.90 a.u, the prepeak at

2.11Å is weakest in intensity in comparison to the principal peak at 2.35Å which has an

intensity of 10.46. As c decreases, the intensity of the peak at 1.93Å increases sharply in

comparison to the principal peak at 2.33Å. At c=0.50 a.u, the intensity at 2.33Å declines

to a shoulder. The relevance of the inherent structure is highlighted by the presence of

prepeaks of intensities 4.16, 1.56 and 0.55 at c=0.60-0.80 where such features are not

observed in the liquid, whereas the large principal peaks for c=0.60-0.90, and the large

prepeak at c=0.50, ostensibly the principal peak, are. Split peaks are observed in both

$g^{IS}_{XX}(r)$ and $g^{IS}_{MM}(r)$. At c=0.90, $g^{IS}_{MM}(r)$, displays similar features to MX$_2$(where

α_X>25 a.u) with edge-sharing and corner-sharing peaks of similar intensity. For

$g^{IS}_{MM}(r)$, the intensity at the corner-sharing peak at 3.58Å forms a shoulder at lower c

values of 0.50 and 0.60. The intensity of the early edge-sharing peak in $g^{IS}_{MM}(r)$ at

~3.04Å varies non-linearly with c: 3.36 at c=0.50 a.u, peaking at 6.27 at c=0.60 a.u, and
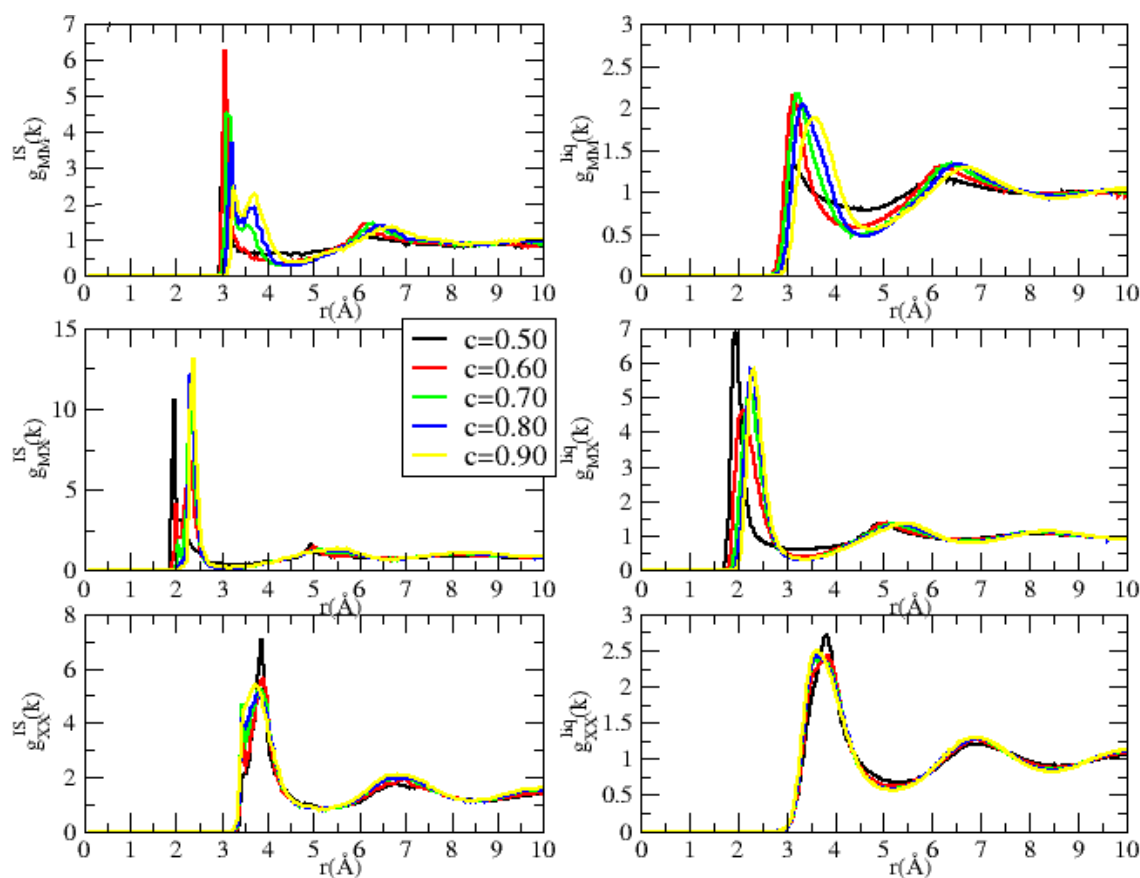
Figure 9.22: Radial distribution functions of the inherent and liquid structure of MX$_2$ systems where the short-range damping parameter c is varied in the range 0.50-0.90 a.u. Black line, 0.50 a.u; red line, 0.60 a.u; green line, 0.70 a.u; blue line, 0.80 a.u; yellow line,0.90 a.u.

then declining to 2.36 at c=0.90. For $g_{XX}^{IS}(r)$, the intensity of the low r principal peak and high r principal peaks, 2.26 and 2.68 respectively, are similar at c=0.90, but diverge sharply at c=0.50 where the values are 1.06 and 3.55.

The bond angle distributions in figure 9.23 are sharpened in comparison to the related liquid configurations. At c=0.90, two significant peaks are present: the first at 86° and a peak at 104°. The latter peak declines sharply in intensity as c declines. A similar pattern emerges from the changes in the X-M-X distribution where the intensity around 110° declines with decreasing c, but in contrast with M-X-M the FWHM increases with intensity at larger angles increases.
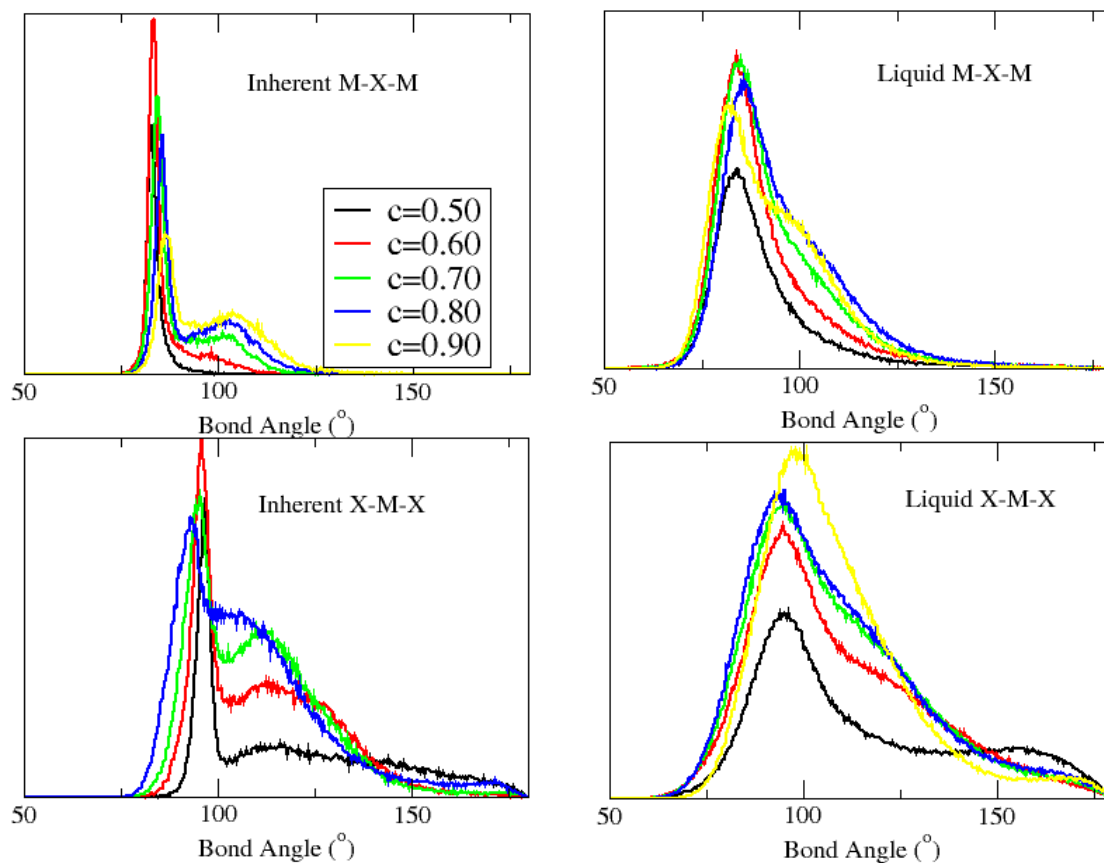
Figure 9.23: Bond angle distribution functions of the inherent and liquid structure of MX$_2$ systems where the short-range damping parameter c is varied in the range 0.50-0.90 a.u. Black line, 0.50 a.u; red line, 0.60 a.u; green line, 0.70 a.u; blue line, 0.80 a.u; yellow line, 0.90 a.u.

The change in the intensities of the principal peak of the radial distribution functions have been dominated by the cation-anion term. This does vary between the systems studied, and in particular with respect to the changes in cation-cation term. Table 9.1 show the values for ratio, Q, given by:

$$Q = \frac{g_{MM}^{IS}(r_{PP}) - g_{MM}^{liq}(r_{PP})}{g_{MX}^{IS}(r_{PP}) - g_{MX}^{liq}(r_{PP})}$$

In most cases, Q >1 indicating that the increase in intensity from the liquid to inherent structure is larger for $g_{MX}(r_{PP})$ than $g_{MM}(r_{PP})$. The relative changes in the intensity of the principal peaks of $g_{MM}^{IS}(r_{PP})$ can be understood through the differences contributions of the vibrational structure of the first coordination shell of M-X compared to M-M and X-X. However, for the *extreme polarisability* system, the increase in principal intensity of $g_{MM}(r)$ from the liquid to the inherent structure is larger than that observed in $g_{MX}(r_{PP})$, as indicated by the Q values of under 1.

	MX₂						*ZnCl₂*	
Section	9.7	9.8(35 a.u)	9.8(15 a.u)	9.8(7000K)	9.10	9.6	9.4	9.4
Parameter	α(a.u) a=10 b=40	ρ(g/cm³) a=3.00 b=4.34**	ρ(g/cm³) a=3.13 b=4.49	ρ(g/cm³) a=2.48 b=3.73**	.c (a.u) a=0.50 b=0.90	r_{eff}^{XX} a=3.67 b=3.84	T(K) a=600 b=1200	P(bar) a=1 b=29000
$g_{MM}^{IS(a-b)}(r)$ / $g_{MM}^{liq(a-b)}(r)$	1.72 1.18	1.15 0.68	1.49 1.42	2.69 1.11	2.39 3.59	1.37 1.52	1.41 1.32	1.39 1.23
$g_{MX}^{IS(a-b)}(r)$ / $g_{MX}^{liq(a-b)}(r)$	2.10 2.72	3.15 1.98	3.98 1.78	2.85 2.91	1.51 2.22	2.89 2.22	2.58 2.79	2.83 2.29
$Q^{(a-b)}$	1.22 2.31	2.74 2.91	2.67 1.25	1.06 2.62	0.63 0.62	1.46 2.11	1.83 2.11	2.04 1.86

Table 9.1: Ratios of changes in the intensities of the principal peaks of $g_{MM}^{IS}(r)$ (row 3) and $g_{MX}^{IS}(r)$ (row 4) from liquid to the inherent structure. The fifth row shows , Q, the ratio which highlights the relative increase in intensity of $g_{MM}^{IS(a-b)}(r)$ compared to $g_{MX}^{IS(a-b)}(r)$ where a and b are the extremes of the ranges highlighted in the 1st row. The top value in each box is from a, the lowest value in the range while the bottom value is b, the highest value in the range.

9.11 Conclusion

In this chapter we have observed that inherent structure calculations elucidate new sructural features within MX_2 liquids previously hidden in the liquid structure and not observed in similar inherent structure calculations on rigid-ion model systems.[14] In comparison to the work of La Violette *et al*[14], who used rigid-ion models, the increase in short-range ordering, as highlighted by a substantial increase in the principal peak of $g_{MX}(r)$, is repeated. The presence of a intermediate peak in the anion-anion separation was not found in the range of systems highlighted, although this occurred at densities much higher than those sampled here.

Earlier inherent structure calculations[6-9] on hard-sphere[6,7] and Lennard-Jones systems[8,9] observed a main feature of a split second peak in the inherent structure g(r). In this chapter, we have focused on the greater changes which occur in the principal peaks of the inherent structure radial distribution functions.A significant difference between these systems and this current study is the presence of a description for polarisability in the range of systems observed here, where differing proportions of corner- and edge-sharing tetrahedra are present, resulting in a greater range of changes in the pair correlation functions. The distinction between corner- and edge-sharing linkages between MX_4 tetrahedra is observed more clearly in the radial distribution functions; the ratio of the intensity of edge- and corner-sharing peaks, resolved in a number of systems analysed, gives a clearer indication as to the specific mixture underlying the liquid configurations. In $g_{MM}(r)$, a peak at ~3.3Å is indicative of the presence of edge-sharing and a corner-sharing peak at ~3.7Å; the relative intensities of these peaks gives an indication of the wide range of mixed corner, corner- and edge-sharing and edge-sharing systems observed in this study.

These changes are also observed in the bond angle distribution functions. In a previous inherent structure study on liquid silicon[16], anomalous changes were observed in a peak upon calculation of the inherent structure with a decline in intensity while others increased with increasing temperature, although not linked to to any structural or dynamic property of the system.[16] In our calculations, increasingly resolved peaks, based on structures from our analysis in earlier chapters have been observed. A number of disparities in the relative intensities observed in the peaks between inherent structure and liquid configurations have been observed. Significantly, the inherent structure bond angle distributions highlight the "rigid" structural ordering present within edge-sharing

tetrahedra in comparison to the corner-sharing peak, as shown by the smaller FWHM of the associated sharp peaks in the X-M-X and M-X-M bond angle distributions and the associated peak in the cation-cation g(r) for systems such as MX_2 (α_X=40 a.u), and $ZnCl_2$ at 1200K at low pressure. In the molten state, this separation between the two geometries becomes less clear giving a strong indication of different types of motion. The greater range of bond angles observed by the vibrational structure in edge-sharing chains is attributed to the floppy motion of edge-sharing chains whereas corner-sharing, which, structurally, is less restricted, observes a relatively smaller range of motion.

This is the first set of calculations where a prepeak in the principal peak of $g_{MX}(r)$ is observed in a number of systems and its origin highlighted. It is related to the miscoordination of the ion-pair X-M, where the anion is singly bonded. This prepeak is observed in the inherent structure of a range of systems and its increasing intensity occurs in $ZnCl_2$ when temperature is increased; in ZnX_2 systems when anion-anion separation increases; and in high temperature MX_2(α_X=35a.u) systems when density declines. For systems with extreme anion polarisability (section 9.10), this effect is so large that the prepeak and principal peak switch places when the short-range parameter c is shifted from 0.50 to 0.90. These systems also observed greater changes in intensity, upon calculation of the inherent structure, in $g_{MM}(r_{PP})$ than $g_{MX}(r_{PP})$. The weakest prepeak intensity was observed in MX_2 systems(α_X=40-10a.u) which displays the most strongly tetrahedral coordination in the range of systems (and subsequent lack of defect, singly coordinated anions) observed in this chapter.

Within classes of systems, a central question is whether the change in IRO as a function of temperature is due to increased motion of ions, an underlying change in structure or a mixture of the two. Inherent structure calculations help our understanding in this regard. In the case of $ZnCl_2$, the inherent structure shows an increase in edge-sharing features, as indicated by the increase in intensity at r~3.3Å with increasing temperature; in contrast, these edge-sharing features decline with increasing pressure. In addition, the prepeak in $g_{MX}(r)$ which increases with increasing temperature, and declines with increasing pressure, is further evidence of structural change. The changes in IRO with increasing temperature can then be understood as a competition between the underlying structure with features more conducive to IRO and the vibrational disorder. This gives a clearer understanding of the structural origin of the "relaxation" of network structure highlighted in systems where the FSDP observes anomalous temperature dependence.[25]

9.12 References

[1] F. H. Stillinger and T. A. Weber. *Phys. Rev. B*, **31**, 5262, (1985).

[2] F. H. Stillinger and T. A. Weber. *Phys. Rev. A*, **25**, 978, (1982).

[3] D. J. Wales. *Energy Landscapes: With applications to clusters, biomolecules and glasses,* Cambridge University Press, Cambridge, (2003).

[4] J. D. Bernal. *Nature*, **183**, 141, (1959).

[5] P. G. Debenedetti, F. H. Stillinger, T. M. Truskett and C. J. Roberts. *J. Phys. Chem. B,* **118**, 8821, (2003).

[6] L. Von. Heimendahl. *J. Phys. F: Metal Phys.,* **5**, L141, (1975).

[7] G. A. N Connell. *Sol. State. Commun.,* **16**, 109, (1975).

[8] W. B. Streett, J. H. Raveché and R. D. Mountain. *J. Chem. Phys.,* **61**, 1960, (1974).

[9] A. Rahman, J. M. Mandell and J. P. McTague. *J. Chem. Phys.,* **64**, 1564, (1976).

[10] L. V. Woodcock, C. A. Angell, P. Cheeseman. *J. Chem. Phys.,* **65**, 1565, (1976).

[11] T. M. Truskett, S. Torquato, S. Sastry, P. G. Debenedetti and F. H. Stillinger. *Phys. Rev. E*, **58**, 3083, (1998).

[12] C. J. Roberts, P. Debenedetti and F. H. Stillinger. *J. Phys. Chem B,* **103**, 10258, (1999).

[13] F. H. Stillinger and T. A. Weber. *J. Phys. Chem.,* **87**, 2833, (1983).

[14] R. A. La Violette, J. L. Budzien and F. H. Stillinger. *J. Chem. Phys.,* **112**, 8072, (2000).

[15] T. A. Weber and F. H. Stillinger. *J. Chem. Phys.,* **80**, 2742, (1984).

[16] C. S. Liu, Z. G. Zhu, J. Xia and D. Y. Sun. *Phys. Rev. B,* **60**, 3194, (1999).

[17] F. H. Stillinger and T. A. Weber. *Phys. Rev. B,* **31***, 5262,* (1985)*.

[18] C. Chakravathy, P. G. Debenedetti and F. H. Stillinger. *J. Chem. Phys.,* **123**, 206101, (2005).

[19] B. Brehler. *Z. Kristallogr.*, **115**, 373, (1961)

[20] J. E. Enderby and A. C. Barnes. *Rep. Prog. Phys.*, **53**, 85, (1990).

[21] R J Newport, R. A. Howe and N. D. Wood. *J. Phys. C: Solid State Phys.,* **18**, 5249, (1985).

[22] A. Di Cicco, A. Taglienti, M. Minicucci and A. Filipponi. *Phys. Rev. B*, **62**, 12001, (2000).

[23] P. S. Salmon and I. Petri. *J. Phys.: Condens. Matter*, **15**, S1509, (2003).

[24] P. S. Salmon, R. A. Martin, P. E. Mason and G. J. Cuello. *Nature (London)*, **435**, 75, (2005).

[25] P. Vashishta, R. K. Kalia and I. Ebbsjö. *Phys. Rev. B*, **39**, 6034, (1989).

Chapter 10

Homopolarity and the effect on IRO

10.1 Introduction.

In previous chapters we have demonstrated the effect of varying anion polarisability and system conditions in terms of controlling liquid network topology. In particular, these factors are shown to control the arrangement of (predominantly) tetrahedral (although both higher and lower ion coordination environments have been shown to have significant effects) units in the network systems, with associated changes in both the intensity and position of the first-sharp diffraction peak (FSDP). The FSDP, we recall, is taken as indicative of significant intermediate-range order (IRO). In this chapter, we investigate the change of structure in a rigid ion system when *homopolar bonds* (bonding of like atoms) are included. The primary goal of this chapter is to demonstrate how such bonding motifs may be included, within a relatively simple model framework, without the need for computationally-demanding electronic structure calculations. These models are not, at present, constructed to give an accurate description of specific systems, but are constructed in a more speculative fashion in order to highlight how the presence of such homopolar bonds may influence liquid structure.

Experimentally, homopolar bonds are observed as small peaks in the like-like radial distribution functions, $g_{MM}(r)$ and $g_{XX}(r)$ for systems of MX_2 stoichiometry. In a chemically-ordered network, such as those described previously in which electrostatic (Coulombic) forces dominate, such bonding motifs may be excluded. In the random covalent network[1], which describes a chemically disordered network, an atom has no preference to bond with like or unlike atoms. In systems of interest to us, such as $GeSe_2$, homopolar bonds can be considered as defects in a chemical ordered network model which arise either through close separation of anions bridging cations or as an isolated homopolar bond between cation-centred units.[2] As a result, such systems can be considered as essentially chemically ordered networks with a significant element of random network. The incidence of homopolar bonds predicted from experiment is a maximum of 25% and 20% of Ge and Se atoms respectively in $GeSe_2$[3,4]. The presence of

homopolar bonds is shown in several Raman[5-10], Mössbauer[11-12] and grazing incidence X-Ray scattering (GIXS) experiments[13]. They are either described as appearing as defects within a tetrahedral network[5-8,13] or as an integral feature of the proposed constituent units[9-12] such as the Ge_6Se_{14} units (shown earlier in figure 4.1) present in the "outrigger-raft" model[9]. Other experiments on $GeSe_2$ have not detected the presence of homopolar bonds[14,15].

In the *ab initio* FPMD model[16] for $GeSe_2$ highlighted in Chapter 4, homopolar bonds between Se atoms exist as a bridge connecting two cation-centred units. The PIM parameter sets used so far are unable to induce homopolar bonds as might be expected for models where Coulombic interactions, resulting from the presence of formal valence charges, are dominant. In early electronic structure calculations[17] on $GeSe_2$, where the local density approximation (LDA)[18] is applied for the exchange and correlation energy, the high proportion of atoms observed to be in homopolar bonds (60% for Se and 25% of Ge) correlated with an absence of a FSDP in the total structure factor. When a generalised gradient approximation (GGA) for electron correlation[19] was introduced, these proportions reduced to 39% for Se and 10% for Ge and a FSDP appeared. This feature was attributed "to the enhancement in chemical order in the form of tetrahedral units, which in turn establish an intermediate-range order featuring a FSDP".[17] Calculations by Drabold[20] and Massobrio[16] on $GeSe_2$ report systems with both the presence of homopolar bonds (26% and 17% of Ge atoms and 24% and 32% of Se atoms in homopolar bonds respectively) and the presence of a FSDP. The LDA results were highlighted as possibly representative of high temperature behaviour for the $GeSe_2$ melt where a large decrease is observed in the intensity of the FSDP in $S_{NN}(k)$.[21] Our results in Chapters 4 and 8 show that structural features of $GeSe_2$: the presence of a FSDP in $S_{CC}(k)$ and high temperature reduction in FSDP, are reproduced without the presence of homopolar bonds. A question of interest, therefore, is what role does the presence of homopolar bonds have on IRO. In addition, the strength of any effects can be probed by systematically varying the number of homopolar bonds within the simulation model (the analogue of controlling the network topology through the anion polarisability).

10.2 Method.

Homopolarity was incorporated into a RIM by means of a Morse potential (referred to now on as the Morse-RIM) which is applied between pairs of like atoms only. The potential takes the form

$$U_{Morse}^{ij}\left(r^{ij} \right) = D_e\left(1 - \exp\left(-a\left(r^{ij} - r_e \right)^2 \right) \right)$$

(10.1)

where R^{ij} is the separation between ions of like charge, r_e. In a standard Morse potential, for example modelling the vibrations of a simple diatomic molecule, r_e and D_e are simply the separation and depth of the energy minimum in the function. In the present work the interaction energy between pairs of like ions will be dominated by the (repulsive) Coulombic interactions. As a result, r_e and D_e are effectively parameters which define the length-scale over which homopolar bonds may be formed and the strength of those bonds respectively. Figure 10.1 highlights the effect of including a Morse potential with the
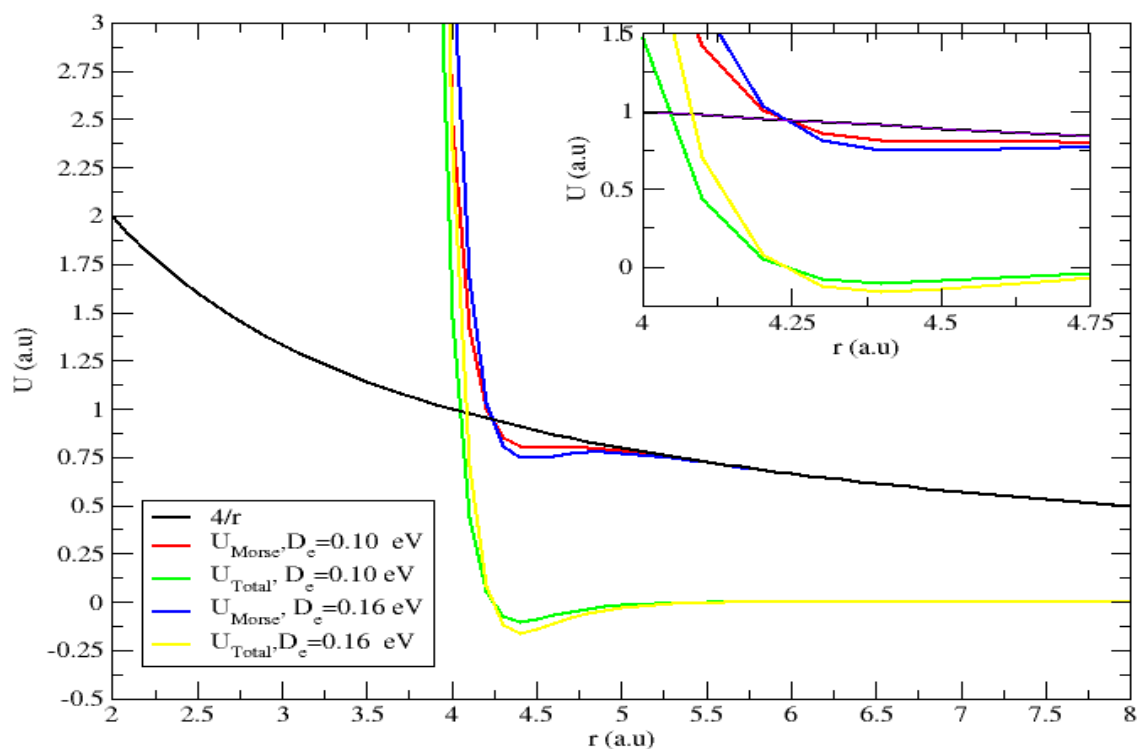
Figure 10.1: Energy diagram for formulation of Morse-RIM potential. Inset: close-up. The function 4/r is an indication of the form of the electrostatic repulsion to which a Morse potential must overcome to induce hompolar bonds . D_e is the dissociation energy, which at D_e=0.10 eV (from original parameterisation) and 0.16 eV (where $H_{XX,}$ the percentage of anions in homopolar bonds, is 100%). The parameter, a, which controls the width of the potential is fixed at 4.0 a.u for both values of D_e.

electrostatic repulsion between two X$^-$ ions. The latter interaction takes the form U=+4/r which is here augmented with the Morse potential which acts to effectively induce a local energy minimum (a "kink") into the total energy function. The presence of this local energy minimum can act to stabilise the relatively close approach of anion pairs.
The total energy of interaction can be written as:

$$U_{Total} = U_{Morse} + U_{Born-Mayer}$$

(10.2)

ij	Fumi-Tosi			Morse		
	a^{ij}(a.u)	B^{ij}(a.u)	C^{ij}(a.u)	r_e (a.u)	A (a.u)	D_e (eV)
XX	1.00	8.00	0.0	4.4	4.0	0.10
MX	1.600	30.00	0.0	-	-	-
MM	1.5564	19.699	40	4.4	4.0	0.10

Table 10.1:Parameter set for Morse-RIM of a MX$_2$ system giving Fumi-Tosi and Morse potential parameters for each ion pair.

10.3 Simulation details.

All calculations in this chapter consists of 324 (108 cations and 216 anions) ions. The initial starting configuration was used from previous calculations at zero pressure where parameters were perturbed to maximise the number of homopolar bonds between anions and to maximise the attractive interaction between the cations. A homopolar bond is defined as any pair of like ions found within a given cut off, defined by the position of the minima in the principal peak of $g_{MM}(r)$ and $g_{XX}(r)$ (~4.69Å for $g_{XX}(r)$ through the H$_{XX}$ range and 5.19Å for $g_{MM}(r)$). To obtain liquid densities for the model a pressure of 3.5x10^{-4} a.u was applied. The temperature of the system was set at 1500K. Table 10.1 lists the parameter set for the model used in this chapter. This parameter set was derived from earlier calculations[22] at zero pressure. To limit the number of variables observed in this chapter, all parameters were kept constant apart from the parameter, D_e^{XX}, which controls the percentage of homopolar bonds. D_e^{XX}, was increased from 0.00 eV in steps of 0.04 eV. The parameter, D_e^{XX}, which controls the depth of the energy well in the anion-anion energy function, was varied from 0.00-0.20 eV, this range being found to yield a percentage of anions in homopolar bonds, H$_{XX}$, from 0-100% (figure 10.2a). Once

the range of anions present in homopolar bonds was understood with 100% being reached at 0.20 eV, more data points were collected in the range of 0.00 eV to 0.20 eV to measure the change in homopolar bonds against network connectivity statistics. The sharpest rise in the number of homopolar bonds occurs in the region of D_e^{XX} =0.06-0.10 eV, where the homopolar percentage jumps from 6 to 80%. The cell size was fixed for the D_e^{XX} range 0-0.20 e.v at 20.87Å, similar to typical liquid densities in this stoichiometry. A simulation was carried out at elevated temperatures of 2500K, well above the melting temperature, to equilibrate the configuration for the model. For each calculation in this chapter, an equilibration run of 50 ps was used and a simulation run of 150 ps under NVT conditions at 1500K was undertaken. Structural quantities were calculated for D_e^{XX} values of 0.00, 0.04, 0.08, 0.09, 0.12 and 0.16 eV which correspond to H_{XX} values of 0%, 3%, 25%, 55%, 80% and 100%.

In section 10.9, calculations at a range of cell sizes were calculated to observe high and low density behaviour of systems with no homopolar bond and a system with many homopolar bonds (H_{XX}=80%). The barostats were relaxed from 3.5 x10^{-4} a.u configuration to 2.5 x 10^{-4} a.u and 1.5 x 10^{-4} a.u resulting in larger cell sizes of 23.56Å and 28.77Å. A higher density configuration of with an average cell size of 19.42Å.was generated by increasing the barostats to 4.5 x 10^{-4} a.u. The configuration were equilibrated for 50 ps and a simulation run of 150 ps under NVT conditions were undertaken.

10.4 Homopolar bonding and changes in network connectivity.

Figure 10.2b indicates that with an increasing percentage of homopolar bonds the percentage of edge-sharing cations rises sharply. The sharpest rise occurs in the range D_e^{XX} =0.04-0.11eV where the fraction of cations labelled "0" change from 82%-3%; those labelled "1" rise from 16% to 36% at 0.09 eV, and then declines to 18%; and those labelled "2" rise from 2% to 87%. The correlation between the fraction of anions in homopolar bonds and the fraction cations in edge-sharing "1" and "2" configurations can be understood as follows. In polarisable ion models, the edge-sharing unit is stabilised by the presence of dipoles on the anion bridges which act to shield the Coulombic repulsion between cation pairs and, as a result, stabilise their relatively close approach. In the Morse-RIM model the formation of homopolar bonds results in an effective build up of

negative charge around two closely spaced *anions* which stabilises the closer separation of cations. Figure 10.3 shows a schematic diagram of such an edge-sharing unit and highlights how the formation of a homopolar bond between the bridging anions acts to stabilise this edge-sharing motif.
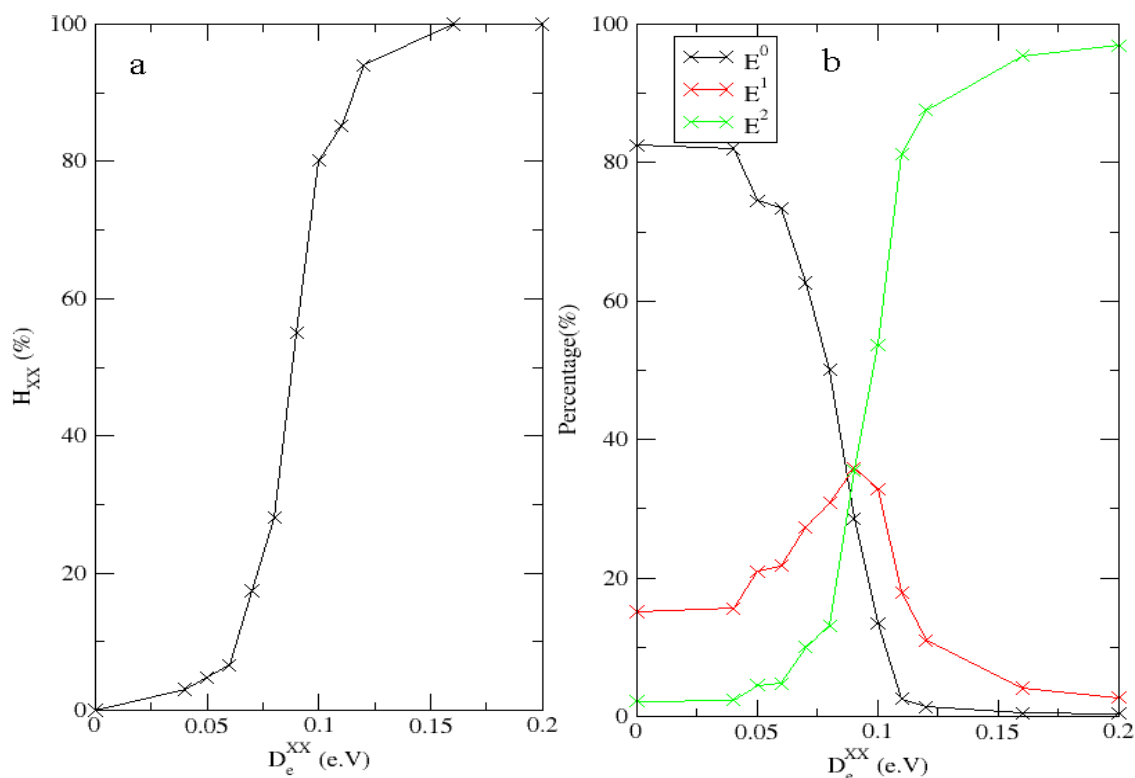
Figure 10.2 (a) Percentage of anions (H_{XX}) in homopolar bonds with varying potential energy well depth, $D_e^{XX}(eV)$ (left). (b) Percentage of cations in different network connectivities with varying
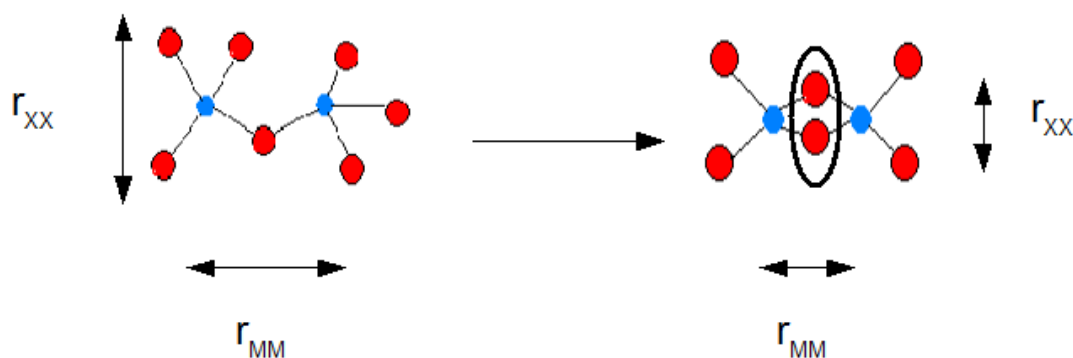
Figure 10.3: Change in connection of two tetrahedral units (red circles are X anions and blue circles are M cations) with increasing homopolarity. The distance r_{XX} and r_{MM} decrease, for the anion-anion interactions this is strong enough to produce a prepeak in $g_{XX}(r)$ but not in $g_{MM}(r)$. An edge-sharing unit is formed by the concentration of negative charge of the two anions in the homopolar bond (circled) which stabilises the closer separation of the cations.

10.5 Changes in the partial structure factor with varying anion homopolarity, H_{XX}.

The partial structure factors calculated are shown in figure 10.4. At low values of H_{XX}, the position of the FSDP in $S_{MM}(k)$ is $\sim 1.45 \text{Å}^{-1}$. This is associated with low polarisability systems where the inter-tetrahedral linkages are predominantly corner-sharing. At $H_{XX}=80\%$, the position of the FSDP shifts dramatically to $\sim 1.07 \text{Å}^{-1}$ which is linked with the increased presence of significant edge-sharing within the tetrahedral framework. The formation of the FSDP at small scattering angles is coupled with a sharp increase in the intensity of the principal peak at 1.92Å^{-1}, from 1.34 at $H_{XX}=0\%$ to 2.76 at 100%. The changes in $S_{MM}(k)$ with increasing H_{XX} mirror the changes observed with increasing polarisability (Chapter 6): the increase in anion polarisability changes the FSDP position from $\sim 1.4 \text{Å}^{-1}$, shifting in position to lower k, with an associated decline in intensity and then, with further increased anion polarisability, an increase, corresponding to systems such as $GeSe_2$ where the intensity of the FSDP approached that of the principal peak. Here we observe a limiting case in terms of induction of homopolar bonds and the ratio of the FSDP intensities of the principal and first-sharp peaks, with values observed (33% and 25% at $H_{XX}=80\%$ and 100% respectively) that are lower than that observed in systems such as $ZnCl_2$ (55%) and $GeSe_2$ (90%).

The FSDP in the cation-anion partial structure factor, $S_{MX}(k)$, shifts from $\sim 1.44 \text{Å}^{-1}$ at $H_{XX}=0$-55% to $\sim 1.13 \text{Å}^{-1}$ at $H_{XX}=80\%$ and $H_{XX}=100\%$. The changes in the principal peak intensity show relatively smaller changes with the fraction of homopolar bonds, with a minimum at $H_{XX}=3\%$ of -1.18 and a maximum of -1.74 occurs at $H_{XX}=80\%$. The increased homopolarity has a more dramatic effect on the *anion-anion* correlations, with a significant FSDP, indicative of the presence IRO in the anion sublattice, appearing as the degree of homopolarity increases. In the range, $H_{XX}=0$-55%, a small FSDP in $S_{XX}(k)$ is present at $\sim 1.41 \text{Å}^{-1}$ with intensity in the range 0.32-0.47. At 80%, the FSDP moves to lower scattering wavevectors of 1.09Å^{-1}. In contrast to the changes in $S_{MM}(k)$, the increase in intensity of a FSDP is coupled with a *decrease* in the intensity of the principal peak, and a shift in position, from 2.83 at 2.00Å^{-1} for $H_{XX}=0\%$ to 1.72 at 1.88Å^{-1} for $H_{XX}=100\%$. This is the first system studied in this thesis where a substantial FSDP in $S_{XX}(k)$ has been observed. It is only upon the formation of significant amounts of homopolar bonds (well beyond that experimentally observed) that significant IRO appears in the anion-anion

correlations in the system. The creation of two lengths scales in $S_{XX}(k)$ is analogous to the mechanism proposed by Wilson and Madden[23] where the closer cation separation enabled by the presence of a dipole on the anion is matched by a corresponding longer length scale. Also, the nature of the FSDPs for all three ion correlations are similar at high H_{XX} values in contrast to other systems previously studied, where the FSDPs in the cation-cation and cation-anion correlations dominate those from anion-anion correlations.

Figure 10.4: Partial structure factors in MX_2 system with varying homopolarity. Black, 0%; red, 3%; green, 25%; blue, 55%;yellow, 80%; brown, 100%.

10.6 Changes in the radial distribution functions.

The radial distribution functions shown in figure 10.5 show similarly large changes with the increase of H_{XX}. Firstly, the existence of homopolar bonds is highlighted by the emergence of a peak at 2.34Å in $g_{XX}(r)$. This peak rises sharply in intensity from 2.91 at $H_{XX}=3\%$ to 15.56 at $H_{XX}=100\%$. The rise in peak intensity is correlated with a shift in the principal peak position to higher r, from 3.67Å to 3.98Å. In comparison with experimentally obtained functions, such as $g_{SeSe}(r)$ in $GeSe_2$, the low-r peak is much

sharper and larger in intensity. The principal peak position in $g_{MX}(r)$ remains constant at 2.24Å but increases in intensity from 5.45 to 7.02 as the homopolar bond percentage changes from 0-55% to 80%-100%. A smaller minima in $g_{MX}(r)$ is observed at H_{XX}=80% and H_{XX}=100% in addition to the splitting effect in the second peak at the same percentage, where two peaks at 4.54Å and 5.94Å are observed.

In a rigid-ion model, the cation-cation and anion-anion separations are expected to be ordered along Coulombic lines; here, an increase in H_{XX} leads to smaller cation-cation separations. At 0%, the principal peak position of $g_{MM}(r)$ is 4.37Å. This figure is similar until H_{XX}=80% when the peak shifts to 3.96Å, corresponding to the increasing edge-sharing behaviour. However, the ratio, $g_{MM}^{PP}(r)$ / $g_{MX}^{PP}(r)$ of 1.77 indicates that, in terms of the classification highlighted in Chapter 6, the system lies in between SiO_2 and $ZnCl_2$, where the respective values are 1.94 and 1.62. In addition, there is an increase intensity in the region 6-8Å for $g_{MM}(r)$ at H_{XX}=80% and 100%, showing significantly greater ordering.
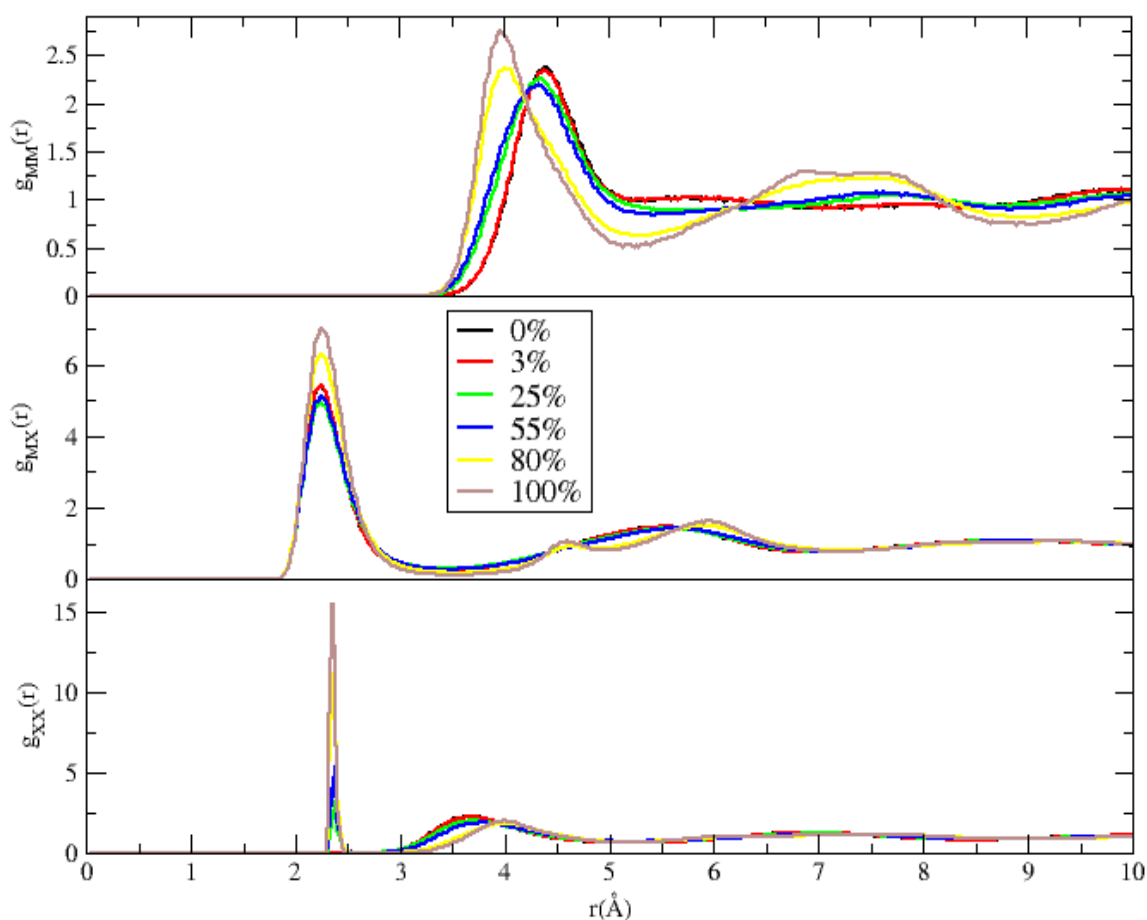
Figure 10.5:Radial distribution functions in MX_2 system with varying homopolarity. Black, 0%; red, 3%; green, 25%; blue, 55%; yellow, 80%; brown, 100%.

10.7 Changes in the bond angle distributions.

The bond angle distributions are shown in figure 10.6. From H_{XX}=0-55%, the M-X-M bond angle is 135°, values typical for corner-sharing tetrahedral systems. At H_{XX}=80%, this peak shifts to ~115° and sharpens in intensity, indicative of the decreased separation of cations with increasing H_{XX}. For the X-M-X function a peak emerges at 50° as the number of homopolar bonds increases. At H_{XX}=80%, this peak rises sharply in intensity and the larger angle peak shifts from ~100° to 118°. This correlates with the presence of homopolar bonds in the system which derive from a close separation of anion pairs in edge-sharing units. As homopolarity becomes increasingly larger, this peak increases in the intensity while the typical X-M-X bond angle shifts to higher values (as can be understood by considering figure 10.3). At H_{XX}=55% the system exhibits an intermediate bond angle distribution, as exemplified by the nascent formation of a peak at 59° in M-M-M, and the peak in M-X-M whose position is closer to the higher H_{XX} distributions, but where the intensity is closer to the lower H_{XX} distributions.
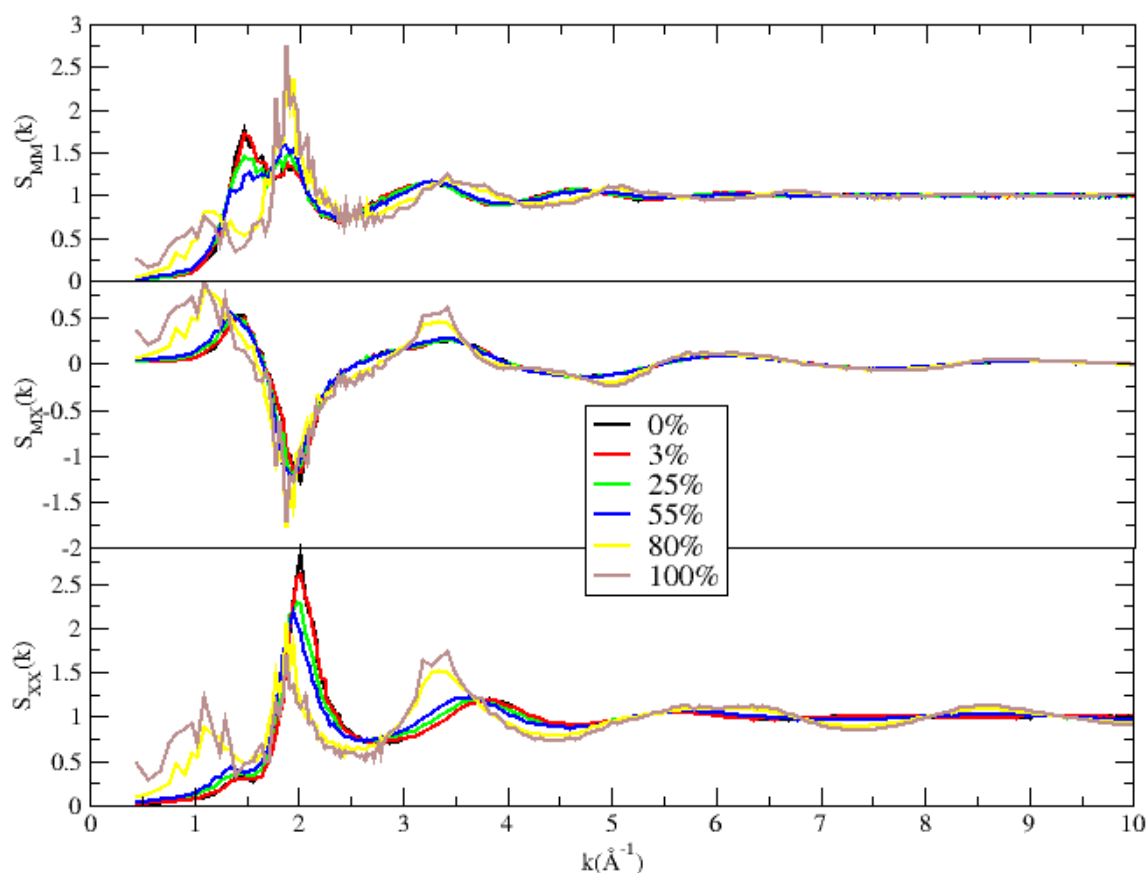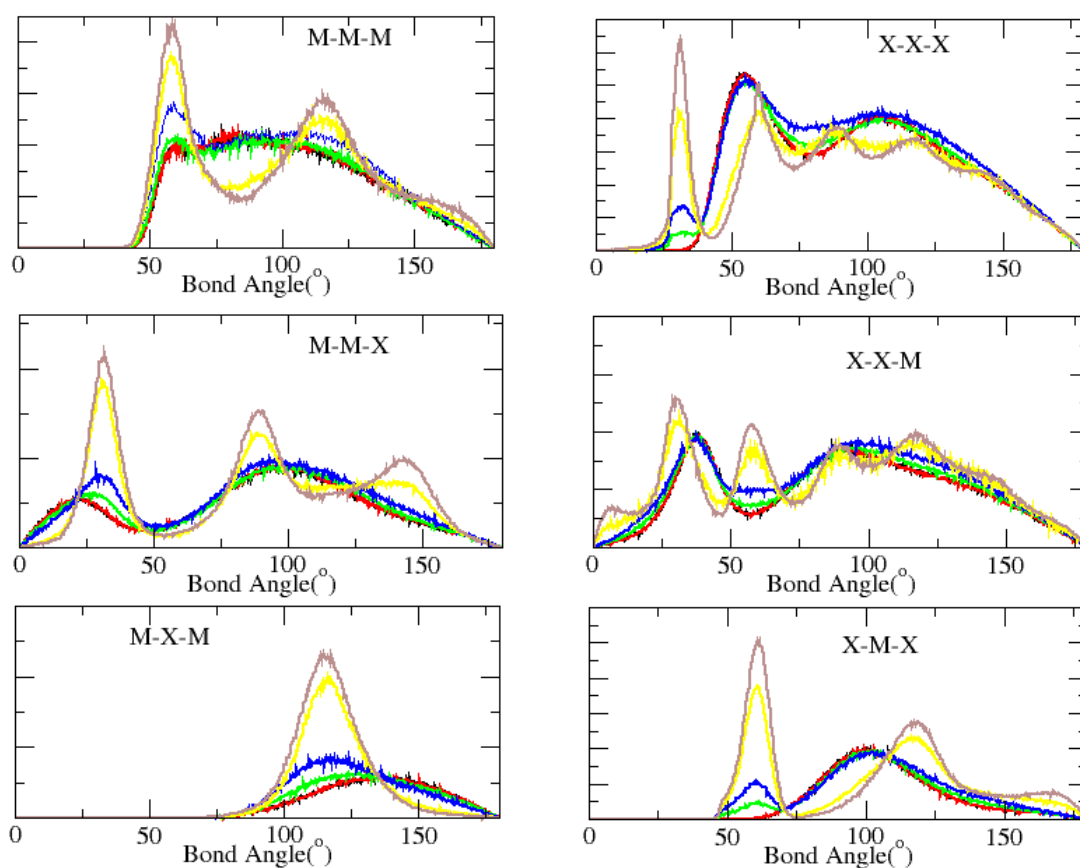

Figure 10.6: Bond angle distributions in MX_2 system with varying homopolarity. Black, 0%; red, 3%; green, 25%; blue, 55%; yellow, 80%; brown, 100%.

10.8 Molecular Graphics.

Figure 10.7 shows graphical snapshots of configurations at H_{XX}=3%, 25%, 80% and 100%, representing contrasting degrees of chemical disorder. The system displaying no homopolar bonds (corresponding to the simple RIM) appears dominated by charge-ordering and hence the system can be well-described in terms of corner-linking MX_4 tetrahedra. The charge ordering also leads to a relatively uniform ionic density distribution with an absence of significant void structure. For high degrees of homopolarity larger voids in the ion structure are evident which correspond to the low k features observed in all three partial structure factors in figure 10.4. The inclusion of homopolar bonds in a system of fixed density promotes the emergence of additional ordering on intermediate length-scales. Similar void structure may be induced into liquid and glassy systems such as $ZnCl_2$ through templating, where ordering across these voids induces the peaks at low k in the underlying structure factors.[24]
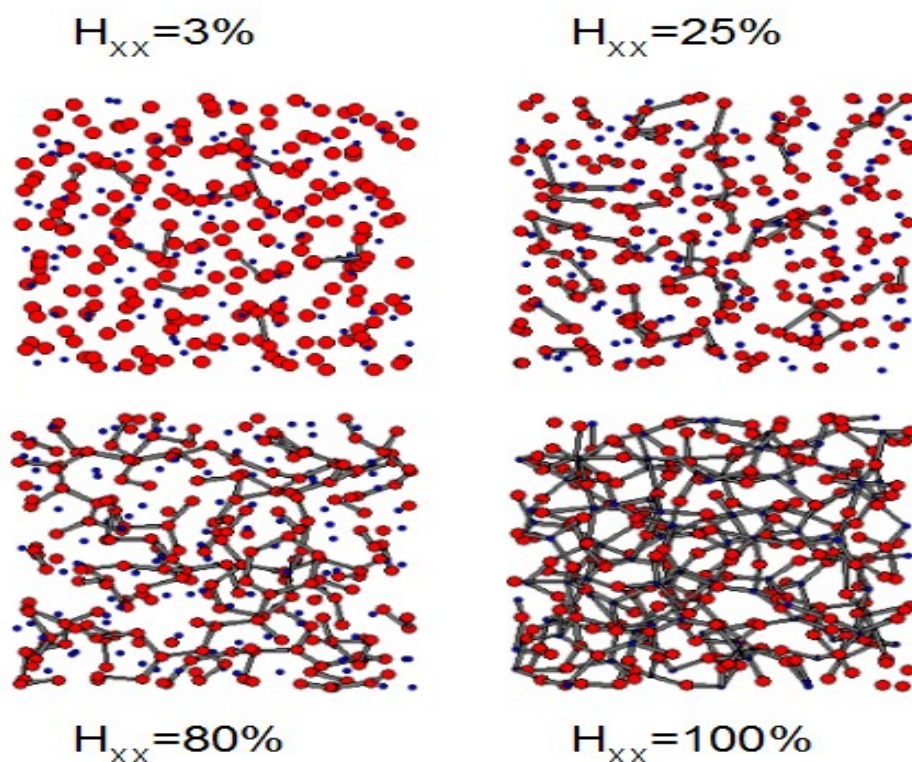
Figure 10.7: Graphical snapshots of Morse-RIM configurations with increasing homopolarity, H_{XX}. Cations are represented by blue circles and aniond by red circles. (Homopolar bonds between anions, where the cutoff is 3.17Å, are shown). With increasing H_{XX}, clustering of both cations and anion increasingly occurs. This is visible with creation of voids observable at H_{XX}=80% and H_{XX}=100% in addition to the evidence from the change in cation coordination numbers and the creation of longer length scales in partial structure factors.

Homopolar coordination	Mean coordination of ion pairs			
	M_{MX}	M_{XM}	M_{XX}	M_{MM}
0%	4.22	2.11	12.91	6.86
3%	4.22	2.11	12.92	6.68
25%	4.38	2.18	12.97	6.71
55%	4.65	2.32	13.54	7.09
80%	5.10	2.55	12.75	6.68
100%	5.48	2.74	12.97	7.04

Table 10.2: Coordination for ion pairs of Morse-RIM MX_2 system.

10.9 Coordination Numbers.

Table 10.2 shows the changes in coordination number with the number of homopolar bonds. At low H_{XX}, the values are closer to a predominantly tetrahedral system: the cation-anion coordination is 4.2, while the anion-cation coordination is 2.1. With increasing homopolar bond percentage, an increase in coordination is observed for all the ion pairs. Whereas increases in coordination are usually associated with increasing system density, the increase in coordination here is accompanied by the stabilisation of larger voids. In other words, the *effective* local system density increases accompanied by the emergence of ordering on an intermediate length-scale associated with larger void formation (regions of low local ion density). The MM and XX coordination numbers appear approximately independent of the number of homopolar bonds.

To highlight the effect of system density additional simulations are performed at three further densities, corresponding to cubic simulation cell lengths, L, of 19.42Å, 23.56Å and 28.77Å, the original simulations being performed at a system density corresponding to a cell length of 20.87Å. The effect of the change in system density is highlighted by the calculation of partial structure factors of systems at high and low values of H_{XX}, (corresponding to H_{XX}=0% and H_{XX}=80% respectively), shown in figure 10.8.

At the lowest density studied (corresponding to L=28.77Å) an effective phase separation (as characterised by an increase in the structure factor intensities as k tends to 0) is observed for $S_{MM}(k)$ and $S_{MX}(k)$ when H_{XX}=80%, in contrast with H_{XX}=0%. For H_{XX}=0%, the lower density configurations show a FSDP tending towards the values observed in higher H_{XX} systems at the same density, with the FSDP shifting in $S_{MM}(k)$

from 1.50Å at 19.42A to 0.98Å^{-1} at 28.77Å. The high density behaviour when H_{XX}=80% displays characteristics similar to changes observed in systems discussed in Chapters 6-8: diminution of the FSDP intensity at ~1Å^{-1} in $S_{MM}(k)$ and a decline in intensity and a shift in position to higher k to 1.35Å^{-1} for $S_{MX}(k)$. The FSDP in $S_{XX}(k)$ declines in intensity to 0.86 and position shifts to 1.35Å^{-1}. For H_{XX}=0%, the split peak in $S_{MM}(k)$ is merged into a single peak at 1.71Å^{-1} at the highest density.
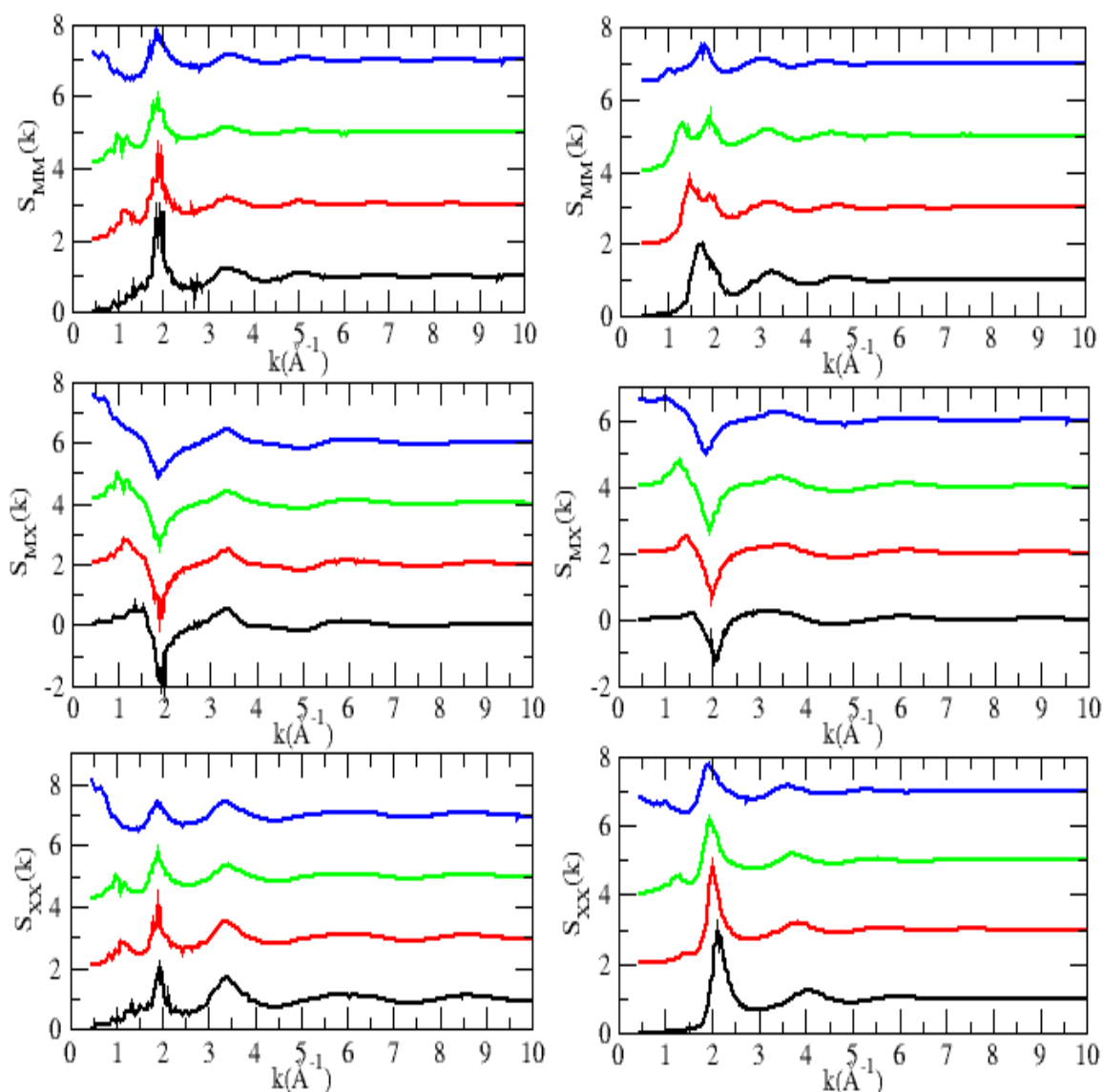
Figure 10.8: Partial structure factors for MX$_2$ system at H_{XX}=80% (left) and H_{XX}=0% (right) at different simulation cell lengths. Black, 19.42Å; red, 20.87Å; green, 23.56Å; blue, 28.77Å.

10.10 Conclusion.

The implementation of a Morse potential in addition to the Born-Mayer potential is able to induce homopolar bonds between anions. When the amount of anions in homopolar bonds, H_{XX}, increases, the percentage of cations in edge-sharing configurations also increases. With increasing H_{XX}, the intermediate-range order changes from that typically observed for systems with anions of low polarisability, with a FSDP in $S_{MM}(k)$ at ~1.5$Å^{-1}$, to that typical of systems containing anions of high polarisability, as evidenced by the change in the position of the FSDP in $S_{MM}(k)$ to ~1$Å^{-1}$. It is, however, important to note that these changes only occur at values of H_{XX} much higher than those typically observed experimentally. The presence of a large proportion of homopolar bonds leads to a significant perturbation in anion-anion correlations leading to a significant FSDP at ~1$Å^{-1}$ in $S_{XX}(k)$. The effect of density changes in such systems were highlighted: at lower densities, configurations with significant amounts of homopolar bonding showed effective phase separation in the partial structure factors, while at higher density, IRO collapses, as it does with configurations which exhibit no homopolar bonds and in keeping with systems such as $ZnCl_2$ as shown in chapter 7. The presence of IRO in this system (where H_{XX}=80%) is much more sensitive to packing effects than that observed for MX_2 (α_X=35a.u) in chapter 8, where, at lower densities, the FSDP intensity increases.

Although approached from a different angle (without the presence of anion polarisability) there are similarities with other systems, such as $GeSe_2$, explored in this thesis: the creation of local density differences by the contraction of the first coordination shell lead to the presence of larger voids with inherent longer-range ordering across them. The evolution of IRO with increasing homopolar bonding is comparable to the change in IRO observed in Chapter 6 although there are number of significant differences. The intensity of the FSDP in $S_{MM}(k)$ is much smaller than observed with systems which change with anion polarisability. There is also a departure from tetrahedral coordination with increased edge-sharing (as shown in figure 10.2) in contrast to the systems in chapter 6 where it is strengthened. However, despite this departure away from tetrahedral coordination, the IRO present in the system increases, stressing the importance of connections between such units rather than the nature of the SRO present. This in contrast with an earlier study[25] which stressed the importance of tetrahedrality in stabilising IRO. In addition, at high proportions of anions in homopolar bonds, the percentage of "2"

cations is higher than that observed previously (indicated by figure 6.15) due to the rapid increase in MX coordination. The variation in changes of network connectivity and the resulting changes in structure between systems explored in C6 and C10 is highlighted by observing the system when percentage of anions in homopolar bonds are at 55%. The respective "0", "1" and "2" cation percentages are 36%, 36% and 28% for the MorseRIM systems closer to the result obtained for $ZnCl_2$ (33%, 40% and 27%) compared to $GeSe_2$ (18%, 49% and 33%). The resulting structure is indicative of systems with smaller anion polarisability however with the FSDP in all three partial correlation functions appearing at $k\sim1.3\text{Å}^{-1}$. By referring to figure 6.5, the anion polarisabililty value which corresponds to a FSDP position of 1.3Å^{-1} is $\alpha_X=20$ a.u (using the position of $S_{MX}(k_{FSDP}=1.3\text{Å}^{-1})$ and $\alpha_X=25$ a.u using $S_{MM}(k_{FSDP}=1.3\text{Å}^{-1})$ indicating the system at $H_{XX}=55\%$ is closer to $ZnCl_2$ than $GeSe_2$.

In contrast with the other systems explored, this mechanism has a similar effect on all three partial correlations whereas, previously, it had been primarily the changes in the cation-cation and cation-anion correlations which dominated the resulting nature of the IRO. The presence of large numbers of homopolar bonds leads to a significant difference in the anion-anion correlations compared with the RIM, which for the first time in this study, displays a significant FSDP at $\sim1\text{Å}^{-1}$ in the structure factor. The difficulty of observing real space correlations responsible for IRO is highlighted by the different changes which occur in the related radial distribution functions: a split second peak observed in $g_{MX}(r)$, a shift in the position of the principal peak for $g_{MM}(r)$ to smaller r values, and a shift in the principal peak in $g_{XX}(r)$ to higher r values. This system is significant that in contrast with other MX_2 systems which display the FSDP, where the IRO present is dependent on cation-cation and cation-anion correlations, anion-anion correlations are also significant. This indicates a single mechanism which contributes equally to all three correlations, in contrast to the evolution of IRO in $ZnCl_2$ with temperature and pressure (observed in chapter 7) where the different rates of change in FSDP properties indicates different mechanisms are responsible.

These are the first set of calculations to look specifically at the effect of inducing homopolar bonds into a tetrahedral network. In previous electronic calculations, the effect of homopolar bond presence has not been separated from other structural features such as the strength of the tetrahedral coordination, in addition to the variety of computational methods used where homopolar bonds are present. In our model, the homopolar bonds are

present in edge-sharing units. In chapter 4, we showed that homopolar bonds in the FPMD are isolated connecting cation-centred units. In the calculations of Cobb and Drabold[20], the majority of Ge and Se atoms involved in homopolar bonds are present in ethane-like units and dimers respectively while for high pressure simulations of $GeSe_2$, chains of Se atoms are predicted. In contrast, other studies do not state specifically in which type of structures the homopolar bonds are present.[26, 27] so as such it is difficult to make comparison with these systems. While these calculations show a varying presence of homopolar bonds, how the resulting structures in which homopolar bonds are present affect the network structure is unclear.

With regards to experimental systems, this simple model broadly correlates the existence of significant homopolar bonding in systems with those systems which display IRO and large presence of edge-sharing units. Experimentally, the range of MX_2 systems which display homopolar bonds include $GeSe_2$ whilst those systems dominated by ionic bonding including $ZnCl_2$, SiO_2, and GeO_2 do not. Systems such as liquid $SiSe_2$ are intermediate between these two groups of systems, displaying a strong presence of edge-sharing tetrahedra, but a much smaller presence of homopolar bonding (1% of Se atoms[28,29]). In contrast with experimental systems, significant homopolar bonding is observed in systems which do not display a FSDP at $\sim 1\text{Å}^{-1}$, a likely feature of using the RIM, which does not account for polarisation effects, in conjunction with the Morse potential.

The system described in this chapter have yet to be observed experimentally and computationally but there are similarities with other systems where the mechanism for the creation of the FSDP has been shown through the creation of void inhomogeneities[30]. Computationally, this has been done on simple crystal packing of a cell of 27000 Lennard Jones atoms by taking out atoms to created voids. By applying the method to a crystalline cell, phase separation was observed in the structure factor, whilst with amorphous systems a FSDP observed; with dimunition of the number of atoms, the position stayed the same, but the intensity of the FSDP increased. One significant difference is that the creation of intermediate length scales is produced by keeping the concentration of the liquid constant. Experimentally, this has been achieved by introduction of voids using alkylammonium templating[24], described earlier in section 1.8.1, although the range of FSDP positions observed with increasing void size ($1.4-0.75\text{Å}^{-1}$) is different from that observed here ($1.45-1.07\text{Å}^{-1}$).

10.11 References.

[1] K. S. Liang, A. Bienenstock and C. W. Bates. *Phys. Rev. B,* **10**, 1528, (1974).

[2] R. M. White. *J. Non-Cryst. Solids,* **16,** 387, (1974).

[3] P. S. Salmon and I. Petri. *J. Phys.: Condens. Matter.,* **15**, S1509 (2003).

[4] I. Petri, P. S. Salmon and H. E. Fischer. *Phys. Rev. Lett.,* **84**, 2413 (2000).

[5] P. Tronc, M. Bensoussan, A. Brenac and C. Sebenne. *Phys. Rev. B*, **8**, 5947, (1973).

[6] R. J. Nemanich, F. L Galeener, J. C. Mikkelsen Jr, G. A. N. Connell, G. Etherington, A. C. Wright and R. N. Sinclair. *Physica B*, **117**, 959, (1983).

[7] R. J. Nemanich, G. A. N.Connell, T. M. Hayes and R. A. Street. *Phys. Rev B,* **18**, 6900, (1978).

[8] S. Sugai. *Phys. Rev. B*, **35**, 1345, (1987).

[9] P. M. Bridenbaugh, G. P. Espinosa, J. E. Griffiths, J. C. Phillips and J. P. Remeika. *Phys. Rev. B,* **20,** 4140, (1979).

[10] W. J. Bresser, P. Boolchand, P. Suranyi and J. P. de Neufville. *Phys. Rev. Lett.*, **46**, 1689, (1981). .

[11] P. Boolchand, J. Grothaus and J. C. Phillips. *Solid State Commun.,* **45**, 183, (1983).

[12] P. Boolchand, J. Grothaus, W. J. Bresser and P. Suranyi. *Phys. Rev B*, **25**, 2975, (1982).

[13] A. Fischer-Colbrie and P. H. Fuoss. *J. Non-Cryst. Solids*, **69**, 271, (1985).

[14] V. Petkov. *J. Am. Ceram. Soc.*, **88**, 2528, (2005).

[15] S. Susman, K. J. Volin, D. G. Montague and D. L. Price. *J. Non-Cryst. Solids*, **125**, 168, (1990).

[16] C. Massobrio, A. Pasquarello and R. Car. *Phys. Rev B*, **64**, 144205, (2001).

[17] C. Massobrio, A. Pasquarello and R. Car. *J. Am. Chem. Soc.,* **121**, 2943, (1999).

[18] J. P. Perdew and A. Zunger. *Phys. Rev. B* **23**, 5048, (1981).

[19] J. P. Perdew, J. A. Chevary, S. H. Vosko, K. A. Jackson, M. R. Pederson, D. J. Singh and C. Fiolhais. *Phys. Rev. B,* **46**, 6671, (1992).

[20] M. Cobb and D. A. Drabold. *Phys. Rev. B*, **56,** 3054**,** (1997)

[21] P. S. Salmon and I. Petri. *J. Phys.:Condens. Matter,* **11**, 10219, (1999).

[22] H. Bhalla. *Homopolar Bond in Ionic Systems*, 4th Year Project, UCL, (2006).

[23] M. Wilson and P. A. Madden. *Phys. Rev. Lett.*, **72**, 3033, (1994).

[24] C. J. D. Martin, S. J. Goettler, N. Fosse and L. Iton. *Nature*, **419**, 381, (2002).

[25] H. Iyetomi and P. Vashishta. *Phys. Rev. B,* **47**, 3063, (1993).

[26] D. Tafen and D. A. Drabold. *Phys. Rev B*, **68**, 165208, (2003).

[27] J. C. Mauro and A. K. Varshneya. *J. Am. Ceram. Soc.*, **89**, 2323, (2006).

[28] P. Boolchand and W. J. Bresser. *Philos. Mag. B*, **80**, 1757, (2000).

[29] M. Arai, D. L. Price, S. Susman, K. J. Volin and U. Walter. *Phys. Rev. B*, **37**, 4240, (1988).

[30] V. P. Voloshin and N. N. Medvedev. *Journal of Structural Chemistry*, **46**, 93, (2005).

Chapter 11

Summary and Conclusions.

11.1 Summary

This study highlighted the variety of ordering, particularly intermediate-range ordering (IRO), displayed in network-forming melts of MX_2 stoichiometry by studying the structure of a range of systems using the Polarisable Ion Model (PIM)[1] which accounts for anion polarisation, Coulombic repulsion and short-range repulsive effects. The changes to short-range ordering (SRO), controlled by variation in the constituent polyhedral units, and IRO that occur with variations in temperature, pressure, anion size, polarisability and homopolarity were examined. The manner in which the constituent polyhedral units, predominantly MX_4 tetrahedra, interconnect, in particular the proportion of edge- and corner-sharing connections present, was shown to be the controlling factor in understanding how the intermediate range order varies.

In chapter 3, an improved PIM representation for $ZnCl_2$ was achieved which showed good correlation with the experimental total structure factors. An additional potential model was produced for $MgCl_2$, which showed increased 5- and 6-MX coordination compared to $ZnCl_2$, with concomitant square-planar and octahedral geometries around the central cation. This had the effect of weakening IRO in comparison to $ZnCl_2$. By using the anion radius as an effective parameter generic ZnX_2 materials were simulated. These systems showed changes in the SRO (increased 3-coordinate cations and associated singly-coordinate anions) which resulted in weaker IRO through a shift to higher scattering angles and a decline in the intensity of the FSDP.

Systems with larger anions were then represented by a new potential model for $GeSe_2$ (requiring the stabilisation of a system with a relatively large anion polarisability, α_X) In terms of the network connectivity structure factors, the representation of Ge-Ge interactions over the range associated with IRO was improved compared to FPMD calculations[2]. The weaknesses of the model include a Se sublattice which shows overstructuring as indicated by the larger intensity of the $S_{SeSe}(k)$ and $S_{GeSe}(k)$ principal peaks and the system observes liquid diffusivities at much higher temperatures (~2500-

3000K) compared to the experimental melting point (1025K). The results showed that the effective balance in ionicity and metallic character is important in reproducing this system, with the PIM, a strongly ionic model, favouring strongly tetrahedral systems with larger amounts of edge-sharing while the FPMD calculations, favouring a metallic description of the bonding, lead to increased miscoordination, both in terms of a reduction in tetrahedrality and the presence of homopolar bonds. The decomposition of $g_{GeGe}(r)$ according to network connectivity showed the difficulty in extracting edge-sharing statistics directly from the network connectivity radial distribution functions.

In chapter 5, the chemical ordering in MX_2 systems was investigated. The variations in the IRO in $ZnCl_2$ and $GeSe_2$ have been attributed to the difference in the number of edge-sharing tetrahedral units present in the two systems. For $GeSe_2$, the larger number of edge-sharing polyhedral units present percolate into persistent charge-neutral pseudo one-dimensional chain structures which act to break up the three-dimensional corner-sharing network predominant in $ZnCl_2$. These chains act to introduce an additional intermediate-ranged length scale leading to an excess intensity in $S_{MM}(k_{FSDP})$ which is not counterbalanced by the corresponding $S_{MX}(k_{FSDP})$ function and hence leads to the FSDP in $S_{CC}(k)$. The key features in systems which contributes to a FSDP in $S_{CC}(k)$ are increased presence of edge-sharing and strong tetrahedral coordination; this was highlighted further by inducing a stronger $S_{CC}(k_{FSDP})$ in $ZnCl_2$ by use of a lower density which favoured these features.

Chapter 6 showed the gradual evolution of intermediate-range order using the anion polarisability as a free parameter in order to control the network topology, starting with the anion polarisability appropiate to the $GeSe_2$ potential. With increasing anion polarisability, the gradual change from corner- to edge-sharing systems was observed. The effect of a large percentage (~50%) of cations labelled "1" percolating through the tetrahedral network was evident in the intensity of FSDP in $S_{CC}(k_{FSDP})$ and the presence of a second peak in the E_g stretch and T_2 bend vibrational modes. The changes in *cation-cation* correlations dominated the variations in IRO, as highlighted by the bond angle distribution functions, which changed significantly compared to anion related terms, and the partial structure factors. The inherent properties of the structure factors were made clearer by constructing additional functions "coloured" in terms of network connectivity.

For example, $S_{MM}^{02}(k)$ showed a resistance to phase separation compared with

$S_{MM}^{22}(k)$ and $S_{MM}^{00}(k)$ at similar concentrations. By use of an amended BeCl$_2$ potential with *extreme anion polarisability*, the system showed distortions from the ionic network with increasing anion polarisability which do not lead to continuous increases in properties associated with IRO. Using the short range damping parameter, c, as a free variable shows a "transition" (when c=0.50) corresponding to a sharp decrease in the intensity of $S_{MM}(k_{FSDP})$, in contrast to a parallel gradual decline in SRO as indicated by the decrease in the intensity of the principal peaks. With increasing polarisation the tetrahedral network was shown to break down owing to the presence of increased presence of singly-coordinated anions.

In chapters 7 and 8, the changes in network topology with temperature and pressure were investigated using systems of low, intermediate and high anion polarisabilites, complementing experimental work which highlighted the analogous changes in IRO in ZnCl$_2$[3-9] and GeSe$_2$[10-12]. As with the experimental results[5-8,12], the FSDP in F(k) decreases noticeably over the experimental neutron diffraction pressure range, with substantial changes with further pressure increases. The change in IRO with increasing temperature is smaller with a decline in intensity. It was shown that the contribution to the FSDP in F(k) from $S_{ZnCl}(k)$ is more stable to changes in temperature and pressure than the cation-cation function. In the radial distribution functions, a shift in the principal peak in $g_{XX}(r)$ is observed with increasing pressure. The changes in the cation-cation correlations were probed by use of a difference function, $P_{\alpha\beta}^{P_n - P_1}(r)$, indicating a change in the fraction of corner- and edge-sharing polyhedra present, with the latter declining with increasing pressure. Large increases in coordination numbers were observed and, in contrast to the systems observed in Chapter 6 which were predominantly tetrahedral, this affected the network connectivity values, and the subsequent interpretation of the variations in E^{0-2}. Greater clarity was achieved by calculating the related structure factors and radial distribution functions according to network connectivity, uncovering greater details of the structural changes occurring, particularly the changes between the interactions of cations labelled "1" with each other in both reciprocal and real space functions. In comparison, the functions based on coordination environment were largely determined by the isotropic distribution of sites.

Chapter 8 focused on the changes in an MX$_2$ system with anion polarisability values higher (α_X=35 a.u) and lower (α_X=15 a.u) than that for ZnCl$_2$ (α_X=20 a.u). At very low densities, MX$_2$ at α_X=15 a.u adopts features associated with systems of higher

polarisability: a shift in FSDP position to $\sim 1\text{Å}^{-1}$ and decreasing nearest-neighbour cation-cation separation. At the higher polarisability, the FSDP position does not shift as significantly but increases in intensity. The existence of different mechanisms in changing network structure was highlighted in the disparity of rates of increase in coordination environment, particularly in the MX first coordination shell. The network connectivity radial distribution functions showed that, at the lowest density, the weak short range ordering of the interaction of the "0" cations with those labelled "2" moved closer to the idealised form due to the reduction in confinement effects, as evidenced by a collapsed principal peak in $g_{MM}^{02}(r)$. At high temperature a sharp reduction in FSDP intensities occurs for $S_{MM}(k)$ and $S_{MX}(k)$. The weakening of short- and intermediate-range ordering is highlighted in the decreasing intensities of network-connectivity structure factors and a weakening of the tetrahedral coordination structure, moving to lower XM and MX coordination.

The inherent structure calculations, undertaken in chapter 9, showed an underlying deformation within constituent polyhedra through the presence of a shortened cation-anion bond length-scale. The signature of such a deformation is indicated through the presence of a prepeak in the inherent structure of $g_{MX}(r)$, correlating with an increase in single anion-cation coordination, such that $N_{XM=1}>\sim 5\%$. The largest prepeak was observed in the MX_2 systems with extreme anion polarisability where a transition is shown with the prepeak effectively becoming the principal peak with declining parameter c. The underlying differences in inter-tetrahedral linkages are highlighted by the radial and bond-angle distribution functions, which exhibit the presence of corner- and edge-sharing tetrahedra through separately resolved peaks, in contrast to that observed in molten configurations. The strength of the separation of these two arrangements, as indicated by the position of the minima between both edge-and corner-sharing arrangements in $g_{MM}(r)$ and in the M-X-M bond angle distribution was greater in systems such $MX_2(\alpha_X>25$ a.u) compared to $ZnCl_2$.

One notable feature present in experimental work[13,14] and electronic structure calculations[2,15] ,but absent in our models so far, was the presence of homopolar bonds. In chapter 10, the effect on structure with varying presence and abundance of homopolar bonds was studied. Although the use of a Morse-RIM potential resulted in homopolar bond between anions only, it had the effect of drawing cations closer than would have otherwise occurred resulting in an increasing proportion of edge-sharing units. The

inducement of substantial amounts of homopolarity (above that observed experimentally) has a similar effect to increasing anion polarisability on IRO. A significant FSDP was observed at $1Å^{-1}$ in $S_{XX}(k)$, which had not been observed in previous chapters, as well as $S_{MM}(k)$ and $S_{MX}(k)$. The radial distribution functions, $g_{XX}(r)$, showed a sharp and intense prepeak which indicated the presence of anion-anion homopolar bonds, while $g_{MX}(r)$ showed the presence of a split second peak with increasing homopolarity. The coordination number distribution, where the MX and XM coordination rises faster than MM and XX, indicates the presence of increased void volume with increasing homopolarity. A further indication of this behaviour occurs by varying the density. In systems with very high homopolarities and lower densities, phase separation occurs in the partial structure factors, a feature not exhibited in the systems studied in earlier chapters.

11.2 Conclusion

Accurate polarisable potential models have been developed for $ZnCl_2$ and $MgCl_2$ which reproduce a number of experimental features including good correlation with total structure factors and radial distribution functions. A new $GeSe_2$ model has been created and has been compared with experimental and computational studies. Its major strengths include the stabilisation of high-proportion of edge-sharing tetrahedra enabling the study of the relationship of corner- and edge-sharing tetrahedra to IRO and elucidation of the structural features responsible for the FSDP in $S_{CC}(k)$.

A greater understanding of the origin of the FSDP in (concentration concentration structure factor) $S_{CC}(k)$ has been achieved. Firstly, the $GeSe_2$ model created exhibited a large FSDP, comparable to that observed experimentally, and significantly greater in intensity than those previously observed in computational studies. Decomposing partial structure factors according to network connectivity (a process not possible from experimental study), we are able to show the features responsible for the peak in $S_{CC}(k)$. The balance between $S_{MM}(k_{FSDP})$ and $S_{MX}(k_{FSDP})$ was shown to be responsible and in $GeSe_2$ the excess intensity of the FSDP in $S_{MM}(k)$ was significant enough to result in a peak at FSDP in $S_{CC}(k)$. The $S_{CC}(k_{FSDP})$ intensity was linked to increasing amounts of edge-sharing units perturbing the corner-sharing network and the greater peak intensity found in $GeSe_2$ compared to $ZnCl_2$ was attributed to the percolation of these units. In comparison, the $S_{CC}(k)$ functions of a range of systems were evaluated showing the

minimum in BeF_2, which is a wholly corner-sharing system; a non-linear change in intensity in low-density $ZnCl_2$, where there is competition between the intermediate-range cation-cation and cation-anion correlations which are of similar intensity; and $BeCl_2$, where the short-range damping parameter (one of the parameters controlling anion polarisability) was varied between c=0.50 and c=0.90. At the lower value, a transition was observed between a system with percolating edge-sharing chains into a molecular system resulting in sharply decreased intermediate-range cation-cation correlations due to the weak interaction of the constituent charge-neutral units. We have shown a limit to $S_{CC}(k_{FSDP})$ intensity in systems of MX_2 stoichiometry such as $GeSe_2$ which are comprised of a mixture of edge- and corner-sharing tetrahedra.

We have shown the evolution of the FSDP in terms of position and intensity with changes in underlying network connectivity. While the presence of corner- and edge-sharing features have been highlighted previously in experimental and simulated systems, the preponderance of these features and their relationship with IRO has been investigated in this thesis by "colouring cations" according to their network connectivity. Novel correlation functions, network connectivity structure and network connectivity radial distribution functions, uncover the details of the structural relationship of the cations within a network system of varying inter-tetrahedral connectivity from corner-sharing, through to mixed edge- and corner-sharing and strongly edge-sharing systems. The network connectivity structure factors uncover different degrees of clustering of the coloured cations, highlighted in an effective "phase separation", and the evolution of IRO with increasing ratio of FSDP intensity to that of the principal peak intensity related to the degree of edge-sharing. In Chapter 6, a limit to the enhancement of the IRO due to anion polarisation in MX_2 systems was shown in systems with extreme anion polarisation, highlighting another 'class' of molecular structures beyond those with percolating edge-sharing chains. This thesis has highlighted the utility of decribing network connectivity in addition to changes in coordination and other structural features such as structure factors and radial distribution functions. These methods could be used in other computational techniques, such as Reverse Monte Carlo modelling, where a particular frame of network connectivity (specified according to the proportion of "0", "1", and "2" cations) could be added as an additional constraint. Furthermore, the related network connectivity functions, and particular properties identified, such the largest ratio of FSDP to principal peak intensity in the function, $S_{MM}^{02}(k)$, could be added.

The effect of pressure and temperature on IRO and structure has been highlighted for a range of systems, particularly in partial structure factors and radial distribution functions which are difficult to obtain experimentally. A decline in the intensity of the FSDP was shown with increasing pressure in $ZnCl_2$ and the related changes in radial distribution functions indicated. The effect of increasing temperature in $ZnCl_2$ was more subtle with an increase in the intensity of $S_{ZnCl}(k_{FSDP})$ in chapter 7 compared to a decline $S_{ZnZn}(k_{FSDP})$, indicating that different structures are responsible for the respective contributions to IRO. In chapter 8, we highlighted that systems of relatively low anion polarisability show a greater rate of coordination change of cation-centred polyhedra than the system at the higher anion polarisability with changing density. The network connectivity radial distribution functions for MX_2 (where α_X=35a.u) shows closer to idealised functions present as 4 MX coordination approaches 100%. In both sytems, a shift of the FSDP to lower scattering wavevectors is observed with declining density.

An attempt has been made to include homopolarity within the framework of ionic models by use of a Morse potential which stabilises short-range separation of like ions in combination with the Born-Mayer potential which treats Coulombic, short-range repulsive and dispersion terms. Homopolar bonds between anions are achieved and the cation-cation separation is reduced leading to the increased formation of edge-sharing units. The induction of homopolarity within a tetrahedral network system is shown to be an analogous mechanism to increasing anion polarisability in inducing concentration fluctuations on long and short-length scales in the ion density. Additionally, at very high fractions of anions in homopolar bonding (H_{XX}=80% and 100%), a system is observed where all three correlations contribute approximately equally to IRO which has not been previously observed.

The inherent structure calculations on the range of MX_2 systems have been carried out highlighting a number of novel structural features not exhibited in previous inherent structure calculations. The presence of a defect feature in the cation-anion radial distribution principal peak, not highlighted previously in both experimental and computational work, is observed. Defect singly-coordinated anions present in a range of systems are uncovered as the structural origin of this feature. Additionally, the features resolved in the cation-cation distribution function, $g_{MM}(r)$, give an indication of the presence of edge- and corner-sharing configurations and indications of deviations away from purely tetrahedral configurations through the intensity of the minimum between

these two peaks. The bond angle distributions from the inherent structure also highlight the rigid bond angle ordering controlling with edge-sharing tetrahedra in the vibrationless structure, indicating that the greater similarity of peaks in the bond angle distributions relating to corner- and edge-sharing geometries in the liquid distributions, is a result of the greater mobility of cations in edge-sharing conformations.

We have calculated the first set of network connectivity diagrams. The underlying change in network connectivity in MX_2 systems was demonstrated over a range of polarisability values (realistic in terms of *ab initio* and experimental results). In this investigation, we have correlated the configuration of "0", "1" and "2" cations with structural properties such as FSDP intensities of $S_{MM}(k)$ and $S_{MX}(k)$. In addition to the structural properties highlighted, this can be used as the basis with which to explore other properties such as liquid fragility, diffusion constants and the onset of network rigidity. In this investigation we observed the evolution of these statistics with IRO in several different environments using different order parameters: largely tetrahedral systems with varying anion polarisability, where the initial cell size at the highest anion polarisability used was at experimental density, and at a lower density where tetrahedral coordination is strengthened; ZnX_2 materials where the order parameter was varying anion-anion repulsion; MX_2 systems (where α_X=15 a.u and 35 a.u) with varying density; and the Morse RIM system, where proportion of anions in homopolar bonds are varied. Future calculations could include effects of homopolar bonds which are isolated from the tetrahedral network (as observed in the calculations of Massobrio[32] highlighted in figure 4.5) and systems of different stoichiometry such as $GeSe_4$.

11. 3 Future Work

The highlighting of network connectivity as a controlling factor in IRO lends itself to a number of further routes of investigation. Firstly, to what extent can the dynamic properties of liquids be understood through the presence of edge-sharing tetrahedra and the links with the character of such liquids in terms of their fragility?[16] Another question is the link of deformed polyhedra, observed by the prepeak feature in $g_{MX}(r)$ in a range of systems, with the possible mechanisms by which diffusion occurs in liquids. Particular structural features observed in liquids through variation of order parameters may link with possible defects present in the crystalline state: the presence and influence

of differing edge- and corner-sharing connections in the liquid structures of $ZnCl_2$ and $GeSe_2$, CS_2 respectively, which contrast in terms of IRO and molecular features.

Further work could utilise the computational advantages of the classical MD methods with FPMD calculations. Early collaborations have focused on oxides alkaline-earth systems[17,18], Al_2O_3[19] and Li_2O[20]; here, density functional calculations are carried out on a small unit cell and the ion forces, multipole moments and cell stresses are then used to parametrise the potential model. In order to produce more advanced models the differences between MD and FPMD need to be fully understood so that further models parametrised in the future retain parameters with physical relevance. This would help in resolving some of the deficiencies in both models: the overstructuring observed for MX and XX in the PIM and the weaker (compared to experimental and PIM) intermediate-range ordering in the FPMD calculations highlighted.[2]

Recent experimental work on filling of carbon nanotubes with molten salts, including MX_2 liquids such as BaI_2[21] and CoI_2[22] leads another route of utilising the systems studied here. Computational work so far[23-29], has studied the mechanism of filling and understanding the internal crystal structure of the filled-in nanotube and their variation with diameter size. With MX_2 systems, simulations have utilised systems with larger sized cations such as $SrCl_2$ which exhibit 5- and 6-MX coordination; further study could observed the effect of anion polarisability on the crystal structures and the effect of confinement effects on IRO in systems investigated here, intermediate-sized cations and a range of anion polarisabilities.

The colouring of structural properties such as network connectivity could be applied further to systems of similar stoichiometry (such as MX_4) in order to effectively build a set of rules regarding the ratios of the FSDP with the principal peak and propensity for phase separation in addition to systems where the anion polarisability is varied. It could also be used to highlight structural features within monatomic liquids and metallic alloys such as NaPb.[30,31]

While homopolarity was studied with a rigid-ion model, the effect of combing such a system, further exploration of the effect of homopolarity in ionic models could be examined by utilising a combined PIM and homopolar model.

11. 3 References

[1] M. Wilson and P. A. Madden. *J. Phys. Condens. Matter*, **5**, 2687, (1993).

[2] C. Massobrio, A. Pasquarello and R. Car. *Phys. Rev B*, **64**, 144205, (2001).

[3] S. N. Yannopoulos, A. G. Kalampounias, A. Chrissanthopoulos and G. N. Papatheodorou. *J. Chem. Phys*., **118**, 3197, (2003).

[4] D. S. Allen, R. A. Howe and N. D. Wood. *J. Chem. Phys*., **94,** 5071, (1991).

[5] T. Pfleiderer, I. Waldner, H. Bertagnolli, K. Todheide and H. E. Fisher. *Phys. Chem. Chem. Phys.,* **5**, 5313, (2003).

[6] V. V. Brazhkin, Y. Katayama, A. G. Lyapin, S. V. Popova, Y. Inamura, H. Saitoh and W. Utsumi. *JETP Letters*, **82**, 713, (2005).

[7] V. V. Brazhkin, A. G. Lyapin, S. V. Popova, Y. Inamura, Y. Katayama, H. Saitoh and W. Utsumi. *Journal of Physics:Condens. Matter,* **19**, 1, (2007).

[8] G. Heusel, H. Bertagnolli, M. Kreitmeir, J. Neuefeind and A. Lemke. *Phys. Chem. Chem. Phys*., **4**, 4155, (2002).

[9] C. Fillaux, B. Couzinet, C. Dreyfus, J. P. Itié and A. Polian. *Physica Scripta,* **T115**, 339, (2005).

[10] I. Petri, P. S. Salmon and W. S. Howells. *J. Phys.:Condens. Matter*, **11**, 10219, (1999).

[11] W. A. Crichton, M. Mezouar, T. Grande, S. Stølen, and A. Grzechnik. *Nature,* **414**, 622, (2001).

[12] Q. Mei, C. J. Benmore, R. T. Hart, E. Bychkov, P. S. Salmon, C. D. Martin, F. M. Michel, S. M. Antao, P. J. Chupas, P. L. Lee, S. D. Shastri, J. B. Parise, K. Leinenweber, S. Amin and J. L. Yarger. *Phys. Rev. B,* **74**, 014203, (2006).

[13] I. Petri, P. S. Salmon, and H. E. Fischer. *Phys. Rev. Lett*., **84**, 2413, (2000).

[14] P. S. Salmon and I. Petri. *J. Phys.: Condens. Matter,* **15**, S1509, (2003).

[15] C. Massobrio, A. Pasquarello, and R. Car. *J. Am. Chem. Soc*., **121**, 2943 (1999).

[16] C. A. Angell. *J. Non-Cryst. Solids*, **102**, 205, (1988).

[17] A. Aguado, L. Bernasconi and P. A. Madden. *Chem. Phys. Lett*., **356**, 437, (2002).

[18] A. Aguado, L. Bernasconi and P. A. Madden. *J. Chem. Phys*., **118**, 5704, (2003).

[19] S. Jahn, P. A. Madden and M. Wilson. *Phys. Rev. B*, **74**, 024112, (2006).

[20] M. Wilson, S. Jahn and P. A. Madden. *J. Phys.: Condens. Matter*, **16**, 82795, (2004).

[21] J. Sloan, S. J. Grosvenor, S. Friedrichs, A. I. Kirkland, J. L. Hutchinson

and M. L. H. Green. *Angew. Chem., Int. Ed.*, **41**, 1156, (2002).

[22] E. Philip, J. Sloan, A. I. Kirkland, R. R. Meyer, S. Friedrichs, J. L. Hutchinson and M. L. H. Green. *Nat. Mater.*, **2**, 788, (2003).

[23] C. L. Bishop and M. Wilson. *J. Phys.: Condens. Matter*, **21**, 115301, (2009).

[24] M. Wilson. *Faraday Discuss.*, **134**, 283, (2007).

[25] M. Wilson and P. F. McMillan. *Phys. Rev. Lett.*, **90**, 135703, (2003).

[26] M. Wilson. *Chem. Phys. Lett.*, **366** , 504, (2002).

[27] M. Wilson. *Nano Lett.*, **4**, 299, (2004).

[28] M. Wilson. *Chem. Phys. Lett.*, **397**, 340, (2004).

[29] M. Wilson. *J. Chem. Phys.*, **124**, 124706, (2006).

[30] H. T. J. Reijers, M.-L. Saboungi, D. L. Price, J. W. Richardson, Jnr and K. J. Volin. *Phys. Rev B*, **40**, 6018, (1989).

[31] H. T. J. Reijers, W. Van der Lugt and M.-L. Saboungi. *Phys. Rev B*, **42**, 3395, (1990).

Publications arising from this work

Work from this thesis is published in the following papers:

Intermediate-range order in molten network-forming systems.
B. K. Sharma and M. Wilson. *Phys. Rev. B*, **73**, 060201, (2006).

Ionicity in disordered GeSe$_2$: A comparison of first-principles and atomistic potential models.
M. Wilson, B. K. Sharma and C. Massobrio. *J. Chem. Phys*, **128**, 244505, (2008).

The evolution of intermediate-range order in molten network-forming materials.
M. Wilson and B. K. Sharma. *J. Chem. Phys*, **128**, 214507, (2008).

Polyamorphism and the evolution of intermediate-range order in molten ZnCl$_2$.
B. K. Sharma and M. Wilson. *J. Phys.:Condens. Matter*, **20**, 244123, (2008).

Appendix A

Potential model parameter tables.

Parameter (a.u)	Compound			
	ZnCl$_2$ PIM (OLD)	ZnCl$_2$ PIM (New)	MgCl$_2$ PIM	ZnX$_2$
a$^-$	1.00	1.5776	1.5564	1.5776
B$^-$	8	87	63	*(103-603)
C	0	183	183.0	183
a^{+-}	1.56	1.5564	1.5564	1.5564
B^{+-}	48	43.71	51.72	43.71
C^{+-}	0	80	18.94	80
a^{++}	1.60	1.5600	1.5564	1.5600
B^{++}	27	27	27	27
C^{++}	0	40	2.2	40
α_X	20	20	20	20
SRDP b	1.55	1.65	1.65	1.65
SRDP c	1	1.4	1.4	1.4
Chapter reference	3	3,4,5,7,9	3,5	3,9

SRDP=Short-range damping parameter. * refers to the parameter which is varied in the range denoted in brackets.

Parameter (a.u)	Compound			
	GeSe$_2$ PIM	MX$_2$	MX$_2$ (BeCl$_2$ PIM)[1]	BeF$_2$ PIM [2]
a$^-$	1.5564	1.5564	1.5564	1.8564
B$^-$	1185.64	1185.64	120.00	16.62
C	1000	1000.60	183.00	0.00
a^{+-}	1.5564	1.5564	1.60	1.8564
B^{+-}	199.38	199.38	53.719	13.10
C^{+-}	380	380.00	80.00	0.00
a^{++}	1.5564	1.5564	1.5564	1.8564
B^{++}	12.25	12.25	27.00	8.245
C^{++}	0	0	40.00	0.00
α_X	40	(40-10)*	20	5.983
SRDP b	1.65	1.65	1.55	1.65
SRDP c	2.00	2.00	*(0.90-0.50)	1.00
Chapter reference	4,5	6,8,9	5,6,8,9	5

[1] M. Wilson and P. A. Madden. *Mol. Phys.,* **92**, 197, (1997).

[2] R Brookes, *Part II Thesis*, *University of Oxford*, (1998).

Appendix B

Calculation of the vibrational frequencies.

The vibrations of polyatomic molecules and ions are considered to be normal modes, which means the vibrations of like atoms within the molecule occur simultaneously within each mode. The motion of the ions may be decomposed into various normal modes which transform as the symmetry operation of the tetrahedron, and then a Fourier transformed velocity autocorrelation function for each of these modes will give the vibrational density of states for that mode.

For the tetrahedral cation, i, at a given time, t, the four bonded anions are identified, $\alpha=1,2,3,4$. The position and velocities of these neighbouring anions relative to the central cation, $\boldsymbol{r}_{i\alpha}$ and $\boldsymbol{v}_{i\alpha}$, are then calculated.

$$\hat{\boldsymbol{r}}_{i\alpha}=\frac{\boldsymbol{r}_{i\alpha}}{|\boldsymbol{r}_{i\alpha}|}=\frac{\boldsymbol{r}_i-\boldsymbol{r}_\alpha}{|\boldsymbol{r}_i-\boldsymbol{r}_\alpha|} \tag{B.1}$$

where $\hat{\boldsymbol{r}}_{i\alpha}$ is the unit vector along the bond between cation i and anion α, and then the velocities are decomposed into components paralled to, $v_{i\alpha}^{\parallel}$, and perpendicular to $v_{i\alpha}^{\perp}$, the bonds, according to

$$v_{i\alpha}^{\parallel}=\boldsymbol{v}_{i\alpha}\cdot\hat{\boldsymbol{r}}_{i\alpha} \tag{B.2}$$

and

$$\boldsymbol{v}_{i\alpha}^{\perp}=\boldsymbol{v}_{i\alpha}-v_{i\alpha}^{\parallel}\hat{\boldsymbol{r}}_{i\alpha} \tag{B.3}$$

The symmetry species of the vibrational normal modes of the tetrahedral species are $A_1+E+T_1+T_2$. The velocity of the central cation, i, in the A_1 (stretching) modes, $V_i^{A_1}$, is then given by

$$V_i^{A_1} = \sum_{i\alpha = 1 \to 4} v_{i\alpha}^{\parallel} \tag{B.4}$$

The two components of the (doubly degenerate) E (bending) modes are given by

$$V_i^{E,1} = (v_{i1}^{\perp} - v_{i2}^{\perp}) \cdot (\hat{\boldsymbol{r}}_{12}) + (v_{i3}^{\perp} - v_{i4}^{\perp}) \cdot (\hat{\boldsymbol{r}}_{34})$$

$$V_i^{E,2} = (v_{i1}^{\perp} - v_{i3}^{\perp}) \cdot (\hat{\boldsymbol{r}}_{13}) + (v_{i2}^{\perp} - v_{i4}^{\perp}) \cdot (\hat{\boldsymbol{r}}_{24})$$

$$V_i^{E} = V_i^{E,1} + V_i^{E,2} \tag{B.5}$$

where $\hat{\boldsymbol{r}}_{\alpha\beta} = \dfrac{\hat{\boldsymbol{r}}_{i\alpha} - \hat{\boldsymbol{r}}_{i\beta}}{|\hat{\boldsymbol{r}}_{i\alpha} - \hat{\boldsymbol{r}}_{i\beta}|}$, i.e $\hat{\boldsymbol{r}}_{\alpha\beta}$ is the unit vector along the line joining anions α and β.

The three components of the (triply degenerate) T_1 (bending) mode are given by

$$V_i^{T_1,1} = v_{i1}^{\parallel} - \{ \boldsymbol{v_{i2}}^{\perp} \cdot \hat{\boldsymbol{r}}_{i1} + v_{i3}^{\perp} \cdot \hat{\boldsymbol{r}}_{i1} + v_{i4}^{\perp} \cdot \hat{\boldsymbol{r}}_{i1} \}$$

$$V_i^{T_1,2} = v_{i2}^{\parallel} - \{ \boldsymbol{v_{i3}}^{\perp} \cdot \hat{\boldsymbol{r}}_{i2} + v_{i4}^{\perp} \cdot \hat{\boldsymbol{r}}_{i2} + v_{i1}^{\perp} \cdot \hat{\boldsymbol{r}}_{i2} \}$$

$$V_i^{T_1,3} = v_{i3}^{\parallel} - \{ \boldsymbol{v_{i4}}^{\perp} \cdot \hat{\boldsymbol{r}}_{i3} + v_{i1}^{\perp} \cdot \hat{\boldsymbol{r}}_{i3} + v_{i2}^{\perp} \cdot \hat{\boldsymbol{r}}_{i3} \}$$

$$V_i^{T_1} = V_i^{T_1,1} + V_i^{T_1,2} + V_i^{T_1,3} \tag{B.6}$$

Finally, the three components of the (triply degenerate) T_2 (stretching mode) are given by

$$V_i^{T_2,1} = v_{i1}^{\parallel} - \frac{1}{3} \{ \boldsymbol{v_{i2}}^{\parallel} + v_{i3}^{\parallel} + v_{i4}^{\parallel} \}$$

$$V_i^{T_2,2} = v_{i2}^{\parallel} - \frac{1}{3} \{ \boldsymbol{v_{i3}}^{\parallel} + v_{i4}^{\parallel} + v_{i1}^{\parallel} \}$$

$$V_i^{T_3,1} = v_{i3}^{\parallel} - \frac{1}{3} \{ \boldsymbol{v_{i4}}^{\parallel} + v_{i1}^{\parallel} + v_{i2}^{\parallel} \}$$

$$V_i^{T_2} = V_i^{T_2,1} + V_i^{T_2,2} + V_i^{T_2,3} \tag{B.7}$$

The density of states for a given symmetry species, $C_{V^{\Gamma}}(\omega)$, with $\Gamma \epsilon A_1, E_1, T_1, T_2$ are then given by

$$C_{V^{\Gamma}}(\omega) = \Re \left\{ \int_0^{\infty} dt\, e^{i\omega t} \frac{1}{N_i} \sum_i \langle V_i^{\Gamma}(t) \rangle V_i^{\Gamma}(0) \right\} \tag{B.8}$$

Appendix C

Atomic Units.

Unit	Name	Conversion Factor
Mass	m_e	9.1095×10^{-37} kg
Time		2.4188×10^{-17} s
Charge	e	1.6022×10^{-19} C
Energy	Hartree	4.3957×10^{-18} J
Length	bohr	0.529177×10^{-10} m
Pressure		2.942×10^{13} Pa

Table C: Conversion factors between atomic units and SI units.